Synthesis of advanced inorganic colloidal nanocrystals

Dissertation

zur

Erlangung des Doktorgrades

der Naturwissenschaften

(Dr. rer. nat.)

dem

Fachbereich Physik

der Philipps-Universiät Marburg

vorgelegt von

Marco Zanella

aus

Thiene (Italien)

Marburg/Lahn, 2008

Vom Fachbereich Physik der Philipps-Universität

Als Dissertation angenommen am: 21.05.2008

Erstgutachter: Prof. Dr. Wolfgang J. Parak

Zweitgutachter: Prof. Dr. Wolfram Heimbrodt

Tag der mündlichen Prüfung: 29.05.2008

Contents

Abstract.

Colloidal nanocrystals are crystalline materials of nanometer size which are colloidally suspended in a solution. Typical nanocrystals are made of few tens to some thousands atoms. Because of their small size they exhibit properties different to the conventional bulk materials. In the nanosize regime, in fact, it is not just the composition which determines the properties of a material but also its size and shape. The possibility to control these parameters allows the fabrications of nanocrystals whose properties can be exploited in several fields such as electronics, diagnostics, catalysis and optoelectronics.

In this dissertation we will focus on semiconductive nanocrystals with particular attention to a new synthesis process which allows us to have a better control on the size and thus the properties. In particular we show that for small nanocrystals the growth is not continuous. Instead the nanocrystals grow discretely, from one stable configuration to the next bigger stable configuration. The possible stable configurations are termed "magic size clusters". For bigger particles growth is continuous. We report the generalization of the process to grow magic size clusters for several semiconductor materials. Also an application of magic size clusters of CdSe for the fabrication of light emitters is reported.

The characterisation and application of particular semiconductive nanomaterials presented in this work will led us to the synthesis of more complex nanostructures such as core@shell nanomaterials and semiconductive-magnetic dimers. We demonstrate in particular the growth of II/VI semiconductor materials on top of FePt nanocrystals. Thus dimeric nanocrystals with a magnetic FePt domain and a II/VI domain are obtained. In these systems it is possible to combine together properties of the different materials in order to fabricate nanoparticles presenting as well a magnetic as a semiconductive domain.

Kolloidale Nanokristalle sind kristalline Materialien mit Nanometer-Größe die stabil in Lösung suspendiert sind. Typische Nanokristalle enthalten einige 10 bis zu einigen 1000 Atomen. Aufgrund ihrer kleinen Größe haben Nanokristalle unterschiedliche Eigenschaften als vergleichbare Volumen-Materialien. Auf der Nanometer-Skala werden die Eigenschaften von Materialien nicht nur durch deren Zusammensetzung, sondern auch durch ihre Größe und Form bestimmt. Die Möglichkeit diese Parameter zu variieren ermöglicht die Herstellung von Nanokristallen deren Eigenschaften sie für den Einsatz in verschiedenen Bereichen, wie Elektronik, Diagnose, Katalyse und Optoelektronik, interessant machen.

In dieser Dissertation haben wir den Schwerpunkt auf Halbleiter-Nanokristalle gelegt. Dabei wurde dem Syntheseprozess besondere Aufmerksamkeit gewidmet, so dass eine bessere Kontrolle der Nanokristallgröße und damit der Eigenschaften ermöglicht wird. Besonders zeigen wir, dass für sehr kleine Nanokristalle deren Wachstum nicht kontinuierlich verläuft. Hingegen wachsen kleine Nanokristalle in diskreten Stufen, von einer stabilen Konfiguration zur nächst größeren stabilen Konfiguration. Die stabilen Konfigurationen werden "magic size cluster" genannt. Für größere Partikel ist der Wachstumsprozess wie gewohnt kontinuierlich. Wir beschreiben die Verallgemeinerung des Wachstums von magic size clusters für verschiedene Halbleiter Materialien. Als Anwendung von magic size clusters wird die Herstellung von Leuchtdioden beschrieben.

Die Charakterisierung und Anwendung von bestimmten Halbleiter Nanomaterialien die in dieser Arbeit vorgestellt werden führt uns zur Synthese noch komplexerer Nanostrukturen wie Kern@Hülle Konfigurationen and halbleitenden-magnetischen Dimer Strukturen. Besonders

beschreiben wir das Wachstum von II/VI Halbleitern auf der Oberfläche von FePt Nanokristallen. Diese Dimere haben sowohl eine magnetische FePt Domäne als auch eine halbleitende II/VI Domäne. So ist es möglich in diesem Systemen zwei verschiedene Eigenschaften in einem einzigen Partikel zu kombinieren, da die Nanopartikel eine magnetische und eine halbleitende Domäne besitzen.

I. Introduction

In the last decade, new directions of modern research have emerged. One of these new fields usually goes under the name "nanoscience and nanotechnology" and joins several areas of research as engineering, physics, chemistry, material science and molecular biology. The research in this direction has been triggered by the recent availability of new revolutionary instruments and techniques which are able to improve our investigation abilities concerning the material properties with a resolution close to atomic scale. Such technological advances have inspirited new pioneering experiments which have revealed new physical properties and effects of matter at an intermediate level between atomic and bulk.
The discovery of these properties, acquired by the materials at these size scale, have driven the desire to fabricate materials with novel or improved characteristics suitable for future advancements in electronics, optoelectronics, diagnostic and catalysis.
These new classes of materials are usually called "nanoscale materials", or "nano-composites" and their properties do not just depend on their composition and size but from their shape too.
Nanomaterials can appear in different forms, some of them are powders, some other can be suspended into a solvent or be embedded in a solid material like glass or a polymer matrix. Their form depends on the process used to synthesize them or their application. Anyway considering the possible applications, in order to maximize the performances of a given nanomaterial some techniques have been developed in order to pass from a form to an other one, for example suspending some nanoparticles into a solvent starting from their powder. Some applications of nanomaterials properties ranging from optic (i.e. optical filters [1,2], LASERs [3], LEDs [4]) to molecular biology (i.e. labelling [5-7] , hyperthermia [8]) has already been realized.
For the fabrication of nanomaterials many techniques have been developed. Here we introduce some of the most diffused.

I.1 Synthesis in solution

The synthesis of nanomaterials in solution is a wet-chemical approach which requires the reaction of precursors injected into a hot reaction flask where some inorganic molecules can be present dissolved into a coordinating solvent (Figure I.1). The temperature of this solution is sufficient to decompose the reagents resulting into a super saturation of precursors in solution. This addition of reagents, hence, raises the precursors concentration above a threshold called "nucleation threshold" in which the precursors present in solution react forming nanocrystals nuclei. This process will be discussed more extensively in the next chapter. For now we can approach the nanoparticle nucleation and growth with a simple example. Let us consider the condensation of steam in water drops at constant temperature. If we keep on increasing the humidity of a certain environment some little drops of water start nucleating and the drops size can increase via water molecule addition or coalescence since the single drops surfaces are not protected. The coalescence or agglomeration of drops do not allow us to control their size.

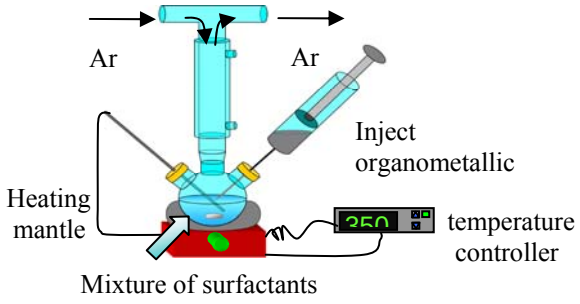

Figure I.1. *Simple sketch of the apparatus for the synthesis of nanomaterials in solution.*

In order to have a control in the nucleation and growth of nanoparticles some organic molecules are used to stabilize the nuclei. These organic molecules, commonly known as surfactants (Figure I.1 and I.2), stick on their surface preventing agglomeration via steric repulsion.

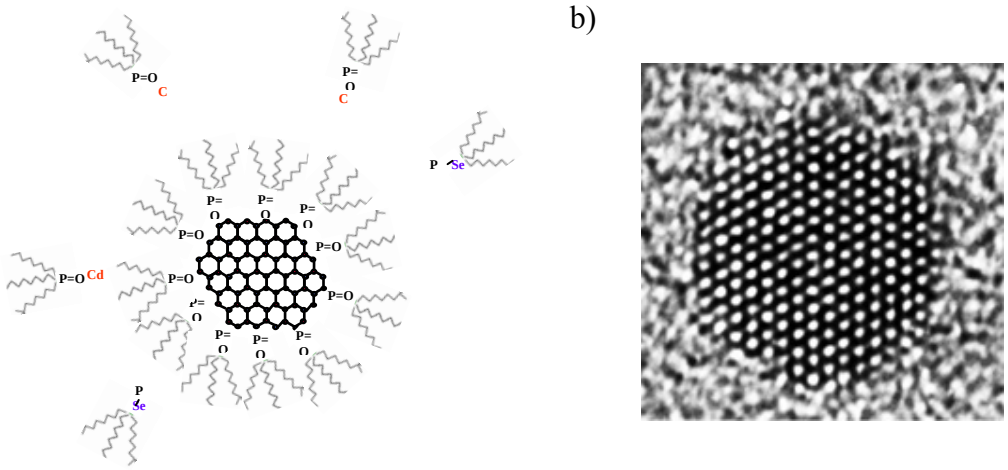

Figure I.2. *a) Sketch of the growth of a nanoparticle of CdSe. The cadmium (red) and selenium (violet) atoms are connected to the organic part forming the relative precursors which surround the nanoparticle in solution. The nanocrystal is stabilized in solution by the surfactants, organic molecule which sticks to its surface avoiding the agglomeration of different cores. b)High resolution TEM micrograph of a spherical nanoparticle. Light grey dots are the nanoparticle atoms (taken from [29]).*

After the nucleation the nanoparticles start growing using the precursors left in solution. In general the NCs size increases over time as more material is added to their surface. One more important factor for the NCs growth, along with the precursor concentration, is the temperature since at higher temperature the rate of atoms addition to the existing nuclei increases. The presence of the surfactant ensure the stability of these particles and the solution itself. Surfactants can be even used in order to drive the nanocrystal shape during the growth (Figure I.3). In fact surfactants can bind more tightly to a NC surface than an other one changing the rate of atoms addition. Or an other strategy is that one which uses two surfactant molecules one that binds tightly to a surface a one that binds weakly to an other one, in order to permit a rapid growth in the second surface and a slow growth in the first.
Reagents can be added to the solution (rapid or drop wise injection if liquid or poring them into the reaction vessel if in powder form) or they can be added to the solution at a temperature in which no reaction is going to occur. In the latter case the temperature will be then risen to the thermal decomposition point to allow the nucleation. Adjusting the reaction parameters, such as reaction time, temperature, precursors and surfactants concentration and type we can control composition, size, shape and the quality of the product. As we will see in the next chapter a high ratio between the concentration of surfactants and precursors in solution led to synthesis of very small nanoparticles.
When the nanoparticles have the required size we can stop the synthesis just by quickly cooling down the solution temperature. The particles are then isolated from the growth solution by adding a solvent that is miscible with that one in which the nanoparticles are but it is incompatible with the NCs surfactants. This incompatibility destabilize the solution and the NPs form big clusters in solution which can be precipitated with a centrifuge or by decantation. The presence of the surfactants on the NPs surface prevent their agglomeration during the precipitation process and the addition of fresh solvent with which the surfactant are compatible led to a stable colloid.

The synthesis in solution is so far one of the most used approach for the synthesis of nanoparticles cause the high number of degree of freedom it allows. It is generally a low cost approach with which is possible to synthesize nanomaterials of several composition ranging from pure metals, semiconductors and insulators to their alloys or doped forms. It allows to finely tune the NCs size (from about 1nm to several hundreds) and shape (i.e. dots, rods, tetrapods, disks Figure I.3).

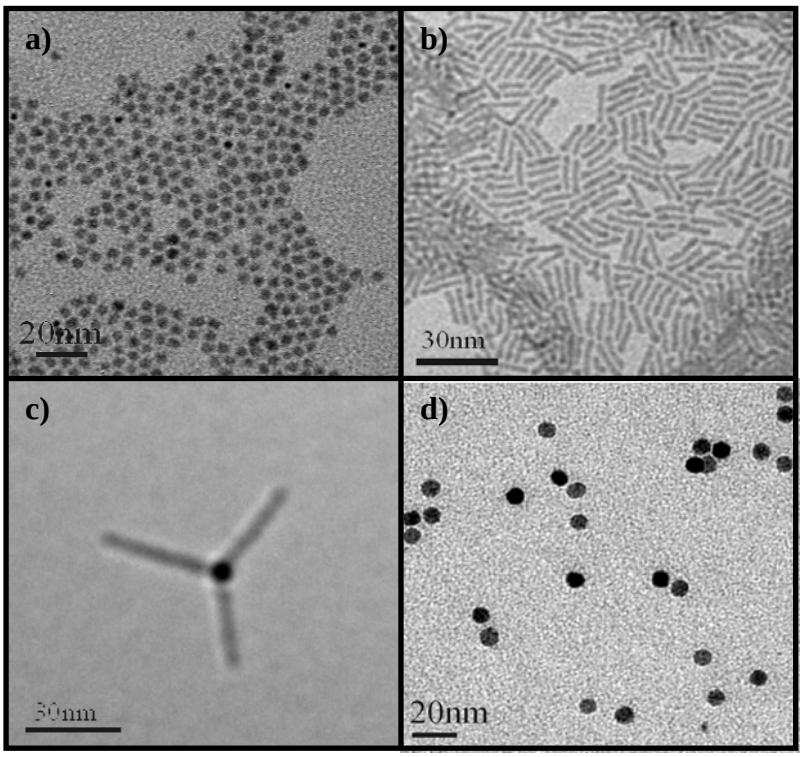

Figure I.3. Some examples of nanocrystals shape control: a) *CdSe nanospheres, b) CdSe nanorods, c) CdTe tetrapods and d) Fe_3O_4 nanodisks, synthesized following the recipes reported in [9].*

An other strength point is the possibility to synthesize particles with a narrow size distribution, fundamental requirement for several applications of these nanomaterials. The final product can be delivered in solution or in a powder form. The possibility to have the sample in solution without any further process make easy the step for mass production and application of nanocolloids in biology and medicine.

For this thesis I have almost exclusively synthesized nanoparticles with the method just described, but this is not the only available. Here are presented some among the most diffused techniques since a complete dissertation is not the object of this thesis.

I.2 Sol-Gel

The sol-gel synthesis is a wet-chemical technique for the fabrication of nanocomposites (typically metal oxides). Typical precursors for this kind of process are metal alkoxides and metal chlorides, which are before hydrolized in solution (**Sol**) and then condensed by solvent evaporation at relatively high temperature. Via these two steps the precursors form a colloid, a system composed of solid particles (the size distribution is quite broad ranging from 1 nm to 1 μm) dispersed in a

solvent which evolves into an inorganic network containing a liquid phase (**Gel***)*. The inorganoc network is made of metal-oxo (M-O-M) or metal-hydroxo (M-OH-M) polymers. The last step of the process is the drying which removes the liquid phase from the gel which led to a powder made of porous material. Among all the ways we can harness this techniue (i.e. metal-oxide thin films, ceramic manifacture) there is the possibility to synthesize nano-micro particles and control their chemical composition, as even a small quantity of dopant can be introduced in the solution and end up in the product finely dispersed. An example of this approach is repoted in [10] where yittrium oxide nanoparticles have been synthesized via sol-gel techique, they have been doped with europium and gadolinium in order to make them red (europium) and green (gadolinium) fluorescent under UV light. We developed even a preocess to suspend them in a solvent starting from the nanoparticles powder. This further process made these materials suitable for future biological application as labels for molecules.

An other very intetresting aspect of the sol-gel technique besides the synthesis of doped nano-micro particles is the formation of porous solid matrices (aerogel and xerogel). To this class of materials belong the world's lightest materials and some of the toughest ceramics.

I.3 Micelles

A micelle is an aggregate of surfactant molecules dispersed in a liquid forming a colloid. The surfactants constituting a micelle is basically made of two parts, one hydrophilic and the other one hydrophobic. This particular composition allows to form two kind of micelles known as "normal" and "inverse" depending on the solvent polarity (Figure I.4).

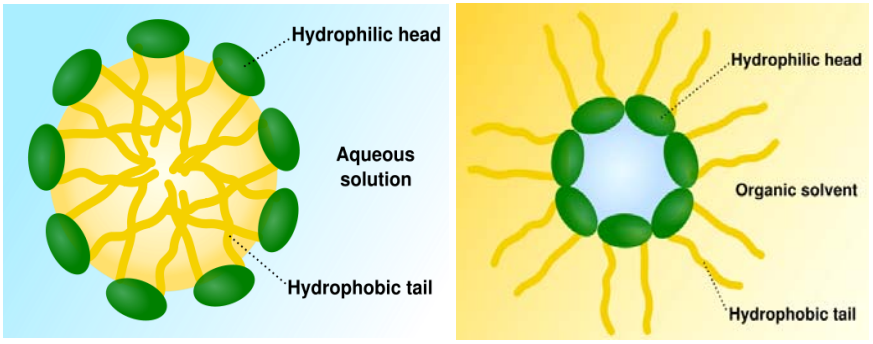

Figure I.4. Scheme of n*ormal (left) and inverse (right) micelle. (Source Internet http://en.wikipedia.org/wiki/Micelle)*

If the main solvent is water the surfactants constituting the micelle will show the hydrophilic part hiding the hydrophobic one on their nuclei. The opposite happens if the main solvent is nonaqueous. The micelles formation from a solution in which some surfactant molecules are suspended occur when the concentration of surfactant molecules exceeds the critical micelle concentration (cmc). Further increases of the concentration can tune the dimension of the micelle cores. Micelles are approximately spherical in shape but other shapes are also possible such as ellipsoids and cylinders. Generally the micelle shape is tailored by using surfactant molecules with different geometry but other factors can influence this feature such as surfactant concentration, temperature, pH and ionic strength. The possibility to tune size and shape of the micelle cores let us to tune the nanoparticles size and shape. Basically the reaction for the synthesis of nanoparticles by using reverse micelles involves a precursor which is dissolved into a solution trapped in the micelle cores since insoluble in the main solvent and an other one which is instead present in solution outside the micelle. The reaction in this case take place by phase exchange. The different precursors could be both trapped into the micelles, in that case the reaction occur via micelle coalescence. In

the case of normal micelles there is no reactants confinement in fact it is the product that is trapped into the micelle which act as a polymer that control the nanoparticle size and stabilize the solution.
With this technique several kinds of metal, metal oxide and semiconductive nanoparticles have been successfully synthesized [11-15].

I.4 Hydrothermal process

Hydrothermal process or hydrothermal synthesis included the various techniques of crystallizing substances from high temperature (150-700°C) and high pressure water solutions. This method harness the solubility in water of almost all the inorganic substance under these condition and the crystallisation of the dissolved material from the fluid. The crystal growth is performed in a autoclave made of steel or titanium alloys with an hot and a cold end which maintain a temperature gradient in the reaction chamber. The growth principle is simple: the reaction chamber is filled with water and reagents, thanks to temperature gradient in the hotter part of the autoclave the reagents are dissolved while in the cooler part there is the nucleation and consequent crystal growth. Usually these kind of synthesis need few hours to several days to be completed.
With this technique it as been possible to produce nanoparticles which are not possible at room temperature cause the peculiar structural properties that reagents and water can have at high temperature and pressure condition. Tuning of parameters such as reaction time, temperature, pressure, reagents type and concentration, allows the synthesis of different kinds of nanoparticles with different size and shape and a good size distribution.
A very interesting example reported by Desvaux et al. [16] in the application of this technique is the synthesis and the self-assembly of FeCo nanoparticles to form directly in the autoclave a mm scale supercrystal (Figure I.5).

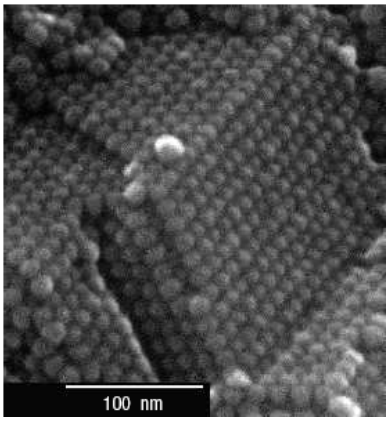

Figure I.5. *SEM-FEG micrograph of a broken FeCo NPs* supercrystal. (taken from [16])

I.5 Photo reduction and role of light in nanoparticles synthesis

Light can be used for the synthesis of nanoparticles too. Well known for the synthesis of carbon nanotubes and fullerenes is the laser ablation technique which is a process of removing material from a solid by irradiating it with a pulsing laser. The amount of material removed depends basically on its optical properties and laser wavelength. Performing the laser ablation on a solid dipped into a solvent in presence of some organic molecules is possible to produce colloidal solution of nanoparticles which have the organic molecules as surfactants. Some examples of this technique are the synthesis of metal nanoparticle colloids such as gold and silver [17-19].

But light can be used as reduction agent for the wet chemical synthesis of nanoparticles. The photochemical reduction of some metal salts dissolved in a solution of surfactants allows the synthesis of metal nanoparticles [20].
Light can even act on the nanoparticles favouring their coalescence and their growth. Some well known examples are the conversion of silver spherical nanoparticles into triangular nanodisks illuminating the solution with a fluorescent lamp [21] and the formation of spherical nanoparticles by irradiating with a pulsing laser a solution of gold nanorods [22].
Other interesting effects of light on nanoparticles recently observed is the formation of hollow nanocrystals starting from spherical one [23] and the mutual transposition between the core and the shell in gold nanoparticles on which surface a platinum shell was grown [24].

I.6 Physical and Chemical Vapour Deposition

Physical vapour deposition (PVD) involves the condensation of materials from their vapour phase. The process is usually performed in a horizontal tube furnace where at one end the material to evaporate is placed and the other end is at lower temperature, in order to favour the condensation, there is a substrate for the nanoparticles growth. The material evaporation is performed in several ways, thermal evaporation, electron beam, sputtering, cathodic arc and pulsed laser. The material is transferred on the growth support through an inert gas flow.

Chemical vapour deposition (CVD) in principle works as the PVD but it involves even a reaction between the materials in vapour phase on the deposition substrate which is usually held at high temperature. Frequently even volatile byproducts are also produced, which are removed by gas flow through the reaction chamber. In same cases catalysts are deposited on the growth substrate in order to accelerate the reactions. This technique can be performed in several conditions which differs from the means by which the chemical process is initiated (i.e. ultrahigh vacuum, atmospheric pressure, atomic layer CVD) which allow different performances. For the growth of nanoparticles is generally used the Stransky-Krastanow growth (SK growth). This technique is basically a two steps process. In the first step several monolayers of materials are grown on a growth substrate, beyond a certain critical layer thickness the growth continues through the nucleation and coalescence of nanoparticles (islands). The critical layer thickness depends on strain and chemical potential of the deposited material.

With this kind of techniques several kind of nanomaterials have been synthesized with different shapes such as nanorods, nanobelts, nanowires, nanosheets and nanosaw [25].

This is just a little list of different techniques which allows the synthesis of nanomaterials. Among these we will focus on the first one with particular emphasis on the synthesis of very small semiconductive nanoparticles and the synthesis of dimers made of magnetic and semiconductive domains.

References:

[1] Hongbo Liao, Weixin Lu, Shengwen Yu, Weijia Wen, and George K. L. Wong, *Optical characteristics of gold nanoparticle-doped multilayer thin film, J. Opt. Soc. Am. B,* **2005**, 9 (22), 1923-1926.

[2] Hiromitsu Takeda, Kenji Adachi, *Near Infrared Absorption of Tungsten Oxide Nanoparticle Dispersions, J. Am. Ceram. Soc.*, **2007**, 90 (12), 4059–4061.

[3] Yinthai Chan, Preston T. Snee, Jean-Michel Caruge, Brian K. Yen, Gautham P. Nair, Daniel G. Nocera, and Moungi G. Bawendi, *A Solvent-Stable Nanocrystal-Silica Composite Laser, J. Am. Chem. Soc.***, 2006**, 128, 3146-3147.

[4] Polina O. Anikeeva, Jonathan E. Halpert, Moungi G. Bawendi and Vladimir Bulovic, E*lectroluminescence from a Mixed Red-Green-Blue Colloidal Quantum Dot Monolayer, Nano Lett.*, **2007,** 7 (8), 2195-2200.

[5] Wolfgang J Parak, Teresa Pellegrino and Christian Plank, *Labelling of cells with quantum dots, Nanotechnology,* **2005**, 16**,** R9–R25.

[6] Wolfgang J Parak, Daniele Gerion, Teresa Pellegrino, Daniela Zanchet, Christine Micheel, Shara CWilliams, Rosanne Boudreau, Mark A Le Gros, Carolyn A Larabell and A Paul Alivisatos, *Biological applications of colloidal nanocrystals, Nanotechnology,* **2003**, 14, R15–R27.

[7] Scott E. McNeil, *Nanotechnology for the biologist, Journal of Leukocyte Biology,* **2005***,* 78, 1-10.

[8] Noriyasu Kawai, Akira Ito, Yoko Nakahara, Mitsuru Futakuchi, Tomoyuki Shirai, Hiroyuki Honda, Takeshi Kobayashi, and Kenjiro Kohri, *Anticancer Effect of Hyperthermia on Prostate Cancer Mediated by Magnetite Cationic Liposomes and Immune-Response Inductionin Transplanted Syngeneic Rats, The Prostate,* **2005**, 64, 373 -381.

[9] (CdSe spheres) Peter Reiss, Joel Bleuse and Adam Pron, *Highly Luminescent CdSe/ZnS Core/ShellNanocrystals of Low Size Dispersion, Nano Lett.,* **2002**, 2(7), 781-784. (CdSe rods*)* Xiaogang Peng, Liberato Manna*,*Weidong Yang, Juanita ickham, Erik Scher, Andreas Kadavanich and A. Paul Alivisatos, *Shape Control of CdSe Nanocrystals, Nature,* **2000**, 404, 59-61. (CdTe tetrapods)Luigi Carbone, Stefan Kudera, Elvio Carlino, Wolfgang J. Parak, Cinzia Giannini, Roberto Cingolani, and Liberato Manna, *Multiple Wurtzite Twinning in CdTe Nanocrystals Induced by Methylphosphonic Acid, J. Am. Chem. Soc.***, 2006**, 128, 748-755. (FeOx nanodisks) Emory M. Chan, Maria F. Casula, A. Paul Alivisatos, David J. Zaziski, Anna Corrias, *The concept of Delayed Nucleation In Nanocrystal Growth Demonstrated for the case of Iron Oxide Nanodisks, J. Am. Chem. Soc.,* **2006**, 128 (5), 1675-1682.

[10] Ashutosh Pandey, M. K. Roy, Anjana Pandey, Marco Zanella, Ralph A. Sperling, W. J. Parak, A. B. Samaddar and H. C. Verma, Chloroform- and water-soluble sol-gel derived Eu^{+++}/Y_2O_3 (red) and Tb^{+++}/Y_2O_3 (green) nanophosphors: synthesis, characterization and surface modification, (Submitted).

[11] Chen-Li Chiang, *Controlled Growth of Gold Nanoparticles in AOT/C12E4/Isooctane Mixed Reverse Micelles, Journal of Colloid and Interface Science,* **2001**, 239**,** 334–341.

[12] Yingwei Xie, Ruqiang Ye, Honglai Liu, N*anoparticles inRreverse Micelles Stabilized by Natural Biosurfactant, Colloids and Surfaces A: Physicochem. Eng. Aspects*, **2006**, 279, 175–178.

[13] Takuya Nakanishi, Hironori Iida and Tetsuya Osaka, *Preparation of Iron Oxide Nanoparticles via Successive Reduction–Oxidation in Reverse Micelles, Chemistry Letters,* **2003,** 12(32), 1166.

[14] W. Xu, D.L. Akins, *Reverse Micellar Synthesis of CdS Nanoparticles and Self-Assembly into a Superlattice, Materials Letters,* **2004**, 58, 2623– 2626.

[15] Saim M. Emin, Ceco D. Dushkin, Seiichiro Nakabayashi, Eiki Adachi, *Central European Journal of Chemistry,* **2007**, 5(2), 590–604.

[16] C´ Eline Desvaux, Catherine Amiens, Peter Fejes, Philippe Renaud, Marc Respaud, Pierre Lecante, Etienne Snoeck and Bruno Chaudret, *Multimillimetre-Large Superlattice of Air-Stable Iron-Cobalt Nanoparticles, Nature Materials,* **2005**, 4, 750-753.

[17] Takeshi Tsuji, Kenzo Iryo, Norihisa Watanabe, Masaharu Tsuji, *Preparation of Silver Nanoparticles by Laser Ablation in Solution:Iinfluence of Laser Wavelength on Particle Size, Applied Surface Science,* **2002**, 202, 80–85.
[18] Fumitaka Mafune´, Jun-ya Kohno, Yoshihiro Takeda, Tamotsu Kondow, Hisahiro Sawabe, *Formation and Size Control of Silver Nanoparticles by Laser Ablation in Aqueous Solution, J. Phys. Chem. B* **2000,** *104,* 9111-9117.
[19] E. Giorgetti, A. Giusti, S. C. Laza, P. Marsili and F. Giammanco, *Production of colloidal gold nanoparticles by picosecond laser ablation in liquids, Phys. Stat. Sol. (a),* 204 (6), 1693-1698.
[20] J. P. Abid, A. W. Wark, P. F. Brevet and H. H. Girault*, Preparation of silver nanoparticles in solution from a silver salt by laser irradiation, Chem. Commun.*, **2002**, 792–793.
[21] A. Callegari, D. Tonti, and M. Chergui, *Photochemically Grown Silver Nanoparticles with Wavelength-Controlled Size and Shape, Nano Lett.,* **2003**, 3 (11), 1565-1568.
[22] S. Link, C. Burda, M. B. Mohamed, B. Nikoobakht, and M. A. El-Sayed, *Laser Photothermal Melting and Fragmentation of Gold Nanorods: Energy and Laser Pulse-Width Dependance,* **1999**, 103 (9), 1165-1170.
[23] Seol J. Kim, Chil S. Ah, and Du-Jeon Jang, *Optical Fabrication of Hollow Platinum Nanospheres by Excavating the Silver Core of Ag@Pt Nanoparticles, Adv. Mater.* **2007**, *19*, 1064–1068.
[24] Chil Seong Ah, Seol Ji Kim, and Du-Jeon Jang, *Laser-Induced Mutual Transposition of the Core and the Shell of a Au@Pt Nanosphere, J. Phys. Chem. B* **2006,** *110,* 5486-5489.
[25] Daniel Moore and Zhong L. Wang, *Growth of Anisotropic One-Dimensional ZnS Nanostructures, J. Mater. Chem.,* **2006**, 16, 3898-3905.
[26] A. P. Alivisatos, *Perspective on the Physical Chemistry of Semiconductor Nanocrystals, J. Phys. Chem.,* 1996, 100(31), 13226-13239.

II. Nucleation, particles growth and ripening

An exhaustive, analytical model for the description of the nanocrystal growth is not available yet, even if several efforts have been made. In this short chapter we will make a simple picture of the topic in order to give some insight to the reader.

The synthesis of nanoparticles can be generally split in three steps:

1) Nucleation
2) Nanoparticles growth
3) Nanoparticles ripening

II.1 Nucleation. Generally there are three kinds of nucleation: primary homogeneous, primary heterogeneous and secondary nucleation. We will focus on the first one which is more suitable with the rest of the discussion and we will just define last two at the end of this paragraph. Homogeneous nucleation occur when the molecules in solution combine themselves to form nuclei. This kind of nucleation can happen when the concentration of monomers in solution raises above a nucleation threshold or a reducing agent or a reagent is injected in a solution in which there is already present an organometallic precursor. The first case is the one usually used to model the nucleation since in the other two the injection of a reagent can be seen as a way to trigger the reaction.
Gibbs-Thompson equation (eq. 1) is commonly used to explain the particles size distribution during nucleation, growth and ripening [1]. Originally this theory was developed to quantify the equilibrium of liquid droplets in a surrounding vapour and it has been adapted to describe the equilibrium of solid particles with radius r in equilibrium with a reaction solution.

$$S_r = S_b \exp(2\sigma V_m / rRT) \quad \text{(eq. 1)}$$

Where: S_b and S_r are respectively the solubilities of the bulk crystals and of the nanoparticles having radius r, V_m is the molar volume of the materials, r is the nuclei radius, R is the gas constant, σ is the surface tension and T is the absolute temperature. Having (eq. 1) as base Sugimoto developed a model [1] about the crystals growth which led to the equation:

$$\frac{dr}{dt} = \frac{2\sigma D V_m^2 S_b}{rRT}\left(\frac{1}{r_{cr}} - \frac{1}{r}\right) \quad \text{(eq. 2)}$$

Where D is the diffusion coefficient and r_{cr} is the critical radius which meaning will be clear in the next pages.
The diffusion coefficient was required because Sugimoto considered that the addition of monomers for the crystal growth was made by a diffusion-controlled mechanism, basically the mechanism that allows the water to form crystals when it is cooled down. But this is not the only mechanism which can allow the formation of crystals. Monomers in fact can react with the elements on the nanoparticle surfaces and we can have a reaction-controlled growth. A very nice model which includes both these growth mechanisms has been reported by Weller group [2] for which the nanoparticle radius evolution is

$$\frac{dr}{dt} = V_m D S_b \left\{ \frac{\frac{[M]_b}{S_b} - \exp\left[\frac{2\sigma V_m}{rRT}\right]}{r + \frac{D}{k_g^{flat}} \exp\left[\alpha \frac{2\sigma V_m}{rRT}\right]} \right\} \quad \text{(eq. 3)}$$

Where $[M]_b$ is the monomer concentration in the bulk of solution in which the nanoparticles grow, α is a transfer coefficient (<1) and k_g^{flat} is the growth rate for a flat (r=∞) surface.
Eq.3 can be simplified defining new variables and parameters in the following manner

$$\frac{dr^*}{dt} = \frac{S - \exp\left(\frac{1}{r^*}\right)}{r^* + K\exp\left(\frac{\alpha}{r^*}\right)} \quad \text{(eq. 4)}$$

In which

$$r^* = \frac{RT}{2\sigma V_m} r \quad \text{(eq. 5) is the dimensionless radius}$$

$$\tau = \frac{R^2T^2DS_b}{4\sigma^2V_m} t \quad \text{(eq. 6) is th dimensionless time}$$

$$K = \frac{RTD}{2\sigma V_m k_g^{flat}} \quad \text{(eq. 7)}$$

is a dimensionless parameter describing the growth process (K<<1 diffusion-controlled growth, K>>1 reaction-controlled process) and

$$S = \frac{[M]_b}{S_b} \quad \text{(eq. 8)}$$

is a dimensionless parameter describing the oversaturation of monomers in solution.
It is interesting to underline that this model which includes the reaction controlled growth can be led to the Sugimoto model if we restrict the growth to just a diffusion process. In fact Eq. 2 can be obtained from eq. 3 when K→0.
In Figure II.1 is reported the nanoparticle growth rate as function of its radius for different values of the parameters K and S.

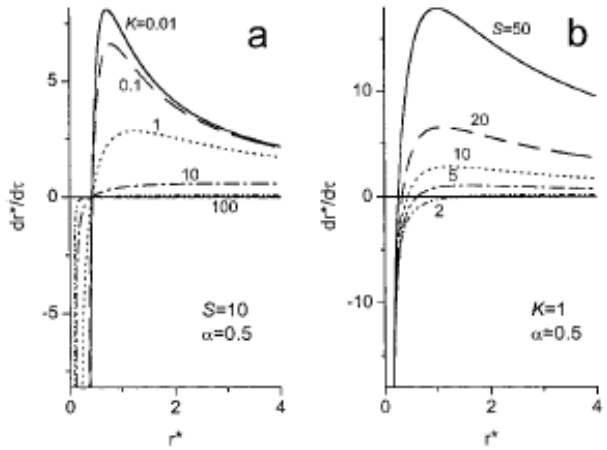

Figure II.1. *Growth rate of a nanoparticle as function of its radius for different values of the parameters S and K (Taken from [2]).*

Form Figure II.1 we see that the growth rate is not always positive which would be what we expect if the particle grows. For small radius, when the nucleation occur, the growth rate assumes even negative values which means that not all the nuclei are stable at the nucleation stage but some of them can dissolve by loosing monomers. The radius corresponding zero growth rate is called critical radius (r_{cr}). Nuclei with a radius bigger than r_{cr} will proceed to the growth stage while the others will be dissolved.
The critical radius is linked to the oversaturation S and the temperature T by the following relation

$$r_{cr} = \frac{2\sigma V_m}{RT\ln(S)} \quad \text{(eq. 9)}$$

In particular the critical radius decreases when the solution oversaturation increases and this is the reason why in order to synthesize very small nanoparticles is necessary to work with high monomers concentration.
A similar interpretation comes analysing the problem from the thermodynamics point of view.
For spherical particles the free energy ΔG can be expressed as sum of a term due to the new volume and an other term due to the new surface created

$$\Delta G = -4\frac{\pi r^3 k_B T\ln(S)}{V_m} + 4\pi r^2\sigma \quad \text{(eq. 10) [3]}$$

where k_B is Boltzmann constant and all the other parameters have been introduced earlier.
When the ratio S>1, ΔG present a positive maximum which is the activation energy for the nucleation. This maximum (Figure II.2) appears at the critical radius (r*) which means that just the nuclei larger than the critical size will decrease their free energy by growing forming particles.

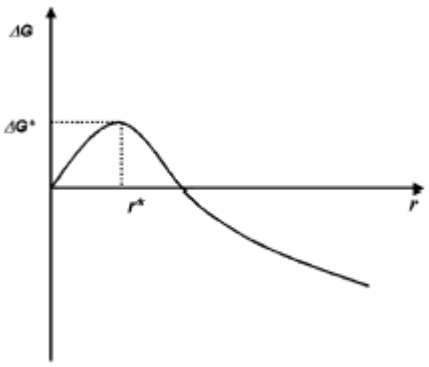

Figure II.2. *Free energy ΔG as function of the growth particle radius.(Taken from [3])*

These theoretical results give us an idea that the homogeneous nucleation has a sort of Darwinian character since after the nucleation has been triggered (i.e. by reagents addition to the starting solution) overcoming the nucleation threshold (Figure II.3), only some of the nuclei are able to become particles while the others are destined to redissolve.
Just out of curiosity we give here a very short description concerning the other two kind of nucleation. Primary heterogeneous nucleation requires the presence of foreign interfaces which support the nucleation reducing nuclei surface energy and increasing the nucleation rate. Concerning modelling aspect the equations describing this process are similar to those used in the homogeneous nucleation. Secondary nucleation occurs when the already present nuclei are broken in solution forming a new generation of smaller nuclei. From this point of view the starting nuclei are usually known as “parents” of the new ones.

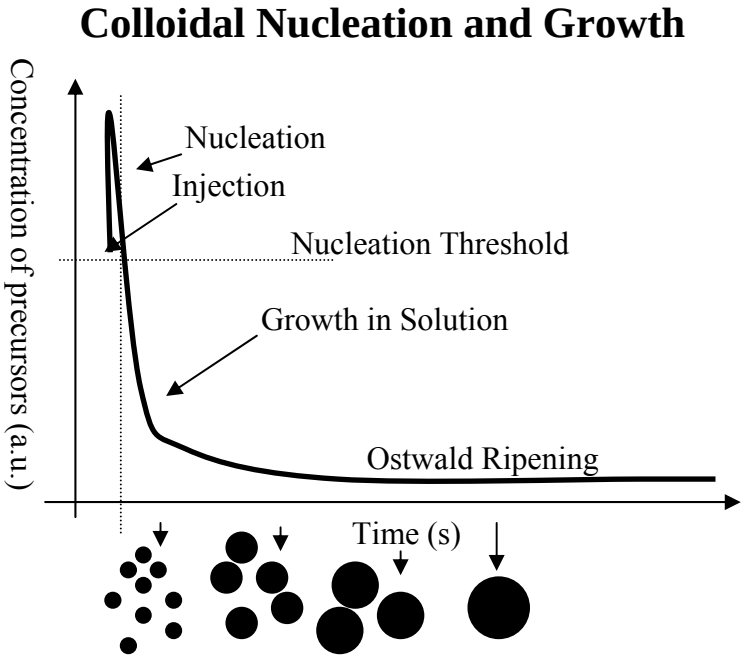

Figure II.3. Figure adapted f*rom [4]. Simple sketch of the nucleation, growth and ripening process. In particular here is possible to see that stopping the synthesis after a certain interval of time from the nucleation is possible to synthesize particles with almost all the same size.*

Growth. When the concentration of monomers drops below the critical level cause the nuclei formation, nucleation stops and the growth process starts (Figure II.3). Nanoparticles grow via monomers addition to their surface but it is not possible to exclude that the growth during and just after the nucleation is driven by the formation of little agglomerates made of at least two nuclei which atoms quickly rearrange after the agglomerate is formed. This process is known under the name "secondary growth". This hypothesis is based on the high reactivity of these materials which atoms are mainly located on the nanoparticle surface.

Just after the nucleation the particles size distribution is characterized by having a broad peak due to the different nuclei size. It has been observed that this size distribution decrease over synthesis time and an explanation of this fact was given by Peng [5] and can be understood considering the negative slope of the curves in Figure II.1. Among all the formed nuclei able to overcome the critical size the growth rate of the smallest is higher than that one of the largest, which means that they grow faster and are able to "catch up" the largest particles over synthesis time.

Ripening. When the reactants concentration is too low to support the nanoparticles growth size defocusing occurs. This process is known usually under the name of "Ostwald ripening" from the name of the german physical chemist who first described it.
At this stage the oversaturation value S is very small which means that the critical radius assumes a value which is the average size of the nanoparticles present in solution. Considering nucleation theory seen above, nanoparticles having a size smaller than the critical one will start dissolving while the larger will grow thanks to the increment of the monomers concentration. This effect led to a broadening (defocusing) of the size distribution.
Once the reaction reaches this stage is difficult to get monodisperse nanoparticles unless the ripening is extended long enough to assure the complete depletion of the smaller particles. A

drawback of this process is that the particles size could leave the nanometer regime to the micrometer one and loose the properties acquired by the material at nanometer scale.

A good understanding of the parameters in control of these process (nucleation, growth and ripening) helps to improve the nanoparticles quality and engineer new synthetic routes which can led to improvements in the impact of these materials on our lives.

References:

[1] Sugimoto Tadao, *Preparation of monodispersed colloidal particles, Adv. Colloid Interfac. Sci*., 1987, 28, 65-108.
[2] Dmitri V. Talapin, Andrey L. Rogach, Markus Haase, and Horst Weller, *Evolution of an Ensemble of Nanoparticles in a Colloidal Solution: Theoretical Study, J. Phys. Chem. B* **2001,** *105,* 12278-12285.
[3] Clemens Burda, Xiaobo Chen, Radha Narayanan, and Mostafa A. El-Sayed, *Chemistry and Properties of Nanocrystals of Different Shapes, Chem. Rev.,* **2005,** 105, 1025-1102.
[4] C. B. Murray, C. R. Kagan, M. G. Bawendi, *Synthesisand Characterisation of Monodisperse Nanocrystals and Close-Paked Nanocrystals Assembly, Annu. Rev. Mater. Sci.* **2000**, 30, 545–610.
[5] Xiaogang Peng, J. Wickham, and A. P. Alivisatos, *Kinetics of II-VI and III-V Colloidal Semiconductor Nanocrystal Growth: "Focusing" of Size Distributions, J. Am. Chem. Soc.* **1998,** *120,* 5343-5344.

III. Magic Size Nanoparticles

As we saw in the first chapter we are able to synthesize nanoparticles of different materials ranging from metals to insulators. Nanoparticles made of semiconductive materials become particularly interesting thanks to their optical properties. Semiconductive nanoparticles present in fact a band gap (Figure III.1) which is dependent on the NPs size. The bigger the nanoparticle the smaller the band gap. This means that just by controlling the NP growth, by stopping the synthesis at a desired nanoparticles size (Figure II.3), we can tailor the material band gap.

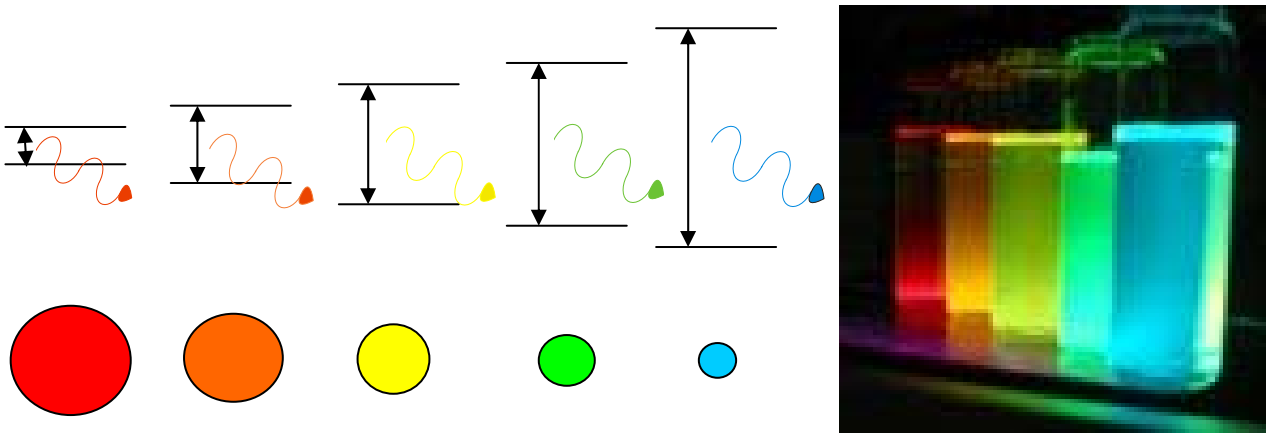

Figure III.1. *Sketch on the relation between nanoparticles size and band gap (left), fluorescence of solution of nanoparticles of different size under UV light (Photo by Liberato Manna).*

This property is extremely important for several technological applications such as electronics, optoelectronics and biological labelling. In order to detect the band gap of a solution of NCs, it is enough to measure its absorbance spectrum. In Figure III.8a the absorbance spectrum of three solutions of CdSe/ZnS core/shell nanocrystals is shown. As we will show in the next chapter, it is possible to grow a shell of an other material, in this case a semiconductor ZnS, which improves the nanoparticles properties. The main peak (at highest wavelength) corresponds to the first exciton of the nanoparticles which is directly related with its band gap. Since the band gap of the nanoparticles gets smaller with the growth of the crystal we will see NCs exciton peak red-shifting to smaller energy values (larger wavelength) and this gives an indirect way to control the nanoparticles growth via optical measurements. In Figure III.8b are reported the fluorescence spectra of the same CdSe/ZnS solutions. Even in this case depending on the nanoparticle size the fluorescence peak position changes and the biggest nanoparticles present a fluorescence at higher wavelength.

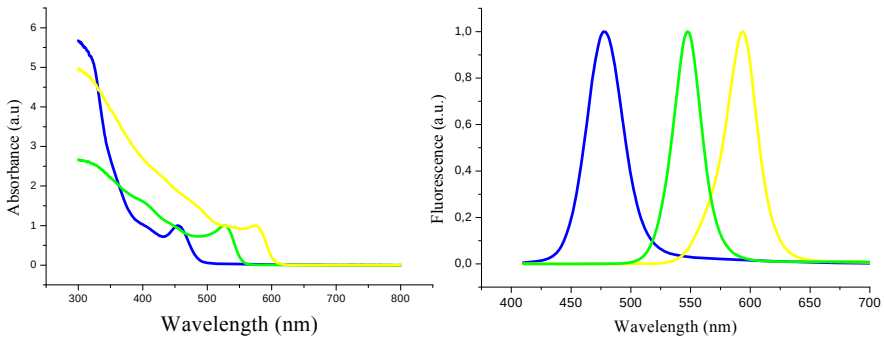

Figure III.8. *Absorbance and fluorescence spectra of different CdSe/ZnS core/shell Qdots. As we will see in the next chapter growing a shell around the CdSe cores enhance the optical properties of the core itself.*

For some application it is very important to be able to synthesize, with high reproducibility, NPs having the same optical properties (i.e. having an absorbance peak always centred at the same wavelength).This usually is not an easy task since for many recipes the nanoparticles growth is too fast to allow a certain precision. Some synthesis can be done at low temperature which slow down the nucleation and growth and allows stopping the synthesis with a better accuracy. Further changes of the synthesis condition can favour the growth in solution of special families of nanoparticles characterized by having fixed electronic and structural properties. These special families of nanoparticles are known with the name of magic size nanocrystals (MSCs). The term "magic" has been associated to clusters in the middle eighties by Teo and Sloane [1] in a paper focused on the number of atoms constituting the different metal clusters discovered till then. Clusters with a "magic number of atoms" resulted to be more common then those in which this feature was not present underlining the stability of these structures. In the case of semiconductive materials the magic size crystals are characterized by a specific absorbance spectrum as shown in Figure III.9.

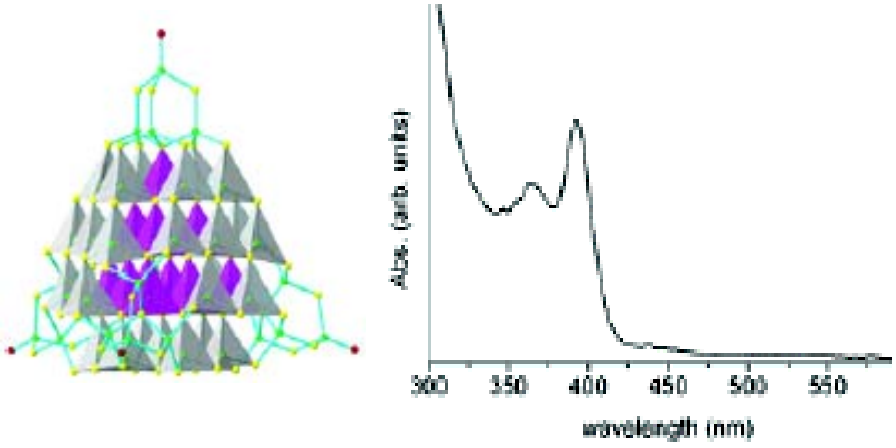

Figure III.9. *Structural diagram and the absorbance of a solution of* $[Cd54X32(SPh)48(H2O)4]^{4-}$ *(X= S or Se)in DMF[3].*

The example in Figure III.9 is one among several reported in literature about semiconductive magic size crystals. The synthesis of this structures can be done via laser ablation [2], in autoclave [3], using micelles [2] but those which present the best performances in terms of fluorescence are those synthesized in solution. In general synthesis are able to yield one or two MSCs at the same time and their crystalline structure could be defined via single crystal XRD once the MSCs are self organized in a superlattice [4,5,2]. We recently reported [6] a sequential growth of CdSe MSCs growth in a solution in which it is possible to follow indirectly the formation of six different MSCs families over time. The temporal evolution of the absorbance spectrum of the synthesis solution is reported in Figure III.10. Some minutes after the injection of the selenium precursor in a solution in which some surfactants and a cadmium precursor are present, several well-defined absorption peaks appear. That one at highest energy (the first to appear) was centred at 330 nm. As the synthesis proceed, new peaks appear at longer wavelengths, over minutes and even over several hours. The position of all these peaks remain constant over time, while their relative intensities vary so that the peak at longest wavelength exhibit increasing intensity with respect to those at shorter wavelength, which eventually disappear. This behaviour points to an evolution of the system through different families of clusters with high stabilities.

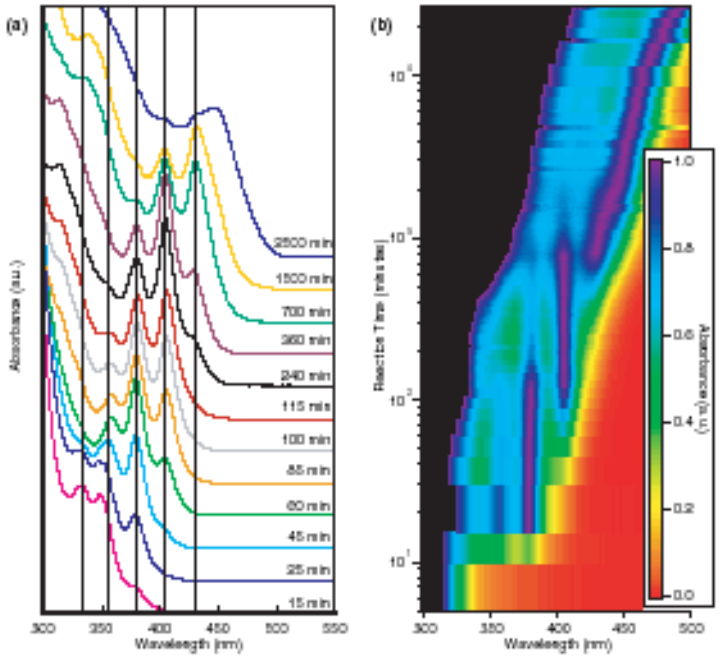

Figure III.10. *a) Absorption spectra of the growth solution recorded at different times and containing different populations of MSCs. b) This graph is built by stacking several horizontal stripes on top of each other, each of which corresponds to a color-coded plot of an optical-absorption spectrum, which were collected at progressively longer reaction times. (Taken from [6]).*

If indeed only one family of clusters were present, and these clusters were steadily increasing their size, then a single absorption peak would be seen, and this would be shifting gradually towards longer wavelengths (Figure III.8). Instead, the optical spectra indicate the formation of new families of MSCs having larger sizes. Over time, the average cluster size within each family remains constant, while the relative population of the various families changes in favour of the one present with the largest size. In addition, the width of the various absorption peaks (Figure III.10) suggests that the size distribution within each family is quite narrow.
The mechanism by which the growth of these clusters proceeds in solution is definitely fascinating. In the second chapter we introduced the basic ideas concerning the nucleation and the growth of a nanoparticle. A continuous growth can support a temporal evolution as that one of Figure III.8 but it is not able to justify a behaviour like that one of Figure III.10. This could be instead justified if we think the growth a competition between the attachment and detachment of single atoms onto its surface or if nanoparticles belonging to new MSCs families are due to the coalescence of smaller MSCs. In [6] we proposed a growth model based on the first picture which resulted to be in good agreement whit the experimental data. The key assumption of our model states that once a cluster has grown to a magic size, such a size is so stable that no atoms can detach from it. Therefore it can only grow further, but it cannot shrink. Any cluster with a size intermediate between two magic sizes can either grow to reach the larger of the two magic sizes, or shrink to the smaller one.
A model based on the aggregation of small clusters was discarded as it was not able to reproduce the experimental trends as well as the model described above. An example of CdTe MSCs which growth model is based on the agglomeration of smaller particles has been reported by Dagtepe [7]. In Dagtepe paper as support to this model where presented some high resolution TEM (HRTEM) images showing some net differences in the orientation of the crystal structure in different parts of the nanoparticle (Figure III.11). These differences were justified as due to the different orientation with which the different component of a nanoparticle stuck together.

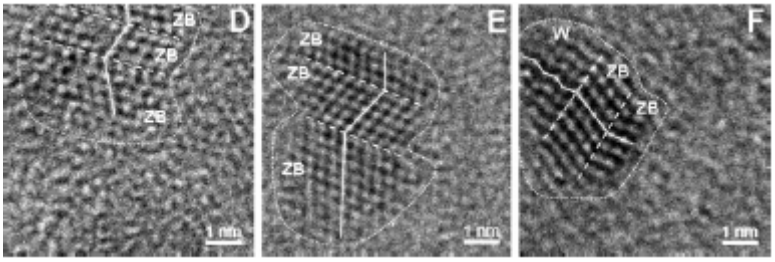

Figure III.11. *Examples of MSCs obtained by coalescence of smaller nanoparticles reported by Dagtepe [7]. The presence of different crystal orientation in the same nanoparticle has been justified as an agglomeration of smaller crystals to form a larger one.*

In our case, since the synthesis condition are different the growth can occur in a different way. In [9] we reported the characterisation of CdS, CdTe, ZnSe and ZnO MSCs synthesized with techniques similar to that one used for the CdSe MSCs [6] and in the HRTEM images there is no evidence of coalescence mechanism. Furthermore, we performed [6] a control experiment with the CdSe MSCs which supports our growth model and that discredits any aggregation mechanism. A synthesis of CdSe MSCs was performed and the nanocrystals were extracted from the solution by precipitation and were purified by repeated washing. This sample, which contained different families of MSCs, was redissolved in the same mixture of surfactants used for the synthesis of MSCs and the mixture was heated at 80° C for several hours. Therefore, all conditions were similar to those used for the synthesis of MSCs, with the only difference that no free monomers were present in this experiment. Optical absorption spectra on aliquots taken from this mixture at different times during the heating did not show any remarkable variation in the intensity of the various peaks, nor any shift in their positions, indicating no further evolution in the distribution of the families of MSCs. The results of this control experiment have two important implications, namely that the various MSCs are stable and that they do not undergo any shrinking or ripening process, and in addition that no aggregation occurs among smaller clusters to form larger clusters. Both implications support a growth model with attachment and deattachment of monomers.
An interesting hypothesis about the MSCs formation was formulated by Peng [8]. Peng converted the solubilities S_r and S_b in Gibbs-Thomson equation (eq.1) in the chemical potential of nanocrystals having radius r and infinite size considering that $\mu_x = RT \ln S_x$ (x=r or b). Gibbs-Thomson equation assume then the following form

$$\mu_r = \mu_b + \frac{2\sigma V_m}{rRT} \quad \text{(eq.11)}$$

In [8] Peng says that the monomers high concentration complicates the nucleation process producing critical nuclei which are smaller than the one observed for the usual dots synthesis. In this very small size regime Gibbs-Thomson equation is no more able to describe the growth process and need to be revised. Peng then suggested that the chemical potential curve assumed, at MSCs size regime, a shape as in Figure III.12.

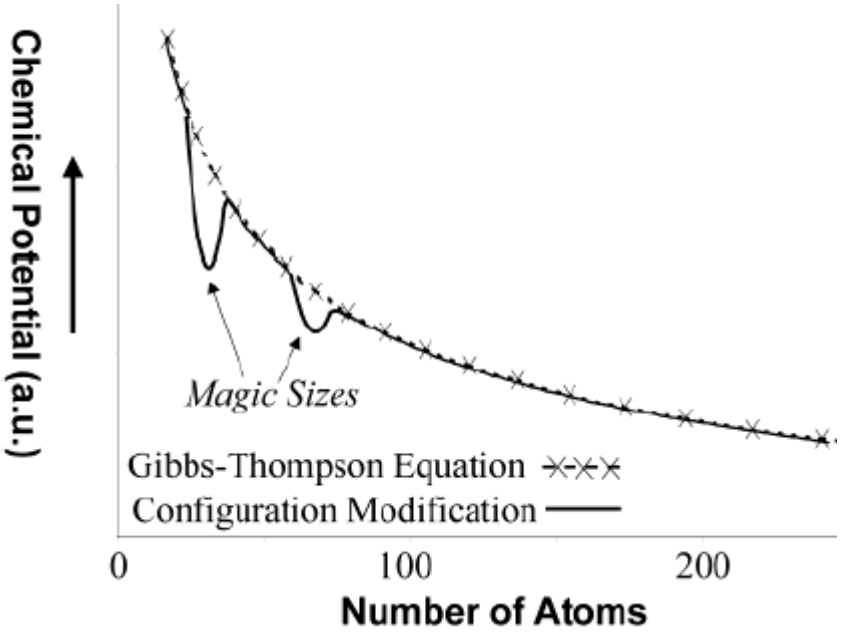

Figure III.12. *Schematic illustration of the chemical potential μ_r as function of the cluster number of atoms at MSCs size regime. (taken from [8])*

In an usual synthesis after the nucleation the critical nuclei have a certain chemical potential which decreases with the nanoparticle growth (dot-cross curve in Figure III.12). In order to describe the formation and the stability of the MSCs Peng introduced some wells in the Gibbs-Thomson curve (continuous curve of Figure III.12) suggesting a tunnelling mechanism for the formation of bigger MSCs. Starting from the introduction of the wells in the chemical potential landscape we would like to consider the sequential growth of MSCs from a different point of view.
For sake of simplicity we will consider for the moment only the CdSe MSCs growth introducing the similarities and the differences with the other MSCs growth later as support or extension of this qualitative model.
Considering the temporal evolution of the absorbance spectrum of CdSe MSCs (Figure III.10) the shape of the absorbance peak of each MSCs family can be approximated with a gaussian bell in which the FWHM is dependent on the NPs size distribution. We could assume that even the shape of the wells representing the MSCs families in the chemical potential landscape could be drawn as gaussian bells. The chemical potential equation could then be then written as

$$\mu_r \propto \frac{1}{r} - \sum_i \frac{c_i}{\sigma(t)_i \sqrt{2\pi}} \exp\left(\frac{-(r-m_i)^2}{2\sigma_i(t)^2}\right) \quad \text{(eq. 12)}$$

Where μ_r is the chemical potential of the nanoparticles with radius r, c_i is a proportional constant, m_i is the centre of the gaussian well we can assume to be the average radius of the magic size crystal, σ_i is the standard deviation of the gaussian well. The sum is extended on all the *i* MSCs families of a given material. In the case of a material having two MSC families the chemical potential would look like Figure III.13a. At this point two models can be used to describe the MSCs sequential growth which do not discredit the monomers attachment deattachment model. In the first one the gaussian bell standard deviation is time dependent as the concentration of the monomers in solution and the landscape of the chemical potential evolves over time as in Figure 12b, c, d.

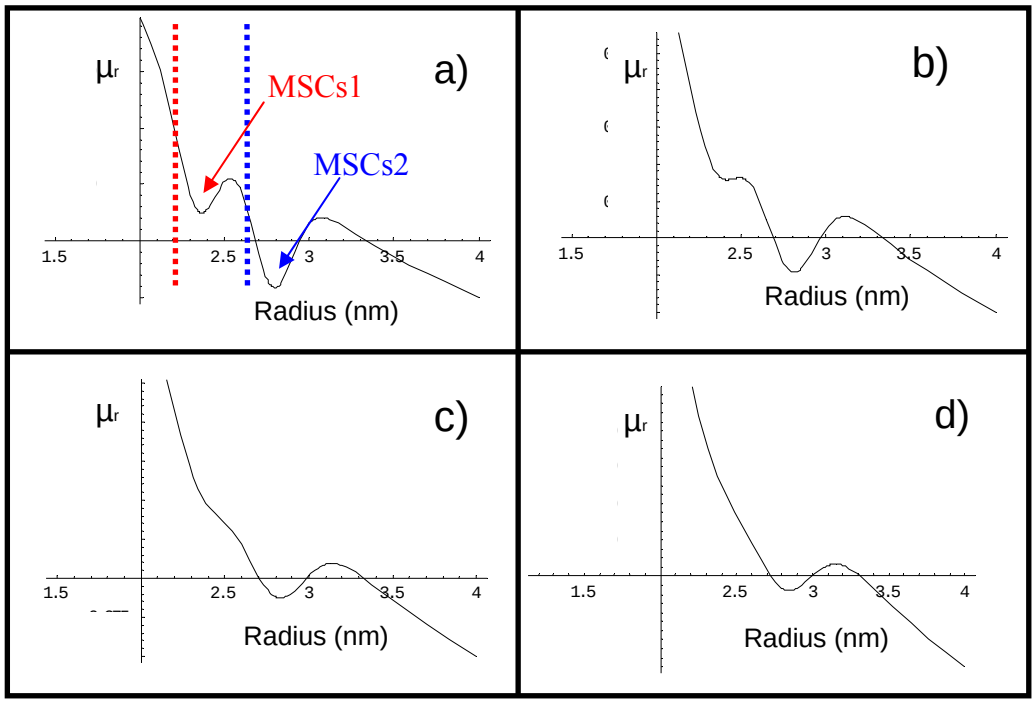

Figure III.13. *Temporal evolution of the chemical potential of a solution of MSCs. a) Chemical potential (μ_r) of a solution in which two MSCs (two MSCs wells) will form over time. Nanoparticles will start increasing their radius with a continuous growth and their chemical potential will fall on the first well minimum. Over time b), c) and d) with the decreasing of the monomer concentration this minimum will be lifted till the barrier between the wells will be small enough to let some particles to slide to the next well forming the second MSCs family. The process can continue with other wells with the formations of other families.*

As we said each gaussian would be centred on the MSCs average size and we would have as many of them as the observed peaks in the absorbance temporal evolution. From Figure III.10 we see that with the growth of a new peak led a peak at lower wavelength to disappear. The higher energy absorbance peak (lower radius well) disappear because no more MSCs belonging to that family are formed, and this could be represented with a gaussian well which depth decreases over time till its complete disappearing as in Figure III.13d. The decreasing of the well depth favours the formation of the next family of MSCs since the barrier between a well and the next one becomes smaller over time. But there is even the possibility the chemical potential to be time independent. In fact with the decreasing of the concentration of the monomers in solution the critical size increases (eq.9 in chapter II). According to the nucleation theory of chapter II the nanoparticles with a size smaller than the critical one shrink releasing monomers back in solution. This might explain just what we observe in the sequential growth of MSCs as we can understand considering Figure III.13a. If the concentration of precursors is high enough to define a critical size smaller than that one characteristic of the red vertical line the nuclei will easily fall in the first well increasing the number of the MSCs1 belonging to the first well (we see it because the absorbance peak intensity, characteristic of MSCs1, will increase). Over time the critical size will shift over the red line to the blue one which define a critical size which is bigger than MSCs1. The particles belonging to MSCs1 will then start shrinking (their absorbance intensity peak decreases) and new nuclei belonging to MSCs2 will start forming. The process will be then repeated for the next MSCs families if present in the chemical potential landscape.

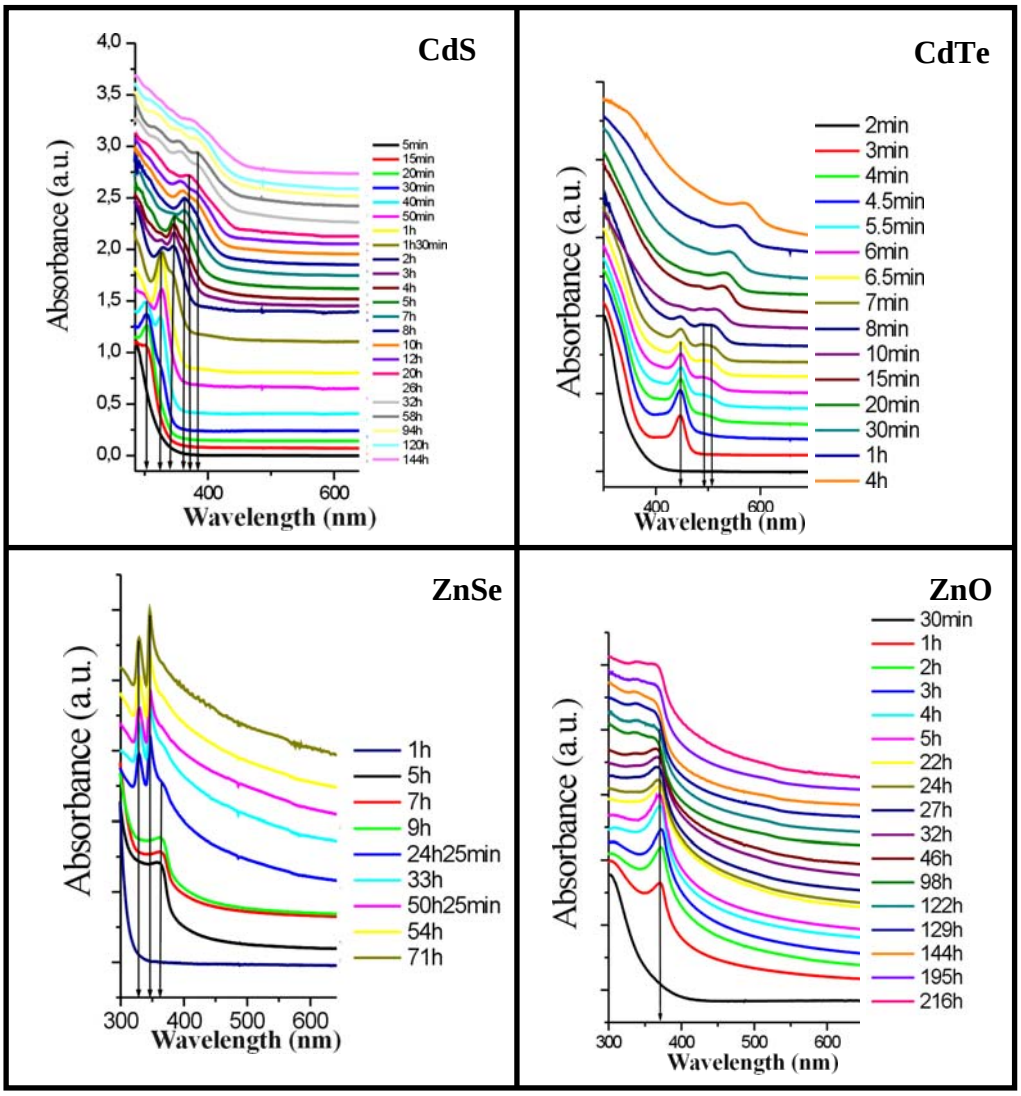

Figure III.14. *Absorbance spectra time evolution of different magic size crystals solutions. (Taken from [9])*

Both these two models might be able to describe the growth of MSCs avoiding the growth via agglomeration of smaller particle which effects were never observed in HRTEM analysis.
As introduced earlier the extension of the MSCs sequential growth to other materials is possible performing synthesis with slight changes. In Figure III.14 the temporal evolution of the MSCs absorbance spectrum of CdS, CdTe, ZnSe and ZnO is shown.
The average absorbance peak position of the MSCs belonging to these four materials are collected in Table 1 while all the other main characteristics such as HRTEM images, composition and crystalline structure can be found in [9]. The MSCs families of CdS and CdTe present similar characteristics just presented in the CdSe case and via size selective precipitation is possible to prepare solution in which the nanoparticles belong almost exclusively to one family. It is interesting to notice instead the unusual growth of the peaks in the case of the ZnSe which is characterized by the formation of a larger crystal followed by the growth of two families made of smaller nanoparticles. This type of sequential growth do not allow us to separate the families as we did in the cadmium case. We could anyway separate the bigger particles from the smallest by stopping the synthesis before they were present in solution. Considering the family of curves of Figure III.14, if we stop the synthesis after 9h it is possible to precipitate just the biggest ZnSe MSCs family avoiding the presence in solution of the smallest MSCs. The reason why the largest size MSCs family shows up before the smallest is still under investigation in our group. In [9] we proposed a model similar to that one reported in Figure III.13 with three MSCs wells in which the

weight of the one characterizing the largest size is, at the beginning of the synthesis, large enough to cover the smallest size ones. Considering a time dependent chemical potential landscape the over time evanescing importance of the largest size well would reveal the presence of the two other wells which show their increasing contribute in the absorbance spectrum (Figure III.13c). Since HRTEM images do not support an aggregation growth mechanism we do not support the possibility to have a second nucleation (see chapter II) due to the snap of the largest nanoparticles into smaller ones. It would be anyway hard to explain why the effect of a second nucleation occur after several hours from the appearance of the largest nanoparticles and not since the beginning.
In the case of ZnO (see Figure III.14) the main peak is centred at about 370nm which is actually a too long wavelength to be attributed to the ZnO for which bulk band gap is 3,3eV (about 360nm). Srikant and Clarke [10], considering the red shift of the absorbance peak reported in several papers about the fabrication of devices based on ZnO films, found that the responsible of this shift is the contribution of a valence band-donor transition at about 3.15eV. This transition can contribute to the optical absorption but can even dominate it depending on the measuring conditions. A further interesting feature of these particles is the fact that they might be doped with some carbon atoms. Carbon atoms could be present in solution cause the decomposition of the nonanoic acid which is also the oxygen provider during the synthesis.

Material	**CdS I**	**CdS II**	**CdS III**	**CdS IV**	**CdS V**	**CdS VI**
Abs Peak Position (nm)	**303,7±0,5**	**326,7±0,5**	**347±1**	**362,7±0,6**	**367±1**	**382±1**
Material	**ZnSe I**	**ZnSe II**	**ZnSe III**	**ZnO**	**CdTe I**	**CdTe II - III**
Abs Peak Position (nm)	**328,2±0,9**	**346±1,1**	**378±1,8**	**370±1,4**	**445,3±1,5**	**490,6±2,5 506±1,5**

Table 1. *Average peak position of different families of MSCs of CdS, CdTe, ZnSe and ZnO. (Taken from [9])*

The presence of carbon atoms in the ZnO lattice could enrich this semiconductive material of magnetic properties as it has been recently reported for ZnO thin films [11]. By using ZnO MSCs we a
re now trying to extend these magnetic properties from films to nanoparticles in order to synthesize nanomaterials having both semiconductive and magnetic behaviors. In the next chapter we will see the importance of synthesizing nanoparticles having as properties the combination of characteristics belonging to single materials and some of the new effects observed making effort in this direction.

References:

[1] Boon K. Teo and N. J. **A.** Sloane, *Magic Numbers in Polygonal and Polyhedral Clusters, Inorg. Chem.* **1985**, *24,* 4545-4558.
[2] A. Kasuya, R. Sivamohan, Y. A. Barnakov, I. M. Dmitruk, T. Nirasawa, V. R. Romanyuk, V. Kamur, S.V. Mamykin, K. Tohji, B.Jeyadevan, K. Shinoda, T. Kudo, O. Terasaky, Z. Liu, R.V. Belosludov, V.Sudararajan, Y. Kawazoe, *Nat. Mater.* **2004**, 3, 99.
[3] Nanfeng Zheng, Xianhui Bu, Haiwei Lu, Qichun Zhang, and Pingyun Feng, *Crystalline Superlattices from Single-Sized Quantum Dots, J. Am. Chem.. Soc.,* **2005**, 127, 11963-11965.
[4] V. N. Soloviev, A. Eichho1fer, D. Fenske, and U. Banin, *Size-Dependent Optical Spectroscopy of a Homologous Series of CdSe Cluster Molecules, J. Am. Chem. Soc.* **2001,** *123,* 2354-2364.
[5] V. N. Soloviev, A. Eichho¨fer, D. Fenske, and U. Banin, *Molecular Limit of a Bulk Semiconductor: Size Dependence of the "Band Gap" in CdSe Cluster Molecules, J. Am. Chem. Soc.* **2000,** *122,* 2673-2674.
[6] Stefan Kudera, Marco Zanella, Cinzia Giannini, Aurora Rizzo, Yanqin Li, Giuseppe Gigli, Roberto Cingolani, Giuseppe Ciccarella, Werner Spahl, Wolfgang J. Parak, and Liberato Manna, *Sequential Growth of Magic-Size CdSe Nanocrystals, Adv. Mater.* **2007**, *19*, 548–552.
[7] Pinar Dagtepe, Viktor Chikan, Jacek Jasinski, and Valerie J. Leppert, *Quantized Growth of CdTe Quantum Dots; Observation of Magic-Sized CdTe Quantum Dots, J. Phys. Chem. C* **2007,** *111,* 14977-14983.
[8] Z. Adam Peng and Xiaogang Peng, *Nearly Monodisperse and Shape-Controlled CdSe Nanocrystals via Alternative Routes: Nucleation and Growth, J. Am. Chem. Soc.,* **2002**, 124, 3343-3353.
[9] Marco Zanella, Azhar Zahoor Abbasi, Andreas Schaper and Wolfgang J. Parak, *General Approach to II-VI Semiconductor Magic Size Nanoparticles, (Submitted)*
[10] V. Srikant and D. R. Clarke, *On optical bandgap of zinc oxide*, *Journal of Applied Physics,* **1998**, 83 (10), 5447-5451.
[11] H. Pan, J. B. Yi, L. Shen, R. Q. Wu, J. Y. Lin, Y. P. Feng, J. Ding, L. H. Van and J. H. Yin, *Room Temperature Ferromagnetism in Carbon-Doped ZnO,* **2007**, PRL, **2007**, 99, 127201-1 - 127201-4.

IV. Hybrid nanocrystals

The main object of the earlier three chapters were nanoparticles made of different materials and size. Their properties depend strongly on this two parameters as we saw in the case of semiconductive nanoparticles and if we think about nanoparticles made of magnetic materials. Magnetic nanoparticles could be harvest with a magnet [3] and find interesting application in modern medicine (i.e. hyperthermia [1,2]).
Hyperthermia is an extremely interesting effect which could be used for the treatment of several diseases and cancers. It harness the energy losses as heat that a magnetic material experience in an alternating magnetic field and the sensitivity of cancer cells to temperature. In fact cancer cells can not live if their temperature is risen above 46°C while the cells of the rest of the body do. A fascinating result concerning the treatment of cancer via hyperthermia on mice was reported by Suzuki et al. [2]. They injected iron oxide nanoparticles on the tumour site of a group of mice and their temperature was risen to 46°C with an alternating magnetic field. Naturally, since the nanoparticles distribution is localized, just on the tumour site the temperature rises leaving the rest of the body at its normal temperature. Heating with this technique the tumour cells at 46°C for 30min twice let to a total regression of the cancer in 90% of the mice. This extraordinary result is now the base for tests on human being since iron oxide nanoparticles are compatible with human metabolism.
Considering then all the properties and the possible applications of nanoparticles of different materials it is natural to consider the possibility to combine many properties in a single nanocrystals. For example the combination of a semiconductive and a magnetic material in one nanoparticle could be really advantageous for several application. The magnetic part could be used for the magnetic harvesting of the nanoparticles in order to separate them from other undesired objects or for hyperthermia as seen above. The presence of a fluorescent semiconductive part on the same nanoparticle might allow us to track the nanoparticle trajectory in a given solution. This is just a simple example which motivated the development of the so called “hybrid nanoparticles” in which domains of different materials can be assembled together in a single nano-object.
With the purpose to fabricate these kind of complex structures different techniques have been developed. These techniques harness parameters like the difference between the materials lattice constants and surface reactivity. The first approach and the most used for the synthesis of nanoparticles which are the combination of two or more materials is the “seeded growth” where some nanoparticles previously synthesized are employed as “seeds” for the growth of the new structures. In the next paragraph we will introduce some examples of the application of this technique introducing even some interesting new effects discovered during the development of the synthesis of these structures.

IV.1 Synthesis of core-shell hybrid nanomaterials

When the lattice constant between two materials do not differ significantly the growth of a material on the existing cores led to the formation of core-shell structures (Figure IV.1).

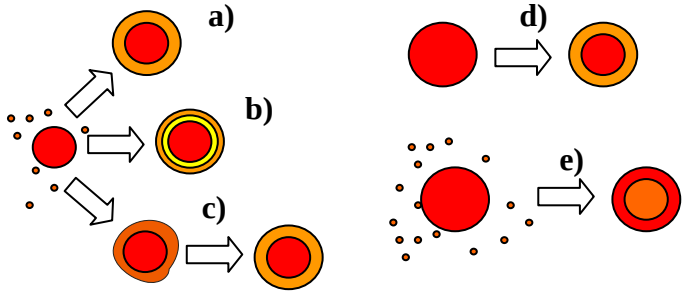

Figure IV.1. *Sketch of the most employed mechanisms for the synthesis of core-shell nanoparticles.*

The shell can be grown via addition (dropwise or fast injection) of all the needed precursors (Figure IV.1a) [4], growing alternating monolayers of different materials one after the other one (Figure IV.1b) [5]. The quality of the shell grew in this way could be improved by sample annealing if necessary (Figure IV.1c)[6]. Other ways to form a core shell structure is the redox reaction of the cores with suitable reagents which led to the conversion of the core outer layers to a shell (Figure IV.1d) [7] and the diffusion of materials into the existing cores leading to a core shell structure where the starting core material will constitute the shell of the reaction product (Figure IV.1e) [8]. This is one of the new interesting nanomaterial effects discovered accidentally during the synthesis of hybrid materials.

Most of the report concerning the growth of a shell are related to fluorescent semiconductor nanoparticles since the discovery of the enhancement of the core optical properties due to the presence of a shell [4,9]. In Figure IV.2 the absorbance and fluorescent spectra of a CdSe MSCs before and after the growth of a ZnS shell are shown. We have already seen in the previous chapter that semiconductive nanoparticles show fluorescence if properly excited. Generally cause the inevitable surface defects present on the nanopaticles the fluorescence of the cores is affected by "trap states" effects. In a nutshell the presence of defects on the nanoparticles surface (surface Cd or Se vacancies in the case of CdSe nanoparticles) led to the localisation (electron- holes traps) of those electrons which could participate to the photon emission via energy relaxation and the formation of some electron-hole energy levels (trap states) in the band gap which are responsible of the nanoparticles lower energy emission (Figure IV.2 orange curve). The reason why the surface defects are considered responsible for the trap state presence is because their effects are reduced for bigger nanoparticles which have a smaller surface to volume ratio.

Obviously the electrons-holes localisation strongly reduces the nanoparticles optical properties and it has been discovered the growth of a semiconductive shell on the cores strongly reduces these undesired effects (Figure IV.2 red curve). During the shell growth, in fact, the surface defects (vacancies) are replaced by the atoms constituting the shell. Removing the defects gets rid of the "trap states" and the optical properties of the nanoparticle are enhanced since more electron can contribute to the photon emission.

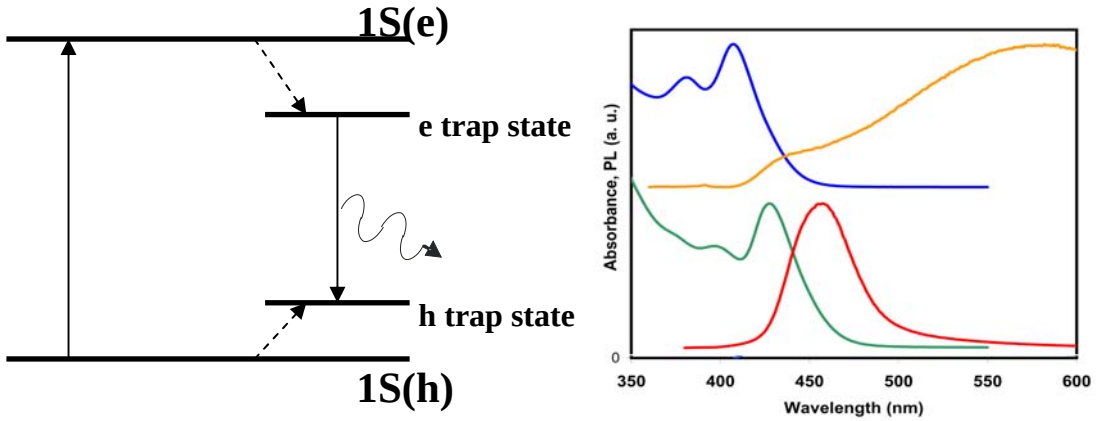

Figure IV.2. *(left) Sketch of a nanoparticles band gap. Due to the surface defects the trap states for holes (h) and electrons (e) appear into the band gap. After the excitation form the valence band (1S(h) is the valence band edge) to the conduction band (1S(e) is the conduction band edge) some electrons and holes relax into the trap state without photons emission (dashed arrows). Their recombination is responsible of the broad peak at high wavelength present in the orange curve on the right. (right) Absorbance (blue curve) and fluorescent emission (orange curve) of CdSe MSCs in chloroform. Absorbance (green curve) and fluorescence (red curve) of CdSe@ZnS core@shell nanoparticles. After the shell growth the fluorescence characteristic change considerably, the trap states emission has been removed and the band gap nanoparticle emission presents the prominent emission (taken from [10]).*

The red shift of the absorbance and fluorescence peaks of the core@shell nanoparticles is due to the lattice mismatch between the core and the shell which led to a stress in the cores crystalline structure. This kind of stress increases with the shell thickness leading to a decrease of the core optical properties. The shell growth is then stopped at the beginning of this decreasing step in order to produce sample with the best possible optical characteristics.
Other interesting results on semiconductors shell growth consider the growth of a material with a band gap smaller than that one present in the cores [11] and multishell nanoparticles. The latter can led to systems where the red shift due to the lattice mismatch is reduced and the optical properties are further enhanced [12] and display new interesting effects like the confinement of the carriers in an intermediate layer introducing the "quantum shell" effect [13].
Several other materials have been produced following the techniques described in Figure IV.1 as Co-CdSe core-shell structure [3]. This is a typical example of the system described in the beginning of this chapter. In this case the semiconductive shell make the core shell material able to express both magnetic and fluorescence characteristic even if the performances of these particles are lower than the single Co and CdSe nanoparticles.

Synthesis of hetherodimers and oligomers

Hetherodimers and oligomes nanomaterials are nanoparticles in which the different materials occupy different domains. All these domains are accessible from outside which allows the exploitation of all the different materials surfaces conversely to what generally occur with the core-shell geometry. Actually it has been reported that some reaction with the cores via diffusion through the shell are possible [14] but the presence of the shell can not allow the selective adhesion of molecules to the core surface.
One of the parameters responsible for the formation of nanoparticles with dimers and oligomers geometry is the materials surface reactivity which can be different in the different nanocrystals facets. This allows the growth of materials just on the facets where the surface reactivity allows it with the consequent formation of dimers and oligomers [15]. This anyway is not the only way used for achieving such geometries.

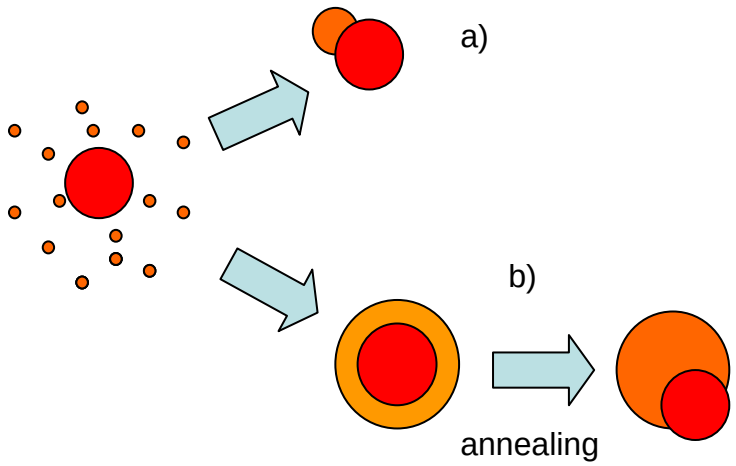

Figure IV.3. *Sketch of two of the most diffused techniques for the formations of dimers nanoparticles.*

The synthesis of dimers and oligomers by selective nucleation on a pre-existing seeds described above is pictured in Figure IV.3a. The shape of the starting seed can be different than spherical. A very interesting example of this process is the growth of gold tips on CdSe rods and tetrapods [16] which was followed by the observation of a very interesting effect of formation of CdSe rod- gold

single tip when the dropwise addition of gold precursor was prolonged over the formation of the gold–CdSe-gold nanodumbbell [17] (Figure IV.4).

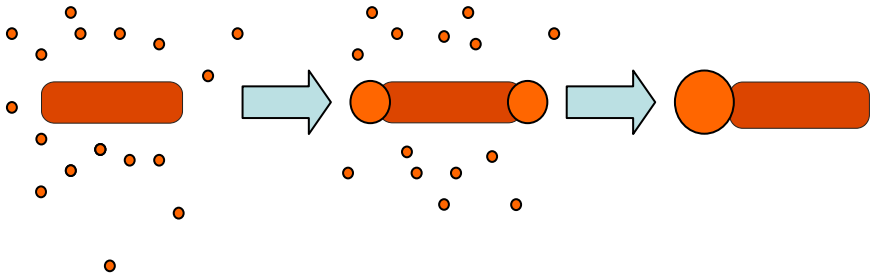

Figure IV.4. *Simple picture describing the mechanism of formation of gold-CdSe sphere-rod dimers passing by the gold-CdSe-gold dumbbell geometry starting from nanorods as seeds.*

An other approach for the formation of dimers starts with the formation of an amorphous shell around the pre-existing cores which forms a separate domain after its annealing (Figure IV.3b). This technique has been employed for the synthesis of FePt-CdS and FePt-CdSe nanodimers [18, 19, 20] which present both semiconductive and magnetic properties. For the synthesis of FePt-CdS dimers the process of Figure IV.5 was followed.

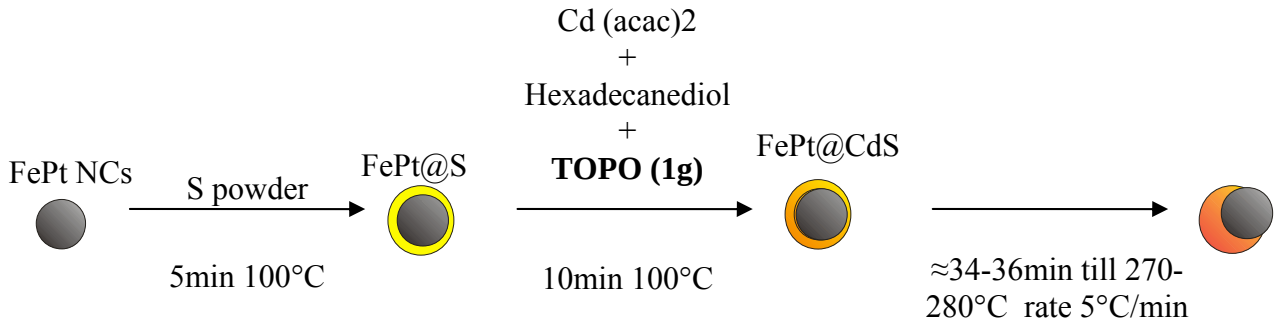

Figure 5. *Sketch of the approach used for the synthesis of FePt-CdS dimers starting from FePt nanoparticles as seeds.*

After the synthesis of the FePt nanoparticles, in the same reaction flask without purification steps, the S powder was poured and left reacting with the magnetic cores for 5min at 100°C. This step led to the formation of an amorphous S shell around the FePt nanoparticles (FePt@S) which is turned in a CdS amorphous shell with the addition of cadmium precursors (FePt@CdS). In order to stabilize the nanoparticles solution 1g of surfactant powder (tri-octyl phosphine oxide, TOPO) was added to the solution too. After the formation of the semiconductive shell the annealing of the nanoparticle led to the formation of magnetic-semiconductive dimers FePt-CdS. We recently reported [20] the extension of this process to other materials as FePt-CdSe dimers which imply the formation of FePt@Se core@shell nanoparticles which reacts with the cadmium precursor before the annealing procedure.
In Figure IV.6 the TEM micrographs of FePt-CdSe dimers is shown.

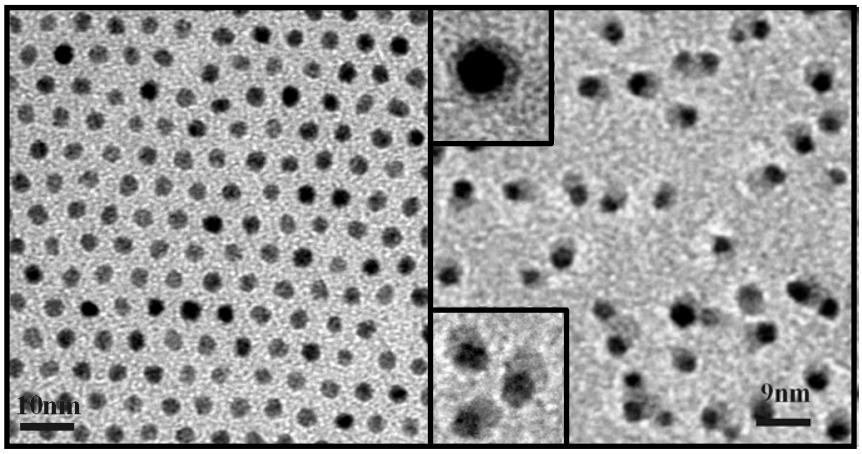

Figure IV.6. *TEM micrograph of plain FePt nanoparticles (left) and FePt-CdSe dimers (right). The dimers solution presents as byproduct even some nanoparticles in which two FePt cores are connected via a semiconductive nanoparticle. On the right the image of a FePt@CdSe core@shell nanoparticles is shown as inset along with a higher magnification of some dimers.*

In order to avoid the formation of free semiconductive nanoparticles the amorphous shell was grown reacting one shell precursor at a time with the FePt cores. The possibilities to deposit before a cadmium shell followed by the reaction with chalcogens has been reported too [19]. Extending this process to other semiconductive materials including zinc and lead chalcogens [20] not always led to formations of dimers even if the synthesis conditions (reaction temperature and annealing rate) are changed. As example, substituting the cadmium acetyl acetonate with lead acetyl acetonate in the reaction with FePt@Se nanoparticles do not lead to the formation of core@shell nanoparticles not even when the reaction occur at low temperature (35°C). The high reactivity of the lead precursors is able to etch the Se layer yielding solution with almost free FePt nanoparticles, and agglomerates of PbSe and FePt nanoparticles. XRD characterisation of the sample shows the presence of small PbPt4 nanoparticles suggesting the reaction of the lead acetyl acetonate with the platinum precursor left in solution after the synthesis of the FePt nanoparticles (Figure IV.7b).

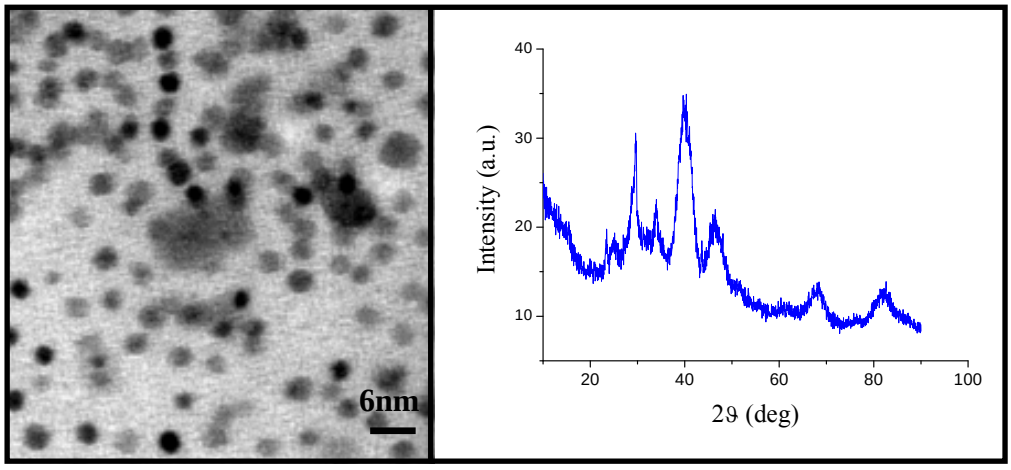

Figure IV.7. *TEM micrograph and XRD spectrum of a sample of FePt@Se nanoparticles after the reaction with lead acetyl acetonate at 35°C. The peaks between 20 and 40deg show the formation of crystalline PbSe and PbPt4.*

In the cases in which the process could led to the dimers structures (FePt-CdS, FePt-CdSe, FePt-ZnS and FePt-PbS) we observed that fluorescence emission of dimers solutions was not due to the nanoparticles but to some fluorophores synthesized in solution along with the nanoparticles.

The evidence of this problem was found comparing the fluorescence of dimers made of a different semiconductor material (Figure IV.8).

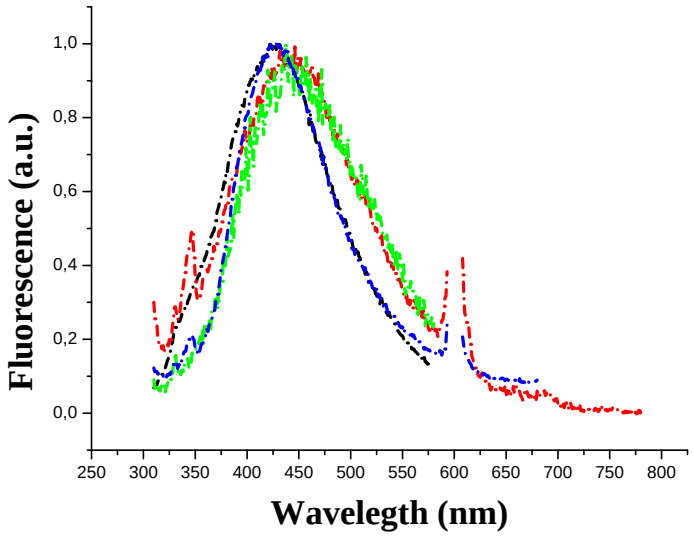

Figure IV.8. *Fluorescence spectra of different particle combinations after one round of purification from excess surfactant molecules. The samples were excited at 300 nm. The intensities of all fluorescence spectra were normalized to the same value. Black curve: FePt-CdS dimers, green curve: FePt-ZnS dimers, red curve: FePt-CdSe dimers, blue curve: aggregates of FePt-PbSe. The peak at 600 nm is an instrumental artifact at the double wavelength of excitation.*

Different semiconductive materials in fact have a different band gaps which means that even their emission band is different. The fact then that the emission bands are almost the same even if the semiconductive material is different is a clear signal that something else is responsible for the observed fluorescence, in our case one or more fluorophores.
These fluorophores can be separated from the dimers with several rounds of purification leading to no fluorescent nanoparticles solutions.
Responsible for this emission quenching is the presence of the FePt part and the trapping states created on the interface between the two domains which trap a large amount of electrons which would contribute to the emission. The quenching of fluorescent nanoparticles [16] and molecules [21] attempting to synthesize dimers has been already reported. These are all example of the fact that to synthesize nanoparticles as combination of different materials does not necessary means that the properties of the single parts are preserved. In the core/shell case the properties of the combined systems definitely enhance the material performances and make them useful for several applications. Considering the synthesis of semiconductive-magnetic dimers, despite the initial enthusiasm, the enhancement or at least the preservation of the properties of the single materials seems to be still a challenge.

References:

[1] Noriyasu Kawai, Akira Ito, Yoko Nakahara, Mitsuru Futakuchi, Tomoyuki Shirai, Hiroyuki Honda, Takeshi Kobayashi, and Kenjiro Kohri, *Anticancer Effects of Hyperthermia on Prostate Cancer Mediated by Magnetic Cationic Liposomes and Immune-Response Induction in Transplanted Syngeneic Rats*,*The Prostate*, **2005**, 64, 373-381.
[2] Suzuki M., Shinkai M., Honda H., Kobayashi T., *Anticancer Effect and Immune Induction by Hyperthermia of Malignant Melanoma Using Magnetite Cationic Liposomes, Melanoma Res.*, **2003**, 13(2), 129-35.
[3] Hyungrak Kim, Marc Achermann, Laurent P. Balet, Jennifer A. Hollingsworth and Victor I. Klimov, *Synthesis and Characterization of Co/CdSe Core/Shell Nanocomposites: Bifunctional Magnetic Optical Nanocrystals, J. Am. Chem. Soc.,* **2004**, 127, 544-546.
[4] B. O. Dabbousi, J. RodriguezViejo, F. V. Mikulec, J. R. Heine, H. Mattoussi, R. Ober, K. F. Jensen and M. G. Bawendi, *J. Phys. Chem. B*, **1997**, 101(46), 9463.
[5] J. J. Li, Y. A. Wang, W. Z. Guo, J. C. Keay, T. D. Mishima, M. B. Johnson and X. G. Peng, *J. Am. Chem. Soc.*, **2003**, 125(41), 12567.
[6] H. Kim, M. Achermann, L. P. Balet, J. A. Hollingsworth and V. I. Klimov, *J. Am. Chem. Soc.*, **2005**, 127(2), 544.
[7] J. I. Park and J. Cheon, *J. Am. Chem. Soc*., **2001**, 123(24), 5743.
[8] Taleb Mokari, Assaf Aharoni, Inna Popov and Uri Banin, *Diffusion of Gold into InAs Nanocrystals, Angew. Chem. Int. Ed.,* **2006**, 45, 8001-8005.
[9] X. G. Peng, M. C. Schlamp, A. V. Kadavanich and A. P. Alivisatos, *J. Am. Chem. Soc.*, **1997**, 119(30), 7019.
[10] Stefan Kudera, Marco Zanella, Cinzia Giannini, Aurora Rizzo, Yanqin Li, Giuseppe Gigli, Roberto Cingolani, Giuseppe Ciccarella, Werner Spahl, Wolfgang J. Parak, and Liberato Manna, *Sequential Growth of Magic-Size CdSe Nanocrystals, Adv. Mater.* **2007**, *19*, 548–552.
[11] S. Kim, B. Fisher, H. J. Eisler and M. Bawendi, *J. Am. Chem. Soc*., **2003**, 125(38), 11466.
[12] D. V. Talapin, I. Mekis, S. Gotzinger, A. Kornowski, O. Benson and H. Weller, *J. Phys. Chem. B*, **2004**, 108(49), 18826.
[13] A. Eychmuller, A. Mews and H. Weller, *Chem. Phys. Lett*., **1993**, 208(1–2), 59.
[14] P. Mulvaney, L. M. Liz-Marzan, M. Giersig and T. Ung, *J. Mater. Chem*., **2000**, 10(6), 1259.
[15] P. D. Cozzoli, T. Pellegrino and L. Manna, *Synthesis, properties and perspectives of hybrid nanocrystal structures*, *Chem. Soc. Rev*., **2006**, 35, 1195–1208
[16] Mokari, T., Rothenberg, E., Popov, I., Costi, R. & Banin, U., *Selective growth of metal tips onto semiconductor quantum rods and tetrapods*. *Science,* 2004, 304**,** 1787–1790.
[17] Taleb Mokari, Claudia G. Sztrum, Asaf Salant, Eran Rabani and Uri Banin, *Formation of asymmetric one-sided metal-tipped semiconductor nanocrystal dots and rods, Nature Materials,* **2005**, 4, 855-863.
[18] Hongwei Gu, Rongkun Zheng, XiXiang Zhang, and Bing Xu, *Facile One-Pot Synthesis of Bifunctional Heterodimers of Nanoparticles: A Conjugate of Quantum Dot and Magnetic Nanoparticles, J. Am. Chem. Soc.,* 2004, 126, 5664-5665.
[19] Jinhao Gao, Bei Zhang, Yuan Gao, Yue Pan, Xixiang Zhang, and Bing Xu, *Fluorescent Magnetic Nanocrystals by Sequential Addition of Reagents in a One-Pot Reaction: A Simple Preparation for Multifunctional Nanostructures,J. Am. Chem. Soc.,* **2007**, 129, 11928-11935.
[20] Marco Zanella, Andrea Falqui, Stefan Kudera, Liberato Manna, Maria F. Casula, Wolfgang J. Parak, *Growth of colloidal hybrid nanoparticles of fluorescent group II/VI particles on top of magnetic iron-platinum, (Accepted for publication).*
[21] E. Dulkeith, A. C. Morteani, T. Niedereichholtz, T. A. Klar, J. Feldmann, S. A. Levi, F. C. J. M. van Veggel and D. N. Reinhoudt, M. Moller, D. I. Gittins, *Fluorescence Quenching of Dye Molecules near Gold Nanoparticles: Radiative and Nonradiative Effects, Physical Review Letters,* 89 (20), 203002.

V. Conclusions and Perspectives.

An introduction to the synthesis techniques, the nucleation and growth theory and some examples of fabrication of simple and complex nanostructures has been reported. Along with some very interesting new effects discovered during the nanomaterials synthesis development we showed the sequential growth of magic size nanoparticles of different kinds of semiconductive materials. Their selective precipitation allowed the characterisation of the properties of these new materials and make them suitable for next process like shell growth, which improves their optical properties for technical-scientific applications [1,2].
In progress in our lab is the doping of semiconductive MSCs. Well known are the properties improvements due to the presence of impurities in the lattice of bulk semiconductors and their exploitation for the fabrication of electronic devices. The introduction of impurities in the lattice of a nanocrystal can strongly change their optical properties [3,4] as is possible to see in Figure V.1 where the first results concerning the doping of CdS MSCs with Hg is shown.

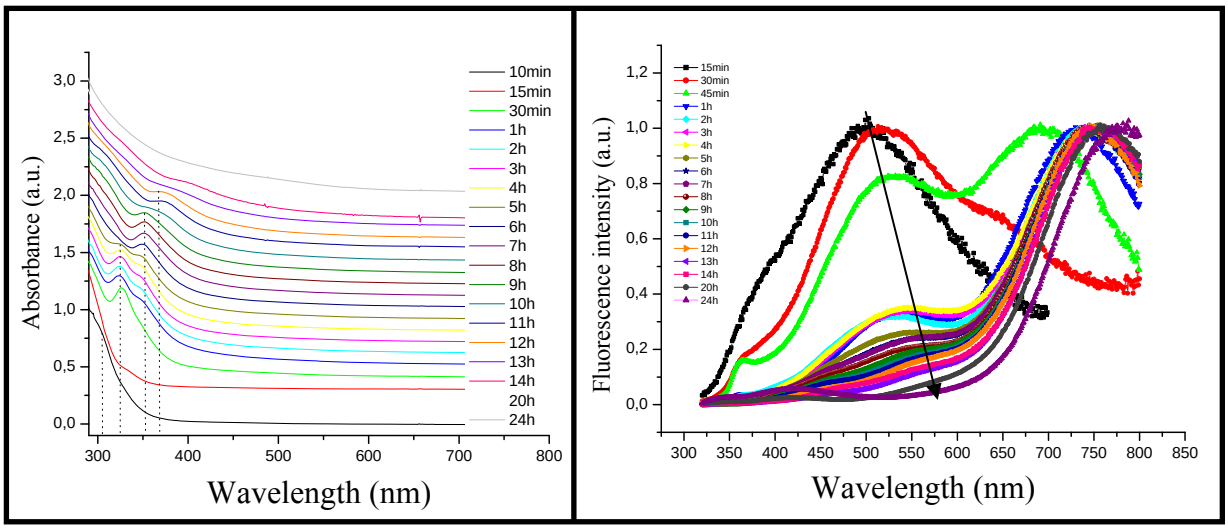

Figure V.1. *Absorbance (left) and fluorescence (right) temporal evolution of the synthesis solution of CdS MSCs doped with Hg (CdHgS MSCs). For simplicity all the fluorescent spectra have been normalized to the Hg emission peak maximum.*

The absorbance temporal evolution still shows the peaks formation and the typical sequential growth behaviour observed in the case of undoped nanoparticles synthesis. Even if in presence of mercury the peak at lower lambda (about 303nm) is less intense and the peak centred at about 373nm is a little red shifted as compared to the undoped CdS MSCs. While other peaks preserve the same position the presence of dopants in the lattice do not allows the formation of large wavelength magic size crystals (CdS V and CdS VI) . The fluorescence temporal evolution clearly shows the effect of the presence of Hg impurities in the lattice of the CdS MSCs. The Fluorescence due to the pure CdS is quenched over time (see arrow in Figure V.1) while the contribute to the emission due to the Hg ions (dark red- NIR) grows. The synthesis protocol for these particles still needs some refinements but this results tell us we are on the right track for the fabrication of doped MSCs. Their isolation via size selective precipitation is allowing us to make the first steps on the characterisation (size, composition, crystalline structure) of these new materials which could hopefully be employed in some application (i.e. NIR light emitters, nanolabels).
The application of semiconductive nanoparticles in electrochemistry experiments is now under investigation in our group [5]. A simple Sketch of the apparatus used for this kind of experiments is shown in Figure V.2. When the semiconductive nanoparticles are illuminated with light having a

proper frequency electron-hole pairs are generated and thanks to the electric field between the counter and the working electrode a photocurrent can be detected. The presence of particular enzymes or proteins in solution can increase this current which makes the system suitable as biosensor.

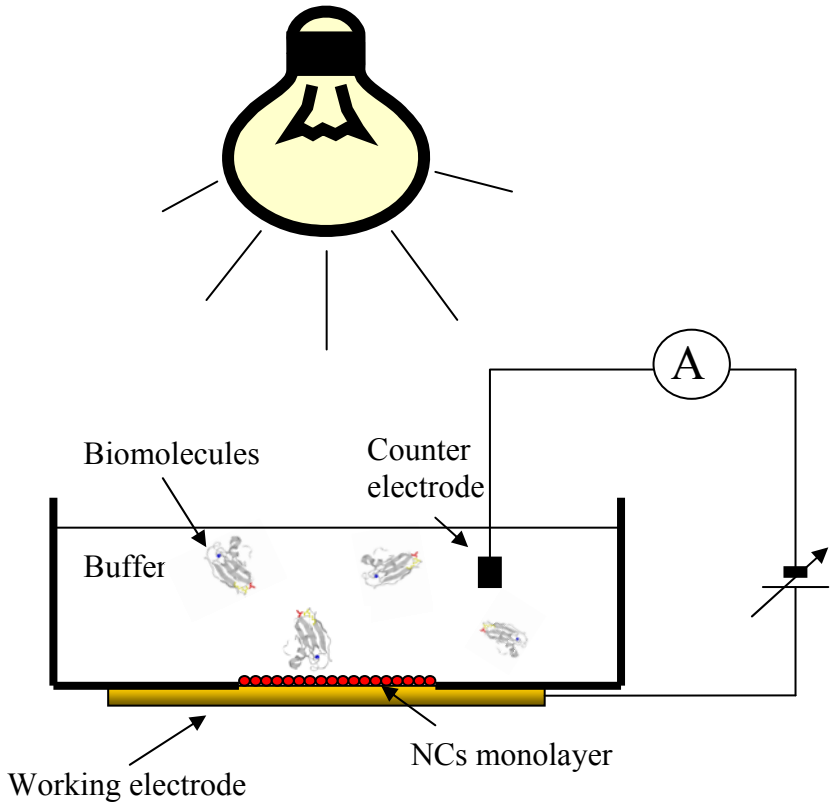

Figure V.2. *Simple sketch of the electrochemistry apparatus used in our laboratory.*

The optical properties quenching of the semiconductive nanoparticles is not important for these kind of experiments since the semiconductive part is employed just in the formations of photocurrents via photo generation of electron-hole pairs.
The presence of catalysts in contact with the solution where the biomolecules to be detected are, could change the kinetic of the electrochemical reactions.
For this reason we are performing some experiments using semiconductive-magnetic dimers at the place of the plain semiconductive nanoparticles. The presence of platinum atoms in the dimers magnetic core, combined with the electron-hole pairs generated in the semiconductive domain of the dimers could be exploited for the fabrication of high sensitive biosensors.
The application of semiconductive nanoparticles having different shape (i.e. rods or tetrapods see Figure 3 of chapter I) in the fabrication of sensors is an other interesting topic. Nanorods have already been employed for the fabrication of solar cells harnessing the higher photocurrent produced by material having this geometry compared to the nanospheres [6].
Cause their three-dimensional extension nanotetrapods will require the deposition of a layer of resin in order to avoid electrical shortcuts between the working electrode and the solution in which the biomolecules are dispersed (Figure V.3). The possibility to grow gold on the tetrapods tips reported by Mokari et al. in [7] allows to covalently anchor the nanoparticles on the di-thiol molecules monolayer present on the working electrode surface. This solution lead to the fabrication of surfaces more resistant to the resin deposition.

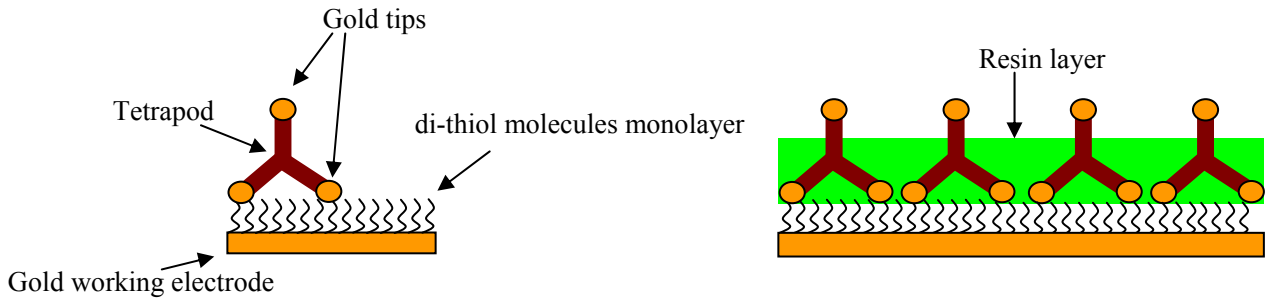

Figure V.3. *Simple sketch about the formation of nanotetrapod monolayers on the working electrode (left) and the deposition of the resin protective layer (right).*

References:

[1] Stefan Kudera, Marco Zanella, Cinzia Giannini, Aurora Rizzo, Yanqin Li, Giuseppe Gigli, Roberto Cingolani, Giuseppe Ciccarella, Werner Spahl, Wolfgang J. Parak, and Liberato Manna, *Sequential Growth of Magic-Size CdSe Nanocrystals, Adv. Mater.* **2007**, *19*, 548–552.
[2] Aurora Rizzo, Yanquin Li, Stefan Kudera, Fabio Della Sala, Marco Zanella, Wolfgang Parak, Roberto Cingolani, Liberato Manna and Giuseppe Gigli, *Blue emitting diodes based on fluorescente CdSe/ZnS nanocrystals, Applied Physics Letters,* **2007**, 90, 051106.
[3] Frederic V. Mikulec, Masaru Kuno, Marina Bennati, Dennis A. Hall, Robert G. Griffin, and Moungi G. Bawendi, *Organometallic Synthesis and Spectroscopic Characterization of Manganese-Doped CdSe Nanocrystals*, *J. Am. Chem. Soc.* **2000,** *122,* 2532-2540.
[4] D. J. Norris, Nan Yao and F. T. Charnock and T. A. Kennedy, *High-Quality Manganese-Doped ZnSe Nanocrystals*, *Nano Lett.,* **2001,** 1(1), 3-7.
[5] Ch. Stoll, C. Gehring, M. Zanella, W. J. Parak, F. Lisdat, *Photoelectrochemical signal chain sensitive to superoxide radicals in solution, (Accepted for publication).*
[6] Wendy U. Huynh, Janke J. Dittmer, A. Paul Alivisatos, *Hybrid Nanorod-Polymer Solar Cells*, *Science*, **2002**, 5564 (295), 2425-2427.
[7] Mokari, T., Rothenberg, E., Popov, I., Costi, R. & Banin, U., *Selective growth ofmetal tips onto semiconductor quantum rods and tetrapods*. *Science,* 2004, 304**,** 1787–1790.

Publications

ADVANCED MATERIALS

DOI: 10.1002/adma.200601015

Sequential Growth of Magic-Size CdSe Nanocrystals**

By *Stefan Kudera*, *Marco Zanella*, *Cinzia Giannini*, *Aurora Rizzo*, *Yanqin Li*, *Giuseppe Gigli*, *Roberto Cingolani*, *Giuseppe Ciccarella*, *Werner Spahl*, *Wolfgang J. Parak*, and *Liberato Manna**

Colloidal semiconductor nanocrystals have been exploited in several applications in which they serve as fluorophores, because of the tunability of the wavelength of the emitted light.[1–3] The possibility of exactly controlling the size of nanocrystals is of great importance in the development of these materials, as this will lead to nano-objects with well-defined and reproducible properties. Whereas this goal seems to be hard to achieve with large nanocrystals, it might be viable for clusters consisting of a few tens or hundreds of atoms, as in this size regime a handful of structures can have an exceptionally high stability and therefore would form preferentially over any other combination of atoms. This concept is already well-known for several metal clusters, as for some of them several "magic" structures exist that are formed by closed shells of atoms.[4–7] Cluster molecules that can be considered as the smallest building units of semiconductors have been investigated in the past.

As an example several tetrahedral cluster molecules based on the general formula $[E_wM_x(SR)_y]^{z-}$ (where E = S or Se; M = Zn or Cd; and R = alkyl or aryl) or similar were reported some years ago.[8,9] The series was formed only by clusters containing a well-defined number of atoms, and therefore, characterized by particularly stable structures; thus, these structures can also be termed "magic-size clusters" (MSCs). Different families of almost monodisperse CdS clusters of sizes down to 1.3 nm were reported by Vossmeyer et al.,[10] whereas CdSe MSCs were observed later in the solution growth of colloidal nanocrystals[11] and the various cluster sizes found were explained as arising from the aggregation of smaller clusters. Soloviev et al. synthesized and crystallized a homologous series of CdSe cluster molecules[12,13] (very similar in structure to those reported earlier[8,9]) that were capped by selenophenol ligands. Also in many high-temperature organometallic syntheses of colloidal CdSe nanocrystals, either the transient formation of ultrasmall, highly stable CdSe clusters was noticed,[14,15] or these clusters could be isolated using size-selective precipitation.[16,17] Recently, one type of CdSe MSC has been synthesized in a water-in-oil reverse-micelle system.[18]

Here, we report a method for controlling the sequential growth in solution of CdSe MSCs of progressively larger sizes. Each of these types of clusters is characterized by a sharp optical-absorption feature at a well-defined energy. During the synthesis, the relative populations of the different families of MSCs varied, as smaller MSCs evolved into larger MSCs. We can model the time evolution of the concentration of the various magic sizes using a modification of a continuous-growth model, by taking into account the much higher stability of the various MSCs over nanocrystals of any intermediate size.

For the synthesis of the CdSe MSCs reported here a mixture of dodecylamine and nonanoic acid was used to decompose cadmium oxide at 200 °C under an inert atmosphere. The resulting solution was stabilized at 80 °C and a stock solution of selenium in trioctylphosphine was injected into the flask. The temperature was kept at 80 °C throughout the synthesis. The low temperature ensured both slow nucleation and growth, as it produced large activation barriers for the two processes. The optical spectra of several aliquots taken during the synthesis are shown in Figure 1a. Some minutes after the injection, two well-defined absorption peaks appeared at 330 and 350–360 nm, as well as a shoulder around 384 nm. Over time, the peak at 330 nm disappeared, the peak at 360 nm kept losing intensity, the shoulder at 384 nm became a well-distinct peak, and a new peak showed up at 406 nm. Later, another shoulder appeared at longer wavelengths, which developed into a new absorption peak centered at 431 nm, followed by yet another peak at 447 nm. The position of all these peaks remained constant over time, whereas their rela-

[*] Dr. L. Manna, S. Kudera, A. Rizzo, Dr. Y. Li, Prof. G. Gigli, Prof. R. Cingolani, Dr. G. Ciccarella
National Nanotechnology Laboratory of CNR-INFM
Distretto Tecnologico – ISUFI
Via Arnesano, 73100 Lecce (Italy)
E-mail: liberato.manna@unile.it
S. Kudera, M. Zanella, Prof. W. J. Parak
Center for Nanoscience
Ludwig Maximilians Universität
Amalienstraße 54, 80799 München (Germany)
Dr. C. Giannini
CNR-Istituto di Cristallografia (IC)
Via Amendola 122/O, 70126 Bari (Italy)
Dr. W. Spahl
Department of Chemistry and Biochemistry
Ludwig Maximilians Universität
Butenandtstr. 5-13 F, 81377 München (Germany)

[**] S. Kudera and M. Zanella contributed equally to this work. This work was supported by the European projects SA-NANO (contract number STRP 013698) and OLLA (contract number IST 004607), by the Italian MIUR 297 project (contract number 13587) by the Italian project FIRB NG-lab (contract number RBLA03ER38) and by the German research foundation (DFG, Emmy Noether program). We acknowledge Dr. Davide Cozzoli, Dr. Elvio Carlino, and Hermann Gumpp for many inspiring discussions. Supporting information is available online from Wiley InterScience or from the author.

ADVANCED MATERIALS

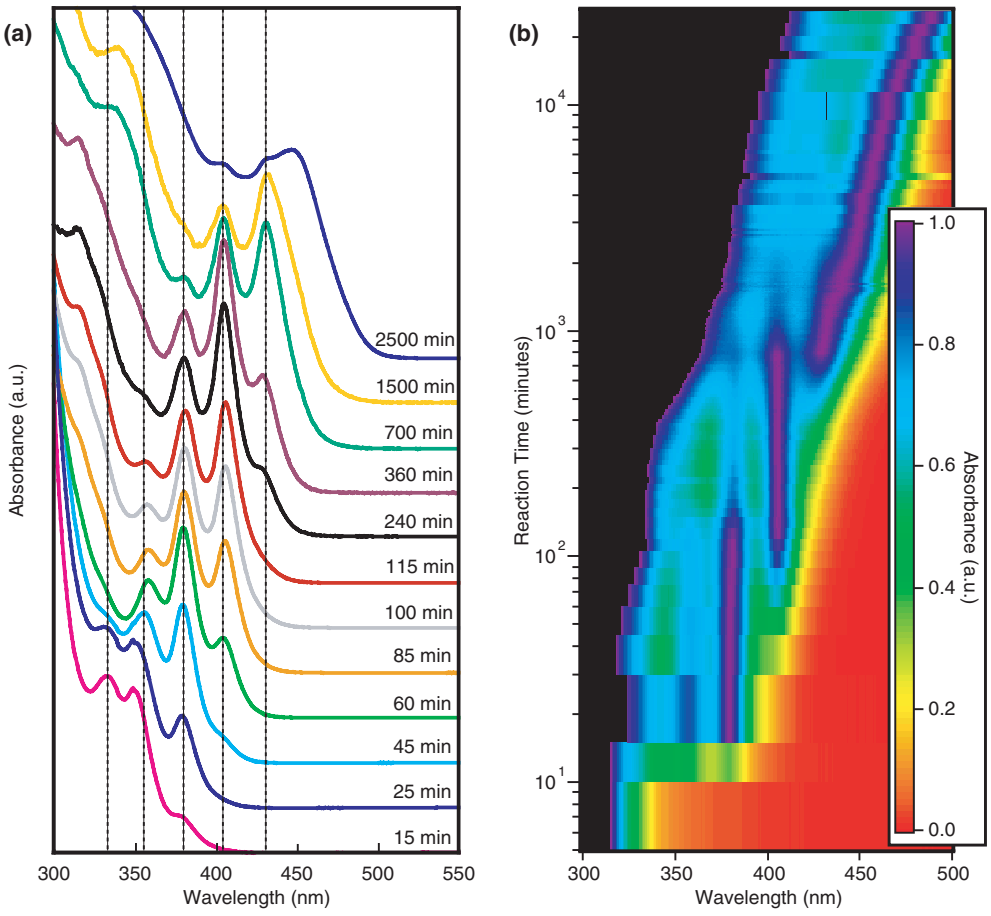

Figure 1. a) Absorption spectra of the growth solution recorded at different times and containing different populations of MSCs. b) This graph is built by stacking several horizontal stripes on top of each other, each of which corresponds to a color-coded plot of an optical-absorption spectrum, which were collected at progressively longer reaction times.

tive intensities varied so that the peak at the longest wavelength exhibited increasing intensity with respect to those at shorter wavelength, which eventually disappeared.

This behavior points to a size evolution through different families of increasingly larger clusters with high stabilities. If in fact these peaks corresponded to various excitonic transitions of a single family of cluster sizes in solution, and these clusters were steadily growing in size, then the spectral positions of the peaks would be shifting gradually towards longer wavelengths, and in addition their relative separation and their width would change (as their electronic structure is strongly sensitive to size[19]). Instead, the time evolution of the optical spectra did not point to a continuous growth but rather to the formation of new families of MSCs having larger sizes. Also the optical emission spectra of diluted samples of the growth solution showed the contribution of different families of MSCs (see Supporting Information). Over time, the average cluster size within each family remained constant, whereas the relative population of the various families changed in favor of the one with the largest size.

The graph in Figure 1b is built by stacking several horizontal stripes on top of each other, each of which corresponds to a color-coded plot of an optical absorption spectrum that had been collected at progressively longer reaction times. Each spectrum, that is, each horizontal stripe, is normalized to the intensity of its dominant peak. Spectra were recorded roughly every 15 min. On the overall plot, therefore, the wavelength is reported on the horizontal axis, whereas the reaction time is reported on the vertical axis. At shorter reaction times ($t < 10^2$ min) only a limited number of spectra could be collected and therefore the corresponding plots were replicated along the time scale until a new plot was available. As a consequence of this approach in constructing the overall plot, artificially sharp transitions are seen in it at these short times. The overall plot shows clearly the persistence over time of the peaks at 350–360 nm, 384 nm, 406 nm, and 431 nm, which therefore appear as vertical stripes. Once the various families of MSCs have evolved such that the peaks at 431–447 nm are the most intense ones, the overall spectral trends reflect rather the "continuous" size evolution of traditional nanocrystal growth kinetics.

The width of the various absorption peaks (see Fig. 1a) suggests that the size distribution within each family was quite narrow. As an example, the width-at-half-maximum of the

peak centered at 406 nm was approximately 20 nm (150 meV), which is rather close to the one reported by Kasuya et al.[18] for ultrasmall, extremely monodisperse CdSe nanoparticles prepared in reverse micelles and absorbing strongly at 415 nm (also approximately 20 nm or only slightly narrower). The overall growth kinetics did not change much neither for syntheses carried out at lower temperatures (peak widths could not be narrowed further) nor at moderately higher temperatures (peak widths were slightly broader), as in both cases the changes over time in the relative populations of the various families of MSCs followed the same trend as above.

The mechanism by which the growth of these clusters proceeded in solution is definitely fascinating. At the very simplest level, the size evolution of a nanocrystal can be thought of as being the result of a competition between the attachment and detachment of single atoms to its surface. Based on this picture, we have developed a growth model that reproduces the time evolution of the relevant absorption features of the various families of MSCs. The experimental parameters for the various families of MSCs were extracted by performing a Gaussian deconvolution of the absorption spectra. For this fit we assumed that the contribution of a single family of MSCs consisted of a narrow Gaussian function that represents the lowest exciton peak and of a much broader Gaussian that models the absorbance at shorter wavelengths (see the Supporting Information for details). The key assumption of our model states that once a cluster has grown to a magic size, such a size is so stable that no atoms can detach from it. Therefore it can only grow further, but it cannot shrink. Any cluster with a size intermediate between two magic sizes can either grow to reach the larger of the two magic sizes, or shrink to the smaller one. Figure 2 reports with different marker types the intensities of the exciton peaks from the various families of MSCs over reaction time as derived from the fit to the experimental spectra, whereas solid lines represent the trends in the intensities of such peaks as derived from the proposed growth model. This fitting procedure reflects qualitatively the actual trends in the growth of the various families of MSCs.

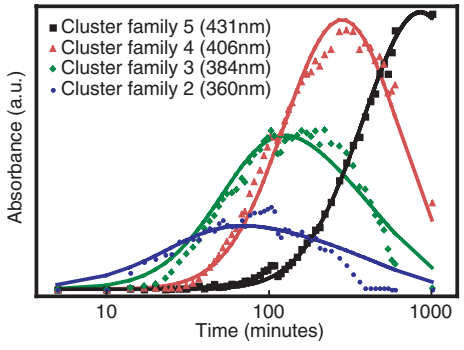

Figure 2. Development over time of the intensities of the individual absorption peaks from the various MSCs. These were extracted from the normalized optical absorption spectra, as shown in Figure 1. The families of smallest MSCs as identified from the optical spectra (those showing a peak at 330 nm) were not considered in the fit, as their absorption spectra became too weak a few minutes after their formation. Solid lines represent the fits to these trends using the proposed growth model.

A control experiment that supports our model was carried out. A synthesis of MSCs was performed and thereby the nanocrystals were extracted from the solution using precipitation and purified by repeated washing. This sample, which contained different families of MSCs, was redissolved in the same mixture of surfactants used for the synthesis of MSCs and the mixture was heated at 80 °C for several hours. Therefore, all conditions were similar to those used for the synthesis of MSCs, with the only difference being that no free monomers were present in this experiment. Optical-absorption spectra on aliquots taken from this mixture at different times during the heating did not show any remarkable variation in the intensity of the various peaks, nor any shift in their positions, indicating no further evolution in the distribution of the families of MSCs. The results of this control experiment have two important implications. One is that the various MSCs were stable and that they did not undergo any shrinking or ripening process, as opposed to the classical case of a sample containing a wide distribution of colloidal crystal sizes, for which Oswald-ripening processes dominate if there is a shortage of monomers.[20] The other is that no aggregation occurred among smaller clusters to form larger clusters. Both implications support our growth model.

The novelty of the synthetic approach developed here is that it yields only MSCs. These are not a side product of a synthesis that yields much larger nanocrystals, nor are much larger nanocrystals formed as a side product in our syntheses. Furthermore, as the growth is slow, the synthesis is reproducible and indeed it can be stopped whenever a given distribution of various families of MSCs is reached. Then, from this final solution, the largest family of MSCs present can be isolated using a size-selective precipitation. A typical set of optical absorption spectra before and after size-selective precipitation is reported in Figure 3a. The isolation of MSCs of smaller sizes from this solution is in principle possible but laborious, as they are contaminated by a small percentage of the largest MSCs.

Transmission electron microscopy (TEM) analysis on aliquots extracted from the growth solution and on size-selected samples revealed that these MSCs have roughly spherical shapes and that they are not aggregated. However, a more detailed analysis based on electron microscopy and aimed at determining average sizes and size distributions was strongly limited by the extremely small sizes of such clusters. Wide-angle X-ray diffraction analysis on size-selected samples indicated cluster sizes ranging from 1.5 to 2.0 nm for the families of largest MSCs (those absorbing strongly at 406, 431, and 447 nm, respectively) and elemental analysis of these size-selected and purified clusters showed that they are all Cd-rich, with Cd/Se ratios ranging from 1.1 to 1.3. No further structural information could be inferred from mass spectrometry, as the ionization of these samples in a matrix-assisted laser desorption ionization time-of-flight mass spectrometry (MALDI-

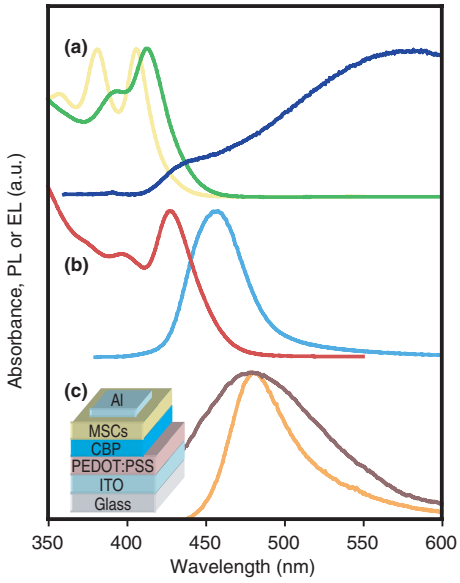

Figure 3. a) Optical absorption spectra of a sample (yellow) before size-selective precipitation, and optical absorption (green) and fluorescence spectra (blue) after size-selective precipitation. b) Optical absorption (red) and fluorescence spectra (cyan) of the CdSe/ZnS core/shell nanocrystals prepared from the size-selected sample of MSCs shown in (a). c) Photoluminescence from a film of core/shell nanocrystals (light brown) and EL (brown) from a light-emitting diode based on these nanocrystals. The inset displays the schematic layout of the EL device.

TOF-MS) setup yielded very similar fragmentation patterns, even for nanocrystals as large as 3 nm in diameter, but did not yield any clear fingerprints of the original clusters.

The synthesis of different families of MSCs is of technological interest as it yields nanocrystals that always have the same sizes and, therefore, reproducible optical properties, such as, for instance, the range of emitted light. The CdSe clusters reported in this work displayed considerable emission from trap states (see Fig. 3a) and band-edge emission was only clearly visible at very high dilutions. So, after size-selective precipitation, the absorption features were slightly broadened and red-shifted. Both effects could be the result of stripping off of some molecules from the surface of the MSCs during cleaning. This might have resulted in a partial reconstruction of the nanocrystal surface, with a concomitant variation of the overall electronic properties of the clusters.[21,22] By adding fresh surfactants, we could partially cancel this effect. Light emission from these clusters occurred almost exclusively from trap states. However, when a ZnS shell was grown on the size-selected nanocrystals, such as, for instance, on those originally absorbing at 406 nm, the resulting core/shell nanocrystals emitted only from band-edge states (Fig. 3b). The photoluminescence (PL) quantum yield from these samples varied from synthesis to synthesis (in the range between 35 and 60 %), but remained constant for each sample, even for a few months after the synthesis.

A potential application of the blue-light-emitting nanocrystals synthesized in this work is, for instance, a light-emitting diode. There have been several studies of nanocrystal-based light-emitting diodes in the last years,[23–28] but only a few devices have been reported so far in which the blue emission originated from nanocrystals.[26] We built a blue-light-emitting diode in which the active layer was a blend of the blue-light-emitting CdSe/ZnS nanocrystals, prepared as described above, and 4,4′,*N*,*N*′-diphenylcarbazole (CBP). The device, whose geometry and characteristics are displayed in Figure 3c, showed an electroluminescence (EL) peak at 485 nm, which is attributed to the emission of the CdSe/ZnS nanocrystals, in agreement with the PL spectra from a solid film of the same nanocrystals (Fig. 3c). The red-shift in the emission for the clusters in the film relative to that for the clusters in solution is attributed to the energy transfer within the sample.[29] The increase in peak width of the EL is likely to be an effect of both environmental broadening and local heating of the sample under current flow.[25]

In conclusion, we have reported a method to control the sequential growth of CdSe magic-size clusters of progressively larger sizes. We modeled the time evolution of the concentration of the various magic sizes using a slight modification of a continuous-growth model. After the synthesis, we could isolate MSCs of a given size and grow a ZnS shell on them. Finally, we demonstrated the fabrication of a hybrid organic/inorganic light-emitting diode based on these nanocrystals with blue-light emission. The concept of sequential growth of different families of MSCs reported here is of general interest and can be potentially extended to other materials, provided that suitable conditions are found to slow down the nucleation and the growth rate of the nanocrystals. In addition, we believe that this approach can be followed to synthesize more elaborate nanostructures, such as, for instance, doped nanocrystals.[30–36] A route to prepare doped nanocrystals could for instance be through the controlled formation of extremely small clusters, such as those reported in this work, but having a certain number of doping atoms already embedded in them. It might be likely, for instance, that such small cluster molecules could gain an additional stability (and therefore could be formed preferentially) if one or more "impurity atoms" were present in their structure. This possibility is currently under investigation in our groups.

Experimental

Synthesis of Magic-Size CdSe Nanocrystals: 1 g of cadmium oxide (99.99 %), 4 g of dodecylamine (98 %), and 4 g of nonanoic acid (97 %) were mixed in a three-necked flask. The flask was pumped to vacuum at 100 °C for 15 min and then heated to above 200 °C under nitrogen to decompose the CdO. The temperature was then lowered to 80 °C and 20 g of a solution of Se in trioctylphosphine (10 % in weight of Se) was injected. After the injection the temperature dropped and it was allowed to recover to 80 °C (but not higher). During the growth, 0.1 mL of the growth solution was extracted at time intervals ranging from 3 min (at the early stages of growth) to several hours (after several hundred minutes of growth) and diluted into a known amount of toluene. Therefore, all spectra could be scaled according to the dilution factor.

Size-Selective Precipitation: After the synthesis, the growth solution was transferred to a glove-box. Ethyl acetate was added to this solution, followed by methanol until a persistent cloudiness was observed. An amount of methanol ranging from 50 to 150 mL was required, depending on the distribution of MSCs present in the solution. Ethyl acetate was needed to prevent phase segregation, as methanol and trioctylphosphine have a low miscibility. This solution was centrifuged and the precipitate was washed again by adding few milliliters of ethyl acetate and methanol. The final precipitate was redissolved in toluene. By using this procedure, the largest MSCs are almost quantitatively separated from the smaller MSCs present.

ZnS Shell Growth: This was carried out following standard published procedures [37], except for the shell-growth temperature, which was set at 80 °C for the first injection and then steadily raised to 120 °C during the following injections. The starting MSCs could not resist the heating in trioctylphosphine/trioctylphosphine oxide above 80 °C for too long.

Fabrication and Characterization of the Electroluminescent Devices: Devices consisting of ITO/PEDOT-PSS/CBP:CdSe/ZnS/Al were fabricated as follows. A hole-transporting layer (100 nm) of poly(3,4-ethylenedioxythiophene):poly(styrenesulfonate) (PEDOT:PSS), used to lower the hole-injection barrier at the indium tin oxide (ITO) surface, was spin-deposited onto a cleaned ITO-coated glass substrate (120 nm, 15 Ω square^{-1}). The layer was then heated at 110 °C for 10 min to remove residual solvent. Then, a layer of a blend of CdSe/ZnS nanocrystals and CBP (100 nm) was spin-coated from a chloroform solution on the surface of the PEDOT:PSS layer. Finally, a 150 nm thick Al layer was deposited by thermal-evaporation at a pressure of 4×10^{-6} mbar (1 bar = 10^5 Pa). PL spectra were recorded on thin films and $CHCl_3$ solutions, by using a Cary Eclipse fluorescence spectrophotometer with an intense Xenon flash lamp. Absorption measurements were carried out using a Cary 5000 UV-vis spectrophotometer. The EL spectra were measured by a Spectroradiometer OL 770. All the measurements were carried out at room temperature under air.

Received: May 9, 2006
Revised: September 18, 2006
Published online: January 24, 2007

[1] X. Michalet, F. F. Pinaud, L. A. Bentolila, J. M. Tsay, S. Doose, J. J. Li, G. Sundaresan, A. M. Wu, S. S. Gambhir, S. Weiss, *Science* **2005**, *307*, 538.
[2] I. L. Medintz, H. T. Uyeda, E. R. Goldman, H. Mattoussi, *Nature Mater.* **2005**, *4*, 435.
[3] W. J. Parak, T. Pellegrino, C. Plank, *Nanotechnology* **2005**, *16*, R9.
[4] J. Pedersen, S. Bjornholm, J. Borggreen, K. Hansen, T. P. Martin, H. D. Rasmussen, *Nature* **1991**, *353*, 733.
[5] T. P. Martin, T. Bergmann, H. Gohlich, T. Lange, *J. Phys. Chem.* **1991**, *95*, 6421.
[6] T. P. Martin, *Phys. Rep.* **1996**, *273*, 199.
[7] W. Ekardt, *Z. Phys. B: Condens. Matter* **1997**, *103*, 305.
[8] G. S. H. Lee, D. C. Craig, I. Ma, M. L. Scudder, T. D. Bailey, I. G. Dance, *J. Am. Chem. Soc.* **1988**, *110*, 4863.
[9] N. Herron, J. C. Calabrese, W. E. Farneth, Y. Wang, *Science* **1993**, *259*, 1426.
[10] T. Vossmeyer, L. Katsikas, M. Giersig, I. G. Popovic, K. Diesner, A. Chemseddine, A. Eychmüller, H. Weller, *J. Phys. Chem.* **1994**, *98*, 7665.
[11] V. Platschek, T. Schmidt, M. Lerch, G. Müller, L. Spanhel, A. Emmerling, J. Fricke, A. H. Foitzik, E. Langer, *Ber. Bunsenges. Phys. Chem.* **1998**, *102*, 85.
[12] V. N. Soloviev, A. Eichhöfer, D. Fenske, U. Banin, *J. Am. Chem. Soc.* **2000**, *122*, 2673.
[13] V. N. Soloviev, A. Eichhöfer, D. Fenske, U. Banin, *J. Am. Chem. Soc.* **2001**, *123*, 2354.
[14] H. Z. Wang, A. Tashiro, H. Nakamura, M. Uehara, M. Miyazaki, T. Watari, H. Maeda, *J. Mater. Res.* **2004**, *19*, 3157.
[15] Z. A. Peng, X. G. Peng, *J. Am. Chem. Soc.* **2002**, *124*, 3343.
[16] C. B. Murray, D. J. Norris, M. G. Bawendi, *J. Am. Chem. Soc.* **1993**, *115*, 8706.
[17] A. L. Rogach, A. Kornowski, M. Y. Gao, A. Eychmüller, H. Weller, *J. Phys. Chem. B* **1999**, *103*, 3065.
[18] A. Kasuya, R. Sivamohan, Y. A. Barnakov, I. M. Dmitruk, T. Nirasawa, V. R. Romanyuk, V. Kumar, S. V. Mamykin, K. Tohji, B. Jeyadevan, K. Shinoda, T. Kudo, O. Terasaki, Z. Liu, R. V. Belosludov, V. Sundararajan, Y. Kawazoe, *Nat. Mater.* **2004**, *3*, 99.
[19] A. L. Efros, M. Rosen, *Annu. Rev. Mater. Sci.* **2000**, *30*, 475.
[20] T. Sugimoto, *Adv. Colloid Interface Sci.* **1987**, *28*, 65.
[21] A. Puzder, A. J. Williamson, F. Gygi, G. Galli, *Phys. Rev. Lett.* **2004**, *92*, 217 401.
[22] J. Frenzel, J. O. Joswig, P. Sarkar, G. Seifert, M. Springborg, *Eur. J. Inorg. Chem.* **2005**, 3585.
[23] S. Coe, W. K. Woo, M. Bawendi, V. Bulovic, *Nature* **2002**, *420*, 800.
[24] N. Tessler, V. Medvedev, M. Kazes, S. H. Kan, U. Banin, *Science* **2002**, *295*, 1506.
[25] J. L. Zhao, J. Y. Zhang, C. Y. Jiang, J. Bohnenberger, T. Basche, A. Mews, *J. Appl. Phys.* **2004**, *96*, 3206.
[26] J. S. Steckel, J. P. Zimmer, S. Coe-Sullivan, N. E. Stott, V. Bulovic, M. G. Bawendi, *Angew. Chem. Int. Ed.* **2004**, *43*, 2154.
[27] Y. Q. Li, A. Rizzo, M. Mazzeo, L. Carbone, L. Manna, R. Cingolani, G. Gigli, *J. Appl. Phys.* **2005**, *97*, 113 501.
[28] S. Coe-Sullivan, J. S. Steckel, W. K. Woo, M. G. Bawendi, V. Bulovic, *Adv. Funct. Mater.* **2005**, *15*, 1117.
[29] C. R. Kagan, C. B. Murray, M. G. Bawendi, *Phys. Rev. B: Condens. Matter* **1996**, *54*, 8633.
[30] F. V. Mikulec, M. Kuno, M. Bennati, A. D. Hall, R. G. Griffin, M. G. Bawendi, *J. Am. Chem. Soc.* **2000**, *122*, 2532.
[31] D. J. Norris, N. Yao, F. T. Charnock, T. A. Kennedy, *Nano Lett.* **2001**, *1*, 3.
[32] K. M. Hanif, R. W. Meulenberg, G. F. Strouse, *J. Am. Chem. Soc.* **2002**, *124*, 11 495.
[33] D. Yu, C. J. Wang, P. Guyot-Sionnest, *Science* **2003**, *300*, 1277.
[34] D. A. Schwartz, N. S. Norberg, Q. P. Nguyen, J. M. Parker, D. R. Gamelin, *J. Am. Chem. Soc.* **2003**, *125*, 13 205.
[35] S. C. Erwin, L. J. Zu, M. I. Haftel, A. L. Efros, T. A. Kennedy, D. J. Norris, *Nature* **2005**, *436*, 91.
[36] N. Pradhan, D. Goorskey, J. Thessing, X. G. Peng, *J. Am. Chem. Soc.* **2005**, *127*, 17 586.
[37] B. O. Dabbousi, J. Rodriguez Viejo, F. V. Mikulec, J. R. Heine, H. Mattoussi, R. Ober, K. F. Jensen, M. G. Bawendi, *J. Phys. Chem. B* **1997**, *101*, 9463.

ADVANCED MATERIALS

Supporting Information

for

Advanced Materials, adma.200601015

Sequential growth of magic size CdSe nanocrystals

Stefan Kudera[1,2†], Marco Zanella[2†], Dr. Cinzia Giannini[3], Aurora Rizzo[1], Dr. Yanqin Li[1], Prof. Giuseppe Gigli[1], Prof. Roberto Cingolani[1], Dr. Giuseppe Ciccarella[1], Dr. Werner Spahl[4], Prof. Wolfgang J. Parak[2], and Dr. Liberato Manna[1]*

[1] National Nanotechnology Laboratory of CNR-INFM, 73100 Lecce, Italy

[2] Center for Nanoscience, Ludwig Maximilians Universität, 80799 München, Germany

[3] CNR-Istituto di Cristallografia (IC), via Amendola 122/O, 70126 Bari, Italy

[4]Department of Chemistry and Biochemistry, Ludwig Maximilians Universität, München, Germany

[†] These authors have contributed equally to this work

[*] Dr. Liberato Manna
National Nanotechnology Laboratory of CNR-INFM
Distretto Tecnologico – ISUFI, Via Arnesano
email: liberato.manna@unile.it

Supporting information

1. Estimation of the concentration of the various nanocrystal families in solution

Modeling the time evolution of the absorption spectra. In order to extract the concentration of the various clusters present, we attributed to each magic cluster size an absorption spectrum similar to that of a highly monodisperse nanocrystal sample of relatively small size.[1, 2] This is roughly characterized by a strong exciton peak and by a broad, rising absorption towards shorter wavelengths. We modeled the exciton peak with a sharp Gaussian function and the broad contribution with a broad Gaussian function whose peak is at a variable position below 300 nm, in order to place it relatively far from the exciton peak. The width of this broad Gaussian is varied in order to make it vanish for wavelengths longer than those corresponding to the exciton peak position. The curves shown in Figure S1 are examples of how the modeled absorption spectra look like for two different families of MSCs.

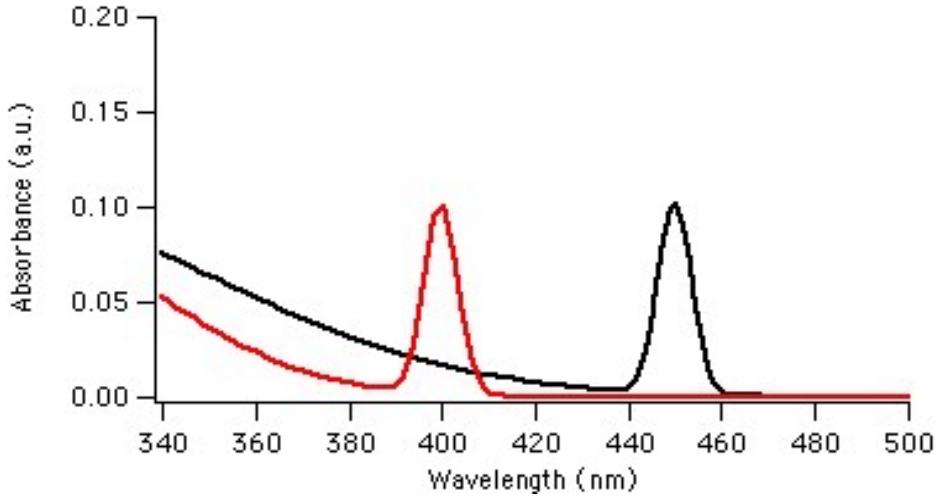

Figure S1. Modeled absorption spectra of two different families of MSCs.

The optical absorption spectrum of an aliquot extracted during the synthesis contained the contribution of several families of MSCs. Therefore, this spectrum had to be fitted with several Gaussian functions. The most important constraint of the fitting procedure was that the position of the individual peaks was kept almost constant for all spectra. The peak positions could vary only in the range of a few nanometers. Also, the peak widths could vary only by a relatively small amount. The short wavelength part of the spectrum was fitted by a single, broad Gaussian function, centered far apart from the area of interest. Through this approach, we could extract the absorption spectra of the single families of clusters. An example of this fit is shown in Figure S2.

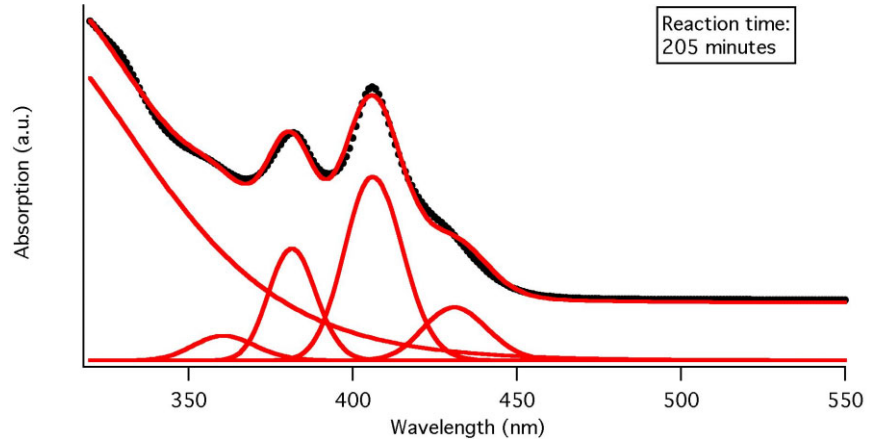

Figure S2: Example of a fit of the optical absorption spectrum (top, the black line is the experimental spectrum, the red line is the result of the fit) with a collection of Gaussian functions (bottom).

2. Simulation of the nanocrystal growth

General description of the model. The basic concept of the model is that the size evolution of a cluster in solution is a process governed by the addition (as well as by the removal) of atoms to (from) its surface. The model describes certain cluster sizes as much more stable than others, so these clusters are actually the "magic size clusters" (MSCs) that we observe in our experiments. The key assumption of the model is that once a cluster has reached such a magic size, it cannot shrink to sizes smaller than this one. Any cluster whose size is intermediate between two magic sizes is unstable and its lifetime in solution will be relatively short. Therefore, either such cluster will grow, by adding a sufficient number of monomers to reach its nearest larger magic size, or it will shrink ultimately to its nearest smaller magic size. As a consequence of this assumption, the dynamics of the growth of a cluster can be considered as unidirectional: Throughout a series of events, a cluster will evolve from one magic size to a larger magic size, and so on.

Let us consider a series of families of MSCs of increasing sizes, with the index i indicating the i^{th} family of this series (a larger i refers to a family of larger MSCs). Let us define with α_i the rate at which a MSC belonging to the i^{th} family evolves to a MSC of the $(i+1)^{th}$ family. This rate can be understood as the depopulation rate of the i^{th} family, and at same as the population rate of the $(i+1)^{th}$ family.

Let us indicate with c_i the concentration of the MSCs belonging to the i^{th} family. In general, the time evolution of c_i is described by the following differential equation:

$$\frac{\mathrm{d}c_i}{\mathrm{d}t} = \alpha_{i-1}c_{i-1} - \alpha_i c_i$$

The first term indicates the rate at which clusters of the $(i\text{-}1)^{th}$ family evolve to the clusters of the i^{th} family, while the second term describes the depopulation rate of the i^{th} family. This set of differential equations can be solved analytically. The solutions consist of a sum of differently weighted exponential decays, with decay rates equal to the rate constants α_i.

Fitting the model to the experimental results. In applying the fitting procedure to extract the concentrations of the various magic clusters, we considered only the first five families of magic clusters that we observed experimentally. The family of the smallest MSCs (denoted with the index 1) was assumed to be the one absorbing strongly at 330 nm. Therefore, the families of the larger MSCs considered here were the ones absorbing at 360 (family 2) , 384 (family 3), 406 (family 4) and 431 nm (family 5), respectively. This assignment was based on the fact that no transient peak below 330 nm was observed in our experiments.

Solution of the differential equations. In order to solve the set of differential equations we had to introduce one initial species, denoted with the index 0, whose population is not fed by any smaller clusters. This species was assumed to be the only family present in the solution at time t=0. Therefore this species can be regarded as the subset of monomers that evolves into MSCs. More importantly, the rate of depopulation of this species, which is equal to the rate of population of the family of the smallest MSCs (family 1), can be interpreted as the nucleation rate in the system.

Estimation of the extinction coefficients. In order to fit the optical absorption data reported in Figure 2 of the manuscript, we had to take into account the fact that the individual families of MSCs have different extinction coefficients. Unfortunately, reliable experimental data exists only for larger clusters. For instance, the calibration curve reported by Yu and co-workers[3] is reliable only for nanocrystals with diameters down to 2 nm. However, as we were interested only in the relative concentrations of the various MSCs in solution, we decided to set the extinction coefficient of the largest MSCs equal to an arbitrary value, and assumed that the extinction coefficients of all MSCs depend linearly on the spectral position of their exciton peak. We were able to fit accurately the time dependence of the optical spectra (Figure 2 of manuscript) even if we varied the slope of this linear dependence over a wide range. The only constraint was that the extinction coefficient ε of the smaller clusters had to be larger than the extinction coefficient of the larger clusters. For the maximum slope that we considered, the extinction coefficient of the smallest MSCs (those absorbing at 360 nm) was 6.6 times larger than that of the MSCs absorbing at 431 nm. For the minimum slope, this was only 1.5 times larger. Such trends in the extinction coefficients are in qualitative agreement with those reported by Soloviev and co-workers.[4]

3. Fluorescence spectra of MSCs

Multimodal distributions in fluorescence. In addition to optical absorption spectra, the presence of different families of MSCs in the growth solution can be inferred from the fluorescence spectra of diluted aliquots. Figure S3 reports a set of fluorescent spectra (a) and of absorption spectra (b) for aliquots extracted at different times during the growth and diluted in toluene. In order to be able to record fluorescent spectra that showed significant emission from band-edge states, the samples had to be significantly diluted, such that for instance the optical density at the exciton peak centred at 406 nm (in absorption) was well below 0.1. In these experiments, the excitation wavelength was peaked at 400 nm.

In principle, a diluted solution containing a sample of fluorescent nanocrystals with a multimodal distribution of sizes would show distinct fluorescence peaks, each corresponding to the band-edge emission from a subset of nanocrystals sizes, if excited with a radiation having an energy higher than all the band gaps present. Indeed, the fluorescence spectra of figure S3 clearly show the contribution from two distinct peaks, whose weight varies over the synthesis in favour of the peak centered at longer

wavelengths, as this is clearly due to a increasing enrichment in the population of the family of largest MSCs during the synthesis run.
Each of the fluorescence spectra reported in Figure S3(a) was fitted with two Gaussians functions, one centered at 528-532 nm (this corresponds to the emission from the family of MSCs absorbing at 406 nm), and the other one centered at 550-552 nm (this corresponds to the emission from the family of MSCs absorbing at 431 nm). The peak heights of the two Gaussian functions for the various spectra are reported in Figure S3(c). As the fluorescence quantum efficiency for the different families of MSCs is not known, we cannot estimate the relative population of the two families of MSCs from this interpolation, so that the trends reported in the left plot of figure S3 are simply indicative of depletion, over time, of the smaller family of MSCs in favour of the larger family. Nevertheless, one should notice that the larger family of MSCs shows a significant contribution in the fluorescence spectrum even when in absorption its contribution is still low (therefore when the population of this family is still relatively small). Consequently, we can easily infer that in this sample the larger MSCs have a much higher fluorescence quantum yield than the smaller MSCs.

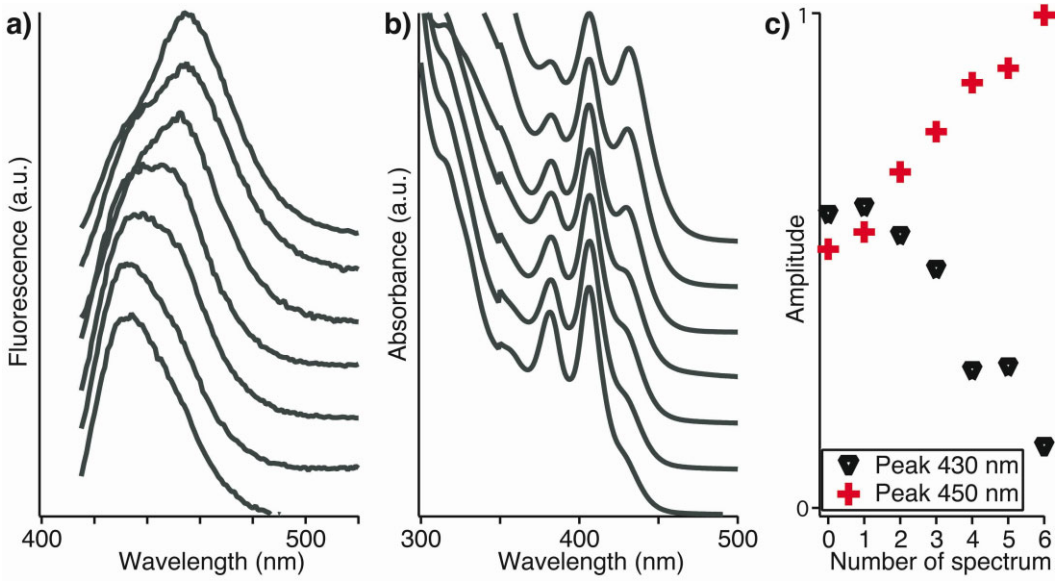

Figure S3: Fluorescence spectra (a) and the corresponding absorption spectra (b) of aliquots extracted from the growth solution at different stages of the synthesis. Spectra recorded at later stages of the reaction are shifted vertically. The fluorescence spectra are normalized to the maximum intensity, the absorptions are normalized to the amplitude of the peak at 406nm. **(c)** Trends in the relative amplitudes of the two Gaussians functions used to fit the fluorescence spectra shown in (a).

Band-edge and trap emission. One remarkable aspect of the fluorescence spectrum from a solution of MSCs is that at concentrations of MSCs higher than the ones discussed in the previous section, for instance when the optical density of the solution is around 0.2 at 406 nm, this is dominated by a broad band that spans the whole visible range (see for instance the spectrum 1 of Figure S4 or the one shown in Figure 5 of the paper). This band can be attributed to emission from trap states. However, when this solution is diluted further (roughly by a factor of 10-20) the band-edge fluorescence increases in intensity over the broad band, as can be seen in the spectra 2 and 3 of Figure S4.
To our opinion, it is unlikely that the almost complete suppression of band edge emission from moderately concentrated samples is due to some self-absorption effect, since at optical densities around 0.2 self-absorption should be still negligible. On the other hand, we know that the solution of MSCs is

contaminated by several un-reacted chemical species and surfactants, which might be adsorbed to the surface of MSCs and which might somehow suppress their band-edge emission. This effect should be less relevant at higher dilutions. This interpretation is however only speculative and more detailed studies are under way in our groups.
At wavelengths below 400 nm the dominant contribution to the fluorescence spectra is the emission from toluene, which takes place between 330 nm and 390 nm. In the range around 600 nm and above in addition to the original signal we find as a main feature the replica of the scattered incident excitation light (peaked at 600 nm), and the replicas of any signal between 300nm and 400nm. This becomes more obvious in spectra 3 and 4.

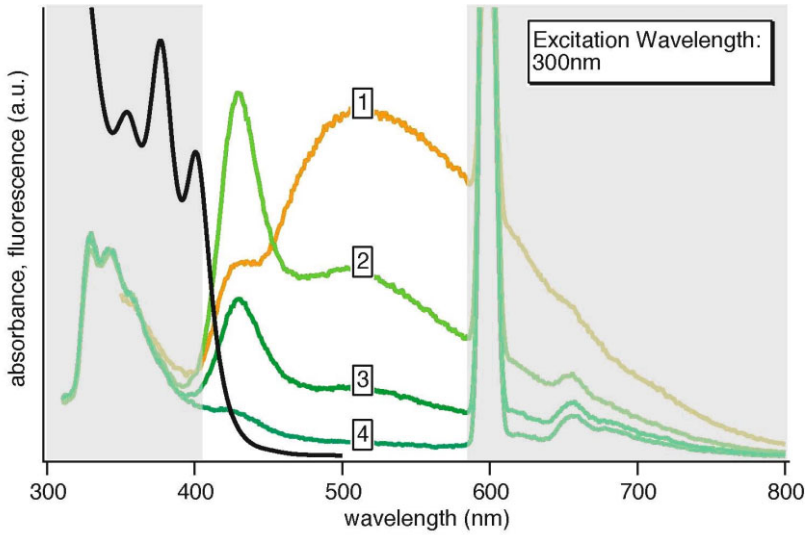

Figure S4: Series of fluorescence spectra (coloured) from the same sample of MSCs in toluene (absorption spectrum in black) but at different concentrations. The concentration of MSCs is reduced gradually from spectrum 1 to spectrum 4 by addition of toluene. The concentration used for spectrum 1 is slightly lower than that used for the spectrum shown in Figure 5a of the paper.

4. Size Selective Precipitation

When the synthesis of MSCs is stopped, the growth solution contains a given distribution of various families of MSCs. In principle, in order to isolate the various families of magic size clusters, a so-called "size selective precipitation" can be carried out, a method that is widely used to isolate monodisperse nanocrystals from a batch containing a broad distribution of sizes. The idea behind this type of separation is that nanocrystals are coated with hydrophobic stabilizing molecules, which cause them to be soluble in non-polar solvents. In a non-polar solvent (such as toluene), surfactant-coated nanocrystals are stabilized by means of hydrophobic interactions between the tails of the surfactant molecules coating the nanocrystals' surface and the solvent molecules (surfactant-solvent interactions). In addition, the inorganic cores of the nanoparticles cannot touch each other as they are ultimately stabilized by the hydrophobic layers of adjacent nanocrystals. If a polar solvent (such as methanol) is gradually added to this solution, the surfactant-solvent interactions are progressively disrupted. As soon as a certain threshold of solvent polarity has been crossed, the nanocrystals start aggregating. This happens because the hydrophobic interactions among the surfactant tails of different nanocrystals (surfactant-surfactant interactions) become much more favourable than the surfactant-solvent interactions. As a consequence of this aggregation, the nanocrystals start precipitating from the

solution. Since larger nanoparticles have a larger radius of curvature than smaller crystals, inter-particle aggregation between larger particles will be significant already in a moderately polar solution. Upon addition of a polar solvent, the larger nanoparticles precipitate first, whereas the smaller particles are still soluble. When large particles are precipitated, the solution is centrifuged so that the larger nanoparticles settle down as a compact precipitate, whereas the smaller ones remain in the solution. The precipitate is then separated from the solution that now contains only the smaller particles (the supernatant). Finally, the precipitate is re-dissolved in a fresh organic solvent, yielding a solution that contains only the largest nanoparticles from the original sample. This process can be applied again to the supernatant obtained from the centrifugation, and so on, so that fractions with different nanoparticles sizes can be obtained form a starting batch of nanocrystals.
In the present case of a solution containing different families of MSCs, the first step of the size-selective precipitation procedure aims at isolating the largest family of MSCs present. Typical optical absorption spectra of an aliquot of the growth solution prior to size selective precipitation, and of the corresponding size-selected largest MSCs, for syntheses stopped at different stages of the growth, are reported in Figure S5.

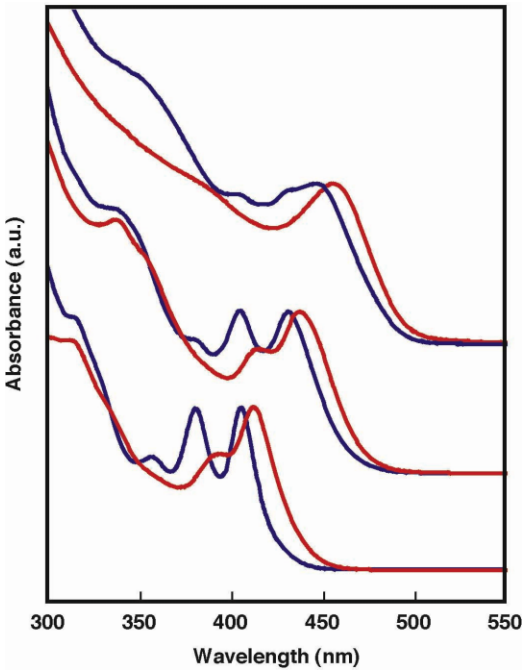

Figure S5. Optical absorption spectra of an aliquot from the growth solution prior to size selective precipitation, and of the corresponding size-selected largest MSCs, for three syntheses stopped at different stages of the growth. The spectrum of each solution before size selective precipitation (diluted in toluene) is reported in blue, while the spectrum of the size-selected largest MSCs, re-dissolved in toluene, is shown in red. The possible reason for the red shift in the absorption spectra of the size-selected samples is discussed in the main paper.

One general limitation of the size selective precipitation is that such a separation procedure is not quantitative and therefore a sample of size-selected nanocrystals is always contaminated by a small fraction of nanocrystals having significantly different sizes. This limitation is particularly critical for the separation of different families of MSCs and this can be seen clearly in Figure S6. The figure reports, for two different syntheses (a, b), the optical absorption spectra of an aliquot from the growth solution prior to size selective precipitation (top), and of the corresponding supernatant solution as well as the solution containing the size-selected, largest MSCs (bottom).

In both cases, one can notice that the solution containing the size-selected largest MSCs is contaminated by a tiny fraction of smaller MSCs. However, more critical is the contamination of the supernatant by the family of largest MSCs (so the precipitation of that family was not quantitative). Consequently, a new size selective precipitation carried out on this supernatant solution yields a precipitate that is certainly richer in the MSCs with intermediate size, but that contains inevitably fractions of both larger and smaller MSCs.

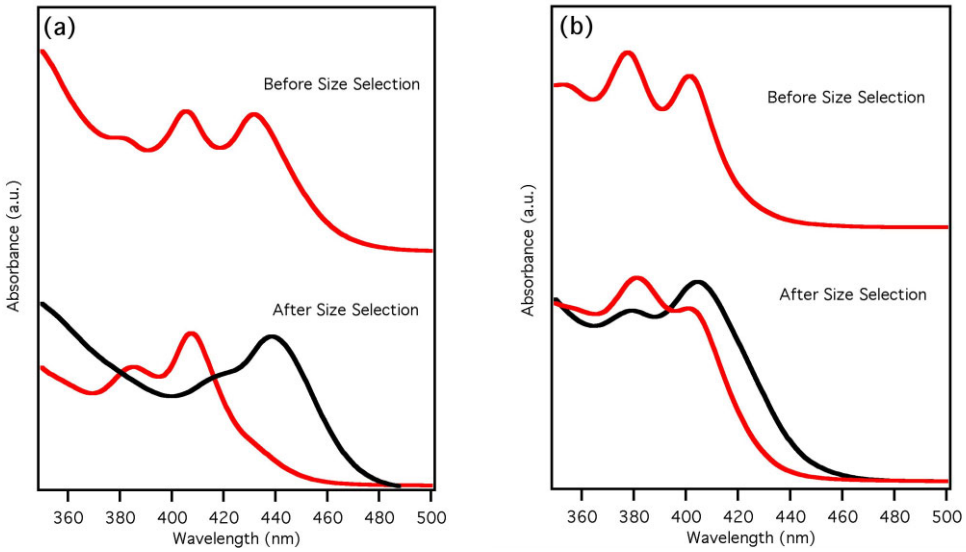

Figure S6: Exemplary optical absorption spectra of precipitate and supernatant solutions after size-selective precipitation. The upper spectra are recorded from the growth solution before size-selective precipitation. The lower spectra are those of the precipitate, i.e. the largest MSCs, (black) and of the supernatant (which contains mainly the families of smaller MSCs, red).

The results of these experiments therefore show that the isolation of a sample that contains virtually only one family of MSCs may be quite laborious. In addition, the size selective precipitation of magic size nanocrystals requires large amounts of methanol, and therefore becomes increasingly unpractical for isolating smaller MSCs from a starting batch. Moreover, MSCs of extremely small sizes, such as those absorbing below 400 nm, cannot be precipitated even by large additions of methanol (several hundreds of ml). As a consequence of these intrinsic difficulties, we found out that it is more favorable to simply carry out a synthesis and stop it when the required family of MSCs is the one present with the largest size. This family will be easy to isolate and will contain as contaminants only smaller MSCs.

5. Elemental analysis and Mass spectrometry

An inductively coupled plasma atomic emission spectrometer (Varian Vista AX) was used to investigate the elemental composition of the nanocrystals. Samples were dissolved in HCl/HNO_3 3:1 (v/v) by using a CEM "MARS 5" microwave digester. For a control experiment, elemental analysis on large CdSe nanocrystals (6 nm diameter) yielded a Cd:Se ratio equal to 1.06, in close agreement with the values reported earlier on large CdSe nanocrystals with the aid of other techniques.[5] Elemental analysis of size-selected and purified clusters (for instance those absorbing strongly at 406, 431 and 447 nm, respectively) showed that they are all Cd-rich, with Cd:Se ratios ranging from 1.1 to 1.3 (see

also table 1 at the end of the supporting information). These findings are in accordance with previous work, as for instance Rosenthal and co-workers found that CdSe nanocrystals are in general Cd-rich.[6] Mass Spectra were recorded on a MALDI/TOF mass spectrometer (Bruker Daltonics autoflex II) without use of a matrix substance. A sample solution was deposited on an anchor chip target plate, dried at ambient temperature and then ionised. Mass spectra of MSCs absorbing at 431 nm and 447 nm, as well as of larger nanocrystals (of roughly 3 nm in diameter) showed that the ionization of all these samples yields naked $(CdSe)_{13}$, $(CdSe)_{33}$ and $(CdSe)_{34}$ clusters, regardless of the starting type of cluster (Figure S7). This indicates that a complete stripping off of surfactant molecules occurs from the surface of the nanocrystals, and that fragmentation of the MSCs could not be avoided, even with such a soft ionisation source as the one used in MALDI/TOF. Similar spectra had been observed previously, with the same technique, on CdSe MSCs prepared in reverse micelles.[2] Such clusters represent very stable aggregates of atoms in the gas phase, as already postulated and observed for similar systems (i.e. ZnS[7]). As these clusters have no direct relation with the CdSe MSCs synthesised in solution, we deduce that the latter might have a rather different structure. Mass spectra on smaller MSCs, those absorbing at 406 nm, did not show any of the characteristic peaks of the $(CdSe)_{13}$, $(CdSe)_{33}$ and $(CdSe)_{34}$ clusters. We deduce therefore that the stripping off of surfactants from these smaller MSCs and their fragmentation leads to the formation of clusters that are even smaller than the smallest "magic" $(CdSe)_{13}$ clusters observed in the gas phase.

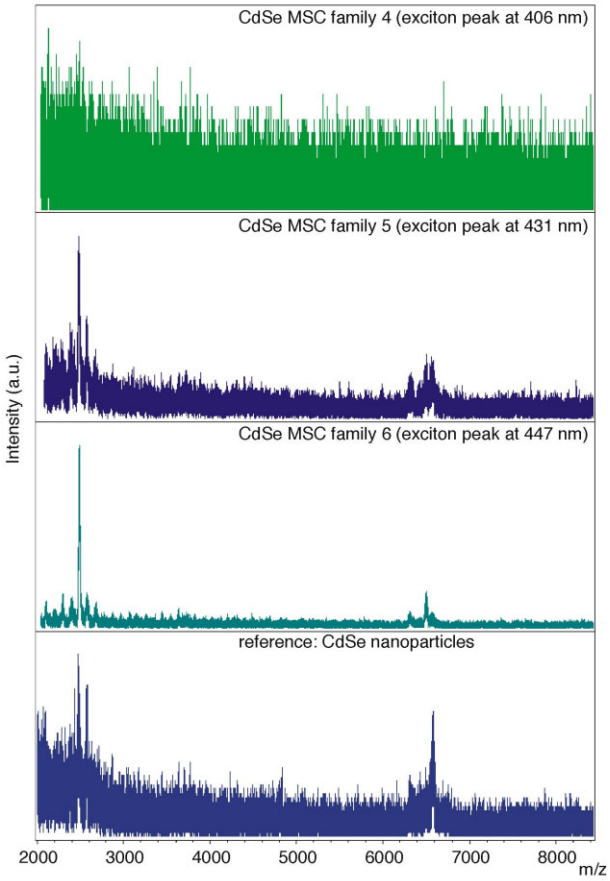

Figure S7. Mass spectra samples of three different MSC families and of a reference sample (bottom) which is based on CdSe nanocrystals having a diameter of about 3 nm.

6. X-ray diffraction spectra

X-ray diffraction spectra were collected with a D8 Bruker diffractometer equipped with a Goebel mirror and a two-bounce V-groove monocromator on the primary beam and a scintillator counter as detector. Samples were deposited on miscut silicon and measured in reflection geometry. The diffraction spectra of these size-selected clusters resemble a zinc-blende like structure. However, for clusters with diameters in the 1-2 nm range, as those reported here, the ratio of surface-to-volume atoms can exceed 50%, adding important surface stress contributions that can strongly affect the internal structure of these clusters.[1, 2, 8, 9] Therefore, the present data cannot be used to fully identify the correct structural model of these clusters. Work is in progress to carry out diffraction experiments with a synchrotron source, in order to possibly distinguish among several structural models.

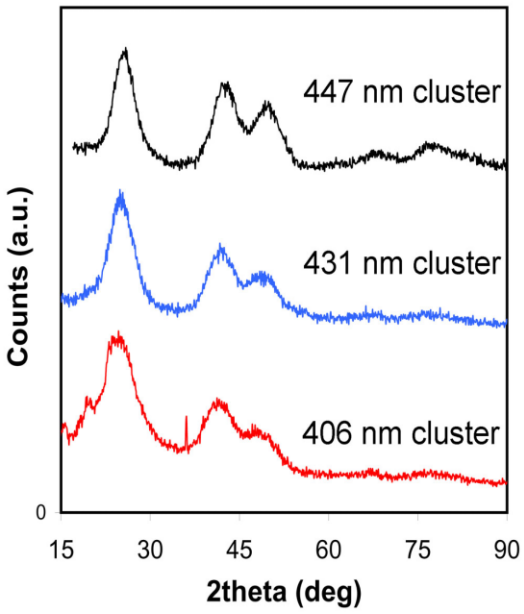

Figure S8. Wide angle, XRD spectra of three different size-selected families of MSCs.

7. Transmission electron microscopy analysis

The samples for transmission electron microscopy (TEM) were prepared by dispersing dilute solutions of nanocrystals onto carbon-coated copper grids. Low-magnification TEM images were recorded on a Jeol Jem 1011 microscope operated at 100 KV. TEM observations were particularly difficult due to extremely small size of such clusters, for which the contrast variation under the beam often did not differ sufficiently enough from the normal fluctuations of the carbon support film. In the case of samples absorbing at 406 nm, which have a size around 1.5-1.6 nm (close to the resolution limit of the microscope) we did not succeed to identify clearly the particles. Figure S9 reports TEM micrographs of two different aliquots extracted at different times during the growth, one in which the largest MSCs present are those absorbing at 431 nm (left), and the other in which largest MSCs present are those absorbing at 447 nm (right). On these images it is not possible to carry out a reliable statistical analysis that reveals the relative population of the various families of MSCs, neither we could determine their sizes with an acceptable margin of error. One reason is the limited resolution of the instrument, as the

uncertainty in the size measurement on these images is definitely higher than the separation of two adjacent sizes. Also, as said before, at such small sizes the contrast variation of the carbon support itself introduces critical artefacts in the analysis. Despite these limitations, the TEM images show that MSCs are well dispersed (no aggregation is seen) and that they have a roughly spherical morphology.

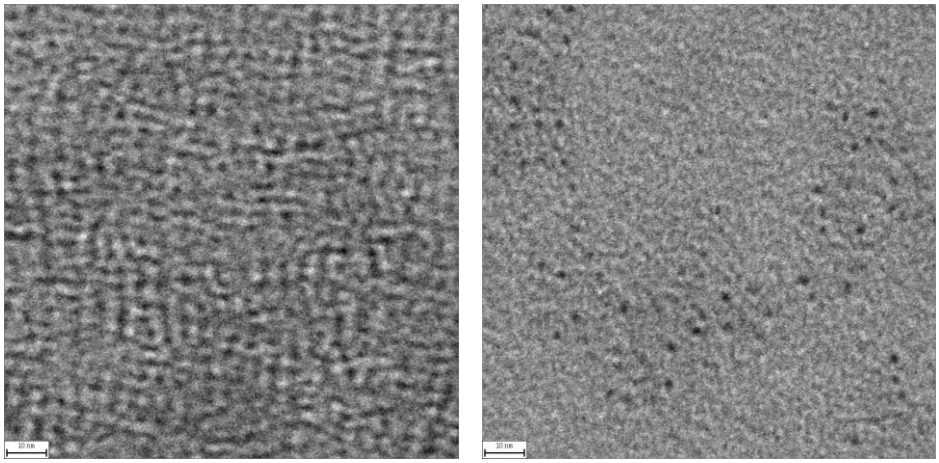

Figure S9: Transmission electron micrographs of a sample with the first absorption feature centred at 431 nm (left) and of a sample with the first absorption feature centred at 447 nm (right). The scale bar is 10 nm.

Peak position (nm)	Diameter (Peng)[3] (nm)	Calculated number of atoms	Cd:Se ratio from elemental analysis
330	0,898	14	-
360	1,185	31	-
384	1,410	53	-
406	1,606	78	1.10 - 1.22
431	1,817	113	1.28 - 1.29
447	1,929	136	1.24 - 1.26

Table 1. Comparison of experimental data with data from the literature. Starting from the measured peak position in the optical absorption spectra of aliquots extracted from the growth solution (Column 1), and by assuming clusters with spherical shape, we estimated a cluster diameter using the calibration curve reported by of Yu co-workers[3] (Column 2) and the number of atoms in each cluster (Column 3). Column 5 reports, for each size-selected family of clusters, the Cd:Se ratio as derived from the elemental analysis.

References

[1] C. B. Murray, D. J. Norris, M. G. Bawendi, *J. Am. Chem. Soc.* **1993**, *115*, 8706.
[2] A. Kasuya, R. Sivamohan, Y. A. Barnakov, I. M. Dmitruk, T. Nirasawa, V. R. Romanyuk, V. Kumar, S. V. Mamykin, K. Tohji, B. Jeyadevan, K. Shinoda, T. Kudo, O. Terasaki, Z. Liu, R. V. Belosludov, V. Sundararajan, Y. Kawazoe, *Nat. Mater.* **2004**, *3*, 99.
[3] W. W. Yu, L. H. Qu, W. Z. Guo, X. G. Peng, *Chem. Mat.* **2003**, *15*, 2854.
[4] V. N. Soloviev, A. Eichhofer, D. Fenske, U. Banin, *J. Am. Chem. Soc.* **2000**, *122*, 2673.
[5] J. E. B. Katari, V. L. Colvin, A. P. Alivisatos, *J. Phys. Chem.* **1994**, *98*, 4109.
[6] J. Taylor, T. Kippeny, S. J. Rosenthal, *J. Cluster Sc.* **2001**, *12*, 571.
[7] T. P. Martin, *Phys. Rep.-Rev. Sec. Phys. Lett.* **1996**, *273*, 199.
[8] A. Puzder, A. J. Williamson, F. Gygi, G. Galli, *Phys. Rev. Lett.* **2004**, *92*, art. n. 217401.
[9] J. Frenzel, J. O. Joswig, P. Sarkar, G. Seifert, M. Springborg, *Eur. J. Inorg. Chem.* **2005**, 3585.

Blue light emitting diodes based on fluorescent CdSe/ZnS nanocrystals

Aurora Rizzo,[a),b)] Yanqin Li, Stefan Kudera, and Fabio Della Sala
National Nanotechnology Laboratory (NNL), CNR-INFM, Università degli Studi Lecce, Via per Arnesano Km 5, 73100 Lecce, Italy

Marco Zanella and Wolfgang J. Parak
Center for Nanoscience, Ludwig Maximilians Universität, Amalienstraße 54 80799 München, Germany

Roberto Cingolani, Liberato Manna, and Giuseppe Gigli[c)]
National Nanotechnology Laboratory (NNL), CNR-INFM, Università degli Studi Lecce, Via per Arnesano Km 5, 73100 Lecce, Italy

(Received 20 September 2006; accepted 28 November 2006; published online 30 January 2007)

The authors report on the blue electroluminescence from CdSe/ZnS core/shell nanocrystals prepared from ultrasmall, magic size CdSe clusters that have a diameter of less than 2 nm. The light emitting device consists of an active layer of nanocrystals blended with 4,4′,*N*,*N*′-diphenylcarbazole and an evaporated electron transporting/hole blocking layer made of 2,9-dimethyl-4,7-diphenyl-1,10-phenanthroline. A blue, stable electroluminescence at 485 nm from the hybrid device was observed, in good agreement with the photoluminescence spectra of a solid film of the same nanocrystals used for the device. © *2007 American Institute of Physics*.
[DOI: 10.1063/1.2426899]

Over the last few years, colloidal semiconductor nanocrystals, also termed as colloidal quantum dots (QDs), have attracted much interest because of their high potential for optoelectronic applications such as organic light emitting diodes (OLEDs)[1–3] and solar cells[4]. The appealing features of these materials, when properly synthesized, are their high fluorescence efficiency,[5] their narrow band emission,[5] their chemical stability,[6] and their tunable light emission. Among the various types of fluorescent colloidal nanocrystals, core/shell CdSe/ZnS nanocrystals are of peculiar interest for practical applications due to the possibility to finely tune their emission wavelength in the visible spectrum by varying their size.[5,7]

Different approaches have been reported so far for the fabrication of light emitting diodes (LEDs) based on colloidal QDs. Hybrid organic/inorganic LEDs, for instance, were fabricated using host/guest systems consisting of a polymer doped with CdSe or CdSe/ZnS nanocrystals.[1] Bilayer structures were also reported which were based on a hole transporting layer made of conductive polymers and an electron transporting layer of QDs.[2] Coe-Sullivan *et al.* have fabricated high luminance devices with electrochemical emission in the green-red region by exploiting the phase segregation between organic molecules, such as 4,4′,*N*,*N*′-diphenylcarbazole (CBP) and *N*,*N*′-diphenyl-*N*,*N*′-bis(3-methylphenyl)-(1,1′-biphenyl)-4,4′-diamine, and aliphatically capped QDs.[3,7] In this approach the problem of poor charge conductivity of QDs, due to the insulating layer of surfactants that coat their surface, was in fact overcome elegantly by the formation of a single monolayer of QDs sandwiched between a hole and an electron transporting organic layer. This geometry separated the charge recombination process (which occurred in the QD layer) from the charge conduction process (which occurred in the two organic layers).

Despite the reported advances in the field, to date LEDs based on core/shell CdSe/ZnS nanocrystals that emit pure blue light have remained difficult to fabricate. This is due to the lack of appropriate synthetic routes to synthesize CdSe nanocrystals with diameters that are sufficiently small (of the order of 1.5 nm) to shift their light emission to the blue-UV region of the visible spectrum, which in addition have a narrow size distribution, good quantum efficiency, chemical stability, and which can be routinely prepared in high yields. These limitations prevent the exploitation of the nanocrystal-based technology in full-color flat display applications, for which chromophores emitting in all the three primary colors are required in order to obtain white light.

In a recent work we have reported a synthetic approach to blue emitting CdSe/ZnS QDs which was based on the sequential growth of CdSe magic size clusters (MSCs) with progressively larger sizes.[8] The method allowed us to grow extremely small colloidal CdSe nanocrystals in a mixture of three surfactants (trioctyl phosphine, dodecylamine, and nonanoic acid) at temperatures (80 °C) that are much lower than those involved in conventional organometallic syntheses of CdSe nanocrystals. Small nanocrystals can be grown as both nucleation and growth rates are considerably reduced, due to the large activation barriers for the two processes at such low temperature.

In order to synthesize blue emitting nanocrystals, we interrupted the growth when the largest MSCs present were the one characterized by an absorption peak at 406 nm. These clusters, which had a diameter of approximately 1.5–1.6 nm, were isolated from smaller MSCs present in the growth solution by size selective precipitation with methanol,[8] and a ZnS shell was grown on them in order to passivate defects and to enhance their band-edge emission. In Fig. 1 we report the absorption and the photoluminescence spectra of core/shell CdSe/ZnS nanocrystals that were prepared from such size-selected MSCs. In a chloroform solution the absorption and PL showed maximum peaks at 427 and 454 nm, respectively. In the solid state, for samples prepared by drop casting the solution of nanocrystals in chloroform on a cleaned

a)Author to whom correspondence should be addressed; FAX: 0039-0832-298238.
b)Electronic mail: aurora.rizzo@unile.it
c)Electronic mail: gigli@mailing.unile.it

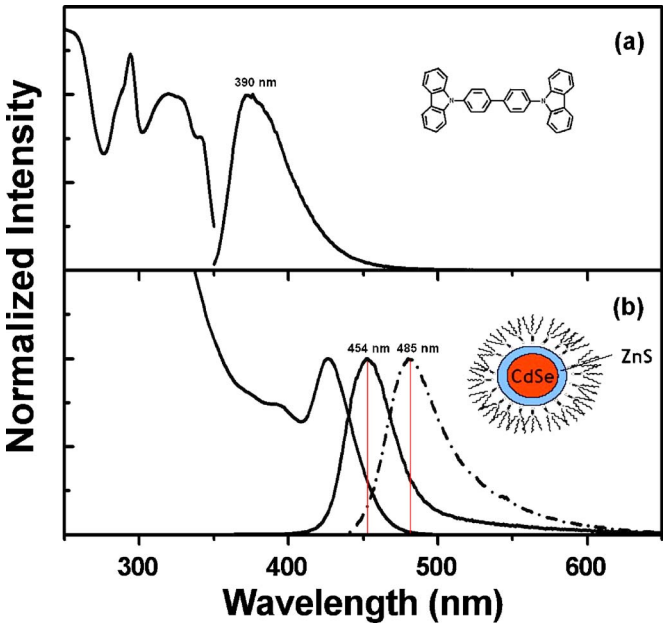

FIG. 1. (Color online) Optical properties of the materials involved in the fabrication of the LED. (a) Absorption and photoluminescence spectra of CBP in chloroform. (Inset) Molecular structure of CBP. (b) Absorption and photoluminescence spectra of core/shell CdSe/ZnS nanocrystals in chloroform (solid) and in film (dash dot). (Inset) Simplified structure of a CdSe/ZnS nanocrystal.

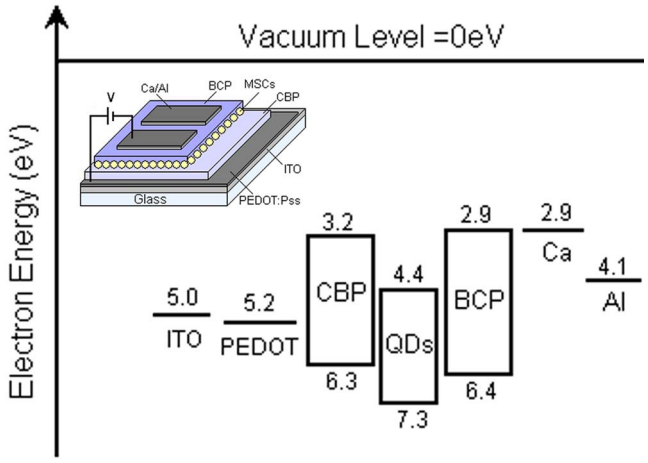

FIG. 2. (Color online) Proposed energy level diagram of the device: ITO‖PEDOT:PSS‖CBP:MSCs‖BCP‖Ca/Al. (Inset) Sketch of the device.

quartz glass, the PL spectrum showed a 30 nm redshift (Fig. 1). It is likely that this shift is due to the Förster energy transfer from smaller (donor) to larger (acceptor) dots within the film, and in nanocrystals it increases with increasing nonhomogeneity of the sample.[9] In the present case, the process of ZnS shell growth leads inevitably to a broadening of the size distribution of the clusters, which is initially remarkably narrow. The Förster theory relates the efficiency of energy transfer due to donor-acceptor dipole-dipole interaction to the spectral overlap of donor emission and acceptor absorption.[10] For a random orientation of transition dipoles, the rate of this process is given by

$$k_F = \tau_D^{-1}\left(\frac{R_0}{r}\right)^6, \tag{1}$$

whereas the Förster radius is

$$R_0 \propto \left(\frac{\varphi_D}{n^4}\int_0^\infty F_D(\tilde{\nu})\varepsilon_A(\tilde{\nu})\frac{d\tilde{\nu}}{\tilde{\nu}^4}\right)^{1/6}. \tag{2}$$

In the former expressions, τ_D is the lifetime of the donor in the absence of the acceptor, r is the distance between the donor and the acceptor, φ_D is the luminescence quantum yield of the donor, n is the refractive index of the QD solid, $F_D(\tilde{\nu})$ is the normalized spectrum of the donor emission, and $\varepsilon_A(\tilde{\nu})$ is the molar extinction coefficient for acceptor absorption. R_0 is a measure of transfer efficiency and defines the distance at which k_F equals the rate of donor deexcitation by competing mechanisms. In our samples, we estimated a Förster radius of about 23 Å from the spectra in Fig. 1, by assuming $n \approx 2.26$,[11] and a molar extinction coefficient at the peak of the first excited state of 2.4×10^4 M^{-1} cm^{-1}.[12] In a recent report by Kasuya *et al.*, the nearest-neighbor interparticle distance for close-packed films of MSCs that were very similar in size to the size-selected MSCs prepared by us was of the order of 16 Å.[13] Such interparticle distance certainly increases in close-packed films of core-shell nanocrystals, as in the present case, but should not be larger than 20 Å, and is therefore shorter than the Förster radius estimated above. We want to remark, however, that the estimate of such Förster radius is certainly affected by large errors, which are due mainly to the large uncertainties in the values of the refractive index and the molar extinction coefficient for nanocrystals with such small sizes. In addition, it is likely that other effects are also responsible for the observed shift. We observed in the absorption spectrum in the film a broadening as well as a very small redshift (about 1.4 nm) of the first absorption peak as compared to the spectrum recorded on the same sample in solution (data not shown). The latter effect can be justified by considering the formation of delocalized states due to the interactions among nanocrystals.[14,15] The small redshift can be explained by considering the changes in the surrounding environment,[15–17] such as the dielectric constant discontinuity at the QD boundary, which is known to increase the exciton ground state energy significantly.[17] However, in our case the effect might be strongly reduced by the presence of the organic surfactants.[18]

PL efficiency of CdSe/ZnS nanocrystals in chloroform solution varied from synthesis to synthesis, in a 30%–60% range. These blue emitting nanocrystals, dispersed in a matrix of (CBP), were used as active emissive layer in OLED devices with a multilayered structure [Fig. 2 inset]. In particular, in order to increase the hole injection from the indium tin oxide (ITO) anode into the active materials and also to improve the film forming properties, a thin layer of poly(3,4-ethylenrdioxythiophene):poly(styrenesulfonate) (PEDOT:PSS) was spin deposited onto the cleaned ITO-coated glass substrate and then heated at 110 °C for 10 min. The nanocrystals and the host material (CBP) were deposited in a single spin-casting step from a chloroform solution.[19] To improve the electron injection in the nanocrystals layer a 35 nm electron transporting/hole blocking layer of 2,9-dimethyl-4,7-diphenyl-1,10-phenanthroline (BCP) was evaporated. Finally, a Ca/Al (50 nm/150 nm) cathode was thermal evaporated at a pressure of 4×10^{-6} mbar using a contact shadow mask.

The electroluminescence spectrum of the device is reported in Fig. 3. It is peaked at the same wavelength as the PL spectrum, although it has a broader line shape. Differences between photo- and electroluminescence are attributed

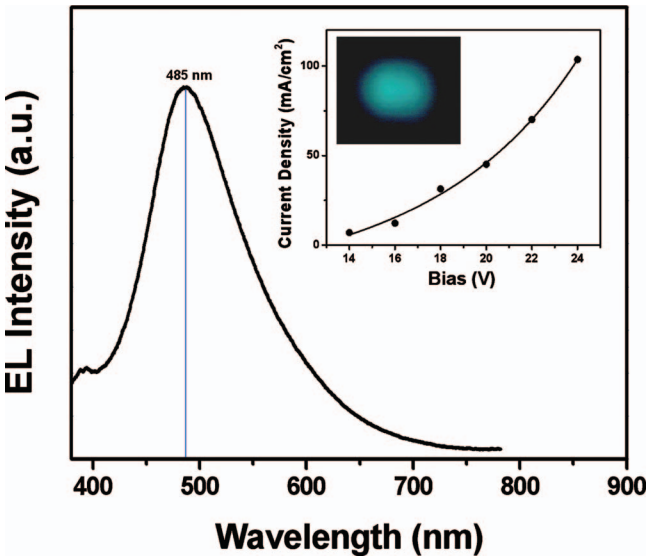

FIG. 3. (Color) Electroluminescence spectrum for the device. (Inset) *V-I* characteristic of the device and a photo taken from the working device.

to the environmental effects, such as energy and charge transfer among nanocrystals or between nanocrystals and the organic molecules.[20] The small shoulder located at 390 nm from CBP is probably due to incomplete exciton energy transfer from CBP molecules to the nanocrystals. We report in Fig. 2 the energy level diagram of the device in order to clarify the processes occurring in the device. Work functions (Φ), band gaps (E_g), ionization energies (IE), and electron affinities (EA) of ITO ($\Phi=-5.0$ eV), PEDOT (IE$=-5.2$ eV), Al ($\Phi=-2.9$ eV), Ca ($\Phi=-4.1$ eV), CBP ($E_g=3.1$ eV, IE$=-6.3$ eV), and BCP ($E_g=3.5$ eV, EA$=-2.9$ eV) were taken from literature.[1,21,22] The IE of the nanocrystals can be obtained approximately by adding the quantization energy to the bulk CdSe IE.[23] For simplicity we treated the nanocrystals as a CdSe sphere of diameter of 1.6 nm and neglected the influence of the ZnS shell on the effective band gap. Atomistic calculations predict for this system a hole quantization energy of about 0.7 eV.[24,25] The resulting IE is thus −7.3 eV, and by subtracting the nanocrystal's optical gap (2.9 eV) estimated from the absorption measurements, we obtain a value of −4.4 eV for the EA.

Based on this diagram, the generation of excitons in the nanocrystals can occur either through direct charge injection or by the Förster energy transfer from the organic molecules. Electrons are injected from the Ca/Al contact through the BCP, due to the energy alignment of the EA of the nanocrystals and the lowest unoccupied molecular orbitals of CBP and BCP. They are eventually transported to the nanocrystals, where they are better confined due to their higher electron affinity. In charged nanocrystals the barrier for hole injection from CBP is reduced, and therefore the holes injected from the anode (ITO) through the PEDOT:PSS into the CBP layer can be trapped on the nanocrystals. By this mechanism excitons are formed on nanocrystals by direct charge injection from CBP and BCP. Excitons as well can be formed on the organic molecules placed in the interstitial spaces of the MSC layer, and then transferred to the nanocrystals by the Förster energy transfer process. According to the Förster energy transfer theory, one of the necessary conditions for an efficient process is a strong overlap of the acceptor absorption and donor photoluminescence spectra.[26,27] As is shown in Fig. 1 this condition is satisfied in the case of the reported device, as the PL of CBP (donor) and the absorption of nanocrystals (acceptor) are well overlapped.

In conclusion, we have fabricated a blue light emitting device based on blue emitting CdSe/ZnS nanocrystals blended in a host material (CBP). A thin layer of a hole blocking/electron transporting material (BCP) is used to control and to balance the emission process. This work demonstrates the potentiality of colloidal semiconductor nanocrystals as blue emitters for light emitting diodes. Furthermore, when mixed with nanocrystals emitting in other colors, they can be exploited for full-color displays and lighting technology.

This work was supported by the European project SA-NANO (contract number STRP 013698) and by the Italian projects MIUR 297 (contract number 13587), FIRB Synergy (RBNE03S8XZ) and FIRB NG-LAB (contract number RBLA03ER38).

[1] Y. Q. Li, A. Rizzo, M. Mazzeo, L. Carbone, L. Manna, R. Cingolani, and G. Gigli, J. Appl. Phys. **97**, 113501 (2005).
[2] H. Mattoussi, L. H. Radzilowski, B. O. Daboussi, E. L. Thomas, M. G. Bawendi, and M. F. Rubner, J. Appl. Phys. **83**, 7965 (1998).
[3] S. Coe, W. K. Woo, M. G. Bawendi, and V. Bulovic, Nature (London) **420**, 800 (2002).
[4] I. Gur, N. A. Fromer, M. L. Geier, and A. P. Alivisatos, Science **310**, 462 (2005).
[5] B. O. Dabboussi, J. Rodriguez-Viejo, F. V. Mikulec, J. R. Heine, H. Mattoussi, R. Ober, K. F. Jensen, and M. G. Bawendi, J. Phys. Chem. B **101**, 9463 (1997).
[6] V. I. Klimov, Los Alamos Sci. **28**, 214 (2003).
[7] S. Coe-Sullivan, J. S. Steckel, W. K. Woo, M. G. Bawendi, and V. Bulovic, Adv. Funct. Mater. **15**, 1117 (2005).
[8] S. Kudera, M. Zanella, C. Giannini, A. Rizzo, Y. Q. Li, G. Gigli, R. Cingolani, G. Ciccarella, W. Spahl, W. J. Parak, and L. Manna, Adv. Mater. (Weinheim, Ger.) (in press).
[9] C. R. Kagan, C. B. Murray, and M. G. Bawendi, Phys. Rev. B **54**, 8633 (1996).
[10] T. Förster, Discuss. Faraday Soc. **27**, 7 (1959).
[11] The refractive index for CdSe cores is calculated from the Moss rule $n^4=77/E_g$ (eV); $E_g=2.95$ eV was estimated from the first optical absorption peak.
[12] W. W. Yu, L. Qu, W. Guo, and X. Peng, Chem. Mater. **15**, 2854 (2003).
[13] A. Kasuya, R. Sivamohan, Y. A. Barnakov, I. M. Dmitruk, T. Nirasawa, V. R. Romanyuk, V. Kumar, S. V. Mamykin, K. Tohji, B. Jeyadevan, K. Shinoda, T. Kudo, O. Terasaki, Z. Liu, R. V. Belosludov, V. Sundararajan, and Y. Kawazoe, Nat. Mater. **3**, 99 (2004).
[14] M. V. Artemyev, A. I. Bibik, L. I. Gurinovich, S. V. Gaponenko, and U. Woggon, Phys. Rev. B **60**, 1504 (1999).
[15] H. Döllefeld, H. Weller, and A. Eychmüller, J. Phys. Chem. B **106**, 5604 (2002).
[16] C. A. Leatherdale and M. G. Bawendi, Phys. Rev. B **63**, 165315 (2001).
[17] V. A. Fonoberov, E. P. Pokatilov, and A. A. Balandin, Phys. Rev. B **66**, 085310 (2002).
[18] B. S. Kim, M. A. Islam, L. E. Brus, and I. P. Herman, J. Appl. Phys. **89**, 8127 (2001).
[19] J. S. Steckel, J. P. Zimmer, S. Coe-Sullivan, N. E. Stott, V. Bulovic, and M. G. Bawendi, Angew. Chem. **43**, 2154 (2004).
[20] J. L. Zhao, J. Y. Zhang, C. Y. Jiang, J. Bohhenberger, T. Basche, and A. Mews, J. Appl. Phys. **96**, 3206 (2004).
[21] I. G. Hill and A. Kahn, J. Appl. Phys. **84**, 5583 (1998).
[22] I. G. Hill and A. Kahn, J. Appl. Phys. **86**, 4515 (1999).
[23] A. H. Nethercot, Phys. Rev. Lett. **33**, 1088 (1974).
[24] L. W. Wang and A. Zuger, Phys. Rev. B **53**, 9579 (1996).
[25] S. Sapra and D. D. Sarma, Phys. Rev. B **69**, 125304 (2004).
[26] S. E. Shaheen, B. Kippelen, and N. Peyghambarian, J. Appl. Phys. **85**, 7939 (1999).
[27] M. Anni, L. Manna, R. Cingolani, D. Valerini, A. Cretì, and M. Lomascolo, Appl. Phys. Lett. **85**, 4169 (2004).

General Approach to II-VI Semiconductor Magic Size Nanoparticles (Submitted)

Marco Zanella[1], Azhar Zahoor Abbasi[1], Andreas Schaper[2]* and Wolfgang J. Parak[1]*

1 Fachbereich Physik, Philipps Universität Marburg, Renthof 7, 35037 Marburg, Germany
2 EM&M Laboratory, Material Science Philipps Universität Marburg, Hans-Meerwein-Str., 35032 Marburg, Germany

*corresponding author: schaper@staff.uni-marburg.de, wolfgang.parak@physik.uni-marburg.de

Abstract. We report a general strategy for the synthesis of II-VI semiconductor magic size crystals (MSCs). CdS, CdTe, ZnSe and ZnO MSCs were synthesized generalizing a method we recently developed for the sequential growth of CdSe MSCs. Harnessing their characteristic sequential growth we could isolate different families of MSCs via size selective precipitation and characterize their optical, structural and compositional properties.

General Approach to II-VI Semiconductor Magic Size Nanoparticles

Marco Zanella[1], Azhar Zahoor Abbasi[1], Andreas Schaper[2]* and Wolfgang J. Parak[1]*

1 Fachbereich Physik, Philipps Universität Marburg, Renthof 7, 35037 Marburg, Germany
2 EM&M Laboratory, Material Science Philipps Universität Marburg, Hans-Meerwein-Str., 35032 Marburg, Germany

*corresponding author: schaper@staff.uni-marburg.de, wolfgang.parak@physik.uni-marburg.de

Abstract. We report a general strategy for the synthesis of II-VI semiconductor magic size crystals (MSCs). CdS, CdTe, ZnSe and ZnO MSCs were synthesized generalizing a method we recently developed for the sequential growth of CdSe MSCs. Harnessing their characteristic sequential growth we could isolate different families of MSCs via size selective precipitation and characterized their optical, structural and compositional properties.

Introduction. Magic size crystals (MSCs) are families of crystals characterized by the fact they have almost the same size which means they have well defined and reproducible properties. The MSCs concept is well known for metal cluster [1-4] and in last few years the interest on these structures and their exclusive properties moved to others materials like semiconductors [5-15] and oxides [16]. Several theoretical results studying the nucleation and the stability, electronic and structural properties of the nanoparticles at the first stages of the growth were reported too [16-29]. Different families of almost monodisperse CdS and CdSe MSCs have been synthesized by high pressure and high temperature methods [30], inverse micellar approach [10], but no one of these nanocrystals present comparable optical properties as those synthesized in solution. We recently reported the synthesis of CdSe MSCs, sequentially grew in solution [31]. The sequential synthesis of these materials in solution allows to study the mechanism which drives their nucleation and growth kinetics, an aspect of MSCs not yet well understood. Other authors have recently reported the sequential growth of CdSe and CdTe MSCs and characterized their properties [32-33].
Here we report a general approach for the synthesis of several families of MSCs of different II-VI semiconductor materials characterizing their optical and structural properties and proposing a simple qualitative model of their growth based on the model we previously reported for the sequential growth of CdSe MSCs.
In Figure 1 the temporal evolution of the absorbance spectrum of CdS, CdTe, ZnSe and ZnO MSCs is shown.

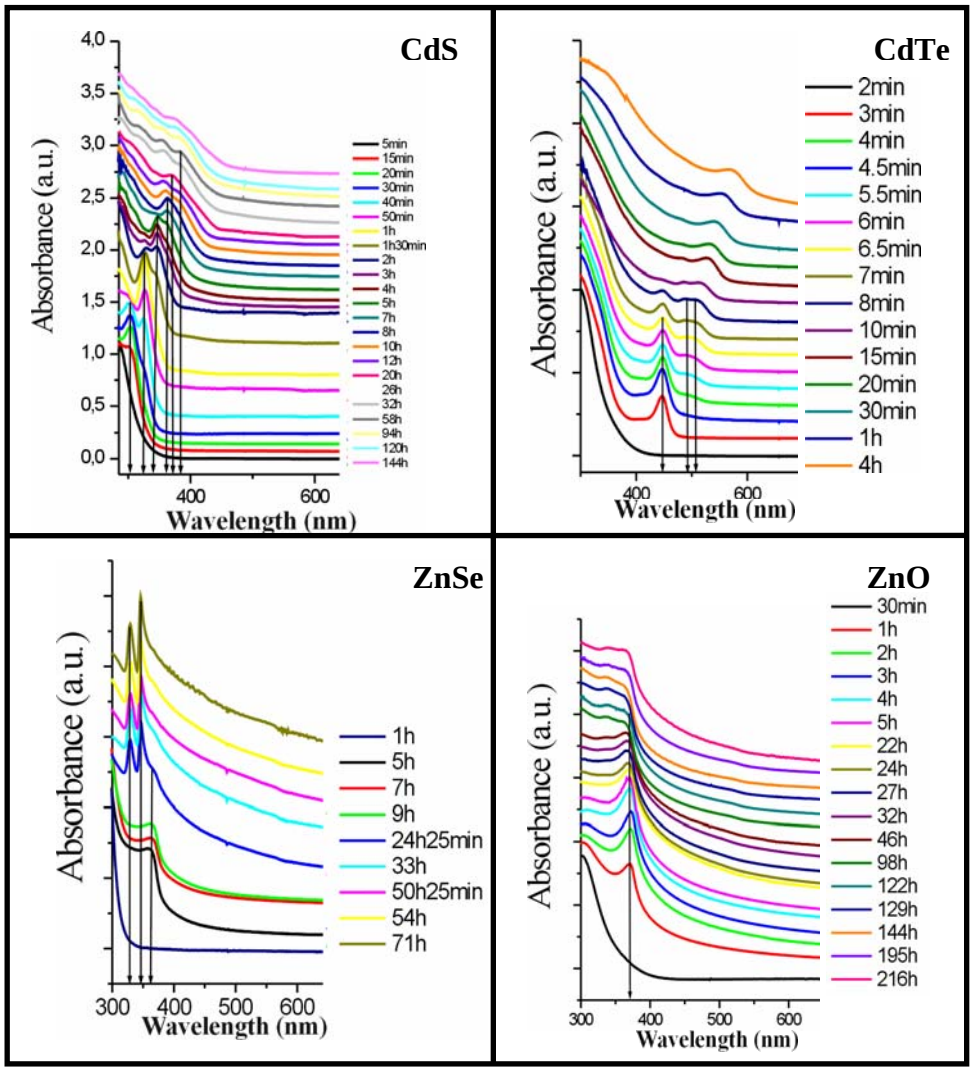

Figure 1. *Absorbance spectra time evolution of different nanoparticles solutions. MSCs characteristic wavelength is pointed with black arrows.*

Each family of spectra is characterized by some peaks which position do not change over time but which intensity does. This intensity enhancement suggests the formation in solution of a family of MSCs characterized by that specific absorbance wavelength. Since the growth of these peaks is sequential it is possible to stop the synthesis when the peak of the particles we want to synthesize reaches its intensity maximum and precipitate the desired nanocrystals with standard procedures. In this ways we could separate different families of MSCs performing a size selective precipitation of the nanoparticles and producing solution in which most of the NCs belong to just one MSCs family. The sample then was ready for further characterizations (i.e. TEM, SAED, XRD and EDX), synthesis steps such as shell growth or seeded growth [37] or to be employed in some applications (i.e. LED, labeling).

CdS MSCs

CdS MSCs were synthesized in a 3 neck flask reacting at low temperature a complex made of cadmium and nonanoic acid with a S:TOP solution in presence of decylamine. The synthesis is described in detail in the experimental part. After the injection of the S:TOP stock solution the

nucleation and the growth of the CdS MSCs was followed taking 0,1ml aliquots from the synthesis solution and dissolving them in 1-2ml of toluene. The temporal evolution of the absorbance spectra of that aliquots is reported in Figure1.
About 15min after the injection of the stock solution a shoulder at about 303nm is clearly visible in the absorbance spectrum (Figure 1 red curve) and this suggests the formation in solution of the first family of CdS MSCs which we will call CdS I. This family of nanoparticles grows over time in solution in fact the shoulder turn into a sharp peak in 5 more minutes (Figure 1 green curve). This peak did not keep on growing alone. After 30 min from the sulphur injection one more peak centered at about 326nm appeared in the absorbance of the solution showing that an other family of CdS MSCs was forming in solution. We will call this new family CdS II. Over time its peak intensity grows overcoming the peak of CdS I till just the peak at 326nm characterize the nanoparticles solution absorbance (Figure 1 pink curve (50min after the S:TOP injection)). This suggests that most of the particles present in solution belong to the CdS II family and just a little fraction of them still belong to CdS I. The process carries on with the sequential formation of four more peaks centered at about 347, 362, 367 and 382nm characterizing the CdS III, CdS IV, CdS V and CdS VI MSCs families. In the reaction between cadmium and sulphur, as it occurred between cadmium and selenium [31] with the same kind of precursors and surfactants, absorbance peaks are sharp and well distinguishable and if the synthesis is not too fast (synthesis temperature too high) is possible to stop it when most of the nanoparticles in solution belong to one family. Precipitating these particles is possible to prepare solution in which basically just one family of particles are present and thus we can synthesize solutions having a fixed excitonic absorbance wavelength. In Figure 2a and 2b are reported the absorbance and the fluorescence of toluene solutions of nanoparticles belonging to the first four families of CdS MSCs taken after the size selective precipitation.
The position of the absorbance peaks is a few nanometers red shifted compare to the synthesis solution (see supporting information) an even the their FWHM (Figure 2a) is a little broader cause the selective precipitation. The NPs fluorescence is prevalently dominated by trap state emission due to the stripping off of the outer atoms during the washing procedure. The surface to volume ratio of this nanocrystal is particularly high cause their small size. In these particles the majority of their atoms is located on their surface. The large amount of surface atoms and the aggressiveness of the washing step led to many dangling bonds which are responsible for the trap state emission. The fluorescence contribute of the semiconductor bandgap is centered at about 368nm for CdS I, 374nm for CdS II, 402nm for CdS III and 415nm for CdS IV. The sharp peak centered at 580nm is due to the excitation wavelength λ_{ex}=290nm. EDX analysis of the samples (see supporting information) show that these particles are richer in cadmium than in selenium even if for their synthesis a higher amount of selenium was required (see Table S1 in the supporting informations).
The fact that a large amount of sulphur is required for the nucleation of the CdS MSCs suggests that the sulphur atoms trigger the magic size crystals formation while the fact that this particles are richer in cadmium tell us that their surface must be mainly made of cadmium atoms.
The analysis of the HRTEM micrographs (Figure 3 for CdS III, for the other families see supporting informations) say that CdS MSCs crystalline structure is mainly cubic. SAED and XRD spectra of the samples (data not shown) do not led to any conclusion cause the broadness of the peaks due to the nanoparticles small size. The analysis of HRTEM images does not give an exhaustive answer to the determination of the NPs crystalline structure. Therefore we can not exclude the hypothesis to have some nanoparticles having a wurtzite structure, even if among all the nanoparticles analyzed this case was never observed. From HRTEM pictures was possible to estimate the size and its distribution for the different families, which values go from about 2 to 4nm. Average values are reported in Table 1.

Material	**CdS I**	**CdS II**	**CdS III**	**CdS IV**	**CdTe I**	**CdTe II - III**
Peak position (nm)	303,7±0,5	326,7±0,5	347±1	362,7±0,6	445,3±1,5	490,6±2,5 506±1,5
Composition	Cd 53% S 47% χ^2=1,11	Cd 53% S 47% χ^2=0,88	Cd 52% S 48% X^2=0,8	Cd 51% S 49% χ^2=1,28	Cd 53% Te 47% χ^2=0,89	Cd 53% Te 47% χ^2=0,89
Crystalline Structure	ZB	ZB	ZB	ZB	W	W
Size distribution (nm)	2,34±0,3	2,78±0,54	2,92±0,84	3,52±0,77	2,44±0,33	3,08±0,78
QY					29%	33%

Table1. *Summary of CdS and CdTe MSCs properties. ZB=zinc blende or cubic, W=wurtzite or hexagonal.*

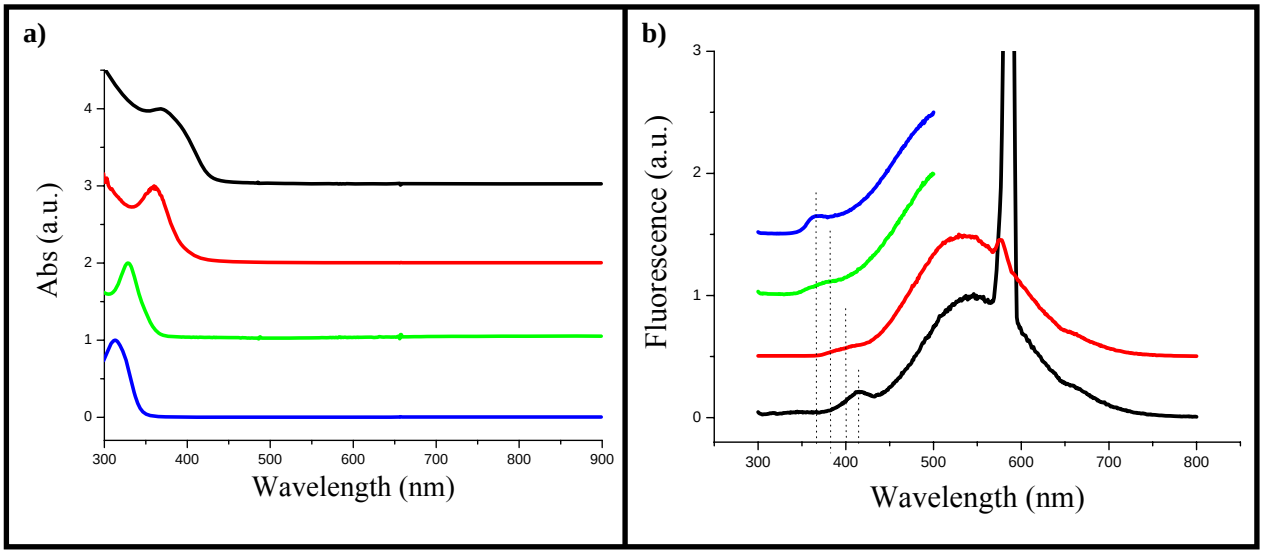

Figure 2. *a) Absorbance and b) Fluorescence of CdS MSC after their size selective precipitation. CdS I(blue curve), CdS II (red curve), CdS III (green curve) and CdS IV (Blue curve). The fluorescence spectra were collected with an excitation wavelength* λ_{ex}*=290nm.*

Comparing our results with others found in literature concerning CdS MSCs we found fundamental differences. Herron et al. reported about Cd32S4(SC6H5)36-DMF4 NCs which were synthesized with high temperature and high pressure process starting from Cd10S4(SC6H5)12 nanoparticles used as precursors [30]. The stoichiometry, the size and the shape of those CdS MSCs is different from those reported here but the absorbance of a Herron's NPs in THF (358nm) is very close to that one of the nanoparticles belonging to CdS IV (362nm). Even the absorbance of the Cd20S13(SPh)22)-8 reported by Farneth et al. [34] (346nm) is very similar to that one reported here for the family CdS III (347nm) although again the size and shape are different. In the same paper Farneth justify the peak at 346nm as the absorbance peak of clusters formed by the agglomerations of Cd10S16Ph12 clusters which present an absorbance maximum at 300nm similar to the value characteristic of CdS I. Vossmeyer et al. [35] reported the absorbance spectra of DMF solution of Cd32S14(SCH2CH(OH)CH3)36-4H2O clusters which present a main peak centred at 325nm along with a less intense peak centred at about 305nm (very close to that one characteristic of CdS II (326nm) and CdS I (303nm) reported here). Clusters reported by Vossmeyer [35] and Herron [30]

have an entirely identical core but a different absorbance peak position which is justified considering the different NPs ligands [35]. The surfactant molecules surrounding the particles object of this report are different from those used by Vossmeyer [35] and Herron [30] as are their size, shape and stoichiometry. The amazing thing is that their absorbance peaks are centred at about the same absorbance wavelength. The values to which the absorbance peaks are centred seem to be a characteristic of the material independent from precursors and surfactants used in the synthesis. It is actually possible that some of the data reported in literature concern agglomerates of MSCs [34] which would express a different absorbance position compare to that ones of the starting building blocks. This would explain why CdS MSCs reported in literature which are smaller than those showed here express similar absorbance wavelength.

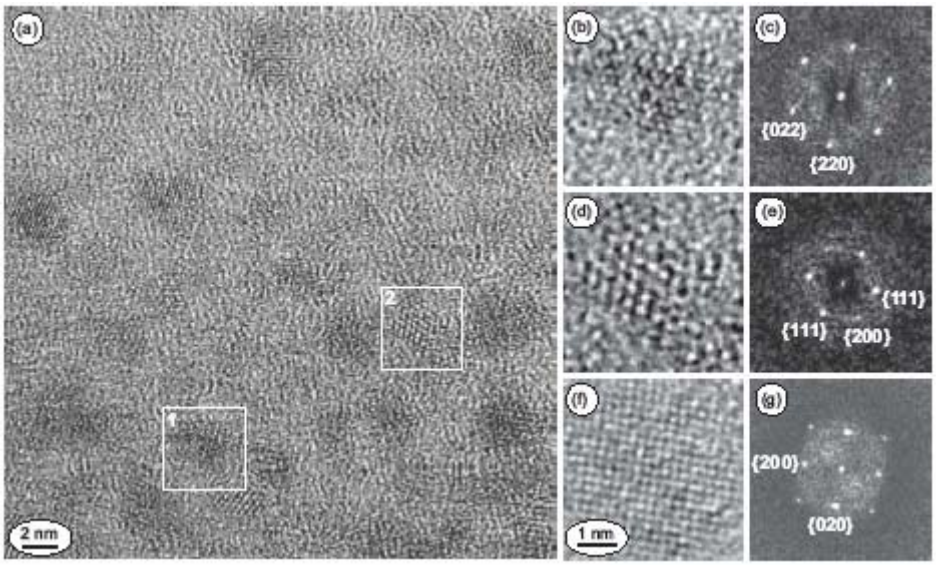

Figure 3. *TEM micrographs of cadmium sulfide nanoparticles of sample CdS III with cubic structure: (a) overview; (b) close-up of the single particle in area 1 with (111) zone axis orientation; (d) close-up of the single particle in area 2 with (110) orientation; (f) single particle in (100) orientation; (c), (e) and (g) are the corresponding diffractograms of the single particle images.*

CdTe MSCs. CdTe MSCs were synthesized following a procedure similar to that one used for the synthesis of CdS MSCs. The cadmium nonanoic acid complex was let reacting at 130°C with a TOP:Te stock solution. Details of the synthesis are collected in the supporting informations. At constant time intervals 0,1ml aliquots of NCs solution were dissolved in 1-2ml of toluene and the solution absorbance spectrum was recorded. In Figure 1 an evolution over time of a typical CdTe MSCs solution absorbance spectrum is shown. After 4min from the injection a narrow peak centred at about 445nm is clearly visible in the solution absorbance spectrum confirming the formation of the first family of CdTe MSCs that we will refer as CdTe I. This peak keeps on growing alone for 30 more seconds till after one minute one more peak appears. This second peak increases its intensity and broadness over time, while the first peak disappears and the absorbance spectrum presents two new peaks (one centred at about 490nm and the other one around 506nm) having a comparable intensity. We will refer to this two new peaks as CdTe II and CdTe III since they represent two magic size families. Over time then the CdTe II peaks disappear while at the same time CdTe III becomes broader and red shifts. Eventually just one broad peak is present in the absorbance spectrum which over time red shifts as in a usual nanoparticles growth.

As it is visible from Figure 1b the growth of the families CdTe II and CdTe III is simultaneous and, at least our synthesis conditions (surfactant and precursors type), it was not possible to observe a sequential growth of these two peaks.
But it was possible to stop the solution when just the peak at 455nm was present. For this reason we decide to apply the size selective precipitation on the solution in which just the family CdTe I was present and on the solution in which CdTe II and III were both present. The absorbance and the fluorescence spectra of these two samples redissolved in toluene are reported in Figure 4.

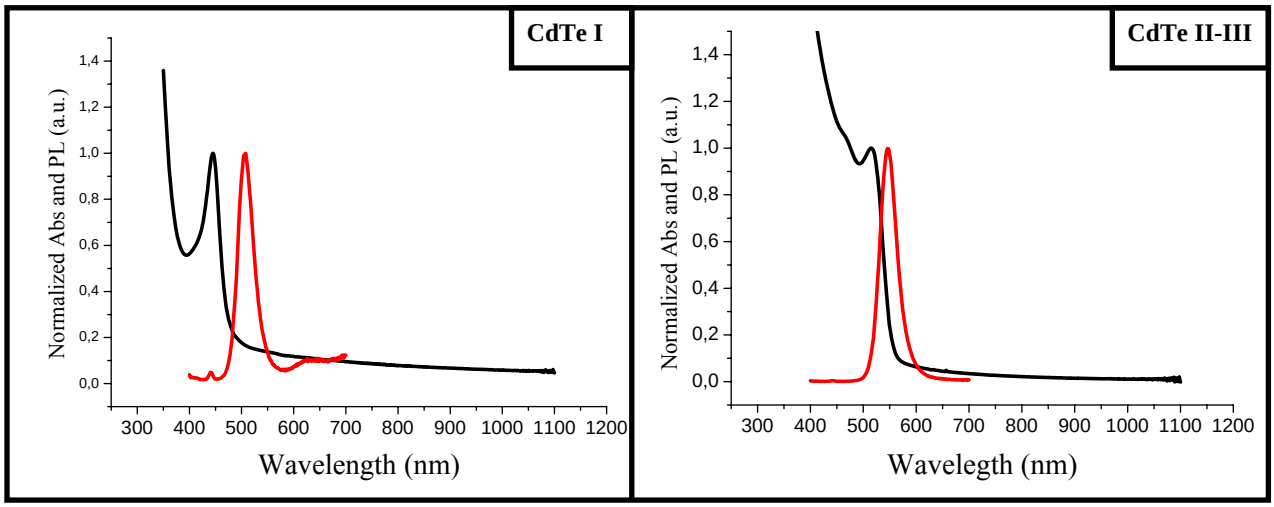

Figure 4. *Normalized absorbance (black) and fluorescence (red) of toluene solution of a sample of CdTe I MSCs (left) and of a sample containing the MSCs belonging to the families CdTe II and CdTe III. For the fluorescence measurement the excitation wavelength was 390nm.*

The absorbance and fluorescence of the CdTe I MSCs present narrow peaks centred at 447 (FWHM≈35nm) and 506nm (FWHM≈35nm). In the fluorescence spectrum a little effect due to trap state emission is present with a much less intense peak at 650nm. The quantum yield of toluene solutions of CdTe I MSCs was ranging around 28-29%
CdTe II and III solution present a less narrow absorbance peak at 512nm which displays a trap state free fluorescence centred at 546nm (FWHM≈42nm) with a quantum yield of about 33%.
The result on the composition of these sample measured performing EDX analysis are reported in Table 1. All the tested families are richer in cadmium than in tellurium which support the hypothesis that they lay on the NCs surface.
The analysis of HRTEM pictures confirmed the wurtzite structure already reported by Peng for the synthesis of CdTe nanoparticles in presence of oleic acid [36]. A measure of the NPs diameter gives around 2,4nm for CdTe I and about 3nm for CdTe II and III (see Table 1) . These values are compatible with those reported by Dagtepe et al. [37] for the synthesis of CdTe magic size crystals using hexilphosphonic acid for the cadmium oxide decomposition. In Dagtepe paper is possible to observe 6 families of MSCs (absorbing at 410, 449, 491, 501, 539 and 588nm) while with our best synthesis conditions (see supporting informations) just 3 were clearly observable (absorbing at about 445, 490 and 506nm). This is probably due to the different molecules used for the cadmium oxide decomposition (carboxylic acid in our case and phosphonic acid in Dagpete synthesis) which can control the number and therefore the dimension of the nuclei at the beginning of the reaction.

ZnSe MSCs. ZnSe MSCs were synthesized following a procedure similar to that one reported for the synthesis of CdSe MSCs [31]. The zinc nonanoic acid complex was let reacting at 150-160°C with a TOP:Se stock solution. Details of the synthesis are collected in the supporting informations. At constant time interval 0,1ml aliquots of NCs solution were dissolved in 1-2ml of toluene and the solution absorbance spectrum was recorded. In Figure 1 an evolution over time of a typical ZnSe

MSCs solution absorbance spectrum is shown. After more than 1h from the injection of Se:TOP stock solution a peak centred at about 378nm shows up and it keeps on growing slowly for several hours hours. This peak is actually quite broad compare to the other peaks characterizing the MSCs but it keeps on growing without shifting which is a typical feature of the MSCs absorbance spectra. We will refer to this peak as ZnSe III which name characterize the third family of ZnSe MSCs observed with this process. At a certain point two more peaks start growing but surprisingly at lower wavelength. These peaks are centred at 328 and 346nm respectively and they are the sharpest MSCs absorbance peaks observed so far (FWHM≈22nm). We will refer to them as ZnSe I (Abs=328nm) and ZnSe II (Abs=346nm). They keep on growing over time while the third peak becomes broader and red shifts. After several hours the peaks at lower lambda become broader and less and less intense (see supporting informations). The fluorescence spectrum of a solution containing all the ZnSe MSCs families present three gaussian peaks (Figure 5a) centred at 345nm (FWHM=20nm), about 368nm (FWHM≈24nm) and 403nm (FWHM=46nm).

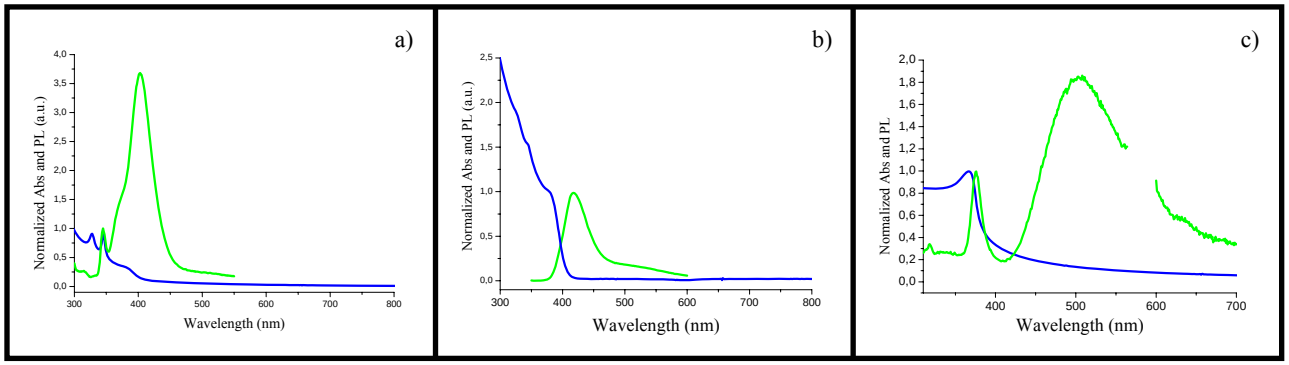

Figure 5. *a) Absorbance and fluorescence peaks of an aliquot containing all the three families of ZnSe MSCs. The aliquot was taken directly from the growth solution and the spectra were taken without any previous purification step. b) Absorbance and fluorescence of a toluene solution of ZnSe III MSCs after the purification step. The nanoparticles were precipitated from the growth solution when just the peak of ZnSe III was present in the solution absorbance spectrum. c) Absorbance and fluorescence spectra of ZnO MSCs in toluene. For all the fluorescence spectra the excitation wavelength was 300nm.*

Cause the peculiar characteristics of the ZnSe MSCs sequential growth, observed here, we could selectively precipitate only the NCs belonging to ZnSe III family. Actually is possible to precipitate all the three families from the solution but a separation via standard selective precipitation used for CdX (X=S,Se,Te) NPs was not very effective in terms of size distribution. In principle other techniques like size selective chromatography might give a better response.
We could anyway precipitate the NPs belonging to the family ZnSe III by stopping the growth when jus the peak at 378nm was present.
The precipitation of the NPs was performed with methanol and the precipitate was redispersed in toluene and the process was repeated at least two times before the characterisation. In Figure 5b) the absorbance and fluorescence of a toluene solution of ZnSe III MSCs is shown. From HRTEM micrographs the NPs crystalline structure was found to be wurtzite even if it is not possible to exclude that some nanoparticles present a cubic lattice as suggested by SAED measurements. Nanoparticles including both phases in their lattice were never directly observed. The average diameter of ZnSe III NPs was found to be about 3,3nm which determination allowed us to define the average diameter of the NCs belonging to ZnSe I and II when we characterized a sample in which all three families were present. The analysis of the HRTEM micrographs of such a sample evidenced the presence of three size distributions centred at about 2, 2,4 and 3,2nm (Table2) which we identified as the particles belonging to the three families of MSCs objective of the characterisation. EDX measurement on this sample displayed a higher presence of selenium which

cover the NPs surface. From the compositional point of view (supporting informations) it was found that as for CdSe and CdS MSCs an higher concentration of chalcogen in solution triggers the MSCs formations.

Material	**ZnSe I**	**ZnSe II**	**ZnSe III**	**ZnO**
Abs peak position (nm)	328,2±0,9	346±1,1	378±1,8	372
Composition		Zn 49% Se 51% χ^2=1,11		Zn 49% O 51% χ^2=2.05
Crystalline structure		ZB and W together		ZB and W together
Size distribution (nm)	1,99±0,22	2,42±0,23	3,23±0,38	5,97±0,7

Table 2. *Summary of ZnSe and ZnO MSCs properties. ZB=zinc blende or cubic, W=wurtzite or hexagonal.*

ZnO MSCs. ZnO MSCs were synthesized following a procedure similar to those reported here for the synthesis of all the other MSCs. The zinc nonanoic acid complex was let reacting at 180°C without addition of any other precursor. Details of the synthesis are collected in the supporting informations. At constant time intervals 0,1ml aliquots of NCs solution were dissolved in 1-2ml toluene and the solution absorbance spectrum was recorded. In Figure 1 an evolution over time of a typical ZnO MSCs solution absorbance spectrum is shown. After about 1h the zinc nonanoic acid complex start forming some ZnO NPs as suggested by the presence of a peak centred at about 365nm growing in the absorbance spectrum of the nanocrystals solution. This peak presents a sharp top but actually a quite broad base as if particles of different size were present in solution along with the ZnO MSCs.
This peak keeps on growing for several hours showing a little red shift of about 3-4nm over time. The fact is probably due to a slight growth of the particles along with the formation of fresh MSCs which nucleation rate decrease over time. When the peak intensity decreases even the absorbance maximum wavelength decreases of about 3-6nm. This might be due to the fact that a portion of the biggest MSCs grows enough to leave the family, and just the fresh MSCs contribute to the main absorbance peak. The biggest NCs which leave the MSCs family do not form a new family since no other sharp peaks are visible in the absorbance spectrum at higher wavelength. Their size distribution appear to become larger as suggested by the broad tail present at wavelength longer than 400nm. While the main absorbance peak is decreasing its intensity an other peak at higher energy appear on the absorbance spectrum. It is centred at about 345nm and it red shift with all the spectrum over time. This peak do not represent an other magic size since it immediately red shifts over time. EDX analysis of the ZnO MSCs says that these particles are richer in oxygen than in zinc and the SAED suggest that their crystalline structure is either cubic or hexagonal (see supporting information). The injection of TOP:Te stock solution to the zinc-nonanoic acid complex do not led to ZnTe nanoparticles but to ZnO MSCs with the same absorbance properties reported above as confirmed by EDX analysis.
In figure 5c) the absorbance and photoluminescence of redispersed ZnO MSCs in toluene is shown. Absorbance main peak is centred at about 368nm while the fluorescence one is centred at 376nm (FWHM=20nm) and it is characterized by trap state emission.

HRTEM on this particle showed that their average diameter is about 6nm (supporting informations).

Growth mechanism. As we already reported in [31] the sequential growth of this kind of MSCs is well described by a continuous growth mechanism in which there is a competition between the adhesion of monomers which lead to bigger crystals and deattachment of monomers which shrink the nanoparticles back to the previous magic size. Our data do not support the hypothesis that the next MSCs family is made by the aggregation of particles belonging to the previous ones [33] since the HRTEM picture do not show any discontinuity in the crystal lattice. Anyway, it is not possible to exclude that very small non stable clusters adhere to the present MSCs quickly rearranging their atoms in order to form a bigger cluster. The present of very small non stable cluster is due to the presence of a characteristic critical radius for the nanoparticles in solution which depend on the solution oversaturation [38]. Below the critical radius the cluster are not stable and tend to dissolve. These clusters are characterized by their high reactivity due to their large surface. This mechanism, combined with adhesion-deadhesion competition seem to be the most probable model for the growth of these materials.

Theoretical discussion . Along with the experimental results the efforts which have been made in order to understand the continuous growth mechanism of nanomaterials has grown. A good understanding of the growth mechanism can let us to improve the synthesis protocols and developing new ones which would led to production of nanoparticles with improved properties and in larger amounts.
A brilliant contribution in understanding the mechanism of NPs growth and Ostwald ripening come from the work of Lifshitz, Slyozov and Wagner (1961) who used the Gibbs-Thomson equation (1) approximating the exponential term by retaining only the first two terms of its Taylor series expansion (2).

$$S_r = S_b \exp(2\gamma V_m / rRT) \quad (1) \qquad S_r \approx S_b\left(1+\frac{2\gamma V_m}{rRT}\right) \quad (2)$$

Where r is the nanocrystal radius, γ is the surface tension, V_m is the molar volume of the precipitate, S_b and S_r are the solubility of the bulk crystal and crystal with a radius r, R is the gas constant and T is the absolute temperature.
Despite to the invaluable insight obtainable from the analytic approach this present some limits just due to the approximation just mentioned. This limits do not let the description of the growth of nanoparticles having a diameter smaller than 20nm [38] for this reason the application of numerical approaches has been a valuable tool for improving our understanding on this matter [38-39]. Peng introduced the formation of MSCs in the general theory concerning the continuous growth of nanoparticles as wells in the chemical potential curve which result to be conversely proportional to the nanoparticles radius (3) [40].

$$\mu_r = \mu_b + \frac{2\gamma V_m}{rRT} \quad (3)$$

Where μ_r and μ_b are the chemical potential of crystals with radius r and with an infinite size. Equation 3 shows that μ_r is conversely proportional to the nanoparticle radius. This chemical potential would describe the continuous growth of a nanoparticle which dynamics is different from the MSCs one. In order to count the formation of MSCs Peng introduced some wells in the

chemical potential landscape and suggest a well-well tunnelling to explain the nanoparticles growth. In our previous report we model the growth of CdSe MSCs as a competition between attachment and deattachment of monomers to the nanoparticles surface which we found fitting the experimental data. We would like to couple this model with Peng assumption in order to find a qualitative description of the sequential growth of MSCs in order to shed some light on this intriguing mechanism.

For sake of simplicity we will consider for the moment only the CdS MSCs growth introducing the similarities and the differences with the other MSCs growth later as support or extension of this qualitative model.

Considering the temporal evolution of the absorbance spectrum of CdS MSCs (Figure1) the shape of the absorbance peak of each MSCs family can be approximated with a gaussian bell which FWHM is dependent on the NPs size distribution. We could assume that even the shape of the wells representing the MSCs families could be drawn as gaussian bells. The chemical potential equation than cold be written as (4)

$$\mu_r \propto \frac{1}{r} - \sum_i \frac{c_i}{\sigma_i \sqrt{2\pi}} \exp\left(\frac{-(r-m_i)^2}{2\sigma_i^2} \right) \quad (4)$$

Where μ_r is the chemical potential of the nanoparticles with radius r, c_i is a proportional constant, m_i is the centre of the gaussian well we can assume to be the average radius of the magic size crystal, σ_i is the standard deviation of the gaussian well. The sum is extended on all the *i* MSCs families of a given material.

In the case of a material having two MSC families the chemical potential would look like Figure 7a.

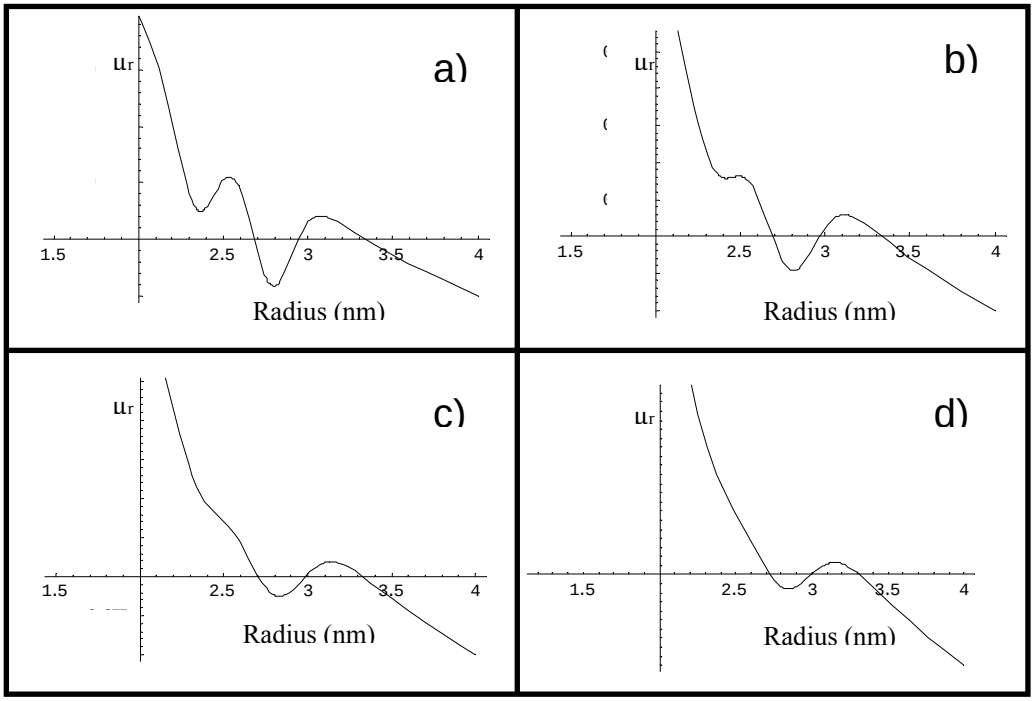

Figure 7. *Temporal evolution of the chemical potential of a solution of MSCs. a) Chemical potential (μ_r) of a solution in which two MSCs (two MSCs wells) will form over time. Nanoparticles will start increasing their radius with a continuous growth and their chemical potential will fall on the first well minimum. Over time b), c) and d) with the decreasing of the monomer concentration this minimum will be lifted till the barrier between the wells will be small enough to let some*

particles to slide to the next well forming the second MSCs family. The process can continue with other wells with the formations of other families.

As we said each gaussian would be centred on the MSCs average size and we would have as many of them as the observed peaks in the absorbance temporal evolution. From Figure 1 we see that with the growth of a new peak led a peak at lower wavelength to disappear. With our approach this would mean that the new chemical potential curve will be time dependent and we will see the wells depth changing over time as in Figure 7. The higher energy absorbance peak (lower radius well) disappear because no more MSCs belonging to that family are formed, and this could be represented with a gaussian well which depth decreases over time till its complete disappearing. The decreasing of the well depth favours the formation of the next family of MSCs if the barrier between a well and the next one become smaller over time. For this purpose we can consider that the gaussian FWHM increases with the decreasing of the well depth. The enlargement of the well FWHM led to an enlargement of the size distribution which slightly grows with the MSCs size. The bigger MSCs are characterized by having Gaussian with larger FWHM since the beginning and this will grow over time. Actually for the last MSCs the FWHM will be large enough to allow the continuous growth of the crystal characterized by the usual red shift of the absorbance spectrum. The new chemical potential landscape will be strongly dependent on the synthesis conditions. We saw already that in the case of semiconductive nanoparticles like those reported here the concentrations of monomers is a fundamental requirement for the MSCs formation. This means that the well depth should be monomer concentration dependent. Considering the results of other authors concerning the synthesis of CdTe and CdSe MSCs we can say that the well properties will depend on the precursors and the surfactant employed for the synthesis too. The higher amount of MSCs family observed by Dagtepe et al. [33] is probably due to the phosphonic acid used for the synthesis.

By using this qualitative model we could explain even the weird behaviour observed in the case of ZnSe MSCs. For this material the sequential growth seems to be reversed since the first two peaks appear after the formation of the third one, moreover the first two peaks appear and grow together without sequential behaviour. The latter effect could be explained if the height of the barrier between the wells related with the first two peak was small enough to allow to the NPs belonging to ZnSe I to grow to become part of ZnSe II while some more ZnSe I are still formed in solution. This "parallel" growth is not unusual since it as already been observer with the absorbance peaks centred at 330 and 350nm for CdSe MSCs and CdTe II and III here reported and they might be due to the employed chemicals which lowers the barrier between the MSCs wells.. The fact that the first two peaks appear after that the third is already developed could be still due to the synthesis conditions and could be explained with our qualitative model considering that the FWHM of the third well and its depth is large enough to reduce the impact of the first two wells.

Over time considering the decreasing of the monomer concentration the contribution of the third well would overtop the contribution of the first two no more and the absorbance peak of ZnSe I and II would show up and start growing. A simple sketch of this effect is reported in Figure 8.

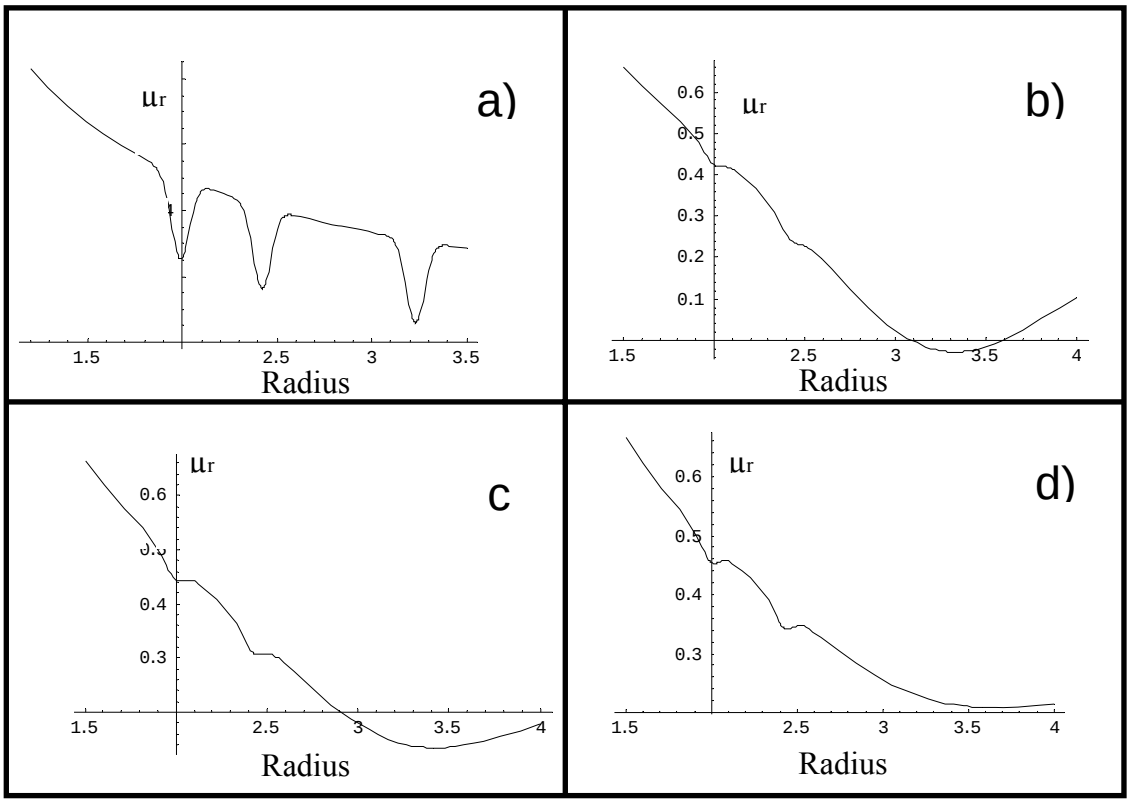

Figure 8. *a) Chemical potential (μ_r) landscape in case of three MSCs. b) If the depth and the of FWHM of the third peak overtops the first two peaks the growth will appear continuous till the dimension of the nanoparticles reach the minimum of the third well and the MSC family growth. In c) and d) we progressively reduced the depth of the third well simulating the effect of monomer concentration decreasing. As result the contribute of first two wells to the landscape become more and more evident.*

In conclusion, we have reported a general method for the sequential growth of CdS, CdTe, ZnSe and ZnO magic size nanocrystals. The procedure and the employed chemicals allows a comparison between the reactivity of the monomers in similar synthesis conditions leading to a general understanding of the behaviour of chalcogens in presence of precursors belonging to the group IIB. The synthesis could be stopped when the desired family of MSCs was the most popular in solution and via size selective precipitation was possible to prepare colloidal solutions composed essentially of these nanoparticles. This allowed the characterisation of the MSCs families and allows the exploitation of their properties for future applications. It is at the moment under investigation in our group the possibility to dope these materials embedding some impurity atoms in their lattice and characterizing their new properties.

Experimental. For the synthesis of CdS MSCs: 514mg of Cadmium oxide, 2 g of decylamine and 2g of nonanoic acid were mixed in a three-neck flask. The flask was pumped to vacuum at 100 for 15 minutes and then heated at 200 °C under nitrogen to decompose the CdO. The temperature was then lowered to 60 °C and 10 g of a solution of S in Trioctylphosphine (10% in weight of S) was injected. The temperature after the injection dropped and was allowed to recover and increased to 80 °C. During the growth, 0.1 ml of the growth solution were extracted at time intervals ranging from 3-5 minutes (at the early stages of growth) to several hours (after several hundreds of minutes of growth) and diluted into toluene.

Size selective precipitation. After the synthesis, the heating mantel was removed and the solution left cooling to room temperature. Two milliliters of toluene were added to this solution, followed by methanol until a persistent cloudiness was observed. This solution was centrifuged and the precipitate was washed again by addition of a few ml of toluene and methanol. The final precipitate was redissolved in toluene. By this procedure the largest magic sizes are almost quantitatively separated from the smaller magic sizes present.

Transmission electron microscopy. TEM investigations were performed using a JEM 3010 high-resolution electron microscope (Jeol Ltd., Tokyo, Japan) operated at 300 kV. For image acquisition a 2 k x 2 k slow scan CCD camera (Mega Scan 794, Gatan Inc., Pleasanton, CA) was used along with the Digital Micrograph software. All samples were prepared by depositing the nanoparticles on 300mesh copper grids covered with thin carbon supporting film. Image processing and Fourier analysis of individual nanoparticles was done making use of the CRISP (Calidris, Sollentuna, Sweden) software, and the Electron Diffraction program by J.-P. Morniroli (Université de Lille, France).

Acknowledgements

The project was funded by the German research foundation (DFG, project PA794/3-1) and supported by the Max Planck Society. Marco Zanella is grateful for a fellowship from the International Graduate School at the Center for Nanoscience.

References

[1] C. E. Briant, B. R. C. Theobald, J W. White, L. K. Bell, D. M. P. Mingos, A. J. Welch, *Chem. Comm.*, **1981,** 5, 201-202.
[2] A. F. Sotelo, A. M. P. Felicissimo, P. Gomez Sal, *Inorganica Chimica Acta*, **2003,**348, 63- 68.
[3] R. C. B. Copley, C. M. Hill, D. M. P. Mingos, *Journal of Cluster Science*, **1995,** 6 (1), 71-91.
[4] D. M. P. Mingos, *Journal of Cluster Science*, **1992**, 3 (4), 397-409.
[5] V. N. Soloviev, A. Eichho¨fer, D. Fenske, U. Banin, *J. Am. Chem. Soc.* **2000,** *122,* 2673-2674.
[6] V. N. Soloviev, A. Eichho¨fer, D. Fenske, U. Banin, *phys. stat. sol. (b)*, **2001**, 224 (1), 285–289.
[7] V. N. Soloviev, A. Eichho1fer, D. Fenske, U. Banin, *J. Am. Chem. Soc.* **2001,** *123,* 2354-2364.
[8] S. F. Wuister, F. van Driel, A. Meijerink, Phys. Chem. Chem. Phys., **2003**, 5, 1253–1258.
[9] A. Kasuya, Y. Noda, I. Dmitruk, V. Romanyuk, Y. Barnakov, K. Tohji, V. Kumar, R. Belosludov, Y. Kawazoe, N. Ohuchi, *Eur. Phys. J. D*, **2005,** 34, 39–41.
[10] A. Kasuya, R. Sivamohan, Y. A. Barnakov, I. M. Dmitruk, T. Nirasawa, V. R. Romanyuk, V. Kamur, S.V. Mamykin, K. Tohji, B.Jeyadevan, K. Shinoda, T. Kudo, O. Terasaky, Z. Liu, R.V. Belosludov, V.Sudararajan, Y. Kawazoe, *Nat. Mater.* **2004**, 3, 99.
[11] T. Kuzuya, Y. Tai, S. Yamamuro, K. Sumiyama, *Chemical Physics Letters*, **2005,** 407, 460–463.
[12] R. Xie, G. W. Bryant, J. Zhao, T. Kar, V. H. Smith Jr., *PHYSICAL REVIEW B* **71**, **2005**, 125422.
[13] I. G. Dance, A. Choy, M. L. Scudder, *J . Am. Chem. Soc.,* **1984,** *106,* 6285-6295.
[14] S. Behrens, M. Bettenhausen, A. Eichhofer, D. Fenske, *Angew. Chem. Int. Ed. Engl.,* **1997***,* 24, 199736.
[15] S. Behrens, M. Bettenhausen, A. C. Deveson, A. Eichhofer, D. Fenske, A. Lohde, U. Woggon, *Angew. Chem. Int. Ed. Engl.,* **1996,** 35 (19), 2215-2218.
[16] A. Aguado, J. M. Lo´pez, *J. Phys. Chem. B* **2000,** *104,* 8398-8405.
[17] S. Kr. Bhattacharya, A. Kshirsagar, *PHYSICAL REVIEW B*, **2007**, 75, 035402.
[18] S. Botti, M. A. L. Marques, *PHYSICAL REVIEW B*, **2007**, 75, 035311.

[19] B. Goswami, S. Pal, P. Sarkar, *PHYSICAL REVIEW B,* **2007**, 76, 045323.
[20] B. Goswami, S. Pal, P. Sarkar, G. Seifert, M. Springborg, *PHYSICAL REVIEW B,* **2006,** 73, 205312.
[21] R. Jose, N. U. Zhanpeisov, H. Fukumura, Y. Baba, M. Ishikawa, *J. Am. Chem. Soc.,* **2006**, 128, 629-636.
[22] J. Joswig, M. Springborg, G. Seifert, *J. Phys. Chem. B,* **2000,** *104,* 2617-2622.
[23] J. Joswig, G. Seifert, T. A. Niehaus, M. Springborg, *J. Phys. Chem. B,* **2003,** *107,* 2897-2902.
[24] J. Joswig, S. Roy, P. Sarkar, M. Springborg, *Chemical Physics Letters,* **2002,** 365, 75–81.
[25] M. L. del Puerto, M. L. Tiago, J. R. Chelikowsky, *PRL*, **2006**, **97,** 096401.
[26] A. Puzder, A. J. Williamson, F. Gygi, G. Galli, *PRL*, **2004**, 92 (21), 217401.
[27] S. Roy, M. Springborg, *J. Phys. Chem. B* **2003,** *107,* 2771-2779.
[28] P. Sarkar, *PHYSICAL REVIEW B*, **2003,** 68, 235409.
[29] M. Yu, G. W. Fernando, R. Li, F. Papadimitrakopoulos, N. Shi, R. Ramprasad, J. Computer-Aided Mater. Des., **2007**, 14,167–174
[30] N. Herron, J.C. Calabrese, W.E. Farneth, Y.Wang, *Science*, **1993**, 259, 1426-1428.
[31]] S. Kudera, M. Zanella, C. Giannini, A. Rizzo, Y. Li, G. Gigli, R. Cingolati, G. Ciccarella, W. Spahl, W.J. Parak, L. Manna, *Adv. Mater.* **2007**, 19, 548-552.
[32] Q. Dai, D. Li, J. Chang, Y. Song, S. Kan, H. Chen, B. Zou, W. Xu, S. Xu, B. Liu, G. Zou, Nanotecnology, **2007**, 18, 405603.
[33] P. Dagtepe, V. Chikan, J. Jasinski, V. J. Leppert, *J. Phys. Chem. C,* **2007,** *111,* 14977-14983.
[34] W. E. Farneth, N. Herron, Y. Wang, *Chem. Mater.,* **1992**, 4, 916-922.
[35] T. Vossmeyer, G. Reck, B. Schulz, L. Katsicas, H. Weller, *J. Am. Chem. Soc.* **1995,** *117, 12881*-12882.
[36] W. W. Yu, Y. A. Wang, X. Peng, *Chem. Mater.* **2003,** *15,* 4300-4308.
[37] L. Carbone, C. Nobile, M. De Giorni, F. Della Sala, G. Morello, P. Pompa, M. Hytch, E. Snoeck, A. Fiore, I. R. Franhini, M. Nadasar, A. F. Silvestre, L. Chiodo, S. Kudera, R. Cingolati, R. Krahne and L. Manna, *Nano Lett.,* **2007**, 7 (10), 2942,2950.
[38] D. V. Talapin, A. L. Rogach, M. Haase, H. Weller, *J. Phys. Chem. B* **2001,** *105,* 12278-12285.
[39] N.V. Mantzaris, *Chemical Engineering Science,* **2005**, 60, 4749-4770.
[40] Z. A Peng, X. Peng, *J. Am. Chem. Soc.,* **2002**, 124, 3343-3353.

General Approach to II-VI Semiconductor Magic Size Nanoparticles

Marco Zanella[1], Azhar Zahoor Abbasi[1], Andreas Schaper[2]* and Wolfgang J. Parak[1]*

1 Fachbereich Physik, Philipps Universität Marburg, Renthof 7, 35037 Marburg, Germany
2 EM&M Laboratory, Material Science Philipps Universität Marburg, Hans-Meerwein-Str., 35032 Marburg, Germany

*corresponding author: schaper@staff.uni-marburg.de, wolfgang.parak@physik.uni-marburg.de

Supporting Information

I) Synthesis

I.1) Chemicals. Cadmium oxide (99.999%), Zinc Oxide (99.999%), nonanoic acid (97%), decylamine (98%), sulphur powder (99.9%, 100mesh), selenium powder (99.9%, 100mesh), tellurium powder (99.8%, 200mesh), water free toluene and methanol were purchased from Sigma while TOP (97%) was purchased from Strem. All the chemicals were used as shipped.

I.2) CdS MSC synthesis. 514mg of Cadmium oxide, 2 g of decylamine and 2g of nonanoic acid were mixed in a three-neck flask. The flask was pumped to vacuum at 100 for 15 minutes and then heated at 200 °C under nitrogen to decompose the CdO. The temperature was then lowered to 60 °C and 10 g of a solution of S in Trioctylphosphine (10% in weight of S) was injected. The temperature after the injection dropped and was allowed to recover and increased to 80 °C. During the growth, 0.1 ml of the growth solution were extracted at time intervals ranging from 3-5 minutes (at the early stages of growth) to several hours (after several hundreds of minutes of growth) and diluted into toluene.

Size selective precipitation. After the synthesis, the heating mantel was removed and the solution left cooling to room temperature. Two milliliters of toluene were added to this solution, followed by methanol until a persistent cloudiness was observed. This solution was centrifuged and the precipitate was washed again by addition of a few ml of toluene and methanol. The final precipitate was redissolved in toluene. By this procedure the largest magic sizes are almost quantitatively separated from the smaller magic sizes present.

I.3) CdTe MSC synthesis. 257mg of Cadmium oxide, 1 g of decylamine and 1g of nonanoic acid were mixed in a three-neck flask. The flask was pumped to vacuum at 100 for 15 minutes and then heated at 200 °C under nitrogen to decompose the CdO. The temperature was then lowered to 90 °C and the tellurium stock solution (255mg of tellurium dissolved in 5g of Trioctylphosphine) was injected. The temperature after the injection dropped and was allowed to recover and increased to 120°C. During the growth, 0.1 ml of the growth solution were extracted at time intervals ranging from 3-5 minutes (at the early stages of growth) to several hours (after several hundreds of minutes of growth) and diluted into toluene.

Size selective precipitation. After the synthesis, the heating mantel was removed and the solution left cooling to room temperature. Methanol was added until a persistent cloudiness was observed. This solution was centrifuged and the precipitate was washed again by addition of a few ml of toluene and methanol. The final precipitate was redissolved in toluene. By this procedure the largest magic sizes are almost quantitatively separated from the smaller magic sizes present.

I.4) ZnSe MSC synthesis. 488mg of Zinc oxide, 2 g of decylamine and 2g of nonanoic acid were mixed in a three-neck flask. The flask was pumped to vacuum at 100 for 15 minutes and then heated at 200 °C under nitrogen to decompose the ZnO. The temperature was then lowered to 130°C and 10 g of a solution of Se in Trioctylphosphine (10% in weight of Se) was injected. The temperature after the injection dropped and was allowed to recover and increased to 170 °C. During the growth, 0.1 ml of the growth solution were extracted at time intervals ranging from 3-5 minutes (at the early stages of growth) to several hours (after several hundreds of minutes of growth) and diluted into toluene.

Size selective precipitation. After the synthesis, the heating mantel was removed and the solution left cooling to room temperature. Two milliliters of toluene were added to this solution, followed by

methanol until a persistent cloudiness was observed. This solution was centrifuged and the precipitate was washed again by addition of a few ml of toluene and methanol. The final precipitate was redissolved in toluene. The injection of Te:TOP stock solution or just TOP with different molar ratio always led to ZnO MSCs but in the case in which the Zn:Te molar ratio is in favor of the chalcogen for which no magic size peak was observed (Table S1 and Figure S13).

I.5) ZnO MSC synthesis. 651mg of Zinc oxide, 3 g of decylamine and 3g of nonanoic acid were mixed in a three-neck flask. The flask was pumped to vacuum at 100 for 15 minutes and then heated at 200 °C under nitrogen to decompose the ZnO. The temperature was then lowered to 180°C for the rest of the synthesis. During the growth, 0.1 ml of the growth solution were extracted at time intervals ranging from 3-5 minutes (at the early stages of growth) to several hours (after several hundreds of minutes of growth) and diluted into 2-3ml of toluene.
After the synthesis, the heating mantel was removed and the solution left cooling to room temperature. Two milliliters of toluene were added to this solution, followed by methanol until a persistent cloudiness was observed. This solution was centrifuged and the precipitate, the final precipitate was redissolved in toluene.

I.6) Comparison of the reaction conditions. Using the same precursors and surfactants in synthesizing these particles allowed us to perform a significant comparison among different materials. No main differences were met for the decomposition of cadmium and zinc. After pumping the vacuum at 100°C for 15-20min ZnO and CdO are well decomposed when the temperature is raised to 200°C and their complex with the nonanoic acid is stable. We observed that the same conditions can be employed for the decomposition of lead oxide which opened the way to the synthesis of lead chalcogenide semiconductors nanoparticles under investigation in our group. In the case of mercury, most of the HgO decomposes into liquid mercury drops during the usual decomposition procedure and just a little amount forms the complex with the nonanoic acid. Since, for the nucleation of the MSC a high concentration of precursors is required in solution probably this kind of protocol is not the proper for the synthesis of mercury chalcogenide MSC.
The main difference between zinc and cadmium concerns their reactivity with the chalcogens solutions (Table S1). For the synthesis of ZnSe and ZnO MSC the growth temperature could be held to 170-180°C and still the crystals required several hour to appear while for cadmium a temperature close to 100°C led to the growth of the smallest families of clusters in a few minutes.
Precursors concentration and molar ratio appear to be paramount for the formation of the MSCs. Generally an high concentration of precursors is required for the synthesis of small nanoparticles in order to increase the amount of nuclei. In the case of CdS, ZnSe (Table S1) and CdSe [1] it has been observed that small Cd:S, Cd:Se and Zn:Se ratios favor the MSCs formation. This fact is very interesting in order to understand which, among the precursors, is responsible for triggering the nucleation. If S and Se are able to trigger the nucleation for CdS, ZnSe and CdSe MSCs, for CdTe and ZnTe it seems the opposite. Although we observed CdTe MSCs even on synthesis with different molar ratios we observed that more peaks are visible with an higher Cd:Te ratio (Table S1). In the case of ZnTe the presence of an higher Zn:Te ratio always guarantee the MSCs nucleation. In general the MSCs reported here can be grown at temperature higher than those here reported without affecting their properties (abs peak position i.e.). Anyway a slow growth allows a better control of the different proportion of families of MSC present in solution which maximize the probability to isolate one family from the others. This can highly improve the quality of the precipitate and the yield of the synthesis.

Cd:S molar ratio	CdO	S:TOP	NNA	DA	MSCs formation
4,59:31,25 (≈1:6)	514mg	1g S: 10g TOP	2g	2g	Yes
4,46:12,65 (≈1:3)	500mg	405mg S: 10g TOP	2g	2g	No

T S:TOP injection: 60°C Growth temperature 75-80°C
2-3ml toluene+ 20ml methanol 2 times for purification

Cd:Te molar ratio	CdO	Te:TOP	NNA	DA	MSCs formation
2:2	257mg	255mg:5g	1g	1g	Yes best result
1:2	257mg	510mg:10g	1g	1g	Yes
2:1	257mg	255mg:5g	2g	2g	Yes

T Te:TOP injection: 90°C T Growth: 120°C
20ml methanol 2 times for the purification.

Zn:Se molar ratio	ZnO	Se:TOP	NNA	DA	MSCs formation
1:0,95	976,43mg	1g:10g	4,5g	4,5g	Yes
1:2	488.4mg	1g:10g	2g	2g	Yes
2:1	488.4mg	237mg:5g	2g	2g	No

T Se:TOP injection: 130°C T Growth: 170°C
2-3ml toluene+ 20ml methanol 2 times for purification

Zn:Te molar ratio	ZnO	Te:TOP	NNA	DA	MSCs formation
1:1	162,8mg	255mg:5g	2g	2g	Yes
1:2	81,4mg	255mg:5g	1g	1g	No
2:1	325mg	255mg:5g	2,5g	2,5g	Yes
4:1	651,2mg	255mg:5g	3g	3g	Yes (even with just TOP)
6:1	976,8mg	255mg:5g	4,5g	4,5g	Yes

T injection: 130°C T Growth: 180°C
2-3ml Toluene+ 20ml methanol for the purification

Table S1. *MSCs synthesis depending from the synthesis conditions. Last column indicate if the MSCs are or not a product of the synthesis. NNA and DA are the amount of nonanoic acid and decylamine employed. Below each chart the different reaction, and purification are reported.*

II) Characterization of structural and compositional properties

II.1) Transmission electron microscopy (TEM). TEM and HRTEM micrographs were recorded with JEOL JEM-3010 (300KV) at the Electron Microscopy & Microanalysis Laboratory (EM&MLab). Samples were prepared by dropping the NCs solution on a TEM grid, and waiting for the solvent evaporation.

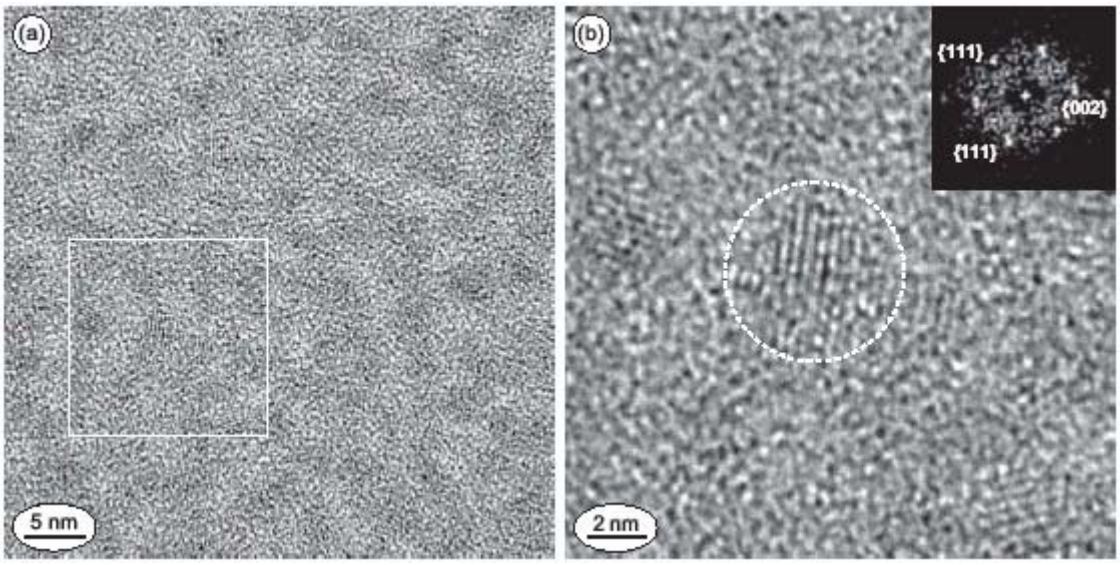

Figure S1. *TEM micrograph of cadmium sulfide nanoparticles of sample CdS I with cubic structure: (a) overview, (b) close-up of the square region marked in (a), inset the diffractogram of the marked circular area revealing (110) zone axis orientation of the single particle.*

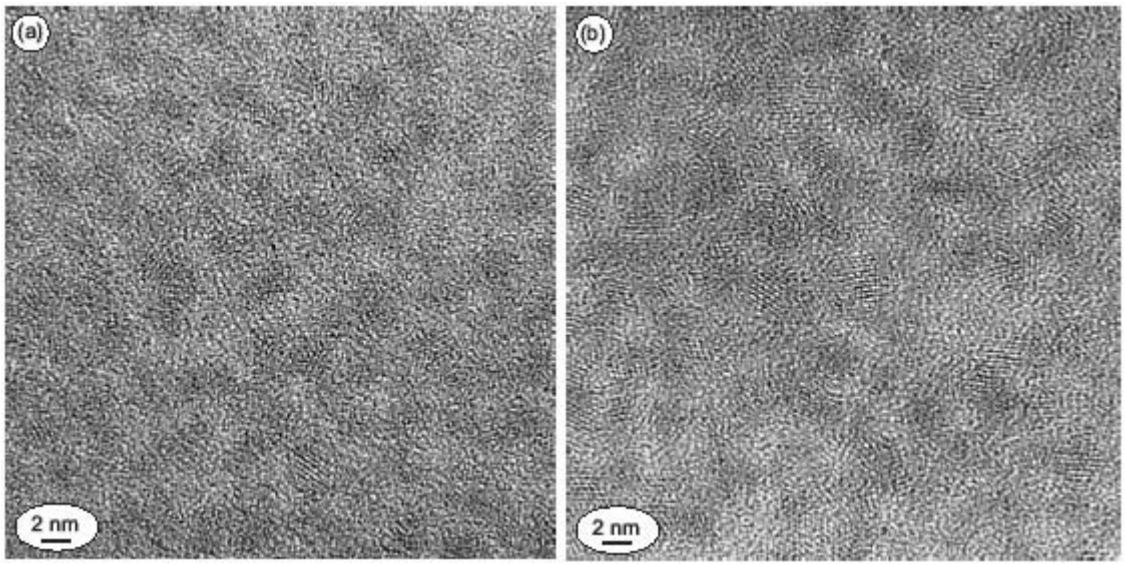

Figure S2. *Overview TEM images of cadmium sulfide nanoparticles of samples CdS II (a) and CdS IV (b).*

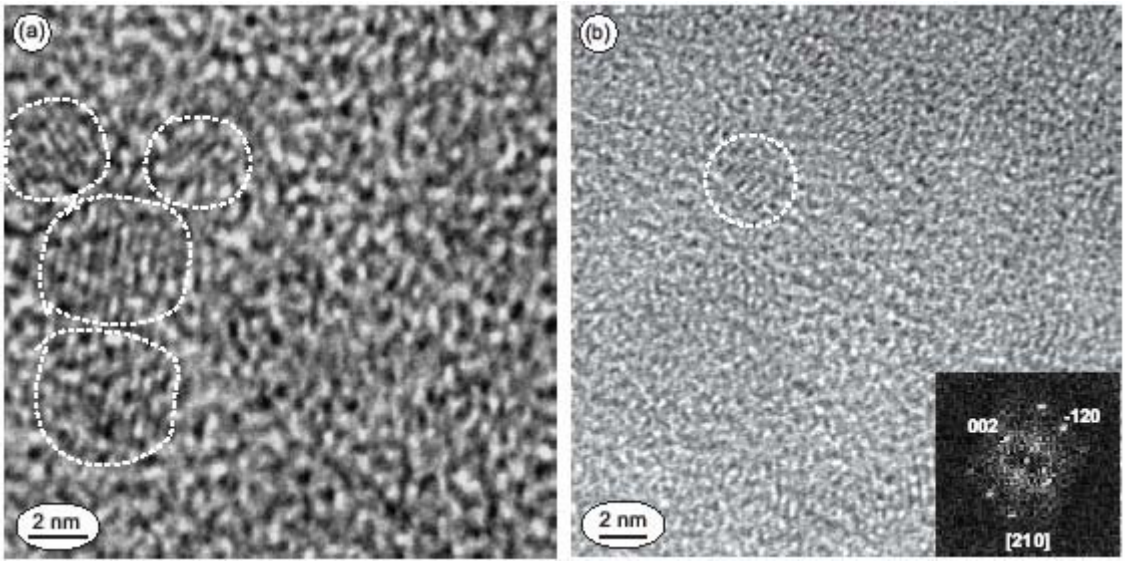

Figure S3. *TEM micrographs of cadmium telluride nanoparticles of samples CdTe I (a) and CdTe II-III (b). In (a) two particles are marked by solid lines, in (b) the diffractogram of the encircled area reveals the hexagonal (210) zone axis orientation of the respective single particle.*

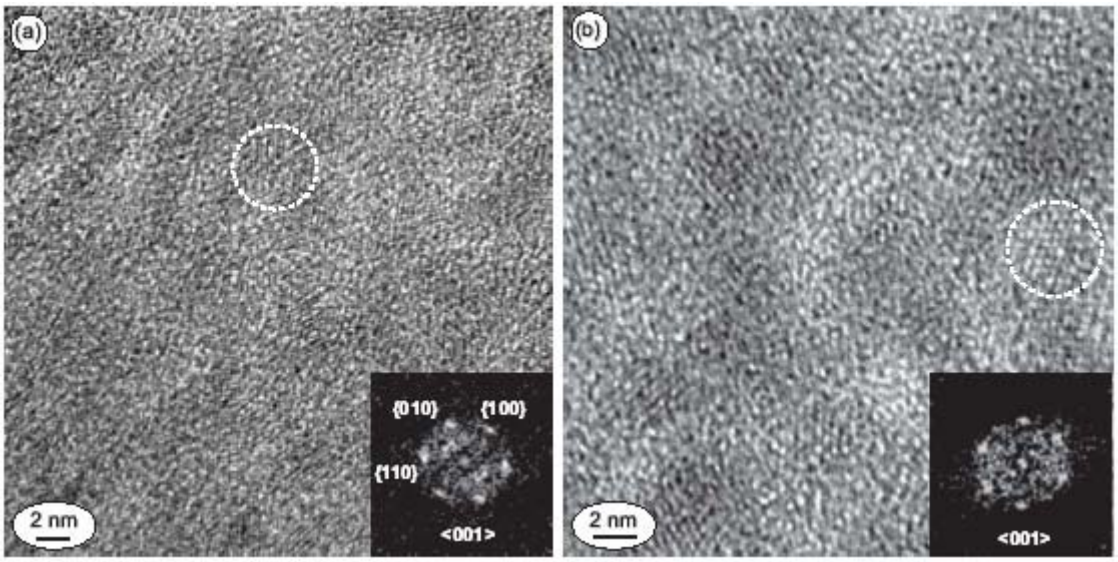

Figure S4. *TEM micrographs of zinc selenide nanoparticles of samples ZnSe including all three MSCs (a) and a sample with particles belonging just to ZnSe III (b). The diffractogram inset of the encircled area in each image reveals the hexagonal (001) zone axis orientation of the respective single particle.*

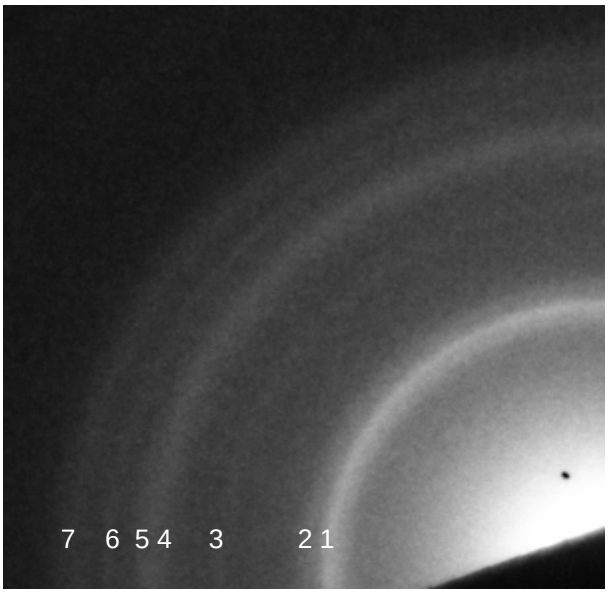

Figure S5. *SAED of ZnSe MSCs. This picture was taken from a sample in which all the ZnSe MSCs families were present. In the picture are clearly visible the rings due to the hexagonal structure (1,2,3,4 (faint)). Anyway the broadness of the rings due to the small particles size does not let us to exclude the presence of some particles with cubic (zinc blende) structure.*

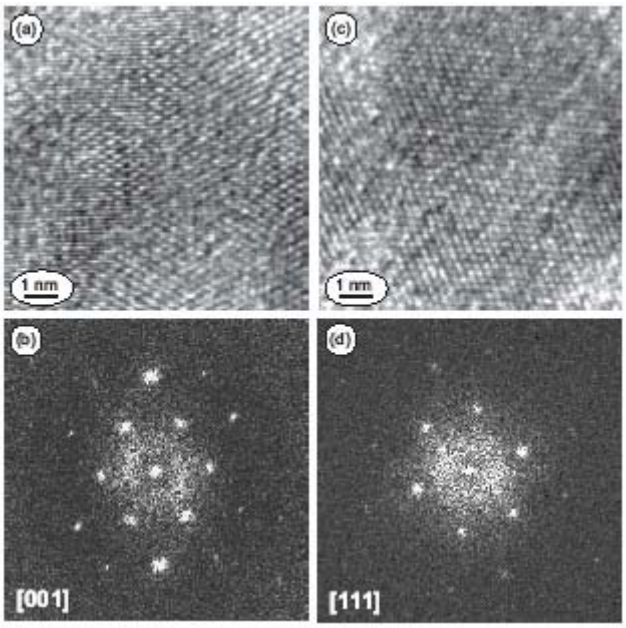

Figure S6. *TEM micrographs of two zinc oxide nanoparticles of sample of ZnO MSCs (a) and (c) with their corresponding diffractograms indicating (b) (001) and (d) (111) zone axis orientation of the hexagonal structure.*

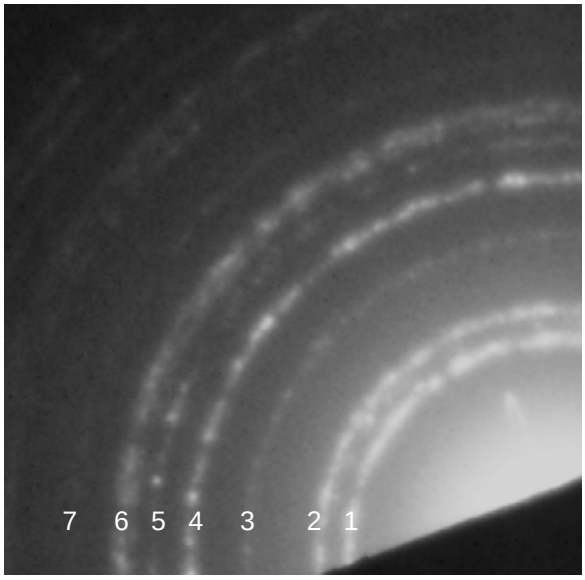

Figure S7. *SAED of ZnO MSCs. In the picture are clearly visible the rings due to the hexagonal structure (1, 2, 3, 4, 6 and 7) but the presence of the ring 5 confirm the presence of same particles having a cubic structure as reported in table S2.*

Ring	**hkl (hexagonal)**	**hkl (cubic)**
1	100	none
2	002	111
3	110	220
4	200	311
5	none	400
6	210	331
7	300	422

Table S2. *Assignment of SAED rings to hexagonal and cubic structure.*

II.2) Energy dispersive X-ray spectroscopy (EDX). EDX graphs were recorded with a SEM CamScan IV at EM&MLab. Nanocrystals were precipitated 3 times and the powder was left drying under nitrogen atmosphere before being spread on a silicon wafer.

CdS MSC EDX

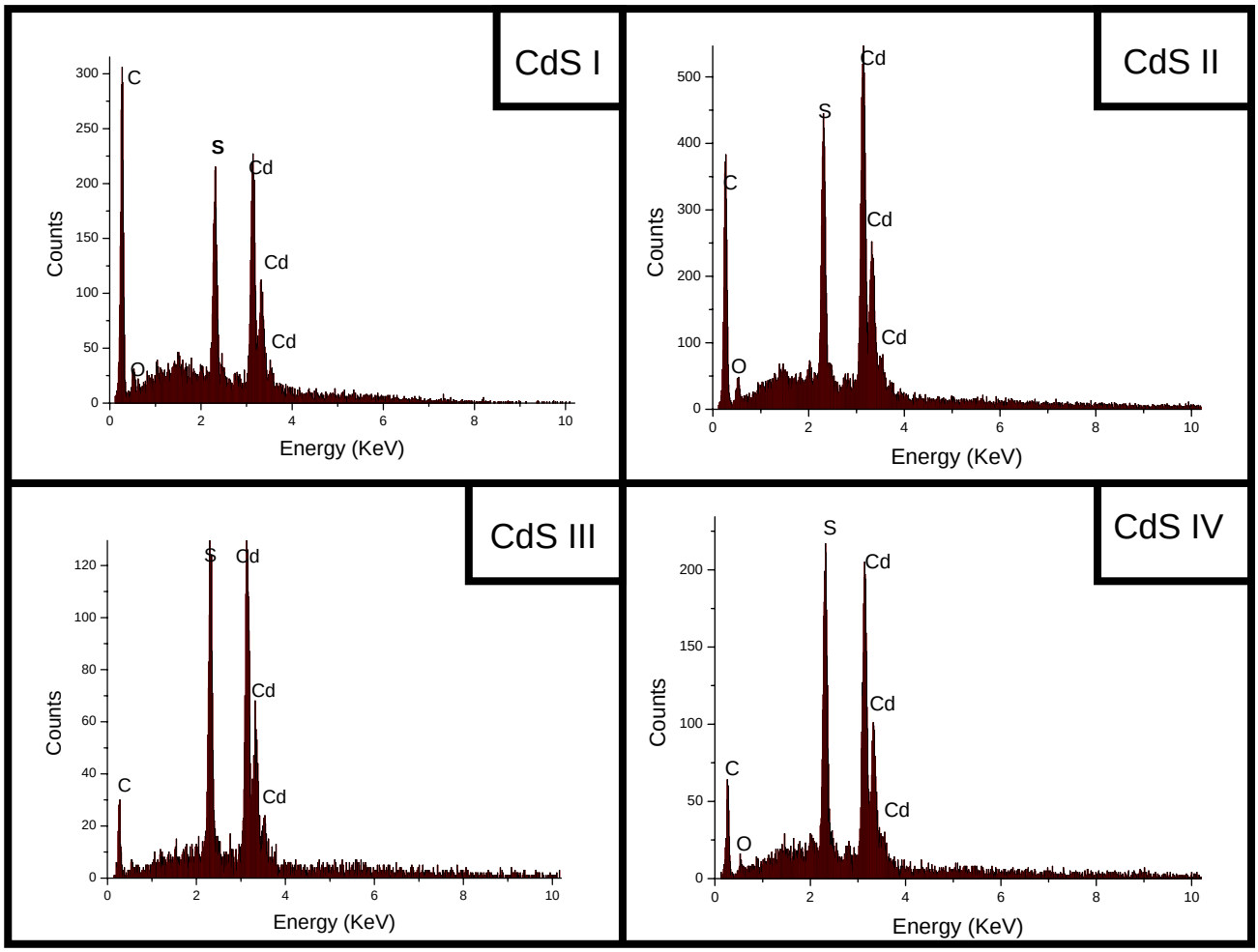

Figure S8. *EDX spectra of the first (CdS I), second (CdS II), third (CdS III) and forth (CdS IV) cadmium sulphide MSC. (Accelerating voltage 15kV, spectra acquisition time 100s).*

Cadmium (Lα1 (3,129KeV), Lβ1 (3,295KeV)) and sulphur (Kα (2,299KeV), Kβ (2,441KeV)) transitions are clearly visible in these spectra. The presence of carbon, oxygen and phosphorous are due to the surfactants still present on the NCs surface after the washing procedure.

CdTe MSC EDX

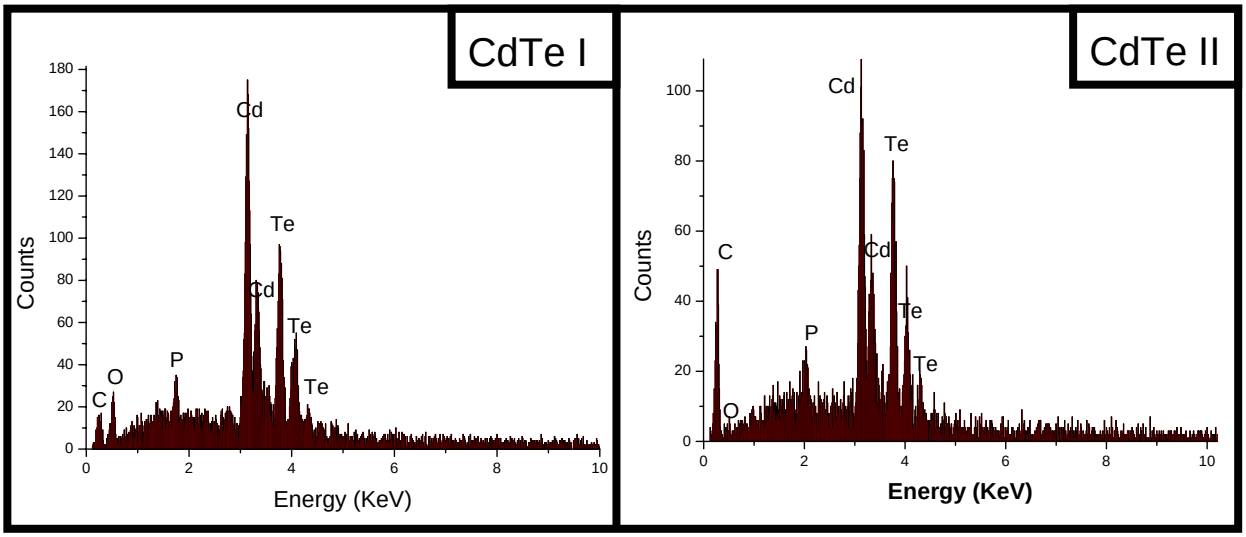

Figure S9. *EDX spectra of the first (CdTe I) and second (CdTe II) cadmium telluride MSC. (Accelerating voltage 15kV, spectra acquisition time 100s).*

Cadmium (Lα1 (3,129KeV), Lβ1 (3,295KeV)) and Tellurium (Lα1 (3,796KeV), Lβ1 (4,006KeV), Lβ2 (4,29KeV)) transitions are clearly visible in these spectra. The presence of carbon, oxygen and phosphorous are due to the surfactants still present on the NCs surface after the washing procedure.

ZnSe MSC EDX

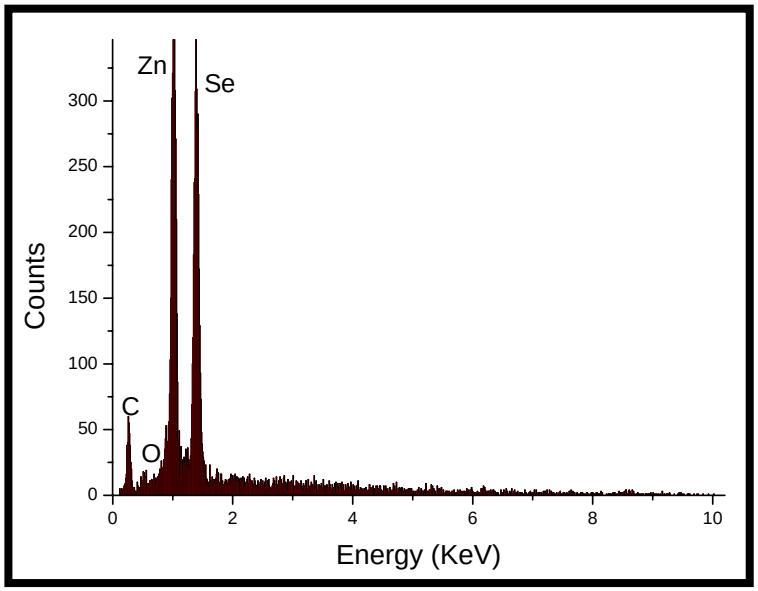

Figure S10. *EDX spectra of the ZnSe MSC without size selective precipitation. In this sample all the three MSCs families were present. (Accelerating voltage 15kV, spectra acquisition time 100s).*

Zinc (L1 (0,877KeV), Lα1 (0,996KeV), Kα1 (08,628KeV), Kβ1 (9,553KeV)) and selenium (Lα1 (1,375KeV)) transitions are clearly visible in this spectrum. The presence of carbon, oxygen and phosphorous are due to the surfactants still present on the NCs surface after the washing procedure.

ZnO MSC EDX

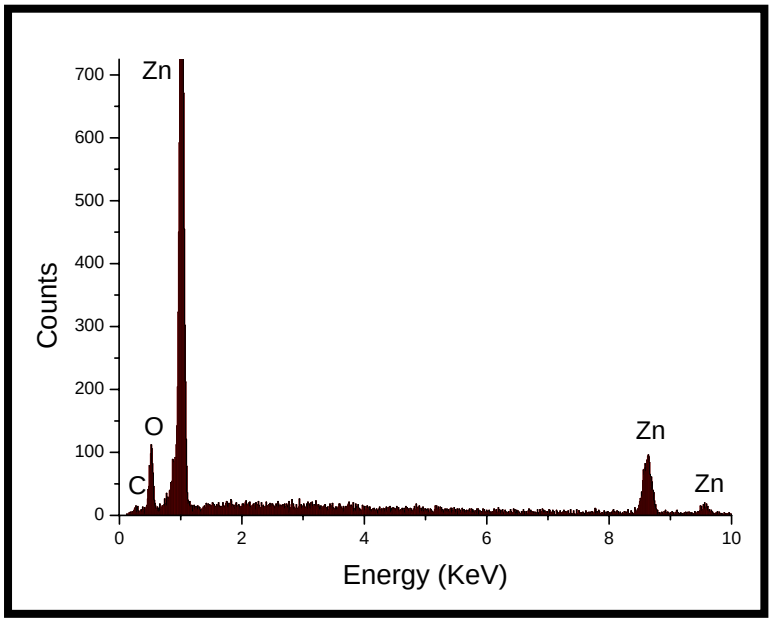

Figure S11. *EDX spectrum of the ZnO MSCs (Accelerating voltage 20kV, spectra acquisition time 100s).*

Zinc (L1 (0,877KeV), Lα1 (0,996KeV), Kα1 (08,628KeV), Kβ1 (9,553KeV)) and oxygen (Kα (0,521KeV) transitions are clearly visible in this spectrum. The presence of carbon, is due to the surfactants still present on the NCs surface after the washing procedure.

III) Characterization of optical properties

III) Absorbance and fluorescence. All the absorbance spectra were collected with an Agilent 8453 UV-vis absorbance spectrometer, while a Fluoromax-3 (JOBIN YVON HORIBA) fluorescence spectrometer was used to record the fluorescence spectra. All the spectra were taken from nanoparticles dissolved in toluene.

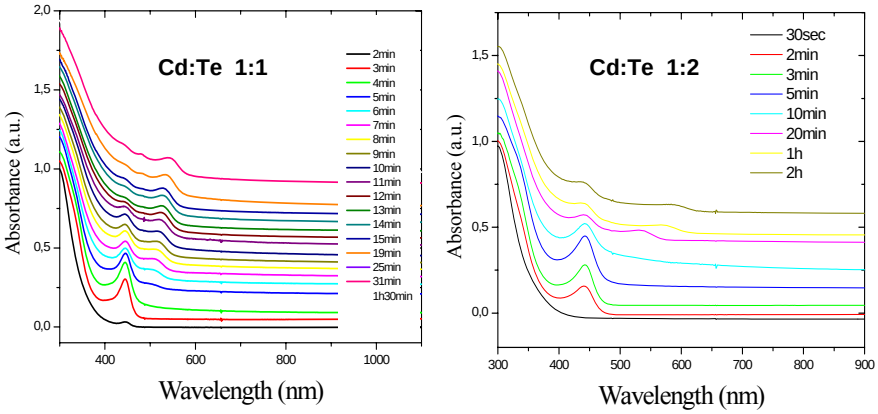

Figure S12. *Absorbance spectrum time evolution of a solution of CdTe MSCs at different Cd:Te ratios. The Te:TOP stock solution was injected at 100°C and the nanoparticles were let growing at 130°C. In each Cd:Te molar ratio tried, the peak characteristic of CdTe I appeared but with different broadness. Increasing the molar ratio this peak gets sharper and even the other peaks become more distinguishable.*

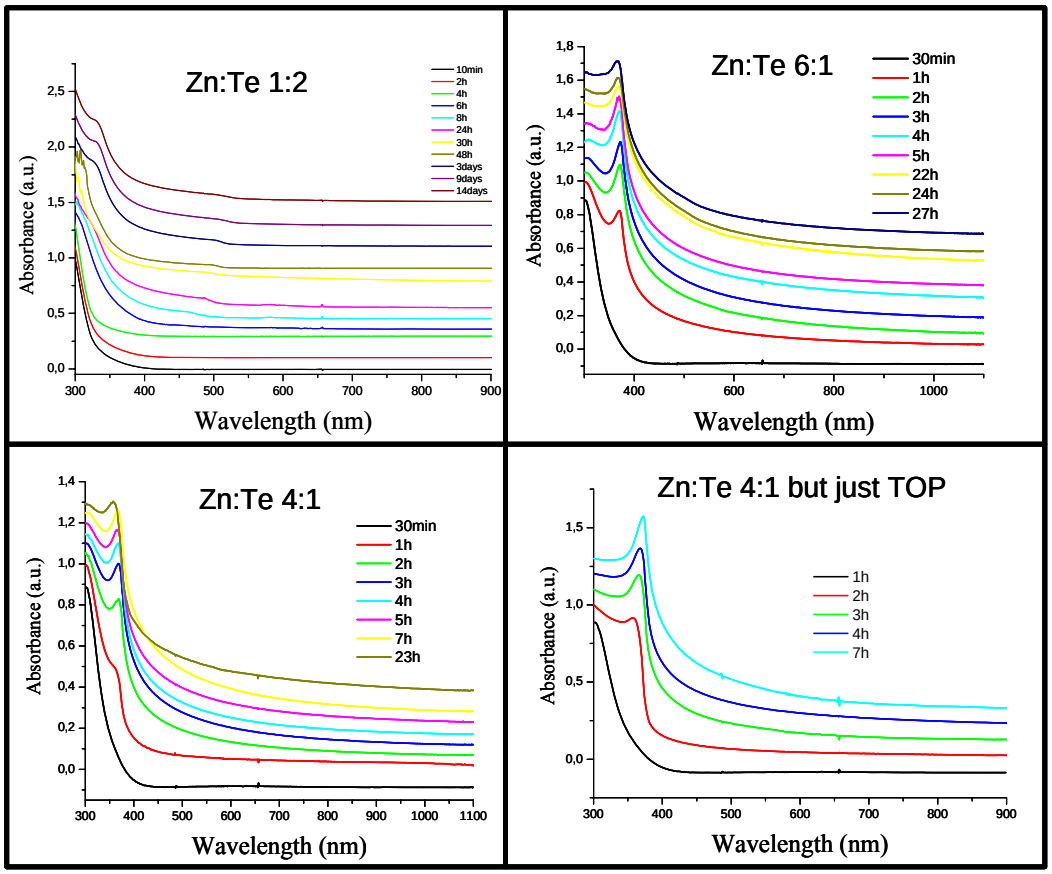

Figure S12. *Absorbance spectra time evolution of a solution of ZnTe MSCs at different Zn:Te ratio. The Te:TOP stock solution was injected at 130°C and the nanoparticles were let growing at 180°C. a) Zn:Te ratio 1:2, b) Zn:Te ratio 6:1, c) Zn:Te ratio 4:1, d) Zn:Te ratio 4:1. in this synthesis the solution just the volume of TOP was the same of synthesis c) but no tellurium was injected.*

IV) References

[1] Kudera S.; Zanella M.; Giannini C.; Rizzo A.; Li Y.; Gigli G.; Cingolati R.; Ciccarella G.; Spahl W.; Parak W.J.; Manna L. Adv. Mater. **2007**, 19, 548-552.

Growth of colloidal hybrid nanoparticles of fluorescent group II/VI particles on top of magnetic iron-platinum (Accepted for publication)

Marco Zanella[1,2], Andrea Falqui[3], Stefan Kudera[2,4,5], Liberato Manna[4], Maria F. Casula[3,*], Wolfgang J. Parak[1,2,*]

[1] Fachbereich Physik, Philipps Universität Marburg, Marburg, Germany
[2] Center for Nanoscience, Ludwig Maximilians Universität München, München, Germany
[3] Dipartimento di Scienze Chimiche and INSTM, Università di Cagliari, Cagliari, Italy
[4] National Nanotechnology Laboratory of CNR-INFM, Lecce, Italy
[5] Max Planck Institute for Metals Research, Dept. New Materials and Biosystems & University of Heidelberg, Dept. of Biophysical Chemistry, postal address: Heisenbergstr. 3, D-70569 Stuttgart, Germany

[*] corresponding authors: casulaf@unica.it, wolfgang.parak@physik.uni-marburg.de

Abstract

Colloidal hybrid nanoparticles with blebs of II-VI particles on top of FePt particles were successfully grown. Whereas in the case of XE = CdS, ZnS, PbS and CdSe, FePt-XE dimer structures were successfully obtained, the growth failed for XE = ZnSe, PbSe. Structural, magnetic, and optical analysis of the structures revealed that though there is only moderate influence of the semiconductor domain on the magnetic properties of the FePt core particle, there is significant fluorescence quenching of the semiconductor bleb due to the underlying FePt particle.

Growth of colloidal hybrid nanoparticles of fluorescent group II/VI particles on top of magnetic iron-platinum

Marco Zanella[1,2], Andrea Falqui[3], Stefan Kudera[2,4,5], Liberato Manna[4], Maria F. Casula[3,*], Wolfgang J. Parak[1,2,*]

[1] Fachbereich Physik, Philipps Universität Marburg, Marburg, Germany
[2] Center for Nanoscience, Ludwig Maximilians Universität München, München, Germany
[3] Dipartimento di Scienze Chimiche and INSTM, Università di Cagliari, Cagliari, Italy
[4] National Nanotechnology Laboratory of CNR-INFM, Lecce, Italy
[5] Max Planck Institute for Metals Research, Dept. New Materials and Biosystems & University of Heidelberg, Dept. of Biophysical Chemistry, postal address: Heisenbergstr. 3, D-70569 Stuttgart, Germany

[*] corresponding authors: casulaf@unica.it, wolfgang.parak@physik.uni-marburg.de

Abstract

Colloidal hybrid nanoparticles with blebs of II-VI particles on top of FePt particles were successfully grown. Whereas in the case of XE = CdS, ZnS, PbS and CdSe, FePt-XE dimer structures were successfully obtained, the growth failed for XE = ZnSe, PbSe. Structural, magnetic, and optical analysis of the structures revealed that though there is only moderate influence of the semiconductor domain on the magnetic properties of the FePt core particle, there is significant fluorescence quenching of the semiconductor bleb due to the underlying FePt particle.

Introduction

For a variety of applications the combination of magnetism and fluorescence within a single particle is desirable. Such particles with magnetic moment could be manipulated by external magnetic field gradients (e.g. spatial separation or accumulation) and observed by their fluorescence. Several approaches to the synthesis of such hybrid particles have been reported in literature, for example by embedding magnetic and fluorescent particles in the same matrix [1-4], by chemically linkage of the magnetic and fluorescent particles [5], and by growing one particle of one type on a particle of the other type [6, 7]. The first two routes are based on the linkage of readily prepared nanocrystals by means of organic molecules, whereas the third route is based on nucleating a particle of the second material directly on top of a particle of the first material that acts as seed [8-10]. Advanced synthesis routes that allow for growing one type of particle on top of another one have been demonstrated for several systems, such as CdS-PbSe, CdSe-PbSe, CdSe-CdTe, and CdS-CdTe [11-13] , CdSe-Au, and CdS-Au [14-16], Au-Fe_3O_4 [17, 18], Au-$CoFe_2O_4$ [19], Au-$CoPt_3$ [20], ZnO-Ag [21], In_2S_3-Cu_2S [22], CdS- Fe_2O_3, HgS- Fe_2O_3, ZnS - Fe_2O_3[23], CdSe-Fe_2O_3[6], and CdS-FePt [7]. In general most of these syntheses are based on using the first type of particle as seed for the nucleation of the particles of the second material. When the initial first particle is highly anisotropic, e.g. of rod- instead of spherical shape, it is often possible to grow a domain of the second material at well-defined locations on top of the first particles, such as for instance on the tips of rod-shaped nanocrystals [11, 14, 15].

For the growth of magnetic-fluorescent hybrid nanoparticles the protocol of Gu et al. [7] has raised particular interest, as it allows for the synthesis of nanoparticles with a good size distribution and uniformity. The starting materials in this protocol are colloidal FePt nanocrystals grown in an

organic solvent in the presence of stabilizer molecules. Addition of sulfur at first leads to the formation of an amorphous sulfur shell around the FePt particles, which is then converted to a CdS shell by subsequent addition of Cd^{2+} ions. Due to the lattice mismatch between CdS and FePt this shell breaks and in a de-wetting process all of the CdS shell material nucleates and anneals at one single location on the surface of each starting FePt nanocrystal. This leads to FePt nanocrystals to which one CdS bleb is attached. Due to the presence of the FePt domain these colloidal hybrid nanoparticles posses a magnetic moment and according to Gu et al. the nanoparticles are also fluorescent due to the presence of the CdS domain [7]. The synthesis could also be generalized to the synthesis of CdSe domains attached to starting FePt nanocrystals [24].

In the present study we want to show that the protocol of Gu et al. [7] can be generalized to a whole class of structures, namely hybrid nanocrystals in which one domain is made of a II-VI semiconductor and the other domain is made of FePt particles. Though adjustment of the synthesis condition for each combination of materials was required, we could successfully grow CdS-FePt, CdSe-FePt, ZnS-FePt and PbS-FePt heterodimers. However, we could not extend Gu's protocol to a high yield synthesis of ZnSe-FePt and PbSe-FePt heterodimers. As each particle comprises two domains of different functionality, i.e. a fluorescent semiconductor domain and a magnetic metal alloy domain, these nanocrystals allow for the investigation of the mutual interactions between the two domains. In this study we studied how the fluorescence of the semiconductor domain and the magnetism of the alloy domain in the hybrid nanocrystals compare to the respective behaviors of the individual, free-standing alloy and semiconductor nanoparticles.

General Synthesis

Our general synthesis strategy followed closely the original protocol by Gu et al. [7] as described above. Two parameters are essential for the formation of the hybrid nanoparticles, namely temperature and reaction time. Conceptually the growth procedure can be divided into two steps, the initial formation of the amorphous semiconductor shell around the FePt particle and the subsequent de-wetting process that is supposed to result in a distinct semiconductor domain on top of the FePt nanoparticle. Too high reaction temperatures lead to a rapid de-wetting process, which results in a splitting of the semiconductor domain from the FePt particle, i.e. to the formation of individual, free-standing semiconductor nanoparticles that are not attached to the FePt particles, and to a fusion of the semiconductor shells, i.e. to inclusion of several FePt particles in a single semiconductor shell.

Following Gu's original protocol on CdS-FePt dimers we observed that during the growth of the amorphous CdS shell around the FePt cores several aggregates were forming in solution. The presence of these agglomerates had been reported already in Gu's paper [7]. By increasing the amount of tri-n-octylphosphine oxide (TOPO) the number of agglomerates could be reduced further and the resulting CdS-FePt core/shell particles and dimers (before and after the de-wetting process, respectively) were stable in solution. Instead of carrying out the synthesis at a constant temperature both during the de-wetting and the annealing phase (as in the original protocol) we decided to increase the temperature linearly at 5°C/min rate until the boiling temperature of octyl ether was reached (see Figure 1). A steeper temperature ramps led to rapid de-wetting and final detachment of CdS from the starting FePt nanoparticles, whereas with a less steep temperature ramp the de-wetting step was too slow and the particles started to agglomerate (see supporting information for low magnification TEM images of samples taken during the different stages of growth).

In Figure 1 we report the reaction conditions (namely temperature ramp reaction time) followed for the syntheses of the various types of heterodimers, while in Figure 2 low-magnification TEM

images of several representative samples of dimers are shown. As an example, the previously described protocol for the synthesis of the CdS-FePt dimers could be extended straightforwardly to the CdSe-FePt system. In this case the adhesion of Se onto the FePt cores took place upon the addition of Se powder to the FePt seed solution at 150°C. After 10 minutes of reaction, TOPO and the Cd precursor were injected, and the resulting mixture was left reacting for 10 min at 150°C. This led to the formation of an amorphous CdSe shell around the starting FePt nanoparticles. The de-wetting/annealing step that led to the formation of the CdSe-FePt dimers was then carried out following the same temperature ramp as for the previous synthesis of CdS-FePt nanoparticles (5°C/min).

In the case of sulfur as constituent of the semiconductor shell the protocol could be extended by substituting Cd either with Zn or with Pb. In the case of ZnS-FePt the above described protocol could be followed directly as well. In the case of Pb on the other hand a "softer" approach was required for the formation of the PbS shell around the FePt seeds. Pb atoms were in fact highly reactive towards the preformed sulfur shell on top of the FePt, and it was therefore necessary to cool down the FePt seed solution (with the already formed sulfur shell) to room temperature before the Pb precursor could be injected. After 5min of reaction the de-wetting step was carried out by increasing the temperature linearly at a 0.6°C/min rate. This slow temperature ramp led to the formation of FePt/PbS dimers as soon as the temperature reached 130-140°C.

When selenium was employed, the formation of a tick amorphous shell of either ZnSe or PbSe around the FePt cores was not very successful, as the high reactivity of Zn and Pb towards the Se layer caused etching of the Se from the FePt surface as soon as the Zn and Pb precursors were injected, even if the injection was carried at room temperature. Therefore attempt to grow ZnSe or PbSe on top of FePt nanoparticles yielded solutions in which FePt nanoparticles remained isolated and various aggregates (most likely of PbSe/ZnSe nanoparticles) were found.

Characterization of Structural Properties

The formation of single colloidal particles with hybrid-structure, i.e. the formation of a semiconductor bleb-like domain on top of each FePt particle, is shown for different II-VI semiconductors in Figure 2. The formation of the hybrid nanocrystals could be monitored by recording TEM images of samples taken at the different stages of the synthesis. In some cases (CdS, CdSe) the core/shell formation and the progressive de-wetting process could be clearly imaged, whereas for the other materials, due to their higher reactivity not even the core/shell formation could be imaged. In all hybrid samples, the FePt core nanocrystal size distribution remained unaltered with respect to the original FePt seeds. From the different contrast of the two phases in the low-magnification TEM images it is possible to identify two spatially separated domains in each nanoparticle.

Crystallinity is very important for the functional properties (fluorescence / magnetism) of the particle domains. Both colloidal FePt and II-VI semiconductor nanoparticles can be synthesized routinely as highly crystalline materials (CdS [25, 26], CdSe [27], FePt [28]). In particular, the FePt nanoparticles used as seed in this study are single domain crystals [28]. Therefore, in order to directly compare the fluorescent and magnetic properties of the hybrid particles with that of individual FePt and II-VI semiconductor nanoparticles, the FePt and the semiconductor domain in the hybrid particles should be crystalline. In the case of synthesis of hybrid particles the II-VI semiconductor domain is formed through heterogeneous nucleation followed by growth and de-wetting and therefore the peculiar crystal formation pathway needs to be monitored in order for the crystallinity to be assessed.

X-ray diffraction (XRD) data clearly indicate the crystallinity of the FePt cores during all steps of the reaction, i.e. for the starting FePt particles, for the FePt particles embedded in the shell of the II-VI semiconductor material, and for the FePt particles with attached II-VI semiconductor bleb. Moreover, no significant variation is observed in XRD peak broadening, indicating that the particle size of the FePt alloy is retained throughout the formation of the hybrid nanoparticle. XRD data also indicate that the initial semiconductor shell around the particles, i.e. the semiconductor before the de-wetting process, is amorphous. On the other hand, the XRD patterns of the hybrid materials after the de-wetting process and annealing show differences with respect to the initial FePt cores. In particular, the presence of a nanocrystalline semiconductor (bleb-shaped) domain is observed in the FePt-CdS, FePt-CdSe, FePt-PbS and FePt-PbSe dimers, whereas in the case of the FePt-ZnS and FePt-ZnSe dimers a broad halo superimposed to the FePt pattern indicates that in this case the semiconductor domain is amorphous. It is remarkable that in the case of the FePt-PbSe dimers the XRD data also suggest the presence of a platinum-lead alloy (all XRD data are shown in the Supporting Information).

In the high resolution TEM images (shown in the Supporting Information) the magnetic and the semiconductor domains can be clearly distinguished, although there are no obvious indications of epitaxial relationships between the two domains at the interface. The size and crystallinity of the magnetic domain is retained throughout the whole dimer formation. On the other hand, the semiconductor domains are more polydisperse in size and their crystallinity depends on the type of semiconductor.

In summary, our structural analysis indicates that the FePt domain in the hybrid particles is crystalline and thus retains the overall structure of the starting domain. XRD patterns also reflect the different reactivities of the various semiconductor materials investigated, which result in domains having different degrees of crystallinity.

Characterization of Magnetic Properties

The magnetic properties of starting FePt nanoparticles are characterized by a static Zero Field Cooled (ZFC) magnetization curve having a main peak centered at 17K, which corresponds to the nanocrystals blocking temperature (T_B), as shown in Figure 3a. In almost all the samples analyzed in this study, a second peak is present in the thermal range between 60K and 70K in the ZFC curves, which is likely due to the presence of a certain amount of bigger FePt nanocrystals in the sample. As reported in Table 1, the crossing temperature (T_{cross}) of the FePt nanoparticles is always above the secondary ZFC maximum of all the samples and corresponds to the temperature of de-blocking of the largest FePt crystals in the samples. T_B is firstly related to the effective magnetic anisotropy K_{eff} of the magnetic domains and to their mean volume. In all the dimer samples T_B is lower than that of the plain FePt. Being the mean volume of the magnetic domain similar for all the samples, the lowering of T_B is therefore related to a corresponding lowering of the effective anisotropy (K_{eff}), which can result from several effects. In fact, it contains all the contributions given to the average anisotropy energy barrier by the magnetocrystalline, surface, stress and shape anisotropy, together with that due to interparticle interactions.

The plain FePt nanoparticles present a hysteresis loop (Figure 3c) with a coercive field H_c of about 1980 Oe, which is the largest recorded among all the samples and is in agreement with the expected very high magnetocrystalline anisotropy of FePt ($K \sim 7 \times 10^7$ erg/cm^3) [29]. The measured value is quite similar to the one reported (1800 Oe) for plain 4nm monodisperse FePt nanoparticles organized in a 120-nm-tick assembly [28]. Even a temperature as low as 2.5K is not enough to

block all the particles' magnetic moment, as can be inferred by the M_r/M_s (absolute / residual magnetization) values that are, for all the samples, well below 0.5, which is the value expected by the Stoner-Wohlfart theory [30] for an assembly of non interacting blocked particles. Moreover, the hysteresis loops of the dimer samples reported in Figure 3b show that the only sample that retains the magnetic behavior of the plain FePt sample is the one with a CdS bleb, for which similar values for H_c and M_r/M_s were found. The other samples show a different behavior: the tendency to the saturation disappears almost completely even at the highest magnetic field, and the M_r/M_s and H_c values decrease dramatically, similar to an antiferromagnetic-like or a spinglass-like phase. This behavior can be ascribed to a possible sulphidation/selenisation that occurs to the FePt cores during the sulphur/selenium adhesion, which could alter the core's magnetic properties. A significant decrease of M_r/M_s and H_c was observed even in the cases where zinc and lead replace cadmium, in the reaction with sulphur. The most likely explanation of such a behavior can be the diffusion of different atoms in the iron platinum core that originates from the presence and from the type of semiconductor. A somehow similar effect was recently observed in Ge/FePt and GePt/FePt bilayer films [31], where the Ge underlayer gave rise to interlayer diffusion that ultimately resulted in the almost complete suppression of the hard ferromagnetic features of the FePt layer. Our data show that lead is particularly aggressive towards the FePt core as it alters its magnetic properties. Moreover, in the FePt/PbS dimers the ZFC main and secondary peak are the broadest among all the samples, suggesting that the diffusion of lead into the FePt cores is not uniform and therefore broadens the corresponding magnetic properties size distribution. This lack of compositional uniformity, *i.e.* the formation in the magnetic core of more than one domain with different composition and magnetic behavior, is supported by the not symmetrical hysteresis loop observed for this sample.

Characterization of Optical Properties

Though Gu et al. have reported a non-negligible quantum yield (QY) for CdS-FePt particles in their original manuscript (3,2%) [7] we were never able to record comparable values of QY on our samples. An important issue in all our experiments was the need for very stringent purification protocols, which were carried out through repeated precipitation and redissolution of the CdS-FePt dimmers, in order to get rid of excess surfactants. The weak fluorescence recorded from our dimmers indicated that the fluorescence of free surfactant in solution cannot be neglected. For instance both TOPO and hexadecylamine (HAD) have a weak blue fluorescence. Even more important mixtures of both surfactants, if heated at the same temperatures as those during dimer growth, yield solutions that emit around 430 nm [32], and thus in the same range of wavelengths as the dimers (see Figure 4). In view of such complications, special care was taken in this study to remove excess surfactant from the dimer solutions before performing the spectroscopic measurements.

In all the dimers synthesized in this study only very weak fluorescence emission could be observed. As the semiconductor blebs are grown on top FePt seed particles (≈ 3.3 nm diameter) the interface between the semiconductor bleb and the underlying FePt metal alloy cannot be neglected. It is well known that organic fluorophores in vicinity of metal-surfaces (in particular of Au) have different fluorescence intensities compared to free fluorophores [33, 34]. Also effects of metal surfaces close to fluorescent semiconductors have been reported [35]. The presence of Au spheres on the tips of CdSe and CdS rods for example has been shown to significantly quench the fluorescence of the CdSe and CdS rods [36]. We believe that also in the case of the case of II-VI semiconductor blebs grown on top of FePt nanoparticles there is significant quenching of the fluorescence of the semiconductor blebs due the underlying FePt surface (here the metal part should act as a sink for both electron and holes that are photo-generated in the semiconductor domain). Another possible

source of quenching could come from doping of the semiconductor with unreacted iron pentacarbonyl which is still present in solution after the iron platinum core synthesis. The presence of iron atoms in the semiconductor ZnS nanocrystals has been shown to cause quenching of their emission [33]. Therefore, several effects could account for the low emission intensity of the dimers.

Our most surprising finding (in accordance with Gao et al. [37]) was that the emission of all material combinations (i.e. CdS-FePt, CdSe-FePt,....) lies in the same range of wavelengths (430-460nm), as can be seen from Figure 4. As the bulk band gaps of the II-VI semiconductors investigated here are significantly different from each other (CdSe: 718nm (1.74eV), CdS: 500nm (2.5eV), ZnS: 340nm (3.68eV), ZnSe: 443nm (2.82eV), PbS: 3048nm (0.41eV), PbSe: 4464nm (0.28eV)) one would assume different wavelength ranges of fluorescence for the different materials in case of blebs of the same size. In order to explain the same wavelengths of emission for different materials Gu et al. argued [7] that the sizes of the blebs in their case (CdS, CdSe) were not the same (3-4 nm for the CdS blebs and 6-8 nm for the CdSe blebds, respectively), so that after taking into account the size-dependence of the band gap [38] both blebs could have a similar band gap and thus color of emission. By this argument they concluded that they observed emission from the CdS and CdSe blebs grown on top of FePt, with a non-negligible quantum yield. Our results show on the other hand that not only the wavelengths of emission of CdSe-FePt and CdS-FePt dimers are comparable, but also those of all the other materials that we have investigated. Our TEM data (Figure 2) also indicate that there is no characteristic dependence of the bleb size on the specific II-VI material. We therefore feel that the assumption that emission from semiconductor blebs on top of FePt nanoparticles can be treated in the same way as the emission from individual semiconductor nanoparticles (quantum dots) should not hold. Though we are not able to propose a detailed alternative mechanism we speculate that the emission of semiconductor blebs is strongly influenced by the underlying FePt particles, which would explain their emission quenching and similar wavelengths of emission. We argue therefore that the emission of blue light by the dimers has a significant contribution from surfactants and/or some polymeric species that form concomitantly during the synthesis of the dimers. The role of surfactant-emission has also been pointed out in similar systems [39]. In this respect we believe that our results and our interpretation are dampening the optimism initially put into new functional fluorescent and magnetic hybrid materials in which both functional domains are in direct contact. The presence of a metal or metal-alloy surface in direct contact with the fluorescent semiconductor is likele to lead to fluorescence quenching. For this reason we believe that in prepare to obtain fluorescent and magnetic hybrid particles more elaborate strategies are required, which for example need to involve a spacer between the semiconductor and the magnetic domain, acting as insulator.

Conclusions

The growth of hybrid nanoparticles is one of the most advanced fields in the area of colloidal nanoparticle synthesis and so far only the synthesis and the related properties of a relatively few structures have been demonstrated. In this study we showed that the synthesis protocol originally introduced by Gu et al. [7] can be adopted to grow a whole class of hybrids which comprise a FePt and a II-VI semiconductor domain. The procedure is highly reproducible and leads to stable nanocrystal solutions. However, in the case of FePt-PbSe and FePt-ZnSe the reaction of lead and zinc precursors with the selenium layer previously attached to the iron platinum cores led to almost complete removal of the selenium layer, even when the reaction occurred at low temperature, which prevented the formation of dimers. Though we failed in the formation of FePt-PbSe and FePt-ZnSe dimmers, from the synthesis point of view the Gu protocol and its modifications are highly satisfactory, as FePt-CdS, FePt-CdSe, FePt-ZnS, FePt-PbS dimers could be reproducibly grown with good quality. On the other hand we debated here that Gu et al. have described the functional

properties of the hybrid particles in an overoptimistic way. Though also our data indicate that there is relatively moderate influence of the semiconductor bleb on top of the FePt on the magnetic properties of the FePt domain, besides the case of PbS in which doping of the FePt with Pb is assumed we believe to have demonstrated evidence that the FePt seed on the other hand strongly influences the fluorescence of the semiconductor blebs. Therefore, to our opinion the fluorescence of the hybrid particles does not follow the same pathway as in the case of individual semiconductor quantum dots and that its low quantum yield practical applications of the present hybrid particles. In our view the synthesis of defined colloidal magnetic / fluorescent hybrid particles is still a challenge, not from the structural point of view, but due to a partial loss of functionality as a result of the creation of an interface between the two domains.

Materials and Methods

FePt cores and FePt-CdS dimers were synthesized according to Gu's original protocol [7]. In order to prepare dimers with other semiconductors, cadmium acetylacetonate was replaced either with zinc acetylacetonate or with lead acetylacetonate and sulfur was substituted by selenium. In case of dimers comprising ZnS the zinc precursor was left reacting with the sulphur layer around the FePt particles at 100°C for 14min in order to form the ZnS shell. In the case of PbS the lead acetyl acetonate was left reacting for 5min at about 40°C. After the formation of the core/shell particles, the annealing and de-wetting step to yield dimmer-like nanoparticles was carried out without any intermediate purification. For the structural characterization XRD patterns were recorded and material phases were identified using the Powder Diffraction Files database. For the magnetic characterization the static Zero Field Cooled (ZFC), the Field Cooled (FC) magnetization, and the isothermal hysteresis loop of the composite particles were measured. For each system the blocking temperature (T_B) and the crossing temperature (T_{cross}) was derived from the recorded data. From the hysteresis loops the coercive field (H_c), and the ratio between the absolute magnetization (M_s) and the residual magnetization (M_r) were derived. All experimental details can be found in the Supporting Information.

Acknowledgements

The project was funded by the German research foundation (DFG, project PA794/3-1) and supported by the Max Planck Society. Marco Zanella is grateful for a fellowship from the International Graduate School at the Center for Nanoscience. The authors are grateful to Abbasi Azhar Zahoor and to Gavin Mountjoy for helpful discussions.

Figures

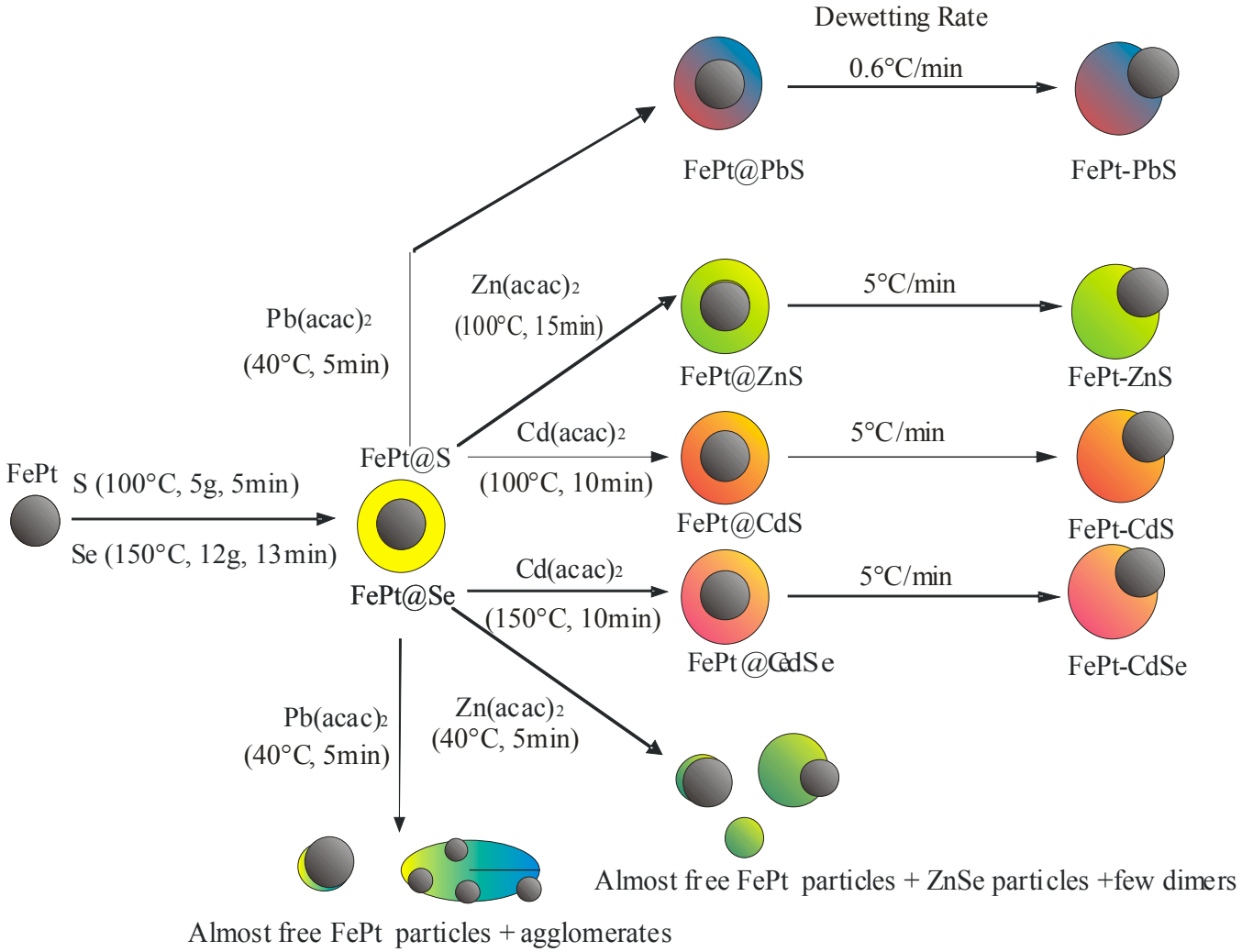

Figure 1: Sketch of the synthesis schemes of the different systems. At first, by adding sulfur and selenium an amorphous sulfur and selenium shell is grown around FePt nanoparticles, respectively. Addition of precursor for the cation (Pb-, Zn-, Cd-acac$_2$; acac = acetylacetonate) and heating at constant temperature leads to the formation of an amorphous II-VI semiconductor shell, with exception in the case of PbSe and ZnSe, where several FePt particles are embedded in one II-VI semiconductor aggregate or complete de-wetting of the II-VI semiconductor shell from the FePt particles occurs. Heating with a linear temperature ramp leads to de-wetting and final formation of a II-VI semiconductor bleb on top of the FePt particles. The corresponding TEM images of the final dimers are shown in Figure 2.

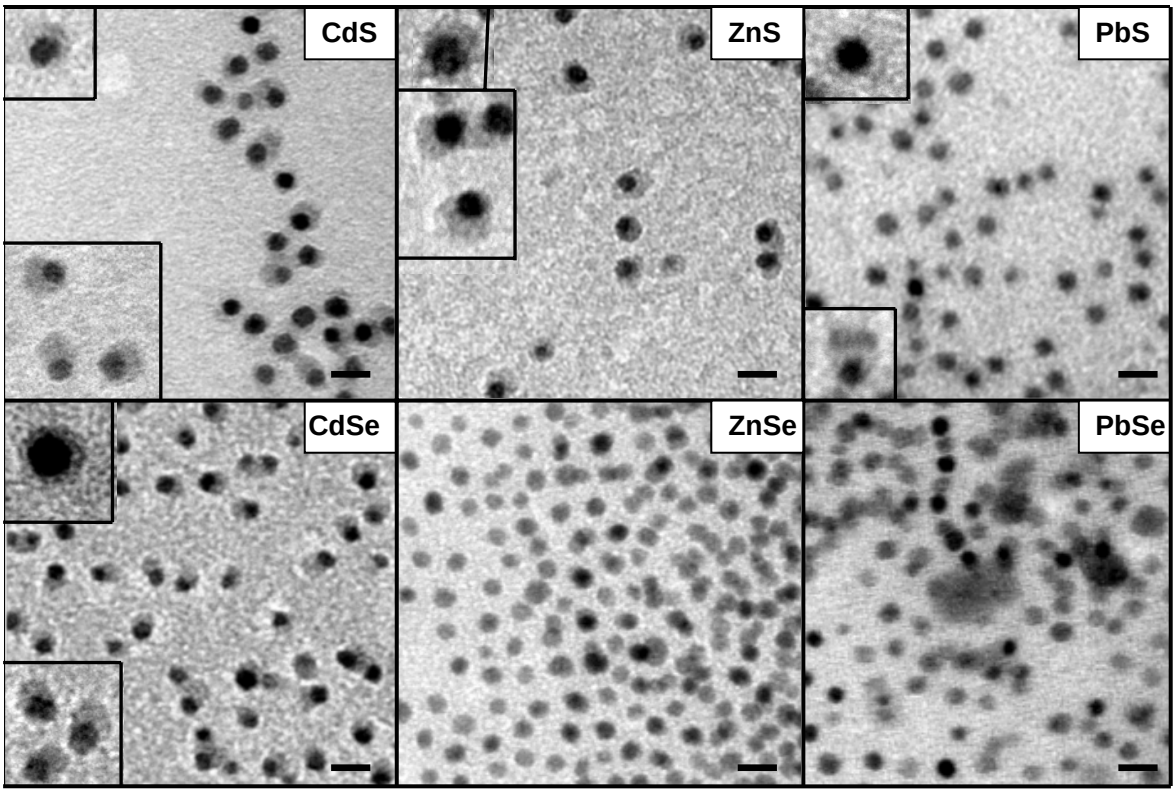

Figure 2: Low resolution transmission electron microscopy (TEM) images of different II-VI semiconductor materials grown on to FePt particles. The darker particles are FePt, the lighter ones are made out of semiconductor material. The scalebars corresponds to 8nm. CdS, ZnS, PbS, CdSe: individual FePt nanoparticles have blebs of the semiconductor material on their surface. Also some particles in which several FePt nanoparticles are embedded in the same II-VI semiconductor matrix are seen as byproduct. The insets show a higher magnification of dimers and corresponding core-shell particles. ZnSe: during the de-wetting process almost all semiconductor material has detached from the FePt cores and besides few FePt-ZnSe dimers mainly free FePt and ZnSe particles can be seen. PbSe: similar to ZnSe a lot of semiconductor material has detached from the FePt cores. In contrast to the ZnSe the PbSe forms not individual particles but rather aggregates, in which some FePt particles are embedded.

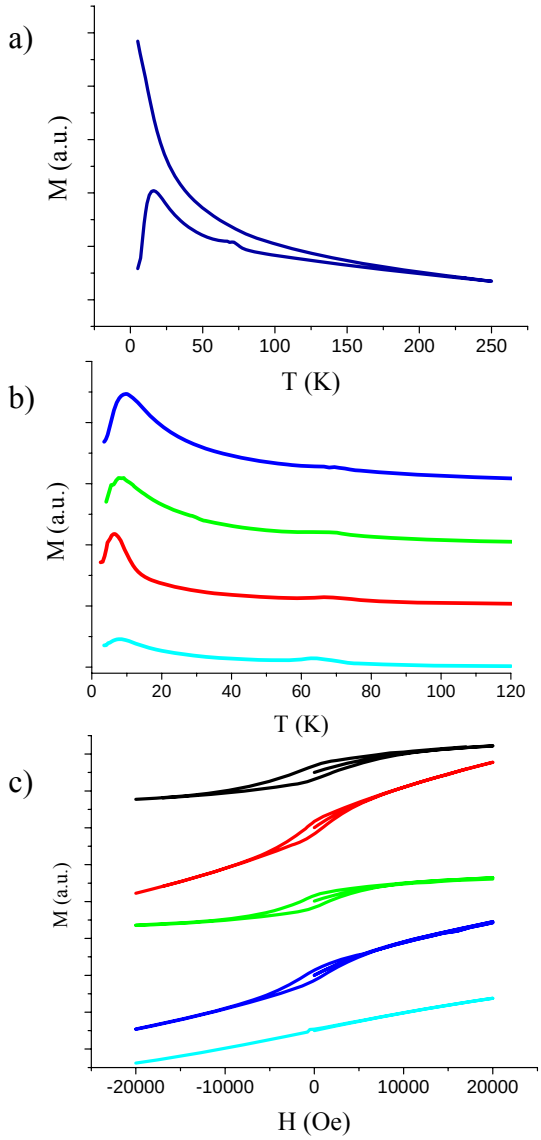

Figure 3: a) Static ZFC and FC magnetization curves of plain FePt particles. b) Static ZFC magnetization curves of FePt-CdSe (blue curve), FePt-CdS (green curve), FePt-ZnS (red curve), and FePt-PbS (light blue curve). c) Hysteresis isothermal loops obtained at T=2.5K of the samples FePt (black), FePt-CdSe (blue), FePt-CdS (green), FePt-ZnS (red) and FePt-PbS (light blue). For clarity the curves are shifted to higher absolute values.

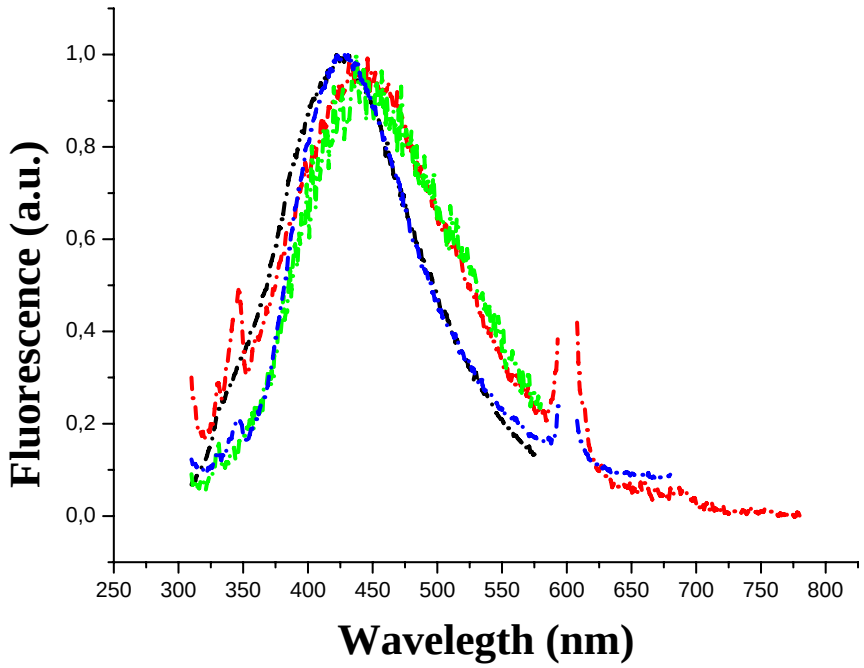

Figure 4: Fluorescence spectra of different particle combinations after one round of purification from excess surfactant molecules. The samples were excited at 300 nm. The intensities of all fluorescence spectra were normalized to the same value. Black curve: FePt-CdS dimers, green curve: FePt-ZnS dimers, red curve: FePt-CdSe dimers, blue curve: aggregates of FePt-PbSe. The peak at 600 nm is an instrumental artifact at the double wavelength of excitation.

Tables

	T_B, T_{cross} (K)	H_c (Oe)	M_r/M_s
FePt	17, 180	1980	0.2
FePt-CdS	9, 240	1464	0.21
FePt-CdSe	10, 66	890	0.03
FePt-ZnS	7, >250	1015	0.03
FePt-PbS	8, >250	560*	0.01

Table 1: Magnetic characterization parameters. The blocking temperature (T_B) is defined as the temperature at which the main maximum of the ZFC (static Zero Field Cooled) magnetization curve appears. The crossing temperature (T_{cross}) is defined as temperature until which the ZFC and FC (Field Cooled) magnetization curves are completely superimposed. From the hysteresis loops the coercive field (H_c) and the ratio between the absolute magnetization (M_s, extrapolated at high field), and the residual magnetization (M_r, measured when the applied field (H) is back to zero after the applied magnetic field reached 5T) were extracted. *This value has been averaged due to a non-symmetrical shape of the recorded data.

References

1. Anker, J.N. and R. Kopelman, Magnetically Modulated Optical Nanoprobes. Applied Physics Letters, 2003. 82: p. 1102-1104.
2. Roberts, T.G., J.N. Anker, and R. Kopelman, Magnetically Modulated Optical Nanospheres (MagMOONS) for Detection and Quantification of Biologically Important Ions Against the Natural Background Fluorescence of Intracellular Environments. J. of Magnetism and Magnetic Materials, 2005. 293: p. 715-724.
3. Zebli, B., et al., Magnetic Targeting and Cellular Uptake of Polymer Microcapsules Simultaneously Functionalized with Magnetic and Luminescent Nanocrystals. Langmuir, 2005. 21: p. 4262-4265.
4. Yi, D.K., et al., Silica-Coated Nanocomposites of Magnetic Nanoparticles and Quantum Dots. Journal of the American Chemical Society, 2005. 127: p. 4990-4991.
5. Wang, D., et al., Superparamagnetic Fe_2O_3 Beads-CdSe/ZnS Quantum Dots Core-Shell Nanocomposite Particles for Cell Separation. Nanoletters, 2004. 4(3): p. 409-413.
6. Selvan, S.T., et al., Synthesis of silica-coated semiconductor and magnetic quantum dots and their use in the imaging of live cells. Angewandte Chemie-International Edition, 2007. 46(14): p. 2448-2452.
7. Gu, H., et al., Facile One-Pot Synthesis of Bifunctional Heterodimers of Nanoparticles: A Conjugate of Quantum Dot and Magnetic Nanoparticles. Journal of the American Chemical Society, 2004. 126(18): p. 5664-5665.
8. Green, M., The Organometallic Synthesis of Bifunctional Core/Shell Nanoparticles. Small, 2005. 1(7): p. 684-686.
9. Murphy, C.J., et al., Anisotropic Metal Nanoparticles: Synthesis, Assembly, and Optical Applications. journal of physical chemistry B, 2005. 109(29): p. 13857-13870.
10. Cozzoli, P.D., T. Pellegrino, and L. Manna, Synthesis, properties and perspectives of hybrid nanocrystal structures. Chemical Society Reviews, 2006. 35(11): p. 1195-1208.
11. Kudera, S., et al., Selective growth of PbSe on one or both tips of colloidal semiconductor nanorods. Nanoletters, 2005. 5(3): p. 445-449.
12. Carbone, L., et al., Selective reactions on the tips of colloidal semiconductor nanorods. Journal Of Materials Chemistry, 2006. 16(40): p. 3952-3956.
13. Milliron, D.J., et al., Colloidal nanocrystal heterostructures with linear and branched topology. Nature, 2004. 430: p. 190-195.
14. Mokari, T., et al., Selective Growth of Metal Tips onto Semiconductor Quantum Rods and Tetrapods. Science, 2004. 304: p. 1787-1790.
15. Mokari, T., et al., Formation of asymmetric one-sided metal-tipped semiconductor nanocrystal dots and rods. Nature Materials, 2005. 4(11): p. 855-863.
16. Cozzoli, P.D. and L. Manna, Asymmetric nanoparticles: Tips on growing nanocrystals. Nature Materials, 2005. 4(11): p. 801-802.
17. Yu, H., et al., Dumbbell-like Bifunctional Au-Fe_3O_4 Nanoparticles. Nanoletters, 2005. 5(2): p. 379-382.
18. Gu, H., et al., Heterodimers of Nanoparticles: Formation at a Liquid-Liquid Interface and Particle-Specific Surface Modification by Functional Molecules. J. Am. Chem. Soc., 2005. 127(1): p. 34-35.
19. Li, Y., et al., Enhanced Magnetooptical Response in Dumbbell-like Ag-CoFe2O4 Nanoparticle Pairs. Nanoletters, 2005. 5: p. 1689-1692.
20. Pellegrino, T., et al., Heterodimers based on CoPt3-Au nanocrystals with tunable domain size. Journal Of The American Chemical Society, 2006. 128(20): p. 6690-6698.
21. Pacholski, C., A. Kornowski, and H. Weller, Site-Specific Photodeposition of Silver on ZnO Nanorods. Angewandte Chemie International Edition, 2004. 43: p. 4774-4777.

22. Choi, S.H., E.G. Kim, and T. Hyeon, One-Pot Synthesis of Copper-Indium Sulfide Nanocrystal Heterostructures with Acorn, Bottle, and Larva Shapes. journal of the american chemical society, 2006. 128(8): p. 2520-2521.
23. Kwon, K.W. and M. Shim, γ-Fe_2O_3/II-IV sulfide nanocrystal heterojunctions. journal of the american chemical society, 2005. 127(29): p. 10269-10275.
24. Gao, J., et al., Fluorescent Magnetic Nanocrystals by Sequential Addition of Reagents in a One-Pot Reaction: A Simple Preparation for Multifunctional Nanostructures. Journal of the American Chemical Society, 2007.
25. Cao, Y.C. and J.H. Wang, One-pot synthesis of high-quality zinc-blende CdS nanocrystals. Journal Of The American Chemical Society, 2004. 126(44): p. 14336-14337.
26. Cao, H.Q., et al., Growth and optical properties of wurtzite-type CdS nanocrystals. Inorganic Chemistry, 2006. 45(13): p. 5103-5108.
27. Mohamed, M.B., et al., Synthesis of high quality zinc blende CdSe nanocrystals. Journal Of Physical Chemistry B, 2005. 109(21): p. 10533-10537.
28. Sun, S., et al., Monodisperse FePt Nanoparticles and Ferromagnetic FePt Nanocrystal Superlattices. Science, 2000. 287(March 17): p. 1989-1992.
29. Inomata, K., T. Sawa, and S. Hashimoto, Effect Of Large Boron Additions To Magnetically Hard Fe-Pt Alloys. Journal Of Applied Physics, 1988. 64(5): p. 2537-2540.
30. Stoner, E.C. and E.P. Wohlfarth, A Mechanism Of Magnetic Hysteresis In Heterogeneous Alloys. Philosophical Transactions Of The Royal Society Of London Series A-Mathematical And Physical Sciences, 1948. 240(826): p. 599-642.
31. Tsai, J.L., et al., Effect of GePt buffer layer on magnetic properties and microstructure of FePt films. Journal of Magnetism and Magnetic Materials, 2006. 303(2): p. e258-e260.
32. de_Mello_Donega, C., et al., Single-step synthesis to control the photoluminescence quantum yield and size dispersion of CdSe nanocrystals. Journal Of Physical Chemistry B, 2003. 107(2): p. 489-496.
33. Borse, P.H., et al., Luminescence quenching in ZnS nanoparticles due to Fe and Ni doping. JOURNAL OF MATERIALS SCIENCE, 1999. 34: p. 6087-6093.
34. Dulkeith, E., et al., Gold Nanoparticles Quench Fluorescence by Phase Induced Radiative Rate Suppression. Nanoletters, 2005. 5(4): p. 585-589.
35. Zhang, W., A.O. Govorov, and G.W. Bryant, Semiconductor-metal nanoparticle molecules: hybrid excitons and the nonlinear fano effect. Physical Review Letters, 2006. 97 / doi:10.1103/PhysRevLett.97.146804(14).
36. Saunders, A.E., I. Popov, and U. Banin, Synthesis of hybrid CdS-Au colloidal nanostructures. Journal Of Physical Chemistry B, 2006. 110(50): p. 25421-25429.
37. Gao, J.H., et al., Fluorescent magnetic nanocrystals by sequential addition of reagents in a one-pot reaction: A simple preparation for multifunctional nanostructures. Journal Of The American Chemical Society, 2007. 129(39): p. 11928-11935.
38. Li, M. and J.C. Li, Size effects on the band-gap of semiconductor compounds. Materials Letters, 2006. 60(20): p. 2526-2529.
39. Gerion, D., et al., Solution Synthesis of Germanium Nanocrystals: Success and Open Challenges. Nanoletters, 2004. 4(4): p. 597-602.

Growth of colloidal hybrid nanoparticles of fluorescent group II/VI particles on top of magnetic iron-platinum

Marco Zanella[1,2], Andrea Falqui[3], Stefan Kudera[2,4,5], Liberato Manna[4], Maria F. Casula[3,*], Wolfgang J. Parak[1,2,*]

[1] Fachbereich Physik, Philipps Universität Marburg, Marburg, Germany
[2] Center for Nanoscience, Ludwig Maximilians Universität München, München, Germany
[3] Dipartimento di Scienze Chimiche and INSTM, Università di Cagliari, Cagliari, Italy.
[4] National Nanotechnology Laboratory of CNR-INFM, Lecce, Italy.
[5] Max Planck Institute for Metals Research, Dept. New Materials and Biosystems & University of Heidelberg, Dept. of Biophysical Chemistry, postal address: Heisenbergstr. 3, D-70569 Stuttgart, Germany

[*] corresponding authors: casulaf@unica.it, wolfgang.parak@physik.uni-marburg.de

Supporting Information

I) Synthesis

I.1) Chemicals

Octyl ether (99%), hexadecanediol (Tech 90%) and iron pentacarbonyl (99.99%), oleic acid (Tech 90%), oleyl amine (Tech 70%), sulphur (100Mesh sublimed) and selenium (99,99% 100Mesh) powder were purchased from Sigma. Tri-n-octylphosphine oxide (TOPO, 98%) was purchased from Alpha Aesar and cadmium acetylacetonate (98%, "water free"), zinc acetylacetonate (98%), lead acetylacetonate (min 95%), and platinum acetylacetonate (98%) were purchased from Strem. All solvents used for precipitation and re-dispersion of the particles (methanol, ethyl acetate, chloroform, toluene and hexane) were purchased as anhydrous solvents from Sigma. Before any synthesis Zinc acetylacetonate was dried under vacuum for 1h at ca. 100°C and then stored under inert atmosphere. All other reactants were used as delivered. The metal compounds and the chalcogens were handled only under an inert (nitrogen) atmosphere.

I.2) FePt synthesis

For the synthesis of the iron platinum cores we followed the recipe previously reported by Sun [1]. In a 50 ml three neck flask 10 ml of octyl ether, 95 mg of platinum acetylacetonate and 195 mg of hexadecanediol were mixed under nitrogen atmosphere. Temperature was raised to 100°C until the solution turned into clear translucent yellow color. A mixture of oleic acid (0.8 ml), oleyl amine (0.8 ml), and iron pentacarbonyl (0.6 ml) was injected quickly under vigorous stirring into the platinum acetylacetonate solution. The temperature was then increased to 280°C with a controlled rate of 12°C/min. The solution was left at that temperature for 15 more minutes. Finally the heating mantle was removed to stop the reaction.

I.3) General concept for growing hybrid particles

The further formation of heterodimers discussed in this work can be divided into three steps as described by Gu et al. [2]. In a first step, an amorphous shell of either sulphur or selenium was formed on FePt nanocrystals. In a second step, a metal (cadmium, zinc or lead) was added to this shell, which at this stage still was amorphous. In the last step a single, crystalline domain was formed out of the amorphous shell. This step can be understood as a dewetting process in which the shell material retracts into a single bleb. The entire reaction from the synthesis of the FePt nanocrystals to the formation of the dimers was carried out in a single pot. No washing steps are involved. However in this study we also stopped the synthesis after the individual steps, in order to perform further characterization of the sample at the different stages. In this case the nanoparticles were purified as follows: The reaction solution was cooled to room temperature and methanol and a small quantity of ethyl acetate were added to it to precipitate the nanoparticles. The ethyl acetate was necessary to enable mixing of the methanol with the reaction solution. After centrifugation the nanoparticles could be collected as the precipitate. Further purification steps involve the re-dispersion of the nanoparticles in a non-polar solvent such as chloroform, toluene or hexane and the subsequent precipitation with methanol. With these three non-polar solvents no further addition of ethyl acetate was necessary. The samples were characterized either after the first precipitation or after several further redispersion/precipitation cycles.

I.4) FePt/S and FePt/Se synthesis

FePt/S nanocrystals were synthesized by following the recipe reported by Gu [2]. Once the iron-platinum nanoparticles were prepared as described above, the reaction solution was cooled down to 100°C and 5 mg of sulphur powder were added under vigorous stirring. Since the whole synthesis was performed in a dry box we could add the powder by simply removing the septum from the flask and pouring the powder into the FePt NCs solution. About 1ml of nanoparticles solution as then used to rinse the vial from the remaining sulphur. After 5min FePt/S nanoparticles were formed (Figure SI-1).

For the characterization of FePt/S the particles then were precipitated from the solution by addition of anhydrous methanol (15ml) and a small quantity of ethyl acetate (2-3 ml) in order to prevent phase separation of the solvents. The supernatant was discarded, and the precipitate could be re-dispersed in chloroform, toluene or hexane. If the precipitation of these particles was performed at a moderate speed (800RPM) the re-dispersed solution resulted stable for months.

With a similar procedure we could synthesize FePt/Se nanocrystals. In this case 12 mg of Se powder were injected (as described before) into the FePt nanocrystals solution at 150°C. The solution was left stirring at that temperature for 12-14 min.

For characterization the solution was cooled down to room temperature and precipitated following the protocol described above. A small insoluble fraction of the nanocrystals was found after the re-dispersion and was discarded as precipitate after additional centrifugation[1].

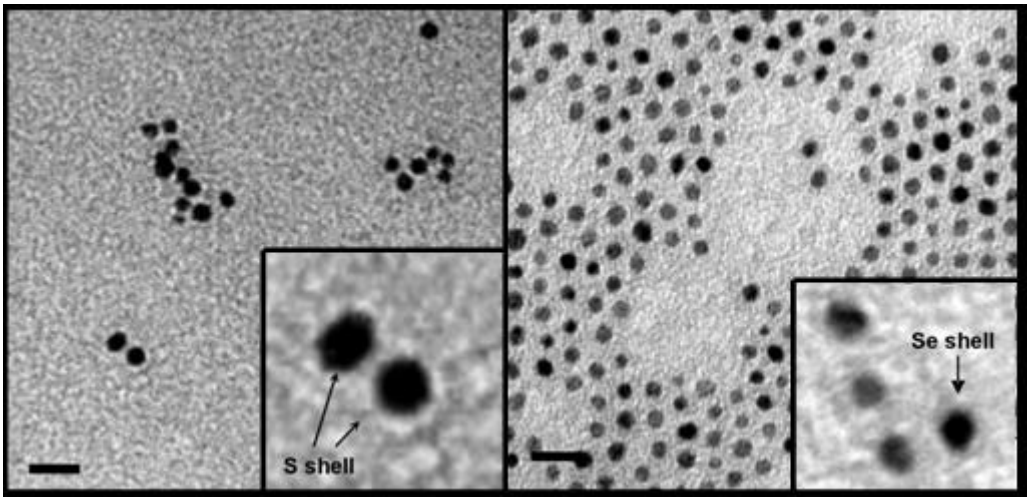

Figure SI-1: *Low resolution TEM image of FePt/S (left) and FePt/Se (right) nanoparticles. Insets show a higher magnification of the same samples. The dark dots are iron platinum particles, while the clear gray shell around them is the chalcogenic shell. The scale bars correspond to 10 nm.*

[1] TEM characterization of this insoluble precipitate showed that it was made of big agglomerates of FePt/Se nanocrystals. We can speculate that these agglomerates formed as by-product either directly during the shell formation or by the stripping off of the surfactants from the nanocrystals' surface occurring during the purification.

I.5) FePt-CdS synthesis

FePt/S nanocrystals were prepared as described in I.4. However, instead of precipitating the FePt/S particles from the solution at the end of the reaction 1g TOPO, 105mg of hexadecanediol and 50mg of cadmium acetylacetonate were added to the hot reaction solution. These chemical were added consecutively to the solution following the same approach used for the S and Se addition thus, pouring most of the powder into the flask and rinsing the remaining powder with about 1-2ml of nanoparticles solution. After 10 min core shell of FePt/CdS core/shell particles were formed. At that point the CdS shell was still amorphous. In order to anneal the crystalline structure, the temperature was risen from 100°C to 260-270°C with a rate of 5°C per minute. Once 260-270°C were reached, the heating mantel was removed and the solution was allowed to cool to room temperature. Dimers were precipitated by centrifugation as described in section I.4. Before characterization, the precipitate was redispersed in chloroform and washed once by precipitation with methanol and subsequent re-dispersion.

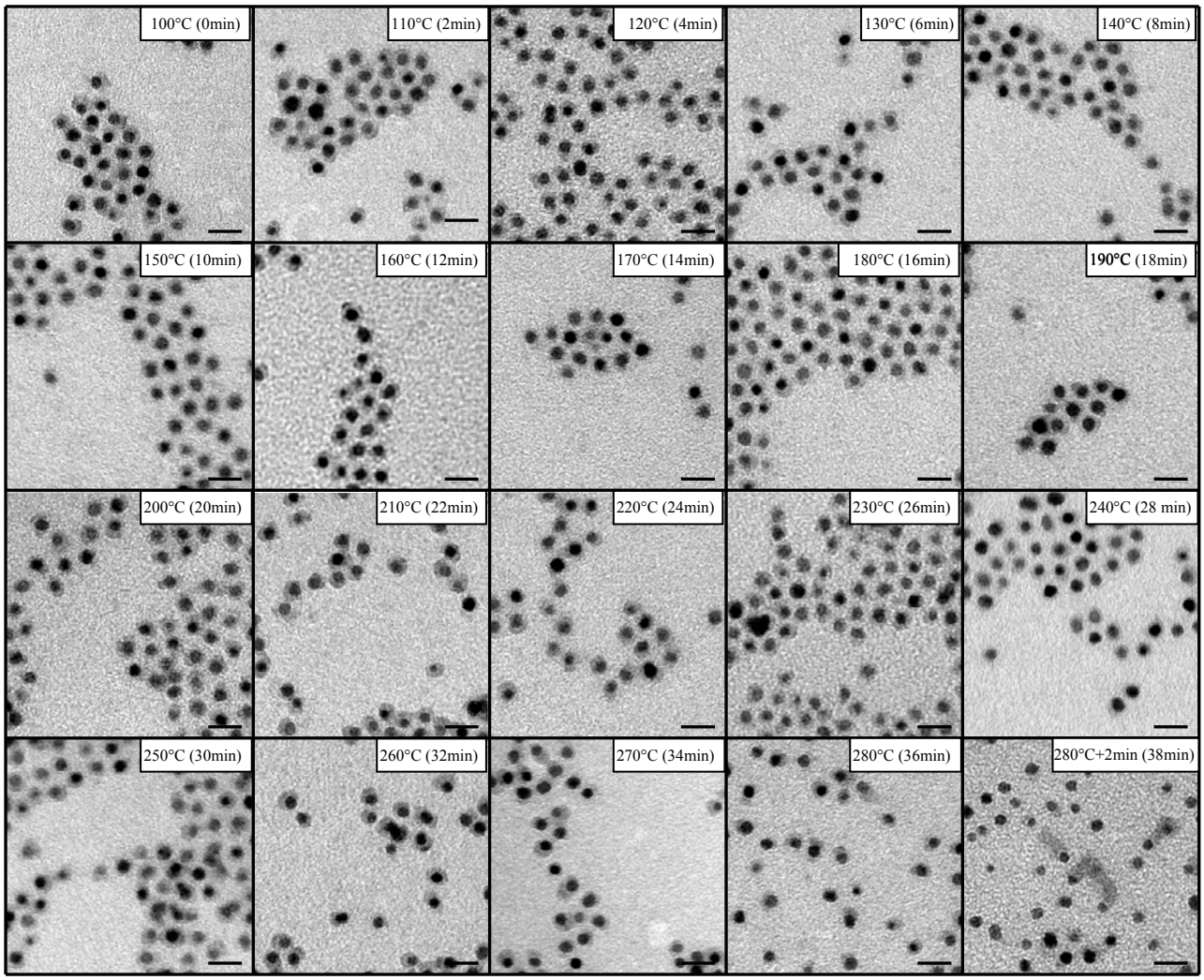

Figure SI-2: *TEM micrographs of FePt-CdS particles at different stages of the annealing process. After the synthesis of the FePt/CdS core/shell particles at 100°C (time 0min) the solution temperature was raised to 280°C with a rate of 5°C/min. About 1ml t of the hot nanoparticles solution was taken from the flask every 2min with a glass syringe and left to cool down to room temperature. This solution was then purified with methanol and ethyl acetate as described above. Precipitate was redispersed in chloroform and TEM samples were prepared by putting a drop of nanoparticles solution on a TEM grid. The picture "280°C+2min" is referred to a sample in which the solution temperature was left at 280°C for 2 more minutes after the annealing ramp.*

I.6) FePt-ZnS synthesis:

The synthesis of FePt/ZnS nanoparticles followed the same route as for the synthesis of the FePt/CdS (see I.5), only that cadmium was replaced by zinc. TOPO (1g), hexadecanediol (105 mg) and dried zinc acetylactonate (40 mg) were consecutively injected in the hot solution (100°C) of FePt/S nanoparticles and left reacting for 10min. For characterization of the FePt/ZnS core/shell particles the sample was washed once as described above by performing two cycles of precipitation, re-dispersion.

For the growth of FePt-ZnS dimers the core/shell particles solution temperature was raised to 260-270°C with a rate of 5°C/min. The annealing of the FePt/ZnS particles led to the formation of dimers composed of a FePt and a ZnS domain. Keeping the solution at high temperature for a longer time produced unstable solutions as in the case of cadmium-containing dimers (See rightmost image in Figure SI-3).

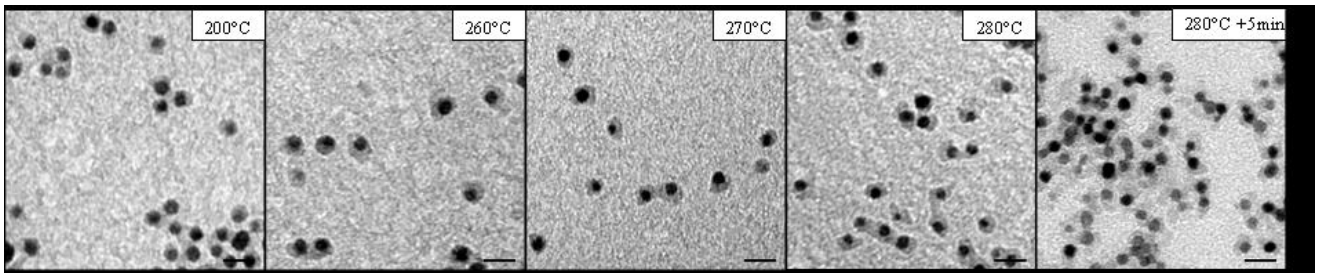

Figure SI-3: *TEM micrographs of FePt-ZnS particles at different stages of the annealing process. The scale bars correspond to 10nm.*

I.7) FePt-PbS synthesis:

The synthesis of FePt-PbS nanoparticles needed a ”softer” approach as compared to the one used for the addition of ZnS and CdS blebs. After the formation of the FePt/S nanoparticles at 100°C the mantel was removed and the solution was allowed to cool to room temperature. When the solution reached 80-90°C TOPO (1 g) and hexadecanediol (105 mg) were added and left dissolving. When the temperature reached 35-40°C lead acetylactonate (40mg) was added and left reacting for about 5min to form FePt/PbS cores/shell particles.

The formation of the FePt-PbS dimers from the core/shell particles was performed by heating the core/shell particles solution to 130-140°C with a rate of 0.6°C/min without any purification step after the synthesis of the of the core/shell particles. The annealing of the FePt/PbS particles led to the formation of FePt-PbS dimers having one iron platinum domain combined with a PbS one. Keeping the solution at high temperature for a longer time resulted in unstable solutions as in the case of CdS and CdSe.

I.8) FePt-CdSe synthesis:

FePt/CdSe core/shell particles were prepared starting from FePt/Se (see section I.4). The further processing was the same as in the case of FePt/CdS core/shell particles, yet the temperature profile of the reaction was different. Cadmium acetylacetonate along with TOPO and hexadecanediol was added at 150°C. After 10min at that temperature the solution was cooled down to room temperature.

For characterization the FePt/CdSe core/shell particles were precipitated with methanol and ethyl acetate following the same procedure as described above.

For the formation of FePt-CdSe dimers the FePt/CdSe core/shell nanocrystals, without any purification step, were annealed and dewetting started at around 150°C. The heating rate was the same as used for the FePt-CdS dimers. TEM and structural analysis displayed the formation of FePt-CdSe dimers at 260-270°C. In these samples most of the particles in solution are dimers while few particles are made of two iron platinum particles connected by a cadmium selenide part, together with a little precipitate. This precipitate was removed with by further centrifugation of the redispersion and by collecting the supernatant.

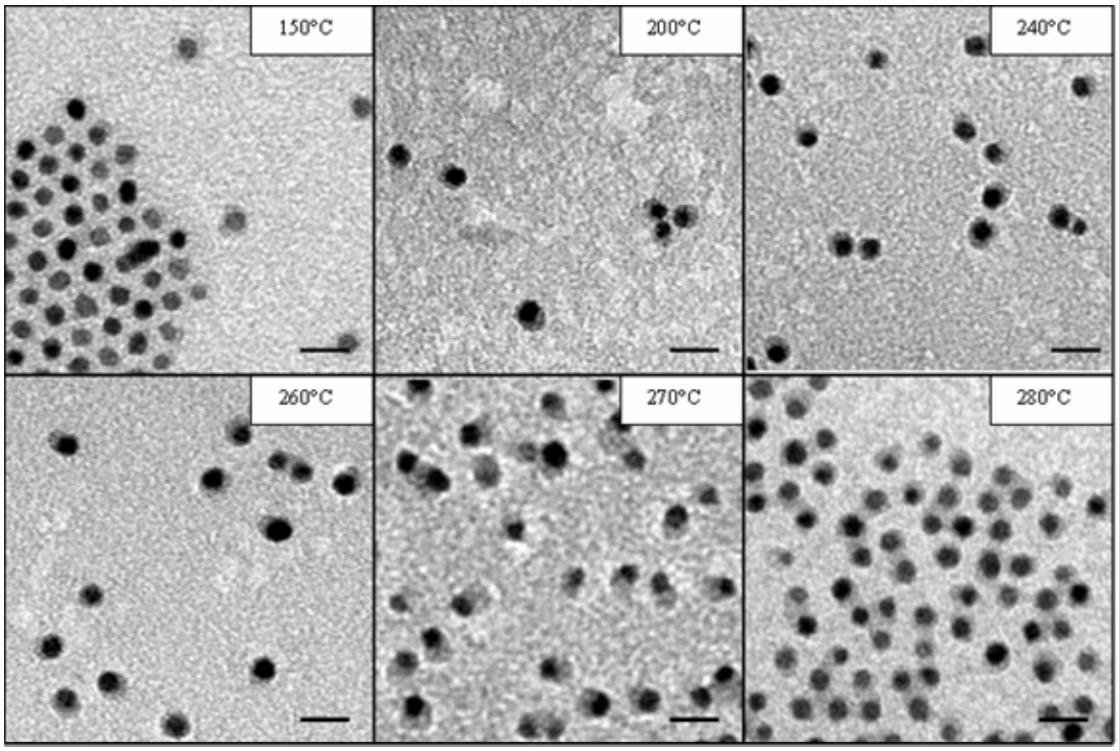

Figure SI-4: *FePt-ZnS particles at different stages of the annealing process. The scale bars correspond to 10nm.*

I.9) FePt-ZnSe synthesis:

After the synthesis of FePt/Se core/shell nanocrystals at 150°C the solution was left cooling down at room temperature to 35-40°C. During the cooling, at about 100°C, TOPO (1g) and hexadecanediol (105mg) were added to the solution in order to favor their dissolution. Once the temperature had reached 35-40°C $Zn(acac)_2$ (40mg) was added and let reacting for about 5min.

It turned out that the addition of zinc acetylacetonate to a solution of FePt/Se NCs at 35°C etches away the selenium layer from the magnetic cores, so that no FePt/ZnSe core/shell particles could be formed.

I.10) FePt-PbSe synthesis:

After the synthesis of FePt/Se nanocrystals at 150°C the solution was left to cool down to 35-40°C. During the cooling, at about 100°C TOPO (1g) and hexadecanediol (105mg) were added to the

solution in order to favor their dissolution. Once at 35-40°C $Pb(acac)_2$ (65mg) was added and let reacting for 3-5min.

The addition of lead acetylacetonate to a solution of FePt/Se NCs at 35°C caused etching away of the selenium layer from the magnetic cores and in addition caused the formation of PbSe agglomerates including an unspecified number of FePt particles. In some cases the PbSe agglomerates include just one FePt particle forming a dimer-like structure with a semiconductor part of different size. Several iron platinum particles seem to be without any shell (i.e. the Se has been etched away), but we cannot exclude that a thin layer or little crystals of PbSe might surround or stick to the magnetic core like the tiny drops of liquid left on a finger tip when dewetting occurs too quickly. The high reactivity of lead ions with the selenium layer is the main cause which prevents the formation of defined FePt/PbSe core/shell nanostructures. The XRD pattern of the sample (shown in Figure SI-6) indicates the presence of nanocrystalline PbSe, suggesting therefore that crystallization of lead selenide occurs despite the low reaction temperature (30-40°C) As discussed later, along with the FePt and PbSe phases the XRD pattern also suggests the formation of Pb_4Pt. The formation of the lead-platinum alloy and of the PbSe may involve the platinum acetylacetonate left in solution after the FePt nanocrystals growth and the selenium left in solution after the Se shell formation.

I.11) Comparison of the reaction conditions

For the synthesis of the FePt/S nanoparticles we followed the protocol reported by Gu.[2]. The sulphur powder was dissolved in the iron platinum nanoparticle solution at 100°C and the sulphur atoms were left reacting with the magnetic core surfaces for 5min in order to form an amorphous shell. The reaction of these materials for the formation of the FePt/XS (X= Cd, Zn, Pb) core/shell particles requires quite different conditions due to the different reactivity the X precursors with the sulphur shell. For cadmium acetylacetonate the reaction at 100°C for 5min was already reported by Gu. The same temperature was kept for zinc acetylacetonate which was left reacting with the sulphur shell for a longer time (about 10 min) in order to allow for a complete reaction of the zinc precursor. Applied to FePt/ZnS the same dewetting rate used for FePt/CdS led to particles with dimer shape at almost 270°C and proceeding with the dewetting big agglomerates were formed. Structural analysis of FePt-ZnS dimers showed that the semiconductor bleb is not yet crystalline. This fact could be due to the lower reactivity of the zinc with sulphur in the shell. When we replaced cadmium with lead at 100°C the product was always found to be unstable. Due to the high reactivity of lead with sulphur low temperature conditions (35-40°C) were required in order to have stable solutions of FePt/PbS particles. To prevent aggregation even the dewetting rate for the dimer formation needed to be very low, about 0.6°C/min versus 5°C/min used for cadmium and zinc.

For the adhesion of selenium on the magnetic nanoparticles a temperature of 150°C was chosen in order to better control the shell growth. This reaction temperature was able to prevent formation of big agglomerates and to minimize the possible doping of the semiconductor material due to the decomposition of the unreacted iron pentacarbonyl. Selenium was left reacting for 12-14min forming a thin amorphous shell around the iron platinum nanocrystals (Figure SI-1). After the formation of FePt/CdSe core/shell particles the dewetting rate applied for the synthesis of the FePt-CdS dimers led to FePt-CdSe dimers when the temperature had reached 270°C. Moving from cadmium to zinc and lead precursors ($Zn(acac)_2$ and $Pb(acac)_2$) we observed that not even the low temperature reaction (35°C) allows for a controlled shell growth.

	FePt-CdS	FePt-ZnS	FePt-PbS	FePt-CdSe
Addition of the S/Se shell				
Temperature at S/Se addition [°C]	100	100	100	150
Reaction time (chalcogen shell) [min]	5	5	5	12-14
Addition of Cd/Zn/Pb				
Reaction time (semiconductor shell) [min]	10	10	5	10
Reaction temperature [°C]	100	100	35-40	150
Dewetting rate [°C/min]	5	5	0,6	5
Temperature for dimer formation [°C]	260-270	260-270	130-140	260-270

Table S1. *Summary of the reaction conditions for the synthesis of FePt-CdS, FePt-CdSe, FePt-ZnS and FePt-PbS dimers.*

II) Structural Characterization:

II.1) X-ray diffraction (XRD)

XRD patterns were recorded on a X3000 Seifert diffractometer equipped with a graphite monochromator on the diffracted beam. The scans were collected using Cu-K_α radiation at 50 kV and 35 mA within the range of 10-100° (2θ). The nanocrystals were precipitated from colloidal solution by addition of ethanol and deposited on a XRD sample holder prior to scan collection. Phase identification was performed by comparison with the Powder Diffraction Files database PDF-2 File [*reference:* PDF-2 File, JCPDS International Centre for Diffraction Data, 1601 Park Lane, Swarthmore, USA].

X-Ray diffraction (XRD) patterns were recorded in order to obtain representative information on the average structural features of the samples at the different steps of the dimer growth. Figure SI-5 shows the pattern of the original plain FePt nanocrystals, of FePt-CdS core/shell particles, and of FePt-CdS dimers. As expected, the composite samples show the reflections of the FePt alloy as main contribution with no significant difference in line broadening. In addition, the dimer sample shows an additional feature centered at about 26° (2θ) due to the formation of nanocrystalline CdS which is not present in the core/shell sample. These data, which were also confirmed by selected area electron diffraction (SAED) collected by conventional TEM, indicate that in case of the core/shell particles the CdS shell is amorphous or anyway highly disordered, whereas the CdS bleb is crytalline in the case of dimers.

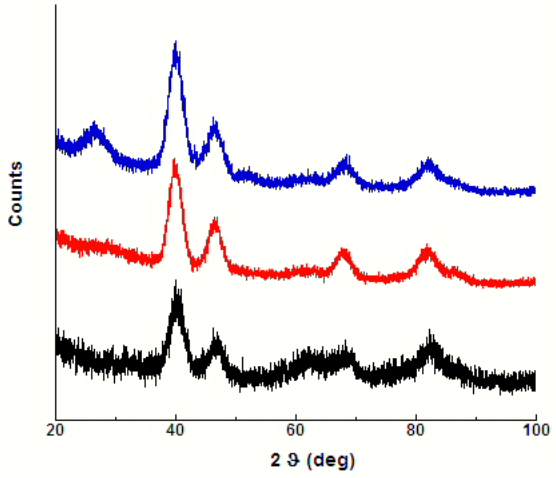

Figure SI-5: *From bottom to top: XRD patterns (Cu-K_α radiation) of plain FePt nanoparticles, of FePt/CdS core/shell nanoparticles, and of the FePt-CdS dimers. For clarity the individual curves are shifted to higher count rates.*

The same result was obtained for all those systems where we could isolate the different products at the different steps of the preparation, i.e. the core/shell samples do not show any diffraction peak in addition to the reflections due to the FePt alloy. As discussed in the manuscript, due to the very high reactivity for some systems only the final dimers could be isolated. The XRD patterns of all the dimer samples are reported in Figure SI-6 and show the presence of the reflections due to the FePt alloy as main contribution. In addition, in the angular range below ~38° (2θ) where no peaks due to iron-platinum are found, extra features are observed, which are broad or well-resolved reflections, depending on the semiconductor material present in the dimer.

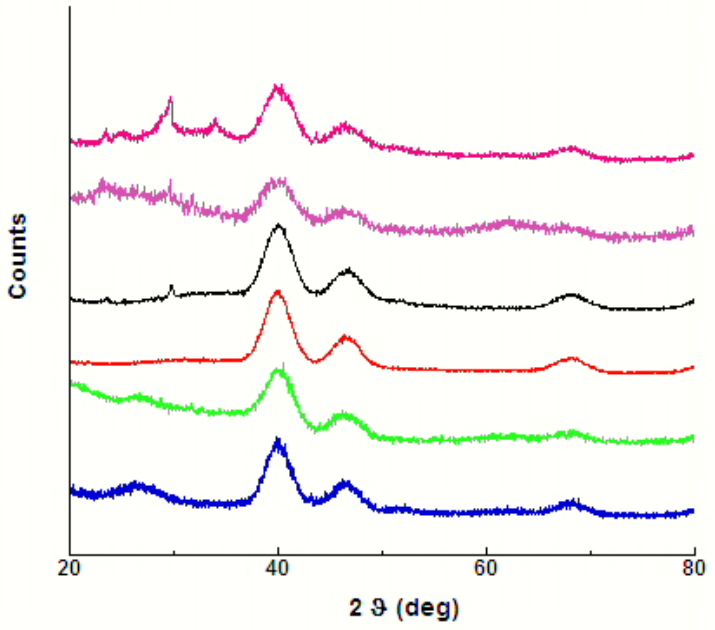

Figure SI-6: *XRD patterns of all dimer samples (Cu-K_α radiation). From bottom to top: FePt-CdS, FePt-CdSe, FePt-ZnS, FePt-ZnSe, FePt-PbS, FePt-PbSe. The individual curves are shifted towards higher count rates.*

In the FePt-CdS and FePt-CdSe dimers a very broad peak can be associated to the formation of nanocrystalline CdS and CdSe respectively. The main reflections of the wurtzite and of the blende structure lie at close angular values and therefore due to the peak broadening associated to the small nanocrystal size it is not straightforward to attribute unambiguously the crystal structure of the CdS and CdSe domain to the zinc blende or to the wurtzite structures. In the FePt-ZnS and FePt-ZnSe sample a halo is observed suggesting that the structure is more disordered or that the crystal domains are smaller, at the limit of detection of XRD technique (~3 nm). The FePt-PbS and FePt-PbSe dimers show sharper peaks which may be attributed to cubic PbS (PbSe) and to a lead-platinum alloy. This is particularly evident in the FePt-PbSe dimer, where the reflections which are not due to FePt can be attributed to the most intense peaks of PbSe and of an alloy richer in lead, Pb_4Pt. These data support the occurrence of diffusion of the atoms from the magnetic to the semiconductor domain (or vice versa) as suggested by magnetic measurements. Due to the extra line broadening of the XRD peaks related to small size effects no significant peak shift or broadening is observed in the reflections due to the FePt alloy due to potential compositional or disorder variations.

II.2) HREM

To gain further insights on the crystal structure of the heterostructures, High Resolution Transmission Electron Microscopy (HRTEM) was performed at the TEMSCAN facility in Toulouse, France, on a JEOL JEM2100F microscope operating at a voltage of 200 kV and equipped with a Field-Emission gun. Prior to observations, samples were deposited by drying a drop of the colloidal solution on top of a holey carbon-coated copper grid. In the HRTEM images of all the samples the FePt alloy core is clearly visible and the size and crystal lattice of the magnetic core is not significantly altered in the heterostructures with respect to the plain alloy nanocrystals. These data are in agreement with conventional TEM and XRD data. It is quite hard to image the lattice fringes of both the semiconductor and the magnetic domain of a given dimer structure because it is unlikely to observe both domains under an appropriate zone axis. However, we have always observed crystalline semiconductor domains which have a less regular shape and broader size

distribution compared to the magnetic domains. Figure SI-7 shows FePt-CdS and FePt-CdSe dimers where coexisting semiconductor and magnetic crystalline domains are visible. The d-spacings observed in the magnetic core are close to the value of 2.23 Å due to the 111 family of planes of the FePt alloy phase. In the semiconductor domains interplanar distances which are only found in the wurtzite structure are observed. In particular, in the FePt-CdS and in the FePt-CdSe dimers interplanar distances due to the 101 family of the wurtzite phase (expected at 3.16 Å and at 3.29 Å in the CdS and CdSe respectively) and which are not present in the zinc blende structure can be observed. The presence of the wurtzite phase is also supported by the observed zig-zag structures which are due to the presence of stacking faults often associated to the occurrence of the wurtzite phase. In all the investigated dimers there is no clear evidence of systematic epitaxial connection between the magnetic and semiconductor domains, even if the low percentage of well oriented dimers does not allow to definitively conclude about such a matter. However, this result is somehow expected on the basis of the proposed mechanism of formation of the heterostructures, as crystallization of the semiconductor domain is concomitant to the dewetting process, and therefore is not due to the growth of the semiconductor on a given facet of the magnetic seed.

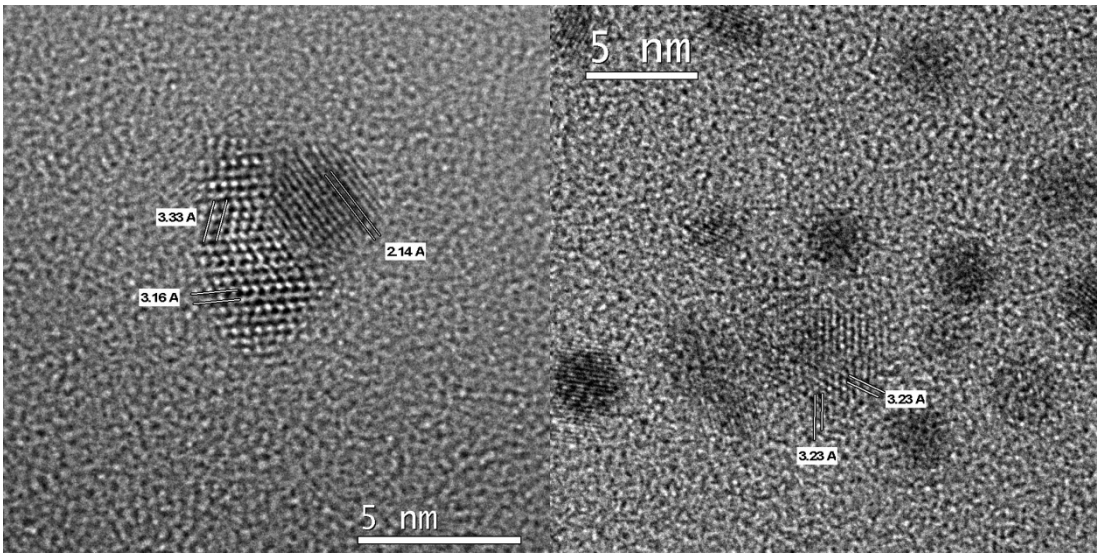

Figure SI-7: *HREM image of the FePt-CdS (left) and FePt-CdSe (right) dimers.*

III) Optical Characterization

For optical characterization an Agilent 8453 UV/vis absorption spectrometer and a Fluoromax-3 (Jobin Yvon Horiba) fluorescence spectrometer were used.

A comparison between the absorption spectra of free FePt nanoparticles and FePt-CdS dimers (both dissolved in chloroform) demonstrates that the dimers present a weak additional peak centered at ca. 400 nm, which is not present in the free iron platinum spectrum and can be explained as absorption feature of the CdS domain. From a calibration curve that relates the position of the absorption peak of free CdS nanoparticles to their size, we can estimate the diameter of the CdS domain as 3-4 nm [3]. Under UV light no emission was visible to the bare eye, but by using a fluorescence spectrometer several peaks could be detected (Figure SI-8). Fluorescence spectra were recorded after subsequent purification steps in order to demonstrate the possible contribution of surfactants to the fluorescence.

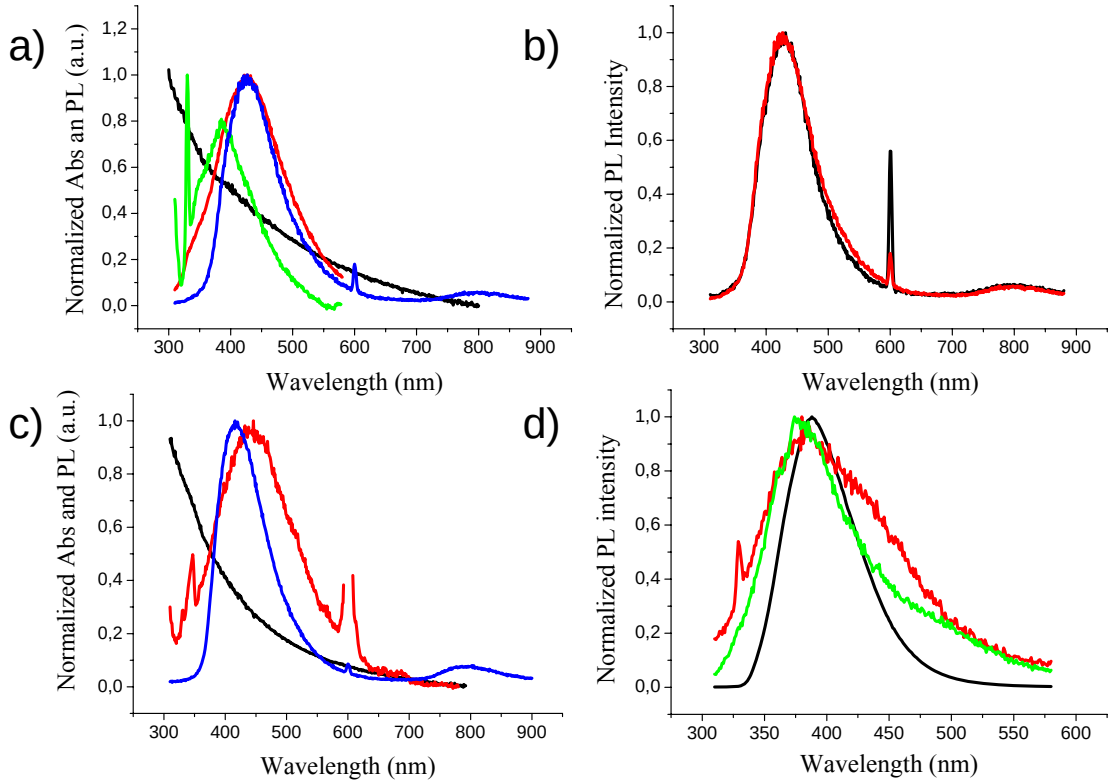

***Figure SI-8**: a) Normalized absorbance (Abs) and fluorescence (PL) spectra of FePt-CdS dimers: absorbance (black curve), fluorescence of the particles after one purification step involving precipitation and redissolution of the precipitate (red curve), fluorescence of the supernatant after the first precipitation which is not supposed to contain particles (blue curve) The peak at ca. 800 nm is a replica of the dominant peak at half the wavelength., fluorescence of the sample after several rounds of purification involving multiple precipitation and redissolution of the precipitate (green curve). b) Normalized fluorescence spectra of the supernatant of a solution of FeP/CdS core/shell particles (black curve) and FePt-CdS dimers (red curve). Both supernatant were collected after precipitation of the particle solution and should not contain particles (which are in the precipitate). c) Normalized absorbance and fluorescence spectra of FePt-CdSe dimers: absorbance (black curve), fluorescence of the particles after one purification step involving precipitation and redissolution of the precipitate (red curve), fluorescence of the supernatant after the first precipitation which is not supposed to contain particles and which is discarded (blue curve). d) Normalized fluorescence spectra of three different surfactants used for the nanoparticles synthesis; TOPO (red curve), oleylamine (green curve), and Oleic acid (black curve). All of them were dissolved in chloroform before the measurement.*

IV) Magnetic Characterization

The magnetic characterization (measurement of static Zero Field Cooled (ZFC) and Field Cooled (FC) magnetization, and of the isothermal hysteresis loop) of the ferromagnet-semiconductor dimeric systems was performed with a Quantum Design MPMS SQUID magnetometer equipped with a superconducting magnet producing fields up to 50 kOe. The samples were prepared by depositing the colloidal nanoparticles into a filter paper and afterward vacuum-drying. ZFC magnetizations were measured by cooling the samples in a zero magnetic field and then increasing the temperature in a static magnetic field of 50 Oe, while the FC curves were obtained by cooling the samples in the same magnetic field. For each system we obtained the blocking temperature (T_B), defined as the temperature at which the main maximum of the ZFC curve appears, and the crossing temperature (T_{cross}), in correspondence of which ZFC and FC curves are completely superimposed. Hysteresis loops were taken once the sample was cooled down at 2.5 K in a zero magnetic field. All the magnetization values are absolutes, since they are referred to an unknown sample mass. From the hysteresis loops we could extrapolate the coercive field (H_c), the ratio between the absolute magnetization (M_S), extrapolated at high field, and the residual magnetization (M_r) measured when the applied field (H) is back to zero after the applied magnetic field reached value 5T.

V) References

1. Sun, S., et al., *Monodisperse FePt Nanoparticles and Ferromagnetic FePt Nanocrystal Superlattices.* Science, 2000. **287**(March 17): p. 1989-1992.
2. Gu, H., et al., *Facile One-Pot Synthesis of Bifunctional Heterodimers of Nanoparticles: A Conjugate of Quantum Dot and Magnetic Nanoparticles.* Journal of the American Chemical Society, 2004. **126**(18): p. 5664-5665.
3. Yu, W.W., et al., *Experimental Determination of the Extinction Coefficient of CdTe, CdSe, and CdS Nanocrystals.* Chemistry of Materials, 2003. **15**(14): p. 2854-2860.

phys. stat. sol. (a) **203**, No. 6, 1329–1336 (2006) / **DOI** 10.1002/pssa.200566182

Synthesis and perspectives of complex crystalline nano-structures

Stefan Kudera[*, 1, 2], **Luigi Carbone**[1], **Marco Zanella**[2], **Roberto Cingolani**[1], **Wolfgang J. Parak**[2], and **Liberato Manna**[1]

[1] National Nanotechnology Laboratories of INFM-CNR, Via Arnesano (km 5), 73100 Lecce, Italy
[2] Center for Nanoscience, Ludwig-Maximilians-Universität, Amalienstr. 54, 80799 München, Germany

Received 17 October 2005, revised 26 February 2006, accepted 26 February 2006
Published online 3 May 2006

PACS 81.07.Be

Research on inorganic colloidal nanocrystals has moved from the synthesis of simple structures, such as spherical nanoparticles, to more elaborate particles with shapes such as rods, stars, discs, and branched nanocrystals, and recently to nanoparticles that are composed out of sections of different materials. Nanocrystal heterostructures represent a convenient approach to the development of nanoscale building blocks, as they merge sections with different functionality in the same particle, without the need of inorganic cross-linkers. The present article gives an overview of synthesis strategies to complex nanocrystals and will highlight their structural properties, as well as discuss some envisaged applications.

1 Introduction

Synthesis techniques for colloidal nanocrystals have seen a fast development over the last years. In the nanometer size-regime the particles of some materials experience already quantum confinement effects. Therefore, by simply varying the size of a particle one can tune its properties over a considerable range, especially in the case of fluorescent semiconductor nanoparticles [1]. The relative ease of fabrication and manipulation combined with the flexibility offered by the possible tuning of their physical properties makes nanomaterials an appealing tool for many applications. This ranges from the development of LEDs [2] solar cells [3–5], lasers [6, 7], to biological tagging with semiconductor particles [8–10] and to biomedical applications of magnetic nanoparticle [11, 12] and also to future electronic devices [13–17].

A recent direction in the field of nanocrystal research is the development of synthetic techniques that allow for controlling the shape of the nanoparticles [18, 19]. Shape-controlled nanoparticles are promising candidates for several new applications. It has been proven for example that semiconductor nanorods enhance the efficiency of solar cells compared to spherical nanocrystals [5]. There are also several fundamental studies on the electronic behavior of semiconductor nanorods [20] and tetrapods [21] as these posses more intriguing shapes with respect to spherical nanocrystals, which might prove advantageous in displays, solar cells, field emitters and in nano-transistors. In addition, by introducing nanoparticles with a complex three-dimensional shape into composite materials, one can expect a strong influence on the materials' mechanical behavior.

The next step in complexity of nanoparticles is the fabrication of hybrid structures. The motivation for research in this direction is clear, as by merging different materials into a single nano-object, such object

[*] Corresponding author: e-mail: stefan.kudera@physik.uni-muenchen.de

might exhibit multiple functionalities. First results have been demonstrated in this field, namely in the fabrication of hybrid materials. In this review we will focus on inorganic colloidal nanocrystals synthesized in hot organic solvents (200–400 °C).

2 Synthesis of spherical nanocrystals

Generally, the synthesis at high temperatures offers the advantage that defects are easily annealed from the crystal lattice. In addition, the nucleation and growth stages can be controlled and tuned easily. The reaction of the particles is started by injecting molecular precursors (which contain the atoms out of which the particle will be made) into a mixture of different organic molecules at a given temperature. These molecules have multiple roles. First, they serve as a solvent for the growing particles. Therefore, they have to support the high temperature without degradation and with negligible evaporation. Second, they also act as surfactants. At the high temperatures of the growth, they bind dynamically to the surface of the particles and by this they control the growth kinetics. When the synthesis is stopped by lowering the reaction temperature, such molecules form a stable monolayer around the particles. For a general overview on synthesis techniques we refer to various reviews [22, 23]. In a very simplified model, the surfactant molecules bind to and unbind from the surface of the nanoparticles, whereby the rates of these two processes are controlled by the temperature. Whenever there is a free site on the surface of a nanocrystal, the surfactants have to compete with the ions/atoms coming from the bulk of the solution for attachment to this site. In order to have a sufficient control on the dynamics of the growth, the surfactants must not bind too strongly to the particle surface, as this would suppress the crystals growth. On the other hand they should not bind too weakly, as otherwise the growth would be uncontrollably fast. This ultimately would result in the formation of large clusters and aggregates of clusters. The surfactant molecules most frequently used for such purpose are for instance phosphine oxides (tri-n-octylphosphine oxide) [1, 24], phosphines (e.g. tri-n-butylphosphine)) [1, 24], phosphonic acids [25], amines [24, 26], and carboxylic acids [27]. In general, nanocrystals of different materials require different surfactants to be grown in a controlled and reproducible way. CdSe, for instance, is frequently grown in a mixture of tri-n-octylphosphine oxide and tri-n-octylphosphine [1], whereas $CoPt_3$ is grown in a mixture of amines, carboxylic acid and hexadecandiol [26], and Fe_2O_3 in oleic acid [27]. At the end of the growth process, when the temperature of the reactor is lowered to room temperature, unreacted excess precursors can be removed by subsequent precipitation and re-dissolution of the particles, by adding solvents to which the surfactant-coated nanocrystals are not soluble. The resulting nanoparticles are hydrophobic because of the monolayer of surfactants bound to their surface. These particles are soluble in many organic solvents and can be also stored as a powder and re-dissolved at whish.

Spherical nanoparticles can be grown for a large variety of different materials. Due to their electronic structure semiconductor materials (such as CdSe, CdS, ZnSe, InAs, CdTe, etc.) are of special interest [28]. These nanoparticles show a size-dependent narrow fluorescence peak. In the case of CdSe, for instance, such peak can be centered anywhere within the visible range from 450 nm to 650 nm, depending on the particle size. Semiconductor nanocrystals also exhibit a size-dependent, continuous absorption spectrum, which is blue-shifted with respect to their bulk counterpart. This clearly distinguishes them from organic dyes, which possess a narrow absorption band at energies slightly higher with respect to their emitted energies. These optical properties and also their superior lifetime [29] compared to fluorescent dyes make semiconductor nanoparticles an attractive tool in fluorescent labeling techniques [30] [31, 32], as they render it easier to observe simultaneously different colours with only one excitation wavelength [8, 10]. Recently, even smaller particles of CdSe have been produced [33, 34] that emit in the blue range. Besides fluorescent, also magnetic particles as $CoPt_3$ [26, 35] or Fe_2O_3 [27] are interesting for many technical applications, such as drug targeting [36, 37] and magnetic storage devices [17].

A more detailed understanding of the growth mechanism of nanocrystals can be obtained in the general framework of the diffusion-controlled growth model [38, 39]. Nanocrystals are crystals and therefore possess facets. One can show that the dynamics of the growth depends on the surface energy of the different crystalline facets onto which new atoms are deposited [40, 41]. In the simplest case, we can

assume that the surface energy for all facets is nearly the same, and in most cases this is a reasonable assumption, as usually the nanocrystals grow isotropically (they have a rather spherical shape). In the theory of colloidal growth one can derive a key parameter, namely the "critical particle size", which is inversely proportional to the concentration of monomers in solution. A particle that has exactly such critical size is in equilibrium with the bulk solution of monomers, therefore monomers unbind and bind at the same rate on it, and thus this particle is not growing nor shrinking. Particles smaller than this critical size exhibit a negative growth rate (they tend to dissolve), whereas particles larger than the critical size are continuously growing. A general equation describing the distribution of growth rate versus size shows a maximum in growth rate for particles which are twice as big as the critical size. Therefore, during the synthesis one should try to arrange the distribution of sizes and the critical size in such a way that even the smallest particles present are significantly larger than the critical size. In this case the smaller particles grow faster than the bigger particles, resulting in a focusing of the size distribution over time [42].

One major complication is that, while the synthesis of nanocrystals is proceeding, the monomers in solution are consumed. This leads to an increase in the critical size and the reaction can ultimately shift into the so-called Ostwald-ripening [43] regime. Here the size distribution is such that the smallest particles present are smaller than the critical size. As soon as these small particles dissolve, they free monomers that can be incorporated into the bigger particles. This regime is characterized therefore by a fast broadening of the size distribution. For this reason, the critical size should be kept always small in order to obtain a narrow distribution of sizes in the final sample. One possibility is to stop the synthesis well before it enters into the broadening regime. Another possibility is to continuously add monomers to the solution [1, 42].

3 Shape control

The assumption of equal surface energies for all facets is most certainly an oversimplified model. For II–VI semiconductor nanoparticles in wurtzite structure, for instance, it has been proven experimentally [44] and theoretically [40, 41] that the different facets exhibit distinguishably different binding strengths for certain surfactant molecules. Especially phosphonic acids are strongly binding to the lateral facets of the wurtzite crystals CdSe, CdS and CdTe, whereas their binding efficiency to the basal facets, that is the (0001) and the $(000\bar{1})$ facets, is much lower. Therefore, the basal facets are more unstable than the prismatic facet and these two types of facets will grow at different rates, depending on the monomer concentration in solution. If the concentration of monomers in the growth environment is high, the basal facets will grow faster, and a rod shape will develop [45]. On the other hand, if the system is in the Oswald ripening regime (monomer concentration is low) and the nanocrystal is shrinking, the basal facets will dissolve at a higher rate than the lateral facets. The synthesis of the rod-shape is well controlled in the case of CdSe, CdS and CdTe. One additional point about the wurtzite structure is that there is also a remarkable difference between the (0001) and $(000\bar{1})$ facets. In the first case the cations expose three dangling bonds, in the second case only one (the opposite is true for the anions). Therefore the two facets are chemically different and have different growth rates [46].

A more complex shape is the tetrapod [19]. In this structure four rods are assembled into one three-dimensional object. A variety of materials may be grown in this shape, e.g. ZnO [47], ZnSe [48], CdS [49], CdSe [50] or CdTe [19, 51]. For type II–VI semiconductors there are two different crystallographic models that can rationalize this structure. In both cases the arms are described as rods that are growing in wurtzite structure. The two models differ in the way they describe the core out of which the arms are growing. The first model relies on the polymorphism of the material, most II–VI and some III–V semiconductors can grow both in the sphalerite and in wurtzite phase [52]. In this model the core consists of a sphalerite particle. The arms, which are in hexagonal phase, branch out of this core through a transition from the cubic to the hexagonal phase. The cubic core has four equivalent (111) facets that are chemically identical to the $(000\bar{1})$ facets of the hexagonal phase. Therefore, through generation of a stacking fault the growth can shift from the cubic to the hexagonal phase. Growth along the (0001) direction is

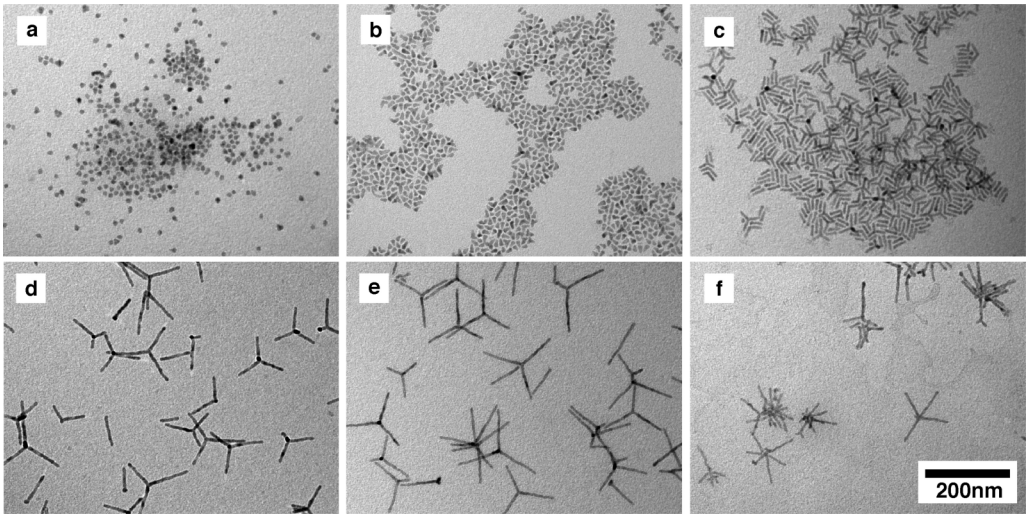

Fig. 1 Transmission electron microscopy (TEM) images of CdTe nanoparticles with different shape.

suppressed due to the better passivation of this facet. The second model describes tetrapods as completely grown in the hexagonal phase, as each couple of arms is interconnected through two twin boundaries to another wurtzite domain located in the core of the tetrapod. In this model the tetrapods core can be considered as an assembly of eight building blocks that are connected to each other through twin boundaries. In the literature on ZnO tetrapods this model is known as the octatwin model [53].

Which of the two mechanism is operative in II–VI nanocrystals is object of investigation in our groups. In the case of CdTe nanocrystals, we are now able to tune the various reaction conditions so that we can synthesize nanocrystals having a variety of different shapes, ranging from spheres to rods, to nanocrystals that are progressively more branched (see Fig. 1). This controlled synthesis has also shed a light on the mechanism of branching in nanocrystals [54].

In a more elaborate approach to nanocrystal synthesis, starting from shape controlled CdSe, CdS or CdTe particles, nanocrystals of other materials, having the same shape or at least a similar shape can be obtained. This is possible for instance through a cation exchange reaction [55], which is even reversible. One demonstrated example is the replacement of Cd^{2+} ions in CdSe rods by Ag^{+} ions to form Ag_2Se nanoparticles.

4 Synthesis of hybrid materials

The combination of different inorganic materials in one particle is desirable, as the resulting new material exhibits the properties of both constituents. Inorganic colloidal particles can be connected with organic, biological molecules in a post-synthesis step. Here the key-lock principle is exploited by binding one type of molecule to the first particle and the complementary molecule to the second type of particles. This technique has been demonstrated for the formation of DNA-connected gold particles of different size [57, 58]. Unfortunately, these structures are very sensitive to environmental changes. DNA linkers are for example not stable against heat, as the double strand would break open. Biological linkers are typically also floppy. In order to get more stable and rigid hybrid materials it is preferable to epitaxially link different materials together.

The most symmetric example of inorganic hybrid materials is the core-shell structure. In this system one particle is embedded into a shell of a different material. For instance fluorescent semiconductor particles can be surrounded by a shell of a semiconducting material with a higher band gap. In the case of CdSe nanoparticles, the growth of a ZnS shell enhances the fluorescence properties of the material and the quantum yield can be increased by more than a tenfold [59].

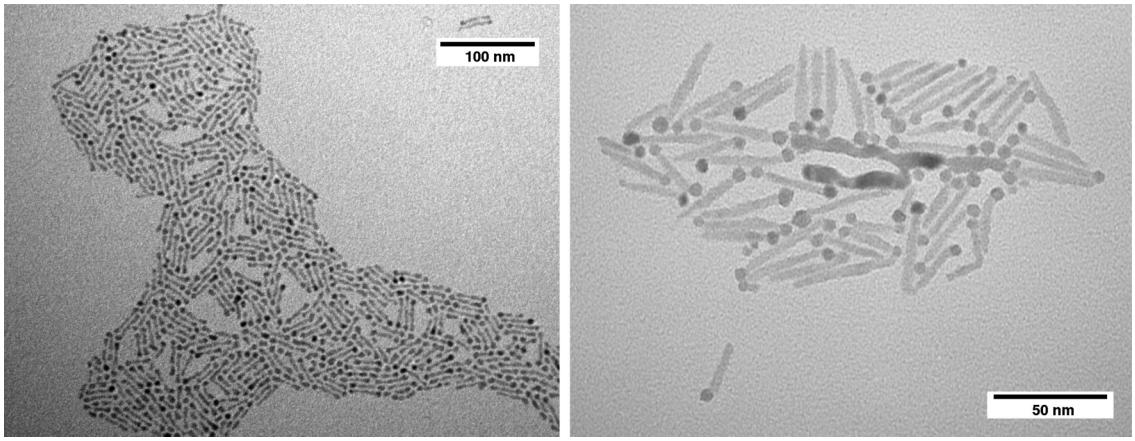

Fig. 2 TEM images of dumbbell and matchstick structures. The left images shows a sample of CdSe rods with PbSe spheres on their tips. The right image shows a sample of CdS rods with a PbSe sphere mainly only on one of their tips. All experimental procedures are reported in Ref. [60].

Other examples of heterostructures are based on nanorods. As discussed above, in the case of rod growth different facets of the crystals have different reactivities. The higher reactivity of the tips or the better passivation of the lateral facets give rise to the possibility to nucleate another material only on the tips of the rods. This scheme can be exploited to grow dumbbell-shaped structures. As an example recently reported by our groups [60] and by the group of Banin [61], first rods of CdSe or CdS can be synthesized and purified. Then, in the presence of these particles, the synthesis of a second material is performed. When the concentration of the monomers of the second material is sufficiently low, the new material nucleates only on the tips of the rods. It seems that stress that is provoked by the lattice mismatch between the two materials does not suppress the formation of such structures. Gold tipped CdSe rods [61] can be produced according to this technique as well as PbSe dots may be grown onto CdSe or CdS rods (see Fig. 2) [60]. In the later case, even the number of dots per particle can be controlled. Instead of dumbbells with two dots, matchsticks with only one dot can be synthesized. With a slightly different approach, ZnO–Ag heterostructures can be produced [62]. Also in this case a two step synthesis is necessary. First the ZnO nanorods are synthesized, then Ag is deposited onto these particles through a photocatalytic reaction. Upon strong UV irradiation, electron–hole pairs are generated in the ZnO rods, the electrons can then reduce the Ag-ions and so trigger the nucleation of Ag-particles on the surface of the rods.

In an *in-situ* approach it is possible to first synthesize rods of a cadmium-based semiconductor material and then grow from its tips linear sections of a different material (CdTe or CdSe). By carefully adjusting the experimental conditions also the shape of the central material (either rod or tetrapod) and the outer material (either linear or branched section) can be controlled [63].

A completely different approach to produce hybrid nanocrystals was followed by Gu and co-workers [64]. They reported the synthesis of hybrids with a CdS and a FePt section. Here, first an amorphous shell of CdS is grown onto FePt particles and then by annealing these samples, crystalline CdS domains form on one side of the FePt, due to a de-wetting process which minimizes the interfacial energy between the two materials.

5 Outlook

By carefully manipulating the thermodynamics and kinetics of crystal growth one can control both the shape and the composition of nanocrystals. It is now possible to grow several materials in complex shapes, such as for instance tetrapods. Starting from these structures, one can synthesize hybrid materials

by exploiting the different passivation efficiencies of surfactant molecules towards the various crystal facets.

These new materials are promising candidates for different applications. First, they might open new perspectives in self-assembly, as in the case of metal tipped semiconductor rods. Reactive groups such as thiols bind strongly to Au, but only relatively weakly to CdSe and CdS surfaces [61]. This facilitates site-selective surface functionalization by organic molecules. By simply exposing CdSe–Au dumbbell structures to biological molecules bearing free thiol-groups, selective attachment of these molecules at the gold-tip regions is expected. First demonstrations in this direction have been reported already for hybrid materials of bigger size [65], namely Au/Ni particles. It was demonstrated that different reactive groups bind selectively to certain domains of a nanocrystal. In particular, thiol-functionalised biomolecules were bound to the gold domains, carboxylic groups were bound to the Ni domain. Also for nanometer-sized CdSe–Au dumbbell structures size-selective surface functionalization has been reported [61]. By adding dithiols, CdSe–Au dumbbells are selectively connected at their Au-ends, which leads to the formation of nanorod chains [61]. Nevertheless, experiments in this direction are just in their infancy and still many questions, such as the role of non-specific interactions remain to be solved. Site-specific functionalization on just one tip of the rods would facilitate new possibilities of arranging particles on surfaces. For an example, by linking rod-shaped objects with their tip to a surface, a brush of vertically aligned particles could be formed (see Fig. 3). This structure would be of great interest for the fabrication of solar cells [5]. Certainly, the possibility to selectively functionalize specific regions of the particles with organic molecules will play an important role in the future for the generation of complex self-assembled structures with an improved degree of programmability.

Other possible applications of hybrid particles are expected in the field of electronics [14, 20]. Gold tipped nanocrystals may render it easier to form electronic contacts with the particles. This might for example help the design of nanocrystal-modified electrodes [66]. In addition, linear junctions of semiconductor particles may provide interesting electronic properties by themselves. The band structure of heterostructures of two types of semiconductor may open up new applications for this material. The reported PbSe–CdSe–PbSe heterostructure [60] could be considered as a light-controlled transistor. Here a high-band gap material (CdSe, $E_g \approx 2$ eV) is situated between two sections of a material with smaller band gap (PbSe, $E_g \approx 0.5$ eV). In this way, communication between the two PbSe sections only is possible when they are in an excited state, that is after the absorption of a photon.

All synthesis procedures and reactions reported so far are dependent on organic molecules bearing long alkyl chains (the surfactants) and therefore the as-grown nanoparticles are hydrophobic. Several methods are now available to transfer these particles to aqueous solution, which work by rendering the surface of these nanocrystals hydrophilic [29, 67]. Water-soluble particles offer a whole new direction of applications, especially in the field of life sciences. We refer here to recent review articles [31, 32, 68]. It is currently under discussion if nanoparticles are compatible with biological applications. There are several investigations on this subjects [69–71], but it seems that this question is not easy to address, as for

Fig. 3 Selective functionalization may be used for the formation of complex architecture as shown in a sketch here. By functionalizing only the tips of the dumbbell structures it may be possible to form chains of these particles (left sketch). This has been demonstrated already [61] by carefully exposing gold tipped nanorods to hexane(1,6)dithiol Providing functional pads (right sketch) on a substrate may enable the formation of brushes of rods. For this approach matchstick-shaped particles with only one functional domain could be of advantage.

instance in the case of gold-nanoparticle there is a strong, non-linear dependence of the toxicity on the size of the particles [72, 73]. Hybrid nanoparticles also open new perspectives in life science applications. Nanoparticles with combined magnetic and fluorescent properties [64] could be directed with magnetic field gradients and detected on a single-particle level by their fluorescence.

We believe that in future the synthesis of nanocrystals should evolve into the development of more complex nano-structures. An appealing field of research would be the synthesis of hybrid nano-materials with increased functionality.

Acknowledgements The authors would like to acknowledge founding by the European Union (SA-NANO STRP 013698), the Deutscher Akademischer Austauschdienst (DAAD) and the DFG Emmy Noether programme.

References

[1] C. B. Murray, D. J. Norris, and M. G. Bawendi, J. Am. Chem. Soc. **115**, 8706–8715 (1993).
[2] N. Tessler et al., Science **295**(5559), 1506–1508 (2002).
[3] B. O'Regan and M. Grätzel, Nature **353**(6346), 737 (1991).
[4] M. Grätzel, Nature **414**(6861), 338 (2001).
[5] W. U. Huynh, J. J. Dittmer, and A. P. Alivisatos, Science **295**(5564), 2425–2427 (2002).
[6] H. J. Eisler et al., Appl. Phys. Lett. **80**(24), 4614–4616 (2002).
[7] P. T. Snee et al., Adv. Mater. **17**(9), 1131–1136 (2005).
[8] M. J. Bruchez et al., Science **281**, 2013–2016 (1998).
[9] W. J. Parak et al., Adv. Mater. **14**(12), 882–885 (2002).
[10] W. C. W. Chan and S. Nie, Science **281**, 2016–2018 (1998).
[11] Q. A. Pankhurst et al., J. Phys. D, Appl. Phys. **36**(13), R167–R181 (2003).
[12] C. C. Berry, J. Mater. Chem. **15**(5), 543–547 (2005).
[13] A. Bezryadin, C. Dekker, and G. Schmid, Appl. Phys. Lett. **71**(9), 1273 (1997).
[14] D. L. Klein et al., Nature **389**(6652), 699 (1997).
[15] R. Krahne et al., Appl. Phys. Lett. **81**(4), 730 (2002).
[16] D. L. Feldheim et al., J. Am. Chem. Soc. **118**(32), 7640–7641 (1996).
[17] D. Weller and A. Moser, IEEE Trans. Magn. **35**(6), 4423–4439 (1999).
[18] X. Peng et al., Nature **404**(6773), 59–61 (2000).
[19] L. Manna et al., Nature Materials **2**, 382–385 (2003).
[20] O. Millo et al., Nanotechnology **15**(1), R1 (2004).
[21] Y. Cui et al., Nano Lett. **5**(7), 1519–1523 (2005).
[22] C. B. Murray, C. R. Kagan, and M. G. Bawendi, Annu. Rev. Mater. Sci. **30**(1), 545–610 (2000).
[23] O. Masala and R. Seshadri, Annu. Rev. Mater. Res. **34**, 41–81 (2004).
[24] P. Reiss, J. Bleuse, and A. Pron, Nanoletters **2**(7), 781–784 (2002).
[25] Z. A. Peng and X. Peng, J. Am. Chem. Soc. **123**(1), 183–184 (2001).
[26] E. V. Shevchenko et al., J. Am. Chem. Soc. **124**, 11480–11485 (2002).
[27] T. Hyeon et al., J. Am. Chem. Soc. **123**, 12798–12801 (2001).
[28] A. P. Alivisatos, J. Phys. Chem. **100**(31), 13226–13239 (1996).
[29] D. Gerion et al., J. Phys. Chem. B **105**(37), 8861–8871 (2001).
[30] W. J. Parak et al., Nanotechnology **14**, R15–R27 (2003).
[31] X. Michalet et al., Science **307**(5709), 538–544 (2005).
[32] I. L. Medintz et al., Nature Materials **4**(6), 435–446 (2005).
[33] A. Kasuya et al., Nature Materials **3**, 99–102 (2004).
[34] H. Z. Wang et al., J. Mater. Res. **19**(11), 3157–3161 (2004).
[35] E. V. Shevchenko et al., J. Am. Chem. Soc. **124**, 11480–11485 (2003).
[36] C. Alexiou et al., Cancer Research **60**(23), 6641–6648 (2000).
[37] B. Zebli et al., Langmuir **21**(10), 4262–4265 (2005).
[38] T. Sugimoto, Adv. Colloid Interface Sci. **28**, 65 (1987).
[39] L. Manna et al., Perspectives of Colloidal Nanocrystals in Nanoscience and Nanotechnology (Enrico Fermi School, 2004).
[40] A. Puzder et al., Nanoletters **4**(12), 2361–2365 (2004).
[41] L. Manna et al., J. Phys. Chem. B **109**(13), 6183–6192 (2005).

[42] X. Peng, J. Wickham, and A. P. Alivisatos, J. Am. Chem. Soc. **120**(21), 5343–5344 (1998).
[43] J. A. Marqusee and J. Ross, J. Chem. Phys. **80**(1), 536–543 (1984).
[44] Z. A. Peng and X. G. Peng, J. Am. Chem. Soc. **123**, 1389–1395 (2001).
[45] Z. A. Peng and X. Peng, J. Am. Chem. Soc. **124**(13), 3343–3353 (2002).
[46] L. Manna, E. C. Scher, and A. P. Alivisatos, J. Cluster Sci. **13**(4), 521–532 (2002).
[47] K. Nishio et al., Philos. Mag. A **76**(4), 889–904 (1997).
[48] J. Hu, Y. Bando, and D. Golberg, Small **1**(1), 95–99 (2005).
[49] Y.-W. Jun et al., J. Am. Chem. Soc. **123**(21), 5150–5151 (2001).
[50] L. Manna, E. C. Scher, and A. P. Alivisatos, J. Am. Chem. Soc. **122**(51), 12700–12706 (2000).
[51] W. W. Yu, Y. A. Wang, and X. Peng, Chem. Mater. **15**, 4300–4308 (2003).
[52] C. Y. Yeh et al., Phys. Rev. B: Condens. Matter **46**, 10086–10097 (1992).
[53] H. Iwanaga, M. Fujii, and S. Takeuchi, Phase Transit. **66**, 147–165 (1998).
[54] L. Carbone, S. Kudera, E. Carlino, W. J. Parak, C. Giannini, R. Cingolani, and L. Manna, J. Am. Chem. Soc. **128**(3), 748–755 (2006).
[55] D. H. Son et al., Science **306**(5698), 1009–1012 (2004).
[56] F. Dumestre et al., Angew. Chem., Int. Ed. **41**(22), 4286–4289 (2002).
[57] R. C. Mucic et al., J. Am. Chem. Soc. **120**(48), 12674–12675 (1998).
[58] C. J. Loweth et al., Angew. Chem. **111**(12), 1925–1929 (1999).
[59] B. O. Dabbousi et al., J. Phys. Chem. B **101**(46), 9463–9475 (1997).
[60] S. Kudera et al., Nanoletters **5**(3), 445–449 (2005).
[61] T. Mokari et al., Science **304**, 1787–1790 (2004).
[62] C. Pacholski, A. Kornowski, and H. Weller, Angew. Chem., Int. Ed. **43**(36), 4774–4777 (2004).
[63] D. J. Milliron et al., Nature **430**(6996), 190–195 (2004).
[64] H. Gu et al., J. Am. Chem. Soc. **126**(18), 5664–5665 (2004).
[65] A. K. Salem, P. C. Searson, and K. W. Leong, Nature Mater. **2**(10), 668–671 (2003).
[66] C. Stoll et al., accepted by Small (2005).
[67] T. Pellegrino et al., Nanoletters **4**(4), 703–707 (2004).
[68] T. Pellegrino et al., Small **1**(1), 48–63 (2005).
[69] A. M. Derfus, W. C. W. Chan, and S. N. Bhatia, Nano Lett. **4**(1), 11–18 (2004).
[70] M. Green and E. Howman, Chem. Commun., No. 1, 121–123 (2005).
[71] C. Kirchner et al., Nanoletters **5**(2), 331–338 (2005).
[72] E. E. Connor et al., Small **1**(3), 325–327 (2005).
[73] M. Tsoli et al., Small **1**(8/9), 841–844 (2005).

Nanoparticles

DOI: 10.1002/smll.200700654

Design of an Amphiphilic Polymer for Nanoparticle Coating and Functionalization**

*Cheng-An J. Lin, Ralph A. Sperling, Jimmy K. Li, Ting-Ya Yang, Pei-Yun Li, Marco Zanella, Walter H. Chang, and Wolfgang J. Parak**

Inorganic colloidal nanoparticles, such as quantum dots or Au nanoparticles, have been extensively investigated for two decades in physics as well as in chemistry. Applications in a variety of fields such as optics, electronics, and biology are envisaged and important proof-of-concept studies have been reported. In particular, with regard to biologically motivated applications, colloidal stability is a key requirement. Apart from nanoparticles stabilized with small ligand molecules,[1–5] lipids, [6–8] and surface silanization,[9–13] amphiphilic polymers have been also used by several groups to disperse originally hydrophobic nanoparticles in aqueous solution.[14–24] This class of amphiphilic particle coatings not only enables the phase transfer of the nanoparticles from organic solvents to aqueous solution, but also serves as a versatile platform for chemical modification and bioconjugation of the particles because biological molecules can be covalently linked to the polymer surface.[14,23,25] Because the stability of the amphiphilic coating around the nanoparticle solely depends on the hydrophobic interaction, this procedure is very general and does, for example, not depend on the material of the inorganic nanoparticle core, as it is the case for ligand exchange protocols. Because of the numerous contact points mediated by hydrophobic interaction, the attachment of the polymer to the particle surface is highly stable and can be improved further by crosslinking of the polymer shell.[5,15,19] Nowadays quantum dots coated with amphiphilic polymers and with various biological molecules attached to their surface are commercially available (e.g., Invitrogen).

The amphiphilic polymers that have been used so far for coating hydrophobic inorganic nanoparticles consist of hydrophobic side chains for the linkage to the nanoparticle surface and a hydrophilic backbone that provides water solubility through charged groups (in general -COO^-) and also acts as an anchor for the attachment of biological molecules with bioconjugate chemistry. In this report, we introduce an amphiphilic polymer which involves a third kind of building block: functional organic molecules. The functional organic molecules are linked to the hydrophobic side chains in a similar way as the hydrophilic backbone and provide additional functionality in the particle surface (Figure 1).

The amphiphilic polymer described here is based on a poly(maleic anhydride) backbone. Reaction of a fraction of the anhydride rings with alkylamines leads to the formation of the hydrophobic side chains that are needed for intercalation with the hydrophobic surfactant layer on the nanoparticle surface. Another fraction of the anhydride rings is used to link functional organic molecules to the backbone. Like the alkylamines, organic molecules bearing amino-groups can be directly linked to the anhydride rings by reaction of the anhydride with the amino group.[26] In this way alkylamines and organic molecules with amino terminations can be linked to the polymer backbone in a one-pot reaction. The resulting amphiphilic polymer is then wrapped around hydrophobic capped nanoparticles and the organic solvent is replaced by aqueous solution according to our previously published procedure.[15] By linking some of the remaining anhydride rings with diamine linkers, the polymer molecules around each nanoparticle are interconnected and, thus, the shell is crosslinked. Upon phase transfer to aqueous solution, the remaining anhydride rings open to yield negatively charged carboxyl groups, which provide electrostatic repulsion resulting in a stable dispersion of the nanoparticles. Apart from negatively charged carboxyl groups, the polymer surface of the nanoparticles also contains embedded functional organic molecules.

The strategy reported here has several advantageous features: 1) The maleic anhydride moieties react spontaneously with high yield with both amino-modified hydrophobic side-chains (such as alkylamines) and functional organic molecules with amino terminal groups. 2) No additional reagents are needed for the coupling. In comparison,

[*] R. A. Sperling,[+] M. Zanella, Prof. W. J. Parak
Fachbereich Physik, Philipps Universität Marburg
Renthof 7, 35037 Marburg (Germany)
E-mail: Wolfgang.Parak@physik.uni-marburg.de

C.-A. J. Lin,[+] R. A. Sperling,[+] P.-Y. Li, M. Zanella, Prof. W. J. Parak
Center for NanoScience
Ludwig-Maximilians-Universität München
Munich (Germany)

C.-A. J. Lin,[+] T.-Y. Yang, W. H. Chang
Department of Biomedical Engineering
Chung Yuan Christian University
Taiwan (ROC)

C.-A. J. Lin,[+] J. K. Li,[#] W. H. Chang
R&D Center for Membrane Technology
Center for Nano Bioengineering
Chung Yuan Christian University
Taiwan (ROC)

[+] These authors contributed equally to this work.

[#] Present address: Institute of Biotechnology, National Cheng Kung University, Taiwan (ROC)

[**] The authors are grateful to the DAAD-NSC sandwich program for facilitating this project. The German and Taiwanese partners were funded by the German research foundation (DFG Emmy Noether fellowship) and the European Union (SA-Nano grant), and by the National Nanotechnology Program (NSC) and the Center of Excellence (MOE) of Taiwan, respectively. Marco Zanella acknowledges a fellowship from the ITKD graduate school at the Center for Nanoscience in Munich. We are very grateful to Prof. Dr. Warren Chan for many important ideas and valuable technical discussions. We are also grateful to Maria Teresa Fernandez and to Dr. Feng Zhang for experimental support and technical discussions at different stages of the project and to Dr. Maria Casula for help in the synthesis of iron oxide nanoparticles.

Supporting Information is available on the WWW under http://www.small-journal.com or from the author.

NANO MICRO small

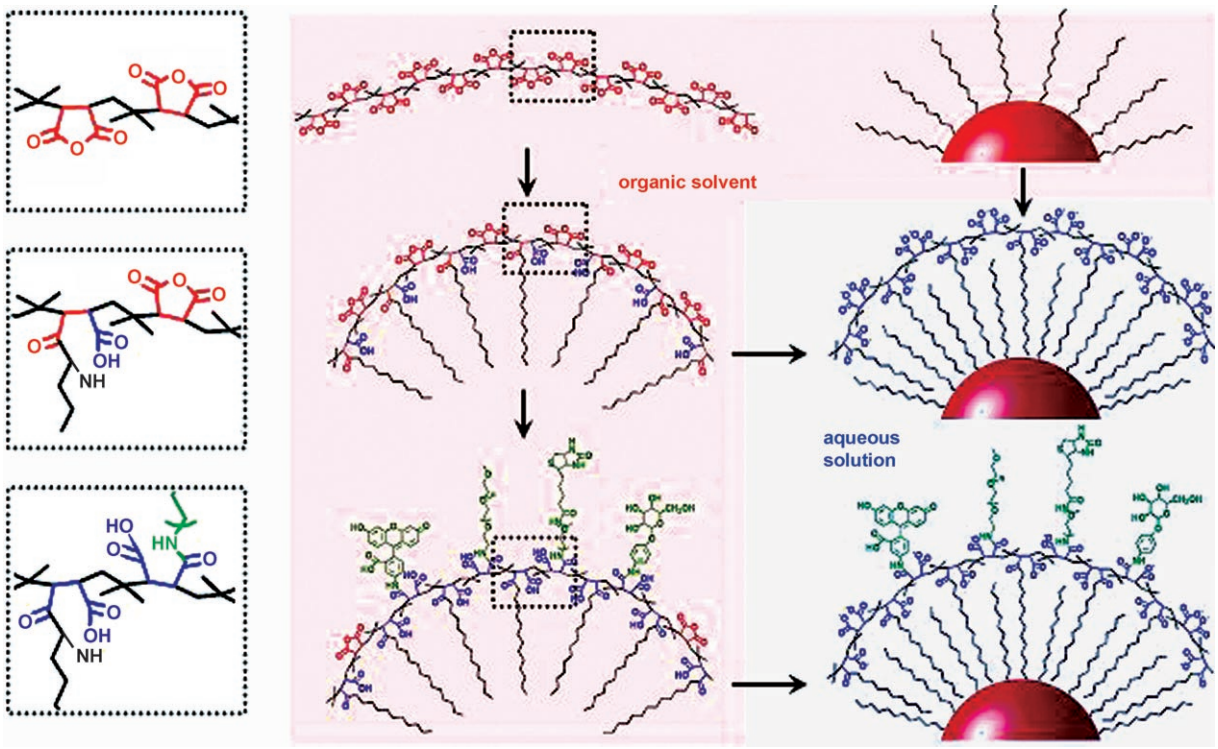

Figure 1. Scheme of the synthesis of the amphiphilic polymer and the coating of nanoparticles. In the center column the synthesis of the amphiphilic polymer is shown. To the polymer backbone, poly(isobutylene-*alt*-maleic anhydride) (top line), alkylamine chains are linked by the direct amidation between maleic anhydride and the amino-ligand (middle line). In an additional step, functional groups (drawn in green) with an amino terminal group are also linked to the polymer (bottom line). In the left column the amide linkage between the amino ligands and the anhydride rings is shown in detail. Nanoparticles with hydrophobic capping (right column, top line) are coated with the amphiphilic polymer by hydrophobic interaction between the alkyl chains of the polymer and the surfactant molecules on the nanoparticles (middle line). This works in the same way for polymers with (bottom) and without (middle) embedded functional molecules. Water solubility is provided by opening the anhydride rings (drawn in red) for carboxylic groups (drawn in blue) which introduces negative charge to the particle surface and leads to electrostatic repulsion between the particles.

crosslinkers such as EDC (1-ethyl-3-(3-dimethylamino propyl) carbodiimide) have to be used in traditional approaches for adding functionality to the particle surface.[25] 3) While EDC-mediated coupling of functional molecules to the polymer shell involves a post-modification of already polymer-coated nanoparticles in aqueous solution, the present protocol is based on coupling functional molecules in organic solvent to the polymer before the actual embedding of the particles in the polymer shell. In this way, functional molecules which are not soluble in aqueous solution, can be introduced to the particle surface as the coupling is performed in organic solvents. 4) By variation of the amount and type of the hydrophobic side-chains, as well as of the functional organic molecules within the amphiphilic polymer, tailored nanoparticle surfaces can be obtained with one universal method.

The commercially available backbone, poly(isobutylene-*alt*-maleic andydride), is an alternating copolymer consisting of maleic anhydride rings connected by butylene residues (Figure 1). Hereafter, one anhydride ring with butylene is referred to as a monomer unit. Maleic anhydride moieties react spontaneously with amines, resulting in an amide bond and one free carboxylic group. As a first step, alkylamines are added to the backbone in hot tetrahydrofuran (THF), resulting in a transparent polymer solution when more than 50% of the maleic anhydride monomers are reacted with an alkylamine. Usually, 75% of the maleic anhydride monomers of the backbone were modified with dodecylamine, leaving 25% of the anhydride rings intact. Part of the remaining anhydride rings were used in a second step for linking additional functional molecules (Figure 1) to the polymer. In practice, a large variety of different functional molecules can be used, as long as they have an amino terminal and are soluble in an organic solvent that is miscible with THF or chloroform. In this study, four different types of functional molecules were chosen to demonstrate the concept: methoxy-PEG-amine, biotin-PEG-amine, aminophenyl galactopyranoside, and fluorescein-amine. All reactions were carried out as one-pot syntheses in water-free solvents (THF or $CHCl_3$) to prevent hydrolysis of the anhyride groups. Because of the quantitative reaction of the amines with the maleic anhydride monomers, the resulting amphiphilic polymer could be used directly, without purification from byproducts or unreacted species.

The resulting amphiphilic polymer showed excellent performance for the phase transfer of hydrophobic nanoparticles to aqueous solution. The coating process was independent of the core material, as demonstrated for Au,[27] CdSe/

ZnS,[28] and Fe_3O_4[29] nanoparticles (Figure 2). Hydrophobic purified nanoparticles dissolved in chloroform were first mixed with appropriate amounts of the amphiphilic polymer, whereby the number of added polymer molecules scaled linearly with the particle surface area. The organic solvents were evaporated and the nanoparticles became water-soluble in alkaline buffer as a result of the repulsion of the negatively charged carboxyl groups on the particle surface (the carboxyl groups originate from maleic anhydride groups through hydrolyzation or linkage to amino-modified molecules, see Figure 1). Empty polymer micelles (i.e. polymer without a nanoparticle inside) were subsequently removed by size-exclusion chromatography (SEC), gel electrophoresis, or ultrafiltration.[30,31] Like our previously published reports, the resulting polymer-coated nanoparticles of various materials were found to be stable for months in aqueous solution (as assessed by gel electrophoresis, SEC, and fluorescence correlation spectroscopy[15,25,30,32]) and single PEG molecules could be attached using EDC chemistry in a postmodification step according to a previous protocol.[25] All experiments are described in detail in the Supporting Information (SI). The results demonstrate that hydrophobic nanoparticles embedded in a shell of amphiphilic polymers with incorporated functional groups show the same colloidal properties as the previously published nanoparticles that have no functional groups in their shells.

PEG was chosen as the first example of a functional organic molecule to be incorporated in the amphiphilic polymer. PEG is known to increase the colloidal stability of nanoparticles in a salt-containing solution due to steric repulsion of the hydrated, and therefore bulky, PEG chains on the particle surface.[6,22,33] Furthermore PEGylated surfaces offer reduced nonspecific interaction with biological molecules and cells.[34,35] The more PEG that is attached to the polymer shell, the bigger the size of the resulting particle.[30] The attachment of amino-modified PEG (Molecular weight, $M_w \geq 5000\ g\ mol^{-1}$) with EDC chemistry in a postmodification step using particles that are already polymer coated has been proven to yield big enough changes in the particle size for them to be resolved as individual band upon gel electrophoresis.[25] Here we demonstrate that PEG can also be directly incorporated into the polymer before the actual polymer coating procedure and that discrete bands of nanoparticles with a different number of PEG molecules bound per particle can be resolved with gel electrophoresis (Figure 2). The more the PEG was incorporated in the polymer, the bigger the polymer-coated nanoparticles became and the more retarded their bands were during gel electrophoresis. Retardation during gel electrophoresis is a clear indication of the presence of PEG molecules on the particle surface. A discrete band resulting from particles with a controllable number of PEG molecules were obtained for Au nanoparticles, quantum dots (CdSe/ZnS), and magnetic iron oxide nanoparticles (Fe_3O_4). This indicates the universality of the approach, which does not depend on the material of the inorganic nanoparticle. A similar study has been recently reported by the Colvin group.[23] PEG molecules on the nanoparticle surface offer the possibility to reduce nonspecific interaction in biological environments, but also allow for preparing particles with a discrete number of free functional groups pointing towards solution.

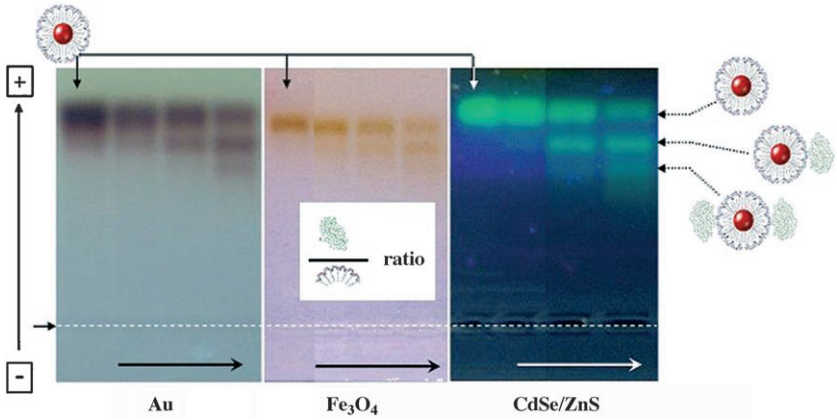

Figure 2. PEG molecules with amino terminal groups ($M_w = 5000\ g\ mol^{-1}$) were incorporated by amidation into the amphiphilic polymer so that 0%, 0.25%, 0.5%, and 1% of the anhydride rings are reacted with the PEG. Gold, iron oxide, and semiconductor nanoparticles were coated with these polymers and the resulting water-soluble particles were run on agarose gels. The arrows on the left indicate the wells where the particles were loaded onto the gel and where they migrated to in the applied electric field. For each material the conjugates with 0 (left lane), 0.25%, 0.5%, and 1% PEG (right lane) were run on one gel. The horizontal arrow on the bottom indicates the direction in which the PEG/polymer ratio is increased. The first lane (0 PEG) serves as a control and corresponds to particles with no PEG in the polymer shell. For increasing PEG/polymer ratios, discrete bands become visible on the gel that correspond to particles with exactly one or exactly two PEG molecules bound per particle.

The streptavidin-biotin system has extensively been used to assemble particles on the nanometer scale[36, 37] and streptavidin (SA)-modified nanoparticles are commercially available, for example, quantum dots and magnetic nanoparticles. In these cases either biotin or SA was attached to the surface of nanoparticles in a postmodification of particles that were already soluble in aqueous solution. In the following we demonstrate that our approach allows us to directly embed biotin into the amphiphilic polymer before the actual polymer-coating procedure. For this purpose PEG of different molecular weights ($M_w = 720\ g\ mol^{-1}$ and $M_w = 5000\ g\ mol^{-1}$) that has an amino group on one end and a biotin group on the other was reacted with the polymer as described above. Because the amino groups reacted with

the anhydride rings on the polymer backbone, the biotinylated ends of the PEG pointed away from the polymer backbone. Gold particles coated with the biotin-PEG-modified polymer were retarded in gel electrophoresis experiments compared to particles coated with the plain polymer, which proves the binding of the biotin-PEG to the particle surface. In the case of biotin-PEG molecules of sufficient molecular weight ($M_w \geq 5000$ g mol^{-1}), nanoparticles with a discrete number of attached biotin molecules could be isolated by gel electrophoresis.

Though gel electrophoresis clearly proved the existence of biotin-PEG in the polymer shell these experiments did not reveal whether biotin was accessible on the particle surface and had therefore preserved its functionality. Biotin is a small biomolecule that specifically binds with high affinity to the natural protein avidin or derivatives such as streptavidin or neutravidin. Because these proteins have four binding sites for biotin, the addition of avidin leads to crosslinking of biotinylated multivalent nanoparticles. In order to exclude uncontrolled binding of SA (additional experiments with avidin and neutravidin are shown in the Supporting Information) to multivalent particles, we used gold particles with no (Au-0), exactly one (Au-1-bio), and exactly two biotin molecules (Au-2-bio) per particle. For each of these particles, a series was prepared in which the Au concentration was kept constant and different amounts of SA were added. The Au–SA mixtures of each series were then analyzed with gel electrophoresis. An example in which SA was added to Au-1-bio particles is shown in Figure 3, whereby the SA–Au-1-bio ration was increased from the left to the right. Au-1-bio with almost no added SA showed the same electrophoretic mobility as Au-1-biotin conjugates. Upon addition of more and more SA per Au-1-bio, first a retarded band and then a doublet of two shifted bands appeared. By increasing the SA–Au-1-bio ratio the intensities within the doublet shift from the less retarded to the more retarded band. The shifts were not visible in the case of SA–Au-0 mixtures (see SI). This demonstrates that the shifts in the band of SA–Au-1-bio mixtures are caused by specific binding of SA to the biotin protruding from the polymer shell around the Au nanoparticle. Under these experimental conditions nonspecific adhesion of SA to the surface of Au nanoparticles can be neglected. When SA was added to Au-2-bio, bigger shifts on the gel were observed. In the case of (divalent) Au-2-bio, networks of crosslinked particles can be formed as each Au particle has two binding sites, whereas the biggest possible conjugate in mixtures of SA and (monovalent) Au-1-bio would be one SA molecule with four Au particles attached (as a result of the four binding sites of SA for biotin). An additional proof for the attachment of SA to biotin-containing Au was performed with fluorescence-labeled FITC-SA. No fluorescence could be observed in the unshifted bands of the Au-particles, whereas fluorescence could be observed in all shifted bands that were associated to SA–Au conjugates. Though we demonstrated specific attachment of SA to mono- and divalent biotinylated Au nanoparticles, we could not unequivocally identify the structure of the conjugates. Transmission electron microscopy (TEM) analysis of the conjugates that had been extracted from the gel showed groupings of Au particles, but in our opinion the data lacked the statistical significance needed to associate the bands to one particular grouping. It also has to be pointed out that the actual shift of the conjugates on the

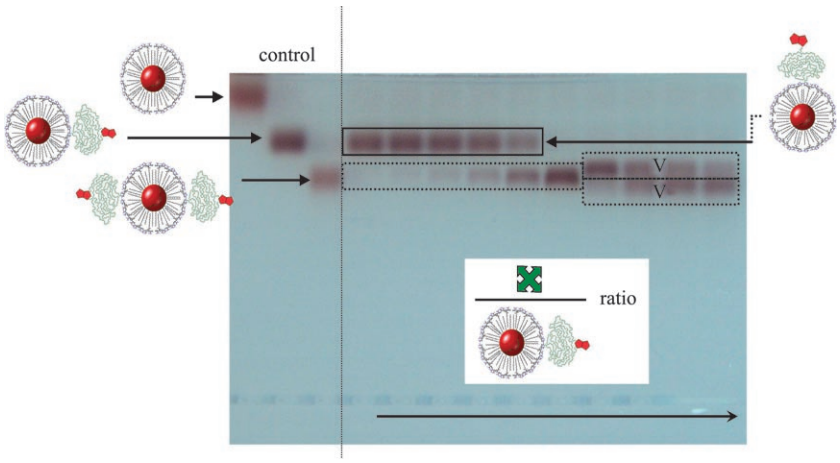

Figure 3. Au particles with no (Au-0), exactly one (Au-1-bio), and exactly two (Au-2-bio) biotin-PEG molecules per particle were run with 1% agarose gel electrophoresis (the samples were loaded in the wells on the bottom of the gel and the particles migrated towards the positive pole that had been arranged close to the top of the gel). The biotin terminal at the free end of the PEG is drawn in red. These three control samples are shown on the three left lanes of the gel. The other lanes correspond to samples to which streptavidin (SA, drawn in green) was added, in different molar ratios, to Au particles with exactly one biotin functionality per particle. The lanes from the left to the right correspond to samples in which the SA–Au-particle ratio has been increased (by a factor of 2 between two adjacent lines, max. 46 SA/Au-NP on the right), while the number of Au nanoparticles was kept constant for all samples. Upon binding of SA to the biotinylated Au particles three different positions of retarded bands can be observed. Though the gel data do not allow for a detailed analysis of the structures of the conjugates, the three bands are in agreement with the following hypothesis: In the condition of a large excess of SA to Au-1-bio (right side on the gel), each SA molecule can be coordinated to at most one Au-1-bio particle (when neglecting nonspecific adhesion). Because of the excess of SA, no Au-1-bio without SA is expected and on the gel there are only retarded bands present (double bands at right of gel). Within the retarded band on the right side of the gel the intensity of the more retarded band gets lower upon decreasing the SA/Au-1-bio ratio. As more Au-1-bio per SA is present for lower SA/Au-1-bio ratios each SA molecule might now be coordinated to two Au particles. On further lowering of the SA–Au-1-bio ratio, at one point there will be less SA molecules than Au-1-biotin particles. This means that each SA molecule can bind up to four Au-1-bio particles, whereas the unbound Au-1-bio particles that remain will appear at the nonretarded position.

gel is caused by a complex interplay of changes in charge and size. As the scope of this study is the modification of particles with functional groups (such as biotin), we did not focus on pursuing the defined assemblies of SA-biotin mediated particle groupings further. Most importantly, we could demonstrate that the biotin molecules, which are incorporated in the polymer shell, are still reactive and specifically bind to SA molecules. The universality of this approach was again shown by performing similar experiment with different types of particles such as Au nanoparticles and colloidal quantum dots. Nanoparticles with biotin on their surface could be used as building blocks for common reactions based on SA–biotin linkages, as for example, for the bioconjugation of biotinylated nanoparticles with biotinylated proteins or other biomolecules through SA.

As another model for a small biomolecule, an amine-containing sugar derivative (4-aminophenyl β-D-galactopyranoside) was directly bound to the polymer using the standard synthetic process shown above. After the coating and phase transfer to aqueous buffers, the galactose-polymer-coated nanoparticles could be detected by the reversible aggregation of the particles after the addition of lectin that binds specifically to galactose moieties.[38–40] By the addition of an excess of free galactose, these molecules compete against the binding of lectin with the galactose attached to the nanoparticles, resulting in the dissolution of nanoparticle aggregates (Figure 4). Nanoparticle aggregation was experimentally determined using UV–vis absorption spectroscopy. Whereas freely dispersed gold nanoparticles formed a clear red translucent solution and did not show absorption at longer wavelengths, aggregated nanoparticles ultimately resulted in dark red precipitate and showed significant absorption at longer wavelengths due to light scattering.[41,42] When aggregates had been formed upon addition of lectin to galactose-modified nanoparticles, the aggregates could be dissolved again by the addition of an excess of free galactose molecules, as the bond formation of galactose and lectin is reversible. Addition of an excess of a different sugar, such as glucose, on the other hand, did not dissolve the lectin-mediated aggregates of galactose-modified nanoparticles because glucose cannot displace galactose bound to lectin. Nanoparticles without galactose in their polymer shell did not show any signs of aggregation on addition of lectins. This demonstrates the incorporation of galactose in the polymer shell and the preservation of the specific binding capability of galactose to lectin. Nanoparticles with sugar molecules present on their surface have, for example, been used for specific recognition by cells.[43,44]

Fluorescein-amine was incorporated into the amphiphilic polymer as an example of organic fluorophores. Au particles coated with unmodified polymer did not exhibit any fluorescence. Dye-modified polymer without nanoparticles was transferred to aqueous solution in order to form empty micelles. After purification from unbound dye molecules by ultrafiltration (100 kDa M_W cut-off), the polymer micelles showed strong green fluorescence (Figure 5). Au particles

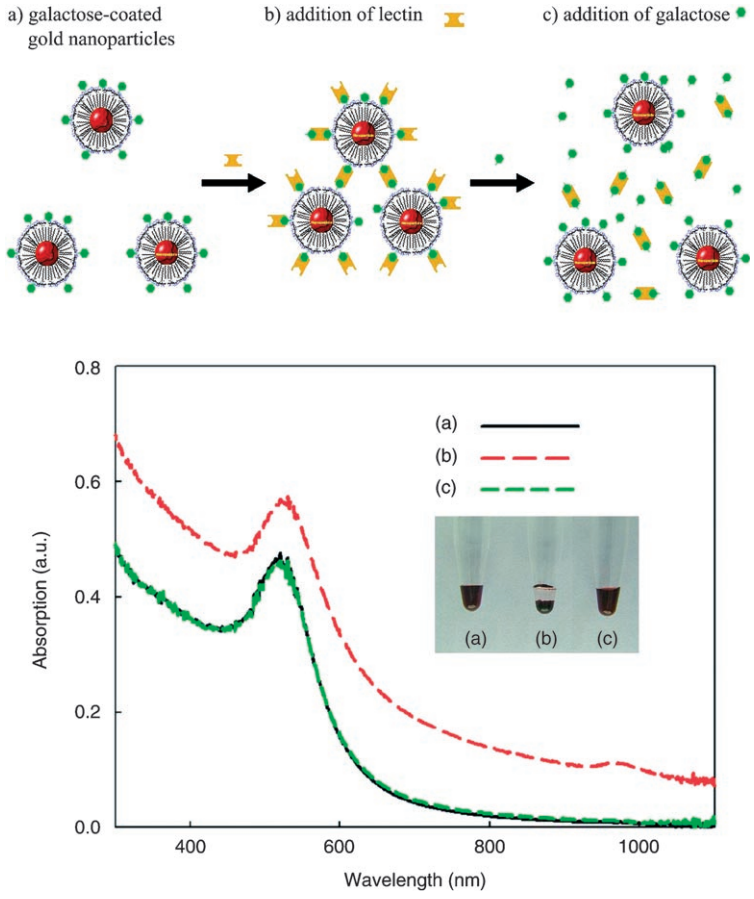

Figure 4. Au nanoparticles have been transferred to aqueous solution by embedding them in an amphiphilic polymer shell. The polymer that was used had 4% anhydride rings that were used to link galactose. These particles form a red translucent solution and have the regular UV–vis absorption spectrum of colloidal gold (sample a). Addition of lectin starts crosslinking the particles. This results in aggregates and ultimately to a dark red precipitate and thus to absorption at longer wavelengths due to light scattering (sample b). Further addition of free excess galactose displaces the bonds between the galactose incorporated in the polymer shell and the lectin and thus the aggregates dissolve again. This results in the original red translucent solution and the normal UV–vis spectrum of colloidal gold with no absorption at longer wavelengths (sample c). The aggregated nanoparticles (sample b) were redispersed by mixing with a pipette before measuring the spectrum.

coated with the dye-modified polymer were purified from empty micelles by gel electrophoresis or SEC. While the UV–vis absorption spectrum of the Au particles coated with the dye-modified polymer is dominated by the absorption of the Au particles, the characteristic peak of fluorescein was found in the emission spectrum (Figure 5).

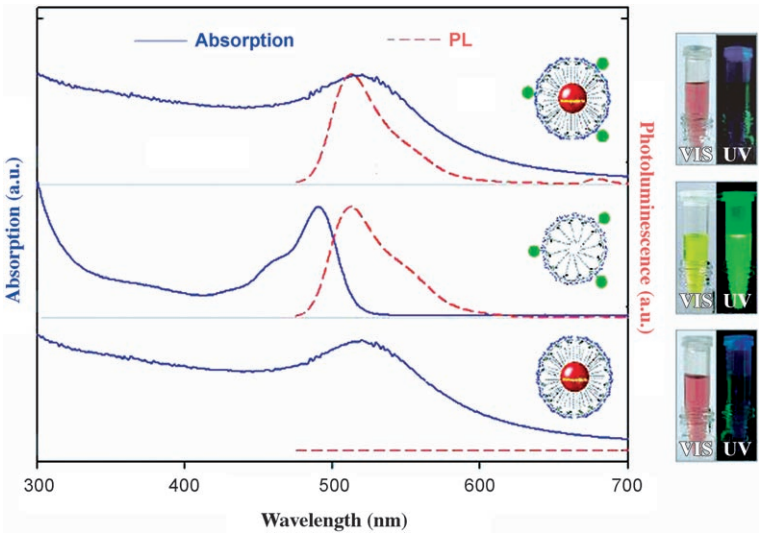

Figure 5. Au particles have been transferred to aqueous solution by an amphiphilic polymer coating in which 1% of the anhydride rings were use to link fluoresceinamine. The normalized absorption and photoluminescence (PL) spectra as well as images of the solution with a digital camera under daylight and upon UV excitation are shown in the top row. The UV–vis absorption spectrum is dominated by the absorption of the Au, which can be seen also in the red color of the translucent solution. Upon UV excitation, weak fluorescence can be observed. If the same polymer coating procedure is applied without the addition of Au particles empty polymer micelles are obtained (middle row). As there is no Au present, the absorption originates from the fluorescein (yellow solution) and there is green fluorescence. As a control Au particles were transferred to aqueous solution with a polymer that did not contain fluorescein (bottom row). The absorption of this solution is again dominated by the Au particles, but there is no fluorescence observed.

However, for fluorescein-containing polymer shells with embedded Au particles, the fluorescence was strongly quenched (by around two orders of magnitude). This phenomenon indicates close proximity of dye to the Au surface. Quenching of fluorophores close to Au surfaces has been investigated in detail by several groups.[45-47] There are two potential applications for inorganic colloidal nanoparticles with a fluorescent dye directly immobilized in their surface coating. First, nanoparticles that do not quench dyes (as it might be the case for magnetic insulators) could be directly fluorescently labeled and visualized with fluorescence microscopy. Second, colloidal quantum dots as donors with acceptor dyes in the polymer shell could be used as fluorescence resonance energy transfer (FRET)-based sensors[31,48–51] because of the close proximity between acceptor and donor.

In this report, a general approach for synthesizing an amphiphilic polymer is described that can be used for the coating of hydrophobic nanoparticles in order to transfer them to aqueous solution. The amphiphilic polymer is based on a poly(maleic anhydride) backbone that is modified with hydrophobic side chains and functional organic molecules. The amphiphilic polymer was used successfully to transfer inorganic colloidal nanoparticles of different materials (Au, CdSe/ZnS, Fe_3O_4) to aqueous solution. As the initial nanoparticles were capped with different hydrophobic surfactant molecules (e.g. trioctylphosphine oxide (TOPO), trioctylphosphine, dodecanethiol), this demonstrates the universality of the approach, in which the attachment of the polymer to the inorganic nanoparticles is only mediated by the hydrophobic interaction and does not depend on the particular surface chemistry of the inorganic nanoparticles. The polymer-coated particles were found to have good colloidal stability, which was assessed by gel electrophoresis. In accordance with previous reports (bio-) molecules such as PEG could be attached with EDC chemistry to the particle surface in a postmodification step. Most importantly, the polymer could be directly modified, before the coating process, with functional amine-containing (bio-) molecules without the need of crosslinker reagents or subsequent purification. This prefunctionalization, that is, the attachment of functional molecules in the polymer before the actual polymer coating, introduces new flexibility. Also (small) functional molecules, which are not soluble in aqueous solution, can be introduced to the particle surface, as the linkage of the functional molecules to the polymer is performed in organic solvent. As the linkage is performed before the actual coating of the particles with the polymer, the reaction can be performed at higher concentration and, therefore, eventual colloidal instabilities during a postmodification step under high salt condition can be circumvented. We have demonstrated, in particular, the linkage of PEG, biotin, galactose, and fluorescein to the polymer. The functionality of the molecules incorporated in the polymer shell around the particles was retained. However, depending on their hydrophobicity, part of the molecules might be inside the polymer shell and thus not accessible on the particle surface. In summary, we introduced one additional degree of control to colloidal nanoparticles. Apart from the functional inorganic core that can be fluorescent (CdSe/ZnS), magnetic (Fe_3O_4) or heatable (Au), additional functionality can be incorporated in the polymer shell around the particles, which can reduce nonspecific adhesion (PEG), introduce specific binding sites (biotin, galactose), or introduce fluorescence (fluorescein). We believe that

such design of particle coatings might bring new impact to bridge hydrophobic nanomaterials with biological and medical applications.

Experimental Section

Polymer synthesis: All reactions were carried out at room temperature and all organic solvents were purchased in anhydrous quality, unless stated otherwise. Polymer(isobutylene-*alt*-maleic anhydride) ($M_w \approx 6000$ g mol^{-1}, Aldrich; corresponding to roughly 39 monomer units per polymer chain) was vigorously mixed with dodecylamine (Sigma) in THF solution (100 mL), whereby the amount of added dodecylamine was sufficient to react with 75% of the anhydride rings. The cloudy solution became transparent upon heating for several hours (60 °C). After evaporation of the solvent, the resulting polymer was redissolved in anhydrous chloroform. For the functionalization of the polymer, appropriate amounts of either methoxy-PEG-amine ($M_w = 5000$ g mol^{-1} from Rapp Polymere or $M_w = 750$ g mol^{-1} from Fluka) dissolved in chloroform, biotin-PEG-amine ($M_w = 5000$ g mol^{-1} from Rapp Polymere (Germany) or $M_w = 720$ g mol^{-1} from Sigma) dissolved in chloroform/THF, aminophenyl β-D-galactopyranoside (Sigma) dissolved in THF, or fluorescein-amine (Aldrich) dissolved in THF were slowly dropped into the diluted polymer solution and reacted overnight under stirring. The amount of added molecules was calculated in such ways that between 0.25% and 4% of the anhydride rings of the polymer backbone were reacted. After evaporation of the organic solvent (chloroform with or without THF) under reduced pressure, the polymer was re-dissolved in chloroform.

Polymer coating: A polymer solution in chloroform and a solution of hydrophobically capped nanoparticles in chloroform were mixed for 30 min at room temperature. The amount of polymer was calculated so that 100 monomers units per nm^2 of nanoparticle surface were used. After evaporating all the solvent under reduced pressure, a solid thin film formed that was then dissolved in alkaline sodium borate buffer (SBB) solution (pH 12). After this phase transfer of the nanoparticles from chloroform to aqueous solution, the buffer was exchanged for one of moderate pH (SBB, pH 9) by two rounds of dilution and reconcentration through a centrifuge filter. The residual polymer was removed by size exclusion chromatography (Agilent 1100 HPLC system with a Sephacryl S-300 HR column, the mobile phase was 150 mM NaCl in 50 mM sodium borate, pH 9.0) and gel electrophoresis.

Experiments with functional polymer: The following molecules were used for selective binding to the functionalized nanoparticle surface: streptavidin (Sigma S4762), streptavidin-FITC (Sigma S3762), lectin RCA_{120} (Sigma L7886), galactose (Sigma–Aldrich, G0625), glucose (Sigma–Aldrich, G5767).

A more detailed description of materials and methods is available in the Supporting Information.

Keywords:

biomolecules · coatings · colloids · conjugation · quantum dots

[1] M. Gao, S. Kirstein, H. Möhwald, A. L. Rogach, A. Kornowski, A. Eychmüller, H. Weller, *J. Phys. Chem. B* **1998**, *102*, 8360.
[2] W. C. W. Chan, S. Nie, *Science* **1998**, *281*, 2016.
[3] F. Pinaud, D. King, H.-P. Moore, S. Weiss, *J. Am. Chem. Soc.* **2004**, *126*, 6115.
[4] A. G. Kanaras, F. S. Kamounah, K. Schaumburg, C. J. Kiely, M. Brust, *Chem. Commun.* **2002**, 2294.
[5] W. Jiang, S. Mardyani, H. Fischer, W. C. W. Chan, *Chem. Mater.* **2006**, *18*, 872.
[6] B. Dubertret, P. Skourides, D. J. Norris, V. Noireaux, A. H. Brivanlou, A. Libchaber, *Science* **2002**, *298*, 1759.
[7] H. Fan, E. W. Leve, C. Scullin, J. Gabaldon, D. Tallant, S. Bunge, T. Boyle, M. C. Wilson, C. J. Brinker, *Nano Lett.* **2005**, *5*, 645.
[8] W. J. M. Mulder, R. Koole, R. J. Brandwijk, G. Storm, P. T. K. Chin, G. J. Strijkers, C. D. Donega, K. Nicolay, A. W. Griffioen, *Nano Lett.* **2006**, *6*, 1.
[9] L. M. Liz-Marzán, M. Giersig, P. Mulvaney, *Chemical Commun.* **1996**, *6*, 731.
[10] M. J. Bruchez, M. Moronne, P. Gin, S. Weiss, A. P. Alivisatos, *Science* **1998**, *281*, 2013.
[11] D. Gerion, F. Pinaud, S. C. Williams, W. J. Parak, D. Zanchet, S. Weiss, A. P. Alivisatos, *J. Phys. Chem. B* **2001**, *105*, 8861.
[12] S. T. Selvan, T. T. Tan, J. Y. Ying, *Adv. Mater.* **2005**, *17*, 1620.
[13] Z. Zhelev, H. Ohba, R. Bakalova, *J. Am. Chem. Soc.* **2006**, *128*, 6324.
[14] M. X. Wu, H. Liu, J. Liu, K. N. Haley, J. A. Treadway, J. P. Larson, N. Ge, F. Peale, M. P. Bruchez, *Nat. Biotechnol.* **2003**, *21*, 41.
[15] T. Pellegrino, L. Manna, S. Kudera, T. Liedl, D. Koktysh, A. L. Rogach, S. Keller, J. Rädler, G. Natile, W. J. Parak, *Nano Lett.* **2004**, *4*, 703.
[16] X. Gao, Y. Cui, R. M. Levenson, L. W. K. Chung, S. Nie, *Nat. Biotechnol.* **2004**, *22*, 969.
[17] T. Nann, *Chem. Commun.* **2005**, 1735.
[18] S. Kim, S. Kim, J. Tracy, A. Jasanoff, M. Bawendi, *J. Am. Chem. Soc.* **2005**, *127*, 4556.
[19] Y. J. Kang, T. A. Taton, *Angew. Chem., Int. Ed.* **2005**, *44*, 409.
[20] C. Luccardini, C. Tribet, F. Vial, V. Marchi-Artzner, M. Dahan, *Langmuir* **2006**, *22*, 2304.
[21] W. W. Yu, E. Chang, C. M. Sayes, R. Drezek, V. L. Colvin, *Nanotechnology* **2006**, *17*, 4483.
[22] M. S. Nikolic, M. Krack, V. Aleksandrovic, A. Kornowski, S. Forster, H. Weller, *Angew. Chem., Int. Ed.* **2006**, *45*, 6577.
[23] W. W. Yu, E. Chang, J. C. Falkner, J. Zhang, A. M. Al-Somali, C. M. Sayes, J. Johns, R. Drezek, V. L. Colvin, *J. Am. Chem. Soc.* **2007**, *129*, 2871.
[24] H. W. Duan, S. M. Nie, *J. Am. Chem. Soc.* **2007**, *129*, 3333.
[25] R. A. Sperling, T. Pellegrino, J. K. Li, W. H. Chang, W. J. Parak, *Adv. Funct. Mater.* **2006**, *16*, 943.
[26] G. H. Hu, J. T. Lindt, *Polym. Bull.* **1992**, *29*, 357.
[27] M. Brust, M. Walker, D. Bethell, D. J. Schiffrin, R. Whyman, *J. Chem. Soc., Chem. Commun.* **1994**, *1994*, 801.
[28] B. O. Dabbousi, J. Rodriguez-Viejo, F. V. Mikulec, J. R. Heine, H. Mattoussi, R. Ober, K. F. Jensen, M. G. Bawendi, *J. Phys. Chem. B* **1997**, *101*, 9463.
[29] M. F. Casula, Y. W. Jun, D. J. Zaziski, E. M. Chan, A. Corrias, A. P. Alivisatos, *J. Am. Chem. Soc.* **2006**, *128*, 1675.
[30] R. A. Sperling, T. Liedl, S. Duhr, S. Kudera, M. Zanella, C.-A. J. Lin, W. Chang, D. Braun, W. J. Parak, *J. Phys. Chem. C* **2007**, *111*, 11552.
[31] M. T. Fernández-Argüelles, A. Yakovlev, R. A. Sperling, C. Luccardini, S. Gaillard, A. S. Medel, J.-M. Mallet, J.-C. Brochon, A. Feltz, M. Oheim, W. J. Parak, *Nano Lett.* **2007**, *7*, 2613–2617.
[32] T. Liedl, S. Keller, F. C. Simmel, J. O. Rädler, W. J. Parak, *Small* **2005**, *1*, 997.
[33] W. J. Parak, D. Gerion, D. Zanchet, A. S. Woerz, T. Pellegrino, C. Micheel, S. C. Williams, M. Seitz, R. E. Bruehl, Z. Bryant, C. Bus-

tamante, C. R. Bertozzi, A. P. Alivisatos, *Chem. Mater.* **2002**, *14*, 2113.
[34] B. Ballou, B. C. Lagerholm, L. A. Ernst, M. P. Bruchez, A. S. Waggoner, *Bioconjugate Chem.* **2004**, *15*, 79.
[35] E. L. Bentzen, I. D. Tomlinson, J. Mason, P. Gresch, M. R. Warnement, D. Wright, E. Sanders-Bush, R. Blakely, S. J. Rosenthal, *Bioconjugate Chem.* **2005**, *16*, 1488.
[36] K. K. Caswell, J. N. Wilson, U. H. F. Bunz, C. J. Murphy, *J. Am. Chem. Soc.* **2003**, *125*, 13914.
[37] A. Salant, E. Amitay-Sadovsky, U. Banin, *J. Am. Chem. Soc.* **2006**, *128*, 10006.
[38] H. Otsuka, Y. Akiyama, Y. Nagasaki, K. Kataoka, *J. Am. Chem. Soc.* **2001**, *123*, 8226.
[39] H. Otsuka, Y. Nagasaki, K. Kataoka, *Adv. Drug Delivery Rev.* **2003**, *55*, 403.
[40] S. R. Popielarski, S. H. Pun, M. E. Davis, *Bioconjugate Chem.* **2005**, *16*, 1063.
[41] C. A. Mirkin, R. L. Letsinger, R. C. Mucic, J. J. Storhoff, *Nature* **1996**, *382*, 607.
[42] T. A. Taton, R. C. Mucic, C. A. Mirkin, R. L. Letsinger, *J. Am. Chem. Soc.* **2000**, *122*, 6305.
[43] J. Rojo, V. Diaz, J. M. d. l. Fuente, I. Segura, A. G. Barrientos, H. H. Riese, A. Bernad, S. Penades, *ChemBioChem* **2004**, *5*, 291.
[44] C. C. Lin, Y. C. Yeh, C. Y. Yang, C. L. Chen, G. F. Chen, C. C. Chen, Y. C. Wu, *J. Am. Chem. Soc.* **2002**, *124*, 3508.
[45] B. Dubertret, M. Calame, A. J. Libchaber, *Nat. Biotechnol.* **2001**, *19*, 365.
[46] E. Dulkeith, A. C. Morteani, T. Niedereichholz, T. A. Klar, J. Feldmann, S. A. Levi, F. C. J. M. van Veggel, D. N. Reinhoudt, M. Möller, D. I. Gittins, *Phys. Rev. Lett.* **2002**, *89*, 203002.
[47] E. Dulkeith, M. Ringler, T. A. Klar, J. Feldmann, A. M. Javier, W. J. Parak, *Nano Lett.* **2005**, *5*, 585.
[48] P. T. Tran, G. P. Anderson, J. M. Mauro, H. Mattoussi, *Phys. Status Solidi B* **2002**, *229*, 427.
[49] I. L. Mednitz, A. R. Clapp, H. Mattoussi, E. R. Goldman, B. Fisher, J. M. Mauro, *Nat. Mater.* **2003**, *2*, 630.
[50] I. L. Mednitz, H. T. Uyeda, E. R. Goldman, H. Mattoussi, *Nat. Mater.* **2005**, *4*, 635.
[51] L. F. Shi, V. De Paoli, N. Rosenzweig, Z. Rosenzweig, *J. Am. Chem. Soc.* **2006**, *128*, 10378.

Received: August 7, 2007
Published online on February 13, 2008

SMALL (3) 301–384 (2008) · ISSN 1613-6810
Volume 4 · No. 3 – March 2008

NANO MICRO

small

www.small-journal.com

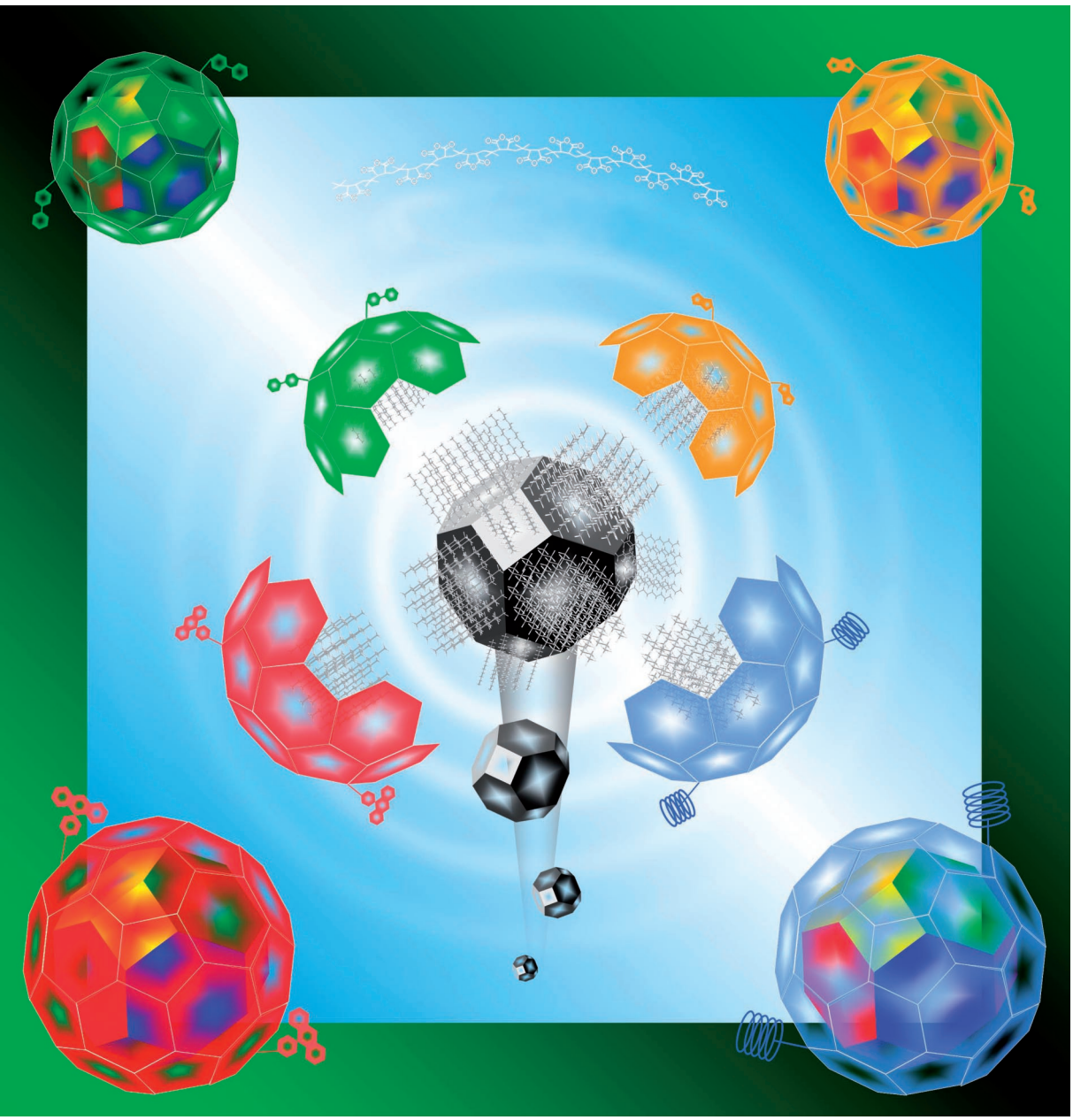

First ISI Impact Factor 6.024

3/2008

WILEY-VCH

Design of an Amphiphilic Polymer for Nanoparticle Coating and Functionalization
W. J. Parak et al.

Shape Control of Colloidal Metal Nanocrystals
P. Yang et al.

Cover picture

Cheng-An J. Lin, Ralph A. Sperling, Jimmy K. Li, Ting-Ya Yang, Pei-Yun Li, Marco Zanella, Walter H. Chang, and Wolfgang J. Parak*

The cover picture shows an amphiphilic polymer that can be used to coat hydrophobic nanoparticles in order to transfer them to aqueous solution. The amphiphilic polymer is based on a poly(maleic anhydride) backbone modified with hydrophobic side chains and functional organic molecules. The polymer successfully transfers inorganic colloidal nanoparticles of different materials (Au, CdSe/ZnS, Fe_3O_4) to aqueous solution. The initial nanoparticles are capped with different hydrophobic surfactant molecules, demonstrating the universality of the approach, in which the attachment of the polymer to the inorganic nanoparticles is only mediated by the hydrophobic interaction and does not depend on the surface chemistry of the inorganic nanoparticles. For more information, please read the Communication, “Design of an Amphiphilic Polymer for Nanoparticle Coating and Functionalization” by W. J. Parak et al., beginning on page 334.

Supporting Information

133

Supporting Information[1]

Design of an amphiphilic polymer for nanoparticle coating and functionalization

Cheng-An J. Lin[a,b,c,#], *Ralph A. Sperling*[a,d,#], *Jimmy K. Li*[c,&], *Ting-Ya Yang*[b], *Pei-Yun Li*[a], *Marco Zanella*[a,d], *Walter H. Chang*[b,c], *Wolfgang J. Parak*[*,a,d]

[a]Center for NanoScience, Ludwig-Maximilians-Universität München, Munich, Germany
[b]Department of Biomedical Engineering, Chung Yuan Christian University, Taiwan, R.O.C.
[c]R&D Center for Membrane Technology, Center for Nano Bioengineering, Chung Yuan Christian University, Taiwan, R.O.C.
[d]Fachbereich Physik, Philipps Universität Marburg, Marburg, Germany

[#]both authors contributed equally to this work
[&]present address: Institute of Biotechnology, National Cheng Kung University, Taiwan, R.O.C.
[*]corresponding author: Prof. Dr. Wolfgang Parak, Fachbereich Physik, Philipps Universität Marburg, Renthof 7, 35037 Marburg, Germany, email: Wolfgang.Parak@physik.uni-marburg.de

[1] The idea of this Supporting Information is to provide the interested reader with a detailed account of the raw data measured. It is by far not meant to be read from the beginning until the end. In contrast, due to the index the reader can access the piece of information that he/she is interested in. All important and relevant information is included in the main paper and this Supporting Information expands on further details to specific points. We have taken great care to describe here everything as detailed as possible, so that a documentation about all experimental and evaluation steps is given.

- Table of Content -

SI1: Synthesis of polymer with different modifications

Functional amphiphilic polymers can be used as a coating for various hydrophobic nanoparticles in order to transfer them to aqueous solution. The polymers developed for this purpose contain two main building blocks: hydrophobic sidechains which are compatible with the nanocrystals surface and a hydrophillic backbone which will be exposed to the aqueous solution.

Hydrophobic domains on the polymer coat intercalate with the hydrophobic tails of the surfactant molecules present around the nanoparticles and the hydrophilic backbone stabilizes the particles by electrostatic repulsion. The synthesis of these amphiphilic polymers is followed by conjugating amino-containing ligands (sidechains) to an anhydride chain (backbone), resulting in a tailored polymer with hydrophobic, hydrophilic, and (optional) functional properties as shown in ***Figure S1***. The illustration of each synthetic unit is described in S1.1 and their designs as well as examples are detailed in S1.2 and S1.3.

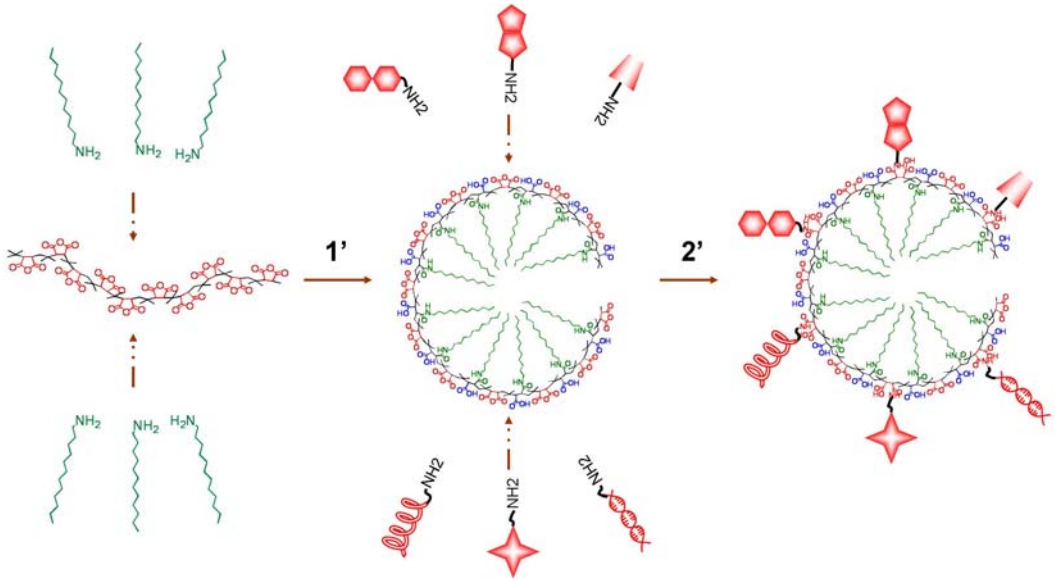

Figure S1. Conceptual scheme of polymer design. The first generation of polymer is created by conjugating alkyl amines to a maleic anhydride chain (1'), forming a basic amphiphilic polymer. The free anhydride groups on the polymer backbone can be covalently modified with functional ligands with amino terminal ($-NH_2$), e.g. fluorescent dyes, sugars, biotin, and polyethylene glycol, giving a multi-functional polymer (2') that can be used as a coating for various hydrophobic nanoparticles. When dispersed in an aqueous solution, the unconjugated maleic anhydride rings hydrolyze and yield two free carboxylic groups each, which stabilize the polymer-coated particles by electrostatic repulsion.

SI1.1 Illustration of synthetic units

Spontaneous reaction

- **maleic anhydride + primary amine**

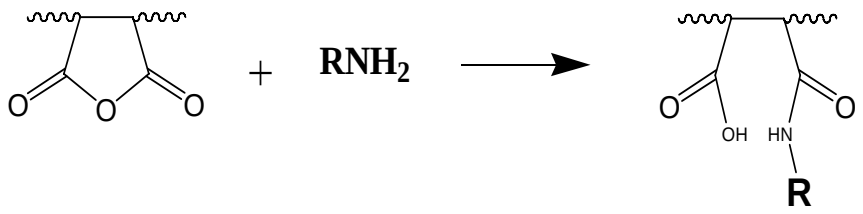

Hydrophilic backbone

- poly(maleic anhydride), e.g. poly(isobutylene-*alt*-maleic anhydride)

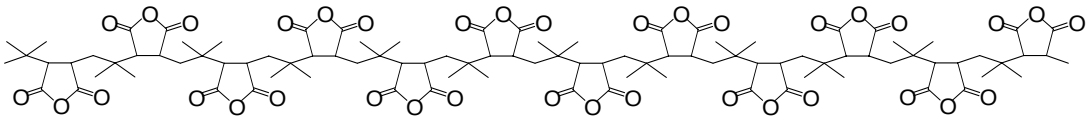

Hydrophobic sidechain

- **Primary alkyl amine** e.g. hexylamine, octylamine, decylamine, dodecylamine, tetradecylamine...

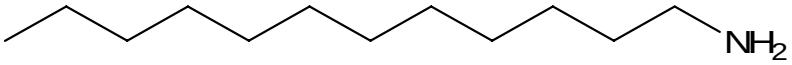

Functional molecules such as PEG, sugars, fluorescent dyes, biotin etc.

(e.g.) amino-PEG

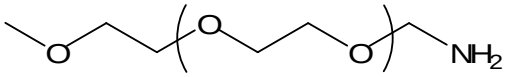

(e.g.) fluorescein-amine

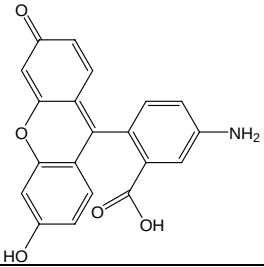

(e.g.) amino-galactose

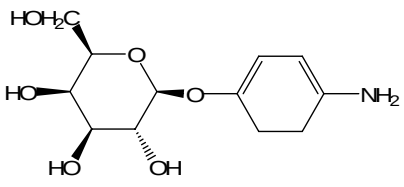

(e.g.) biotin-PEG-amine

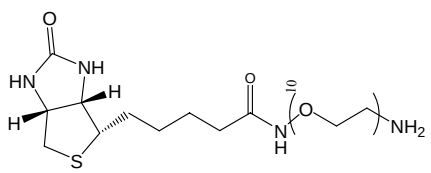

Amphiphilic polymer

- **poly(maleic anhydride) + alkylamine**

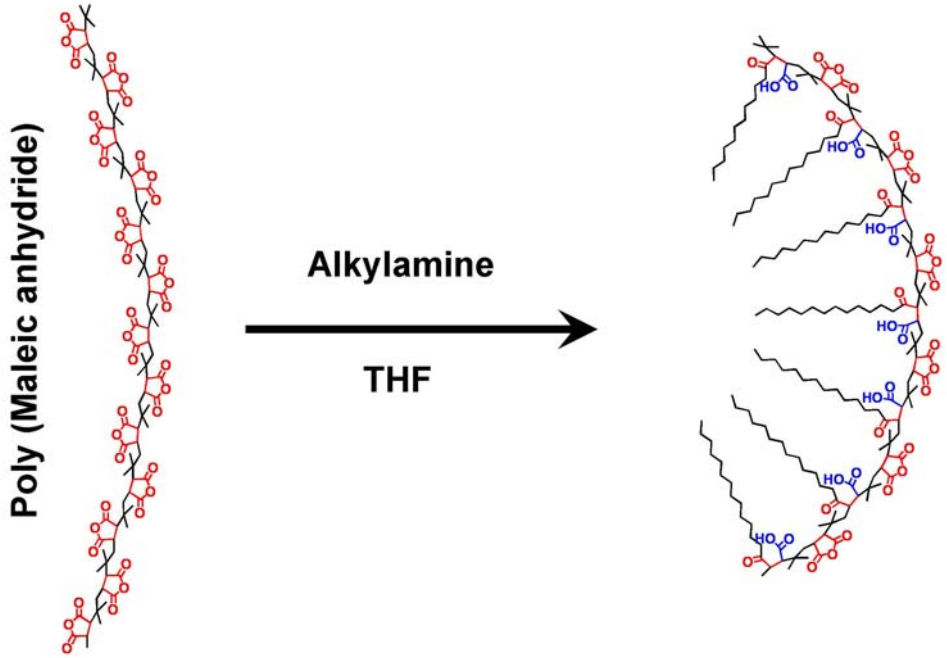

Amphiphilic/ functional polymer

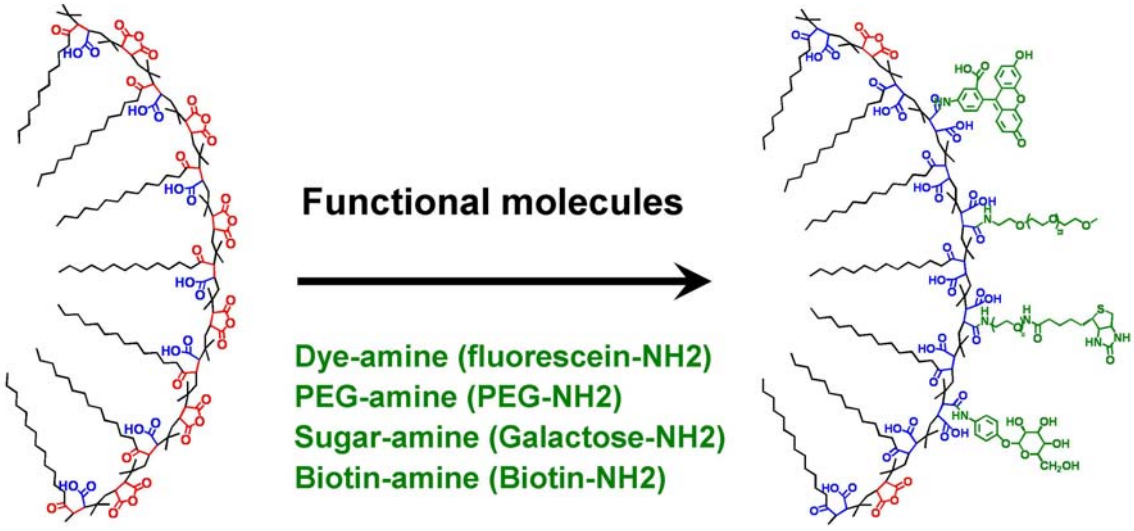

SI1.2 Stoichiometry of polymer synthesis

The maleic anhydride groups of the poly(isobutylene-*alt*-maleic anhydride) backbone were assumed to be 100% reactive to primary amino-ligands through spontaneous amide linkage, which converts one maleic anhydride group into one corresponding amide and one free carboxylic acid group.

Each amino-containing ligand contributes to the final functionality of the amphiphilic polymer, e.g. the hydrophobicity, negative charge, optical properties and biological interaction. Briefly, the polymer contains three parts which include hydrophobic sidechains (from aliphatic modification), hydrophilic groups (from the backbone) and functional molecules[2].

SI1.3 Synthesis of amphiphilic polymer: [*25%Anhydride-75%C12COOH*]

"***25%Anhydride-75%C12COOH***" is defined as a polymer of which x = 75% of its maleic anhydride rings have been reacted with dodecylamine, leaving z = 25% of its anhydride rings intact. The amphiphilic polymer was synthesized by grafting the hydrophobic alkylamine onto the hydrophilic poly(maleic anhydride) backbone through spontaneous amide linkage, which converts one maleic anhydride into one corresponding amide and one free carboxylic acid. In general, 3.084 g (20 mmol monomer) of poly(isobutylene-alt-maleic anhydride) (Mw~6,000 Da, Sigma #531278) were placed in a round flask. Each polymer molecule contains 39 anhydride (= monomer) units on average[3]. It was assumed that the maleic anhydride was 100% reactive. When preparing a 75% hydrophobic modification of amphiphilic co-polymer, 15 mmol dodecylamine (98%, Sigma #D22,220-8) dissolved in 100 ml of anhydrous tetrahydrofurane (THF, ≥99.9%, Aldrich #186562) were quickly injected and vigorously mixed with the polymer powder. The cloudy mixture was sonicated for some seconds and then kept at 60 °C under vigorous stirring. During the spontaneous reaction the solution became transparent within 5 - 10 minutes. In order to quantitatively react the maleic anhydride with the primary amine, the reaction mixture was concentrated roughly up to one fifth of the original volume by a rotavapor system (Laborota 4000, Heidolph) under a reduced pressure (p = 200 - 120 mbar) after 3 hours of reaction. The concentrated solution was further incubated overnight at 60 °C under stirring. The solvent was then slowly evaporated until the polymer was completely dry (pale yellow solid). Finally, the resulting polymer was re-dissolved in anhydrous chloroform and adjusted to a final volume of 25 ml, yielding a calculated concentration of monomer units of 0.8 M[4]. The amphiphilic polymer containing 25% of unreacted maleic anhydride groups was ready for polymer coating or could be further modified with other functional molecules. After the modification of the backbone (6000 g/mol, 39 monomer units) with 75% dodecylamine (185.36 g/mol), the molecular weight of the total (anhydrous) amphiphilic polymer is approximately 11400 g/mol.

[2] If the hydrophobic modification with primary alkylamines consumes x% of the reactive anhydride rings of the backbone, there will be (100 - x)% of anhydride rings left for further amino-ligand modification. With another y% functional amine-containing molecules added for modification, there will be z = (100 – x – y) % of the original number of maleic anhydride rings left. After being dispersed in an aqueous solution, these z% residual anhydride rings will open to yield 2 z% free carboxylic groups, the total percentage of carboxylic groups will thus be (x + y + 2z).

[3] As the polymer has a molecular weight of Mw ~ 6000 g/mol the molecular weight of one polymer unit is Mw ~ 6000 g/mol / 39 ≈ 154 g/mol, as each polymer molecule comprises on average 39 monomer units.

[4] 20 mmol / 25 ml = 0.8 M.

SI1.4 Synthesis of poly(ethylene glycol)-grafted co-polymer: [*75%C12COOH-25%PEG-COOH*]

"***75%C12COOH-25%PEG-COOH***" is defined as a polymer of which x = 75% of its maleic anhydride rings have been reacted with dodecylamine and of which y = 25% of its maleic anhydride rings have been reacted with PEG-amine, leaving no remaining anhydrides unreacted (z = 0%). An appropriate amount of methoxypoly(ethylene glycol) amine (Fluka 07964, mPEG750-amine, Mw~ 750 g/mol) was dissolved in chloroform to make a stock solution of 0.08 M concentration. Then 5 ml mPEG-amine stock solution was dropped into 2 ml of ***25%Anhydride-75%C12COOH*** (0.8 M monomer concentration) under vigorous stirring. Thus, the addition of mPEG-amine was enough to react with 25% of the total amount of anhydride monomers of ***25%Anhydride-75%C12COOH***. In general, the chloroform was evaporated by the rotavapor system and then the dried polymer was re-dissolved in anhydrous chloroform with the final volume of 4 ml, i.e. 0.4 M final concentration. In order to allow complete reaction, the mixture was stirred at room temperature overnight.

SI1.5 Synthesis of fluorescent dye-grafted co-polymer: [*24%Anhydride-75%C12COOH-1%Fluo*]

"***24%Anhydride-75%C12COOH-1%Fluo***" is defined as a polymer of which x = 75% of its maleic anhydride rings have been reacted with dodecylamine and of which y = 1% of its maleic anhydride rings have been reacted with fluorescein-amine, leaving z = 24% of the anhydrides unreacted. In order to anchor directly the fluorescent amino-dye on the polymer in organic phase, it was first prepared as stock solution in anhydrous chloroform. For example, 27.8 mg of fluorescein-amine (Aldrich 201626) were well dissolved in 10 ml of anhydrous THF to obtain a 8 mM fluorescein-amine stock solution (10x). This 10x solution was then further diluted 10 times with anhydrous THF before modification to a 1x stock solution. To obtain the 1% fluorescein-grafted co-polymer, i.e. addition of fluorescein-amine corresponding to 1% of the total amount of anhydride monomers, 0.5 ml of 0.8 M monomer units of ***25%Anhydride-75%C12COOH*** were mixed vigorously with 5 ml of 0.8 mM fluorescein-amine, which were then reacted overnight under stirring at room temperature. The resulting solution was then evaporated by the rotavapor system and the solid powder was re-dissolved in 10 ml of anhydrous chloroform, to yield a final monomer concentration of 40 mM fluorescein-polymer[5].

SI1.6 Synthesis of sugar-grafted co-polymer: [*21%Anhydride-75%C12COOH-4%Galactose*]

"***21%Anhydride-75%C12COOH-4%Galactose***" is defined as a polymer of which x = 75% of its maleic anhydride rings have been reacted with dodecylamine and of which y= 4% of its maleic anhydride rings have been reacted with galactose-amine, leaving z = 21% of anhydride rings intact. In order to anchor the sugar on the polymer, sugar-amine was first prepared in THF as a stock solution. For example, 43.4 mg of aminophenyl galactopyranoside (Sigma A9545) were dissolved in 20 ml of anhydrous THF by sonication to obtain an 8 mM galactose-amine stock solution (10x). The solution was further diluted 10 times with anhydrous THF before modification to yield a 0.8 mM stock solution (1x). To obtain 4% galactose-grafted co-polymer, i.e. addition of galactose-amine corresponding to 4%

[5] (0.5 ml • 0.8 mM) / 10 ml.

of the total amount of monomers (anhydride rings), 0.5 ml of 0.8M monomer of ***25%Anhydride-75%C12COOH*** were mixed vigorously with 20 ml of 0.8 mM galactose-amine, which were then reacted overnight under stirring at room temperature. The resulting solution was then evaporated by the rotavapor system and the solid powder was re-dissolved in 10 ml of anhydrous chloroform, to yield a final concentration of 40 mM monomer concentration of sugar-polymer or galactose-polymer.

SI1.7 Synthesis of biotin-grafted co-polymer: [*21%Anhydride-75%C12COOH-4%Biotin*]

"***21%Anhydride-75%C12COOH-4%Biotin***" is defined as a polymer of which x = 75% of its maleic anhydride rings have been reacted with dodecylamine and of which y = 4% of its maleic anhydride rings have been reacted with biotin-amine, leaving z = 21% of anhydrides unreacted. In order to anchor the biotin molecules on the synthetic polymer, 10 mg of biotin- poly(ethyleneglycol) amine (average Mw = 720 g/mol, Sigma B9931) were first prepared in 0.868 ml of THF (1.6 mM). To obtain a 4% biotin-grafted copolymer, i.e.addition of biotin-amine corresponding to 4% of the total amount of monomers, 0.25 ml of 0.8M monomer concentration of ***25%Anhydride-75%C12COOH*** were vigorously mixed with 10 ml of 0.8 mM biotin-amine (diluted with chloroform), which were reacted overnight under stirring at room temperature. The resulting solution was then evaporated by the rotavapor system and the solid powder was re-dissolved in 5 ml of anhydrous chloroform, to yield a final monomer concentration of 40 mM biotin-polymer.

In addition, the binding efficiency of the functional molecules (e.g. biotin, galactose etc.) to the polymer chain in principle depends on several factors such as the solubility, temperature, concentration and reaction time. As mentioned above, THF is a good solvent substitute for chloroform when the molecule of interest is not well soluble. The synthesis can be carried out in THF or chloroform, selected because of their low vapor point. Furthermore, the reaction efficiency could also be increased by reducing the volume of the polymer solution, i.e. several rounds of evaporation steps after adding THF or chloroform. The protocols above include examples for the synthesis of tailored amphiphilic polymers with several different classes of functional molecules.

141

SI2: Synthesis of different nanoparticles

SI2.1 Synthesis of colloidal gold nanoparticles (4 nm)

The 4-nm gold nanoparticles were synthesized according to the Brust two-phase method, with some modifications. Briefly, the organic phase containing 8.86 g of tetraoctylammonium bromide (TOAB, 98%, Sigma-Aldrich 29,413-6) was dissolved in 320 ml of toluene (Fluka 89682) and the aqueous phase was prepared by dissolving 1.2 g hydrogen tetrachloroaurate (III) (99.9%, Alfa Aesar #12325) in 100 ml of MilliQ water. The two phases were mixed in a 500-ml separation funnel and then the gold precursors (yellow part in water) was then gradually transferred into the oil phase (red color), indicating the formation of tetraoctylammonium-gold pairs. After discarding the aqueous solution (the lower part), the oil phase with gold precursors was transferred to a 500-ml round flask. In another beaker, a reduction agent was freshly prepared by dissolving 1.34 g of sodium borohydride (98%, Sigma-Aldrich #45.288-2) in 100 ml of MilliQ water with stirring, and was then added dropwise within one minute to the gold precursor solution in toluene. Upon vigorous stirring, the color changed from red to red-violet, indicating the nucleation of gold clusters mediated by sodium borohydride. Further growth was mediated by the residue of sodium borohydride, which reduced the remaining gold ions. The solution was transferred to a clean separation funnel after one-hour stirring and then 100 ml of 0.01 M HCl were added to remove the excess of sodium borohydride. The two-phases solution was shaken for minutes and the aqueous phase was discarded. Again, 100 ml of 0.01M NaOH were added in order to remove the excess acid by shaking for minutes and by discarding the aqueous phase. Finally, 100 ml of Milli-Q water were then added to remove the excess ions and the aqueous phase was removed after shaking for minutes. This last step was repeated four times. In order to enhance the stability of particles, 40 ml of 1-dodecanethiol (98%, Sigma-Aldrich #47,136-4) were added after one day stirring and the solution was then incubated at 65°C for 2 hours.

The high binding affinity of thiol to gold would displace the Br- ions and yield dodecanthiol-coated gold nanocrystals. The solution was cooled down to room temperature and larger agglomerates were first removed by centrifuging at 2500 r.p.m. To the collected supernatant, methanol was added until the solution turned cloudy, followed by centrifugation. After discarding the supernatant, the precipitate was dissolved in toluene upon vigorous shaking. To the nanoparticle solution again cold methanol was added until the solution turned cloudy, followed by centrifugation. The supernatant was removed and the precipitate was re-dissolved in 8 ml of toluene. In order to further improve the size distribution of the sample, a size-selective precipitation was carried out by adding 80 µl of cold methanol, followed by centrifugation and discarding of the pellet which comprises bigger particles or aggregates. The average of the inorganic core diameter of the gold nanocrystals was determined by TEM and the particle concentration was determined by UV-VIS absorption measurement (Cary 50, Varian). In this case, gold nanoparticles with an average diameter of 4 nm have the extinction coefficient of 8.7×10^6 $M^{-1}cm^{-1}$ at their plasmon peak around 518 nm. The concentration of the resulting gold nanoparticle solution was typically in the micromolar range.

SI2.2 Synthesis of colloidal gold nanoparticles (6 nm)

The synthesis of 6-nm gold nanoparticles (AuNP) was modified from Peng's protocol[1]. Appropriate amounts of didodecyldimethylammonium bromide (DDAB, Fluka 36785) and decanoic acid (Aldrich W236403) were dissolved separately in toluene to prepare a stock solution of 100 mM concentration. Then an appropriate amount of $AuCl_3$ (Aldrich 379948) was dissolved in DDAB solution to prepare a gold precursor solution of 25 mM concentration. Then, 25 mg of tetrabutylammonium borohydride (TBAB, Fluka 86855) dissolved in 1 ml of DDAB solution were mixed to 2.5 ml decanoic acid

solution. After nucleation by dropping 10 µl of $AuCl_3$ solution into this mixture, 0.8 ml gold precursor solution was then injected during vigorous stirring. The color of the solution changed to deep red within minutes, indicating formation of gold nanoparticles. After one-hour stirring, the solution was heated up to 60°C for 5 minutes in order to improve size distribution. After further adding 0.5 M trioctylphosphine (TOP, Aldrich 117854) which was prepared in toluene the plasmon peak of AuNP was shifted from 530 nm to 520 nm, indicating the successful capping of TOP surfactants on the AuNP, i.e., the phosphine heads were attached onto the gold surface and the alkyl tail protruded out. In most experiments the TOP: gold molar ratio was 1:1. After removing the larger particles by centrifugation (1500 rpm, 5 minutes), the 6-nm AuNP was purified by methanol precipitation and the dried agglomerates of gold nanoparticles were re-dissolved in anhydrous chloroform. The concentration of 6-nm AuNP having the extinction coefficient of 2.87×10^7 $M^{-1}cm^{-1}$ at its plasmon peak was determined by UV-VIS absorption measurement (Cary 50, Varian).

SI2.3 Synthesis of colloidal quantum dots

CdSe

Briefly, 3.86 g of trioctylphosphine oxide (TOPO, 99%, Sigma-Aldrich #22.330-1), 0.78 g of hexadecylamine (HDA, technical grade, Sigma-Aldrich #H7.40-8), 0.268 g of dodecylphosphonic acid (DDPA 98%, Polycarbon Inc.) and 51.4 mg of CdO (99.99+%, Sigma-Aldrich #20.289-4) were mixed in a 50-ml 3-necked flask equipped with a temperature controller stick, a rubber septum for injecting the stock solution, as well as a third neck connected vertically to the Schlenk line assembled in a glove box. First, the mixture was exposed to vacuum at 100 °C for 20 minutes under stirring in order to remove impurities, followed by switching the vacuum to argon flow. The temperature was elevated to 320°C until the color of the mixture turned to transparent pale yellow. At the same time, the Se stock solution was freshly prepared by dissolving 320 mg of Se powder (99.99%, Sigma-Aldrich #22.986-5) in 2 ml of trioctylphosphine (TOP, technical grade, Sigma-Aldrich #11.785-4) under vigorous stirring. After swiftly injecting the Se precursor solution into the hot TOPO solution (320 °C in Ar flow with vigorous stirring under reflux) followed by re-setting the temperature to 240 °C, the color of the solution turned from colorless to yellow-orange and the heating mantle was then removed. In order to synthesize quantum dots of other sizes, heating was continued without removing the heating mantle and the color gradually turned to red, dark red and finally to dark brown in 25-30 minutes after the injection (first exciton absorption peak at 620-630 nm). The growth of quantum dots was monitored by taking aliquots during reaction and by measuring their UV-visible absorption spectrum of the chloroform-diluted sample. The resulting reaction mixture was cooled to room temperature followed by methanol addition. The supernatant was then discarded after centrifugation; the precipitated nanocrystals were re-dissolved in chloroform without further purification. The growth of quantum dots varied slightly from batch to batch, but the synthesis could be stopped as soon as the first exciton peak reached a desired value, which could be easily fitted to an average size through calibration curves from Peng's group[2]. The concentration of quantum dots could also be easily estimated by the optical density in first exciton peak correlated with their extinction coefficient.

CdSe/ZnS

For the growth of ZnS shell on CdSe quantum dots, 4 g of TOPO and 1 g of HDA were weighted in a 50-ml 3-necked flask, pumped to vacuum at 120 °C for 20 minutes under stirring. After switching the vacuum to argon flow, an appropriate amount of CdSe solution (typically 4 ml with concentration of 10^{-5} M) was injected into the TOPO/HDA mixture and the chloroform was then distilled off under vacuum until there was no bubbling. Then the vacuum was switched to argon flow and the temperature was elevated to 140-220 °C depending on the size of nanocrystals according to the literature[3]. The

stock solution for ZnS shell growth was freshly prepared in the glove box by dissolving 0.31 g of diethylzinc solution ($C_4H_{10}Zn$, 1.0 M solution in heptane, Sigma-Aldrich #40.602-3) and 0.45 g of hexamethyldisilathiane ($C_6H_{18}Si_2S$, Aldrich #28.313-4) in 20.0 g TBP, which was then added dropwise to the CdSe/TOPO/HAD mixture. The amount of ZnS solution was calculated according to the size of the CdSe core, the desired number of ZnS monolayers and the concentration of core nanocrystals[3]. After dropping all the ZnS stock solution, the temperature was set to 100°C for the next 2 hours with stirring under argon flow. Then the reaction mixture was cooled down to room temperature followed by addition of methanol. The resulting cloudy solution was centrifuged to discard the supernatant with free surfactants; and the precipitated nanocrystals were re-dissolved in toluene. The concentration of core/shell quantum dots could also be easily estimated by the optical density in the first exciton peak correlated with their extinction coefficient. The prepared CdSe/ZnS quantum dots were nominally covered with two monolayers of ZnS. The solution was then transferred into a vial and stored for the polymer coating experiments.

SI2.4 Synthesis of colloidal iron oxide nanoparticles

Iron oxide nanoparticles were synthesized following Casula's protocol[4]. In a typical synthesis, a solution of tridecanoic acid in octyl ether mixed in a 50-ml 3-necked flask equipped with a temperature controller stick, a rubber septum for injecting the stock solution, as well as a third neck connected vertically to the Schlenk line assembled in a glove-box was out-gassed for 30 minutes and then heated under Ar flow at 293 ºC. Two solutions of iron pentacarbonyl and mCPBA in ether were then rapidly co-injected. The iron molar concentration was 0.1 M, and the iron: surfactant: oxidizer molar ratio was 1:3:1.5. The solution flask was heated at 293 °C for 5 minutes to allow particle growth, after which the solution was cooled to 40 °C, and then ethanol was then added to precipitate nanoparticles from the solution. Following two rounds of centrifugation, re-dispersion in toluene, and precipitation with ethanol, no further size selection procedure was carried out. The iron oxide nanoparticles thus obtained were stored in anhydrous hexane before use.

SI3: Polymer-coating of different systems

SI3.1 General introduction of polymer coating

The general concept of polymer coating has been described previously by Pellegrino et al.[5], in detail in the supporting information of this report. All kinds of colloidal nanoparticles, i.e. CdSe/ZnS quantum dots, gold nanoparticles, and iron oxide nanoparticles, were first cleaned by removing unbound surfactant before applying the polymer coating procedure. Adding an excess of anhydrous methanol to a 10-ml nanoparticle solution resulted in the reversible flocculation of nanoparticles. The flocculates were then separated from the supernatant by centrifugation and re-dispersed in 10 ml of anhydrous chloroform. Second, the amount of (functional) amphiphilic polymer was determined by the total surface area of hydrophobic nanocrystals. For each sample, the average diameter of inorganic nanocrystal core was determined by TEM analysis and the concentration (C) of the nanoparticle solutions were determined either by a gravimetric method[5] or by an absorption measurement[2].

The overall surface area (A_0) of each nanoparticle and the total amount of nanoparticles were calculated using the effective nanoparticle diameter d_{eff}=d_{core}+ 2 $l_{surfactant}$ (nm), i.e., the sum of the diameter of the inorganic core (d) plus the assumed thickness of the surfactant shell ($l_{surfactant}$ = 1 nm), as shown in *Formulas (1) and (2).*

$$A_0 = 4\pi \cdot (d_{eff}/2)^2 = \pi \cdot d_{eff}^{\ 2} \quad \text{..... (1)}$$

$$A = C \cdot V \cdot N_A \cdot A_0 = \pi \cdot C \cdot V \cdot N_A \cdot d_{eff}^{\ 2} \quad \text{..... (2)}$$

A_0 : *Surface area of one single spherical nanoparticle (nm^2)*

A : *Total surface area of all the colloidal nanoparticles in the aliquot solution (nm^2)*

d_{eff} : *Effective diameter of one nanoparticle (nm)*

C : *Concentration of colloidal nanoparticles in the aliquot solution (mol/l)*

V : *Volume of aliquot solution (l)*

N_A : *Avogadro constant, 6.02×10^{23}/mol*

The polymer solution synthesized from the previous section was added to the nanoparticle solution, in which the amount of polymer could be estimated by *formulas (3)* and *(4)*. After 10-20 minutes of stirring the nanoparticles with the polymer, the chloroform was slowly evaporated under reduced pressure by a rotavapor system (Laborota 4000, Heidolph). The cross-linker solution (bis(6-aminohexyl)amine (Sigma-Aldrich # 14506) in chloroform) was then (optionally) added to cross-link the polymer shell which was wrapped around the nanoparticles. The solution was again mixed well for 10 minutes followed by the slow evaporating procedure under reduced pressure to remove all the chloroform. The resulting solids were quickly dissolved in basic buffer solution (0.1 M NaOH or 50 mM sodium borate buffer (SBB, pH12) to yield nanoparticles in aqueous phase. A filtration through a syringe membrane filter (Roth # P818.1, 0.22 μm pore size) helped to remove any remaining aggregates. Then the buffer was changed to sodium borate buffer (SBB, pH 9) by two rounds of

dilution with SBB and reconcentration through 100 kDa MWCO Amicon centrifuge filters (Millipore, Amicon Ultra-15, #UFC9100). Small empty polymer micelles (MW << 100 kDa), which may form from excess polymer, could be removed by ultrafiltration. Most of the remaining polymer micelles could be removed using a size exclusion column (Sephacryl S-300, Pharmacia). Optionally, nanoparticles could also be further purified by gel electrophoresis (Sub-Cell GT electrophoresis cells, Bio-Rad)[6], which lead to a more efficient removal of empty polymer micelles than the purification by size exclusion columns. The concentrated nanoparticles were first loaded into wells of a 2% agarose gel (Invitrogen #15510027) in 0.5 x TBE solution and gel electrophoresis was performed for one hour under an applied electric field of 10 V/cm. The resulting bands which contained nanoparticles were cut out and transferred into a dialysis membrane bag (3500 Da MWCO, Roth) and run through gel electrophoresis again to expel the trapped nanoparticles. The nanoparticles solution was then filtrated with a syringe filter (0.22 μm pores) in order to remove small gel pieces and reconcentrated by ultrafiltration (100 kDa MWCO Amicon centrifuge filter).

$$V_P = \frac{N_P}{C_P} = \frac{A \times R_{P/Area}}{N_A \times C_P} \equiv \frac{\pi \cdot C \cdot V \cdot d_{eff}^{\ 2} \times R_{P/Area}}{C_P} \quad \text{.....(3)}$$

$$V_C = \frac{N_C}{C_C} = \frac{N_P \times r_{C/P}}{N_A \times C_P} = \frac{A \times R_{P/Area} \times r_{C/P}}{N_A \times C_P} \equiv \frac{\pi \cdot C \cdot V \cdot d_{eff}^{\ 2} \times R_{P/Area} \times r_{C/P}}{C_P} \quad \text{..... (4)}$$

V_P, V_C *: Volume of polymer (p) or cross-linker (c) solution added to nanoparticles (l)*

N_P, N_C *: Number of polymer monomers (p) or cross-linkers (c) needed in polymer coating (mol)*

C_P, C_C *: Concentration of polymer monomers (p) or cross-linkers (c) in stock solution (M)*

A *: Total surface area of all colloidal nanoparticles in the aliquot solution (nm^2)*

$R_{P/Area}$ *: Ratio of numbers of polymer monomers (p) added per surface area on nanoparticles (monomer units/nm^2)*

$r_{C/P}$ *: Ratio of added cross-linkers (c) to numbers of polymer monomers added*

Several experiments of polymer coating have been performed. All experiments always lead to a successful transfer of nanoparticles to the aqueous phase although the nanoparticles could vary in size, core material and/or surfactant ligands.

To optimize the parameters for a robust coating procedure, a series of tests were run in order to find the number of polymer monomers per surface area that give the best performance. In the case of gold nanoparticles for example, gold nanoparticles were coated with polymer of 25% anhydride-75% C12-CA with different ratios of added polymer per surface area on nanoparticles, i.e., $R_{P/Area}$ = 5, 10, 50, 100, 500, and 1000 monomer units/nm^2.

[6] In this electrophoresis apparatus, the buffer reservoirs around the electrodes have a much larger cross-section than the gel on the tray, therefore in analogy to a series of resistances the voltage is assumed to drop mainly at the edges of the agarose gel that has a length of 10 cm. With a constant applied voltage of 100 V, the electric field strength is then 10 V/cm.

After HPLC purification the particles were run through gel electrophoresis (10 V/cm, 1 hour). The result of this experiment is shown in Figure S2. As can be seen, there is a safe range ($R_{P/Area}$ = 50-500 units/ nm^2) where bands are sharp, indicating a good coating integrity as well as homogeneity of the polymer shell. Experiments with other nanoparticles led to similar results. Therefore a general protocol for the polymer coating of hydrophobic nanoparticles could be established, regardless of the nanocrystal material. In this protocol, 100 monomer units of polymer are added per nm^2 surface area of nanoparticles and the ratio of cross-linkers to the number of polymer added (in monomer units) is 0.05, i.e. the general values of $R_{P/Area}$ = 100 and $r_{C/P}$ = 0.05 were used in the following. Here we report in detail the protocol applied to three kinds of nanomaterials, namely semiconductor quantum dots (CdSe/ZnS), superparamagnetic nanoparticles (Fe_2O_3), and gold nanoparticles (Au).

The use of cross-linker during the polymer coating described in this study was optional. For our previously published polymer coating procedure (with poly(maleic anhydride alt-1-tetradecene) (Mw ~9000, discontinued product from Sigma-Aldrich, # 452513) and the cross-linker by bis(6-aminohexyl)amine (Fluka # 14506)), it was found that nanocrystals to which only the polymer solution was added, but without undergoing the cross-linking step, did not dissolve well water[5]. In contrast, nanoparticles with polymer coating procedure reported in this study could be quickly dissolved in basic solution (0.1 M NaOH) even without the cross-linker. When the polymer-coated particles were (post-) modified with PEG by means of EDC, it was difficult to reach complete saturation of the particles without precipitation. This was attributed to the smaller number of carboxylic groups on the polymer backbone compared with the commercial polymer used by Pellegrino[5].

The experimental results of the polymer coating of hydrophobic nanoparticles as well as their subsequent PEG modification are illustrated in ***Figure S3.***

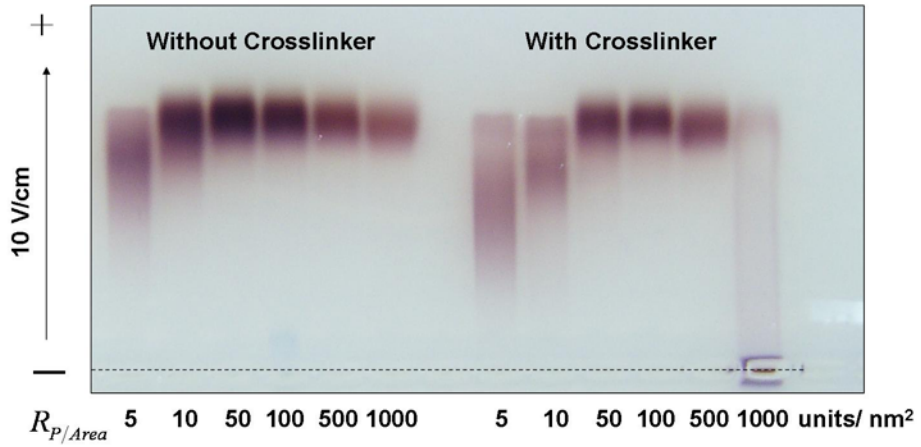

Figure S2. Polymer coating of Au nanoparticles (4-nm core diameter) with different amount of monomer added per surface area ($R_{P/Area}$) with or without crosslinker.

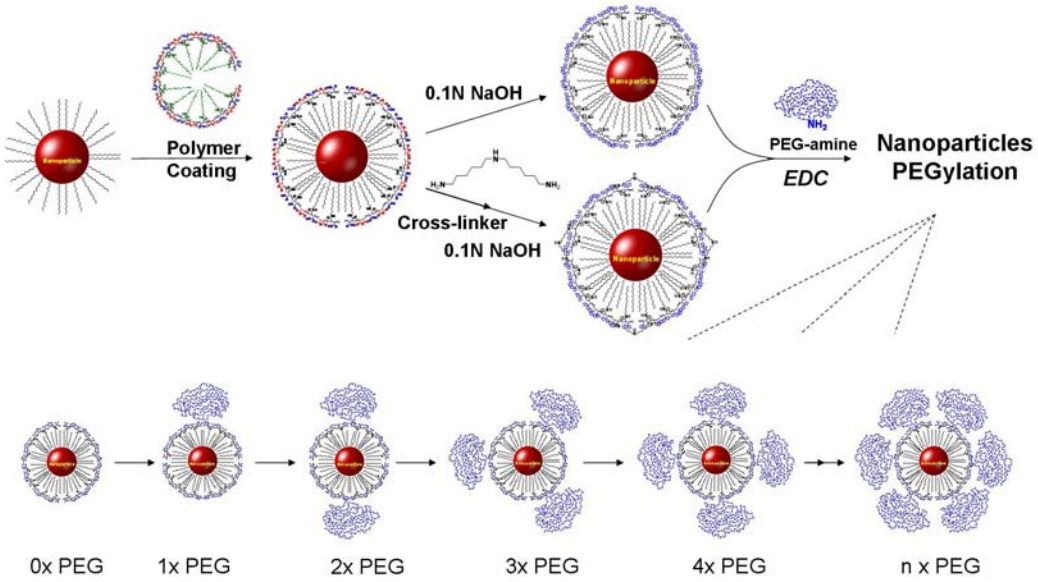

Figure S3. Scheme of polymer coating procedure. The hydrophobic alkyl chains of the polymer intercalate with the surfactant coating on the nanoparticles. The free carboxylic acid and anhydride rings are then located on the surface of these polymer-coated nanoparticles. The amino ends of the optionally added cross-linker open the anhydride ring and link the individual polymer chains for further stabilization. In both cases the nanoparticles become water soluble after 100 mM sodium hydroxide is added. The negative charges of the polymer shell stabilize the particles in water by electrostatic repulsion. Then the exposed carboxylic group on nanoparticles can be further conjugated with amine-containing molecules (e.g. PEG) through EDC chemistry.

SI3.2 Polymer coating of CdSe/ZnS quantum dots and test of PEGylation

The synthesis of CdSe/ZnS quantum dots has been described above. The excess surfactants of as-prepared quantum dots were cleaned by removing the supernatant of a methanol-mediated precipitation and the dried (still wet) agglomerates were then re-dissolved in anhydrous chloroform. The concentration of quantum dots was determined by UV-VIS absorption measurement (Cary 50, Varian). For quantum dots with an average diameter of 2.35 nm (first extinction peak at 500 nm from absorption spectrum) the extinction coefficient of 56047 $M^{-1}cm^{-1}$ was estimated from the literature[2]. The inorganic core diameter (d) was estimated to be 3.75 nm by assuming a thickness of two monolayers of the ZnS shell. Thus the effective diameter (d_{eff}) which comprises the surfactant layer was estimated to be 5.75 nm. In the aliquot solution of CdSe/ZnS nanocrystals (500 µl, 12 µM) the total surface area (A) of colloidal quantum dots was 3.75×10^{17} nm^2 calculated using *formula (1)*. Using a polymer to surface ratio of $R_{P/Area}$ = 100 units / nm^2, means that 62.3 µmol monomer of polymer has to be added to the nanocrystal solution[7]. Therefore 78 µl of polymer stock solution (0.8 M monomer concentration, ***25%Anhydride-75%C12COOH made in SI1.3***) and 2.42 ml of anhydrous chloroform were added to quantum dot solution, giving to a total volume of 3 ml[8]. After stirring for 15 minutes, the solvent was slowly evaporated by the rotavapor system, i.e. set to 200 mbar until no liquid was left and then set to 20 mbar for 10 minutes. For the optional crosslinking 1.56 ml of cross-linker solution (2 mM bis(6-

[7] $A = \pi \cdot 12\ \mu M \cdot 500\ \mu l \cdot 6.01 \cdot 10^{23}\ mol^{-1} \cdot (5.75\ nm)^2 = 3.75 \cdot 10^{17}\ nm^2$.
$N_P = A \cdot R_{P/Area} / N_A = 3.75 \cdot 10^{17}\ nm^2 \cdot 100\ nm^{-2} / 6.01 \cdot 10^{23}\ mol^{-1} = 62.3\ \mu mol$.
[8] 62.3 µmol / 0.8 M = 78 µl.

aminohexyl)amine in chloroform) was added to re-dissolve the resulting particle powder and stirred for 20 minutes. Afterward the solvent was again removed by evaporation, and the resulting powder of quantum dots with polymer shell was quickly dissolved in 2 ml of 0.1 M NaOH. The solution was further diluted to 15 ml by addition of water, filtered through a 0.22-µm syringe filter and finally gave a transparent solution. By two rounds of ultrafiltration with Amicon centrifuge filters (100kD MWCO), the buffer was changed to SBB (sodium borate buffer, 50 mM, pH 9) and the residues of polymer micelles were further removed by passing the solution through a size exclusion column (Sephacryl S-300, Pharmacia). The final concentration of purified quantum dots could be adjusted by concentration on a centrifuge filter. The surface chemistry of quantum dots was also characterized by the attachment of a discrete number of PEG molecules[6], i.e. a simple method that can evaluate the bio-conjugative capability of the nanoparticles. (***Figure S4***)

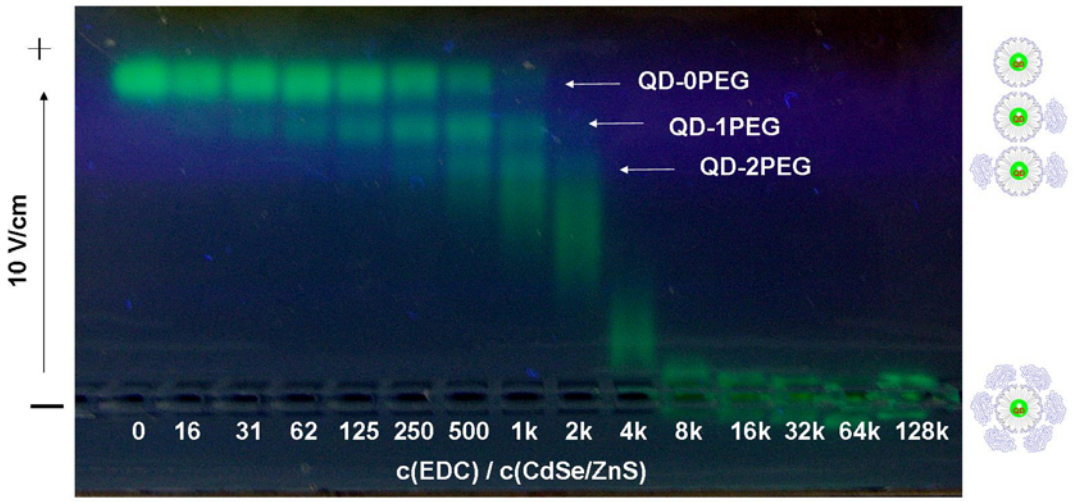

Figure S4. Discrete PEGylation of polymer-coated quantum dots (QD). First, 150 µl of 3 mM of methoxy-poly(ethylene glycol)amine (CH_3O-PEG-NH_2, Mw~5000 g/mol, Rapp Polymere) in SBB were mixed with an equal volume of polymer-coated quantum dots (6 µM, 2.35 nm core diameter) and split into aliquots of 20 µl each. To these samples, 10 µl of an EDC solution of appropriate concentration was added to yield different molar ratios of EDC molecules per nanoparticle, c(EDC)/c(CdSe/ZnS) = 0, 16, 31, 63, 125, 250, 500, 1k, 2k, 4k, 8k, 16k, 32k, 64k, and 128k. After 2 hours of reaction, the series was run by gel electrophoresis (10 V/cm, 1 hour) before the photo was taken under excitation by an UV lamp. The more EDC had been added, the more PEG molecules were bound to the quantum dots, and the more retarded the bands on the gel were. The lanes of the gel correspond to samples with increased EDC concentration from left to right. Discrete bands of particles with 0, 1, 2 ...attached PEG molecules per particles could be resolved in case of c(EDC)/c(CdSe/ZnS) < 2000, which demonstrates the possibility to prepare mono- and divalent quantum dots with the polymer coating procedure described in this report.

SI3.3 Polymer coating and PEGylation of iron oxide nanoparticles (FeNP)

Iron oxide nanoparticles were either synthesized or purchased (USPIO-C18, TAN bead, Taiwan). The concentration of the FeNP solution was determined by gravimetric measurements. Generally, after removing the free surfactants by methanol precipitation, all solvents were evaporated until the sample was completely dry. The weight concentration of FeNP solution was then adjusted to 10 mg/ml by chloroform after weighing the dried FeNP solid. With the bulk density of Fe_2O_3 of 5.24 g/cm^3, the mass of a single FeNP having a diameter of 13 nm (from TEM) was estimated to be 6.03×10^{-18} g. Finally, the molar particle concentration of 2.75 μM was calculated from the weight concentration. The calculation does not take into account the mass of the surfactant coating, which results in an over-estimation of the particle concentration. If we assume that the organic surfactant shell is 1 nm thick, its volume ratio V_{shell}/V_{core} is around 0.54 and the mass ratio M_{shell}/M_{core} is 0.09, the organic shell would contribute around 9 % to the total mass of one particle.

From the inorganic core diameter d = 13 nm the effective diameter d_{eff} = 15 nm was estimated. In the aliquot of FeNP solution (500 μl, 2.75 μM), the total surface area (A) of FeNP was 5.85×10^{17} nm^2 calculated using *formula (2),* $R_{P/Area}$ = 100 nm^{-2}, meaning that 97.2 μM monomer units of polymer had to be added to the nanocrystal solution. Then, 122 μl of polymer stock solution (0.8 M, ***25%Anhydride-75%C12COOH made in SI1.3***) and 2.38 ml of anhydrous chloroform were added to the FeNP solution, giving a total volume of 3 ml. After stirring for 15 minutes, the solvent was slowly evaporated by the rotavapor system, i.e., by setting the pressure to 200 mbar until the solvent was evaporated, and finally to 20 mbar for 10 min until the sample was completely dry. Optionally the polymer shell could be cross-linked. For this 2.43 ml of cross-linker solution (2 mM bis(6-aminohexyl)amine in chloroform) were added to re-dissolve the solid and allowed to react under stirring for 20 minutes. Afterward all solvent was again removed by evaporation, and the solid complex of FeNP with polymer coat was quickly dissolved in 2 ml of basic SBB buffer (SBB, pH12 adjusted by NaOH). The solution was further diluted to 15 ml by the addition of water, filtered through a 0.22-μm syringe filter and finally gave a transparent solution. The SBB buffer exchange was carried out by two rounds of ultrafiltration using Amicon centrifuge filters (100kD MWCO) and residues of polymer micelles were further removed by running the sample through a size exclusion column (Sephacryl S-300, Pharmacia) or the particles were further purified by gel electrophoresis. The final concentration of purified FeNP could be adjusted by ultrafiltration. The surface chemistry of FeNP was also characterized by discrete PEGylation[6] (***Figure S5***).

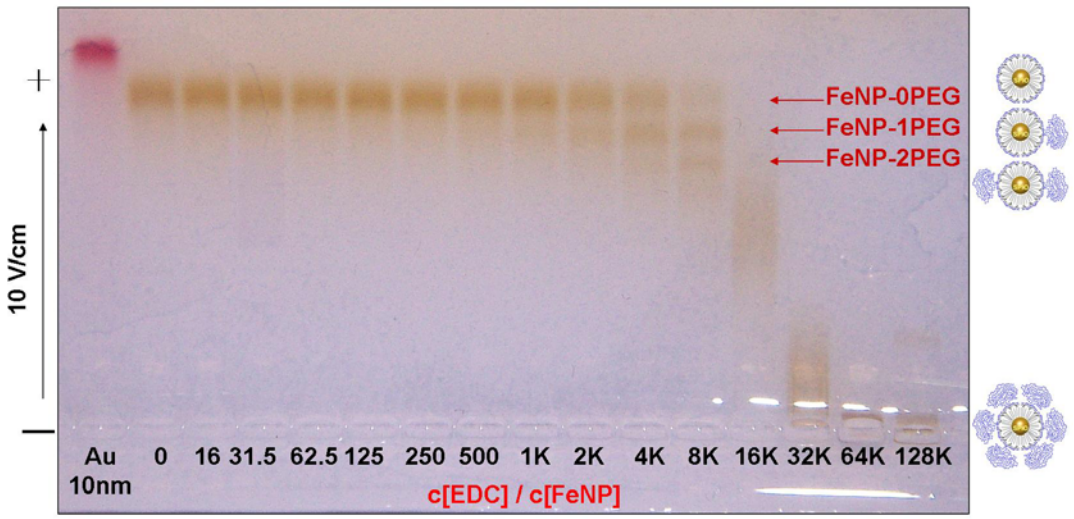

Figure S5. Discrete PEGylation test of polymer-coated iron oxide nanoparticles (FeNP). First, 150 µl of 3mM methoxy-poly(ethylene glycol)amine (CH_3O-PEG-NH_2, Mw~5000 g/mol, Rapp Polymere) in SBB were mixed with an equal volume of polymer-coated FeNP (3 µM, 13 nm core diameter) and split into aliquots of 20 µl each. To these samples, 10 µl of an EDC solution of appropriate concentration were added to yield different molar ratios of EDC molecules per nanoparticle, c(EDC)/c(FeNP) = 0, 16, 31, 63, 125, 250, 500, 1k, 2k, 4k, 8k, 16k, 32k, 64k, and 128k. After 2 hours of reaction, the series was run by gel electrophoresis (10 V/cm, 1 hour, reference sample with phosphine-coated 10-nm Au particles (BBI)). The more EDC had been added, the more PEG molecules were bound to the FeNP, and the more retarded were the bands on the gel. The lanes of the gel correspond to samples with increased EDC concentration from left to right. The discrete bands of particles with 0, 1, 2 ...attached PEG molecules could be resolved in case of 500 < c(EDC)/c(FeNP) < 8k, which demonstrates the possibility to prepare mono- and divalent iron oxide nanoparticles with the polymer coating procedure described in this study.

151

SI3.4 Polymer coating of gold nanoparticles and test of PEGylation

The synthesis of 4-nm of hydrophobic gold nanoparticles (AuNP) has been described previously by Brust et al.. The excess surfactants of as-prepared AuNP were cleaned by removing the supernatant of methanol-mediated precipitation and the dried agglomerates were then re-dissolved in anhydrous chloroform. The concentration of AuNP was determined by UV/Vis absorption measurements (Cary 50, Varian). In the case of AuNP with an average diameter of 4 nm, the gold nanoparticles are assumed to have an extinction coefficient of 8.7×10^6 $M^{-1}cm^{-1}$ at their plasmon peak. The inorganic core diameter (d) was determined to be 4 nm (from TEM) and the effective diameter (d_{eff}) was assumed to be 6 nm (1 nm thickness of the surfactant shell). Of an aliquot of AuNP (500 µl, 7.5 µM) the total surface area (A) of colloidal AuNP was calculated to be 2.55×10^{17} nm^2 using *formula (2),*($R_{P/Area} = 100$ nm^{-2}), meaning that 42.4 µM monomer units of polymer had to be added to the nanocrystal solution. Then, 53 µl of polymer stock solution (0.8 M, ***25%Anhydride-75%C12COOH as described in SI1.3***) and 2.45 ml of anhydrous chloroform were added to the colloidal gold solution, giving a total volume of 3 ml. After stirring for 15 min, the solvent was slowly evaporated by the rotavapor system by setting the vacuum to 200 mbar until the solvent had evaporated, then to 20 mbar for 10 min until the sample was completely dry. In the optional case the polymer shell was cross-linked, 1 ml of cross-linker solution (2 mM bis(6-aminohexyl)amine in chloroform) was then added to re-dissolve the solid particle powder and the sample was stirred for 20 minutes. After this the solvent was again removed by evaporation, and the solid complex of AuNP particle powder with polymer coat was quickly dissolved in 2 ml of 0.1 M NaOH. The solution was further diluted with water, filtered through a 0.22-µm syringe filter, leading to a transparent solution. The buffer was changed to SBB by two rounds of ultrafiltration using Amicon centrifuge filters (100kD MWCO). Residual polymer micelles were further removed by running the sample through a size exclusion column (Sephacryl S-300, Pharmacia) or the particles were further purified by gel electrophoresis. The final concentration of AuNP could be adjusted by ultrafiltration. The surface chemistry of AuNP was also characterized by discrete PEGylation[6] (***Figure S6***).

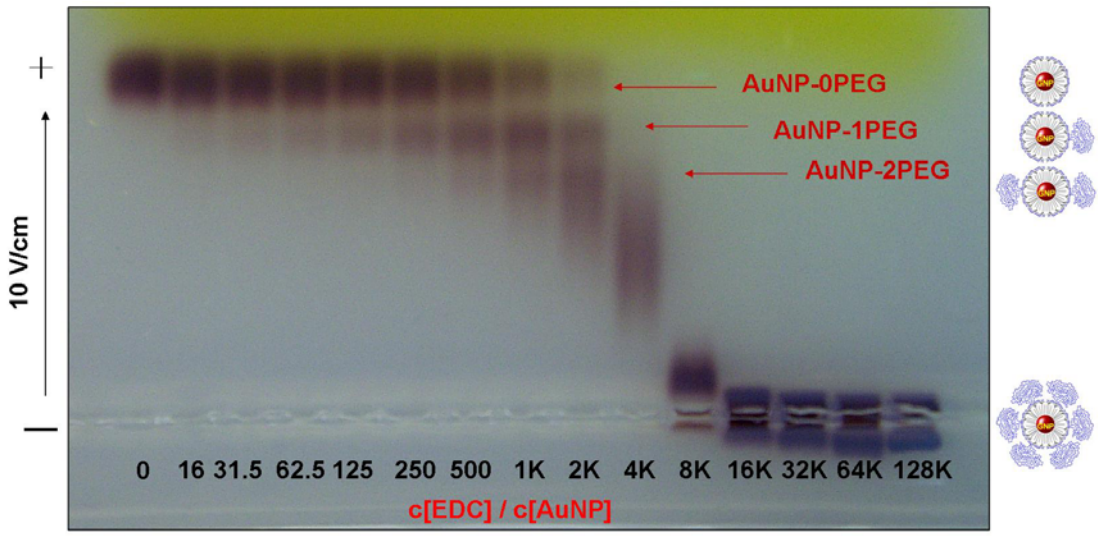

Figure S6. Discrete PEGylation test of polymer-coated gold nanoparticles (AuNP). First, 150 µl of 3 mM of methoxy-poly(ethylene glycol)amine molecules (CH_3O-PEG-NH_2, Mw~5000 g/mol, Rapp Polymere, Germany) in SBB were mixed with equal amounts of polymer-coated AuNP (6 µM, 4 nm core diameter). Then, 10 µl of each fraction was sequentially activated using different concentrations of EDC, i.e. c(EDC)/c(AuNP) = 0, 16, 31, 63, 125, 250, 500, 1k, 2k, 4k, 8k, 16k, 32k, 64k, and 128k. After 2 hours of reaction, all fractions were run with gel electrophoresis (10 V/cm, 1 hour). The more PEG molecules were attached to the gold nanoparticles, the more retardation the gold nanoparticles were run through gel electrophoresis. The lanes in the gel correspond to samples with decreasing EDC concentrations from right to left. Discrete bands of different PEG molecules attached could be resolved in the case of 125 < c(EDC)/c(AuNP) < 4k, which also demonstrates the possibility to make AuNP with single functionality.

SI3.5 Characterization of empty polymer micelles and PEGylation test

It is expected that free polymer molecules will form micelles in an aqueous solution, behaving similar to the polymer-coated nanoparticles, but without nanoparticle inside the polymer shell. To get visible polymer micelles the polymer was modified with fluorescein-amine (***24%Anhydride-75%C12COOH-1%Fluo as described in SI1.5***) to yield fluorescent-labeled micelles. First, 400 µl of fluorescein-polymer stock solution (40 mM monomer units in chloroform) were transferred to a round flask and the solvent was slowly evaporated by the rotavapor system. After drying, the solid film formed by the fluorescein-polymer powder was quickly dissolved in 2 ml of 0.1 M NaOH. The solution was further diluted to 15 ml by the addition of water, filtered through a 0.22-µm syringe filter, and finally gave a yellow transparent solution. The solution was washed by two rounds of ultrafiltration on Amicon centrifuge filters (100kD MWCO) and the polymer micelles in the retentate were collected[9]. Instead of the polymer micelle concentration which could not be directly determined by UV/Vis measurements, the fluorescein concentration of the dye-modified polymer was calculated from the absorption peak of fluorescein (extinction coefficient 72,000 $M^{-1}cm^{-1}$ at 495 nm). With 1% fluorescein modification, the micelle concentration was estimated to be on the order of one µM. The surface chemistry of fluorescein-polymer micelles was also characterized by the discrete PEGylation test[6] (***Figure S7***), however the stoichiometry compared with the series of polymer-coated AuNP might be different due to the uncertainty of the micelle concentration.

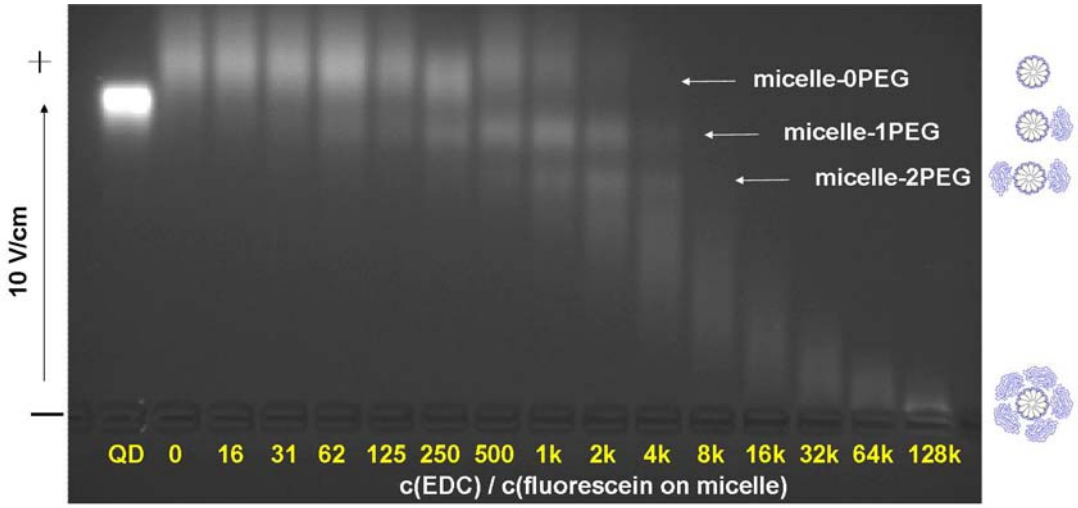

Figure S7. Discrete PEGylation test of fluorescein-modified polymer micelles. First, 150 µl of 3 mM methoxy-poly(ethylene glycol)amine molecules (CH_3O-PEG-NH_2, Mw~5000 g/mol, Rapp Polymere) in SBB were mixed with an equal amount of fluorescein-polymer micelles, i.e., 6 µM of fluorescein concentration. Then, 20 µl of each fraction were sequentially activated with 10 µl of EDC of different concentrations, such thatc(EDC)/c(fluorescein) = 0, 16, 31, 63, 125, 250, 500, 1k, 2k, 4k, 8k, 16k, 32k, 64k, and 128k. After 2 hours of reaction, all samples were run by gel electrophoresis. (10 V/cm, 1 hour). The more PEG molecules were attached per polymer micelle, the more retarded the samples were on the gel. The lanes in the gel correspond to samples with increasing EDC concentration from left to right. The bands of the polymer micelles are running faster and are not as sharp as those from polymer-coated quantum dots (first lane), indicating a smaller size but broader size distribution.

[9] Interestingly, the permeate was also colored, presumably part of the fluorescein-modified polymer formed small micelles that could pass the 100 kDa MWCO membrane.

153

In the same way, also micelles of plain polymer without fluorescein modification were prepared. The absorption and emission spectra of polymer micelles with and without fluorescein modification as well as fluorescein-amine were compared as shown in ***Figure S8***. For the fluorescence spectra, all samples were excited at 455 nm. There was a significant difference in the fluorescence intensity between fluorescein-polymer micelles and free fluorescein-amine. The fluorescence of free fluorescein-amine was quenched in aqueous solution (50 mM SBB pH 9) but was highly fluorescent when conjugated to the polymer[10].

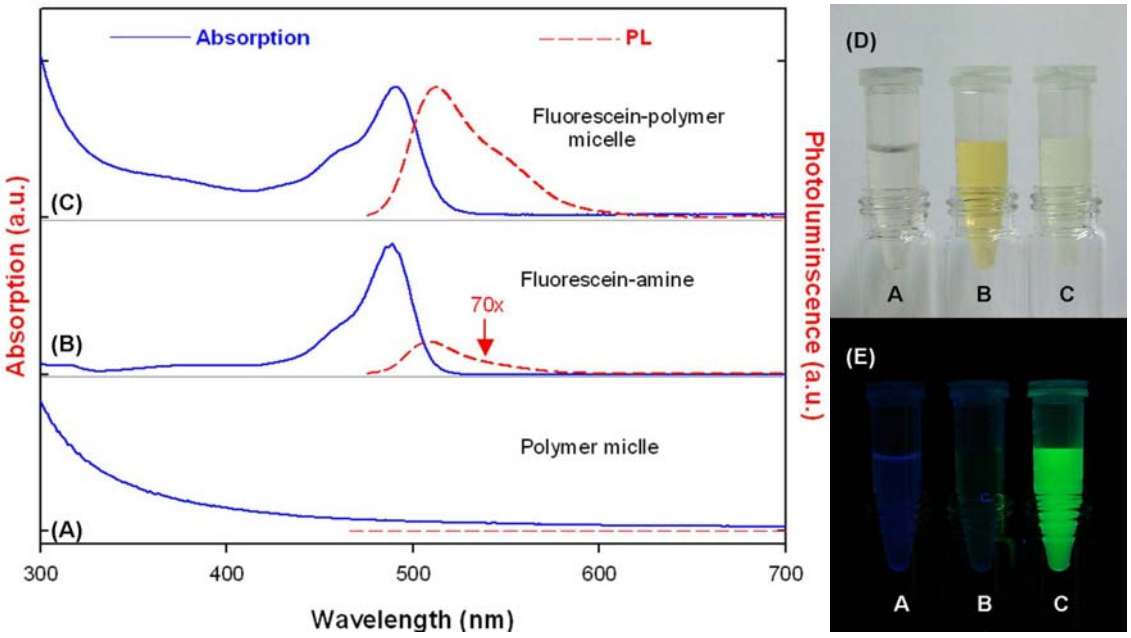

Figure S8. Absorption and photoluminescence (PL) of fluorescein-polymer micelles. First, 1% fluorescein-modified polymer micelles were prepared without inorganic nanoparticles inside and were collected in an (100 kDa MWCO) Amicon centrifuge. (A) plain polymer micelles (Mw > 100 kDa) in SBB (50 mM, pH 9) solution; (B) fluorescein-amine in SBB solution; (C) fluorescein-polymer micelles in SBB solution; white-light image (D) and UV lamp-excited image (E) of the three samples.

[10] In this experiment, the fluorescein concentrations of the different samples were not adjusted to equal values.

SI3.6 Direct PEG modification of the amphiphilic polymer

The amphiphilic polymer described in the previous section consists of a hydrophilic backbone and hydrophobic side-chains. We have demonstrated the possibility to use this amphiphilic polymer to transfer hydrophobic nanoparticles, e.g. quantum dots, iron oxide and gold nanoparticles, into an aqueous solution. The colloidal nanoparticles of different core materials were stable in buffer solution for months, had the same surface chemistry and could be modified with PEG in a post-modification by means of EDC. Alternatively, the PEG can also be attached directly to the polymer in organic solution, before the nanoparticle coating.

Solutions of methoxy-PEG5k-amine (mPEG5k-amine, Rapp Polymere) in anhydrous chloroform were prepared with a concentration of 8, 4, 2, and 1 mM. Then, 2 ml of each mPEG5k-amine solution were dropped into 1 ml of polymer (0.8 M monomer concentration, ***25%Anhydride-75%C12COOH as described in SI1.3***) under vigorous stirring, giving 0.25 - 2 % PEG5k-modified polymer[11]. After stirring overnight at room temperature, the resulting solutions were then evaporated by the rotavapor system and the solid films of dried particle powder were re-dissolved in anhydrous chloroform with a final concentration of 40 mM of monomer units.

Then, 4-nm gold nanoparticles in chloroform were coated with 0.25-2 % mPEG5k-modified polymer by the standard protocol described before and analyzed by gel electrophoresis (10 V/cm, 1 hour), which showed the direct attachment of PEG to the polymer similar to particles that had undergone a post-modification after the polymer-coating and phase transfer to aqueous solution.

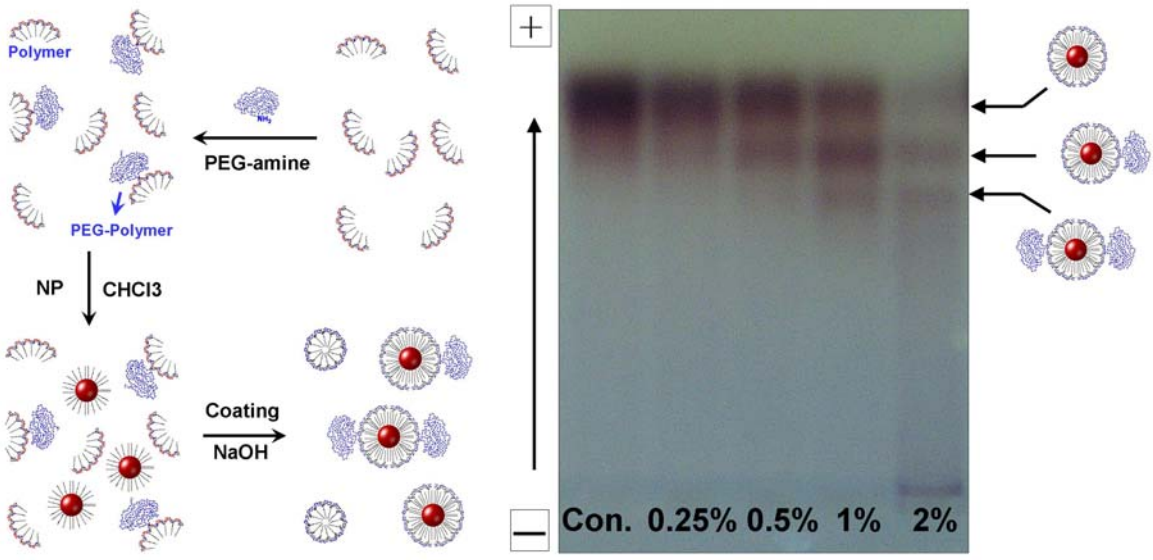

Figure S9. Different mPEG5k-polymer coatings of gold nanoparticles. The polymer was directly modified in organic solution with a different percentage of methoxy-PEG5k-amine, prior to the polymer-coating of gold nanoparticles. In gel electrophoresis, discrete bands from nanoparticles with exactly 0, 1 or 2 covalently attached PEG molecules per particle are observed.

[11] I.e. 0.25 - 2% of the anhydride rings of the polymer were used to attach PEG.

SI4: Characterization of polymer-coated particles with different functionalities

In the following section we select three functional molecules, fluorescein-amine, galactose-amine, and biotin-amine, to demonstrate the possibility of a direct modification of the polymer in order to add functionality before the actual coating process.

SI4.1 Gold nanoparticles coated with sugar-modified polymer

The preparation of 4% galactose-grafted co-polymer has been described in section 1. For the polymer coating of 6-nm gold nanoparticles the inorganic core diameter (d) was determined to be 6 nm (from TEM) and the effective diameter (d_{eff}) was then assumed to be 8 nm. In the sample of gold nanoparticles (500 µl, 1.5 µM) the total surface area (A) of the nanoparticles was 9.08×10^{16} nm^2 calculated using *formula (2),*($R_{P/Area} = 100$ nm^{-2}), meaning that 15.1 µM monomer units of polymer had to be added to the nanocrystal solution. Then, 377 µl of 4% galactose-grafted co-polymer stock solution (40 mM monomer concentration, ***21%Anhydride-75%C12COOH -4%Galactose as described in SI1.6***) and 2.13 ml of anhydrous chloroform were added to the colloidal gold solution giving a total volume of 3 ml. After stirring for 15 minutes, the solvent was slowly evaporated by the rotavapor system until the sample was completely dry. Then, the solid powder of gold nanoparticles with galactose-copolymer shell was quickly dissolved in 2 ml of 0.1M NaOH. The solution was further diluted to 15 ml by the addition of water, filtered through a 0.22-µm syringe filter, and finally gave a transparent solution. The buffer was changed to PBS by two rounds of ultrafiltration with Amicon centrifuge filters (100 kDa MWCO) and the residual empty polymer micelles were further removed by a size exclusion column (Sephacryl S-300, Pharmacia) and again purified by agarose gel electrophoresis. The final concentration of purified gold nanoparticles was adjusted by concentrating the sample with ultrafiltration.

The surface density of galactose on the gold nanoparticles could be controlled by varying the percentage of galactose-modification of the polymer. To examine whether the galactose moieties on the particles were accessible to bind large proteins; the particles were exposed to lectin from *Ricinus communis* (castor bean) Agglutinin (RCA_{120}). RCA_{120} lectin is a 120 kDa lectin biomolecule with two identical and independent galactose-binding sites[7]. When appropriate amounts of galactose-copolymer-coated nanoparticles are mixed with RCA_{120} lectin, agglutination is expected to occur. Such agglutination should also be rapidly reversed when free galactose is added in excess. For the experiment, 10 µl of galactose-coated gold nanoparticles (1 µM in PBS buffer) were mixed with the same volume of RCA_{120} (Sigma L7886), giving a final concentration of 0.25, 0.5, and 1 mg/ml lectin solution. As negative control, plain polymer-coated gold nanoparticles (without galactose) were also treated with 1 mg/ml lectin in PBS buffer but were not found to aggregate.

The results are shown in ***Figure S10***, where the lectin was found to lead to agglutination of the galactose-coated nanoparticles within a few minutes. The particles precipitated completely after 30 minutes of static condition. The cross-linked network scattered light, and the increasing agglutination could be detected by increased absorbance at high wavelengths (in the red / near-IR)[12]. Our data demonstrate that the spectra of the aggregated, galactose-modified particles recovered to the initial values after adding galactose solution (Sigma-Aldrich G0625, 600 mM in PBS), but not in the case

[12] *Note:* all samples (including the precipitated samples) were re-dispersed and diluted to a final volume of 500 µl with PBS buffer before measuring the absorbance.

when excess glucose solution (Sigma-Aldrich G5767, 600 mM in PBS) was added. This demonstrates that the galactose molecules can disassemble the cross-linked network formed by gold nanoparticles and lectin (***Figure S11***).

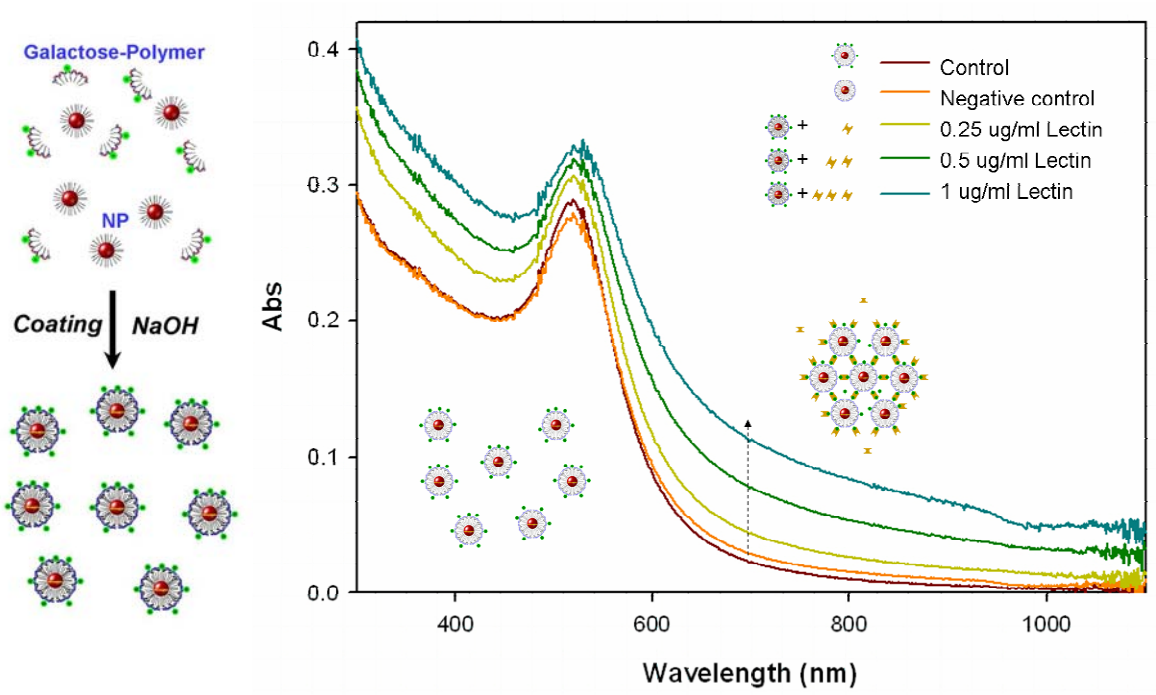

Figure S10. Agglutination effect of galactosylated gold nanoparticles. First, 10 µl of galactose-modified gold nanoparticles (1 µM in PBS) were mixed with equal volumes of RCA_{120} lectin solution with a final concentration of 0.25, 0.5, and 1 mg/ml of RCA_{120} lectin. A negative control of polymer-coated particles without galactose was also treated with 1 mg/ml lectin to examine non-specific binding. All samples were diluted to a final volume of 500 µl before measuring the absorbance. The cross-linked networks of particles scattered light, and the agglutination could be detected by the increased absorbance in the red/near-infrared spectrum. The more lectin was added, the more the galactosylated gold nanoparticles were agglutinated.

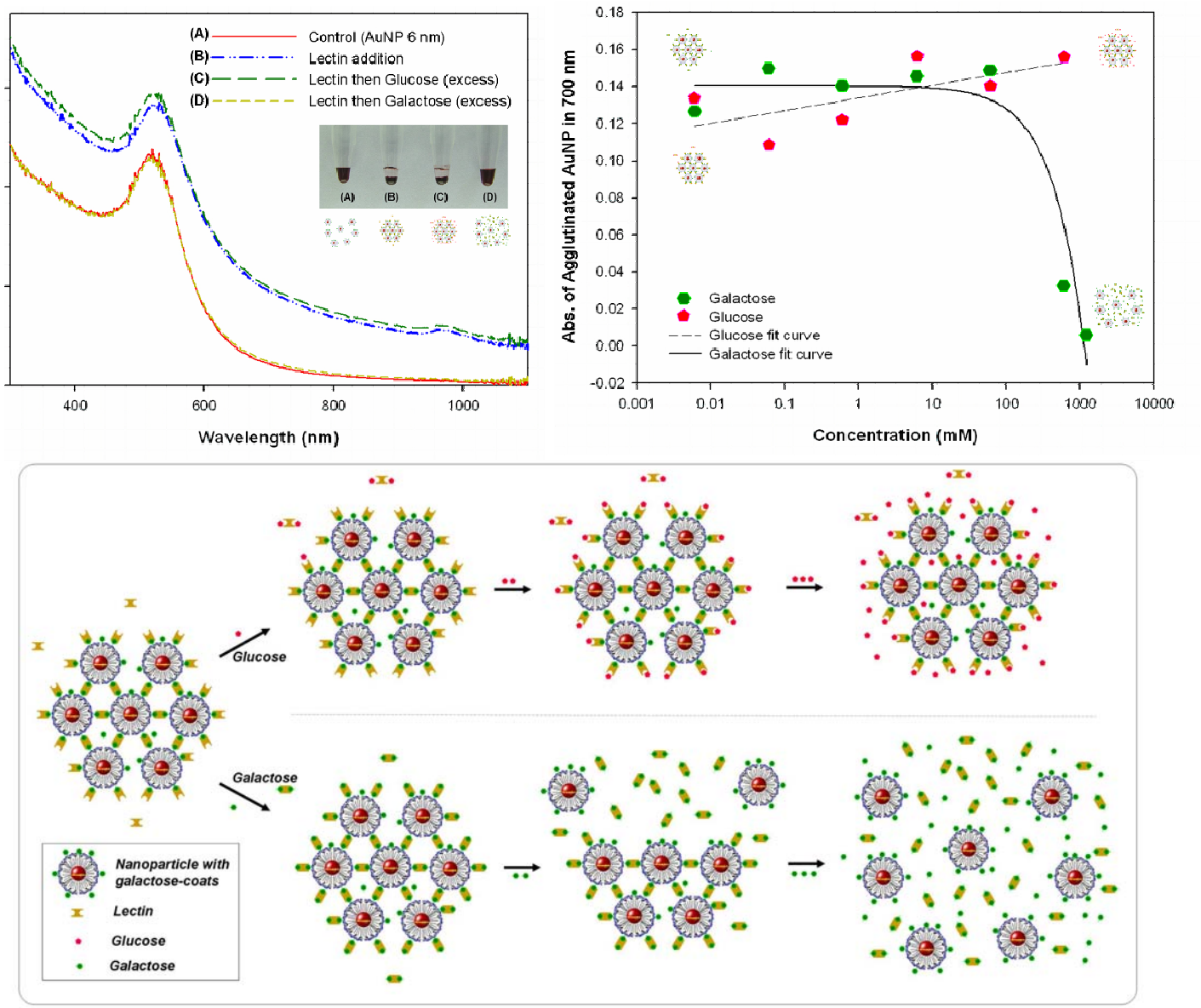

Figure S11. Sugar effects on agglutinated gold nanoparticles (AuNP). ***(Upper-Left figure)*** The agglutinated gold nanoparticles resulting from the lectin cross-linked complex could be selectively disassembled by the addition of excess galactose, but not with excess glucose (the inset picture). The effect could be seen in the absorption spectra of the diluted samples with (A) the galactose-modified AuNP (1 μM); (B) after the addition of RCA_{120} lectin (2 μg/ml) to the AuNP with galactose; (C) after the addition of glucose (600 mM) to sample B; and (D) after the addition of galactose (600 mM) to sample B. The lectin-induced agglutination of gold nanoparticles was fully reversible after adding excess galactose (downward shift). The ***upper-right figure*** shows the optical density of agglutinated gold nanoparticles after the addition of various amounts of sugar solution (with reference to the optical density of sample A at 700 nm). Agglutinated samples were tested with galactose (green) and glucose (red), the lines are curves fitted to the data points. It was found that the agglutinated gold nanoparticles start to disassemble above a concentration of 100 mM galactose, as derived from the decreased optical absorption at 700 nm. This effect is illustrated in the *lower figure* which shows the difference before and after the addition of galactose and glucose to the lectin-agglutinated nanoparticles.

SI4.2 Gold nanoparticles coated with biotin-modified polymer

The preparation of biotin-modified polymer has been described in section 1. To prepare biotin-polymer-coated gold nanoparticles, the inorganic core diameter (d) of gold nanoparticles was determined to be 6 nm (from TEM) and the effective diameter (d_{eff}) was then assumed to be 8 nm. In the sample of gold nanoparticles (500 µl, 1.5 µM) the total surface area (A) of colloidal gold nanoparticles was 9.08×10^{16} nm^2 calculated using *formula (2)*,($R_{P/Area}$ = 100 nm^{-2}). Therefore, 15.1 µmol monomer units of polymer were added to the nanocrystal solution. For this, 377 µl of biotin-modified polymer stock solution (40 mM monomer concentration, ***21%Anhydride-75%C12COOH-4%Biotin as described in SI1.7***) and 2.13 ml of anhydrous chloroform were added to the colloidal gold solution, giving a total volume of 3 ml. After stirring for 15 min, the solvent was slowly evaporated by the rotavapor system (200 mbar until all solvent was evaporated, then the pressure was set to 20 mbar for 10 minutes until the sample was completely dry). After all solvent had been removed by evaporation, the solid complex of the powder of gold nanoparticles with the biotin-modified polymer was quickly dissolved in 2 ml of 0.1 M NaOH. The solution was further diluted to 15 ml by the addition of water, filtered through a 0.22-µm syringe filter to give finally a transparent solution. The buffer was changed to SBB by two rounds of ultrafiltration on Amicon centrifuge filters (100 kDa MWCO) and residual polymer micelles were further removed by a size exclusion column (Sephacryl S-300, Pharmacia) or optionally purified by gel electrophoresis. The final concentration of purified gold nanoparticles coated with 4%- biotin-polymer could be adjusted by concentration with ultrafiltration.

To examine whether the biotin-groups on the particles were accessible to bind avidin molecules, the particles were exposed to 2 types of biotin-binding proteins: avidin and streptavidin. Avidin is a 66 kDa glycoprotein from egg white with four identical and independent biotin binding sites[7]. Streptavidin is a derivative of avidin produced by the bacterium *Streptomyces avidinii* and has like avidin four binding sites for biotin. Both have been extensively used in biotechnology, such as immunochemical systems, conjugation to antibodies, enzymes or fluorochromes. However, avidin (pI~10.5) has higher isoelectric point than streptavidin (pI~5-6). When streptavidin (or avidin) is added in excess to biotinylated gold nanoparticles, the protein is expected to bind to the nanoparticles and thus to increase the diameter of nanoparticles by the protein layer.

For the experiment, aliquots of 10 µl of streptavidin (Sigma S4762) or avidin (Sigma A9275) with different concentrations were mixed each with 10 µl (1 µM) of 4 % biotinylated gold nanoparticles solution and incubated for 30 min at room temperature. The electrophoretic mobility of each sample was analyzed through gel electrophoresis (10 V/cm, 1 hour) as shown in ***Figure S12***.

Non-biotinylated gold nanoparticles without ("control") and with streptavidin added ("negative") were tested for their non-specific binding. Both samples had the same mobility on the gel, indicating that no streptavidin is bound to the particles without biotin (under the here-used conditions).

The samples coated with biotin-modified polymer (without streptavidin added, lane "0") were slightly retarded on the gel when compared with the plain polymer-coated nanoparticles without biotin. This indicates a slight increase in particle size due to the additional biotin molecules attached to a short PEG spacer (MW 720 g/mol).

When the streptavidin concentration of the solution added to biotin-modified particles was increased, the nanoparticles were more and more retarded and discrete bands became visible, indicating the binding of streptavidin molecules to the particles. At high concentrations, a molar excess of streptavidin was added to the particles, so every particle could bind several streptavidin molecules. Their number could not be resolved anymore as discrete bands on the gel. At low streptavidin concentration, more nanoparticles than streptavidin were in the reaction mixture, but the nanoparticles

did not precipitate, indicating the absence of large cross-linked nanoparticle-streptavidin networks.

In case of avidin, the particles were much more retarded on the gel, even the control sample of plain polymer-coated gold nanoparticles (data not shown). This is probably due to the high isoelectric point of avidin. The electrostatic attraction between the gold nanoparticles (negative charge) and avidin (positive charge) in the SBB solution might have been responsible for the observed non-specific binding (data not shown).

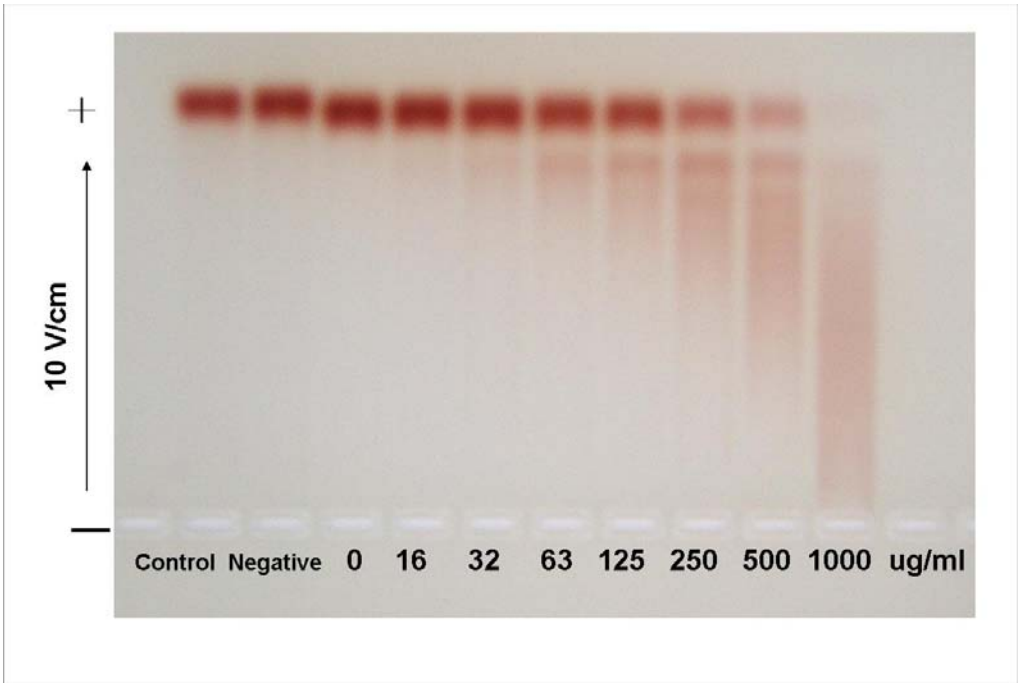

Figure S12 4% biotinylated gold nanoparticles (AuNP). First, 10 µl of each fraction from 4 % biotinylated gold nanoparticles (1 µM) were sequentially mixed using different concentrations of streptavidin solution, i.e. the resulting concentrations of streptavidin were equal to 0, 16, 31, 63, 125, 250, 500, and 1000 µg/ml. Non-biotinylated gold nanoparticles (as control) and their mixture with streptavidin (as negative control) were also tested for their non-specific binding. After 2 hours of reaction, all fractions were run through gel electrophoresis. (10 V/cm, 1 hour) The more streptavidin molecules were added, the more the AuNP-streptavidin complexes were retarded on the gel. The lanes in the gel correspond to samples with decreasing streptavidin concentrations from right to left. Discrete bands appeared for 63 µg/ml $<$ c(streptavidin) $<$ 500 µg/ml, which indicates the binding of streptavidin to the gold nanoparticles coated with biotin-modified polymer. There was no non-specific binding between plain gold nanoparticles and streptavidin observed. The slight shift between particles coated with the plain polymer (without biotin) and the biotin-modified polymer is due to the increase in size with biotin-PEG molecules used for the modification of the polymer.

SI4.3 Gold nanoparticles coated with fluorescein-modified polymer

The preparation of fluorescein-modified polymer has been described in Section 1. Of a sample of Au NP, the inorganic core diameter (d) of gold nanoparticles was 6 nm (determined with TEM) and the effective diameter (d_{eff}) was assumed to be 8 nm. In the aliquot of gold nanoparticles (0.5 ml, 1.5 µM) the total surface area (A) of colloidal gold nanoparticles was 9.08×10^{16} nm^2 calculated using *formula (2),*($R_{P/Area}$ = 100 nm^{-2}), meaning that 15.1 µM monomer units of polymer were required for the polymer coating. For that, 377 µl of fluorescein-grafted co-polymer stock solution (40 mM monomer concentration, ***24%Anhydride-75%C12COOH-1%Fluo as described in SI1.5***) and 2.13 ml of anhydrous chloroform were added to the colloidal gold solution, giving a total volume of 3 ml. The concentration of gold nanoparticles in this solution, i.e. ~0.25 µM, was sufficiently low to avoid cross-linking effects among nanocrystals and the polymer could efficiently coat the gold nanoparticles, forming the polymer shell. After stirring for 15 minutes, the solvent was slowly evaporated with a rotavapor system. After all the solvent had been removed by evaporation, the completely dry solid of gold nanoparticles with fluorescein-modified polymer shell was quickly dissolved in 2 ml of 0.1 M NaOH. The solution was further diluted to 15 ml by the addition of water, filtered through a 0.22-µm syringe filter, and finally gave a transparent solution. The sample was washed with PBS buffer by two rounds of ultrafiltration on Amicon centrifuge filters (100 kDa MWCO) and residual polymer micelles were further removed by a size exclusion column (Sephacryl S-300, Pharmacia) and the particles could be optionally further purified by gel electrophoresis. The final concentration of purified gold nanoparticles coated with 1% fluorescein-polymer could be adjusted by ultrafiltration. For comparison plain polymer-coated nanoparticles (without fluorescein) were prepared and purified by the same procedures. The high fluorescence of the fluorescein-polymer was affected by quenching after coating the gold nanoparticles (***Figure S13***), which could be due to the spectral overlap between the gold plasmon absorption and the emission of the fluorescein. The extinction coefficient of gold nanoparticles (6 nm) was also two orders higher than that of fluorescein, resulting in a non-detectable fluorescein absorption for the sample of Au NP coated with the fluorescein-modified polymer.

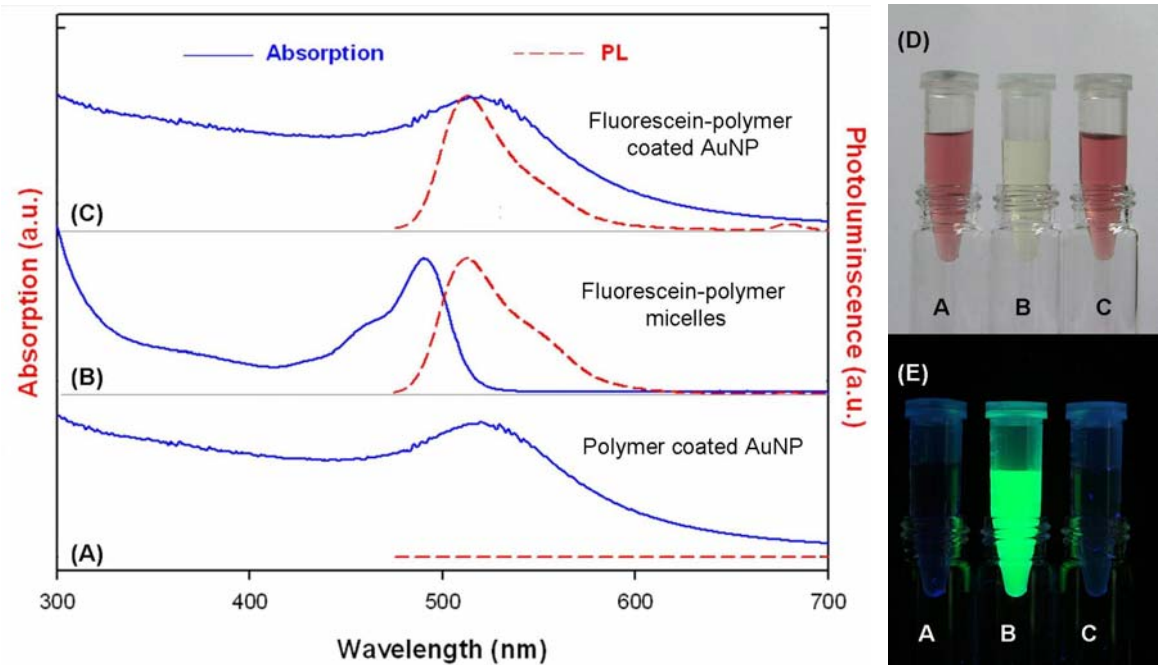

Figure S13. Absorption and photoluminescence (PL) of fluorescein-polymer gold nanoparticles (AuNP). Gold nanoparticles (6 nm core diameter) were coated with 1 % fluorescein-modified polymer, for comparison also empty micelles of the fluorescein-polymer and Au particles coated with the plain polymer (without fluorescein) were prepared. (The excitation wavelength for the PL measurements was 455 nm.) (A) The plain-polymer coated AuNP; (B) the fluorescein-modified polymer micelles; (C) the fluorescein-polymer coated AuNP. On the right: samples under white-light (D) and UV lamp excitation (E).

SI5: Protein-mediated Assembly of 1- or 2-Biotin Functionalized Nanoparticles

SI5.1 Description of nanoparticle assembly

After polymer coating and phase-transfer to aqueous solution, the originally hydrophobic nanoparticles are negatively charged. If there is a large number of (bio-) functional groups on the nanoparticles (e.g. biotin or galactose), the nanoparticles start to assemble when a binding partner (e.g. avidin or lectin, respectively) is added. Generally, the aggregation depends on the valency of both nanoparticles and biomolecules and their stoichiometry. Thus, it is hard to predict size and shape of each assembled nanostructure when the number of bio-functional groups on the particles is unknown.

Poly(ethylene glycol) is a biocompatible and linear polymer which can have functional groups at its two ends. For the polymer-coated nanoparticles described here, it has been demonstrated that by means of PEG molecules with a MW $\geq$ 5000 g/mol it is possible to separate particles with exactly no, one or two covalently bound PEG molecules per particle. In the case of bifunctional PEG this means particles with exactly no, one or two free (bio-) functional groups per particle. In ***Figure S14***, polymer-coated gold and CdSe/ZnS nanoparticles were reacted with PEG of different molecular weight, and discrete bands indicating the attachment of a discrete number of PEG molecules per particle can be resolved by gel electrophoresis with PEG of a molecular weight of 5000, 10000 or 20000 g/mol. In the following experiments, gold nanoparticles have been modified with biotin-PEG-amine (5000 g/mol), by binding the amine terminal covalently to the carboxylic groups of the polymer-coated particles by means of EDC chemistry. By the separation of the particle fractions with 0, 1 or 2 PEG molecules per particle, particles with exactly 0, 1 or 2 biotin groups were prepared.

One single (strept)avidin molecule offers four binding sites for biotin, allowing for a relatively simple model system to study the assembly of predictable nanostructure through the biotin-avidin systems.

SI5.2 Isolation of 1- or 2-biotin functionalized nanoparticles

The PEG modification (***Figure S14***) of polymer-coated gold particles (or quantum dots) was examined again with biotin-PEG5k-amine and by varying the amount of EDC in order to find the optimum stoichiometry to prepare particles with 0, 1, or 2 PEG molecules per particle. For that, 150 µl of 0.3 mM biotin-poly(ethylene glycol)amine molecules (biotin-PEG5k-amine, Mw~5000 g/mol, Rapp Polymere) in SBB were mixed with an equal volume of polymer-coated gold nanoparticles (AuNP, 6 µM, 4 nm core diameter). Here we used a smaller ratio of PEG per particle in order to reduce the needed amount of biotin-PEG5k-amine, i.e. PEG:AuNP = 50:1. Then, 20 µl of each fraction were sequentially activated by adding 10 µl of EDC solution of different concentrations, whereby in the final reaction mixtures the molar ratios were c(EDC)/c(AuNP) = 0, 16, 31, 63, 125, 250, 500, 1k, 2k, 4k, 8k, 16k, 32k, 64k, and 128k. After 2 hours of reaction, all aliquots were run by gel electrophoresis (10 V/cm, 1 hour). Usually discrete bands appeared clearly in the range of 500 < c(EDC)/c(AuNP) < 8000. Based on these data we selected the ratio of c(EDC)/c(AuNP) = 2000 as best condition for a the production of larger amounts of sample. For that, 2 ml of gold nanoparticle solution (6 µM) were mixed with 2 ml of biotin-PEG5k-amine solution (0.3 mM) in a 20-ml glass vial, followed by the addition of 2 ml of freshly prepared EDC solution. The reaction mixture was shaken overnight and then concentrated by ultrafiltration on Amicon centrifuge filters (100 kDa). The resulting samples were loaded into the wells of 2 % agarose gels, followed by gel eletrophoresis (10 V/cm, 1 - 2 hours). The discrete bands of 0-, 1-, 2-biotin gold nanoparticles (i.e. gold particles with exactly 0, 1, 2 biotin molecules per particle) were cut out from the gel, transferred into a dialysis membrane bag (3500 Da

MWCO, Roth), and run again with gel electrophoresis to elute the nanoparticles from the gel. The resulting nanoparticle solution was taken out, filtered with a 0.22 µm syringe filter and concentrated on a 100 kDa MWCO Amicon centrifuge filter. Then, the samples were purified by a second round of gel electrophoresis in order to remove residual particles of other fractions (Figure S15 (D)). The final nanoparticle samples were adjusted to a concentration of 1.5 µM for further experiments (***Figure S15***).

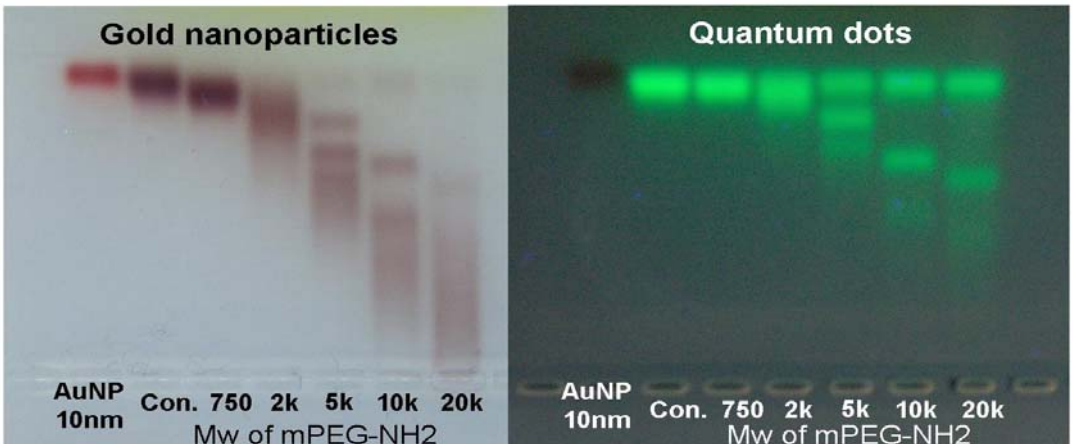

Figure S14. Polymer-coated Au and CdSe/ZnS nanoparticles conjugated with PEG molecules of different molecular weight. Each sample of 10 µl of 4-nm gold nanoparticles (left) or quantum dots (right) was individually mixed with the equal volume of methoxy-PEG-amine solution, i.e. 3 mM mPEG-amine with 0, 750, 2k, 5k, 10k, and 20 kDa in SBB solution. Then 10 µl of 6 mM EDC solution prepared freshly in SBB were added to each AuNP/PEG (or QD/PEG) aliquot and reacted for 2 hours. The resulting reaction mixtures were run on 1% agarose gel (Invitrogen #15510027) by gel electrophoresis (10 V/cm, 1 hour). As reference, 10 nm gold nanoparticles (BBInternational) stabilized with bis(*p*-sulphonatophenyl) phenylphosphine (Strem Chemicals) were run in the first lane of both gels. The discrete bands appeared only in case of PEG with molecular weight ≥ 5000 g/mol.

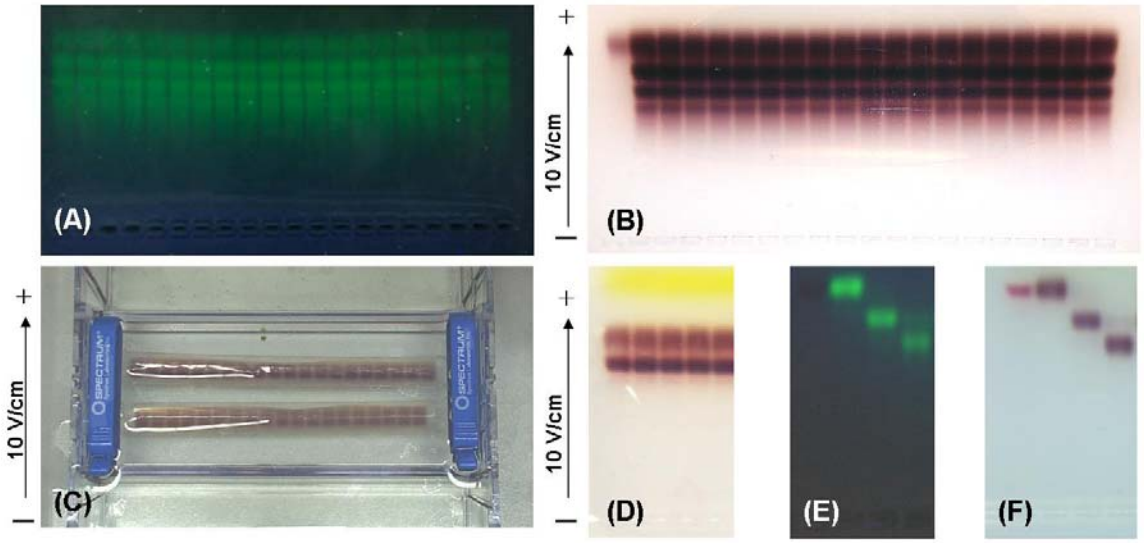

Figure S15. Isolation of 1- or 2-biotin functionalized nanoparticles. First, 2 ml of gold nanoparticles (Au) or quantum dots (QD) solution (6 µM) were mixed with 2 ml of biotin-PEG5k-amine solution (0.3 mM) in a 20-ml glass vial, followed by the addition of 2 ml of fresh EDC solution. The molar ratio was c(EDC)/c(NP) = 2000. The reaction mixture was shaken overnight and then concentrated by ultrafiltration (100 kDa). The resulting sample was loaded into the wells of a 2% agarose gel, followed by gel eletrophoresis (10 V/cm, 1 hour). The results are shown in (A) for the QDs and in (B) for Au. The discrete bands of 0-, 1-, 2-biotin Au were cut out separately, then transferred to a dialysis membrane bag (3500 Da MWCO, Roth) and run again with gel electrophoresis to elute the nanoparticles (C). The obtained nanoparticle solutions were purified using a syringe filter (0.22 µm), and were re-concentrated through 100 kDa MWCO Amicon centrifuge filters. Then the samples were purified in a second round of gel electrophoresis in order to remove residual particles of the other fractions (D). Finally, a part of the purified nanoparticles with 0-, 1-, 2-biotin molecules per particle was run again for control purpose on a 1 % agarose gel, giving a clear band for each fraction of the QDs (E) and Au particles (F).

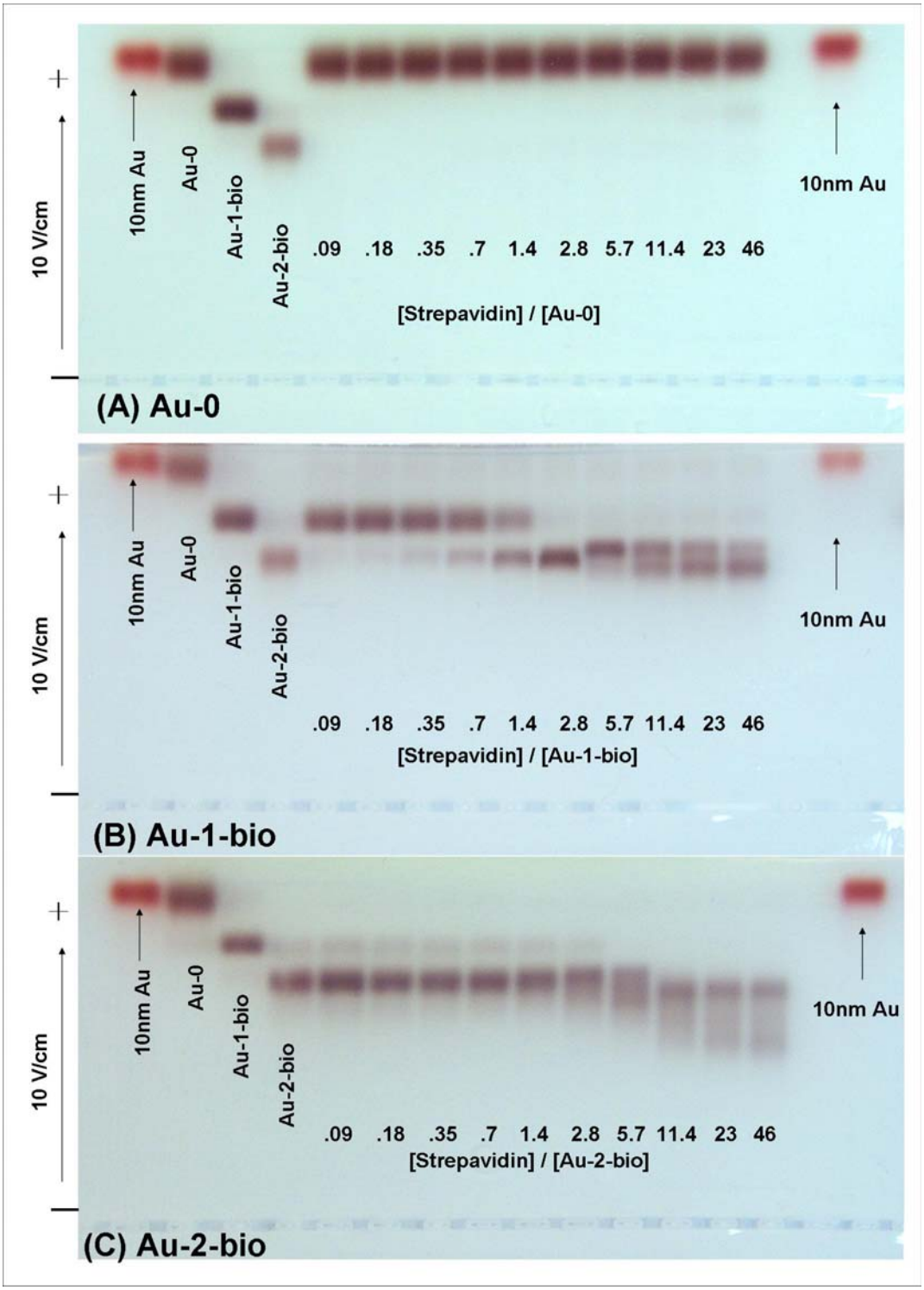

Figure S16. Assembly of 0-, 1- or 2-biotin gold nanoparticles (Au-x-bio) with streptavidin (SA). The lanes of each gel from left to right comprise four kinds of references (10-nm phosphine stabilized Au nanoparticles, Au-0, Au-1-bio, and Au-2-bio, i.e. gold particles with 0, 1, and 2 biotin molecules attached per particle), and SA-Au-x-bio conjugates with increasing molar ratios of c(streptavidin)/ c(Au-x-bio). For these conjugates the amount of c(Au-x-bio) =1.5 µM x 10 µl was kept constant, whereas the amount of streptavidin was varied. (A) gradient of c(SA)/ c(Au-0); (B) gradient of c(SA)/ c(Au-1-bio); and (C) gradient of c(SA)/ c(Au-2-bio). All samples were run through 1% agarose gel at 10 V/cm for 1 hour.

SI5.3 Assembly of 1- or 2-biotin nanoparticles

The purified gold nanoparticles (Au) with x-biotin (x = 0, 1, 2) were adjusted to a concentration of 1.5 μM by ultrafiltration. Then different proteins from the avidin family, such as streptavidin (Sigma S4762), avidin (Sigma A 9275), NeutrAvidin (Pierce #31000), streptavidin-FITC (Sigma S3762), neutravidin-FITC (Pierce #31006), were prepared with 4 mg/ml in double destilled water and stored at 4°C before use. Au-x-bio solutions were incubated at room temperature with a concentration series of the protein solutions and then analyzed by gel electrophoresis on 1% agarose gels. For the concentration series, each 10 μl of streptavidin solution were prepared by diluting the 4 mg/ml stock solution, i.e. with a concentration of 4×2^{-n} mg/ml (n = 0, 1, 2, 3, 4, 5, 6, 7, 8, and 9) or the corresponding molar concentration of 66×2^{-n} μM (n = 0, 1, 2, 3, 4, 5, 6, 7, 8, and 9). Each aliquot of streptavidin solution was mixed with an equal volume of Au-x-bio solution (x = 0, 1, or 2), the resulting molar ratios are shown in the figures. After overnight reaction, each sample of Au-streptavidin mixture was loaded into the wells of 1% gels and run by gel electrophoresis. (***Figure S16***). Then, 10-nm gold nanoparticles (BBInternational) stabilized with bis(*p*-sulphonatophenyl) phenylphosphine (Strem Chemicals) in the first lane were run as reference. The following three lanes were nanoparticles without proteins, i.e. Au-0, Au-1-bio, Au-2-bio. The Au-0-bio sample was first tested to see the effect of non-specific binding between streptavidin and polymer-coated gold nanoparticles (***Figure S16A***). If there were proteins attached to the nanoparticles, their increased size would retard the particles on the gel. Clearly, streptavidin showed a negligible non-specific binding from the gel results under the here used conditions. However, Au-1-bio particles with streptavidin resulted in one retarded band. When the streptavidin concentration was further increased, this band seemed to split into two bands.

In the same way, the interaction of the biotinylated AuNP was also studied with avidin and neutravidin, resulting in similar retarded bands on the gel. However, gold nanoparticles showed now a serious retardation when avidin was added at high concentration to Au-2-bio as well as for Au-1-bio and Au-0-bio, indicating the formation of larger particle-protein networks that lead to aggregation (***Figure S17***). This indicates unspecific (electrostatic) interactions stronger for avidin than for the other analogues due its higher isoelectric point (10 – 10.5, streptavidin: ~ 5, neutravidin: ~ 6.3).

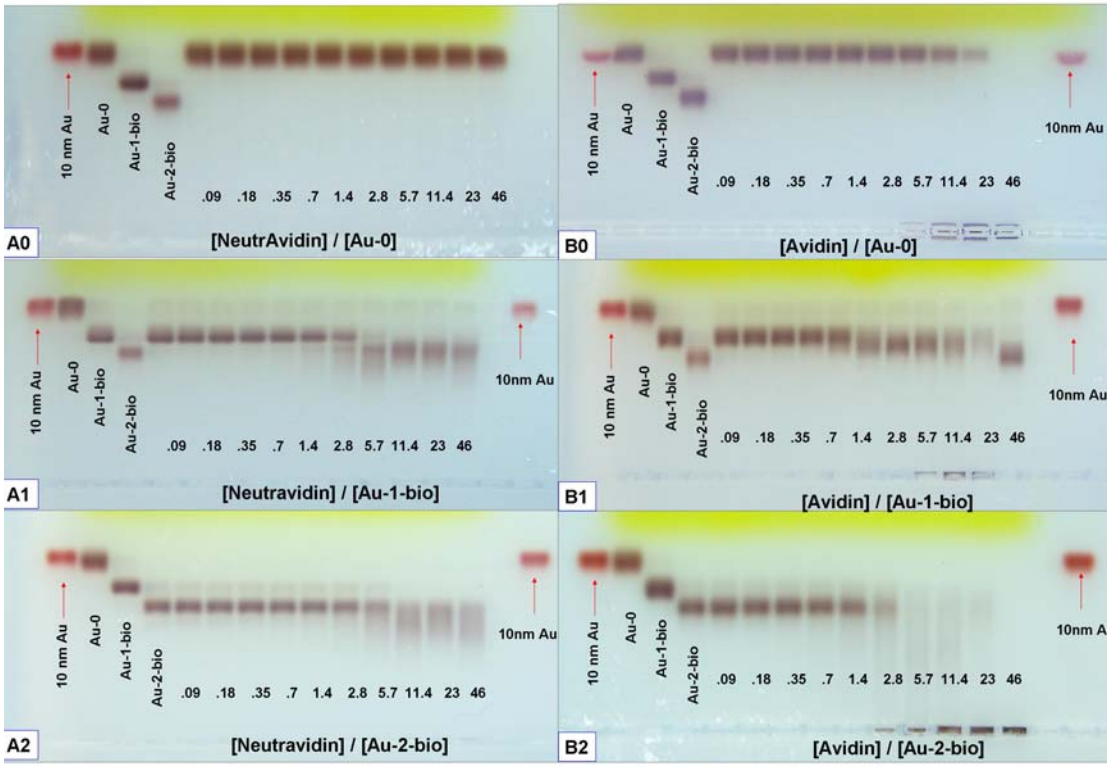

Figure S17. Assembly of 0-, 1- or 2-biotin gold nanoparticles (Au-x-bio) with neutravidin and avidin. The lanes of each gel from left to right comprise four kinds of references (10-nm Au nanoparticles, Au-0, Au-1-bio, and Au-2-bio), increasing molar ratios of c(Avidin or Neutravidin)/ c(Au-x-bio) with a constant amount of c(Au-x-bio) =1.5 µM x 10 µl, blank, and again 10-nm Au; (*Abbreviation: Neutravidin, NA; Avidin, AV*); (A0) gradient of c(NA)/ c(Au-0); (A1) gradient of c(NA)/ (Au-1-bio); (A2) gradient of c(NA)/ (Au-2-bio); (B0) gradient of c(AV)/ c(Au-0); (B1) gradient of c(AV)/ c(Au-1-bio); (B2) gradient of c(AV)/ (Au-2-bio). All samples were run through 1% agarose gels @10 V/cm for 1 hour (the yellow color is from Orange G that has been added to the gel-loading buffer).

In addition, the previous experiments were repeated with fluorescence-labeled streptavidin-FITC (Sigma S3762) and neutravidin-FITC (Pierce #31006). The fluorescence-labeled proteins allowed for localizing the protein on the gel. The experimental results were basically the same as those with the unlabeled streptavidin and neutravidin, but now the proteins could be found co-located with the gold particles, a clear indication for the formation of NP-protein structures. The visible and UV images were taken by a gel documentation system (BioRad GelDoc). The color images were taken by Pentax Optio MX4 digital camera. (***Figure S18, Figure S19***)

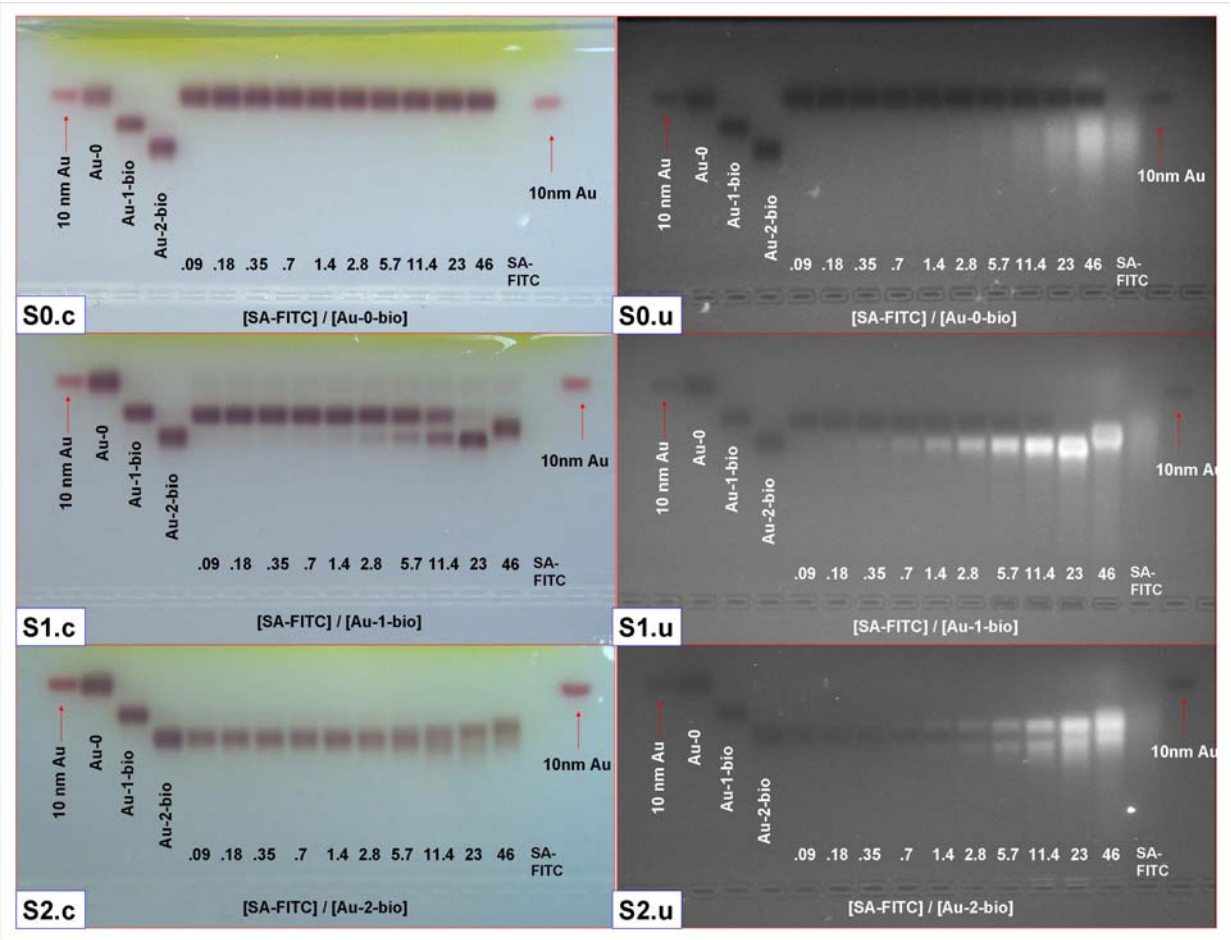

Figure S18. Assembly of 0-, 1- or 2-biotin gold nanoparticles (Au-x-bio) with streptavidin-FITC (SA-FITC). The lanes of each gel from left to right comprise four kinds of references (10 nm phosphine stabilized Au nanoparticles, Au-0, Au-1-bio, and Au-2-bio), increasing molar ratios of c(SA-FITC)/ c(Au-x-bio) with a constant amount of c(Au-x-bio) =1.5 µM x 10 µl, SA-FITC, and again 10-nm Au; in the left column is color picture of the gradient of c(SA-FITC)/ c(Au-0) *(S0.c)*, c(SA-FITC)/ c(Au-1-bio) *(S1.c)*, or c(SA-FITC)/ c(Au-2-bio) *(S2.c)*; and the right column shows UV light images of gradients of c(SA-FITC)/ c(Au-0) *(S0.u)*, c(SA-FITC)/ c(Au-1-bio) *(S1.u)*, and c(SA-FITC)/ c(Au-2-bio) *(S2.u)*; All samples were run through 1% agarose gel, 10 V/cm for 1 hour.

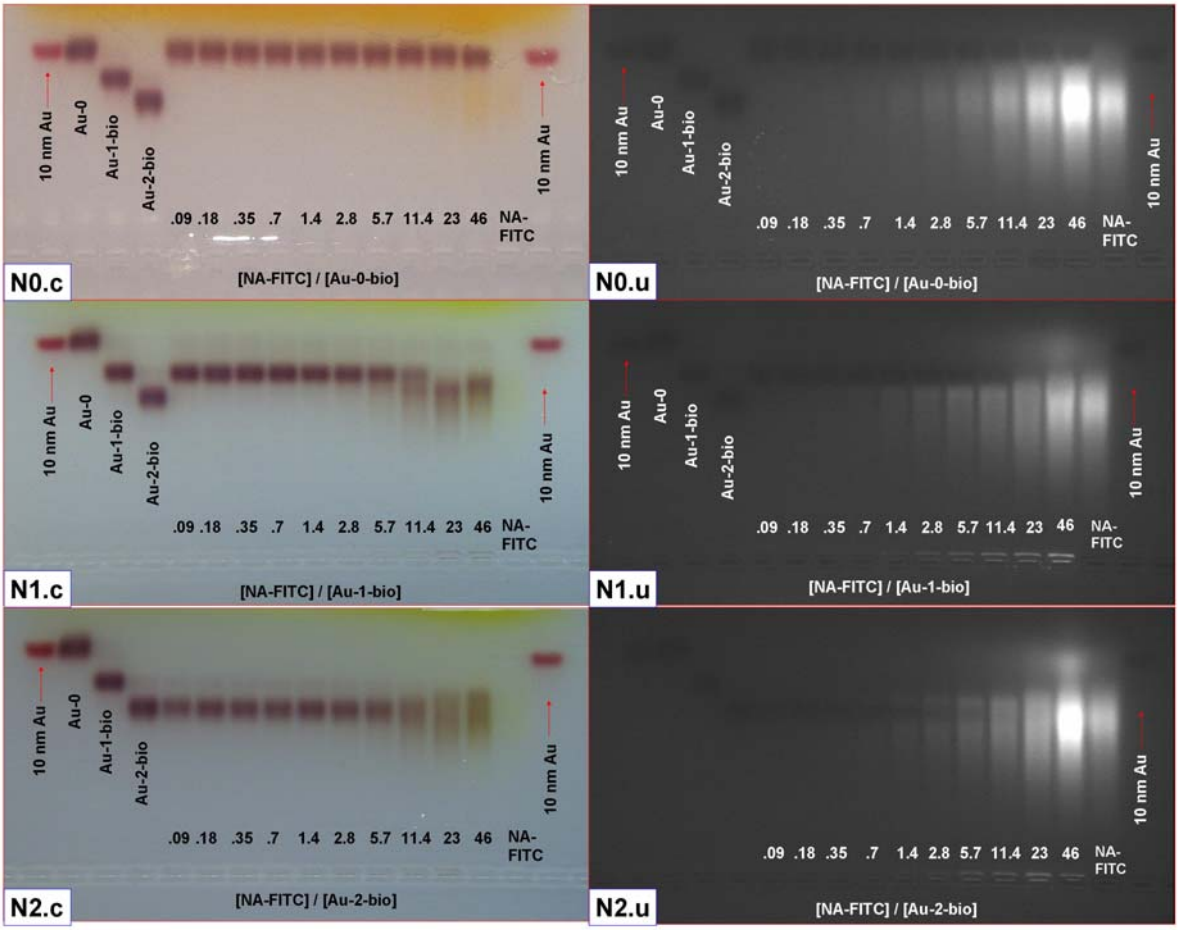

Figure S19. Assembly of 0-, 1- or 2-biotin gold nanoparticles (Au-x-bio) with neutrAvidin-FITC (NA-FITC). The lanes of each gel from left to right comprise four kinds of references (10-nm Au nanoparticles, Au-0, Au-1-bio, and Au-2-bio), increasing molar ratios of c(NA-FITC)/ c(Au-x-bio) with a constant amount of c(Au-x-bio) =1.5 µM x 10 µl, NA-FITC, and again 10 nm AuNP; The left columns show white light color pictures of gradients of c(NA-FITC)/ c(Au-0) *(N0.c)*, c(NA-FITC)/ c(Au-1-bio) *(N1.c)*, or c(NA-FITC)/ c(Au-2-bio) *(N2.c)*; and the right columns show UV light images of gradients of c(NA-FITC)/ c(Au-0) *(N0.u)*, c(NA-FITC)/ c(Au-1-bio) *(N1.u)*, and c(NA-FITC)/ c(Au-2-bio) *(N2.u)*; All samples were run through 1% agarose gels, 10 V/cm for 1 hour.

SI5.4 Assembly of 1- biotin quantum dots with streptavidin

Quantum dots (QD) with a defined number of biotin molecules, i.e. the QD-0, QD-1-bio and QD-2-bio, were prepared in the same way as gold nanoparticles (see details in SI5.2). Briefly, the discrete PEGylation test of polymer-coated quantum dots (previously prepared) was examined again with biotin-PEG5k-amine in order to find the optimal conditions for the attachment of single biotin-PEG molecules. For that, 150 µl of 0.3 mM biotin-poly(ethylene glycol)amine (biotin-PEG5k-amine, Mw 5000 g/mol, Rapp Polymere) in SBB were mixed with an equal volume of polymer-coated CdSe/ZnS QDs (6 µM, 3.75 nm core/shell diameter). Here a smaller molar ratio of PEG molecules per particle was used in order to use as little biotin-PEG5k-amine as possible, i.e. PEG:QD=50:1. Then each 20 µl of the mixture were sequentially activated by EDC of different concentration, i.e., c(EDC)/c(QD) = 0, 16, 31, 63, 125, 250, 500, 1k, 2k, 4k, 8k, 16k, 32k, 64k, and 128k. After 2 hours of reaction, all aliquots were run by gel electrophoresis (10 V/cm, 1 hour). Usually the discrete band appeared clearly in the range of 500 < c(EDC)/c(QD) < 8000. From this small-scale screening experiment we selected a molar

ratio of c(EDC)/c(QD) = 2000 as the condition for a scaled-up reaction. For this, 2 ml of QD solution (6 μM) were mixed with 2 ml of biotin-PEG5k-amine solution (0.3 mM) in a 20-ml glass vial, followed by the addition of 2 ml of freshly prepared EDC solution. The reaction mixture was shaken overnight and then concentrated by ultrafiltration (Amicon centrifuge filters, 100 kDa MWCO). The resulting sample was loaded into the wells of a 2% agarose gel, followed by gel electrophoresis (10 V/cm, 1 - 2 hours) as shown in ***Figure S15A***. The discrete bands of 0-, 1-, 2-biotin QD were then cut out separately and transferred to dialysis membrane bags (3500 Da MWCO, Roth) and run through gel electrophoresis again to elute the trapped nanoparticles. The resulting nanoparticle samples were filtered using a syringe filter (0.22 μm) and reconcentrated on a 100 kDa MWCO Amicon centrifuge filter. Then the samples were purified again by a second round of gel electrophoresis in order to remove residual neighbor fractions. The final nanoparticle samples were adjusted to a concentration of 1.5 μM by ultrafiltration for further experiments.

Aliquots of 10 μl of streptavidin solution with concentrations of 4 mg/ml were prepared by a dilution series, i.e. 4 x 2^{-n} mg/ml (n=0, 1, 2, 3, 4, 5, 6, 7, 8, and 9) or the corresponding molar concentrations of 66 x 2^{-n} μM (n=0, 1, 2, 3, 4, 5, 6, 7, 8, and 9). Each streptavidin solution was quickly mixed with an equal volume of QD-1-bio solution. After overnight reaction, each sample of QD-streptavidin mixture was loaded into the wells of 1% agarose gels and run through gel electrophoresis under an applied electrical field in order to resolve the nanoparticle-streptavidin groupings (***Figure S20***). Similarly, QD-1-bio also yields three different retarded bands when increasing the streptavidin concentration, as compared with the experiments on Au-1-bio.

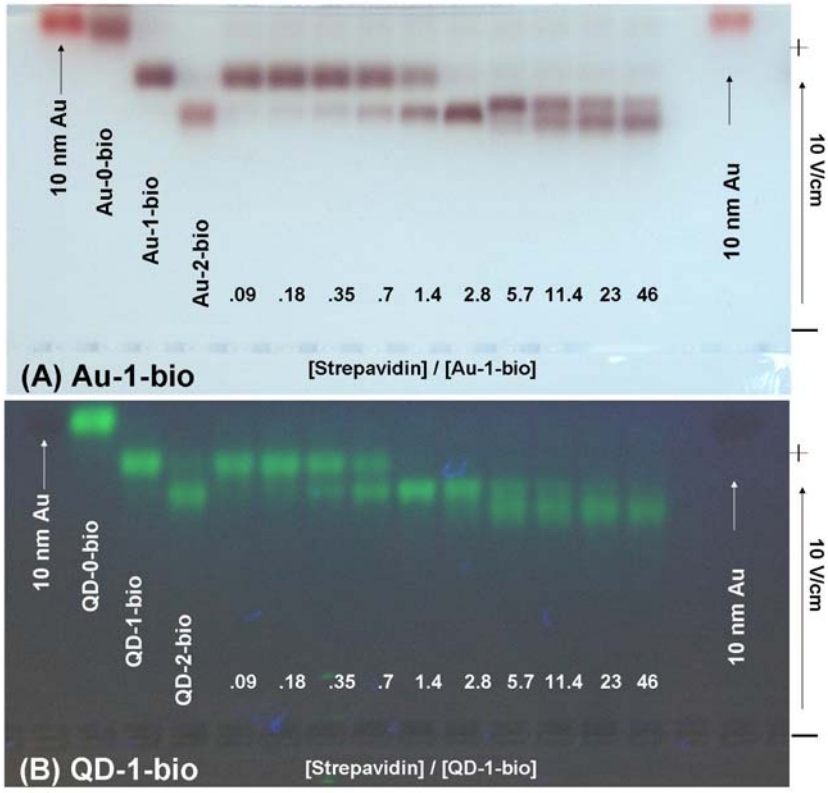

Figure S20. Assembly of 1-biotin nanoparticles with streptavidin (SA). The single biotin on gold nanoparticles (Au) or quantum dots (QD) that were assembled with different concentrations of streptavidin was tested. (A): the lanes of each gel from left to right consist four kinds of standards (10 nm Au nanoparticles, Au-0, Au-1-bio, and Au-2-bio), the increasing ratio of c(Streptavidin)/ c(Au-1-bio) with a constant amount of c(Au-1-bio) = 1.5 μM, blank, and again 10 nm Au; (B): the lanes of each gel from left to right comprise four kinds of references (10-nm Au nanoparticles, QD-0, QD-1-bio, and QD-2-bio), increasing ratios of c(Streptavidin)/ c(QD-1-bio) with a constant amount of c(QD-1-bio) =1.5 μM, blank, and again 10 nm phosphine stabilized Au.

169

SI6: References

[1] N. R. Jana, X. G. Peng, *Journal of the American Chemical Society* **2003**, *125*, 14280.

[2] W. W. Yu, L. Qu, W. Guo, X. Peng, *Chemistry of Materials* **2003**, *15*, 2854.

[3] B. O. Dabbousi, J. Rodriguez-Viejo, F. V. Mikulec, J. R. Heine, H. Mattoussi, R. Ober, K. F. Jensen, M. G. Bawendi, *Journal of Physical Chemistry B* **1997**, *101*, 9463.

[4] M. F. Casula, Y. W. Jun, D. J. Zaziski, E. M. Chan, A. Corrias, A. P. Alivisatos, *Journal of the American Chemical Society* **2006**, *128*, 1675.

[5] T. Pellegrino, L. Manna, S. Kudera, T. Liedl, D. Koktysh, A. L. Rogach, S. Keller, J. Rädler, G. Natile, W. J. Parak, *Nanoletters* **2004**, *4*, 703.

[6] R. A. Sperling, T. Pellegrino, J. K. Li, W. H. Chang, W. J. Parak, *Advanced Functional Materials* **2006**, *16*, 943.

[7] J. P. Van Wauwe, F. G. Loontiens, C. K. De Bruyne, *Biochim Biophys Acta* **1973**, *313*, 99.

Size Determination of (Bio)conjugated Water-Soluble Colloidal Nanoparticles: A Comparison of Different Techniques

R. A. Sperling,[†] T. Liedl,[†] S. Duhr,[†] S. Kudera,[†] M. Zanella,[†] C.-A. J. Lin,[†,‡] W. H. Chang,[‡] D. Braun,[†] and W. J. Parak*[,†]

Center for Nanoscience, Ludwig Maximilians Universität, München, Germany, and Center for Nano Bioengineering and R&D Center for Membrane Technology, Chung Yuan Christian University, Taiwan, R.O.C.

Received: February 5, 2007; In Final Form: April 21, 2007

The size of inorganic colloidal nanoparticles coated with organic layers of different thickness has been measured with different techniques, including transmission electron microscopy, gel electrophoresis, size exclusion chromatography, fluorescence correlation spectroscopy, and thermophoresis. The results are critically compared, and the advantages and disadvantages of the respective methods are discussed.

Introduction

In the past decades, improved synthesis techniques have influenced significantly research and applications of inorganic colloidal nanoparticles. This is mainly due to advances in the control of particle growth. Nowadays, samples with very narrow size distribution and controlled shape can be grown.[1−3] Colloidal stability is provided by a layer of organic molecules around the inorganic particle core. This layer can be either hydrophobic or hydrophilic, and the respective particles are soluble in organic solvents or aqueous solution. Naturally, this layer contributes to the overall diameter of the particles. Whereas the colloidal stability of particles in organic solvents is usually achieved by a monolayer of hydrophobic molecules,[4] thicker (hydrophilic) layers are often used to stabilize particles in aqueous solution, which in turn results in significantly increased particle diameters.[5,6] The effective diameter of the particles increases further when additional (biological) molecules are bound to the particle surface in order to provide functionality. In particular, for biological applications, it is important to know the effective diameter of the particles, as bigger particles, for example, might not be able to enter pores of a certain size. However, due to the composite nature of the particles—a "hard" inorganic core and a "soft" organic shell with attached biological molecules—this is not a trivial task. The problem is that some techniques are more sensitive for the inorganic part, and others may eventually influence the conformation and thus the size of the organic part.

The size of the first generation of colloidal semiconductor nanoparticles was investigated extensively several years ago by the group of Henglein and Weller.[7−9] These particles were directly synthesized in water, and the organic shell around the inorganic cores comprised just a monolayer of mercaptocarbonic acid molecules. In this study, we want to investigate the size of more complex nanoparticles that first have been synthesized in organic solvents, then have been transferred to aqueous solution by embedding them in a hydrophilic polymer shell,[10−13] and finally have been modified by the conjugation of polyethylene glycol (PEG) molecules with different molecular weight.[14] These particles represent the general case where the samples differ in the thickness of a (soft) organic shell, while the (hard) inorganic particle core is the same.

For this work, nanoparticle size was characterized by the following methods: transmission electron microscopy (TEM),[15−17] gel electrophoresis,[9,18−24] size exclusion chromatography (SEC),[7,8,21,25−35] fluorescence correlation spectroscopy (FCS),[11,36−44] and thermophoresis.[45−47] These and other relevant methods not used in this study are described in more detail in the Supporting Information (SI).

Materials and Methods

Particle Synthesis. CdSe/ZnS core/shell nanoparticles were synthesized in organic solvent according to standard protocols[48,49] and transferred to aqueous solution by embedding them in a shell of an amphiphilic polymer.[11] All protocols are reported in detail in the Supporting Information (SI §I.1−§I.5). The first exciton peak in the absorption spectrum of the CdSe cores was at 610 nm (corresponding to a diameter of the inorganic core of 4.7 nm[50]) and, after overcoating with the ZnS shell, at 614nm (see Table 1). PEG molecules of different molecular weight, which were modified with an amino group on one end, were attached at different coverages by standard EDC chemistry to the polymer shell around the nanoparticles[14] (SI §I.6). Sketches of the resulting particles are drawn in Tables 1−3. For particles whose surfaces were saturated with PEG, unbound excess PEG molecules were removed in five subsequent purification steps with centrifuge filters. Mixtures of particles with a discrete number of PEG molecules attached per particle were first run on 1% agarose gels in order to separate particles with zero, one, two, and three PEG molecules attached per particle. After extraction of the particles from the gel, they were purified on a desalting column. As additional samples, Au nanoparticles[16,51] with the same modifications as those described for the CdSe/ZnS particles were also used. Detailed protocols have been published previously.[11,14] We also measured the diameter of commercially available quantum dots with and without streptavidin modification (Table 4).

Transmission Electron Microscopy. TEM images of CdSe/ZnS particles dissolved in chloroform and water were recorded before and after embedding them in a shell of amphiphilic

* Corresponding author. E-mail: Wolfgang.Parak@physik.uni-muenchen.de.
† Ludwig Maximilians Universität.
‡ Chung Yuan Christian University.

10.1021/jp070999d CCC: $37.00
Published on Web 07/13/2007

TABLE 1: The Inorganic Hard Core Diameter $<d>$ and the Effective Diameters $<d_{eff}>$ of CdSe, CdSe/ZnS, and Au Particles (Drawn in Gray) Determined with Optical Methods and by TEM Images

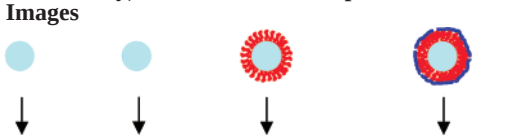

particle type	$<d>_{abs}$ [nm][a]	$<d>_{TEM}$ [nm][b]	$<d_{eff}>_{TEM}$ [nm] before polymer coating	$<d_{eff}>_{TEM}$ [nm] after polymer coating[c]
CdSe	5.1	4.7	6.0	
CdSe/ZnS	5.3	5.3	6.4	9.6
Au		4.6	5.6	9.0

[a] For the CdSe particles, the diameter was derived from absorption spectra.[50] [b] By analyzing the spacing between the particles in the TEM images, the effective diameters $<d_{eff}>$, which comprise the inorganic particles plus the organic layers (drawn in red and blue) attached to their surfaces, were determined before and after coating the particles with an amphiphilic polymer. Before the polymer coating, the particle is just surrounded by the hydrophobic surfactant layer (drawn in red). After the polymer coating, an amphiphilic polymer (with hydrophobic tails drawn in red and a hydrophilic backbone drawn in blue) is also wrapped around the particles.[11,14] [c] These values have to be considered as an approximation (see SI §II.2).

polymer. Drops of the particle solution were placed on TEM grids, and images were recorded after evaporation of the solvent. The distribution of the inorganic particle diameters and the distances between the centers of adjacent particles were derived from the images by an image analysis program (SI §II.1).

Gel Electrophoresis. CdSe/ZnS and Au particles saturated with PEG molecules of different length were run on agarose gels (1−2%, 1−2 h, 100 V). As a control, phosphine-stabilized 10 nm Au particles were also run on the same gel.[19,20] After running the particles on the gel, the bands of the CdSe/ZnS and Au particles were identified by their fluorescence and red color, respectively (see Figure 1) (SI §III). The mobilities of the different particles were determined from their position on the gel relative to the position where they had been loaded to the gel.[19,20] For CdSe/ZnS and Au particles with a discrete number of PEG molecules attached per particle, a low amount of PEG molecules of different length was reacted to the polymer-coated CdSe/ZnS and Au particles, and the reaction mixtures were run on agarose gels. After running the gel, discrete bands corresponding to CdSe/ZnS and Au particles with no, exactly one, exactly two, and exactly three PEG molecules bound per particle were observed as individual bands on the gel (see Figure 1).[19,20] The bands were extracted from the gel, and the obtained CdSe/ZnS− and Au−PEG conjugates with a different number of PEG molecules attached per particle were purified on a desalting column before using them for the SEC, FCS, and thermophoresis experiments. From gel electrophoresis, the mobilities m of all conjugates were then transformed in corresponding effective diameters d_{eff} by using a mobility−diameter calibration curve created with phosphine-stabilized Au nanoparticles[20] (SI §III):

$$d_{eff,1\%}(m) = -85.0 \cdot \ln[(m/m_{10nm,1\%})/1.05] + 6 \text{ [nm]}$$

$$d_{eff,2\%}(m) = -37.7 \cdot \ln[(m/m_{10nm,2\%})/1.12] + 6 \text{ [nm]} \quad \text{(Formula 1)}$$

Here, $m/m_{10nm,y}$ refers to the electrophoretic mobility of the conjugates (m) in relation to the mobility of 10 nm phosphine-stabilized Au particles ($m_{10nm,y}$) that have been run on a gel with the same agarose concentration y (y = 1% or 2%).[19,20]

Size Exclusion Chromatography. CdSe/ZnS and Au particles saturated with PEG molecules of different molecular weight were run on different high-performance liquid chromatography (HPLC) size exclusion columns, and the elution volume v_e (i.e., the total volume of the mobile phase when the particles come out of the column) of the particles was measured (similarly, elution times t_e, i.e., the time after which the particle fraction is eluted from the column, could have been measured) (see Figure 2) (SI §IV). In order to normalize the data to one universal curve, the elution volumes v_e were transformed into partition coefficients K_{SEC}.[52,53] The partition coefficient corresponds to the fraction of accessible pore volume for sample particles and can obtain values $0 \le K_{SEC} \le 1$. Very small particles or molecules can occupy the total pore volume (as they are small enough to fully penetrate the pores of the gel), and $K_{SEC} = 1$. Very large particles are totally excluded from the pore volume, and $K_{SEC} = 0$. In this way, the K_{SEC} value is a measure of the size of the particles: the smaller and larger the particles are, the closer their K_{SEC} values come to 1 and 0, respectively. In contrast to elution volumes or elution times, the K_{SEC} values are normalized quantities and thus do not depend in first order on experimental parameters such as sample volume, flow rate, or column geometry (SI §IV):

$$\begin{aligned} K_{SEC}(\text{particle}) &= [(t_e(\text{particle}) - t_e(\text{biggest particle})]/ \\ &\quad [(t_e(\text{smallest particle}) - t_e(\text{biggest particle})] \\ &= [(v_e(\text{particle}) - v_e(\text{biggest particle})]/ \\ &\quad [(v_e(\text{smallest particle}) - v_e(\text{biggest particle})] \\ &= [(v_e(\text{particle}) - v_0]/[v_t - v_0] \end{aligned} \quad \text{(Formula 2)}$$

The elution volume of the very small particles is referred to as the total liquid volume v_t, and the elution volume of the very large particles is referred to as dead or void volume v_0. In order to experimentally obtain v_t and v_0, aceton (a very small particle) and λ-DNA (a very big particle) were run, and their elution volumes (= v_t and v_0) were measured. For generating a calibration curve that relates partition coefficients K_{SEC} to effective diameters d_{eff}, protein standards were run through the columns, and their elution volumes were determined from the elution peak maxima and converted into partition coefficients. The size d_{eff} of each protein standard was estimated as 2 times the hydrodynamic radius of the protein.[53] By plotting the partition coefficients of different proteins versus their effective diameter and extrapolating these data, a calibration curve d_{eff}-(K_{SEC}) was obtained (see Figure 2). By using this calibration curve, the partition coefficients derived for the CdSe/ZnS−PEG and Au−PEG conjugates could be converted into effective diameters. As for the gel electrophoresis experiments, the effective diameters are obtained by a comparison with standard samples of known diameter. In the case of the gel electrophoresis experiments, phosphine-stabilized Au nanoparticles were used. These particles could not be used for the SEC measurements, as they got stuck in the columns. Therefore a series of globular proteins had to be used as standard samples for the SEC measurements.

Fluorescence Correlation Spectroscopy. Samples of CdSe/ZnS−PEG conjugates were mounted on an Axiovert200 confocal microscope with a 40× water immersion objective (C-Apochromat, NA = 1.2) and a ConfoCor2 FCS module (whole setup: Zeiss, Germany). Fluorescence was excited with the 488 nm line of an Ar ion laser. The focal volume was calibrated with Alexa488 (diffusion coefficient D = 316 $\mu m^2 s^{-1}$, Molecular Probes). The nanocrystals were diluted to a concentration

TABLE 2: Effective Diameters d_{eff} [nm] of CdSe/ZnS-PEG Conjugates

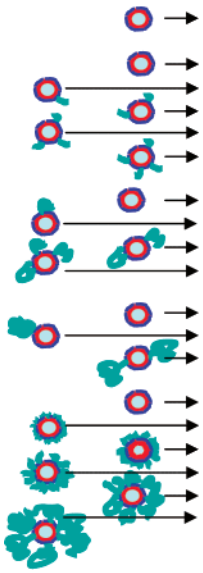

PEG/ polymer-coated CdSe/ZnS particle[a]	M(PEG) [g/mol]	$\langle d_{eff}\rangle_{TEM}$ [nm]	$\langle d_{eff}\rangle_{gel,1\%}$ [nm]	$\langle d_{eff}\rangle_{gel,2\%}$ [nm]	$\langle d_{eff}\rangle_{SEC}$ [nm]	$\langle d_{eff}\rangle_{FCS}$ [nm]	$\langle d_{eff}\rangle_{Therm}$ [nm]
0	-	9.6[b]	14.5	-	-	20.5	-
0	5000	-	14.5	14.5	-	20.1	-
1	5000	-	24.5	19.3	-	22.8	-
2	5000	-	34.2	24.1	-	24.4	-
3	5000	-	43.6	28.5	-	25.8	-
4	5000	-	51.9[c]	32.8	-	-	-
0	10000	-	14.5	-	-	25.0	-
1	10000	-	29.4	-	-	25.8	-
2	10000	-	43.5	-	-	26.6	-
3	10000	-	56.5[c]	-	-	-	-
0	20000	-	14.5	-	-	22.2	8.2
1	20000	-	39.6	-	-	26.3	12.2
2	20000	-	62.7[c]	-	-	29.2	30.2
0	-	-	-	14.5	12.6	19.4	12.2
sat.	750	-	-	46.1[c]	14.6	25.4	22.0
sat.	2000	-	-	180.2[c]	18.3	25.6	23.6
sat.	5000	-	-	neg.[c]	23.9	27.6	25.0
sat.	10000	-	-	neg.[c]	26.2	30.2	30.0
sat.	20000	-	-	neg.[c]	34.8	34.2	40.0

[a] PEG molecules (drawn in green) of different molecular weight M_w have been attached to the surface of polymer-coated CdSe/ZnS particles, as already sketched in Table 1.[14] Either zero, one, two, three, or as many as possible ("sat.") PEG molecules were attached per particle, and the effective particle diameter $\langle d_{eff}\rangle$ was measured with TEM, gel electrophoresis ("gel",1% and 2% agarose concentration), FCS, SEC, and thermophoresis ("Therm"). The particles with single PEGs attached per particle (first 13 samples) had been separated with gel electrophoresis with subsequent extraction from the gel and purification before their diameters were measured with SEC, FCS, and thermophoresis. [b] This value has to be considered as approximation. [c] These values are not realistic (as they are either too big or negative) due to limitations of the applied technique (see SI §II.2).

TABLE 3: Effective Diameters d_{eff} [nm] of Au−PEG Conjugates

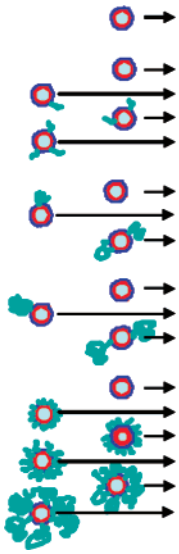

PEG/ polymer-coated Au particle[a]	M(PEG) [g/mol]	$\langle d_{eff}\rangle_{TEM}$ [nm]	$\langle d_{eff}\rangle_{gel,1\%}$ [nm]	$\langle d_{eff}\rangle_{gel,2\%}$ [nm]	$\langle d_{eff}\rangle_{SEC}$ [nm]
0	-	8.6	12.7	12.5	-
0	5000	-	12.7	12.5	-
1	5000	-	26.3	18.4	-
2	5000	-	38.2[b]	24.5	-
3	5000	-	-	29.9	-
0	10000	-	13.4	12.5	-
1	10000	-	44.5[b]	21.6	-
2	10000	-	70.7[b]	29.3	-
0	20000	-	14.4	12.5	-
1	20000	-	52.5[b]	27.7	-
2	20000	-	83.5[b]	40.2	-
0	-	-	-	12.5	11.1
sat.	750	-	-	49.7[b]	12.5
sat.	2000	-	-	140.1[b]	16.5
sat.	5000	-	-	neg.[b]	21.0
sat.	10000	-	-	neg.[b]	28.8
sat.	20000	-	-	neg.[b]	34.8

[a] PEG molecules of different molecular weight M_w have been attached to the surface of polymer-coated Au particles.[14] Either zero, one, two, three, or as many as possible ("sat.") PEG molecules were attached per particle, and the effective particle diameter $\langle d_{eff}\rangle$ was measured with gel electrophoresis ("gel",1% and 2% agarose concentration) and SEC. [b] These values cannot be taken into account (as they are too big or negative) and demonstrate the limitations of gel electrophoresis for size measurements (see SI §II.2).

of ~10 nM, which corresponds to roughly one particle per focal volume. Time traces of the fluorescence intensity were recorded with an avalanche photodiode with single-photon sensitivity. From the fluorescence intensity traces, autocorrelation functions were calculated (see Figure 3) (SI §V). By fitting the experimentally obtained autocorrelation functions with model functions for freely diffusing particles, the diffusion coefficients of the particles were obtained as fit parameters.[37−39,54] The diffusion

TABLE 4: Effective Diameters d_{eff} of Commercially Available Quantum Dots[a,b]

sample	$<d_{eff}>_{gel,2\%}$ [nm]	$<d_{eff}>_{SEC}$ [nm]	$<d_{eff}>_{Therm}$ [nm]	$<d_{eff}>_{mean-value}$ [nm]
QD655 carboxyl	16.6	11.8	14.0	14.1 ± 2.4[d]
QD655 SA	133.0[c]	20.5	25.6	23.1 ± 1.6

[a] Quantum Dot Corporation, 655 nm emission, polymer shell with carboxyl groups and with additional streptavidin (SA) modification (Qdot655 ITK carboxyl, #2132-1, and Qdot655 streptavidin conjugate, #1012-01). [b] The values were obtained with gel electrophoresis (2% agarose gels), SEC (column with Sephadex S-400), and thermophoresis. [c] This value cannot be taken into account due to charge effects (see SI §II.2). [d] This value is in the same range as the diameter obtained from Pons et al[24] for particles with slightly smaller cores.

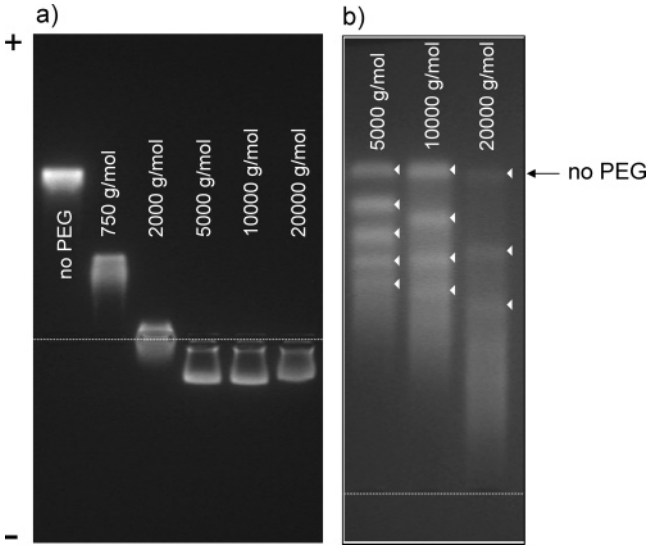

Figure 1. 1. Gel electrophoresis for polymer-coated CdSe/ZnS nanoparticles. The "+" and "−" symbols indicate the direction of the applied electric field, and the dashed line marks the position where the samples have been loaded into the wells of the gel. (a) 2% agarose gel with particles with no PEG and particles whose surface has been saturated with PEG of 750, 2000, 5000, 10000, and 20000 Da molecular weight. (b) 1% agarose gel of particles to whose surface only a few PEG molecules of different molecular weight have been bound. The particles with no, one, two, and so forth PEG molecules attached per particle yield discrete bands on the gel.

coefficients were then converted into effective diameters by using the Stokes−Einstein relation. In contrast to the gel electrophoresis and HPLC measurements, the effective diameters obtained with FCS measurements are absolute values and do not depend on a direct comparison with standard samples of known diameter. However, the setup has to be calibrated with a dye of known diffusion constant for all measurements. Since the Au−PEG conjugates do not fluoresce, they could not be analyzed with FCS.

Thermophoresis. Strong local temperature gradients were used to manipulate concentration patterns in solution, all optically. Figure 4a shows the typical time course of an experiment. A solution of nanoparticles was continuously monitored by fluorescence microscopy, and the local fluorescence was used as measure for the particle concentration. An infrared laser was then used to introduce an inhomogeneous radial symmetric concentration pattern by inducing thermophoretic motion. After a few seconds, when the concentration in the center of the heat spot had decreased to at least 90% of the initial condition, the heating source was turned off. The temperature relaxed nearly instantaneously and was followed by the much slower flattening of the concentration profile by diffusion. These time-resolved concentration profile data were compared with data obtained in a one-dimensional (1D) radial simulation over time (Figure 4b). By comparison of the experimental and simulated data, the mean diffusion coefficient of the fluorescent particles in solution was obtained, and from this the hydrodynamic diameter of the particles was derived using the Stokes−Einstein relation (SI §VI). In contrast to the gel electrophoresis and HPLC measurements the effective diameters obtained with thermophoresis measurements do not depend on a comparison with standard samples of known diameter, but are absolute values. Since the Au−PEG conjugates do not fluoresce, they could not be analyzed with thermophoresis.

PEG Radius. The increase in size of particles with a PEG shell should correspond to the dimensions of the PEG molecules. The effective diameters of free PEG molecules can be calculated from Formula 3, which was obtained by SEC,[55] whereby r_h is the hydrodynamic radius, and M_w is the molecular weight of the PEG:

$$d_{eff,PEG} = 2r_h = 0.03824\, M_w^{0.559} \qquad \text{(Formula 3)}$$

Results and Discussion

Transmission Electron Microscopy. The results for the TEM analysis on particles without PEG modification are summarized in Table 1. However, these values have to be considered as very rough estimates with only limited reliability (SI §II.2). First of all, measurements had to be performed on dried samples. While, in solution, the hydrophobic surfactant chains repel each other, on a TEM grid, the particles can come so close to each other that the surfactant chains intercalate. More severe, the size distribution after the polymer coating, that is, the size-distribution of the entire system inorganic core plus organic shell, is by far not as good as that of the original particle solution, and the particles therefore do not assemble anymore nicely into two-dimensional lattices. Therefore, the particle-to-particle distance curves are smeared out, and the derived effective particle diameters have to be interpreted with care. As the particles have to be measured in the dried state, the effective diameters as determined by TEM do not contain any interaction with the solvent (as, for example, a cloud of counterions). Therefore, the values obtained for the effective diameter for CdSe/ZnS as well as Au particles with TEM are significantly smaller than the effective diameters determined with methods in which the particles are dispersed in their solvents (see first lines of Tables 2 and 3).

Gel Electrophoresis. In Figure 1, examples for particles separated by gel electrophoresis are shown. As with SEC, not only can the particle diameter be estimated, but the particles can also be sorted and fractionated by size in small preparative scale. In comparison to SEC, the size resolution of gel electrophoresis is significantly better, as particles with zero, one, two, and so forth PEG molecules can be clearly separated by gel electrophoresis, but not with the columns used for SEC. However, there are severe limitations for the determination of effective diameters. The particles need to possess a very high colloidal stability in the electrolytic solution, which is needed to drive the current, otherwise they agglomerate and get stuck on the gel. The biggest problem, however, is obtaining an appropriate calibration curve that relates electrophoretic mobility to effective size. As electrophoretic mobility depends on both size and charge, any calibration curve for size can only be valid for objects of similar charge. Furthermore, the physical properties such as stiffness and flexibility of the particles used to obtain

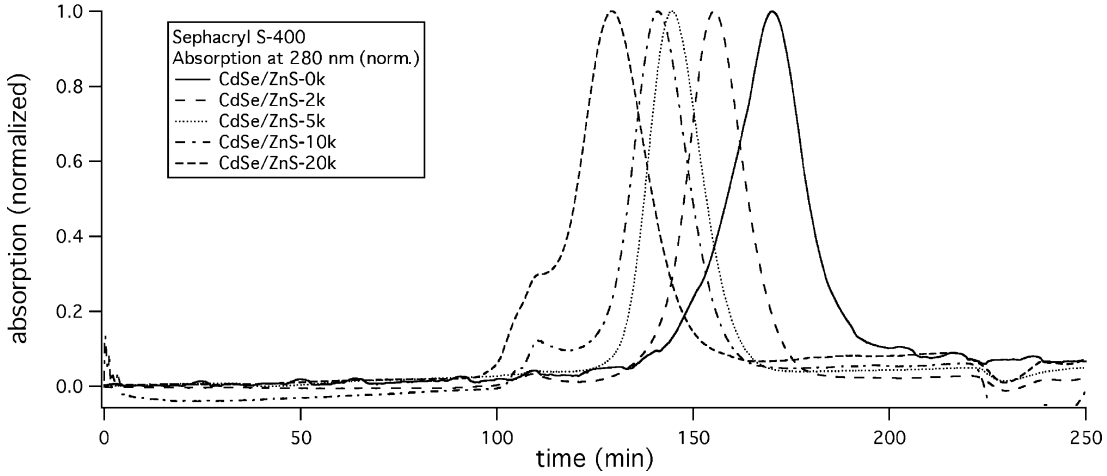

Figure 2. Size exclusion chromatograph (SEC) with a Sephacryl S-400 filled column of CdSe/ZnS nanoparticles whose surface is saturated with PEG molecules of different molecular weight (no PEG, 2 kDa, 5 kDa, 10 kDa, 20 kDa). Plotted is the absorption of the eluted solution versus the elution time. The bigger the particles are, due to the attachment of PEG of higher molecular weight, the earlier they are eluted from the column.

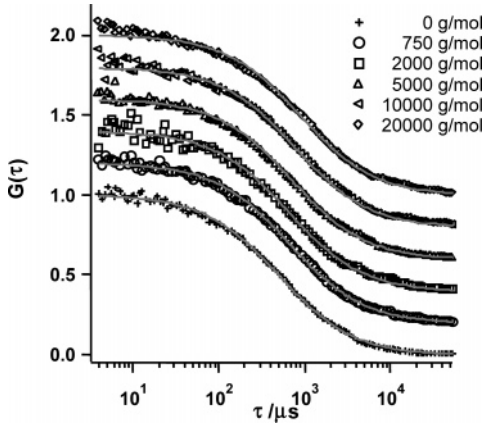

Figure 3. Autocorrelation functions $G(\tau)$ obtained from the FCS data for polymer-coated CdSe/ZnS particles whose surface is saturated with PEG molecules of different molecular weight (750 g/mol, 2 kg/mol, 5 kg/mol, 10 kg/mol, 20 kg/mol). The curves for the respective particles are shifted along the *y*-axis for the purpose of better visualization. The particles with no PEG attached are referred to as particles with PEG of molecular weight 0 (bottom graph). The experimental data were fitted with an analytical function (shown as gray lines), which yielded the effective diffusion coefficient as one fit parameter (see SI §V).

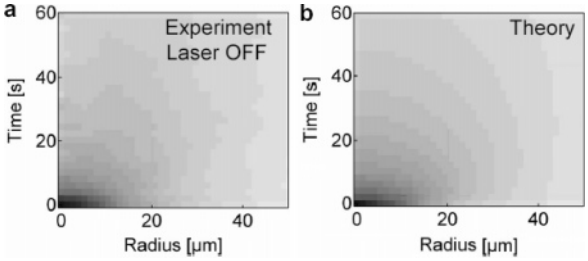

Figure 4. Thermophoresis and back-diffusion of nanometer-sized particles in solution. Thermodiffusion is used to form a concentration gradient in solution by heating a micrometer-sized spot. (a) (experiment) The graph shows the development of radial concentration averages over time after the heating laser is switched off (black: low concentration; gray: high concentration). As can be seen from the plot, the concentration inhomogeneity relaxes within 60 s. The data shown correspond to a particle size of approximately 30 nm in diameter. (b) (theory) The diffusion constant D is obtained by performing 1D finite element simulations with D as a free parameter, until the theory in b matches the experiment in a.

the calibration curve must be similar to those of the particles that are to be investigated. Basically, two different types of particles could be used in order to obtain calibration curves: biological macromolecules or colloidal nanoparticles. We have tried oligonucleotides[19,20] as well as proteins for calibration, but both yielded very different mobility values compared to the ones obtained for colloidal nanoparticles. As linear flexible molecules, oligonucleotides can move in a different way through the pores of a gel compared to rigid inorganic colloidal nanoparticles. On the other hand, the surface charge density of oligonucleotides is, in first order, constant, therefore oligonucleotides are sorted by size and not by charge. In contrast to average oligonucleotides, proteins possess a secondary and tertiary structure and can be thought of in crude approximation as elastic spherical particles. However, proteins can have different surface charge densities comprising the full spectra from negative to neutral to positive. Because it is hard to find a set of proteins with different sizes but with the same charge density as the particles that are to be investigated, proteins are also not suited as standard particles for obtaining a calibration curve that relates electrophoretic mobilities to size. Therefore we have chosen inorganic colloidal nanoparticles of different size but with identical negatively charged surface coatings (bis(*p*-sulfonatophenyl)-phenylphosphine dihydrate) as size standards. There are known problems for these standards as well. First, there is an inherent uncertainty in the standard, as the effective hydrodynamic diameter is not known and is assumed to be the hard core Au particle diameter plus 2 times the length of the phosphine molecules, without taking into account the cloud of counterions.[20] However, comparison with the literature data obtained from dynamic light scattering shows that they are in good agreement with the assumed values. Second, attached macromolecules (such as DNA[20]) form a soft shell around the hard inorganic core, which can be compressed by the gel. This can be seen in the data of Tables 2 and 3: the effective diameters derived from 1% agarose gels are always larger than the ones from 2% agarose gels, as the soft shell is compressed more on gels of higher percentage. This difference in data obtained with gels of different percentages has already been observed with DNA-modified sulfonate-stabilized Au particles.[20] Even in this case where there is only a minor influence of charge on the electrophoretic mobilities, the diameters obtained with gels of different percentages differed significantly, whereby the differences were most significant for long DNA strands and particles with a lot of attached DNA (= thick soft shells). In this study, PEG molecules were used for particle modification. As has already been reported,[14] attachment of sufficient amounts of PEG to negatively charged polymer-coated particles can reverse

the polarity of the particles to a positive net charge, so that they migrate toward the negative electrode during gel electrophoresis (see Figure 1). This effect might be due to positive ions adsorbed to the PEG.[56] At any rate, this charge effect makes the determination of effective diameters of PEGylated particles with gel electrophoresis almost impossible. Due to the charge effect, the derived diameters are too large, and, for particles saturated with long PEG, no diameter can be derived due to the change in polarity (see Tables 2 and 3). The more PEG is attached per particle and the higher the molecular weight of the PEG, the more unreliable the results become. Although, in our experience, gel electrophoresis is the most sensitive of the here-described methods to resolve changes in size (e.g., the attachment of a single molecule), reliable absolute numbers of effective diameters can be only derived under very restricted conditions when the charge density of the sample to be investigated is highly similar to that of the particles used as size standards.

Size Exclusion Chromatography. Analogous to gel electrophoresis, SEC is not only an analytical method, but particles of different diameter can be fractionated on a preparative scale. Here, sorting by size is also achieved by a porous matrix, but, in contrast to gel electrophoresis where particles are driven by an electric current and small particles run faster, in SEC smaller particles are retarded because they can access a larger pore volume of the column packing. For all the columns used in this study, the resolution by size was lower for SEC compared to gel electrophoresis, since, with SEC, particles with zero, one, two, three, and so forth PEG molecules bound per particle could never be separated, while this was easily achieved with gel electrophoresis. Size measurements with both methods rely on appropriate size standards. In SEC, charge effects, that is, electrostatic interaction of charged particles with charges in the gel, are typically reduced by a mobile phase with a high salt concentration that screens residual charges of the column material. Unfortunately, this rules out the use of the sulfonate-stabilized Au particles that were used for gel electrophoresis as size standards, as these particles tend to agglomerate at high salt concentrations and get stuck in the columns. We therefore used globular proteins as size standards, as we could exclude charge effects as in the case of gel electrophoresis. Good estimates for effective hydrodynamic diameters exist for many proteins. On the other hand, the size range of available proteins is limited. We were unable to find spherically shaped (globular) proteins with a diameter as large as the largest of our PEG-modified nanoparticles (ca. 40 nm). The derived effective diameters for PEGylated nanoparticles from the extrapolated calibration curve are therefore more reliable the smaller the particles are (see Tables 2 and 3 and Figure 2).

Fluorescence Correlation Spectroscopy. Unlike gel electrophoresis or SEC, FCS is a purely analytical method and does not allow for separation and subsequent collection of fractions of particles with different diameters. The effective diameters derived from the FCS measurements (see Table 2 and Figure 3) are consistent with our previous findings[11,41] and also consistent within themselves. The more and the longer PEG is added to the particles, the bigger the measured effective diameters are. Since FCS is based on single-particle experiments, each effective diameter reported in Table 2 corresponds to the mean value of the diameters of hundreds of particles from each sample. Within one sample series (i.e., different PEGs have been attached to the same batch of polymer-coated particles and the measurements were performed directly after each other with exactly the same FCS setup conditions), even the attachment of single PEG molecules could be resolved, that is, the resolution limit is better than that for the increase in diameters for particles upon attachment of zero, one, two, and three PEGs per particle (see Table 2). However, the absolute values of effective diameters that have been recorded on the same type of particles but under different experimental conditions (i.e., when the particles were extracted from different gels before the measurements, when the FCS setup was recalibrated, etc.) vary significantly. As an example, we take the mean diameters for plain polymer-coated particles (i.e., zero PEGs per particle) from the different series from Table 2. The mean effective diameter and standard deviation of the five different samples ($<d_{\mathrm{eff,FCS}}>$ = <20.5 nm, 20.1 nm, 25.0 nm, 22.2 nm, 19.4 nm>) is 22.0 ± 2.8 nm. The standard deviation has to be seen as an error bar for absolute measurements. The error bar is in the same range as the increase in the particle diameter upon the attachment of individual PEG molecules per particle. We therefore conclude that, although relative changes in the effective particle diameter upon the attachment of molecules within the same batch of particles and under the same setup conditions can be resolved with good precision, there is a significant error of about 3 nm in the determination of absolute effective diameters. There are two main sources for systematic errors in deriving absolute effective diameters: (i) Although FCS does not need a size standard, the focal volume has to be calibrated for each set of measurements with a dye molecule of known diffusion constant and thus known hydrodynamic diameter. Each error of the calibration is propagated to the results of the following measurements. (ii) In contrast to organic fluorophores, colloidal quantum dots exhibit no exponential triplet state decay but rather blinking behavior on all time-scales, which influences the recorded florescence intensity time traces. To our knowledge, so far, no analytical expression has been derived to account for this fact.[11,41,42]

Thermophoresis. The values obtained by thermophoresis increase as expected with the molecular weight of the covalently coupled PEG molecules. The method measures the mean diffusion coefficients of the whole ensemble. Species without or with less surface modification would, in principle, lead to a higher overall diffusion coefficient and smaller radius, respectively. The sizes obtained for nanoparticles saturated with PEG molecules are listed in Table 2, and a typical experiment is shown in Figure 4. In contrast to gel electrophoresis and SEC, no calibration curve of size standards is needed to obtain the effective diameters. Although thermophoresis, like FCS, is based on obtaining effective diameters by measuring the diffusion of the dispersed particles, the values obtained with both methods differ significantly (see Table 2). The standard deviation in the measurements between similar samples is in the same range as that with FCS (polymer-coated CdSe/ZnS with no PEG: $<d_{\mathrm{eff,Therm}}>$ = <8.2 nm, 12.2 nm> = 10.2 ± 2.8 nm; see last column of Table 2; the deviations within one method are attributed to variations in the sample, e.g., due to differences in the gel extraction procedure). The difference in the effective diameter of about a factor of 2 ($<d_{\mathrm{eff,Therm}}> \approx$ 10 nm; $<d_{\mathrm{eff,FCS}}> \approx$ 22 nm) for plain polymer-coated nanoparticles as determined with thermophoresis and FCS can therefore not be explained by the resolution limit due to sample variations (≈ 3 nm) of both methods. Although we cannot explain the origin of this discrepancy, we speculate that it might arise from the different particle concentrations used for the measurements. Whereas FCS is a single-molecule-based method and thus requires extremely diluted particle solutions, thermophoresis is an ensemble-based method, and typically more

TABLE 5: Polymer-Coated Au and CdSe/ZnSe Nanoparticles Coated with Saturated Layers of PEG Molecules of Different Molecular Weight M_w[a]

M_w (PEG) [g/mol]	$<d_{eff}>_{SEC}$ [nm] Au core	$<d_{eff}>_{SEC}$ [nm] CdSe/ZnS core	$<d_{eff}>_{FCS}$ [nm] CdSe/ZnS core	$<d_{eff}>_{Therm}$ [nm] CdSe/ZnS core	$1/2\Delta d_{eff,SEC}$ [nm] Au core	$1/2\Delta d_{eff,SEC}$ [nm] CdSe/ZnS core	$1/2\Delta d_{eff,FCS}$ [nm] CdSe/ZnS core	$1/2\Delta d_{eff,Therm}$ [nm] Au core	$1/2<\Delta d_{eff}>$ [nm]	$d_{eff,PEG}$ [nm]
0	11.1	12.6	19.4	12.2						
750	12.5	14.6	25.4	22.0	0.7	1.0	3.0	4.9	2.4 ± 2.0	1.5
2000	16.5	18. 3	25.6	23.6	2.7	2.9	3.1	5.7	3.6 ± 1.4	2.7
5000	21.0	23.9	27.6	25.0	5.0	5.7	4.1	6.4	5.3 ± 1.0	4.5
10000	28.8	26.2	30.2	30.0	8.9	6.8	5.4	8.9	7.5 ± 1.7	6.6
20000	34.8	34.8	34.2	40.0	11.9	11.1	7.4	13.9	11.1 ± 2.7	9.7

[a] The first line hereby corresponds to plain polymer-coated nanoparticles without PEG modification. In columns 2−5, the mean effective diameters $<d_{eff}>$ of the particles as determined with different methods are listed. These values originate from the data in Tables 2 and 3. The thickness of the PEG layers of different molecular weight around polymer-coated particles are derived as half of the difference of the total diameters of the PEG-coated and the plain polymer-coated particles: $1/2\Delta d_{eff}(M_w(\mathrm{PEG}) = \mathrm{X}) = (<d_{eff}(M_w(\mathrm{PEG}) = \mathrm{X})> - <d_{eff}(M_w(\mathrm{PEG}) = 0)>)/2$. These values are listed in columns 6−9. In column 10, the mean thickness of the PEG layers (as the average value of the different methods) $1/2\Delta d_{eff}$ is given. The last column shows the diameters of free PEG molecules as calculated with Formula 3.[55]

concentrated particle solutions are used in order to obtain signals with sufficient intensity. Particle−particle interaction plays a different role under both conditions. Also the statistical effect of a certain amount of aggregated particles is different. We estimate the relative concentration of aggregates to contribute less than linearly to the diffusion coefficient measured by thermophoresis, since larger particles are depleted more strongly and the back diffusion is slower. Thus, the measured signal stems mostly from single-particle diffusion. The role of particle interactions will be analyzed in future experiments under optimized conditions with particle concentrations of less than 10 nM. This would allow direct comparison with FCS experiments. The values obtained with SEC in ensemble measurements of relatively concentrated particle solutions for plain polymer-coated particles correspond more to the values obtained with thermophoresis than those obtained with FCS, which also gives some indication about the importance of the particle concentration used for the measurements.

Thickness of Organic Coating Layers. In the following, we focus on the polymer-coated particles according to our own procedure (Tables 2 and 3). The mean value of all our different methods for the effective diameters of polymer-coated CdSe/ZnS is $<d_{eff,gel}, (d_{eff,FCS}), d_{eff,SEC}, d_{eff,Therm}> = <14.4, 12.6, (19.5), 12.2> = 13.1 \pm 1.2$ nm (14.7 ± 3.4 nm with the value obtained with FCS), and, for Au nanoparticles, it is $<d_{eff,gel}, d_{eff,SEC}, d_{eff,Therm}> = <12.5, 11.6> = 12.0 \pm 0.6$ nm. The hard core diameter as determined by TEM is 5.3 nm for CdSe/ZnS and 4.6 nm for the Au nanoparticles. This leads to an effective thickness of the organic shell of $(13.1 - 5.3)$ nm/2 = 3.9 nm in the case of CdSe/ZnS and $(12.0 - 4.6)$ nm/2 = 3.7 nm in the case of Au. Besides the values obtained with FCS, the values derived with the other techniques correspond well, and we conclude that, after polymer coating, the effective thickness of the organic layer around the inorganic particle core is around 3.5−4.0 nm. Whereas this value for the plain polymer-coated particles seems quite reliable, the uncertainties in absolute size determination get higher the larger the molecules attached to the polymer shell are. The addition of a saturated layer of 20 kDa PEG molecules to the polymer surface increases the thickness of the organic layer by $<\Delta d_{eff,gel}, \Delta d_{eff,FCS}, \Delta d_{eff,SEC}>/2 = <(34.8 - 12.6), (34.2 - 19.4), (40.0 - 12.2)>$ nm/2 = 10.8 ± 3.3 nm in the case of the CdSe/ZnS particles.

In Table 5, the thickness of the saturated layer of the PEG molecules bound to the particle surface is compared with the effective diameter of free PEG molecules as determined by Formula 3, whereby the thickness of the PEG layer was calculated as half of the difference in diameter of the PEG-coated and plain polymer-coated particles. All obtained values for the PEG molecules bound to the nanoparticles are slightly larger than those of free PEG molecules. This finding can be explained by a more stretched configuration of the random coil of the PEG molecules when they are attached by one end to the densely occupied surface of a saturated nanoparticle, compared to the presumably more symmetric configuration of PEG molecules in free solution. In any case, the agreement demonstrates that relative increments in particle size can be determined with much higher accuracy than absolute diameters.

Conclusions

The total particle diameter can be estimated by the core diameter plus 2 times the thickness of the organic layer, which is, for simple coatings, the length of the surfactant molecule. While this eventually works well for short molecules when the length of these molecules is small compared to the particle, it becomes more complicated for longer and more complex molecules or even complex polymer (multi)layers. Here the size depends strongly on assumptions about the steric configuration of the molecules on the curved nanoparticle surface. Furthermore, the effective hydrodynamic diameter also depends on hydration: interaction of the particles with the solvent results in larger effective sizes,[57] even in the most simple case where the stabilizer molecules form a monolayer around the inorganic core. Although several studies exist in which the effective diameters of particles have been measured, most of these studies are either based on only one method or only one type of particle surface.[24,58,59] A more detailed discussion can be found in the Supporting Information.

The more molecules are attached and thus the bigger the particles become, the more unreliable size measurements are. First, the hybrid nature of the particles with a rigid inner inorganic core and a soft organic shell becomes more pronounced, which eventually leads to problems for the methods in which the measurements take place in a matrix that can compress the particles. Especially, a random coil of a linear polymer such as PEG can be easily deformed depending on the technique used for the size determination. Second, for the methods using calibration with size standards, there is the problem of a lack of appropriate size standards of sufficient size. Third, the charge composition can also change (in particular, if positively charged molecules are attached), which leads to the failure of gel electrophoresis but might also affect the other methods.

Thus, depending on the actual particle nature but also on the intended application, the adequate method for measurement has

to be chosen with great care. For instance, when particles are designed to enter into pores, the diameter determined by gel electrophoresis or SEC might be better suited than the one determined by free diffusion.

Different methods to measure effective sizes of colloidal nanoparticles are based on different physical principles, resulting in deviations of the resulting particle diameters between the different methods. This finding is not surprising and points to a general problem and uncertainty: although within one measurement effective diameters can be determined in a consistent way with relatively small errors, bigger discrepancies arise between values obtained with different methods. This implies that the comparison with control samples (e.g., before and after a certain conjugation step) remains indispensable and that all derived absolute numbers for nanoparticle diameters have to be considered with care.

Acknowledgment. The authors would like to thank Andrea Rauh for help with the analysis of the TEM images and Dr. Fritz Simmel and Prof. Dr. Joachim Rädler for helpful discussion. The authors are grateful to Prof. Dr. Joachim Rädler for providing the FCS setup and expertise of his institute. Quantum dots with organic and streptavidin coating were a gift from Quantum Dots Corp. The project was funded by the Deutsche Forschungsgemeinschaft (DFG Emmy Noether Grant) and the European Union (STREP NanoInteract grant). M.Z. is grateful for a fellowship from the International Doctorate Program Nano-Bio-Technology at the Center for Nanoscience.

Supporting Information Available: Details of particle synthesis, TEM analysis, gel electrophoresis, SEC, FCS, and thermophoresis experiments, and a comparison of the different methods. This material is available free of charge via the Internet at http://pubs.acs.org.

References and Notes

(1) Scher, E. C.; Manna, L.; Alivisatos, A. P. *Philos. Trans. R. Soc. London, Ser. A* **2002**, *361*, 241.
(2) Kumar, S.; Nann, T. *Small* **2006**, *2*, 316.
(3) Kudera, S.; Carbone, L.; Zanella, M.; Cingolani, R.; Parak, W. J.; Manna, L. *Phys. Status Solidi C* **2006**, *203*, 1329.
(4) Templeton, A. C.; Wuelfing, W. P.; Murray, R. W. *Acc. Chem. Res.* **2000**, *33*, 27.
(5) Michalet, X.; Pinaud, F. F.; Bentolila, L. A.; Tsay, J. M.; Doose, S.; Li, J. J.; Sundaresan, G.; Wu, A. M.; Gambhir, S. S.; Weiss, S. *Science* **2005**, *307*, 538.
(6) Pellegrino, T.; Kudera, S.; Liedl, T.; Javier, A. M.; Manna, L.; Parak, W. J. *Small* **2005**, *1*, 48.
(7) Fischer, C.-H.; Lilie, J.; Weller, H.; Katsikas, L.; Henglein, A. *Ber. Bunsen-Ges. Phys. Chem.* **1989**, *93*, 61.
(8) Fischer, C.-H.; Weller, H.; Katsikas, L.; Henglein, A. *Langmuir* **1989**, *5*, 429.
(9) Eychmüller, A.; Katsikas, L.; Weller, H. *Langmuir* **1990**, *6*, 1605.
(10) Wu, M. X.; Liu, H.; Liu, J.; Haley, K. N.; Treadway, J. A.; Larson, J. P.; Ge, N.; Peale, F.; Bruchez, M. P. *Nat. Biotechnol.* **2003**, *21*, 41.
(11) Pellegrino, T.; Manna, L.; Kudera, S.; Liedl, T.; Koktysh, D.; Rogach, A. L.; Keller, S.; Rädler, J.; Natile, G.; Parak, W. J. *Nano Lett.* **2004**, *4*, 703.
(12) Luccardini, C.; Tribet, C.; Vial, F.; Marchi-Artzner, V.; Dahan, M. *Langmuir* **2006**, *22*, 2304.
(13) Nann, T. *Chem. Commun.* **2005**, *2005*, 1735.
(14) Sperling, R. A.; Pellegrino, T.; Li, J. K.; Chang, W. H.; Parak, W. J. *Adv. Funct. Mater.* **2006**, *16*, 943.
(15) Zanchet, D.; Moreno, M. S.; Ugarte, D. *Phys. Rev. Lett.* **1999**, *82*, 5277.
(16) Fink, J.; Kiely, C. J.; Bethell, D.; Schiffrin, D. J. *Chem. Mater.* **1998**, *10*, 922.
(17) Yonezawa, T.; Onoue, S.-y.; Kimizuka, N. *Langmuir* **2001**, *17*, 2291.
(18) Zanchet, D.; Micheel, C. M.; Parak, W. J.; Gerion, D.; Alivisatos, A. P. *Nano Lett.* **2001**, *1*, 32.
(19) Parak, W. J.; Pellegrino, T.; Micheel, C. M.; Gerion, D.; Williams, S. C.; Alivisatos, A. P. *Nano Lett.* **2003**, *3*, 33.
(20) Pellegrino, T.; Sperling, R. A.; Alivisatos, A. P.; Parak, W. J. *J. Biomed. Biotechnol.*, submitted for publication, 2007.
(21) Pinaud, F.; King, D.; Moore, H.-P.; Weiss, S. *J. Am. Chem. Soc.* **2004**, *126*, 6115.
(22) Song, X.; Li, L.; Qian, H.; Fang, N.; Ren, J. *Electrophoresis* **2006**, *27*, 1341.
(23) Nehilla, B. J.; Vu, T. Q.; Desai, T. A. *J. Phys. Chem. B* **2005**, *109*, 20724.
(24) Pons, T.; Uyeda, H. T.; Medintz, I. L.; Mattoussi, H. *J. Phys. Chem. B* **2006**, *110*, 20308.
(25) Wilcoxon, J. P.; Provencio, P. P. *J. Phys. Chem. B* **2005**, *109*, 13461.
(26) Siebrands, T.; Giersig, M.; Mulvaney, P.; Fischer, C.-H. *Langmuir* **1993**, *9*, 2297.
(27) Fischer, C.-H.; Giersig, M.; Siebrands, T. *J. Chromatogr., A* **1994**, *670*, 89.
(28) Fischer, C.-H.; Kenndler, E. *J. Chromatogr., A* **1997**, *773*, 179.
(29) Wei, G.-T.; Liu, F.-K. *J. Chromatogr., A* **1999**, *836*, 253.
(30) Wei, G.-T.; Liu, F.-K.; Wang, C. R. C. *Anal. Chem.* **1999**, *71*, 2085.
(31) Jimenez, V. L.; Leopold, M. C.; Mazzitelli, C.; Jorgenson, J. W.; Murray, R. W. *Anal. Chem.* **2003**, *75*, 199.
(32) Al-Somali, A. M.; Krueger, K. M.; Falkner, J. C.; Colvin, V. L. *Anal. Chem.* **2004**, *76*, 5903.
(33) Krueger, K. M.; Al-Somali, A. M.; Falkner, J. C.; Colvin, V. L. *Anal. Chem.* **2005**, *77*, 3511.
(34) Kuga, S. *J. Chromatogr., A* **1981**, *206*, 449.
(35) Holtzhauer, M.; Rudolph, M. *J. Chromatogr., A* **1992**, *605*, 193.
(36) Magde, D.; Elson, E.; Webb, W. W. *Phys. Rev. Lett.* **1972**, *29*, 705.
(37) Eigen, M.; Rigler, R. *Proc. Natl. Acad. Sci. U.S.A.* **1994**, *91*, 5740.
(38) Schwille, P.; Bieschke, J.; Oehlenschläger, F. *Biophys. Chem.* **1997**, *66*, 211.
(39) Krichevsky, O.; Bonnet, G. *Rep. Prog. Phys.* **2002**, *65*, 251.
(40) Zhang, P.; Li, L.; Dong, C.; Qian, H.; Ren, J. *Anal. Chim. Acta* **2005**, *546*, 46.
(41) Liedl, T.; Keller, S.; Simmel, F. C.; Rädler, J. O.; Parak, W. J. *Small* **2005**, *1*, 997.
(42) Doose, S.; Tsay, J. M.; Pinaud, F.; Weiss, S. *Anal. Chem.* **2005**, *77*, 2235.
(43) Dong, C.; Bi, R.; Qian, H.; Li, L.; Ren, J. *Small* **2006**, *2*, 534.
(44) Jin, T.; Fujii, F.; Yamada, E.; Nodasaka, Y.; Kinjo, M. *J. Am. Chem. Soc.* **2006**, *128*, 9288.
(45) Duhr, S.; Arduini, S.; Braun, D. *Eur. Phys. J. E* **2004**, *15*, 277.
(46) Duhr, S.; Braun, D. *Phys. Rev. Lett.* **2006**, *96*, 168301.
(47) Duhr, S.; Braun, D. *Proc. Natl. Acad. Sci. U.S.A.* **2006**, *103*, 19678.
(48) Reiss, P.; Bleuse, J.; Pron, A. *Nano Lett.* **2002**, *2*, 781.
(49) Dabbousi, B. O.; Rodriguez-Viejo, J.; Mikulec, F. V.; Heine, J. R.; Mattoussi, H.; Ober, R.; Jensen, K. F.; Bawendi, M. G. *J. Phys. Chem. B* **1997**, *101*, 9463.
(50) Yu, W. W.; Qu, L.; Guo, W.; Peng, X. *Chem. Mater.* **2003**, *15*, 2854.
(51) Brust, M.; Walker, M.; Bethell, D.; Schiffrin, D. J.; Whyman, R. *J. Chem. Soc., Chem. Commun.* **1994**, 801.
(52) Mori, S.; Barth, H. G. *Size Exclusion Chromatography*; Springer: New York, 1999.
(53) Hagel, L. Gel Filtration. In *Protein Purification. Principles, High Resolution Methods and Applications*, 2nd ed.; Janson, J.-C., Ryden, L., Eds.; John Wiley & Sons: New York, 1998.
(54) Amediek, A.; Haustein, E.; Scherfeld, D.; Schwille, P. *Single Mol.* **2002**, *3*, 201.
(55) Fee, C. J.; Alstine, J. M. V. *Bioconjugate Chem.* **2004**, *15*, 1304.
(56) Sartori, R.; Sepulveda, L.; Quina, F.; Lissi, E.; Abuin, E. *Macromolecules* **1990**, *23*, 3878.
(57) Xu, X.; Rosi, N. L.; Wang, Y.; Huo, F.; Mirkin, C. A. *J. Am. Chem. Soc.* **2006**, *128*, 9286.
(58) Smith, A. M.; Duan, H.; Rhyner, M. N.; Ruan, G.; Nie, S. *Phys. Chem. Chem. Phys.* **2006**, *8*, 3895.
(59) Yu, W. W.; Chang, E.; Falkner, J. C.; Zhang, J.; Al-Somali, A. M.; Sayes, C. M.; Johns, J.; Drezek, R.; Colvin, V. L. *J. Am. Chem. Soc.* **2007**, *129*, 2871.

R. A. Sperling[1], T. Liedl[1], S. Duhr[1], S. Kudera[1], M. Zanella[1], C.-A. J. Lin[1,2], W. H. Chang[2], D. Braun[1], W. J. Parak[1*]

Size determination of (bio-) conjugated water-soluble colloidal nanoparticles - a comparison of different techniques

[1]Center for Nanoscience, Ludwig Maximilians Universität, München, Germany
[2]Center for Nano Bioengineering and R&D Center for Membrane Technology, Chung Yuan Christian University, Taiwan, R.O.C.
[*] Corresponding author: Wolfgang.Parak@physik.uni-muenchen.de

Supporting Information[1]

[1] The idea of this Supporting Information is to provide the interested reader with a detailed account of the raw data measured. It is by far not meant to be read from the beginning until the end. In contrast, due to the index on this page the reader can access the piece of information that he/she is interested in. All important and relevant information is included in the main paper and this Supporting Information expands on further details to specific points. We have taken great care to describe here everything as detailed as possible, so that a documentation about all experimental and evaluation steps is given.

I) Particle synthesis

I.1) Synthesis protocol for CdSe and CdSe/ZnS particles

Chemicals: Tri-n-octylphosphine oxide (TOPO, 99%, #22.330-1), tri-n-octylphosphine (TOP, 90%, 11.785-4), hexadecylamine (HDA, 90%, #H7.40-8), nonanoic acid (97%, #N5502), CdO (99.99+%, #20.289-4), Se (99.99%, #22.986-5), diethylzinc (#40.602-3), hexamethyldisilthiane ($(TMS)_2S$, #28.313-4), octanoic acid (>99.5%, #15.375-3), octanethiol (98.5+%, #47.183-6), octylamine (99%, #O580-2) were purchased from Sigma-Aldrich. Tri-n-butylphosphine (TBP, 99%, #15-5800) was purchased from Strem. Dodecylphosphonic acid (DDPA, technical grade) was purchased from Polycarbon Industries. A stock solution of Se in TBP was prepared as 20%wt.

Synthesis of CdSe nanoparticles: The synthesis of CdSe nanoparticles was performed according to the procedure described by Reiss et al.[1]: 5.76 g HDA, 2.26 g TOPO, 2.20 g DDPA and 0.50 g CdO were mixed in a 50 mL flask. The powders were molten under nitrogen and then degassed for ca. 20 minutes at 130 °C. Under nitrogen, the solution was heated to 290 – 310 °C until the color of the solution changed from brownish to transparent. The solution should not reach a temperature higher than ca. 320 °C, as at this temperature HDA will evaporate. Once the solution was clear, 1 mL TBP was injected into the flask and the remaining undissolved CdO was removed from the walls of the flask by agitating the flask. The temperature was then stabilized at 270°C and 1.6 g of Se:TBP was injected rapidly into the solution. After ca. 1 minute the solution showed a light yellow color indicating the nucleation of CdSe particles. The reaction was allowed to proceed for 20 minutes, and then it was stopped by removing the heat-source. The particles as prepared by now could not be directly precipitated by methanol as they would be stuck in a polymer-gel that presumably forms out of the free surfactants (mainly DDPA). In other words, the particles would be trapped in a big amount of organic material. In order to obtain free particles the gel has to be removed, which will be described in the following. Unfortunately there is no procedure available which works always and there is no other way than "playing". We try to describe strategies to remove the gel to the best of our knowledge.

The general strategy to remove gel bound to the surface of the particles is to add nonanoic acid which prevents formation of chains of DDPA-molecules. DDPA has two binding sites for Cd, as well as Cd has two binding sites for DDPA. Apparently for steric reasons a Cd ion cannot saturate both bonds of the DDPA. Nonanoic acid in turn has only one binding site for Cd, thus $(NNA)_2Cd$ is formed and the formation of the gel is suppressed. In practise, after the reaction was stopped the solution was cooled down to ca. 100°C and 3 mL of toluene and 5 mL of nonanoic acid were added to the flask and the product was precipitated rapidly by addition of methanol as soon as it had cooled down to below 40-50 °C. The precipitate was dissolved in 5-10 mL toluene. Apart from the approach described above, there are several slightly different approaches to extract the particles from the gel. Which of these approaches yields the best results depends on the nature of the sample and certainly also on the exact composition of the growth solution, i.e. on the type of impurity and thus ultimately on the producer of the individual compounds. Generally one should try to wash the sample as fast as possible after the reaction. On the other hand, the methanol for the precipitation should not be added at a too high temperature. All approaches used in our group involve the addition of a solvent such as toluene or chloroform, nonanoic acid, and the precipitation of the particles with methanol. In the easiest case, it is sufficient to simply add a considerable amount (5-10 mL) of nonanoic acid to the reaction solution when it has cooled down to ca. 100 °C and then precipitate the particles from

the solution. Additionally the solution can be kept at ca. 90 °C after the addition of the nonanoic acid until the precipitation (for ca. one hour). This approach bears the danger to destroy the size distribution of the sample. In most cases we observed an enlargement of the fluorescence peak, and even the appearance of a second fluorescence line. We could show that in the presence of nonanoic acid new CdSe-particles can nucleate even at that low temperature [2].

A second approach is to first precipitate the particles out of the growth solution by addition of methanol. In this case, a sufficient amount (ca. 5 mL) of toluene has to be added to the warm (ca. 80 °C) growth solution in order to prevent solidification of the organic material. Generally this yields a huge precipitate that is hard to dissolve in toluene. From this gel, the particles can be extracted by the addition of toluene and nonanoic acid in equal parts. By heavy agitation and eventual moderate heating of the sample the gel can be dispersed in the solvent. Subsequent centrifugation yields a precipitate of the same size as the first precipitate and a very clear supernatant that is now colored red, indicating the presence of nanoparticles. The supernatant can be transferred carefully to another vial. By repetition of this process more particles can be extracted from the gel. In this process it makes a difference if one uses toluene or chloroform. Toluene is lighter than the gel, thus in the centrifugation the gel is found as the lower phase. When chloroform is used, the lower phase is the clear gel-free phase, and therefore it is fairly difficult to extract this phase from the vial without polluting it with the gel.

In all cases, once a gel-free solution with free particles had been obtained, this had to be washed to remove the residual free reactants. To do so, the particles were precipitated twice by addition of methanol to the solution and subsequent re-dissolution in toluene. Methanol for the precipitation was added until the solution turned completely cloudy. Generally this was obtained when the ratio solvent-to-nonsolvent was roughly 1:1. When a shell growth on the CdSe-core is intended it is of advantage to dissolve the final sample in chloroform, as this solvent can be easily evaporated from the growth-solution for the shell-growth. At this point the CdSe cores are freely dispersed in chloroform. To characterize the samples absorption- and fluorescence-spectra, and transmission-electron microscopy (TEM) images were recorded. These data are shown in Figure SI-I.1.

Growth of a ZnS shell onto the CdSe particles: In order to increase the fluorescence intensity of the CdSe-nanoparticles, a shell of a different material is grown around the particles. This shell consists of the ZnS, which has a wider bandgap than CdSe and thus enhances the confinement of the exciton in the volume of the CdSe core. The synthesis is carried out according to the protocol described by Dabboussi et al. [3]. In detail, a typical protocol reads as follows: 6 g TOPO (technical grade, purchased from Sigma-Aldrich, #34.618-7) was molten and degassed at 130 °C. Then 1.5 mL TOP were added and ca. a sixth of the yield of the CdSe-synthesis was added in chloroform and the solution was degassed again to remove the chloroform. Then the particles were heated to 160 °C and a readily prepared stock-solution of Zn and S precursors (5.73 g TBP, 0.76 g diethylzinc, 0.22 g $(TMS)_2S$) was added dropwise to the particles. After each addition of 0.5 mL of stock solution the quantum yield of an aliquot was measured with respect to the initial bare CdSe-sample. The growth of the shell was stopped by cooling down the solution when the sample had just passed the maximum quantum yield. 5-10mL of butanol were added to prevent solidification of the TOPO. The sample was washed twice by repeated precipitation with methanol and subsequent re-dissolution in chloroform. At this point the CdSe/ZnS core/shell particles are freely dispersed in chloroform. To characterize the samples absorption- and fluorescence-spectra, and transmission-electron microscopy (TEM) images were recorded. These data are shown in Figure SI-I.1 and Table SI-I.1.

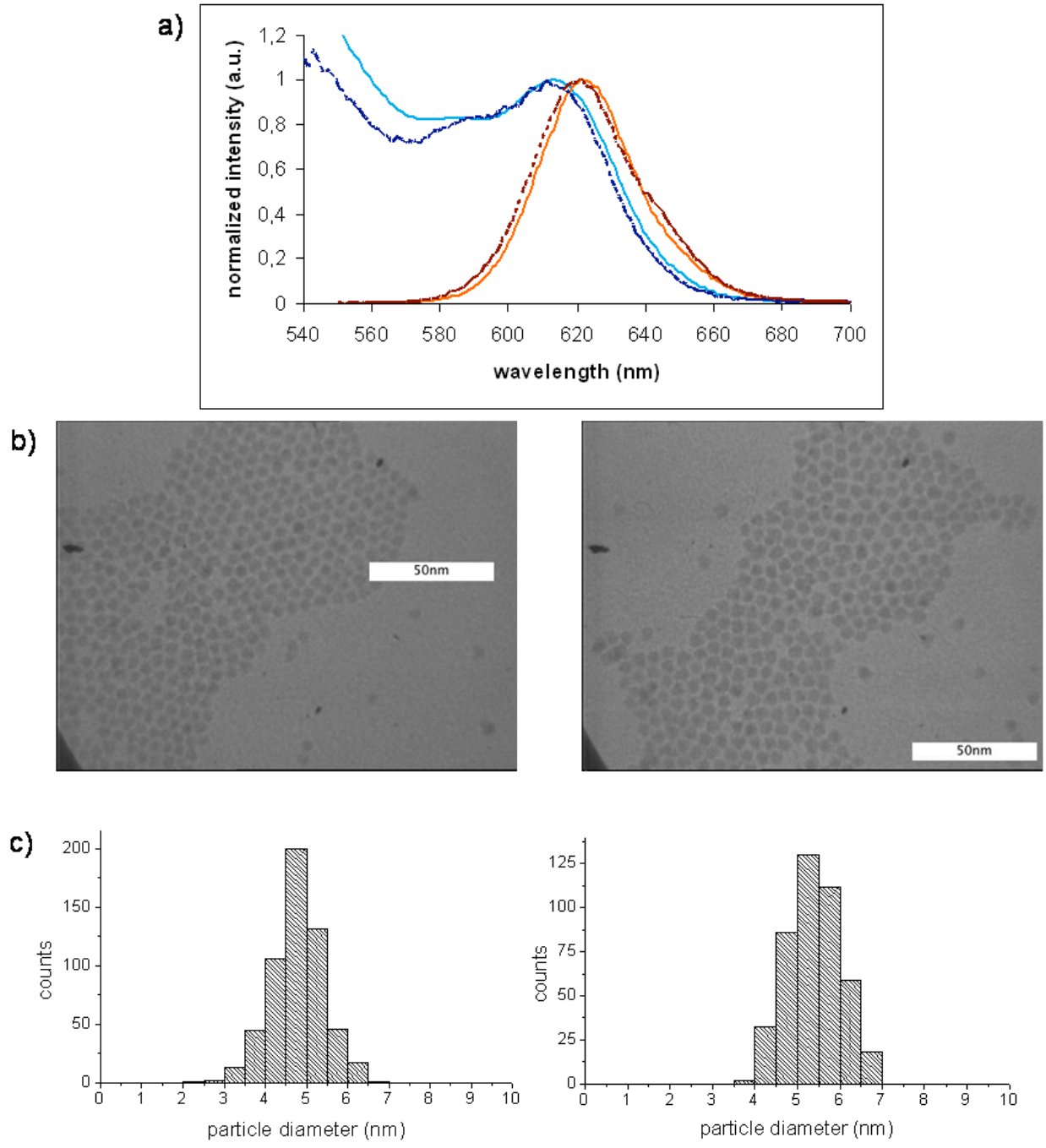

Figure SI-I.1: Characterization of hydrophobic CdSe and CdSe/ZnS particles that are soluble in chloroform. a) Absorption (blue) and emission spectra (red) of CdSe (dark color) and CdSe/ZnS (light color) particles. The wavelengths of the absorption of the first excition peaks are 610 nm and 614 nm and the wavelengths of the maximum of the emission peak are 620 nm and 624 nm for CdSe and CdSe/ZnS particles, respectively. b) Transmission electron microscopy (TEM) images for CdSe (left) and CdSe/ZnS (right) particles. The scale bars correspond to 50 nm. c) Histograms of the size distribution of the diameter <d> of the inorganic CdSe (left, <d> = 4.7 nm) and CdSe/ZnS (right, <d> = 5.3 nm) particles as obtained from the TEM images.

I.2) Synthesis protocol for CdTe particles

Before the actual synthesis, a stock solution of Tellurium in tri-n-octylphosphine (TOP, 90% Sigma) was prepared: 1 g Te was mixed with 9 g TOP under nitrogen. In order to completely dissolve the Te, the mixture was heated to 200 °C for more than one hour. Residual undissolved Te was removed by centrifugation.

The synthesis was adapted from Yu et al. [4]. 3.70 g tri-n-octylphosphine oxide (TOPO, 99% Sigma), 0.270g octadecyl phosphonic acid (ODPA, Polycarbon Industries) and 0.051 g CdO (99.99+%, Sigma-Aldrich) were mixed in a 50 ml flask. The mixture was melted under nitrogen and degassed for ca. 20 minutes at 130 °C. The brown solution was then heated to above 340 °C under nitrogen until it turned transparent. To this clear solution, 1 mL of TOP was added. The temperature was then stabilized at 370 °C and the reaction was started by the fast injection 0.550 g of the Te:TOP solution. Nucleation was observed after ca. 10 seconds by a sudden darkening of the solution. The particles were allowed to grow for 90 seconds. The reaction was stopped by removing the heating mantle from the flask. When the solution had reached a temperature below 100 °C, 3 mL of anhydrous toluene was added to the solution to prevent solidification of the solvents. The solution was transferred to a glove-box and washed twice by repeated precipitation with anhydrous methanol and subsequent redissolution in toluene. The purified sample was dissolved in chloroform. At this point the CdTe core particles are freely dispersed in chloroform. To characterize the samples absorption- and fluorescence-spectra, and transmission-electron microscopy (TEM) images were recorded. These data are shown in Figure SI-I.2 and Table SI-I.1.

particle	λ_{abs} [nm]	λ_{em} [nm]
CdSe	610	620
CdSe/ZnS	614	624
CdTe	668	688

Table SI-I.1: Wavelength of the first exciton peak (λ_{abs}) in the absorption spectra and the corresponding wavelength of the maximum in the fluorescence emission (λ_{em}) for the CdSe, CdSe/ZnS, and CdTe particles that have been used in this study.

183

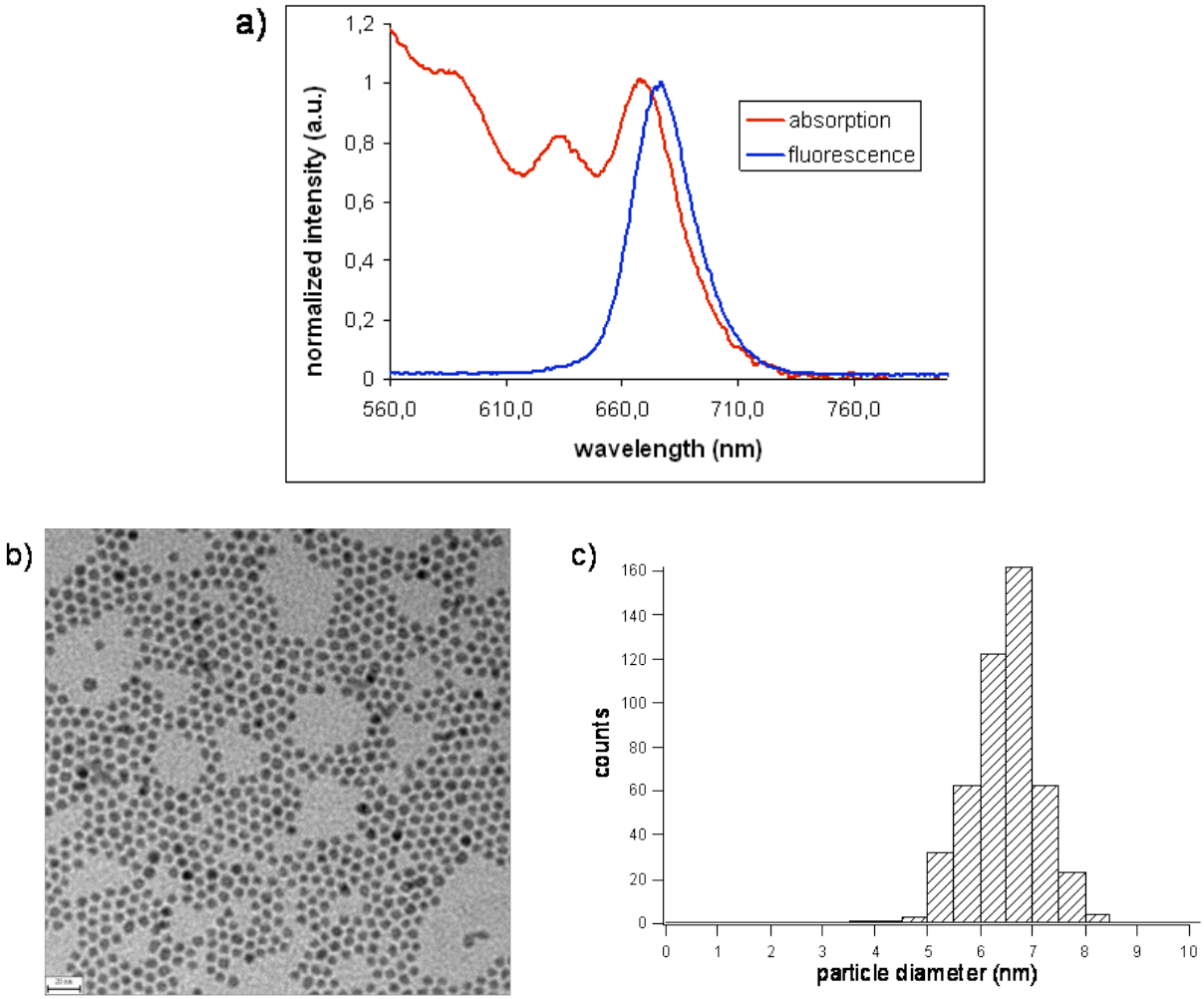

Figure SI-I.2: Characterization of hydrophobic CdTe particles that are soluble in chloroform. a) absorption (blue) and emission spectra (red) of CdTe particles. The wavelength of the absorption of the first excition peak is 668 nm and the wavelength of the maximum of the emission peak is 677 nm. b) Transmission electron microscopy (TEM) image for CdTe particles. The scale bar corresponds to 20 nm. c) Histogram of the size distribution of the diameter <d> of the inorganic CdTe particles (<d> = 6.3 nm) as obtained from the TEM images.

I.3) Synthesis protocol for Au particles

Colloidal Au nanocrystals were synthesized according to standard protocols [5,6]. The detailed procedure as used for the particles in this report is based on these initial publications and has been published in our previous manuscripts [7,8]. All glassware was carefully cleaned in a KOH/isopropanol bath and carefully rinsed with water before use. All reactions were carried out at room temperature under ambient conditions.

In a beaker, 2.17 g of tetraoctylammonium bromide ($(C_8H_{17})_4NBr$ 98 %, Sigma-Aldrich #294136) were dissolved in 80 ml of HPLC grade toluene (C_6H_5Me) and transferred into a 250 ml separation funnel. 300 mg tetrachloroauric acid (hydrogen tetrachloroaurate (III): $HAuCl_4 \bullet xH_2O$ 99.9 %, Alfa Aesar #12325) was weighted into a 20 ml vial, 25 ml Millipore water was added in three washing steps to yield a yellow translucent solution which was transferred to the separation funnel. The funnel was shaken for about 5 minutes in order to transfer the $AuCl_4^-$ ions into the organic phase. During this time the initially colorless toluene phase ("tol", on the top) turned dark red and the initially yellow aqueous phase ("aq", on the bottom) turned colorless, indicating the formation of tetraoctylammonium-gold ion pairs in the organic phase:

$$AuCl_4^-(aq) + N(C_8H_{17})_4^+(tol) \rightarrow N(C_8H_{17})_4^+ AuCl_4^-(tol)$$

The aqueous phase was discarded and the toluene phase was transferred to a 250 ml round flask. In a beaker, 334 mg of sodium borohydride ($NaBH_4$ 98 %, Sigma-Aldrich #452882) was dissolved in 25 ml of Millipore water under vigorous stirring by means of a stirring magnet. The appearing small bubbles indicate the formation of hydrogen:

$$BH_4^-(aq) + 3H_2O \rightarrow B(OH)_3(aq) + 2H_2(\uparrow) + e^-$$

This clear solution was then pipetted dropwise within one minute into the red solution of tetraoctylammonium-gold in toluene. Upon stirring for few seconds, the color changed from red to red-violet. This color change indicates the nucleation of gold clusters mediated by sodium borohydride. The residual sodium borohydride in solution reduces the remaining gold ions, providing additional monomers for the growth of the nuclei

$$nAuCl_4^-(tol) + 3ne^- \rightarrow 4nCl^-(aq) + Au_n$$

The Br^- ions are supposed to be attached on the surface of the gold clusters, attracting again the $N(C_8H_{17})_4^+$ counterions [6]. The solution was stirred for 1 hour, transferred to the cleaned separation funnel and 25 ml of 10 mM HCl were added in order to remove the excess sodium borohydride. The funnel was shaken for 1 minute and the aqueous phase on the bottom was discarded. 25 ml of 10 mM NaOH were added to the funnel to remove the excess acid and after shaking for 1 minute the aqueous phase was again discarded. Finally, 25 ml of Millipore water were added to remove excess ions, the funnel was shaken for 1 minute and the aqueous phase was discarded. This last washing step was repeated 2 more times. The aqueous phase and the eventually remaining emulsion were discarded. The organic phase was then transferred to a 100 ml round flask and stirred over night to allow the particles to Ostwald ripen to a thermodynamically stable average size and size distribution.

After the synthesis, a surfactant exchange procedure was carried out. For this, 10 ml of dodecanethiol ($C_{12}H_{25}SH$ 98 %, Sigma-Aldrich #471364) were added to the Au nanocrystals in

toluene. The solution was heated to 65 °C and stirred for 2 – 3 hours. During this process the mercapto groups of the dodecanethiol molecules displace the Br^- and tetraoctylammonium ions and yield dodecanethiol capped Au nanocrystals. The solution was then cooled to room temperature and split into several half–filled 20 ml vials.

The Au nanocrystals were precipitated by the addition of about the same amount of methanol, followed by centrifugation for 2 min. After discarding the clear supernatant, the precipitate of each vial was dissolved in little toluene and these samples were pooled, yielding a total volume of 11 ml. This and the following precipitation steps removed the excess dodecanethiol molecules. The nanocrystals were then centrifuged for two minutes to precipitate larger aggregates, the supernatant was taken out and precipitated again by the addition of about 6 ml of methanol followed by centrifugation. The slightly colored supernatant was discarded and the precipitate was redissolved in 4 ml of toluene, yielding a solution of dodecanethiol capped Au particle with a concentration of usually 20 – 25 µM. The optical absorption spectrum, a TEM image and the size distribution of the particles are shown in Figure SI-1.3. The particle concentration was determined from the absorption at the plasmon peak (at around 515 nm) by using a molar extinction coefficient of $8.63 \cdot 10^6$ $M^{-1}cm^{-1}$. From the size-distribution of the TEM images a mean diameter of the inorganic Au-core of <d> = 4.6 nm was determined. (see Table SI-I.2).

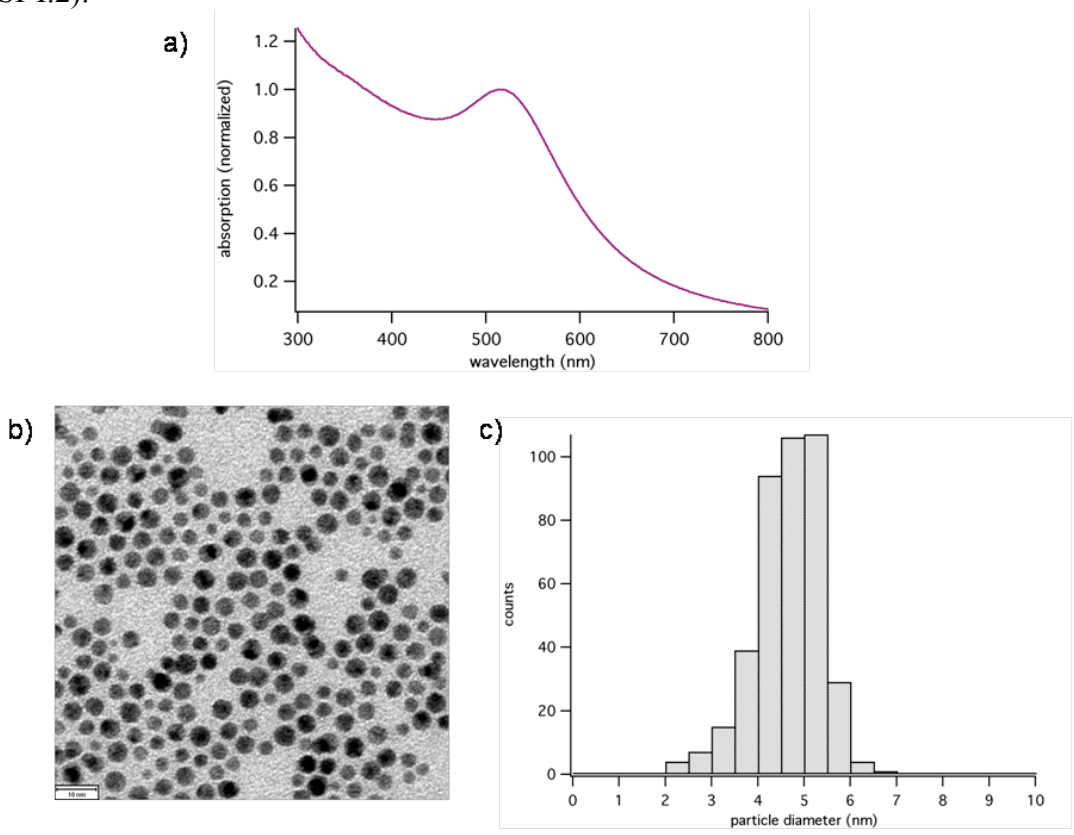

Figure SI-1.3: Characterization of hydrophobic Au particles that are soluble in chloroform. a) absorption spectra of Au particles. The wavelength of the plasmom peak is 515 nm. b) Transmission electron microscopy (TEM) image for Au particles. The scale bar corresponds to 10 nm. c) Histogram of the size distribution of the diameter <d> of the inorganic Au particles (<d> = 4.6 nm) as obtained from the TEM images.

I.4) Polymer coating to convert hydrophobic into hydrophilic particles

This protocol has been adapted from previously published reports [7,8]. As described therein, 100 monomer units of an amphiphilic polymer (poly(maleic anhydride alt-1-tetradecene), Sigma-Aldrich # 452513) and 10 crosslinker molecules (bis(hexamethylene)triamine, Sigma-Aldrich # 14506) were added per nm2 of the total surface A of the hydrophobically capped nanoparticles (as synthesized as described in Sections I.1 - I.3). For all particle samples, this total surface A of the particles was estimated by

$$A = V\ c\ N_A \cdot {}^4/_3\ \pi\ (r + r_{surf})^3$$

with the volume V of the particle solution, the particle concentration c, Avogardro's number N_A, the hardcore particle radius r and the length of the surfactant molecules r_{surf}. Besides the length of the surfactant molecules, that was assumed as r_{surf} = 1.1 nm for all particles[2], the inorganic core diameters were assumed for the different particle species as listed in Table SI-I.2.

	<d> (nm)	<r> (nm)	$<r + r_{surf}> = <r_{eff}>$ (nm)	ε ($cm^{-1}M^{-1}$)
CdSe/ZnS	5.3	2.7	3.8	$4.79 \cdot 10^5$
CdTe	4.8	2.4	3.5	$2.79 \cdot 10^5$
Au	4.6	2.2	3.3	$8.63 \cdot 10^6$

Table SI-I.2: Diameters d, radii r, and extinction coefficients ε of the CdSe/ZnS, CdTe, and Au particles used in this study. <d> and <r> = <d>/2 always refer to the diameter and radius of the inorganic part of the nanoparticle, e.g. the CdSe/ZnS hardcore, the CdTe hardcore, and the Au hardcore. Actually the CdSe/ZnS hardcore is composed out of an inorganic CdSe core and an inorganic ZnS shell around it, but in this context we refer to the whole inorganic part as "core". The most straightforward way to determine <d> is to make TEM images of the particles and to measure the size of the inorganic particles from them (the organic surfactant shell does not give contrast and is thus invisible). For the particles used in this study the following values were obtained: CdSe/ZnS: $<d>_{TEM}$ = 5.3 nm (see Figure SI-I.1c), CdTe: $<d>_{TEM}$ = 6.3 nm (see Figure SI-I.2c), Au: $<d>_{TEM}$ = 4.6 nm (see Figure SI-I.3c). Since recording TEM images is some kind of laborious in general we derived the particles diameters not from TEM images, but either from the absorption spectra or by guessing. In the case of CdSe/ZnS and CdTe we typically derived the inorganic particle diameters by a calibration curve [9], in which the diameter of CdSe (!) and CdTe particles is listed versus the extinction coefficient of the particles at the first exciton peak. The values in this table for <d> have been obtained with this method: $<d>_{abs}$ = 5.4 nm for CdSe/ZnS and 4.8 nm for CdTe (see also Table SI-II.1). The described Au synthesis yielded typically particles with an inorganic diameter of <d> = 4.0 nm and we just assumed this value, also the actual value as measured by TEM can vary between different syntheses. Since the polymer coating procedure is relatively uncritical to the amounts of used polymer and crosslinker we therefore often use the guessed values, instead of measuring the actual values by TEM. The additional increase in radius due to the layer of organic surfactant molecules on the particle is roughly assumed to be r_{surf} = 1.1 nm, regardless of the actually used surfactant molecules. The effective particle diameter is the diameter of the inorganic core plus two times the thickness of the surfactant layer: $<d_{eff}> = <d> + 2\ r_{surf}$. This corresponds to the effective particle diameter before (!) the polymer coating (see also Table SI-II.1).

[2] It has to be pointed out that for a refined model, the length of the surfactant can be estimated more precisely for the actual molecule, e.g. r_{surf}(dodecanethiol) ≈ 1.6 nm, r_{surf}(TOPO) ≈ 1.2 nm, and some correction for the geometric orientation of the molecules in respect to the particle surface. However, it was found that the polymer coating procedure is quite robust in regard to small changes, it worked well for all particles with the assumed value of r_{surf} = 1.1 nm.

For the polymer coating, all particles were dispersed in chloroform and the concentration was determined by the absorption spectra with the extinction coefficients from Table SI-I.2. Typically, the molar particle concentration of the stock solutions as used for the polymer coating was in the range of 5 – 20 µM. Of the polymer (poly(maleic anhydride alt-1-tetradecene, Sigma-Aldrich # 452513), a stock solution of 200 mM in regard of the monomer units (294.4 g/mol) in chloroform was prepared. The crosslinker (bis(hexamethylene)triamine, Sigma-Aldrich # 14506) was prepared as a 20 mM solution in chloroform.

The amount of polymer corresponding to 100 monomers/nm^2 was added to the nanoparticles in a round flask and the solvent was evaporated within 5 minutes at room temperature under reduced pressure. When the sample was dried, the amount of crosslinker corresponding to 10 molecules/nm^2 was diluted in some ml additional chloroform and added to the nanoparticles. The flask was shaken until all particles were redissolved in the solution, prior to the evaporation of the solvent within 5 minutes. The flask with the dried sample was vented and evacuated two times to assure that all solvent was evaporated[3]. Then, 10 – 20 ml of 50 mM sodium borate buffer pH 9 (SBB) or 0.5 x TBE (Sigma-Aldrich # T3919) was added and the flask was shaken until all solid had redissolved to yield a clear solution.

The nanoparticle solution was filtered through a syringe filter with a 0.22 µm CME membrane (Millipore, Roth #P818.1), and washed by diafiltration with SBB on Centriplus YM100 (Millipore # 4424) or Amicon-15 100k (Millipore # UFC910096) ultrafiltration devices.

Not all added polymer is wrapped around the particles. Some unbound polymer molecules can form polymer micells. These are stable assemblies of several (crosslinked) polymer molecules, in which the hydrophobic tails point towards the inside of the micell and the hydrophobic backbones are exposed to the outside, see Figure SI-I.4.

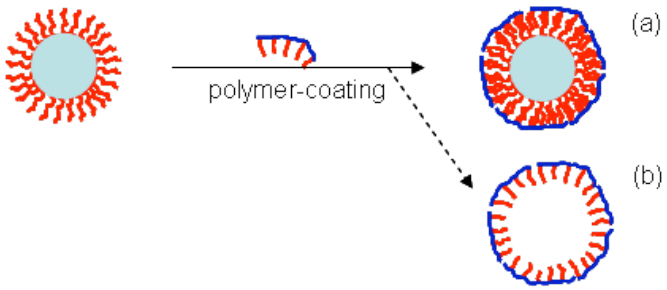

Figure SI-I.4: During the polymer coating procedure besides polymer coated particles (a) also polymer micells are formed (b). They can be thought as "empty" polymer shells without embedded inorganic particles. As the polymer shell around the particles also the micells are bound together by hydrophobic interaction. The hydrophobic tails of the amphiphilic polymer are drawn in red, the hydrophilic backbone in blue, the hydrophobic surfactant changes bound to the surface of the inorganic nanoparticle in red, and the nanoparticle in grey.

[3] The polymer coating did not work properly in case there was still some chloroform left.

I.5) Gel filtration chromatography

After the polymer-coating, the nanoparticles were routinely purified on a size exclusion gel filtration column (Sephacryl S-300 HR, GE Healthcare, #17-0599-10) connected to a standard HPLC system (Agilent 1100). The mobile phase was 50 mM sodium borate buffer with 100 mM NaCl, pH 9.0. The flow rate was set to 0.5 ml/min. The setup and the detailed procedure is described in Paragraph SI-IV. Usually, 1 ml of sample was injected in each run, the fractions containing the nanoparticles as observed by the absorption were collected and pooled, and the vials containing the front and tail fractions were discarded. Figure SI-I.5 shows examples of the elution profiles of CdSe/ZnS, CdTe, and Au particles directly after the polymer coating as described in Section I.4. The nanoparticles have a continuous absorption spectrum below their first exciton peak (for the semiconductors) and below their surface plasmon peak (for the gold), see Figures SI-I.1a, SI-I.2a, SI-I.3a. They therefore absorb in the visible close to their characteristic peak and in the UV range, while the polymer absorbs in the UV only. As mentioned in Section I.4 the polymer-coating procedure yields in addition to the polymer coated nanoparticles also some "empty" polymeric micells. Typically the polymer-coated nanoparticles are larger than the micelles of unbound polymer and therefore elute earlier on the size exclusion columns. In this way excess polymer (in the form of micells) can be separated from the polymer-coated particles. The solution containing the collected purified polymer-coated particles was diafiltrated three times with SBB pH 9 on Centriplus YM100 or Amicon 15 ultrafiltration devices to exchange the buffer and to concentrate the nanoparticles to a final concentration of 6.0 µM.

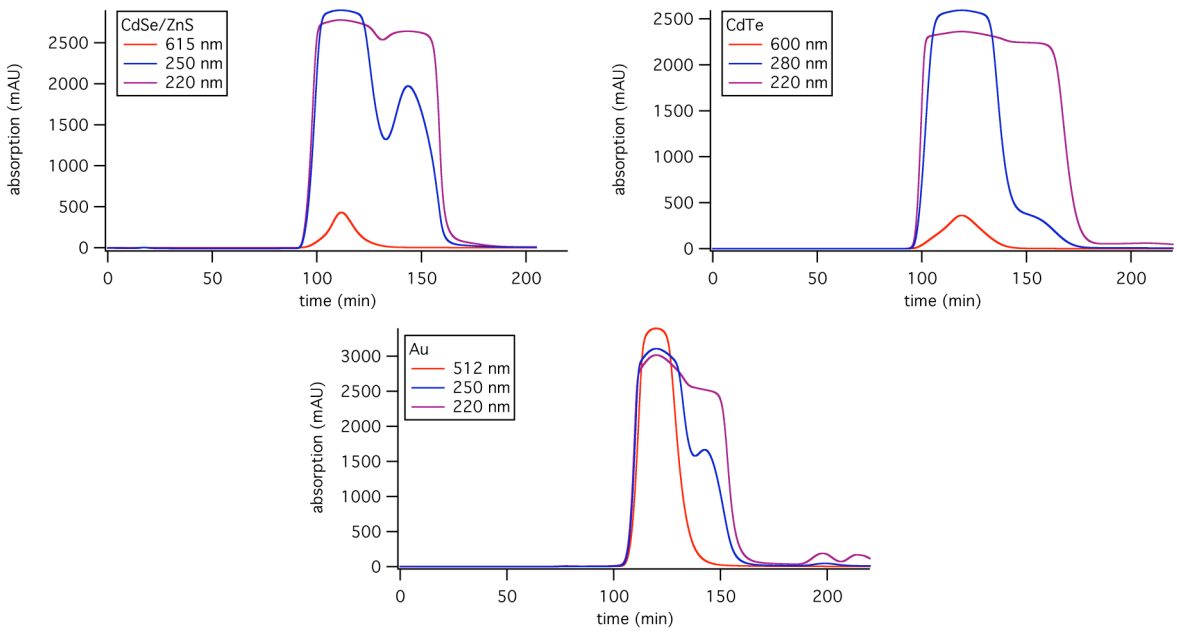

Figure SI-I.5: HPLC elution profiles of CdSe/ZnS, CdTe and Au nanoparticles after the polymer-coating. The absorption of the eluted samples is plotted versus the time. The bigger the particles are, the faster they pass the column and the earlier they are eluted. By the absorption at different wavelengths, the inorganic particle cores (absorbing in the visible and UV range) can be distinguished from the polymer (blue and purple lines, absorbing only in the UV at 250-280 nm and 220 nm). By stopping the sample collection at the end of the peak where only the inorganic cores absorb (red lines absorption in the visible at the characteristic absorption peak of the inorganic particles at 615 nm, 600 nm, 512 nm), most of the free polymer can be eliminated and only the purified polymer-coated nanoparticles are collected. The particles were run on a Sephacryl S-300 column at 0.5 ml/min with 50 mM sodium borate buffer with 100 mM NaCl, pH 9.0. Although the detector signal for the short wavelengths is saturated, a good separation of the particles from the free polymer could be observed.

I.6) Modification of the particle surface with polyethylene glycol (PEG)

Amino-modified PEG was attached to the carboxyl-groups present on the surface of polymer coated particles by EDC chemistry, see Figure SI-I.6. This protocol has been adjusted based on a previously published report [8]. Stock solutions of 3 mM methoxy-PEG-amine with a molecular weight of 750 g/mol (Sigma-Aldrich # 07964), 2000 g/mol (SunBio # P1AM-2), 5000 g/mol (Nektar Therapeutics # 2M2U0H01), 10000 g/mol (Sigma-Aldrich # 07965), and 20000 g/mol (Sigma-Aldrich # 07966) were prepared with by dissolving aliquots of some mg of PEG in sodium borate buffer (SBB) of pH 9.

Figure SI-I.6: PEG molecules (drawn in green) are bound to the surface of polymer coated nanoparticles, in a way that 1, 2, 3 PEG molecules are bound per particle or that the particles surface is saturated with PEG.

For CdSe/ZnS particles saturated with PEG, to 70 µl of the 6 µM particle solution 70 µl of the 3 mM PEG was added, resulting in a ratio of 500 PEG molecules per nanoparticle. Then, 70 µl of a fresh EDC solution (Sigma-Aldrich # E7750, 384 mM in SBB) was added, yielding a ratio of 64000 EDC molecules per nanoparticle and a final particle concentration of 2 µM in the reaction mixture. The samples were allowed to react 3 h before they were diafiltrated once with SBB on Centricon YM100 ultrafiltration devices.

For CdSe/ZnS particles with a defined number of attached molecules, 100 µl of a 3 mM PEG solution (M_W 5000 g/mol, 10000 g/mol, and 20000 g/mol) were added to 100 µl of 6 µM nanoparticles, yielding a ratio of 500 PEG molecules/nanoparticle. The ratio of EDC molecules per nanoparticle was experimentally determined by preparing a test-series with variable EDC concentration and running these particles on an agarose gel [8]. For the following reactions the EDC concentration at which discrete bands on gel of the test-series appeared was used. It has to be noted that the efficiency of the coupling reaction appears to be slightly higher at larger reaction volumes. For the CdSe/ZnS samples described here, 100 µl of a 1.74 mM solution of EDC in SBB was added to the nanoparticles with PEG, resulting in a ratio of 100 EDC molecules per nanoparticle. After allowing the mixture to react at least for 3 h, the samples were run on a 1 % agarose gel (Invitrogen #15510027) in 0.5 x TBE buffer (Sigma-Aldrich, # T3913) for typically 60 – 120 min at 100 V. The separation of the individual bands was controlled with an UV hand lamp before they were cut out by means of a scalpel. The gel cubes containing the bands were cut into smaller pieces and immersed in 50 mM SBB of pH 9 over night to 3 days. In this time the particles diffused out of the gel into solution. It was found that the fluorescence of the particles was reduced significantly or even totally when the extraction was carried out in 0.5 x TBE buffer. The samples were then concentrated to < 1 ml on Centricon YM100 ultrafiltration devices (Millipore) and desalted on NAP-25 columns (GE Healthcare, #17-0852-02) equilibrated with MilliQ water, while the elution was observed under illumination with an UV hand lamp. The attachment of PEG to Au particles was carried out in the same way for CdSe/ZnS particles, but instead of cutting out the bands the samples were only run on a 2 % agarose gel in order to derive the effective radii of particles with a discrete number of PEG molecules.

II) Transmission electron microscopy (TEM) analysis of the particles

II.1) Description of the image analysis

When nanoparticles are deposited on a surface, as for instance on a TEM-grid, the particles tend to form a 2D-lattice. By looking closer, one can observe that two neighboring particles do not touch each other, but leave a gap between them, see for example Figures SI-I.1b and SI-I.2b. This gap can be interpreted as the contribution of the organic surfactants that are adsorbed to the inorganic particle surface to the effective particle diameter, which consist of the inorganic particle core plus the surfactant layer. The surfactants consist mainly of alkyl-chains and therefore show only a very low contrast in the TEM.

The purpose of the image analysis as described here is to determine the thickness of the gap and in this way to determine the thickness of the surfactant layer. In order to do so, we measure the distance between the centers of two adjacent particles and subtract the diameter of a single particle. In this work this has been done by comparing different statistics. The diameter has been measured on about 500 individual particles and the results are reported in the histograms in Figure SI-I.1c and SI-I.2c. The distance between two particles has been determined with an automated image-analysis routine, which is described in the following paragraph. As it simply calculates the distance between all particles on one image, in the statistics (see Figures SI-II.2 and SI-II.3b) we find a peak not only for the first neighbors but also one combined peak for the second and third neighbors and some higher orders (not shown).

In order to determine the centers of the particles, one cannot just use the standard particle-analysis routine delivered with most analysis programs (as for instance Igor Pro (Wavemetrics) or ImageJ (NIH)). The general procedure for this type of analysis is to first transform the image into a binary image by reducing the color-range of each pixel to just black or white. In order to do so, a threshold is set. All pixels that have a grey value darker than this threshold are counted as black, the others as white. In a second step all closed areas of one of the two colors are marked as a particle. Applying this procedure to our TEM-images yields a quite faulty result, as frequently two adjacent particles are recognized as just one particle. The gap between two particles is usually not perfectly white, but has a grey-value only slightly different from that of the particles. Therefore the setting of the threshold always leads to a trade-off between erroneous connection of particles and an incomplete recognition of only the darkest particles.

To recognize the particles with a higher efficiency, we introduced a preprocessing step. We applied a Gaussian convolution-filter. This can be understood as a pattern search for circular structures. As a result, ideally we obtain very sharp and intense peaks as the positions of the centers of the particles. After this treatment the image analysis yields better results. The improvement is twice. First, adjacent particles, which show only little contrast in the gap are identified as separate particles and second fluctuations in the background are not identified as particles. This is demonstrated in the Figure SI-II.1.

191

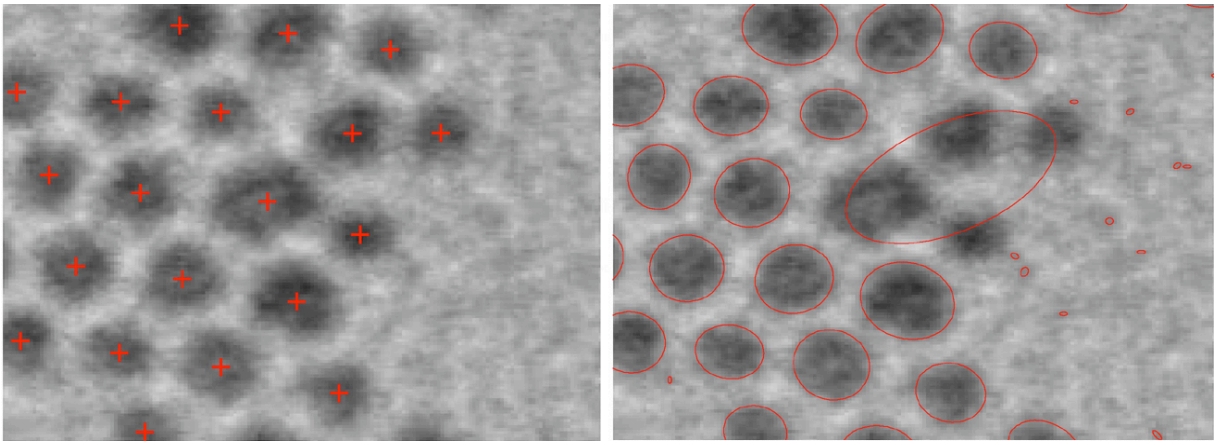

Figure SI-II.1: Demonstration of the improved particles analysis. The left panel shows the recognized centers of the particles with a cross mark. In this case a preprocessing step has been applied. In the right panel only the standard procedure was used. The particle areas are marked with red ellipses. In this case some adjacent particles are recognized as one and also some tiny spots are falsely identified as particles.

II.2) Results of the TEM analysis

The mean diameter of the inorganic part of the CdSe and CdSe/ZnS particles was directly extracted as $<d>_{TEM}$ = 4.7 nm and 5.3 nm from the TEM images as maximum in the histogram of the diameter distribution, see Figure SI-II.2. Yu et al. [9] have published a calibration curve which relates the wavelength of the first exciton peak to the diameter of the particle core. Absorption at 610 nm and 614 nm corresponds to a diameter of $<d>_{abs}$ = 5.1 nm and 5.3 nm for CdSe and CdSe/ZnS particles, respectively (the table actually has been made for CdSe particles; however, as first approximation we used the same table for CdSe/ZnS particles). Thus the resultant diameters from Yu et al. correspond well to our own data. All data are enlisted in Table SI-II.1.

The surfaces of two adjacent particles cannot get closer than two times the thickness of the organic shell around the inorganic particles. In Figure SI-II.2 the distribution of the distances of the centers of all particles are given for hydrophobic CdSe and CdSe/ZnS particles. The first maximum corresponds to two times the particle radius plus twice the thickness of the organic layer on the particle surface, which gives a number for the effective particle diameter $<d_{eff}>_{TEM}$ that comprises both, the inorganic and organic part. Since TEM images need to be recorded with dried particles these values have to be interpreted as lower limits. For the hydrophobic particles the effective diameter is around $<d_{eff}>_{TEM}$ = 6.0 nm and 6.4 nm for CdSe and CdSe/ZnS particles, respectively, see also Table SI-II.1. This corresponds to a thickness of the organic layer (that mainly consists out of trioctylphosphine oxide (TOPO) and hexadecylamine (HDA) molecules) of $(<d_{eff}> - <d>)_{TEM} / 2$ = (6.0 nm - 4.7 nm) / 2 = 0.7 nm in the case of CdSe and $(<d_{eff}> - <d>)_{TEM} / 2$ = (6.4 nm - 5.3 nm) / 2 = 0.6 nm in the case of CdSe/ZnS. This value lies in the expected range of the length of TOPO and HDA molecules. As mentioned above, the measured distance will be certainly underestimated.

Unfortunately we did not have a sufficient amount of CdSe/ZnS particles left to finish all TEM experiments (for all experiments with all different methods the same batch of CdSe/ZnS was used). Therefore for the analysis of polymer-coated particles we had to use a different batch of particles. It is very laborious to obtain two batches of CdSe/ZnS with the same properties. Since CdTe particles can be synthesized with a more regular spherical shape we used them for the determination of the thickness of the polymer shell. The surface chemistry of hydrophobically capped CdTe and CdSe/ZnS is very similar. We are aware that for this reason the obtained values have to be related with care to the data obtained with CdSe/ZnS. The following analysis about the thickness of the polymer layer is performed on CdTe and not on CdSe/ZnS.

193

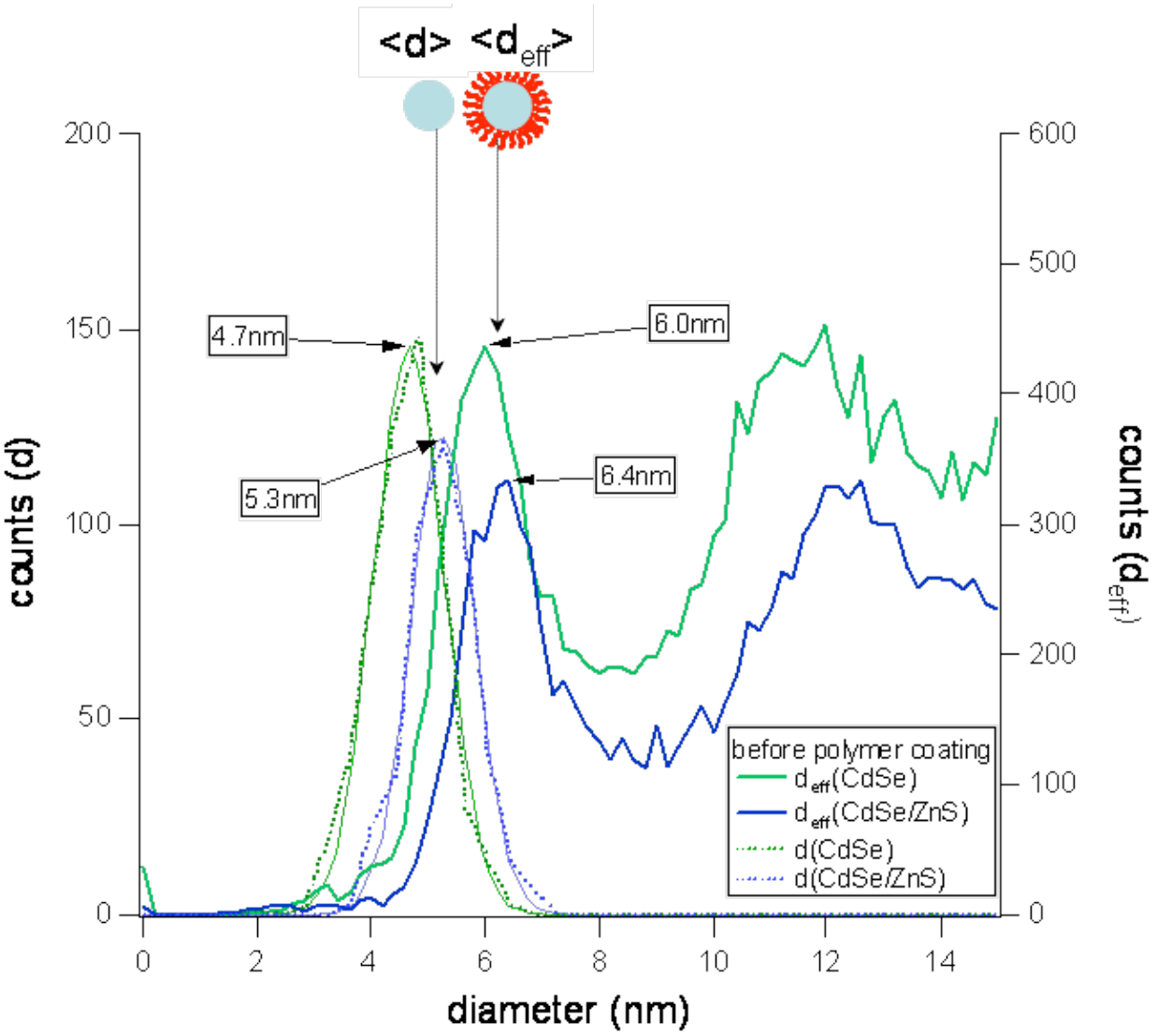

Figure SI-II.2: The inorganic particle core (CdSe or CdSe/ZnS gray) of the hydrophobic particles is stabilized by surfactant molecules (red). On the left side graphics a histograms of the particle diameters d that have been measured from many TEM images and a fits to the histograms are shown. The data are plotted in green and blue for CdSe and CdSe/ZnS particles, respectively. The fits of the histograms (thin, solid lines) peak at $\langle d \rangle_{TEM}$ = 4.7 nm and 5.3 nm for CdSe and CdSe/ZnS, respectively. This can be interpreted as the mean diameter of the inorganic part of the CdSe and CdSe/ZnS particles. The graph also contains the distribution of the distances between the centers of the particles for hydrophobic particles. The first peak in this distribution function can be interpreted as lower limit for effective particle diameter $\langle d_{eff} \rangle_{TEM}$, i.e. the diameter of the inorganic particle plus the organic shell around the particle.

The mean diameter of the inorganic part of the CdTe particles was directly extracted as $\langle d \rangle_{TEM}$ = 6.3 nm from the TEM images as maximum in the histogram of the diameter distribution, see Figure SI-II.3. This is somehow different to the value of <d> = 4.8 nm from a calibration curve reported by Yu et al. [9] that correlates the wavelength of the first exciton peak to particle diameters. We have double checked this by using two synthesis and analyses involving different persons and transmission electron microscopes. Therefore the Yu data seem not to be valid for all types of CdTe synthesis. On samples produced at different times, the correlation was quite reliable.

a)

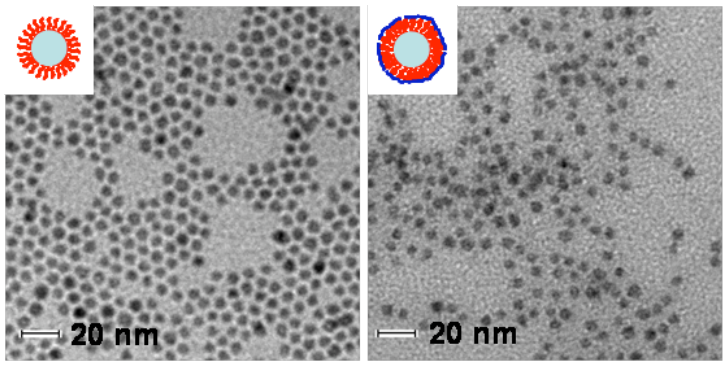

b)

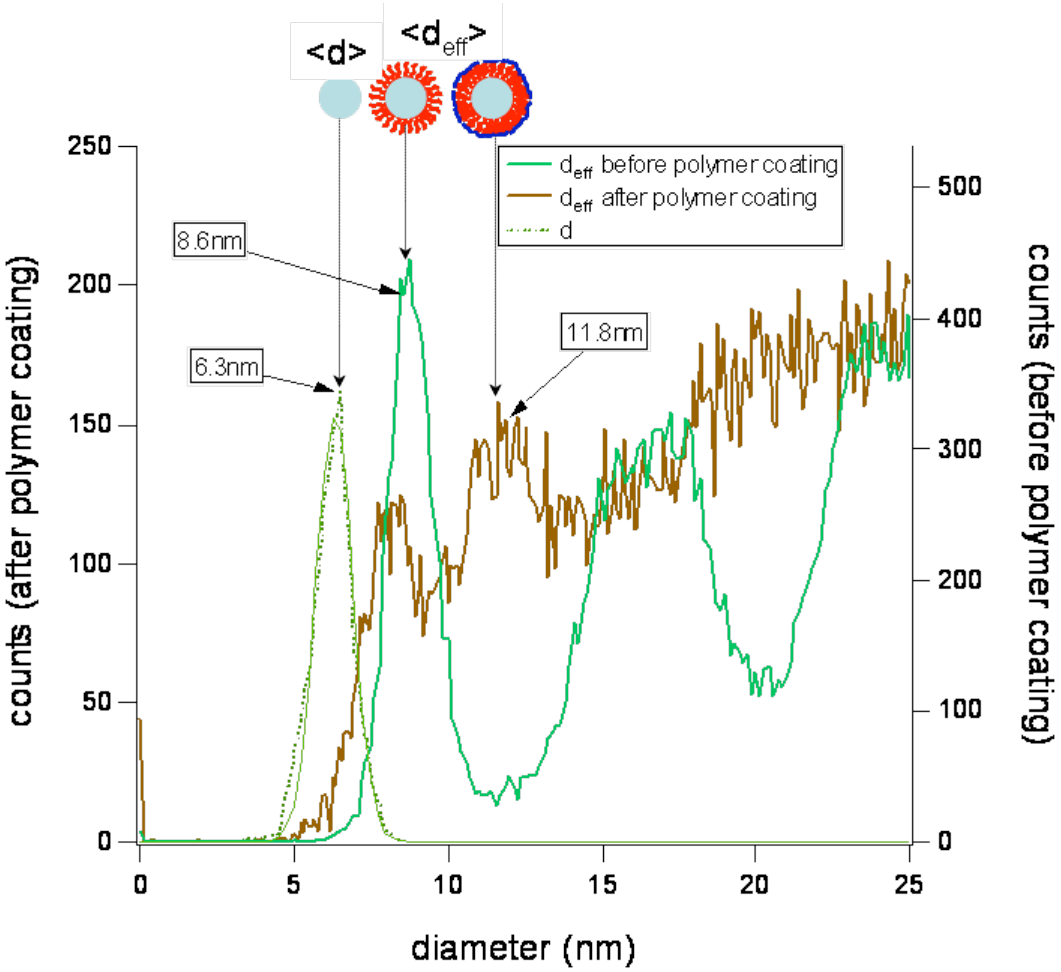

Figure SI-II.3: a) TEM images of hydrophobic and hydrophilic CdTe particles are shown on the left and right side, respectively. The inorganic particle core (gray) of the hydrophobic particles is stabilized by surfactant molecules (red). The hydrophilic particles have an additional amphiphilic polymer shell wrapped around the particle, whereby the hydrophobic side chains are drawn in red and the hydrophilic backbone in blue [7]. b) On the left side of the graphics a histogram of the particle diameters d that have been measured from many TEM images and a fit to the histogram is shown. The fit of the histogram peaks at <d> = 6.3 nm (as well for hydrophobic as for hydrophilic particles), which can be interpreted as the mean diameter of the inorganic part of the CdTe particles. The graph also contains the distribution of the distances between the centers of the particles for hydrophobic (green) and hydrophilic (brown) particles. The first peak in this distribution function can be interpreted as lower limit for effective particle diameter $<d_{eff}>_{TEM}$, i.e. the diameter of the inorganic CdTe particle plus the organic shell around the particle. In the case of hydrophobic particles the organic shell corresponds to the TOPO layer ($<d_{eff}>_{TEM}$ = 8.6 nm), in the case of hydrophilic particles to the TOPO layer plus the amphiphilic polymer around it ($<d_{eff}>_{TEM}$ = 11.8 nm).

In Figure SI-II.3b the distribution of the distances of the centers of all particles are given. The first maximum corresponds to two times the particle radius plus twice the thickness of the organic layer on the particle surface, which gives a number for the effective particle diameter $\langle d_{eff} \rangle_{TEM}$ comprising both the inorganic and organic part. Since TEM images need to be recorded with dried particles these values have to be interpreted as lower limits. For the hydrophobic particles the effective diameter is around $\langle d_{eff} \rangle_{TEM}$ = 8.6 nm. This corresponds to a thickness of the organic layer (that mainly consists out of trioctylphosphine oxide (TOPO) molecules) of $(\langle d_{eff} \rangle - \langle d \rangle)_{TEM} / 2$ = (8.6 nm - 6.3 nm) / 2 = 1.2 nm, see Table SI-II.2. This value lies in the expected range of the length of TOPO molecules. As mentioned above the measured distance is certainly underestimated. For the hydrophilic particles the peaks in the distance distribution function are less pronounced. The first peak can be found at the same position as for the hydrophobic particles. There is a second peak at around 11.8 nm, which is not present for the hydrophobic particles. The first peak in the distribution of distances could be attributed to particles that are only partly coated by the polymer and the second peak could be attributed to particles that are completely coated with polymer. In this way the thickness of the organic layer (TOPO + polymer) would be estimated as $(\langle d_{eff} \rangle - \langle d \rangle)_{TEM} / 2$ = (11.8 nm – 6.3 nm) / 2 = 2.8 nm, see Table SI-II.2. This suggests that in the dried state the additional increase in particle radius due to the polymer layer is around 2.8 nm - 1.2 nm = 1.6 nm. However, the arrangement of the hydrophilic particles on the TEM grid is much less regular than the one of the hydrophobic ones. The reduced ability of the polymer coated particles to arrange in a 2D-lattice might be due to several facts. First, the softness of their shell might lead to variable distances. Second, more than two particles might be wrapped in within the same polymer-shell. However, the results obtained with gel electrophoresis show that this cannot be a dominant process. Third, one might assume that the polymer coating is not very homogeneous and the broad distance distribution might result from the fact, that the polymer is not wrapped as nicely around the particles as assumed [7]. We assume this third possibility to be the most likely one. The data are compared in Table SI-II.1.

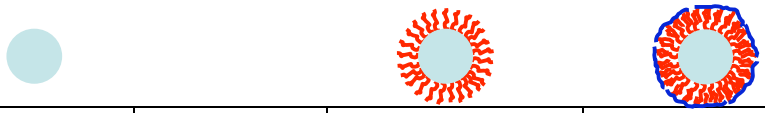

particle	$\langle d \rangle_{TEM}$ [nm]	$\langle d \rangle_{abs}$ [nm]	$\langle d_{eff} \rangle_{TEM}$ [nm] (before polymer coating)	$\langle d_{eff} \rangle_{TEM}$ [nm] (after polymer coating)
CdSe	4.7	5.1	6.0	-
CdSe/ZnS	5.3	5.3	6.4	-
CdTe	6.3	4.8	8.6	11.8
Au[4]	3.9	-	4.9	8.6

Table SI-II.1: Diameters of different particles. $\langle d \rangle_{TEM}$ is the mean diameter of the inorganic part as determined from the histograms of the diameter distribution from TEM images. $\langle d \rangle_{abs}$ corresponds to the mean diameter of the inorganic part as derived from the absorption spectra using a calibration curve in case of the semiconductor particles. This calibration curve created by Yu et al. [9] relates the wavelength of the first excition peak in the absorption spectra to a diameter (that had been also determined by TEM). The effective particle diameters were obtained as the mean distance between the centers of adjacent particles. The effective diameters $\langle d_{eff} \rangle_{TEM}$ comprise the inorganic core of the particles plus the organic layer adsorbed to it. These values were obtained before and after the polymer coating.

[4] As in the case of Au particle the diameter of the Au core changed due to the fractioning process during the size exclusion chromatography purification from 4.6 nm to 3.9 nm in this table the effective before the polymer coating is referred to the core diameter of the hydrophilic cores. This means 0.7 nm have been subtracted from the effective diameter before polymer coating (as this refers to cores that are 0.7 nm bigger in diameter): 5.6 nm - 0.7 nm = 4.9 nm.

Unfortunately as described above because of running out of sample we were not able to determine with TEM the effective diameter of polymer coated CdSe/ZnS particles from the batch that has been used for all the rest of the experiments. Therefore, we decided to make a rough approximation. The thickness of the polymer layer in case of the CdTe particles has been estimated to 1.6 nm as described above. In first approximation we assume that this should be similar for CdSe/ZnS particles. Since the diameter of hydrophobic CdSe/ZnS particles (before polymer coating) is 6.4 nm we assume the diameter of hydrophilic CdSe/ZnS particles (after polymer coating) to be $<d_{eff}>_{TEM}$ (CdSe/ZnS after polymer coating) = 6.4 nm + 2× 1.6 nm = 9.6 nm. We have used this value in the main part of the paper. As already mentioned this has to be understood as a rough approximation. However, since the effective diameters obtained from the TEM experiments can be questioned at any rate because they were measured on dry samples and the data sets also do not shown unequivocally interpretable peaks, we are convinced that this approximation does not reduce the value of the presented work.

The same analysis as described above for CdSe/ZnS and CdTe particles was also applied to Au particles. Gold particles either capped with dodecanethiol (i.e. hydrophobic) or coated with an additional amphiphilic polymer shell (i.e. hydrophilic) were studied by TEM. Figure SI-II.4 shows the histograms of the Au core diameters d_{TEM} and the distribution of the distances between the centers of the particles for hydrophobic and hydrophilic particles. The first peak in this distribution function can be interpreted as lower limit for the effective particle diameter $<d_{eff}>_{TEM}$, i.e. the diameter of the inorganic Au core plus the organic shell around the particle. In the case of hydrophobic particles the organic shell corresponds to the dodecanethiol layer, in the case of hydrophilic particles to the dodecanethiol layer plus the amphiphilic polymer around it.

The obtained core diameters of both samples are not the same, the polymer-coated particles have a slightly smaller core diameter ($<d>_{TEM}$ = 3.9 nm) than the hydrophobic ones ($<d>_{TEM}$ = 4.6 nm, see also Table SI-I.2 and Figure SI-I.3) although both were prepared from the very same batch of particles. This is due to the fractionating of the sample by the size exclusion column: After the polymer coating, only the center fractions eluted from the column were pooled to yield the final sample. Both front and tail shoulders containing larger or smaller particles were discarded, not necessarily yielding a symmetrically sharper size-distribution.

The effective diameters of the particles before and after polymer coating (which correspond to the particle Au core plus the organic layer around it) are derived from the first peak in the distance distribution function. In the case of the hydrophobic Au particles the effective particle diameter $<d_{eff}>_{TEM}$ has been determined to be 5.6 nm, whereby the diameter of the Au cores $<d>_{TEM}$ was 4.6 nm. . In the case of the hydrophobic Au particles the effective particle diameter has been determined to be 8.6 nm, whereby the diameter of the Au cores was 3.9 nm. As in the case of the semiconductor particles the thickness of the organic layer was calculated as $(<d_{eff}>_{TEM} - <d>_{TEM})/2$, the numeric values are shown in Table SI-II.2. The thickness of the dodecane thiol layer of the Au particles differs from the TOPO / HDA layer of the CdSe/ZnS or CdTe nanoparticles[5].

[5] From the length of the molecule, one would expect a thicker layer for dodecanethiol than for TOPO. However, also steric effects of the organic molecules might play a role: Dodecanethiol consists of one linear C12 (dodecyl) chain while TOPO has three C8 (octyl) chains. The latter might be more densely packed while the longer chains could allow an intercalation of the organic molecules which would lead to a smaller distance between the particles, especially in the dry state when prepared on the TEM grid. However, the differences are also within the error bars of our method.

197

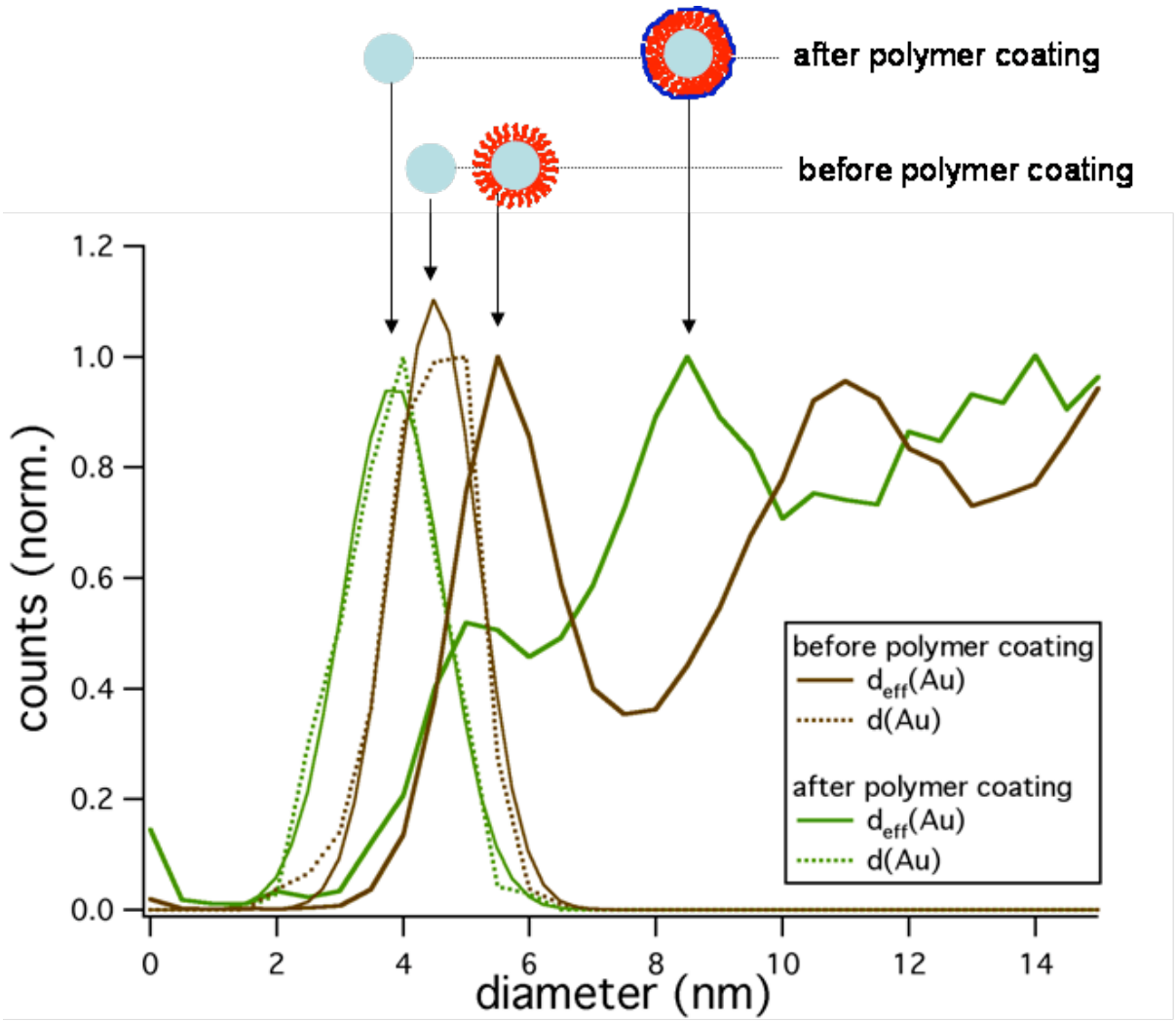

Figure SI-II.4: *Histograms of the core diameters <d> (solid lines) of Au nanoparticles capped with dodecanethiol (green) and coated with the amphiphilic polymer (brown) as obtained by TEM analysis. The graph also contains the distribution of the distances between the centers of the particles (dashed lines) for hydrophobic (green) and hydrophilic particles (brown), see Chapter II.1. The first peak in this distribution function can be interpreted as lower limit for the effective particle diameter $<d_{eff}>_{TEM}$, i.e. the diameter of the inorganic Au core plus the organic shell around the particle. In the case of hydrophobic particles the organic shell corresponds to the dodecanethiol layer ($<d_{eff}>_{TEM}$ = 5.6 nm), in the case of hydrophilic particles to the dodecanethiol layer plus the amphiphilic polymer around it ($<d_{eff}>_{TEM}$ = 8.6 nm).*

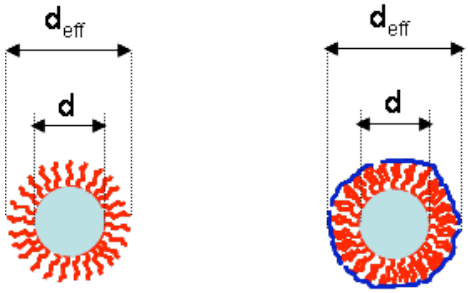

particle	thickness of the organic layer ($<d_{eff}>_{TEM}$ -$<d>_{TEM}$)/2 before polymer coating	thickness of the organic layer ($<d_{eff}>_{TEM}$ -$<d>_{TEM}$)/2 after polymer coating
CdTe	1.2 nm	2.8 nm
Au	0.5 nm	2.4 nm

Table SI-II.2: Thickness of the organic layer around the particles. $<d>_{TEM}$ is the mean diameter of the inorganic cores as determined from the histograms of the diameter distribution from the TEM images. The effective particle diameters $<d_{eff}>_{TEM}$ were obtained as the mean distance between the centers of adjacent particles. The effective diameters comprise the inorganic core of the particles plus the organic layer adsorbed to it. Before the polymer-coating the organic layer around the (hydrophobic) particles is TOPO/HDA and dodecanethiol in the cases of CdTe and Au particles. After the polymer-coating an additional layer of amphiphilic polymer adds to the organic layer of the (hydrophilic) particles. Again, the linear dodecanethiol molecules could allow a deeper intercalation with both the dodecanethiol capping of adjacent particles and the hydrophobic side-chains of the polymer, which could explain the smaller values for the thickness of the organic layer before and after the polymer coating in case of the Au particles.

III) Gelelectrophoresis experiments

Agarose gels of different w/v percentage were prepared with Agarose UltraPure (Invitrogen #15510027) and 0.5 x TBE buffer (Sigma-Aldrich, # T3913). For a typical 1% and 2 % gel, 1.5 g and 3 g of agarose were added to 150 ml 0.5 x TBE buffer in an Erlenmeyer flask, respectively, covered by a Petry dish and heated in a microwave oven. The heating was interrupted several times to shake the flask before boiling, so that the agarose could hydrate and finally form a homogeneous clear solution without sticking to the bottom of the flask. The agarose was left for about a minute in the microwave oven and was cast still hot into the gel tray mounted in the gel caster (Biorad Sub-Cell GT), before a comb for the wells was inserted. After the gels had become solid, the comb was removed and the gel was placed into the electrophoresis device (Biorad, #170-4401 Sub-Cell GT electrophoresis cells, 15 x 10 cm tray) filled with 0.5 x TBE. The electrophoresis was performed at 100 V constant voltage, after 60 min or more the gel was taken out and a digital picture was taken (Biorad GelDoc 2000). The electric field strength was estimated to be 10 V/cm.

Due to their negative charge the polymer-coated nanoparticles used in this study migrate towards the positive electrode. As control 10 nm phosphine coated Au nanoparticles were run on the same gel [10].

For each particle the length of the migration length l was measured and normalized to the migration length l_{10nm} of the phosphine-coated 10 nm Au particles to yield the relative electrophoretic mobility m/m_{10nm} of the particle (see Figure SI-III.1):

$$m_y/m_{10nm,y} = l_y / l_{10nm,y} \quad (1)$$

y hereby refers to the gel percentage (1% or 2%). In previous work [10] we have obtained a calibration curve (2) which relates the relative mobilities $m_y/m_{10nm,y}$ to effective diameters d_{eff}[6]:

$$d_{eff} = -T \ln (m_y/m_{10nm,y} / A) + 6 \text{ nm} \quad (2)$$

with the parameters A = 1.049 and 1.12) and T = 85 and 37.7 for 1 % and 2 % agarose gels [10]. Examples of gels are shown in Figures SI-III.1 and SI-III.2 and the derived effective diameters are enlisted in Tables SI-III.1 and SI-III.2.

When a few PEG molecules are attached per particle discrete bands can be resolved which correspond to Au particles with no, one, two, three, etc. PEG molecules per particle. In accordance with previous results [8] the spacing between the discrete bands increases with the molecular weight for both Au and CdSe/ZnS particles. The effective size of particles modified with one PEG molecule with a high molecular weight is always smaller than the same particles modified with two PEG molecules with each half the molecular weight. This is plausible since the radius of a polymer coil does not scale linearly with its molecular weight, thus two small polymer coils add more to the effective radius of a nanoparticle than one polymer molecule of the double molecular weight.

[6] This calibration curve was obtained by running particle standards with a known size on gels of the the same percentage. Phosphine-coated Au particles of known size (core diameter 5, 10, 15, 20, … nm) were used and their effective diameters were estimated as the core diameter + 1 nm for the phosphine layer. The relative mobility versus the effective particle diameter was fitted with a monoexponential fit function for each gel percentage.

Also the nanoparticles saturated with PEG are more retarded when modified with PEG of higher molecular weight. With a molecular weight ≥ 5000 g/mol, the saturated nanoparticles migrate towards the negative electrode, indicating a positive net charge of the conjugated particles. This has already been found in earlier experiments and is always reproducible, yet the origin of the positive charge is not clear. We mention again the hypothesis of ion binding [8,11] to the originally neutral PEG chains that have a similar structure to crown ethers when coiled.

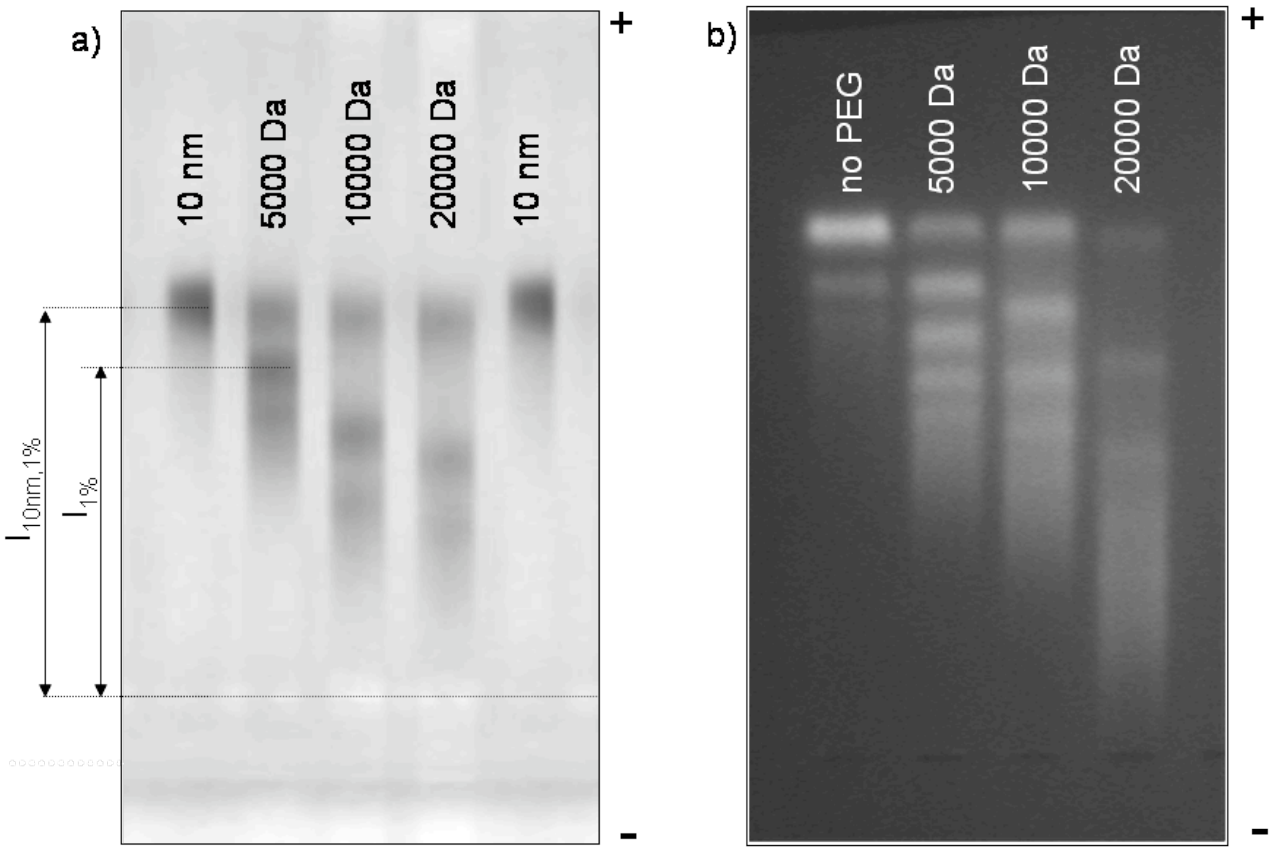

Figure SI-III.1: Polymer-coated Au (a) and CdSe/ZnS (b) nanoparticles to whose surface a small number of PEG molecules of different weight (5 kDa, 10 kDa, and 20 kDa) was attached were run for 1 @ 100 V on 1% agarose gels. The position of the bands on the gel was then recorded by taking a digital photograph of the gel. In the case of the fluorescent CdSe/ZnS particles the gel had been illuminated with an UV table during the photographing procedure. As the polymer coated particles are negatively charged the migrate towards the positive electrode. In the gel shown here with the Au particles (a) phosphine-coated Au particles of 10 nm Au-diameter were run as control on the gel [10]. In the case of the gel shown here for CdSe/ZnS particles plain polymer-coated CdSe/ZnS particles (i.e. without PEG) were run as control on the gel (b). For each band the length of migration $l_{1\%}$, i.e. the distance between the final position of the band on the gel and the position were the particles had been loaded into the gel, is measured. In order to obtain the relative mobility $m_{1\%}/m_{10nm,1\%}$ of the particles this length of migration is related to the length of migration of phosphine-coated Au particles of 10 nm Au diameter $l_{10nm,1\%}$ with Formula (1). Sometimes, as on the gel shown in (b) no 10 nm phosphine-coated Au-particles were run on the same gel. In this case an additional gel was run in which the mobility of the polymer-coated particles (without PEG) was related to the mobility of the 10 nm phosphine-coated Au-particles. More details about the evaluation of our gel electrophoresis experiments can be found in a previous report [10]. The discrete bands on the gel correspond to particles with no, one, two, etc. PEG molecules bound per particle [8].

201

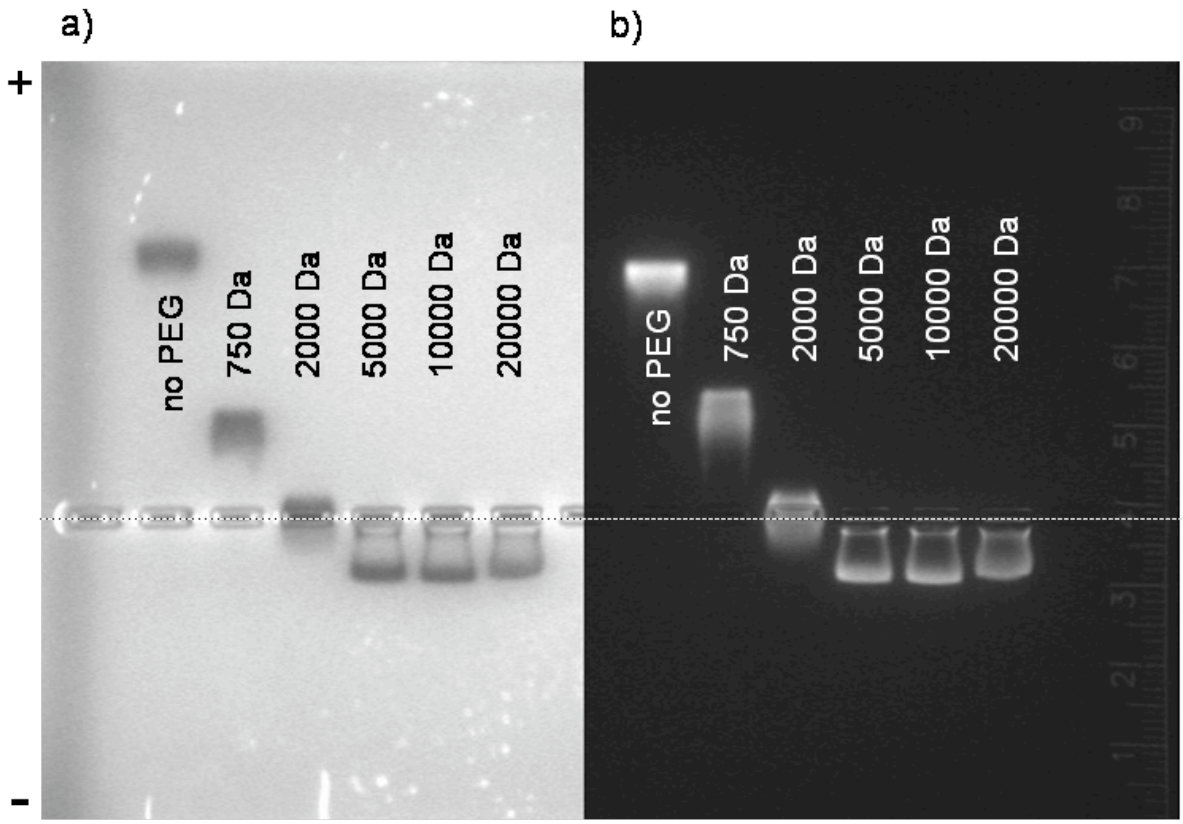

Figure SI-III.2: : Polymer coated Au (a) and CdSe/ZnS (b) nanoparticles to whose was saturated with PEG molecules of different weight (0.75 kDa, 2kDa, 5 kDa, 10 kDa, and 20 kDa) were run for 1 @ 100 V on 2% agarose gels. The gels were photographed and the migration length of each band $l_{2\%}$ was measured and related to the migration length of phosphine-coated Au particles with 10 nm Au diameter (not shown on the gels presented here) in order to obtain relative mobilities with Formula (1). Upon saturation with PEG of molecular weight ≥ 5 kDa the particles migrate towards the negative electrode and therefore must posses an overall positive charge. The position where the particles had been loaded on the gel is marked with a dashed line.

There are several restrictions on deriving effective diameters from relative mobilities with a calibration curve (2)[7] [10]. The particles used to obtain the calibration curve (2) were phosphine-coated Au nanoparticles and thus different in nature from the here used polymer-coated particles with attached PEG molecules. These particles were negatively charged and the particles of different diameter had the same charge density. However, for the particles used here upon attaching PEG not only the diameter but also the charge changes. Therefore, for the particles with a lot of PEG gel electrophoresis is not an adequate method to determine their effective diameter, since it is in this case evident that the changes in mobility are not only due to the particles' size but also due to their change in charge that even changes the sign. The calibration curve (2) can only be applied for particles which are similar in nature to phosphine-coated Au particles. For polymer-coated Au particles with only few PEG molecules attached per particle the charge effect upon binding PEG can be neglected and curve (2) can be applied. The values obtained with (2) for particles saturated with PEG of high molecular weight on the other hand have to be disregarded.

[7] The calibration curve is a fit to effective mobility of particles whose effective diameters are known or can be estimated. As it is a fit values derived from the fit do not necessarily match exactly the values which have been used to generate the fit.

PEG/ polymer-coated CdSe/ZnS particle	M(PEG) [g/mol]	$m_{1\%}/m_{10nm,1\%}$	$m_{2\%}/m_{10nm,2\%}$	$<d_{eff}>_{gel(1\%)}$ [nm]	$<d_{eff}>_{gel(2\%)}$ [nm]
0	5000	0.95	0.89	14.5	14.5
1	5000	0.84	0.79	24.5	19.3
2	5000	0.75	0.69	34.2	24.1
3	5000	0.67	0.62	43.6	28.5
4	5000	0.61	0.55	51.9	32.8
5	5000	-	0.50	-	36.7
6	5000	-	0.44	-	40.8
0	10000	0.95	-	14.5	-
1	10000	0.80	-	29.4	-
2	10000	0.67	-	43.5	-
3	10000	0.60	-	56.5	-
0	20000	0.95	-	14.5	-
1	20000	0.71	-	39.6	-
2	20000	0.54	-	62.7	-
0	-	-	0.89	-	14.5
sat.	750	-	0.39	-	46.1
sat.	2000	-	0.01	-	180.2
sat.	5000	-	-0.22	-	* neg.
sat.	10000	-	-0.22	-	* neg.
sat.	20000	-	-0.21	-	* neg.

<u>Table SI-III.1</u>: Relative mobilities $m_y/m_{10nm,y}$ and effective particle diameters $<d_{eff}>_{gel,y}$ for polymer-coated CdSe/ZnS particle with attached PEG molecules of different molecular weight. y codes the gel percentage (1% or 2%). In the upper columns particles with a discrete number of PEG molecules (0, 1, 2, ... PEGs per particle) are enlisted. In the lasts columns particles whose surface had been saturated with PEG are enlisted. The relative mobilities $m_y/m_{10nm,y}$ were derived by measuring the migration lengths l_y of the particles and normalizing them to the migration lengths $l_{10nm,y}$ of phosphine-coated Au particles of 10 nm Au diameter by using Formula (1). The effective diameters were derived from the relative mobilities by using a calibration curves (Formula (2)) which had been obtained previously [10]. In case of particles saturated with PEG of high molecular weight the mobilities became very small or even negative. Negative mobilities mean that the particles migrated towards the negative instead of the positive electrode. This comes due to a charge effect and in this case the calibration curve (2) can no longer be applied. The values labeled with (*) therefore have to be disregarded.

PEG/ polymer-coated Au particle	M(PEG) [g/mol]	$m_{1\%}/m_{10nm,1\%}$	$m_{2\%}/m_{10nm,2\%}$	$<d_{eff}>_{gel(1\%)}$ [nm]	$<d_{eff}>_{gel(2\%)}$ [nm]
0	5000	0.97	0.94	12.7	12.5
1	5000	0.83	0.81	26.3	18.4
2	5000	0.72	0.69	38.2	24.5
3	5000	-	0.59	-	29.9
0	10000	0.96	0.94	13.4	12.5
1	10000	0.67	0.74	44.5	21.6
2	10000	0.49	0.60	70.7	29.3
0	20000	0.95	0.94	14.4	12.5
1	20000	0.61	0.63	52.5	27.7
2	20000	0.42	0.45	83.5	40.2
0	-	-	0.94	-	12.5
sat.	750	-	0.35	-	49.7
sat.	2000	-	0.03	-	140.1
sat.	5000	-	-0.20	-	* neg.
sat.	10000	-	-0.21	-	* neg.
sat.	20000	-	-0.20	-	* neg.

Table SI-III.2: Relative mobilities $m_y/m_{10nm,y}$ and effective particle diameters $<d_{eff}>_{gel,y}$ for polymer-coated Au particle with attached PEG molecules of different molecular weight. y codes the gel percentage (1% or 2%). In the upper columns particles with a discrete number of PEG molecules (0, 1, 2, ... PEGs per particle) are enlisted. In the lasts columns particles whose surface had been saturated with PEG are enlisted. The relative mobilities $m_y/m_{10nm,y}$ were derived by measuring the migration lengths l_y of the particles and normalizing them to the migration lengths $l_{10nm,y}$ of phosphine-coated Au particles of 10 nm Au diameter by using Formula (1). The effective diameters were derived from the relative mobilities by using a calibration curves (Formula (2)) which had been obtained previously [10]. In case of particles saturated with PEG of high molecular weight the mobilities became very small or even negative. Negative mobilities mean that the particles migrated towards the negative instead of the positive electrode. This comes due to a charge effect and in this case the calibration curve (2) can no longer be applied. The values labeled with (*) therefore have to be disregarded.

If one analysis the band of polymer-coated CdSe/ZnS particles in Figure SI-III.1b carefully one can observe three bands, whereby the fastest one corresponds to single polymer-coated CdSe/ZnS particles. As there was no PEG linked to these particles one would not expect the two additional bands. Their corresponding diameters (1% gel, diameters derived with (2) from the relative mobilities) are enlisted in Table SI-III.3. As these particles never have been in contact with any PEG they can be explained in two ways: first, two or three particles might be embedded in the same polymer shell, and second, two or three polymer-coated particles might stick nonspecifically together. We cannot decide which of the two possibilities is true. We have to point out that the same effect (3 bands) is true for the commercially available polymer-coated CdSe/ZnS particles from the Quantum Dot Corp. However, if one compares the intensities of the bands it is obvious, that the fraction of particles in the 2nd and 3rd band is very small compared to the 1st band with the single polymer-coated particles. The 2nd and 3rd band only can be observed in the case of CdSe/ZnS, as these bands are much sharper, but not in the case of Au, where the bands cannot be resolved as well (see Figure III.3.1). Therefore these impurities can be neglected. It is also important to point out that these impurities have nothing to do with

the bands generated by the attachment of PEG. The higher the molecular weight of single PEG molecules attached to the particles, the bigger their shift on the gel becomes. Therefore, the discrete bands in the case of attachment of single PEG molecules are a specific effect with high yield and must not be confused with the small impurities in the plain particle samples. This effect has also been observed with commercial (plain polymer-coated) nanoparticles (QuantumDots QD655 ITK carboxyl, data not shown).

band #	$d_{eff,1\%}$ [nm]
1	14.5
2	23.7
3	30.2

Table SI-III.3: Effective diameters corresponding to the bands resolved with plain polymer-coated CdSe/ZnS particles on a 1% agarose gel by using Formula (2). The first band corresponds to the actual single polymer-coated CdSe/ZnS particles, whereas the two slower bands are impurities. The first band corresponds to the data shown in Table SI-III.1 for CdSe/ZnS particles with no PEG attached per particle.

IV) Size exclusion chromatography (SEC) experiments

The setup consisted of an Agilent 1100 HPLC system, comprising a vacuum degasser (G1322A), a quaternary pump (G1311A), an autosampler (G1313A ALS) with 900 ul injection upgrade kit (G1363A) and multidraw upgrade kit (G1313-68711), a column oven with column switching valve (G1316A), a diode array detector DAD (G1365B with upgrade G1315), a FLD (G1321A) and a fraction collector (G1364A), operated with the Chemstation B.01.03 software. All components before the column were connected by stainless steel or PEEK capillaries of an inner diameter (ID) of 0.17 - 0.3 mm, and after the column of ID 0.5 mm in order to reduce the back pressure at the column.

The mobile phase for all experiments was 50 mM sodium borate buffer with 100 mM NaCl, pH 9.0 ("SBBS") at a flow rate of 0.5 ml/min. The elution was observed with the DAD by measuring the absorption simultaneously at different wavelengths in the UV and visible range, optionally also the fluorescence. All experiments were performed with the column at room temperature. As stationary phase, different polymer-based gels (GE Healtcare Sephacryl S-300, S-400, S-500 and S-1000 and Tosoh Toyopearl HW75-F and HW65-S) were packed into empty columns (GE Healthcare XK16-70 or Omnifit ID x L = 15 x 750 mm) according to the instructions of the manufacturer. The column dimensions were chosen so that the columns could also be used for injection volumes of 1 ml per run for preparative purposes. Glass columns were preferred because they have the advantage of easy visual control of the gel bed in case of gaps, cracks, air or other contamination.

For the column calibration, first the void volume v_0 and the total liquid column volume v_t, that is accessible for small molecules and the mobile phase, were determined with λ-DNA and 3 % acetone, respectively. λ-DNA consists of 48.5 kbp, has a molecular weight of $31.5 \cdot 10^6$ g/mol and a gyration radius in the order of 600 nm, which is still small compared to the particle size of the stationary phase (47 μm for the Sephacryl media). The λ-DNA was assumed to be totally excluded from the gel pores since it eluted always earlier than the often used blue dextran (M_W $2 \cdot 10^6$ g/mol, e.g. Sigma-Aldrich # D5751), and yielded a much more symmetric peak. That means for the column materials used in these experiments, that the blue dextran could enter the pores of the gel beads at least partially and is therefore not a good standard. To prepare the standard sample solution for the determination of v_0 and v_t, 40 μl of a λ-DNA stock (Fermentas #SD0021, as received) and 30 μl of acetone were added to 930 μl SBBS and mixed well with a pipette prior to injection.

A slight dependence of the flow rate and injection volume on the elution volume v_e was observed. Therefore the flow rate was set to 0.5 ml/min and the injection volume to 200 μl for all measurements that have been performed in this study. In order to compare the resolution of different packing materials in different columns, the distribution coefficient K_{SEC} was calculated from the elution volume v_e at the peak maxima with the total liquid volume v_t and the void volume v_0

$$K_{SEC} = (v_e - v_0)/(v_t - v_0) = (t_e - t_0) / (t_t - t_0) \quad (1)$$

Formula (1) can also be written in the same way by using elution times t instead of elution volumes. When the retardation of a sample is due to size exclusion only (without any attractive forces between the eluent and stationary phase), the partition coefficient K_{SEC} is found by principle between 0 and 1 and equals to the fraction of the pore volume ($v_t - v_0$) of the

stationary phase that is accessible for the molecule or particle of interest. By referring to the partition coefficient K_{SEC}, differences in the dimensions or filling of different columns is cancelled out and the resolution range of the different materials can be directly compared. Thus K_{SEC} in first order does not depend on the actually used columns, but only on the different gels with which the columns are filled with.

In Figure SI-IV.1, the partition coefficients K_{SEC} for a number of samples run on size-exclusion columns with different polymer-based materials are shown. The column materials were chosen because they have relative large pores which are needed to resolve nanoparticles of different size, and they are stable at basic pH (in contrast to silica-based materials) where the polymer-coated nanoparticles are most stable. The column dimensions inner diameter times length (ID x L) of 16 mm x 700 mm (GE Healthcare XK16/70) and 15 mm x 750 mm (Omnifit) were chosen because they also allow for small-scale preparative runs with an injection volume of 1 ml/run. Running two columns in series would only improve the total separation in regard of elution time or volume, and eventually the separation of discrete peaks, but the relative separation in terms of K_{SEC} would be the same.

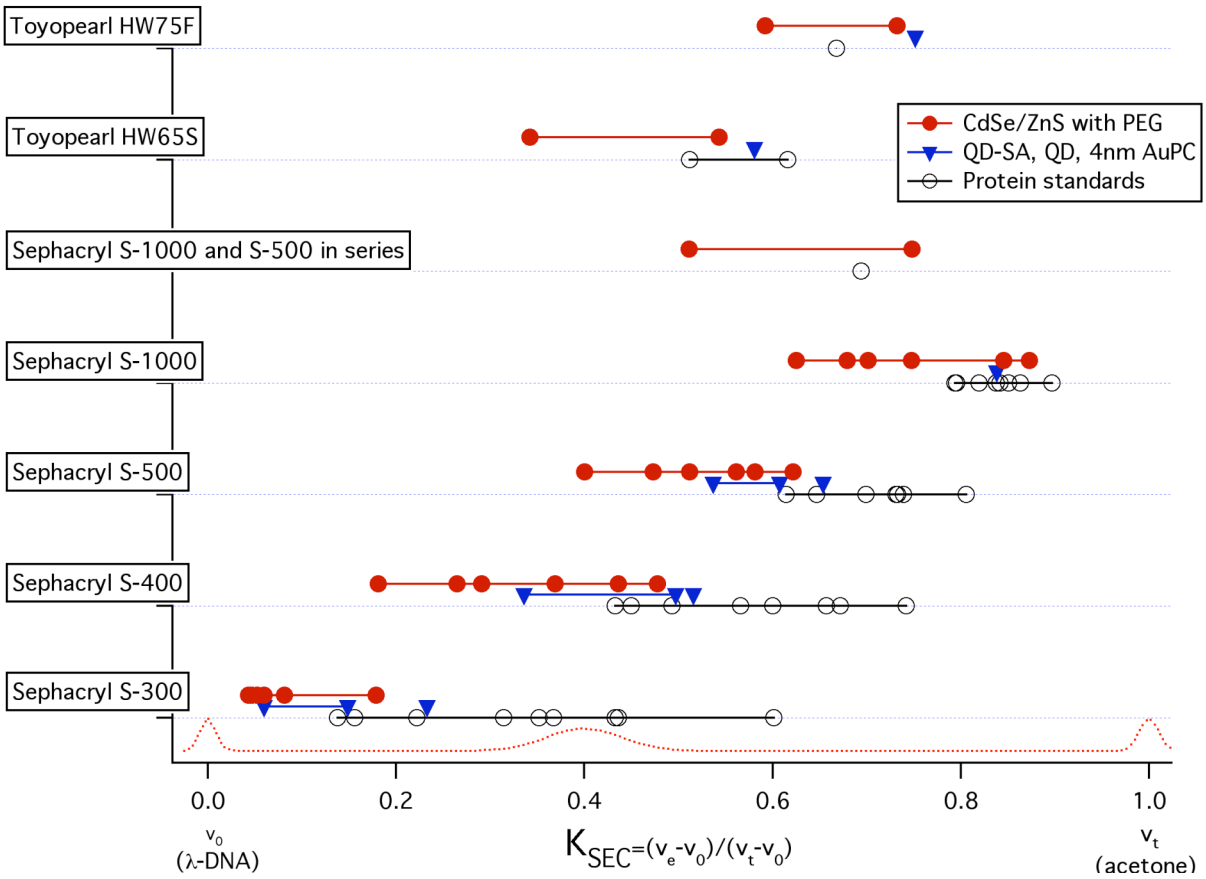

Figure SI-IV.1: Partition coefficients K_{SEC} of different standard samples and particles measured on different columns. The partition coefficient of different protein standards are plotted as black circles. The partition coefficients of CdSe/ZnS samples which are saturated with PEG molecules of different molecular weight are plotted as red circles. The partition coefficients of Au samples and commercially available quantum dot samples are plotted as blue triangles. For the purpose of size-determination of nanoparticles the column material is best suited, which offers the best overlap of the range of partition coefficients spanned by the protein standards with the range needed for the nanoparticles. All values are enlisted in Table SI-IV.1.

sample name	Sephacryl S-300	Sephacryl S-400	Sephacryl S-500	Sephacryl S-1000	Sephacryl S-1000 + Sephacryl S-500	Toyopearl HW65S	Toyopearl HW75F
Thyroglobulin bovine	0.156	0.450	0.615	0.820	0.694	0.512	0.668
Thyroglobulin porcine	0.138	0.433	0.615		-	-	-
Apoferritin	0.222	0.493	0.647	0.796	-	-	-
Beta-Amylase	0.315	0.566	0.699	0.837	-	-	-
Alcohol Dehydrogenase	0.367	0.600	0.739	0.863	-	-	-
Albumin	0.433	0.657	0.731	0.842	-	-	-
HSA	0.436	0.672	-		-	0.616	-
Carbonic Anhydrase	0.601	0.742	0.806	0.897	-	-	-
CdSe/ZnS	0.179	0.478	0.622	0.873	0.749	0.543	0.718
CdSe/ZnS + M_W 750 PEG	0.060	0.436	0.581	0.846	-	-	-
CdSe/ZnS + M_W 2000 PEG	0.082	0.369	0.562	0.748	-	-	-
CdSe/ZnS + M_W 5000 PEG	0.053	0.291	0.512	0.702	-	-	-
CdSe/ZnS + M_W 10000 PEG	0.047	0.265	0.473	0.680	-	-	-
CdSe/ZnS + M_W 20000 PEG	0.043	0.181	0.400	0.625	0.511	0.616	0.570
Au	0.233	0.516	0.653	0.838	-	0.581	0.738
QD655 carboxyl	0.149	0.497	0.607	-	-	-	-
QD655 SA	0.060	0.336	0.537	-	-	-	-

Table SI-IV.1: Partition coefficients of different standard samples and particles measured on different columns. In the first column the names of the different samples are given. The first nine samples are different protein standards (see Table SI-IV.2 for more information). The next 6 samples are the polymer-coated CdSe/ZnS samples used for this study (see Chapter I.1, I.4, and I.6). The surface of these particles is saturated with PEG molecules of different molecular weights (no PEG, 750, 2000, 5000, 10000, 20000 g/mol). The next sample is polymer-coated Au used for this study: 4 nm polymer-coated Au particles (see Chapter I.3, I.4). The two last samples are commercial quantum dots (Quantum Dot Corp., Hayward, CA, USA: CdSe/ZnS with polymer shell fluorescent at 655 nm with carboxyl-, and streptavidin- (SA) modification). The data are graphically displayed in Figure SI-IV.1.

The results of Figure SI-IV.1 demonstrate that different column materials resolve particles of different size. This can be seen very nicely in the "family" of Sephacryl gels, which from S-300 to S-1000 have pores with increasing size. For the gel with the biggest pores (Sephadex S-1000) the protein standards elute at very high partition coefficients (close to the limit $K_{SEC} = 1$ ultimately small molecules). For the gels with smaller pores the protein standards are eluted at much lower elution times and they also span from the smallest to the biggest protein a larger range in the interval $0 \leq K_{SEC} \leq 1$. The standard protein samples shown in Figure SI-IV.1 therefore certainly can be best resolved by size with the Sephadex S-300 gel. As it becomes also obvious from the data of Figure SI-IV.1 the nanoparticles samples used in this study are

significantly bigger than the protein standards. Therefore they are eluted at smaller partition coefficients. This already points out a severe limitation of size measurements of nanoparticles with size exclusion columns: There are no appropriate size-standards easily available. The nanoparticles are best resolved with the gel with the biggest pores (biggest interval in K_{SEC} for Sephacryl S-1000), but for this gel the protein standards are not resolved well, as they are too small. When comparing the interval of K_{SEC} values that is spanned by the series of protein standards or nanoparticle samples, the Sephacryl S-400 material shows the best performance for both protein standards and nanoparticle samples. Thus in the following, the evaluation is focused on this material and the Sephacryl S-300 and S-500 with smaller or larger pores, respectively.

For size determination by size exclusion chromatography, columns have to be calibrated with standards of known molecular weight and/or radius, and from the elution time, volume or K_{SEC} value of a sample its size can be derived. For SEC with aqueous mobile phases several types of standards exist like synthetic polymers and proteins [12], also nanoparticles have already been used for column characterization [13]. Actually, the elution volume of a sample does not directly depend on the molecular weight, but on its hydrodynamic volume. The hydrodynamic volume naturally depends on the molecular weight of a given molecule, but the M_W-volume relation might depend on the kind of molecule. By taking into account the hydrodynamic volume (or hydrodynamic radius r_h by assuming spherical molecules) instead of M_W, different standards can be used for a so-called universal calibration [14].

Globuar proteins have a compact shape and can be approximated as spheres with a hydrodynamic radius r_h (in nm) dependent of the molecular weight M_W (in g/mol) by the following expression [15,16]:

$$r_h = 0.081\ M_W^{1/3} \qquad (2)$$

Name of the molecule	#	M_W (g/mol)	r_h (nm)	K_{SEC} S-300	K_{SEC} S-400	K_{SEC} S-500
λ-DNA (48502 base pairs)	v_0	31500000	≥ 500	0	0	0
Thyroglobulin bovine (MWGF1000)	1a	669000	7.084	0.156	0.450	0.615
Thyroglobulin porcine (#89387)	1b	669000	7.084	0.138	0.433	0.615
Apoferritin (MWGF1000)	2	443000	6.175	0.222	0.493	0.647
Beta-Amylase (MWGF1000)	4	200000	4.737	0.315	0.566	0.699
Alcohol Dehydrogenase (MWGF1000)	5	150000	4.304	0.367	0.600	0.739
Albumin (MWGF1000)	6	66000	3.273	0.433	0.657	0.731
HSA (A3782)	7	60000	3.171	0.436	0.672	-
Carbonic Anhydrase (MWGF1000)	8	29000	2.489	0.601	0.742	0.806
acetone	v_t	58	< 0.5	1	1	1

Table SI-IV.2: Molecular weights and estimated hydrodynamic radii (derived with Formula (2) of several protein standards, and their K_{SEC} values for three different Sephacryl columns. The numbers in parentheses indicate the product number from Sigma-Aldrich. λ-DNA and acetone are used as limit for big and small molecules, respectively. The K_{SEC} values for the Sephacryl S-400 gel have been derived from the measurements shown in Figure SI-IV.2.

In Table SI-IV.2 a number of proteins with radii derived by their molecular weight according to Formula (2) are enlisted. It has to be noted that for globular proteins, other radii than the ones derived with Formula (2) have been reported in literature [17], and even if the protein structure is

known, sizes obtained from protein crystals (e.g. from the RCSB Protein Data Bank) are naturally not the same for hydrated proteins in solution

For each of the protein standards the partition coefficient was determined for different gels. In Figure SI-IV.2 the measurements for the Sephacryl S-400 filled column are shown. The partitions coefficients derived from this measurement according to Formula (1) and also the ones obtained with other gels are enlisted in Table SI-IV.1.

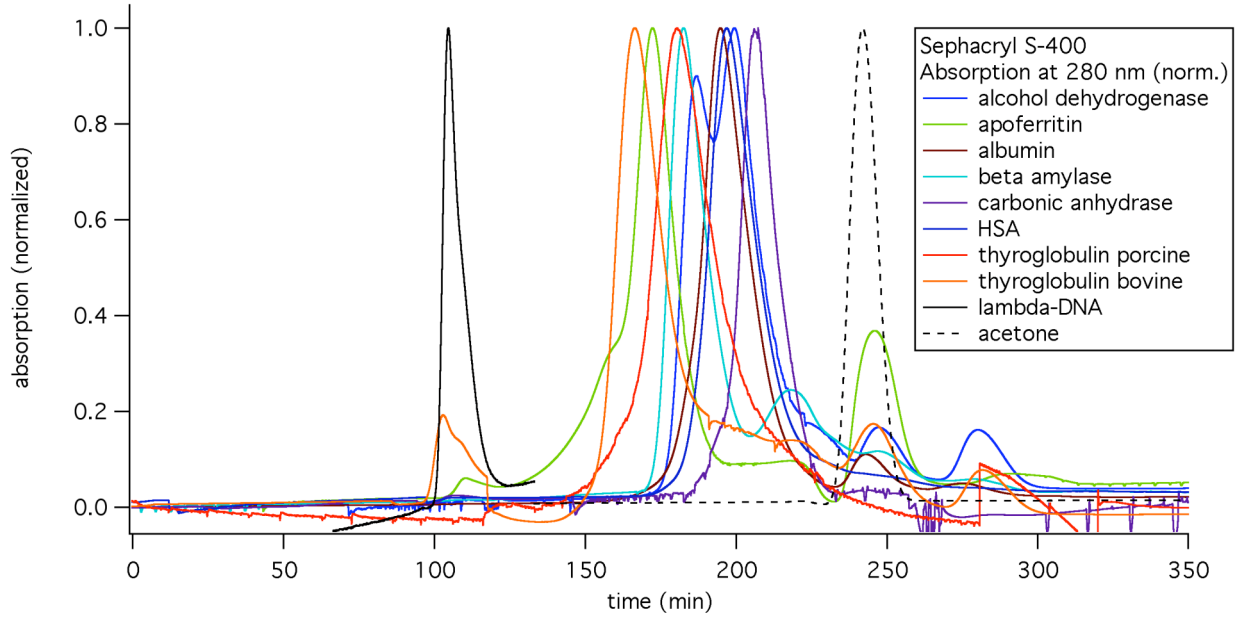

Figure SI-IV.2: Chromatograms of protein standards. The normalized absorption at 280 nm of the elute solution is plotted versus the elution time. Larger proteins elute first. The elution times of the peak maxima were used to calculate the K_{SEC} values shown in Table SI-IV.2. Lambda-DNA and acetone were injected in the same run, for clarity the peaks are normalized separately for this graph.

The elution time, volume or respectively K_{SEC}, now can be related to the hydrodynamic radius according to Table SI-IV.2 (and Formula (2) which leads to a calibration curve that relates partition coefficients K_{SEC} to hydrodynamic radii r_h, see Figure SI-IV.3. An empirical finding for globular proteins is that in a certain range for a size-exclusion column there is a linear dependence between the logarithm of the molecular weight and the elution time, volume or partition coefficient K_{SEC}. According to Formula (2) this also yields to a linear relation between the logarithm of the hydrodynamic radius r_h and the partition coefficient K_{SEC}:

$$\log r_h = a \cdot K_{SEC} + b \qquad (3)$$

It is obvious that Formula (3) can only be valid for an intermediate range $0 << K_{SEC} << 1$. $K_{SEC} = 0$ refers to the exclusion volume and therefore to the M_W or radius of the standard sample (here λ-DNA) with a molecular weight of at least one order of magnitude bigger compared to the samples of interest. However, K_{SEC} would be also = 0 for any molecule bigger than λ-DNA. The case $K_{SEC} = 1$ (here determined with acetone) refers to ideally small molecules, with a M_W or radius close to 0. However, K_{SEC} would be also = 1 for any molecule smaller than acetone. Therefore the linear relation between log r_h and K_{SEC} is not valid for K_{SEC} close to 1 or close to 0. Also various other models and functions have been used to describe the relation between r_h and K_{SEC} alternative to Formula (3) [15]. Formula (3) has rather to be seen as an empirical instead of an analytical function. In addition, the exact shape of the $r_h(K_{SEC})$ calibration curve also

depends on parameters that are not at all included in the model, e.g. the shape and size distribution of the pores of the stationary phase, or any possible non-ideal behavior like electrostatic or hydrophobic interactions between the sample and the column.

The K_{SEC} data shown in Table SI-IV.2 for different protein standards with known r_h were fitted with Equation (3) with the fit parameters A and B. The fits are shown for three different column materials in Figure SI-IV.3 and the resultant fit parameters are summarized in Table SI-IV.3. By inverting Equation (3) now any measured K_{SEC} value can be converted in a corresponding hydrodynamic radius r_h:

$$r_h(K_{SEC}) = A \exp(-B\, K_{SEC}) \qquad (4)$$

Expression (4) was then used in the following to convert the K_{SEC} values obtained for nanoparticles into hydrodynamic radii.

Effective diameters are assumed as two times the hydrodynamic radius:

$$d_{eff} = 2 \cdot r_h \qquad (5)$$

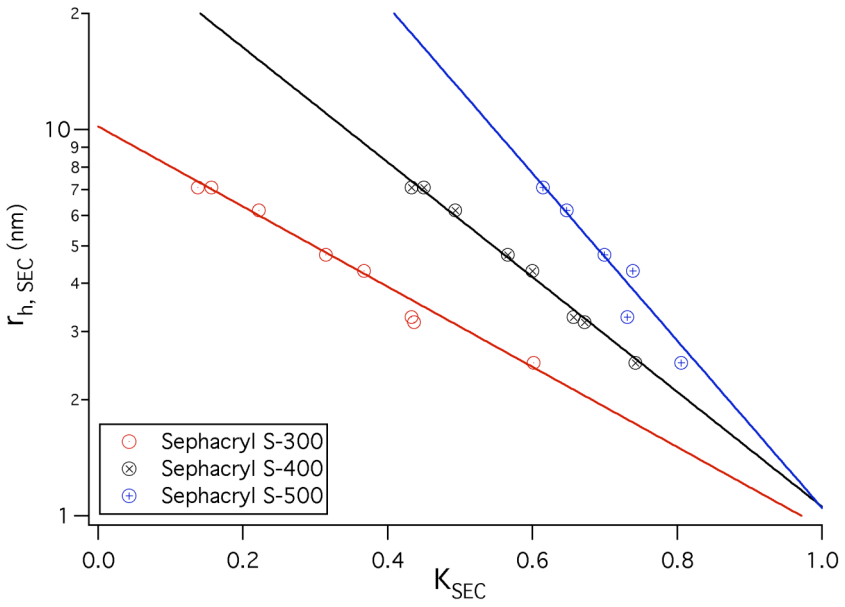

Figure SI-IV.3: K_{SEC} values obtained from protein standards for different column materials. The hydrodynamic radii of the proteins r_h are plotted as derived from Equation (2) (numerical values as in Table SI-IV.2). A mono-exponential function $r_H = A \exp(-B\, K_{SEC})$ has been fitted to the data points with the fit parameters A and B. The resulting fit parameters are enlisted in Table SI-IV.3.

Column material	Fit parameter A	Fit parameter B	range of K_{SEC} for used proteins
Sephacryl S-300	10.2 ± 1.3	2.39 ± 0.47	0.14 – 0.60
Sephacryl S-400	32.4 ± 5.7	3.42 ± 0.34	0.43 – 0.74
Sephacryl S-500	154 ± 166	4.99 ± 1.62	0.62 – 0.81

Table SI-IV.3: Parameters A and B of Function (3) which can be used to relate partition coefficients K_{SEC} with hydrodynamic radii r_h. A and B have been determined from the data shown in Figure SI-IV.3.

All the protein standards are eluted in different K_{SEC} ranges (Table SI-IV.3) as expected for the three Sephacryl materials with their three different pore sizes. The nanoparticle samples elute always before or around the biggest protein standard (thyroglobulin), so that the fit function has to be extrapolated in order to derive their hydrodynamic radii. In case of the column material with the smallest pores (Sephacryl S-300), the protein standards fit best to the well-resolved range, while the nanoparticle samples are "squeezed" close to the void volume v_0, or respectively $K_{SEC} = 0$. The assumed linear dependence holds not for K_{SEC} values close to 0 where the real slope has to become much steeper towards 0, so the simple exponential fit (3) delivers too small radii for any K_{SEC} value close to 0. In case of the column material with large pores (Sephacryl S-500), the proteins standards are "squeezed" into a range of K_{SEC} close to 1. Because the fit of the exponential function is now based on a very small range $K_{SEC} = 0.62 - 0.81$, the extrapolation to smaller K_{SEC} values cannot be reliable. The resolution of the column material Sephacryl S-400 is relatively good for both, the protein standards and nanoparticle samples, therefore it was chosen as the gel to be used best for the size characterization. For preparative purposes the situation can be different: E.g. for the separation of polymer-coated nanoparticles from unbound polymer (micelles), the Sephacryl S-300 shows a better performance.

As nanoparticle samples, the series of Au and CdSe/ZnS particles saturated with PEG of different molecular weight described above was run on the size exclusion columns. Figures SI-IV.4 and SI-IV.5 show as an example the chromatograms of CdSe/ZnS nanoparticles (absorption measured at 280 nm, due to the better signal-to-noise ratio compared to the wavelength of their exciton peak) and of Au nanopartcivles (absorption measured at 515 nm) and) run on a Sephacryl S-400 column. Similar to the protein standards, the elution times (peak maxima) were converted to K_{SEC} values (Tables SI-IV.1 and SI-IV.4.). From the K_{SEC} values then the hydrodynamic radii r_h were calculated by the inverse fit function (4) together with the fit parameters A and B (Table SI-IV.3) that were obtained from the protein standards. The hydrodynamic radii are enlisted in Table SI-IV.4.

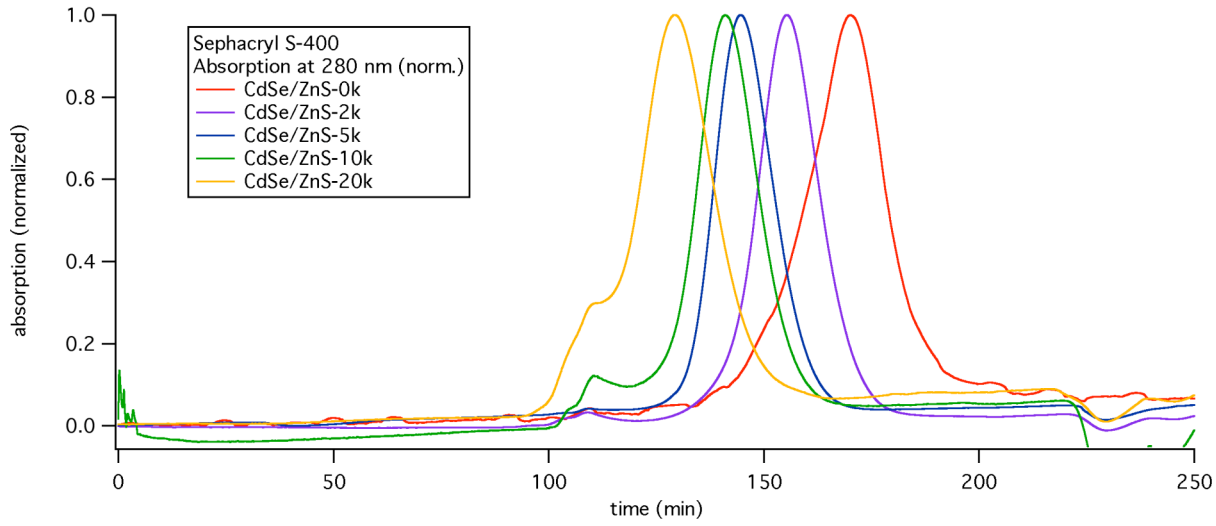

Figure SI-IV.4: Chromatograms of CdSe/ZnS nanoparticles saturated with PEG of different molecular weight.

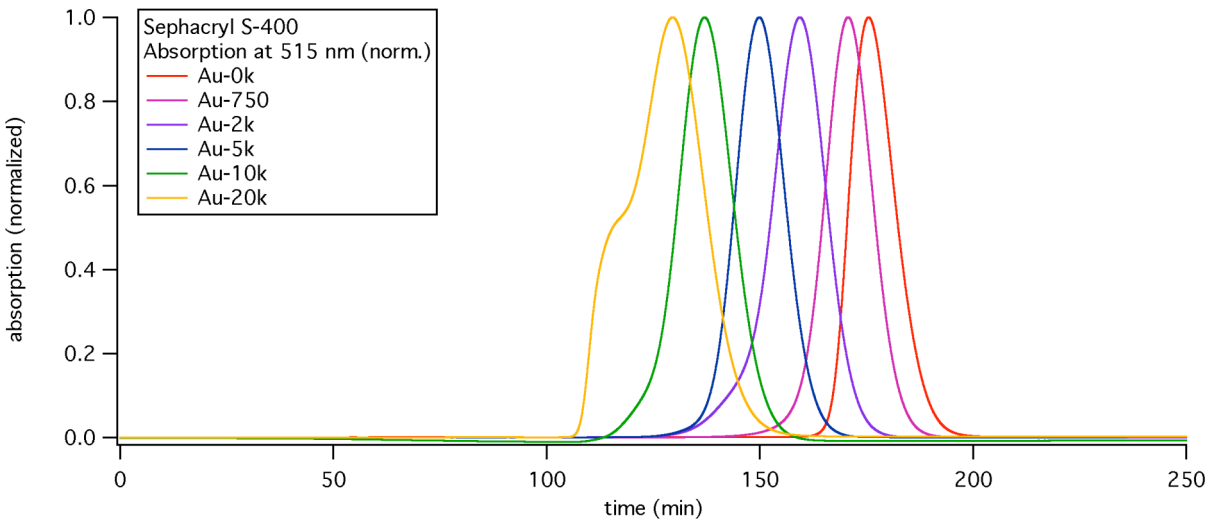

Figure SI-IV.5: Chromatograms of Au nanoparticles saturated with PEG of different molecular weight.

In Figure SI-IV.6, the calculated radii for Au and CdSe/ZnS particles with polymer-coating and PEG of different molecular weight are plotted. In contrast to Figure SI-IV.3 the scale for the hydrodynamic radius r_h is now linear, and also the 95 % expectation interval (internal functions of Igor software (Wavemetrics, V5.05)) is plotted. Based on the expectation interval, an error of about ± 2 nm in the determined size can be estimated for the larger PEG-modified nanoparticles in the case of the column packed with Sephacryl S-400.

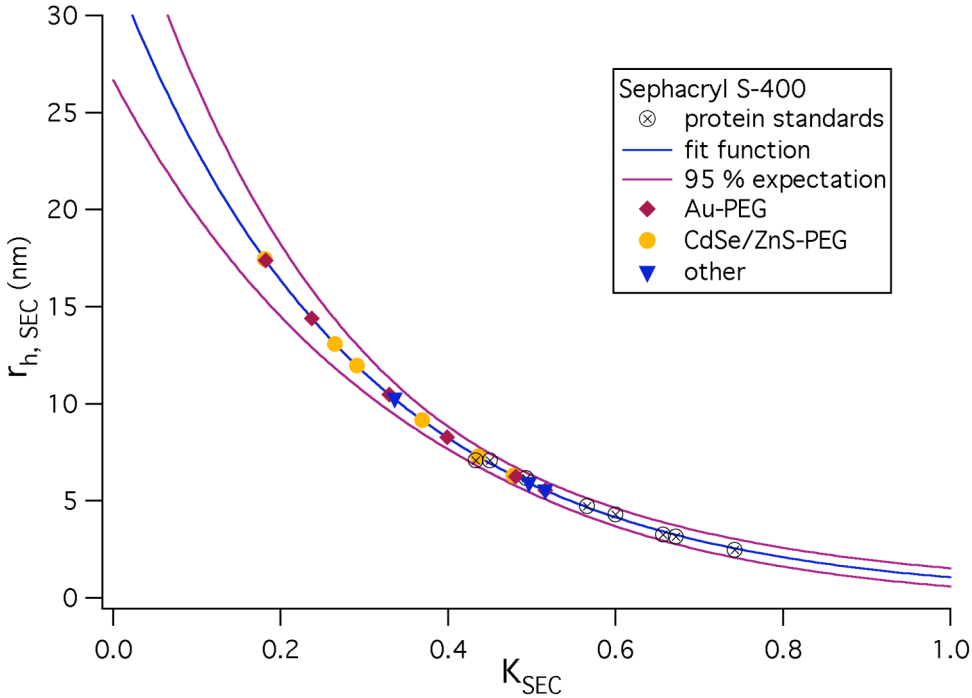

Figure SI-IV.6: The protein standards with the fitted and extrapolated exponential function (4) are shown here with a linear scale, together with the 95 % expectation interval. The radii of the nanoparticle samples were calculated from their K_{SEC} value with the same fit function. The numeric values are given in table SI-IV.4. This Figure demonstrates the error in the derived hydrodynamic radii due to deviations in the parameters A and B in the fit function.

Particles	Mw(PEG)	S-300 K_{SEC}	S-300 $r_{h,}$ (nm)	S-400 K_{SEC}	S-400 $r_{h,}$ (nm)	S-500 K_{SEC}	S-500 $r_{h,}$ (nm)
CdSe/ZnS	0	0.179	6.65	0.478	6.31	0.622	6.91
CdSe/ZnS	750	0.082	8.39	0.436	7.29	0.581	8.44
CdSe/ZnS	2000	0.060	8.84	0.369	9.17	0.562	9.32
CdSe/ZnS	5000	0.053	9.00	0.291	11.97	0.512	11.93
CdSe/ZnS	10000	0.047	9.12	0.265	13.08	0.473	14.48
CdSe/ZnS	20000	0.043	9.20	0.181	17.44	0.400	20.83
Au	0	0.233	5.85	0.516	5.54	0.653	5.89
Au	750	0.172	6.76	0.481	6.25	0.629	6.67
Au	2000	0.113	7.78	0.399	8.27	0.579	8.53
Au	5000	0.055	8.93	0.330	10.47	0.546	10.07
Au	10000	0.042	9.23	0.237	14.40	0.456	15.76
Au	20000	0.039	9.28	0.182	17.38	0.407	20.11
QD655 carboxyl		0.149	7.15	0.497	5.91	0.607	7.41
QD655 SA		0.060	8.84	0.336	10.26	0.537	10.54

Table SI-IV.4: Nanoparticles run on Sephacryl S-300, S-400, and S-500 columns. Enlisted are the K_{SEC} values and the hydrodynamic radii r_h derived by fit function (4) with the parameters from Table SI-IV.3.

For the size calibration, the series of globular proteins were run on the columns and the peak position was recorded at the maxium at 280 nm, where proteins as well as lambda-DNA and acetone absorb light. Protein solutions were prepared at a concentration of 2 – 10 mg/ml in either SBBS or 1 x protein stabilizing cocktail (Pierce #89806). Alcohol dehydrogenase eluted later after longer storage, so the solution was always prepared freshly prior to injection. Catalase (from bovine liver, Sigma-Aldrich #C1345) yielded a slightly turbid solution and precipitated over time. Since also the K_{SEC} values were larger than expected from the molecular weight and did not fit to the calibration curve, the data was not taken into account.

It has to be noted that the particle radii are derived from a function extrapolated from the data points of the protein standards. It would be desirable to have larger particle standards available in order to be able to have a truly *interpolated* calibration curve also for radii between e.g. 10 and 20 nm. For the column calibration, also commercial Au particles (British Biocell) of diameters between 5 and 15 nm were tried, with different surface modifications: the particles were coated with phosphine (bis(p-sulfonatophenyl)phenylphosphine dihydrate dipotassium salt, Strem Chemicals #15-0463), and MPA (mercaptopropionic acid, Sigma-Aldrich # M5081) by incubating the Au particle solution with some mg phosphine or MPA for several days, so that the citrate shell was replaced. An empty disposable plastic syringe was packed with some Sephacryl medium after the outlet had been stuffed with some glass wool, and equilibrated with SBB or SBBS driven by gravity. However, even in the case of SBB, 5 nm particles coated with MPA or phosphine got stuck in the stationary phase and were visible as a bluish band. For both cases, no free MPA or phosphine had been added to the mobile phase. Also 55 nm blue latex beads (Sigma-Aldrich #L1148) did not pass the small test column. In lack of a refractive index detector, plain PEG standards could not be measured since it shows no optical absorption or fluorescence in the wavelength range 200 – 800 nm.

There are already a number of publications about SEC with colloidal nanoparticles in both aqueous [18-22] or organic solvents [23-25], however in most cases either surfactants or precursors for the core material were added to the mobile phase in order to insure the stability of the colloids. For a reliable comparison, both size standards and samples should be run in the same mobile phase. Our approach in which the usual conditions that are also used for the preparative purification of nanoparticles, no additives were necessary for the polymer coated nanoparticles with or without PEG modification.

215

V) FCS experiments

FCS was established by Madge et al. (1972) [26] as a way for measuring the diffusion constants of fluorescent particles dispersed in a solvent. From the diffusion constant of a particle it is possible to derive then its hydrodynamic radius through the Stokes-Einstein relation. Here, we first give a short overview of the FCS theory (details are discussed elsewhere [27-29]), and then we describe the experimental procedure for determining the average radius of the nanocrystals in the present work, using the FCS theory.

Let us assume that an excitation light source is focused on a tiny volume (V_{eff}) of the solution containing the fluorescent particles. On average, <N> particles will be sampled in this volume. However, the number of particles N(t) in this volume will fluctuate over time, because the particles can diffuse in and out of it. In the case of dilute solutions (so only few particles are present in the focus volume, on average), the fluctuation in the number of particles can be described by a Poisson distribution:

$$\sqrt{\frac{\langle(\delta N)^2\rangle}{N}} = \frac{1}{\sqrt{N}} \qquad (1)$$

$\delta N(t) = N(t) - \langle N \rangle$ is the fluctuation of the number of particles, and $\langle N \rangle$ is the mean number of particles in the volume. Now, the concentration of the particles must be high enough to guarantee a good signal to noise ratio, but low enough to observe free particle diffusion. A good compromise would correspond roughly to 1 particle per femtoliter of the focus-volume V_{eff}. The FCS theory demonstrates that it is possible to derive the diffusion constant of the particles from $\delta N(t)$, and the principle can be understood in terms of a simple model. The time a particle needs to diffuse in and out of the focus volume depends indeed on its diffusion coefficient. The larger the diffusion coefficient, the faster the particles can diffuse in and out of the focus, and consequently faster time scale will characterize the fluctuations of the number of particles in V_{eff}. The analysis of the time scales involved in the fluctuations can be carried out by means of an autocorrelation function.

To a first approximation, we assume a constant value for the fluorescence emission from each particle inside the focus volume. In this simplified approach fluorescence fluctuations due to fluctuations in the absorption cross-section and in the quantum yield and blinking of the particles are neglected. Particles are also assumed to have a spherical shape.

The number of particles in the focus at a given time t can be experimentally determined by the total fluorescence F(t) collected. Since the excitation light is focused on a tiny volume V_{eff}, only the particles within this volume contribute to the fluorescence signal. The fluctuation $\delta F(t) = F(t) - \langle F \rangle$ of the fluorescence signal is defined as the deviation from the mean fluorescence signal $\langle F \rangle$, which is given by:

$$\langle F \rangle = \frac{1}{T}\int_0^T F(t)dt \qquad (2)$$

The number of particles N(t) in the focus can be written as an integral over the local particle concentration $c(\underline{r}, t)$:

$$N(t) = \int_{V_{eff}} c(\underline{r}, t)dV \tag{3}$$

We now assume that the fluctuations in the fluorescence signal are only due to local changes in the concentration $\delta c(\underline{r}, t)$ in the effective focus-volume V_{eff} . In addition, we merge the spatial parameters of the illumination to a function $W(\underline{r})$ that is written as:

$$W(\underline{r}) = e^{-2(x^2+y^2)/r_0^2} \cdot e^{-2z^2/z_0^2} \tag{4}$$

W(r) is the so called Molecule Detection Efficiency which gives the probability of exciting and detecting a fluorescent particle in the solution. It is therefore the product of the excitation profile of the focused laser and the spatial collection efficiency of the confocal detection optics. Under carefully chosen setup conditions $W(\underline{r})$ can be approximated as a 3-dimensional Gaussian ellipsoid, as has been assumed in Equation (4). $\underline{r}$ = (x, y, z) describes the coordinates in the three-dimensional space. Here r_0 is the radius in the focal plane where the excitation intensity of the laser has dropped to $1/e^2$ compared to the center. The parameter z_0 gives the extension of the effective detection volume on the z-axis and is mainly determined by the used objective and the size of the pinhole.

The fluctuation of the fluorescence signal can then be written as:

$$\delta F(t) = \eta \int_{V_{eff}} W(\underline{r}) \cdot \delta c(\underline{r}, t)dV \tag{5}$$

The constant value η contains the quantum efficiency of the dye, detection efficiency and absorption cross-section. The normalized autocorrelation function G(τ) for fluorescence fluctuations δF(t) is defined as:

$$G(\tau) = \frac{\langle \delta F(t) \cdot \delta F(t+\tau) \rangle}{\langle F(t) \rangle^2} \tag{6}$$

G(τ) is a measure of the self-similarity of the fluorescence signal after a delay-time τ. Thus G(0) is the variance $\langle \delta F(t)^2 \rangle / \langle F \rangle^2$. By inserting equation (5) in equation (6) the autocorrelation function becomes:

$$G(\tau) = \frac{\int\int_{V\,V'} W(\underline{r}) \cdot W(\underline{r}') \cdot \langle \delta c(\underline{r},0) \cdot \delta c(\underline{r}', \hat{o}) \rangle \, dVdV'}{\left(\langle c \rangle \int_V W(\underline{r})dV \right)^2} \tag{7}$$

Under the assumption that the particles can diffuse freely in all three spatial directions (Brownian diffusion), we can derive an expression for the concentration fluctuations $\delta c(\underline{r},t)$ if we solve the diffusion equation, where D is the diffusion coefficient.

$$\frac{\delta c(\underline{r},t)}{\ddot{a}t} = DV^2\delta c(\underline{r},t) \tag{8}$$

We can use the following expression for $\delta c(\underline{r},t)$:

$$\delta c(\underline{r},t) = \delta c(\underline{r},0)\cdot e^{-\underline{r}^2/Dt} \tag{9}$$

The solution of the diffusion equation using (9) yields:

$$\langle \delta c(\underline{r},0)\delta c(\underline{r}',\tau)\rangle = \langle c\rangle \frac{1}{(4\pi D\tau)^{\frac{3}{2}}}\cdot e^{\frac{(\underline{r}-\underline{r}')^2}{4D\tau}} \tag{10}$$

Insertion of (10) into (7), followed by integration over the volume, finally leads to the autocorrelation function for freely diffusing particles (11).

$$G(\tau) = G_{motion}(\tau) = \frac{1}{V_{eff}\langle c\rangle}\cdot\frac{1}{(1+\frac{\tau}{\tau_D})}\cdot\frac{1}{\sqrt{1+\frac{\tau}{\tau_D\cdot s^2}}} \tag{11}$$

with the characteristic diffusion-time τ_D given by

$$\tau_D = \frac{r_0^2}{4D} \tag{12}$$

and the structure parameter s given by

$$s = \frac{z_0}{r_0} \tag{13}$$

The effective focus volume V_{eff} is then defined as

$$V_{eff} = \frac{\left(\int_V W(\underline{r})dV\right)^2}{\int_V W^2(\underline{r})dV} = \frac{\left(\int e^{-2\frac{x^2+y^2}{r_0^2}}\cdot e^{-2\frac{z^2}{z_0^2}}dV\right)^2}{\int e^{-4\frac{x^2+y^2}{r_0^2}}\cdot e^{-4\frac{z^2}{z_0^2}}dV} = \pi^{\frac{3}{2}}\cdot r_0^2\cdot z_0 \tag{14}$$

For fluorescent colloidal nanoparticles formula (11) has been proven to fit well to the experimental data[8]. For organic fluorophores a more advanced approach is applied: The correlation function G_{motion} (which describes only changes in fluorescence due to the motion of

[8] In our first manuscript (7) we have used Formula (16) also to fit the autocorrelation functions of CdSe/ZnS. However, in the following manuscript (30) we have used Formula (11) to the autocorrelation functions of CdSe/ZnS, since they described the results better. Also in this manuscript we use (11) to fit the autocorrelation functions of CdSe/ZnS. For organic fluorophores the more complex Formula (16) has to be applied.

the particles) is therefore multiplied by a kinetic factor that accounts for blinking / flickering [29,31] in the fluorescence of the particles

$$X_{triplet} = \frac{1 - T_{trip} + T_{trip} \cdot \exp\frac{\hat{o}}{\hat{o}_{trip}}}{1 - T_{trip}} \quad (15)$$

The entire fit function than reads

$$G(\tau) = 1 + X_{triplet}\, G(\tau) \quad (16)$$

For measurements involving CdSe/ZnS quantum dots only the simple approach (11) was used, for measurement of organic fluorophore approach (16).

The hydrodynamic radius r_h of the spherical particles can be obtained by inserting the diffusion constant D (from equation (12)) into the Stokes-Einstein-equation:

$$r_h = \frac{kT}{6\pi\eta D} \quad (17)$$

In our work we define the effective diameter d_{eff} of nanoparticle conjugates as two times their measured hydrodynamic radius:

$$d_{eff(FCS)} = 2 \cdot r_h \quad (18)$$

Having given a brief overview of the FCS theory, we now describe the experimental procedure followed for the determination of the average diameter of the polymer coated nanocrystals synthesized in the present work.

Figure SI-V.1 shows a sketch of the experimental setup. A laser beam is focused by an objective with a high numerical aperture. Fluorescent light that is collected by the same objective can pass through the dichroic mirror as it is slightly shifted to higher wavelengths compared to the excitation. A 50/50 beamsplitter gives half of the intensity to two independent detection channels. With the filters the desired detection wavelengths can be chosen. Behind the pinholes of variable size the photons are detected with avalanche photodiodes giving the intensity versus time F(t). An autocorrelation of the signal is done by a correlator card attached to a computer.

The Experiments were performed with a Confocor2 FCS-setup from Zeiss™. The laser light from a HeNe-Laser (Lasos/Zeiss, 633 nm wavelength) was coupled into the system via a dichroic mirror and was focused with a Zeiss C-Apochromat water immersion objective (40x; numerical aperture: 1.2) to a small volume within the diluted sample. The fluorescence signal emitted from the particles passed through a dichroic mirror and the focal plane was selected by a pinhole with 90 μm diameter. The signal was split by a 50/50 beamsplitter and collected by two Avalanche Photo Diodes (after passing appropriate filters).

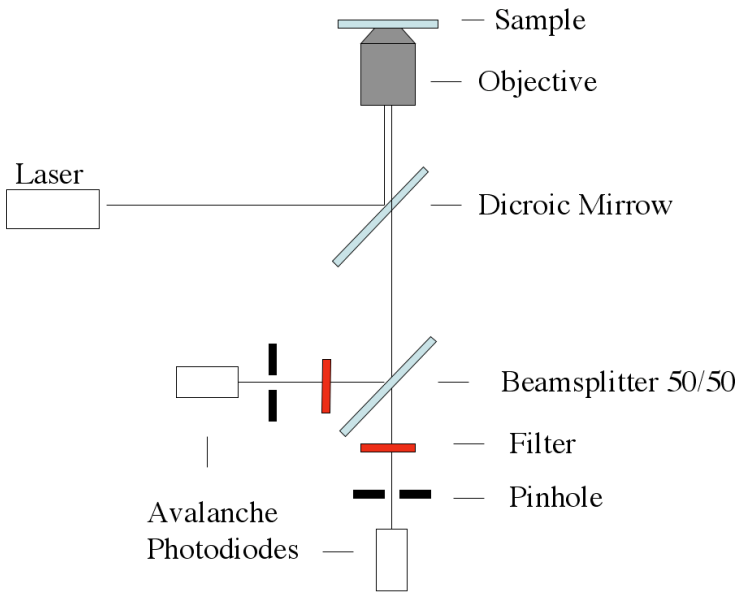

Figure SI-V.1: FCS setup. An Ar-ion-Laser (Lasos/Zeiss) was used, the cut-off wavelength of the dicroic mirror was 510 nm, and 510 nm longpass filters were used to observe the emitted fluorescence.

First of all, the system had to be calibrated. In particular the volume of the focus had to be determined experimentally. For this purpose fluorescent molecules with a known diffusion constant were used as calibration sample. We used a solution of Cy5 dye (Molecular Probes, excitation maximum 649 nm, emission maximum 670 nm) dissolved in water (10 nM concentration), as this dye has a fluorescence in the red similar to the CdSe/ZnS nanoparticles that are investigated in this study. The time trace of the fluorescence signal F(t) from this sample was recorded 10 times, each time for 20 seconds (Figure SI-V.2). For each measurement, the autocorrelation function $G(\tau)$ for the fluorescence fluctuations $\delta F(t)$ was calculated by using equation (6) (Figure SI-V.3). The experimental data for the autocorrelation function were fitted with equation (16), using the 5 fit parameters τ_{trip}, T_{trip}, τ_D, s, and $\langle N \rangle = V_{eff}\langle c \rangle$. Since the diffusion constant for Cy5 is known ($D = 250\ \mu m^2/s$), the focal radius r_0 could be derived via (12) using for τ_D the value obtained from the fit. Similarly, z_0 could be derived via (13) by using the fit results for the structure parameter s and r_0. The mean values for r_0 and z_0 (and thus also for s) obtained from the ten individual measurements where then used for all the measurements on CdSe/ZnS nanocrystal samples.

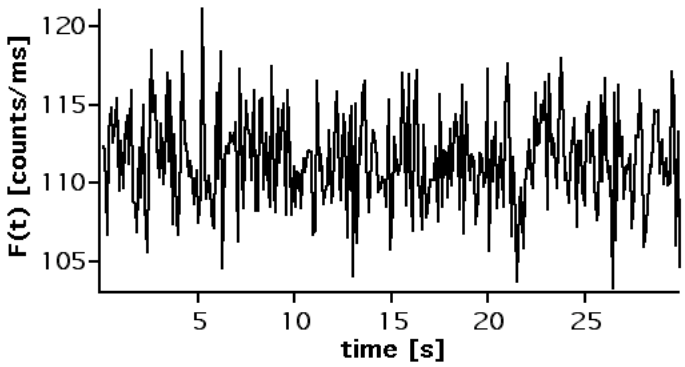

Figure SI-V.2: Time trace of the recorded fluorescence intensity F(t) of a Cy5 fluorescent dye solution.

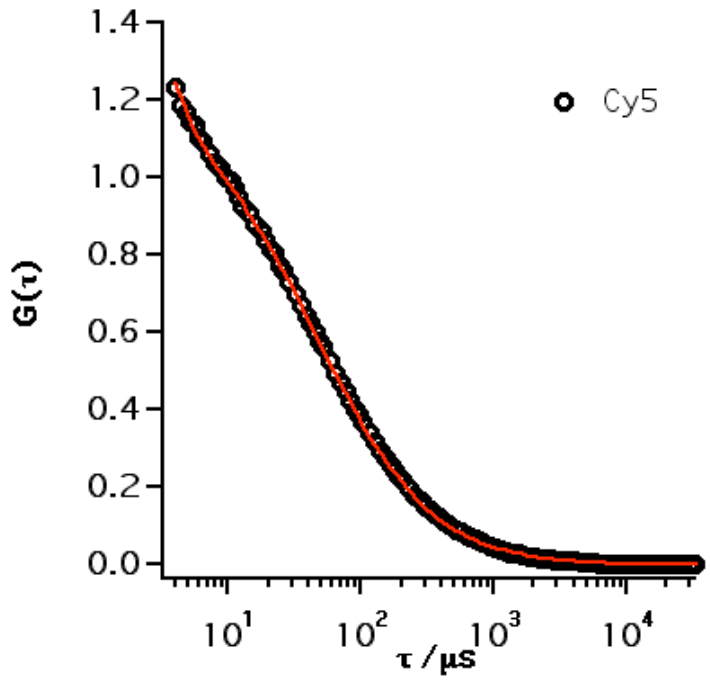

Figure SI-V.3: Autocorrelation function G(τ) calculated from the F(t) data shown in Figure SI-V.2 (dotted line). The curve was fitted with the function given in equation (16). The fit yielded the five fit parameters: Triplet time τ_{trip} = 3 µs, a triplet fraction of 11% (T_{trip} = 0.11), the characteristic diffusion time τ_D = 46 µs, structure parameter s = 8, and average number of dye molecules within the focal volume $\langle N \rangle = V_{eff}\langle c \rangle$ = 0.85. The focal radius r_0 was calculated by means of (12), using the known diffusion-constant of Cy5 (D = 250 µm²/s), and was equal to 215 nm.

For the measurements on the nanocrystal samples, nanocrystal solutions with a concentration of approximately 50 nM were deposited on a coverslip over the objective (the same as for the Cy5 dye solution). The time trace of the fluorescence signal F(t) was recorded at least ten times, each time for 20 seconds. The corresponding autocorrelation functions G(τ) were calculated using equation (6) and were fitted with (11). This time only two fit parameters were used: τ_D and $\langle N \rangle = V_{eff}\langle c \rangle$. The geometrical parameters for the focus volume (r_0 and z_0, as well as s) where in fact known from the previous calibration with the Cy5 solution. The diffusion constant for the nanocrystals D could be calculated via (12), using the diffusion time τ_D, as determined from the fit, and the known focal radius r_0. Finally, the hydrodynamic radius of the nanocrystals was calculated using the Stokes-Einstein-equation (17). As viscosity of water η_{water} = 0.98 mPa·s respectively was assumed at 20 °C. At least 10 individual measurements were performed for each sample, and the resulting hydrodynamic radius was determined as the mean value of the measurements.

In Figures SI-V.5 and SI-V.6 the correlation functions that have been determined in this work for different CdSe/ZnS - PEG conjugates are shown. The effective diameters derived from the fits are presented in the main text of this manuscript.

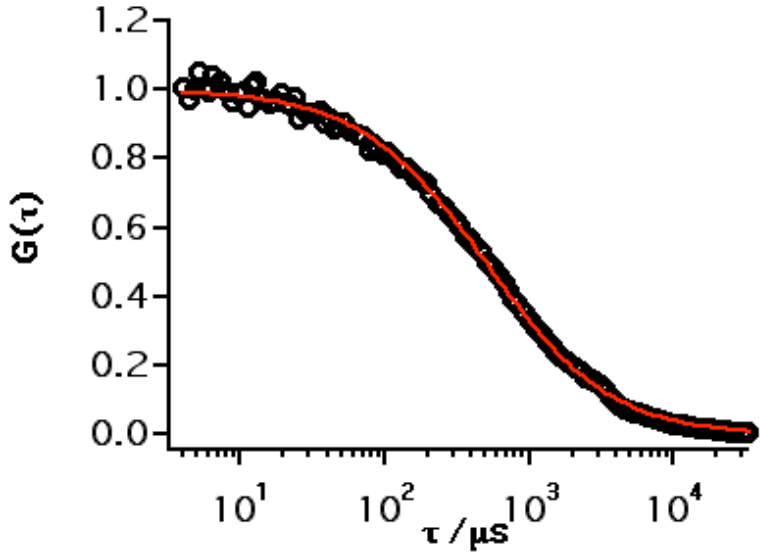

Figure SI-V.4: Autocorrelation function G(τ) calculated from the F(t) data recorded on a sample of red fluorescent, polymer-coated CdSe/ZnS nanocrystals dissolved in water (dotted line). The curve was fitted with the function given in equation (11), whereby the structure parameter (as determined from the calibration with Cy5) was kept fixed at s = 8. The fit yielded the following the characteristic diffusion time τ_D = 524 µs. With the known value for r_0 =215 nm the diffusion constant was determined via (12) to be D = 22 µm^2/s. According to the Stokes-Einstein relation this corresponds to a hydrodynamic radius of r_h = 11.3 nm.

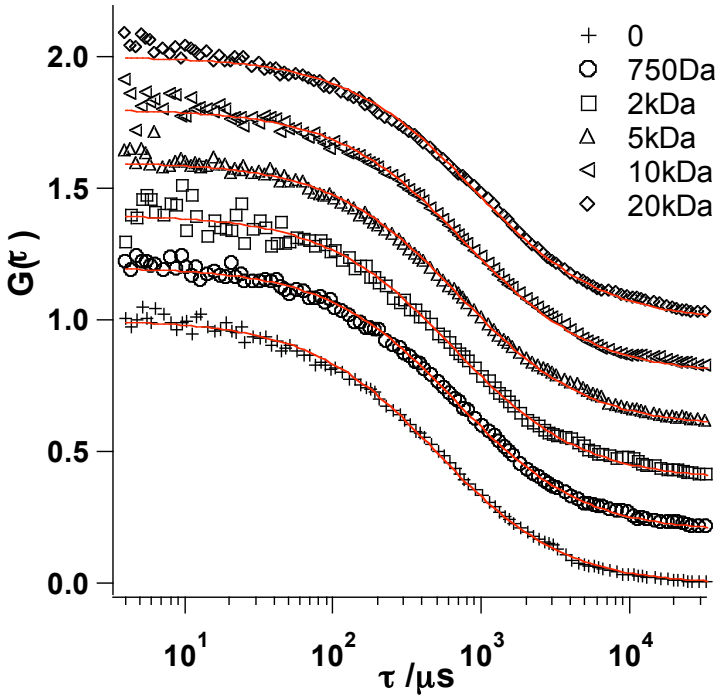

Figure SI-V.5: Correlation functions (experimental data: black points; fits: red lines) for polymer coated CdSe/ZnS nanoparticles that have been saturated with PEG molecules of different molecular weight.

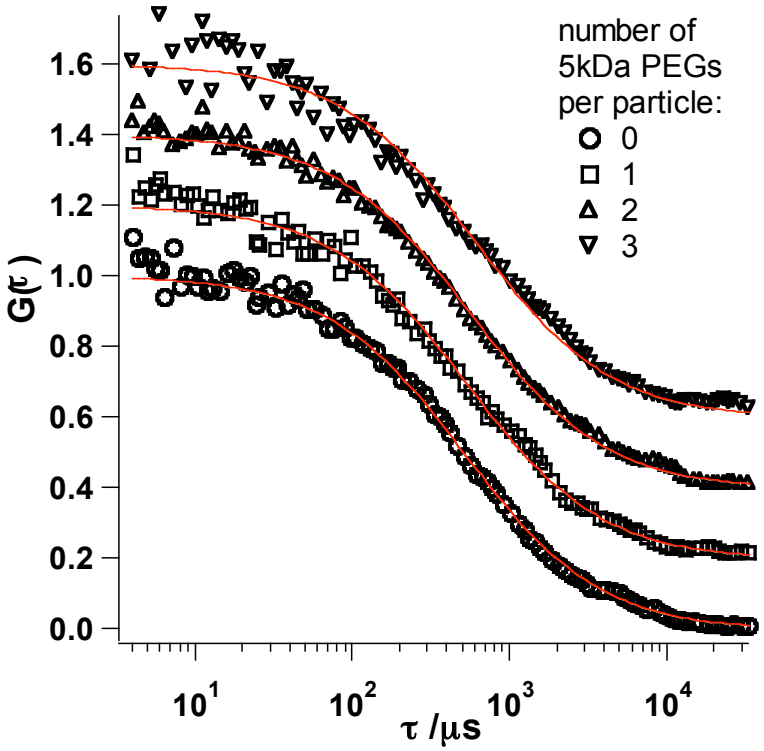

Figure SI-V.6: Correlation functions (experimental data: black points; fits: red lines) for polymer coated CdSe/ZnS nanoparticles that have been modified with 0, 1, 2, 3 PEG molecules per particle. The PEG had a molecular weight of 5 kDa.

VI) Thermophoresis experiments

Introduction: Thermophoresis, also named Soret Effect, is known for 150 years and describes the movement of molecules in temperature gradients, which is usually observed from hot to cold. A general theoretical description for behavior of molecules in solution was missing until recently [32]. With our method we create strong temperature gradients on the micron scale by infrared laser heating. A measure for the magnitude of the thermophoretic effect is the Soret coefficient S_T. It can be obtained from the steady state profile at constant laser heating typically after 100 seconds for the given geometry and diffusion coefficient. Given the temperature at radius r obtained from temperature dependent fluorescence, the concentration of fluorescent particles c(r) can be fitted with the steady state thermophoretic profile given by

$$c(r) = c_0 e^{-S_T(T(r)-T_0)} \quad (1)$$

with the chamber temperature T_0 and the bulk particle concentration c_0. Since S_T relates the concentration change exponentially to the temperature difference in principal very strong depletion can be expected at small temperature increase. If local equilibrium condition holds [33], the Soret coefficient is related to the solvation entropy ΔS by the expression

$$S_T = -\Delta S / kT \quad (2)$$

The build-up of a concentration gradient and the steady state are used to obtain important parameters of the fluorescent particles like effective charge and entropy of solvation [32]. Two contributions dominate the particle entropy S in water: the entropy of ionic shielding and the temperature sensitive entropy of water hydration. The interplay of these quantities determines whether particles move from hot to cold or vice versa. In some cases a balance of certain surface modifications may cancel out any thermophoretic motion. An important application has been established to obtain particle sizes by measuring the diffusion coefficients as described in the following.

Detecting molecules / particles: The technique is based on fluorescence microscopy were imaging was provided with an AxioTech Vario fluorescence microscope (Zeiss), illuminated with a high power LED (Luxeon) or Xenon-lamp (XBO, Osram) and imaged with the CCD Camera SensiCamQE (PCO). The filter sets allowed for a fluorescence excitation between 450 and 500 nm, while emission was detected at wavelengths > 560 nm. Nanoparticle concentration was inferred from fluorescence images, that were measured with a 40 x oil objective (NA =1.3). This relates to a field of view of 200 x 200 µm.

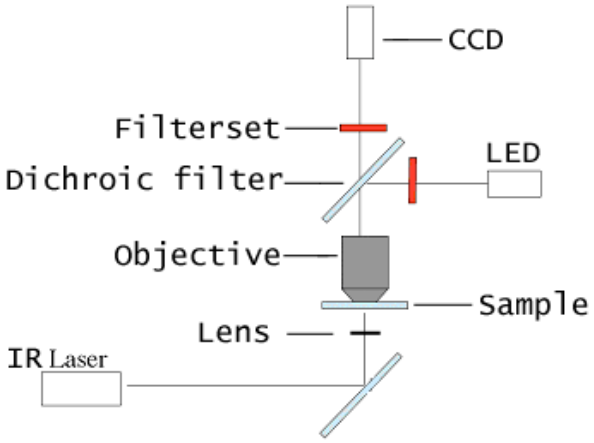

Figure SI-VI.1: Experimental Setup. An IR laser is coupled into a aqueous sample from below. Fluorescence excitation is provided by LED illumination and imaging is performed by a CCD camera device.

Manipulating molecules / particles: Thermophoresis is an all optical method to manipulate even small molecules / particles in solution. A localized temperature distribution is created in aqueous solution by means of infrared laser heating and particles move (typically to colder regions) to maximize their entropy of solvation. The velocity of the movement and the respective steady state, were thermodiffusion is balanced by backdiffusion, are strongly dependent on particle properties like charge and size. The temperature gradients used to induce thermodiffusive motions were created by aqueous absorption of an infrared laser at 1480 nm wavelength and a maximum power of 320 mW (Furukawa). Water strongly absorbs at this wavelength with an attenuation length of κ = 320 µm. The laser beam was moderately focused with a lens of 8 mm focal distance (Thorlabs, C240TM-C). Typically, the temperature in the solution was raised by 2 - 15 K in the beam center. The laser was focused into the sample from below the sample holder and the beam position in the x/y plane could be adjusted by two galvanoometrically controlled infrared mirrors (Cambridge Technology 6200-XY Scanner with Driver 67120).

Temperature calibration: Temperatures have been measured with the temperature dependent fluorescence signal of the dye BCECF, diluted to 50 µM in 10 mM TRIS buffer. Details of bleaching correction and temperature extraction were described previously[34]. From the total temperature dependence of BCECF of -2.8 %/K, only -1.3 % /K stems from pH drift of the used TRIS buffer. The remaining -1.5 % /K are the result of thermodiffusion of the dye itself, measured to be S_T = 0.015 /K with the concentration over time method described below. Determining the exact temperature distribution is important to quantify the thermophoretic effect, but not necessary to measure diffusion of particles [34].

Measurement: Measurements were performed in thin microfluidic chambers of 20 µm in height. A droplet of 1.8µl was sandwiched between an object slide and cover slide (Roth, Karlsruhe). To avoid evaporation the chamber was sealed with nail polish. Beside the low consumption of sample volume the low sample thickness provides several advantages. Convection is largely suppressed by this geometry and the sample is homogeneously heated throughout its height since only a fraction of the laser power is absorbed on this lengthscale. Diffusion constants and the respective radii are measured as described in the following. The

sample was illuminated and fluorescence was recorded without heating with a frequency up to 20 Hz, depending on the fluorescence intensity. This determined the 100 % relative concentration level. Then the laser was turned on, and immediately the concentration in the heated center decreased until steady state was reached. The laser was turned off and images were recorded until the established concentration gradient had relaxed completely. Please note that thermal relaxation is much faster and established before 100 ms. For the sizes measured throughout this work a typical experiment was performed within 10 s. We obtained the diffusion constant D by analyzing the flattening of the concentration profile over time after turning the infrared laser beam off. First we calculated radial concentration averages, since we had heated with a round symmetric heatspot. The concentration profile obtained after thermal relaxation (> 100 ms) was fitted polynomically. The fit is the starting point to calculate the backdiffusion in a one dimensional finite element model in radial coordinates (FEMLab, Comsol) over time. The experimentally measured radial concentration timecourse was fitted by adjusting the diffusion coefficient used in the numerical calculation. The hydrodynamic particle radius r_h has been calculated by using the Einstein relation

$$D = kT / \pi\eta r_h \qquad (3)$$

In contrast to the gel electrophoresis and size exclusion chromatography measurements the effective diameters $d_{eff} = 2 \cdot r_h$ obtained with thermophoresis measurements do not depend on a comparison with standard samples of known diameter, but are absolute values. Since the Au-PEG conjugates do not fluoresce they could not be analyzed with thermophoresis. The measurement is also not sensitive to impurities even though they may be fluorescent. In Table VI.1 some results are listed.

sample	D [m^2/s]	r_h [nm]
QD655 carboxyl	$3.0 \cdot 10^{-11}$	7.0 ± 1.0
QD655 SA	$1.6 \cdot 10^{-11}$	12.8 ± 1.0
λ-DNA	$6.0 \cdot 10^{-13}$	348 ± 3.0

Table SI-VI.1: Nanoparticles investigated with thermophoresis. Enlisted are the diffusion constants D and the hydrodynamic radii r_h. The samples are the same as in Tables SI-IV.1 and SI-IV.2.

VII) Comparison of different methods

VII.1) Introduction to the differences of the methods

The most straight-forward way to determine the size of a particle is to make an image of the particle from which the size can be directly obtained. Due to their small size **optical microscopy** is obviously not suitable for this purpose due to the lateral resolution which is limited by diffraction. When electron- instead of light waves are used the resolution is increased by orders of magnitudes and thus individual single nanoparticles can be imaged with **transmission electron microscopy** (TEM). However, the contrast of the inorganic core is much higher than that of its organic shell. Therefore, in most cases only the inorganic particle core can be seen on a TEM image and it is not possible to directly measure the effective total particle diameter, although exceptions exist as for example for relatively thick silica layers around an inorganic particle core [35]. When TEM grids are prepared with the appropriate concentration of nanoparticles, the particles can self-assemble to 2-dimensional lattices [36]. In this way the size of the surfactant layer can be estimated as two times the minimum distance between the two adjacent inorganic particle cores [6,37]. For TEM imaging particles have to be deposited on a substrate and the solution in which the particles are dispersed must be evaporated. The thickness of the organic layer is likely to be underestimated due to the drying procedure. It is known for example that the organic layers of two adjacent particles can intercalate [6,37]. In **atomic force microscopy** (AFM) the surface of a substrate is probed with a tiny cantilever-tip and the deflection of the tip is a measure for the height profile of the sample. In this way the height of individual nanoparticles that are adsorbed on a substrate can be measured [38] and even the attachment of biological molecules can be analyzed [39,40]. Although nanoparticles have to be attached to a substrate, measurements can in principle be performed in solution. The measured height of the particles is a direct equivalent for their effective diameter. Due to the lateral resolution of the AFM which is limited by the sharpness of the probing tip, information about the effective diameter cannot be taken from the image of the surface but must be derived from the height profile. Potential problems include compression of the soft organic shell around the hard inorganic particle core which leads to too small effective diameters, although this problem can be reduced when the AFM is operated in tapping mode. Electrostatic and other interactions between the tip and the particle can also lead to wrong effective diameters [41]. AFM is an effective but also laborious method (if statistics have to be obtained) for directly measuring the effective diameter of single particles [38].

In contrast to the above described imaging methods the size of nanoparticles can also be determined by size-selective sorting. With **size exclusion chromatography** (SEC) nanoparticles can be sorted by size with size exclusion columns [18-25,42-45]. Size exclusion columns comprise a porous gel matrix through which the particles are run by the flow of the mobile phase. Smaller particles can diffuse into the pores and are therefore eluted later than bigger particles. By using particles with known size (such as protein calibration standards) a calibration curve between the elution time versus the effective particle size can be obtained [12, Holtzhauer, 1992 #10875]. By running a sample of nanoparticles through the same size exclusion column and by measuring the elution time the effective diameter of the particles can be interpolated from the calibration curve [24,25]. Size determination with SEC is an ensemble measurement. Although the particles are dispersed in their natural solvent the analysis relies on a stationary phase, i.e. a gel matrix, and the effective diameter of the particles can be influenced by interactions with the gel which can lead to non-ideal effects, e.g. the retardation of the sample by electrostatic or hydrophilic-hydrophobic interactions. Another size-selective sorting technique is **gel electrophoresis**. Here charged particles are run through a gel matrix by

applying an electric field along the gel. The bigger the particles are the slower they migrate on the gel and the smaller their electrophoretic mobility is [10,40,44,46-50]. Analogous to SEC, particles with known diameter can be run on the gel which can be used to generate a calibration curve that relates the electrophoretic mobility of particles to their effective diameter. In this way the effective diameter of particles can be determined by measuring their electrophoretic mobility. Of course the electrophoretic mobility of particles also depends on their charge and therefore size-selective sorting by gel electrophoresis can only be used for particles with similar surface charge. Like SEC, gel electrophoresis is an ensemble measurement in which the particles are dispersed in their solvent. However, interactions with the gel matrix, such as squeezing of the soft organic shell around the hard inorganic particle core, can lead to errors in the determination of the effective particle diameter. Particle sorting can also be achieved by free flow **capillary electrophoresis** (CE) without involving a gel matrix [51,52]. However, the resolution of the sorting usually decreases without gel matrix.

The size of particles can be derived from their diffusion coefficient via the Stokes-Einstein-relation. Diffusion coefficients of particles dispersed in a solvent can be experimentally determined with several techniques. In all this methods particles can be freely dispersed in the solvent without the need for a gel matrix or substrate to be attached to the particles. With **dynamic light scattering** (DLS) fluctuations in the light that has been scattered from a particle solution are analyzed by calculating the autocorrelation function [45,50,53-58]. The diffusion constant can be directly derived as absolute value from the correlation function with an analytical model for free diffusion. Quantitative analysis is hampered by the hybrid nature of the nanoparticles, whose refraction index of the inner inorganic core is significantly different from the refraction index of their organic shell. This complicates the transformation of the measured intensity distribution to a number distribution of particles size. Whereas light scattering works with relatively concentrated samples, **fluorescence correlation spectroscopy** (FCS) [26-29] measures the fluorescence of particles in a very diluted solution, in such way that on average there is always only one particle in the focal volume of a confocal fluorescence microscope. By this means, the signal of the recorded fluorescence reflects the light fluctuations caused by particles diffusing through the gaussian excitation profile of a focused laser. The mean diffusion constant of the particles is derived from the autocorrelation function of the intensity fluctuations of the recorded fluorescence [7,30,59-62]. In a simplified picture, a particle with a smaller diffusion coefficient that is moving with Brownian motion, remains longer in the focus of the excitation light and therefore fluctuations of the recorded intensity will be found on a slower time scale which is derived by the decay of the autocorrelation function of the measured intensity signal. The effective size of the particles is then again derived by the Stokes-Einstein-relation. Since the volume of the excitation focus is not known initially, it has to be determined by means of a dye with a known diffusion constant. In **thermophoresis** a solution that contains dispersed fluorescent particles is locally heated with an IR laser. Due to the heat gradient particles move into or out of the heated area. The direction of motion depends on the surface properties of the particle. The heat gradient results in an inhomogeneous concentration distribution imaged by fluorescence microscopy. After the heat source is removed the system equilibrates by diffusion and the fluorescence distribution becomes again homogeneous. By recording the changes in concentration the mean diffusion coefficient of the particle ensemble can be determined [32-34].

We also have to mention other methods that were not employed in this study, such as **X-ray diffraction** (XRD) [63,64], small angle scattering with x-rays (**small angle x-ray scattering**, SAXS) [63] and neutrons (**small angle neutron scattering**, SANS) [65]. Whereas XRD is insensitive to organic shells around the inorganic particle core, small angle scattering is

sensitive to it. However, it is very complicated to extract quantitative data for inhomogeneous systems, which are composed of various organic layers with inhomogeneous thickness, since numbers only can be obtained via fitting the data with layer-models. Furthermore, particles can be separated by their effective diameter by **analytical centrifugation** [55,66,67]. While this method yields good results for particles with a homogeneous mass density, in the case of core-shell nanoparticles the average mass density changes with the thickness of the (organic) shell, which complicates the calibration of the density gradient and a quantitative evaluation of particle size distributions. A summary of all the methods is shown in Table SI-VII.1.

Method	**Limited to nanoparticles that are**	**Particle state during measurement**
Fluorescence correlation spectroscopy (FCS)	fluorescent	in solution
Thermophoresis	fluorescent	in solution
Dynamic light scattering (DLS)		in solution
Gel electrophoresis	charged	in solution (gel)
Size exclusion chromatography (SEC)		in solution (gel)
Capillary electrophoresis (CE)	charged	in solution (free or gel)
Analytical centrifugation		in solution (density gradient)
Transmission electron microscopy (TEM)	composed out of atoms with high numbers Z of nucleons	on surface (dry)
Atomic force microscopy (AFM)		on surface (wet or dry)
X-ray diffraction (XRD)	crystalline	powder
Small-angle X-ray or neutron scattering (SAXS, SANS)		in solution

Table SI-VII.1: Overview and classification of analytical methods for determining nanoparticle diameters in respect to nanoparticle type and state.

229

VII.2) Comparison of our results with values from literature

Though several studies exist in which the effective diameters of particles have been measured most of these studies are either based on only one method or only one type of particle surface. The groups of Mattoussi [50] and Nie [58] have reported extensive studies in which data obtained with DLS and gel electrophoresis [50], and particles with different surface modification [58] were compared. As particles with different surface modification were used in these studies we cannot directly compare these values with those we obtained in our present study. Pons et al. determined an effective diameter of about 14.2 nm for polymer-coated CdSe/ZnS particles with fluorescence at 565 nm, as well with gel electrophoresis as with DLS, whereby their polymer-coating procedure was not exactly the same as the one we used for our study [50]. This lies in the same range as we determined with several methods for our plain polymer-coated CdSe/ZnS particles (cfg. Tables 2 and 3 of the main paper), though our particle cores were slightly larger (fluorescence at 625 nm). Very recently, Yu et al. have published SEC and DLS data [68] of polymer-coated nanoparticles modified with PEG. Their diameters are in good agreement with our data, but slightly larger. This could be due to the longer sidechains of the polymer (octadecene instead of tetradecene). For a meaningful comparison of the thickness of both polymer and PEG shell with our results, data from particles coated with the plain polymer would be helpful. A specialized review about the size characterization of colloidal nanoparticles could be helpful to researchers to get a more complete overview of work that has already been done by others.

VIII) References

(1) Reiss, P.; Bleuse, J.; Pron, A. *Nanoletters* 2002, *2*, 781.
(2) Kudera, S.; Zanella, M.; Giannini, C.; Rizzo, A.; Li, Y.; Gigli, G.; Cingolani, R.; Ciccarella, G.; Spahl, W.; Parak, W. J.; Manna, L. *Advanced Materials* 2007, *19*, 548.
(3) Dabbousi, B. O.; Rodriguez-Viejo, J.; Mikulec, F. V.; Heine, J. R.; Mattoussi, H.; Ober, R.; Jensen, K. F.; Bawendi, M. G. *Journal of Physical Chemistry B* 1997, *101*, 9463.
(4) Yu, W. W.; Wang, Y. A.; Peng, X. *Chemistry of Materials* 2003, *15*, 4300.
(5) Brust, M.; Walker, M.; Bethell, D.; Schiffrin, D. J.; Whyman, R. *J. Chem. Soc., Chem. Commun.* 1994, *1994*, 801.
(6) Fink, J.; Kiely, C. J.; Bethell, D.; Schiffrin, D. J. *Chemistry of Materials* 1998, *10*, 922.
(7) Pellegrino, T.; Manna, L.; Kudera, S.; Liedl, T.; Koktysh, D.; Rogach, A. L.; Keller, S.; Rädler, J.; Natile, G.; Parak, W. J. *Nanoletters* 2004, *4*, 703.
(8) Sperling, R. A.; Pellegrino, T.; Li, J. K.; Chang, W. H.; Parak, W. J. *Advanced Functional Materials* 2006, *16*, 943.
(9) Yu, W. W.; Qu, L.; Guo, W.; Peng, X. *Chemistry of Materials* 2003, *15*, 2854.
(10) Pellegrino, T.; Sperling, R. A.; Alivisatos, A. P.; Parak, W. J. *Journal of Biomedicine and Biotechnology* 2007, *submitted*.
(11) Sartori, R.; Sepulveda, L.; Quina, F.; Lissi, E.; Abuin, E. *Macromolecules* 1990, *23*, 3878.
(12) Kuga, S. *Journal of Chromatography A* 1981, *206*, 449.
(13) Holtzhauer, M.; Rudolph, M. *Journal of Chromatography A* 1992, *605*, 193.
(14) Grubisic, Z.; Rempp, P.; Benoit, H. *Journal Of Polymer Science Part B-Polymer Letters* 1967, *5*, 753.
(15) Hagel, L. Gel Filtration. In *Protein Purification. Principles, High Resolution Methods and Applications*; 2 ed.; Janson, J.-C., Ryden, L., Eds.; John Wiley & Sons: New York, 1998.
(16) Fee, C. J.; Alstine, J. M. V. *Bioconjugate Chemistry* 2004, *15*, 1304.
(17) Dubin, P. L.; Edwards, S. L.; Mehta, M. S.; Tomalia, D. *Journal of Chromatography* 1993, *635*, 51.
(18) Siebrands, T.; Giersig, M.; Mulvaney, P.; Fischer, C.-H. *Langmuir* 1993, *9*, 2297.
(19) Fischer, C.-H.; Giersig, M.; Siebrands, T. *Journal of Chromatography A* 1994, *670*, 89.
(20) Fischer, C.-H.; Kenndler, E. *Journal of Chromatography A* 1997, *773*, 179.
(21) Wei, G.-T.; Liu, F.-K. *Journal of Chromatography A* 1999, *836*, 253–260.
(22) Wei, G.-T.; Liu, F.-K.; Wang, C. R. C. *Analytical Chemistry* 1999, *71*, 2085.
(23) Jimenez, V. L.; Leopold, M. C.; Mazzitelli, C.; Jorgenson, J. W.; Murray, R. W. *Analytical Chemistry* 2003, *75*, 199.
(24) Al-Somali, A. M.; Krueger, K. M.; Falkner, J. C.; Colvin, V. L. *Analytical Chemistry* 2004, *76*, 5903.
(25) Krueger, K. M.; Al-Somali, A. M.; Falkner, J. C.; Colvin, V. L. *Analytical Chemistry* 2005, *77*, 3511.
(26) Magde, D.; Elson, E.; Webb, W. W. *Physical Review Letters* 1972, *29*, 705.
(27) Eigen, M.; Rigler, R. *Proc. Natl. Acad. Sci. USA* 1994, *91*, 5740.

(28) Schwille, P.; Bieschke, J.; Oehlenschläger, F. *Biophysical Chemistry* 1997, *66*, 211.
(29) Krichevsky, O.; Bonnet, G. *Rep. Prog. Phys.* 2002, *65*, 251.
(30) Liedl, T.; Keller, S.; Simmel, F. C.; Rädler, J. O.; Parak, W. J. *Small* 2005, *1*, 997.
(31) Amediek, A.; Haustein, E.; Scherfeld, D.; Schwille, P. *Single Molecules* 2002, *3*, 201.
(32) Duhr, S.; Braun, D. *PNAS* 2006, *103*, 19678.
(33) Duhr, S.; Braun, D. *Physical Review Letters* 2006, *96*, 168301.
(34) Duhr, S.; Arduini, S.; Braun, D. *European Physical Journal E* 2004, *15*, 277.
(35) Kobayashi, Y.; Horie, M.; Konno, M.; Rodriguez-Gonzalez, B.; Liz-Marzan, L. M. *J. Phys. Chem. B* 2003, *107*, 7420.
(36) Zanchet, D.; Moreno, M. S.; Ugarte, D. *Physical Review Letters* 1999, *82*, 5277.
(37) Yonezawa, T.; Onoue, S.-y.; Kimizuka, N. *Langmuir* 2001, *17*, 2291.
(38) Gerion, D.; Pinaud, F.; Williams, S. C.; Parak, W. J.; Zanchet, D.; Weiss, S.; Alivisatos, A. P. *Journal of Physical Chemistry B* 2001, *105*, 8861.
(39) Cai, W.; Shin, D.-W.; Chen, K.; Gheysens, O.; Cao, Q.; Wang, S. X.; Gambhir, S. S.; Chen, X. *Nano Letters* 2006, *6*, 669.
(40) Nehilla, B. J.; Vu, T. Q.; Desai, T. A. *Journal of Physical Chemistry B* 2005, *109*, 20724.
(41) Ebenstein, Y.; Nahum, E.; Banin, U. *Nanoletters* 2002, *2*, 945.
(42) Fischer, C.-H.; Lilie, J.; Weller, H.; Katsikas, L.; Henglein, A. *Ber. Bunsenges. Phys. Chem.* 1989, *93*, 61.
(43) Fischer, C.-H.; Weller, H.; Katsikas, L.; Henglein, A. *Langmuir* 1989, *5*, 429.
(44) Pinaud, F.; King, D.; Moore, H.-P.; Weiss, S. *Journal of the American Chemical Society* 2004, *126*, 6115.
(45) Wilcoxon, J. P.; Provencio, P. P. *Journal of Physical Chemistry B* 2005, *109*, 13461.
(46) Eychmüller, A.; Katsikas, L.; Weller, H. *Langmuir* 1990, *6*, 1605.
(47) Zanchet, D.; Micheel, C. M.; Parak, W. J.; Gerion, D.; Alivisatos, A. P. *Nanoletters* 2001, *1*, 32.
(48) Parak, W. J.; Pellegrino, T.; Micheel, C. M.; Gerion, D.; Williams, S. C.; Alivisatos, A. P. *Nanoletters* 2003, *3*, 33.
(49) Song, X.; Li, L.; Qian, H.; Fang, N.; Ren, J. *Electrophoresis* 2006, *27*, 1341.
(50) Pons, T.; Uyeda, H. T.; Medintz, I. L.; Mattoussi, H. *Journal Of Physical Chemistry B* 2006, *110*, 20308.
(51) Peterson, R. R.; Cliffel, D. E. *Analytical Chemistry* 2005, *77*, 4348.
(52) Bücking, W.; Nann, T. *IEE proceedings - Nanobiotechnology* 2006, *153*, 47.
(53) Cardenas, M.; Schillen, K.; Nylander, T.; Jansson, J.; Lindman, B. *Physical Chemistry Chemical Physics* 2004, *6*, 1603.
(54) Cardenas, M.; Schillen, K.; Pebalk, D.; Nylander, T.; Lindman, B. *Biomacromolecules* 2005, *6*, 832.
(55) Luccardini, C.; Tribet, C.; Vial, F.; Marchi-Artzner, V.; Dahan, M. *Langmuir* 2006, *22*, 2304.
(56) Jiang, W.; Mardyani, S.; Fischer, H.; Chan, W. C. W. *Chemistry of Materials* 2006, *18*, 872.
(57) Ipe, B. I.; Shukla, A.; Lu, H.; Zou, B.; Rehage, H.; Niemeyer, C. M. *ChemPhysChem* 2006, *7*, 1112.
(58) Smith, A. M.; Duan, H.; Rhyner, M. N.; Ruan, G.; Nie, S. *Phys. Chem. Chem. Phys.* 2006, *8*, 3895.

(59) Zhang, P.; Li, L.; Dong, C.; Qian, H.; Ren, J. *Analytica Chimica Acta* 2005, *546*, 46.
(60) Doose, S.; Tsay, J. M.; Pinaud, F.; Weiss, S. *Anal. Chem.* 2005, *77*, 2235.
(61) Dong, C.; Bi, R.; Qian, H.; Li, L.; Ren, J. *SMALL* 2006, *2*, 534.
(62) Jin, T.; Fujii, F.; Yamada, E.; Nodasaka, Y.; Kinjo, M. *Journal of the American Chemical Society* 2006, *128*, 9288.
(63) Borchert, H.; Shevchenko, E. V.; Robert, A.; Mekis, I.; Kornowski, A.; Grübel, G.; Weller, H. *Langmuir* 2005, *21*, 1931.
(64) Petkov, V.; Peng, Y.; Williams, G.; Huang, B.; Tomalia, D.; Ren, Y. *PHYSICAL REVIEW B* 2005, *72*, 195402.
(65) Zackrisson, M.; Stradner, A.; Schurtenberger, P.; Bergenholtz, J. *Langmuir* 2005, *21*, 10835.
(66) Calabretta, M.; Jamison, J. A.; Falkner, J. C.; Liu, Y. P.; Yuhas, B. D.; Matthews, K. S.; Colvin, V. L. *Nano Letters* 2005, *5*, 963.
(67) Slocik, J. M.; Stone, M. O.; Naik, R. R. *Small* 2005, *1*, 1048.
(68) Yu, W. W.; Chang, E.; Falkner, J. C.; Zhang, J.; Al-Somali, A. M.; Sayes, C. M.; Johns, J.; Drezek, R.; Colvin, V. L. *J. Am. Chem. Soc.* 2007, *129*, 2871.

Biological Applications of Gold Nanoparticles (Accepted for publication)

Ralph A. Sperling, Pilar Rivera Gil, Feng Zhang, Marco Zanella, Wolfgang J. Parak*

Fachbereich Physik, Philipps Universität Marburg, Renthof 7, 35037 Marburg, Germany
*corresponding author: wolfgang.parak@physik.uni-marburg.de

Synopsis. This review gives a short compilation of the widespread use of gold nanoparticles in biology. We have identified four classes of applications in which gold nanoparticles have been used so far: labeling, delivering, heating, and sensing. For each of these applications the underlying mechanisms and concepts, the specific features of the gold nanoparticles needed for this application, as well as several examples are described.

Biological Applications of Gold Nanoparticles

Ralph A. Sperling, Pilar Rivera Gil, Feng Zhang, Marco Zanella, Wolfgang J. Parak*

Fachbereich Physik, Philipps Universität Marburg, Renthof 7, 35037 Marburg, Germany
*corresponding author: wolfgang.parak@physik.uni-marburg.de

Synopsis. This review gives a short compilation of the widespread use of gold nanoparticles in biology. We have identified four classes of applications in which gold nanoparticles have been used so far: labeling, delivering, heating, and sensing. For each of these applications the underlying mechanisms and concepts, the specific features of the gold nanoparticles needed for this application, as well as several examples are described.

1. Introduction

Colloidal gold nanoparticles have been technologically used since ancient times due to their optical properties, in particular for staining glass. Systematic researches on gold colloids go back to the days of Faraday, though in particular their use for biological applications the break-through just happened in the last decade [1]. This goes hand in hand with the advent of (bio-) nanotechnology, which nowadays allows for controlled synthesis and functionalization of materials on the nanometer scale and thus provides a toolbox that did not exist before. It is a legitimate question to ask whether the rising use of gold nanoparticles in biology is just an effect of the "nano-hype", or whether colloidal gold offers particular properties which go beyond the performance of previously used materials. The purpose of this review is to outline the conceptual properties of colloidal gold nanoparticles and to outline the motivation for their uses in different areas of biologically related researches. We have classified the uses of gold nanoparticles in four concepts of applications: labeling, delivering, heating, and sensing.

2. Some aspects about the synthesis and properties of gold nanoparticles

2.1 Synthesis and phase transfer

The synthesis of Au nanoparticles with diameters ranging from a few nm to several hundreds of nm is well established as well in aqueous solution as in organic solvents. In typical syntheses, gold salts such as $AuCl_3$ are reduced by the addition of a reducing agent which leads to the nucleation of Au ions to nanoparticles. In addition also a stabilizing agent is required which is either adsorbed or chemically bound to the surface of the Au nanoparticles. This stabilizing agent is typically charged, so that the equally charged nanoparticles repel each other so that they are colloidally stable. For the most common used synthesis route in aqueous solution, citric acid is as well used to reduce the gold salt and thus trigger nucleation, as upon adsorption to the particles it provides colloidal stability to the particles by its negative charges [2, 3]. Similar synthesis routes can be also performed in organic solvents [4], though in this case the reducing agent is different from the stabilizing agent. For particles dispersed in organic solvent which require a hydrophobic surface frequently alkane chains bound to the particle surface provide colloidal stability. A sketch of the geometry of Au nanoparticles is depicted in Figure 1. Besides growing of particle with spherical shape also other geometries such as rod-shaped particles can be synthesized [5, 6].

2.2 Surface modification and bioconjugation

Colloidal gold nanoparticles are surrounded by a shell of stabilizing molecules. With one of their ends these molecules are either adsorbed or chemically linked to the gold surface, while the other end points towards solutions and provides colloidal stability. After synthesis of the particles the stabilizer molecules (often also called surfactant molecules) can be replaced by other stabilizer molecules in a ligand exchange reaction. As thiol-moieties bind with good affinity to gold surface most frequently thiol-modified ligands are use which bind to the surface of the Au particles (which are from several groups also called monolayer protected clusters) by formation of Au-sulfur bonds [7]. Ligand exchange is motivated by several aspects. Ligand exchange allows for example for transferring Au particles from aqueous to organic phase (and vice versa) by exchanging hydrophilic to hydrophobic surfactants (and vice versa) [8]. In this way it is possible to adjust the surface properties of the particles. For applications in aqueous solution typically ligands with carboxy groups at their ends (mercaptocarbonic acids) pointing towards solution are used as due to their negative charges that provide colloidal stability and also because they can be used as anchor points for the further attachment of biological molecules. Often also poly(ethylene glycol) (PEG) is used as ligand as PEG reduces nonspecific adsorption of molecules to the particle surface and also provides colloidal stability as particles with PEG brushes on their surface repel each other for steric reasons [9]. Also other surface coatings as embedding particles in a glass shell have are used by several groups [10]. Biological molecules can be attached to the particles in several ways. In case the biological molecules have a functional group which can bind to the gold surface (like thiols or specific peptide sequences) then the biological molecules can replace some of the original stabilizer molecules when they are added directly in excess to the particle solution or in a ligand exchange reaction. In this way molecules like oligonucleotides, peptides or PEG can be readily linked to Au particles and subsequent sorting techniques allow even for obtaining particles with an exactly defined number of attached molecules per particle [11, 12]. Alternatively biological molecules can be also attached to the shell of stabilizer molecules around the Au particles by bioconjugate chemistry. The most frequent protocol is the linkage of amino-groups on the biological molecules with carboxy groups at the free ends of stabilizer molecules using EDC (1-ethyl-3-(3-dimethylaminopropyl)carbodiimide-HCl) [13, 14]. With related strategies almost all types of biological molecules can be attached to the particle surface. Though such protocols are relatively well established, bioconjugation of Au nanoparticles still is not trivial and characterization of synthesized conjugates is necessary, in particular to rule out any aggregation effect during the conjugation reaction. In particular in many conjugation protocols the number of attached molecules per gold nanoparticle is only a rough estimate, as no standard method for determining the surface coverage of particles modified with molecules has been yet established [15, 16].

2.3 Cytotoxicity

Though gold nanoparticles are composed of an inert material still biocompatibility issues have to be considered. Cells exposed to gold nanoparticles will incorporate the particles (similar to nanoparticles of other materials) and the particles are stored inside the cells in vesicular structures close to the cell nucleus [17, 18]. Due to particle internalization cells or tissues in contact with gold nanoparticles will be exposed to the particles for extended periods of time. Concerning cytotoxic effects [19] one has to distinguish between effects related to the nature of gold and to effects common between nanoparticles of inert materials. Also for inert particles such as gold inflammatory effects in tissues caused by particles has been demonstrated.

However, in cell culture experiments Au nanoparticles are regarded as biocompatible, and acute cytotoxicity has not been observed so far[20]. In particular no release of toxic ions as in the case of cadmium-based nanoparticles [21] has been reported. On the other hand there are few examples of toxic effects related to the nature of Au, which might depend on the cell line [18, 22], on surface chemistry [23], and on the nanoparticle size [24]. Actin fibers inside the cell for example can be affected by the presence of nanoparticles [25], and very small Au-clusters have been demonstrated to fit into the grooves of DNA molecules and thus cause cytotoxic effects [24, 26]. A more detailed discussion can be found in another article in this issue [27].

3. Gold nanoparticles for labeling and visualizing

Historically Au nanoparticles have been first used in labeling applications. In this regard the particles are directed and enriched at the region of interest and they provide contrast for the observation and visualization of this region. The particles are used here as "passive" reporters, there is no change of particles properties required for the read-out as it is the case for active sensor applications (see section 6). Gold nanoparticles are a very attractive contrast agent as they can be visualized with a large variety of different techniques. The most of prominent detection techniques are based on the interaction between gold nanoparticles and light [28]. Gold particles strongly absorb and scatter visible light. Upon light absorption the light energy excites the free electrons in the Au particles to a collective oscillation, the so called surface plasmons [29]. In particular close to the plasmon resonance frequency the absorption cross section is very high. The excited electron gas relaxes by transferring the thermal energy to the gold lattice and thus light absorption leads to heating of the gold particles. Interaction with light can be used for the visualization of particles in several ways. Gold particles bigger than around 20 nm can be directly imaged with optical microscopy in phase contrast or differential interference contrast (DIC) mode [30]. By using dark field microscopy light scattered from gold particles is detected with an optical microscope [31] whereby particles bigger than 20-30 nm can also be imaged. As the color of the light scattered by gold particles depends on their sizes and shapes gold particles can be used as the label with different colors [29, 32]. For small particles the scattering cross section decreases rapidly whereas the absorption cross section decreases less. Absorbed light ultimately leads to heating of the particles and upon heat transfer subsequently to heating of the environment. This can be observed in two ways. Photothermal imaging records density fluctuations of the liquid environment around the particles by differential interference contrast (DIC) microscopy [33, 34]. Photoacoustic imaging on the other hand makes use of the fact that the liquids expand due to heat. A local heat-pulse due to light absorption leads to expansion of the liquid surrounding the gold particles and thus to the creation of a sound wave which can be detected by a microphone [35, 36]. Both, photothermal and photoacoustic imaging are making use of the big light absorption cross section of gold nanoparticles. Small gold particles have recently also been reported to emit fluorescence light upon photo-excitation and thus can be visualized with fluorescence microscopy [37, 38]. All of the above mentioned methods involving photo excitation (phase contrast / interference contrast microscopy, dark field microcopy, photothermal imaging, photoacoustic imaging, and fluorescence microscopy) are sensitive enough to allow for the detection on a single particle level. Besides the interaction with visible light, the interaction with both electron waves and X-rays can also be used for visualization of Au nanoparticles. Due to their high atomic weight Au nanoparticles provide high contrast in transmission electron microscopy (TEM) [39]. Au particles also efficiently scatter X-rays and thus provide contrast in X-ray imaging [40]. Finally Au nanoparticles can be also radioactively labeled by neutron activation [41] and can be detected in this way by gamma radiation.

3.1 Immunostaining

Immunostaining is one of the traditional uses of Au nanoparticles in biology before the advent of "nanobiotechnology". The idea of immunostaining is labeling specific molecules or compartments of cells (see Figure 2.1). Without labeling, molecules / compartments cannot be distinguished from the rest of the cells because of a lack of contrast, so that a label is necessary to provide enough contrast for visualization. For immunostaining, cells are typically fixed and permeated and Au nanoparticles conjugated with antibodies specific to the molecules / compartments of interest are added. Guided by molecular recognition the antibody-modified Au particles will bind to the target regions. As the cells are fixed and permeated, targets outside as well as inside cells can be labeled with gold particles in this way. The Au particles provide excellent contrast for TEM imaging with high lateral resolution [42] and bigger structures can be also imaged with optical microscopy [43]. Compared to fluorescence labeling Au particles are more stable as they do not suffer from photobleaching which is a major limitation for fluorescence based methods, and in case of TEM imaging also better lateral resolutions with high contrast can be obtained. In immunostaining, molecules / structures are labeled with an excess of Au nanoparticles so that virtually all molecules / structures present are labeled and that each molecule / structure is labeled with several Au nanoparticles in order to provide high contrast. In this case the local density of Au particles at the sites where the labeled molecules / structures are present is quite high. Therefore the resolution limit of the optical microscope (of a few hundreds of nm) does not allow for optically resolving individual receptors and thus antibody-conjugated Au nanoparticles (with a few tens of nm in diameter) bound to it, as the distance between adjacent Au nanoparticles is smaller than the optical resolution limit. However, due to better lateral resolution individual receptors can be resolved by visualizing the bound Au nanoparticles with TEM. Immunostaining is also possible without fixing and permeating cells, but in this case only structures / domains on the surface of the cell can be labeled. For immunostaining of the outer cell surface also photoacoustic imaging is used besides the imaging techniques mentioned above. Photoacoustic imaging provides an additional feature in contrasting. When Au nanoparticles come close together (i.e. form small aggregates) the frequency of the plasmon resonance shifts to higher wavelengths. In case freely dispersed colloidal Au nanoparticles are optically excited at wavelengths well above their plasmon resonance the light can not be absorbed and thus there will not be any photoacoustic signal. Small aggregates of Au nanoparticles on the other hand can absorb light at wavelengths above the plasmon resonance of freely dispersed Au particles. If therefore light with a wavelength above the plasmon resonance of freely dispersed Au particles is used for excitation there will be a photoacoustic signal for aggregates of Au nanoparticles, but not for single dispersed Au nanoparticles. If Au nanoparticles modified with antibodies against membrane receptors are used they will bind to the regions of the outer cell surface where the receptors are present. As several Au nanoparticles will bind to such regions there is a local "aggregation" of Au nanoparticles present which provides a photoacoustic signal, whereas Au nanoparticles which are still in solution or which are randomly distributed on the cell surface due to nonspecific adsorption will not exhibit any photoacoustic signal [35].

3.2 Single particle tracking

The molecules / structures on the outer cell surface can be labeled with Au nanoparticles which are conjugated with specific antibodies against these molecules / structures. In contrast to immunostaining for single particle tracking only few antibody-conjugated Au nanoparticles are added, so that after binding to the cell the particle labels present on the cell surface are very

diluted. As in this case the average distance between adjacent Au nanoparticles is higher than the optical resolution limit, individual Au nanoparticles can be optically resolved. For imaging the movement of molecules / structure, living cells without fixation and permeation have to be used, which limits the labeling to molecules / structures on the outer cell surface and the visualization to optical (+ acoustic) techniques (phase / interference contrast microscopy, dark field microscopy, photothermal imaging, photoacoustic imaging, fluorescence imaging). Most frequently membrane bound receptor molecules are investigated with single particle tracking. By time resolved imaging of the receptors which are labeled with Au nanoparticles their trajectories and thus their diffusion within the cell membrane can be observed (see Figure 2.2) [44]. Movement of Au nanoparticles bigger than around 40 nm can be traced directly with phase contrast or differential interference contrast microscopy [45]. For gold particles bigger than around 20-30 nm the light scattered by individual Au nanoparticles can be recorded with dark field microscopy [46]. Movement of receptors labeled with even smaller Au nanoparticles (down to 5 nm) has been visualized with photothermal imaging [47, 48]. Also other labels are used for the tracking of single receptors on cell surfaces and each of the methods has certain intrinsic advantages and disadvantages. The bigger the (particle-) label is, the easier (regarding the required set-up) it can be optically imaged. The principle is the same for 40 nm Au nanoparticles as for latex and silica beads, whereby the beads also can be impregnated with organic fluorophores and thus can be imaged also with fluorescence microcopy [49]. One could argue that gold nanoparticles can be easier conjugated with antibodies than latex / silica beads (due to the thiol-gold chemistry), though surely the fluorescence of beads provides a better signal-to-noise ratio. At any rate attachment of particles bigger than around 40 nm to receptors might severely change the diffusion properties of the receptor molecules. For this reason the real challenge of single particle tracking is using as small (and as stable) labels as possible. Organic fluorophores exist that are smaller than colloidal particles, however, they suffer from photobleaching and therefore their fluorescence can be traced only for limited periods of time. Alternatively colloidal fluorescent semiconductor nanoparticles (so called quantum dots) can be used for single particle tracking of membrane molecules [50]. Though they are slightly bigger than small organic fluorophores they suffer much less from photobleaching and thus allow for extended observation periods. Colloidally stable quantum dots are typically bigger than 10 nm in diameter, as sophisticated coatings are needed to warrant colloidal stability. On the other hand, movement of gold particles down to 5 nm diameter can be imaged with photothermal microscopy [47, 48] and as no fluorescence detection method is used there is no limitation in observation times by photobleaching. For this reason photothermal microscopy of small Au nanoparticles is in particular advantageous when long periods of observation are required.

3.3 Contrast agents for X-rays

Whereas immunostaining and single particle tracking are used for visualizing structures within single cells, the same concept can also be applied for providing contrast in-vivo to whole organs in animals and potentially in humans. Again the Au particles are conjugated with antibodies or ligands which bind as specific as possible to the organ of interest in the animal. When particles are administered to the blood circulation a part of them will eventually bind via receptor-ligand interaction at the designated organ. The particles bound to the organ provide contrast for imaging and resolving the structure of the organ (see Figure 2.3). However, the big general problem of contrasting organs with colloidal nanoparticles is their short circulation time in the blood stream, so that only a fraction of the particles has a chance to bind to the designated organ whereas a significant part is cleared from the blood stream by the liver. On the other hand, colloidal nanoparticles can provide better contrast compared to organic molecules. Gold nanoparticles can be for example imaged with high signal-to-noise ratio with X-ray computer

tomography [40, 51] and therefore only short exposure times are required, which helps to reduce radiation damage of surrounding tissues. X-rays penetrate skin and therefore also organs deep inside the body can be imaged or addressed for therapy [52]. Furthermore X-ray tomography set-ups are readily available in many hospitals. Again Au nanoparticles have to compete with fluorescent semiconductor nanoparticles (quantum dots) [53, 54]. In order to reduce X-ray exposure of patients certainly fluorescence detection would be preferable compared to imaging with X-rays. On the other hand light is absorbed by tissues even partly in the infrared (IR), so that fluorescence contrasting of organs deep inside the body is complicated. Furthermore colloidal gold nanoparticles are less likely to cause cytotoxic damage than the generation of colloidal quantum dots presently used.

3.4 Phagokinetic tracks

Albrecht Bühler has introduced a very nice way of imaging the movement of adherent cells along a substrate [55-57]. For this purpose the surface of the substrate is coated with a layer of colloidal gold nanoparticles (see Figure 2.4). Cells adherent to the substrate incorporate the Au particles. In this way cells migrating along the substrate leave behind a trail called phagokinetic track in the nanoparticle layer. By imaging the particle layer with transmission microscopy of TEM a blue print of the migration pathway of the cells is obtained. Compared to time lapse tracing of the migration of cells which requires online video microscopy of individual cells phagokinetic tracks do not need to be recorded online. Many trails can be recorded on the same substrate and the trails can be imaged ex-situ, as they consist of areas permanently free of nanoparticles in the nanoparticle layer. Although recently the same technique has been also introduced with both fluorescent quantum dots [58] and fluorescent latex beads, still gold is the predominantly used label for recording phagokinetic tracks.

4. Gold nanoparticles as vehicle for delivery

Gold nanoparticles have been used since long time for delivery of molecules into cells. For this purpose the molecules are adsorbed to the surface of the Au particles and the whole conjugate is introduced into the cells. Introduction into cells can be either forced as in the case of gene guns or naturally by particle ingestion. Inside cells the molecules will eventually detach from the Au particles.

4.1 Gene guns

The idea of gene guns is using Au particles as massive nano-bullets for ballistic introduction of DNA into cells (see Figure 3.1) [59]. DNA is adsorbed onto the surface of gold particles which are then shot into the cells. The ballistic acceleration of the gene-loaded micro- or nanoparticles is realized by different means like macroscopic bullets, gas pressure or electric discharges [60] and some types of guns are commercially available. Traditionally gene guns have been used for the introduction of plasmid DNA into plant cells [61, 62], which results in expression of the corresponding proteins inside the cells. In this case ballistic introduction with massive particles is advantageous as it allows for traversing the rigid cell walls which surround the membranes of plant cells. However, gene guns are also used for delivery of DNA into animal cells, which do not posses cell walls [63].

4.2 Uptake by cells

Cells naturally ingest colloidal nanoparticles [17] whereby particle incorporation can be specific (via receptor-ligand interaction) or nonspecific. The goal is again to transfer molecules which are adsorbed to the surface of the Au particles into the cells (see Figure 3.2). For specific uptake ligands specific to receptors on the cell membrane, such as transferrin which binds to membrane bound transferrin receptors [64-66], are conjugated to the surface of the gold particles. As specific uptake is more efficient than nonspecific uptake in this way ligands modified Au particles are predominantly incorporated by cells which posses receptors for these ligands, but not by other cells. In this way it is for example possible to direct particles specifically to cancer cells by conjugating them with ligands specific to receptors which are overexpressed on the surface of cancer cells but are less present on healthy cells [67]. After incorporation nanoparticles are stored in endosomal / lysosomal vesicular structures inside cells [68]. In order to release the particles from the vesicular structures to the cytosol their surface can be coated with membrane-disruptive peptides or the particles can be modified with peptides which allow for direct transfer across the cell membrane [69-72]. In this way it is possible to deliver molecules which are adsorbed to the surface of the Au particles upon particle incorporation inside the cells [73, 74]. Particle uptake mediated delivery of molecules into cells is used mainly for two applications. First, in gene therapy DNA is introduced into cells, which subsequently causes the expression of the corresponding proteins [75-77]. Second, in drug targeting anti-cancer drugs are delivered specifically to cancer tissue [67, 78]. Particle-mediated drug delivery by adsorbing molecules onto colloidal particles and transferring them into cells allows for delivery of molecules inside cells which would not have been ingested into the cells by themselves. This is based on the fact that colloidal nanoparticles are taken up by cells. As besides loading with the molecules to be delivered, particles can be also conjugated with ligands through which specific uptake by target cells can be facilitated. For such delivery applications no special property of gold particles is exploited, besides that they are small, colloidally stable, relatively easy to conjugate with ligands via thiol-gold bonds, and that they are inert and thus relatively biocompatible. Similar applications can be performed with colloidal silica, polymer, and iron oxide nanoparticles. Nevertheless, there are a few studies that already make use of the optical properties of Au nanoparticles for detection (which the other types of particles do not offer), after they have been ingested by cells [79, 80].

5. Gold nanoparticles as heat source

When gold particles absorb light the free electrons in the gold particles are excited. Excitation at the plasmon resonance frequency causes a collective oscillation of the free electrons. Upon interaction between the electrons and the crystal lattice of the gold particles, the electrons relax and the thermal energy is transferred to the lattice. Subsequently the heat from the gold particles is dissipated in the surrounding environment [81]. Besides its combination with imaging techniques (see above in section 3), controlled heating of gold particles can be used in several ways for manipulating the surrounding tissues [82].

5.1 Hyperthermia

Cells are very sensitive to small increases in temperature. Even temperature raises of a few degrees can lead to cell death. For human beings temperatures above 37°C lead to fever and temperatures above 42°C are lethal. This fact can be harnessed for the anti-cancer therapy in a concept called hyperthermia. The idea is to direct colloidal nanoparticles to the cancerous tissue. This can be done by conjugating the particle surface with ligands that are specific to receptors overexpressed on cancer cells. The particles are then locally enriched in the cancerous

tissue (either adherent to the cell membranes or inside the cells after internalization). If the particles can be heated by external stimuli then the temperature of cells close to the particles is raised and in this way cells in the vicinity of the particles can be selectively killed [83]. As mentioned above Au particles can be heated by absorption of light, whereby the absorbed light energy is converted into thermal energy. Thus the idea is to enrich cancerous tissues with gold nanoparticles and to illuminate the tissue. Due to the head mediated by the gold particles to the surrounding tissue, cancerous tissues could be locally destroyed (see Figure 4.1) [84-86] without exposing the entire organism to elevated temperatures. Besides the general problem of local particle enrichment in the target tissue there is also a principle problem involved. Tissues absorb light in the visible, and even infrared (IR) light can only penetrate thin tissues. For this reason gold nanoparticles are needed which absorb light rather in the IR than in the visible range, such as gold rods or shells [87]. Nevertheless hyperthermia by photo-induced heating of gold nanoparticles will work best for tissue close to the skin. For tissues deep inside bodies heating with magnetic particles is favorable. Upon irradiating magnetic particles with radio frequency (RF) fields, heat is generated by repetitive cycling of the magnetic hysteresis loop [88, 89]. Compared with the optical excitation of Au nanoparticles at wavelengths of ca. 500 nm - 1000 nm, the excitation of magnetic nanoparticles works at lower frequencies (RF). As those are absorbed much less by normal tissues, also particles deep inside the body can be heated. On the other hand it is much more complicated to focus microwaves or radiofrequency waves than visible light and therefore photo-induced heating of gold particles is favorable for local heating of only small parts of tissue.

5.2 Optically triggered opening of bonds

Photo-induced heating of gold nanoparticles can be also used for the opening of chemical bonds (see Figure 4.2). The binding of complementary oligonucleotides (hybridization) to double stranded DNA for example is temperature dependent. Upon heating, double stranded DNA melts into single strands. If DNA is linked to the surface of gold nanoparticles then local melting can be triggered by illuminating and thus heating of the Au particles [90, 91]. As light can be easily focused to micrometer spot size a high degree of spatial control is possible which allows for very local heating. Similar concepts have been also used for the disassembly of protein aggregates by local heating [92].

5.3 Opening of containers

Finally photo-induced heating of gold nanoparticle can be also used for remotely controlled release of cargo molecules from containers (see Figure 4.3). This concept is based on embedding cargo molecules in containers, such as polymer capsules, whereby the walls of the containers are functionalized with gold nanoparticles. Upon optical excitation the gold nanoparticles are heated which causes local ruptures in the container walls and thus release of the cargo from the inside of the container [93, 94]. Light-induced opening of polymer capsules can be performed on a single capsule level and it has already been demonstrated that upon photo-induce heating cargo molecules can be released from capsules inside living cells [95]. Moveover, cell membranes themselves can be perforated with the help of nanoparticles [96].

6. Gold nanoparticles as sensors

Besides using gold nanoparticles as (passive) label they can be also used for (active) sensor applications. Their aim to a sensor is to specifically register the presence of analyte molecules

and to provide a read-out that indicates the concentration of the analyte. In case an optical read-out is used, the presence of analyte can be for example indicated by changes in the optical properties of gold nanoparticles. Due to their small size, gold-particle based sensors could have an important impact in diagnostics [80].

6.1 Surface plasmons

The plasmon resonance frequency is a very reliable intrinsic feature present in gold nanoparticles (with wavelengths around 510-530 nm for Au nanoparticles of around 4-40 nm diameter) that can be used for sensing [97]. The binding of molecules to the particle surface can change the plasmon resonance frequency directly [98], which is observable by their scattered light in dark field microscopy, in particular on the single particle level. On the other hand the plasmon resonance frequency is dramatically changed when the average distance between Au particles is reduced to that they form small aggregates [99]. This effect of plasmon coupling can be used for colorimetric detection of analytes (see Figure 5.1). The method has been pioneered by Mirkin and coworkers and is nowadays maybe the most well known example of gold-based sensors [100-102]. The original assay was developed for the detection of DNA. Gold nanoparticles are conjugated with oligonucleotides that are complementary to the target sequence which is to be detected. Without the presence of the target sequence the gold particles are freely dispersed and the colloidal solution appears in red color. Upon the presence of the target sequence the gold particles bind to the target by hybridization of complementary strands of DNA. As each gold nanoparticle is bearing several oligonucleotides, hybridization results in the formation of small aggregates of Au particles, which will lead to a change in the plasmon resonance and the colloidal solution appears in violet/blue color. When the sample is heated, even single sequence mismatches result in a different melting temperature of the aggregates which causes color change. Several DNA assays have been derived from this concept and nowadays the method is established in a way that quantitative detection of DNA sequences of very low concentrations [103]. The same concept can be also applied for analytes others than DNA. Gold particles can be for example connected by DNA in a way that the average inter-particle distance is high enough to prevent changes in the plasmon resonance frequency. By using DNA sequences that change their conformation upon specific binding (such sequences are called aptamers) of metals [104] or proteins [105, 106] the inter-particle distance is reduced upon binding of the metals / proteins to the DNA and thus the color of the gold colloids changes from red to violet/blue. Also enzyme activity can be monitored with such colorimetric assays, for example by the enzymatic biotinylation of nanoparticles and subsequent formation of aggregates with streptavidin-modified nanoparticles [107], and in case in the presence of an enzyme inhibitor, the first nanoparticles are not modified and no aggregation occurs. Besides the detection of analytes, the inter-particle distance mediated color changes of gold colloids can be also used to measure distances. The concept of such "rulers on the nanometer scale" is again based on color changes of gold particles if the gold particles are in close vicinity. Different sites of a macromolecule can be linked to gold particles. By observing the color of the gold particles the distance between these sites can be measured and in this way for example conformation changes in molecules can be observed [108].

6.2 Fluorescence quenching

The fluorescence of many fluorophores is quenched when they are in close proximity to gold surfaces [109-111]. This effect can be used for several sensor strategies (see Figure 5.2). The first one is based on competitive displacement. For quantitative detection of a certain analyte, gold particles are conjugated with ligands that specifically bind to this analyte. Then the binding

sites of the ligands are blocked by saturating them with analyte molecules (or molecules of similar structure that bind to the ligand), whereby these molecules are modified with fluorophores. As the fluorophores are in this way closely linked to the Au particles their fluorescence is quenched. After washing, these gold particles with blocked ligands are now added to the solution in which the concentration of the analyte should be detected. In case no analyte is present there will be no fluorescence, as the fluorophores are quenched by the gold particles. Analyte molecules present in solution on the other hand will compete with the fluorophore-labeled analytes previously bound to the Au particles for the binding sites of the ligands on the Au surface [15]. In a continuous dynamic equilibrium analyte molecules in solution will displace analyte molecules bound to the ligands present on the particle surface. For reasons of simple statistics, the higher the concentration of analyte molecules in solution is, the fewer of the fluorophore-labeled prebound molecules will remain on the particle surface in equilibrium. This means that higher the concentration of analyte molecules is, the more fluorophore-labeled molecules will be released from the Au particle surface into solution and as there is no quenching in solution the higher the resulting fluorescence signal will be. A variation of this concept includes using Au nanoparticles as quenchers for quantum dots which are replaced by the analyte. When the Au nanoparticles are released, the fluorescence of the quantum dots increases [112]. A second detection scheme works slightly different. In this case a molecule is needed which changes its conformation upon binding of the analyte. This molecule is used as spacer to link fluorophores to gold nanoparticles. Without the presence of the analyte the spacer molecule is extended and there is no quenching of the fluorescence of the fluorophore. Analyte molecules on the other hand will bind to the spacer which then changes its conformation in a way that the attached fluorophore will be brought into close proximity of the Au surface, which results in quenching of the fluorescence. The higher the concentration of analyte in solution, the lower the recorded fluorescence signal will be. The same principle can be used in the opposite way when binding of the analyte stretches the spacer attached to the particles, and the quenched fluorescence increases after binding [113-115]. Due to dynamic binding and unbinding of the analytes to the ligand (spacer) molecules present on the Au surface, both of the above introduced sensor concepts are reversible. In contrast to fluorescence quenching by metal nanoparticles, it remains to note that there are also recent findings of metal-*enhanced* fluorescence and ideas about the exploitation of this effect for future applications [116].

6.3 Surface enhanced Raman scattering

Due to their characteristic spectra, many (macro) molecules can be detected by Raman scattering [117]. In Raman scattering the incident light is scattered with a low probability on vibrational and rotational states of the molecule. The scattering process is inelastic, and thus the scattered light can have a smaller (Stokes, by depositing energy into the molecule) or higher energy (anti-Stokes, by gaining energy from the molecule) than the incident light. The energy shift is characteristic for the chemical structure where the scattering occurred and complex molecules have therefore a characteristic Raman spectrum that allows for detection and identification. While the scattering efficiency might depend on the wavelength of the incident light, the energy shift remains the same. Typically Raman signals are quite weak and therefore a sufficient analyte concentration is needed in order to provide enough signals. Raman scattering is dramatically enhanced if the molecules are close to a gold surface with very high curvature, as for example small gold nanoparticles. This effect is called surface enhanced Raman scattering (SERS) [118-120]. Due to the plasmon resonance of metal nanoparticles there is a strong enhancement of the electric field in close proximity to the particles, compared with the field strength of the incident light. This results in a much higher scatter probability and thus in a

gain of several orders of magnitude of the Raman-scattered light intensity that is detected. SERS can be used for the detection of analytes (see Figure 5.3). Again the surface of Au nanoparticles is modified with ligands that can specifically bind the analyte. Upon binding of the analyte to the Au particle its Raman signal is dramatically enhanced, which can be used for its detection [121, 122]. Recent developments include Au nanoparticles modified with Raman-active reporter molecules for the detection of DNA [123] or proteins [124, 125], and two-photon excitation [126].

6.4 Gold stains

Instead of using fluorophores or absorbing dyes as read-out for ELISA-like assays (enzyme-linked immunosorbent assays) also gold nanoparticles can be used. The aim of such assays is the specific quantitative or quantitative detection of analytes and is conceptually related to immunostaining (see section 3.1). For this purpose the analyte is immobilized on a surface, either by simple adsorption or specific binding e.g. by a capture antibody. Instead of enzyme-labeled antibodies, analyte-specific antibodies are conjugated to the surface of gold nanoparticles. The presence of analyte in the assay thus results in binding of gold particles to the surface [127, 128]. The concentration of analyte molecules can be quantified by the optical absorption of the gold spot which is a function of the analyte concentration. Sensitivity can be enhanced by involving secondary antibodies and silver enhancement, where the gold nanoparticles catalyze the reduction of silver and are thus grown larger by a silver coating [129]. Similar assays of using gold stains as read-out can be also applied for receptor-ligand systems without involving antibodies, such as the detection of target DNA sequences with complementary DNA [130, 131]. In a similar way antibody-conjugated gold nanoparticles can be used for the detection of proteins or DNA after blotting the molecules from a gel onto a membrane [132]. For many years, gold nanoparticles conjugated with a variety of antibodies (“immunogold”) are commercially available, and they are also used to enhance the contrast in electron microcopy (e.g. section 3.1). Alternatively, conjugated Au nanoparticles can be used to detect antigens (e.g. proteins [133] or DNA [134]) present on an electronic chip. The binding of the nanoparticles is read out by voltammetry, and again the Au nanoparticles can be enhanced by silver deposition in order to amplify the signal.

6.5 Electron transfer

Finally gold nanoparticles also can be used for the transfer of electrons in redox reactions [135]. The idea of such assays is to detect analytes which are substrates to redox enzymes. The enzyme can specifically oxidize (or reduce) the analyte molecules. The flow of electrons released (or required) in this redox reaction can be measured as electrical current. For this purpose the enzyme is conjugated to the surface of the gold particles [136]. The enzyme-particle conjugates are then immobilized on the surface of an electrode (gold) which is connected to an amplifier for current detection, e.g. by cyclic voltammetry. Alternatively, the gold nanoparticles can be first immobilized on the electrode and then be modified with enzymes [137]. In principle the enzyme could be directly immobilized on the flat gold electrode of the chip. However, the introduction of Au nanoparticles has several advantages. First an electrode covered with a layer of nanoparticles has a much higher surface roughness and thus larger surface area, which leads to higher currents. Second, because of the small curvature of small gold particles the contact of the Au particle to the enzyme can be more "intimate", i.e. located in proximity to the reactive center, which can facilitate the electron transport [138, 139].

7. Outlook

Colloidal Au nanoparticles posses a lot of interesting properties that make them useful for biological applications. Though similar applications could be also performed with colloidal nanoparticles of different materials, such as quantum dots, there are several features unique to gold particles. So far there is no indication of Au particle corrosion, and Au particles are inert, which makes them relatively biocompatible. Gold nanoparticles can be easily synthesized, they are colloidally stable, and they can be conjugated with biological molecules in a straight forward way. Due to their optical properties, in particular the surface plasmon resonance they can be visualized with different methods and sensors based on changes of the plasmon resonance have been demonstrated. For this reason gold particles are now also used for different applications besides the "classic" examples of gene guns and immunostaining. Though to our opinion gold nanoparticles never will play a "dominant" role in biology we predict that they will be routinely used within several standard assays and kits and that there is still plenty room for new researches. In particular we believe that the shift in plasmon resonance upon binding of molecules or changing the inter-particle distance will lead to many sensor assays for the detection of analytes, which will be also commercially available.

8. Acknowledgements

This work has been supported by the German Research Foundation (DFG, SPP Bio-Nano-Responses, PA 794/4-1).

9. Figures

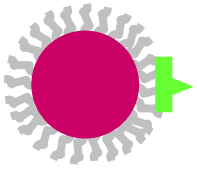

Figure 1: Scheme of a ligand-conjugated gold nanoparticle. The gold core (red) is surrounded by stabilizer molecules (grey) which provide colloidal stability. Ligands (green) can be either linked to the shell of stabilizer molecules (as shown here) or directly attached to the gold surface by replacing parts of the stabilizer molecules.

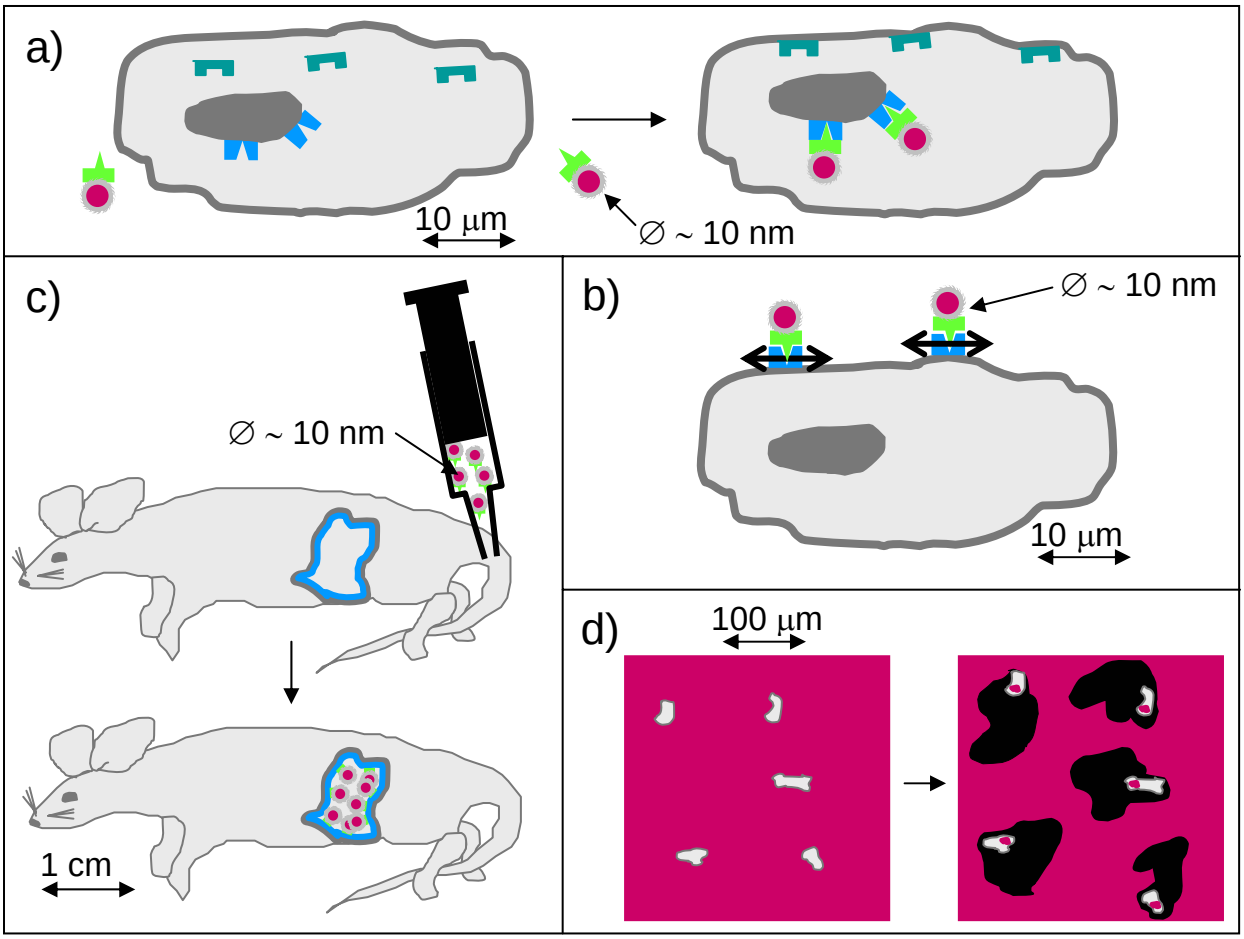

Figure 2: Labeling with gold nanoparticles. Gold nanoparticles (core in red, ligand shell in grey) are conjugated with ligands (green) which bind to specific receptors (blue) but not to other structures (as the receptors shown in dark green). a) Immunostaining: Gold nanoparticles conjugated with ligands against the structures to be labeled are added to fixed and permeated cells (shown in grey). Guided by molecular recognition they bind to the designated structures which are in this way stained with gold particles. In the image the particles are conjugated with ligands that bind to receptors on the surface of the nucleus, but for example not to other receptors present at the inner cell membrane. b) Single-particle tracking: Gold particles conjugated with ligands specific for membrane-bound molecules are added to living cells. In this way individual membrane-bound molecules are labeled with gold particles and their diffusion within the cell membrane can be traced via observation of the gold particles. c) X-ray contrasting: Gold particles conjugated with ligands that warrant for specific uptake in target organs are injected into the blood stream of animals. The organ then can be visualized by X-ray tomography due to the enriched gold particles. d) Phagokinetic tracks: a surface is covered with a layer of gold nanoparticles. When cells (shown in grey) are cultured on top of the surface they will ingested the underlying nanoparticles. Upon cellular migration along the surface the cells incorporate all nanoparticles along their pathway leaving behind area free of nanoparticles, which are a blueprint of their migration pathway. All images are not drawn to scale and important lengths scales are indicated in the images.

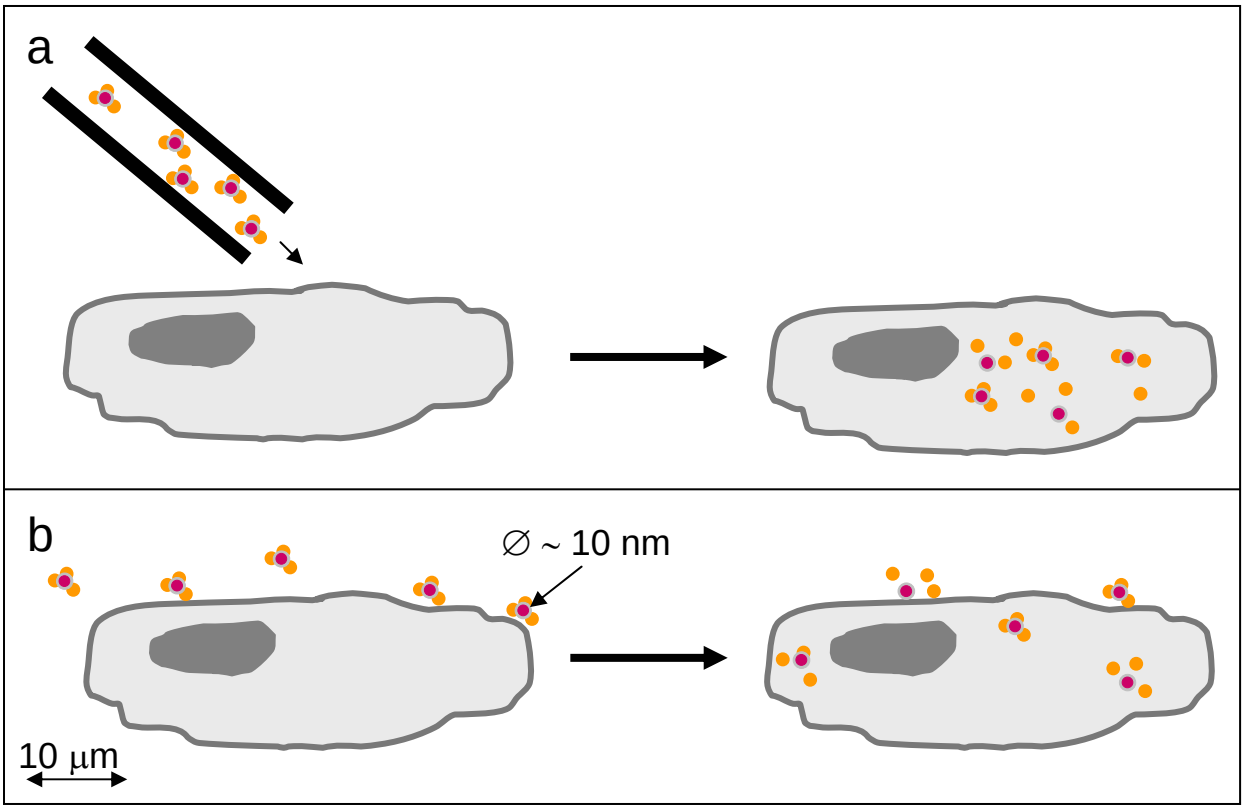

Figure 3: Delivering with gold nanoparticles. Molecules (shown in orange) which are to be delivered inside cells are adsorbed on the surface of gold nanoparticles (core in red, ligand shell in grey). Once inside the cell these molecules eventually will detach from the surface of the nanoparticles. a) Gene guns: The nanoparticles are shot as ballistic projectile into the cells using so called gene gun system. b) Incorporation by cells: The nanoparticles are either specifically or nonspecifically incorporated by cells. After ingestion the particles are stored in vesicular compartments inside the cells.

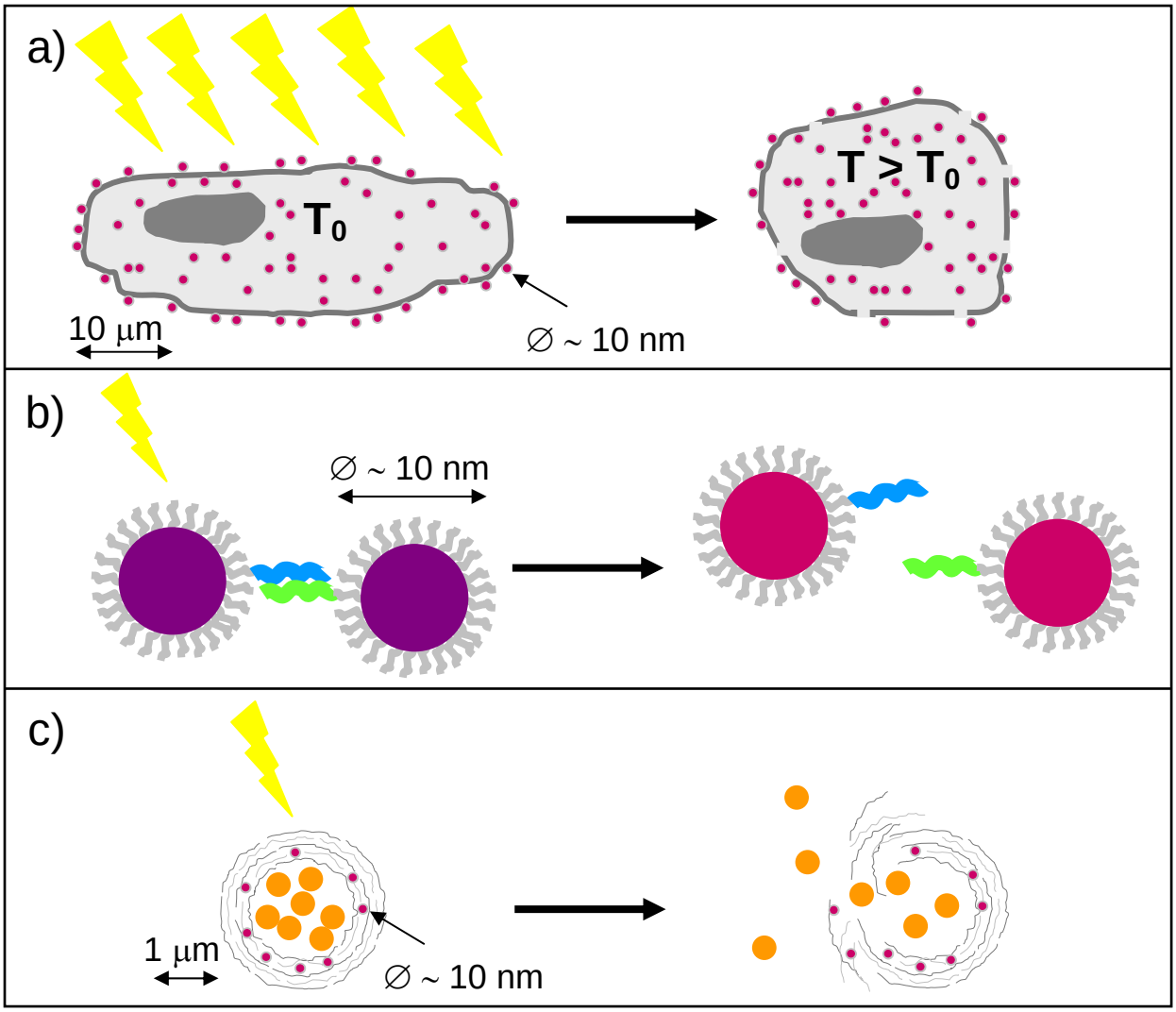

Figure 4: Heating with gold nanoparticles. Gold particles (core in red, ligand shell in grey) are heated upon absorption of light (shown as yellow ray) and mediate the heat to their local environment. a) Hyperthemia: the temperature inside cells (drawn in grey) is raised by illumination of gold particles. A temperature increase of only a few degrees is enough to kill cells. b) Breaking of bonds: When gold nanoparticles (core in red, ligand shell in grey) are conjugated with ligands (shown in green) that are specific to receptors (shown in blue) which are bound to other gold particles, these two kinds of gold particles will be linked to assemblies mediated by receptor-ligand binding. As the distance between the particles in such aggregates is low, their plasmon resonance is shifted to higher wavelengths and the particle solution appears violet/blue. Upon illumination the gold particles get heated and the bonds of the receptor-ligand pairs melt. Therefore the assemblies are dissolved, the average distance between the particles is increased and the particle solution appears red. c) Light-controlled opening of individual polymer capsules (drawn in grey) by local heating mediated by Au nanoparticles: Gold nanoparticles are embedded in the walls of polyelectrolyte capsules. The capsule cavity is loaded with cargo molecules (drawn in orange). Upon illumination with light the heat created by the nanoparticles causes local ruptures in the capsule walls and thus release of the cargo.

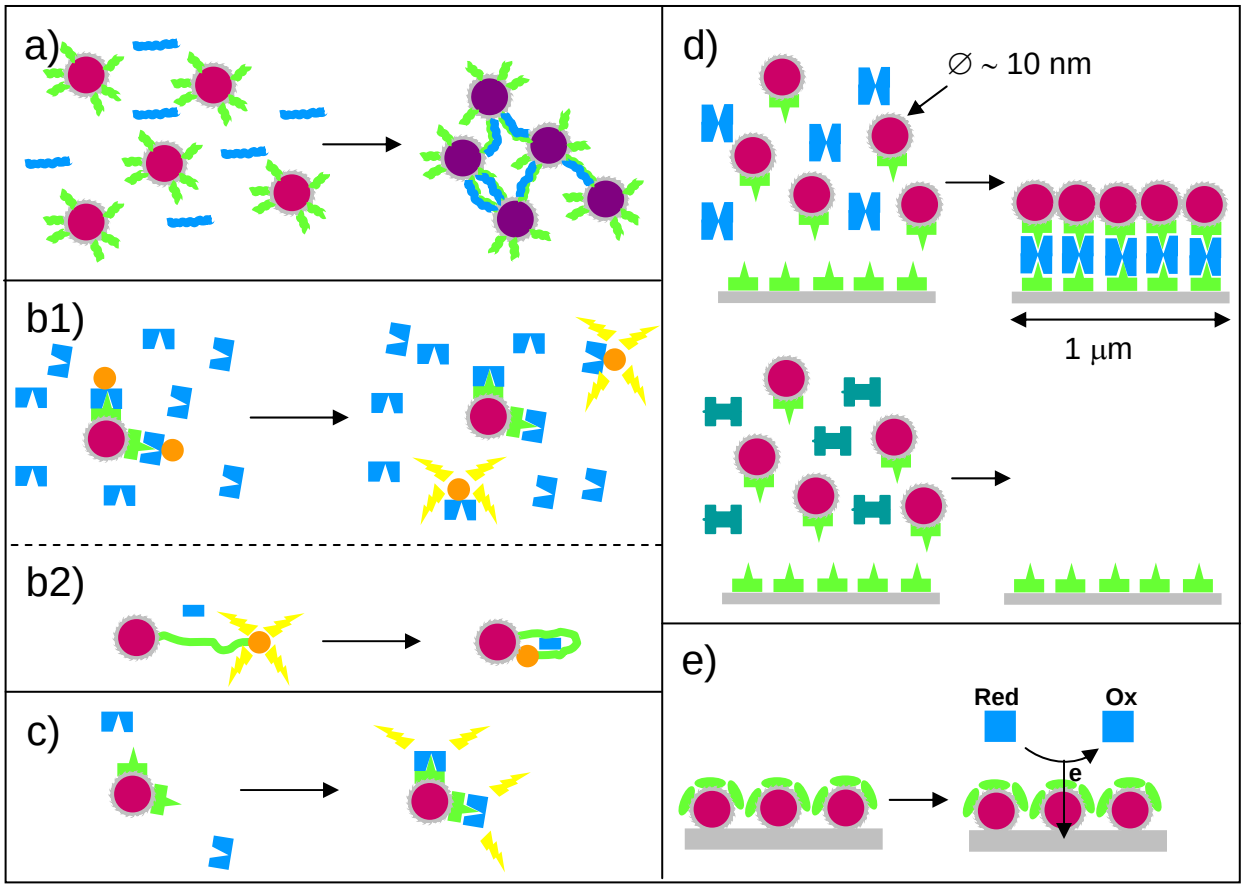

Figure 5: Sensing with gold nanoparticles. For the specific detection of analytes (shown in blue) gold nanoparticles (core in red, ligand shell in grey) are conjugated with ligands (shown in green) that selectively bind to the analyte. a) Colorimetric assays: Binding of the analyte to the ligands links several particles together to small aggregates and the red color of the colloidal gold solution shifts to purple / blue. b) Quenching of fluorophores: 1) Gold nanoparticles are conjugated with ligands that specifically bind to the analyte to be detected. The ligands on the nanoparticle surface are then saturated with molecules that bind to the ligands (shown in blue) and that have a fluorophore (drawn in orange) attached. As the fluorophores are in close vicinity to the surface of the Au particles their fluorescence is quenched. The presence of analyte molecules competitively displaces part of the molecules with the fluorophores from the nanoparticle surface. As these fluorophores are no longer in contact with Au particles their fluorescence (symbolized as yellow rays) can be detected. 2) Fluorophores (drawn in orange) are attached via linker molecules (drawn in green) to the surface of Au nanoparticle. Due to the length of the linker the distance between the fluorophore and the gold particles is big enough so that no quenching of the fluorescence of the fluorophore occurs. Presence of the analyte (drawn in blue) changes the conformation of the linker molecules and as the fluorophores then are in close vicinity of the Au surface so their fluorescence is quenched. c) Surface enhanced Raman scattering: Gold nanoparticles are conjugated to ligand molecules which specifically bind to the analyte to be detected. The analyte (drawn in blue) in solution provides only a week Raman signal. Upon binding of the analyte to the ligands present on the Au surface the analyte comes into close vicinity of the gold particles and the Raman signal is dramatically enhanced (as symbolized with the yellow rays). d) Gold stains: Ligands specific to the analyte to be detected are immobilized as well on a plain surface as on the surface of Au nanoparticles. Presence of the analyte (drawn in blue) causes the binding of the particles to the surface. Other molecules (drawn in dark green) do not cause binding of the particles to the surface and thus a washing

step removes all gold particles. The presence of the analyte is then quantified by the number of Au particles bound to the surface. e) Redox reactions. Redox enzymes (drawn in green) are conjugated to the surface of Au nanoparticles (core in red, ligand shell in grey) which are immobilized on top of an electrode (drawn in grey). The enzymes oxidize their present substrates (drawn in blue) from the reduced form to the oxidize oneand the released electrons are transferred via the gold nanoparticles to the electrode, which can be measured as current.

10. References

1. Jennings, T. and G. Strouse, Past, present, and future of gold nanoparticles, in Bio-Applications Of Nanoparticles. 2007. p. 34-47.
2. Turkevich, J., P.C. Stevenson, and J. Hillier, A study of the nucleation and growth processes in the synthesis of colloidal golde. J. Discuss. Faraday Soc., 1951: p. 55-75.
3. Kimling, J., et al., Turkevich Method for Gold Nanoparticle Synthesis Revisited. J. Phys. Chem. B, 2006. 110(32): p. 15700-15707.
4. Brust, M., et al., Synthesis of thiol-derivatised gold nanoparticles in a two-phase liquid-liquid system. J. Chem. Soc., Chem. Commun., 1994. 1994: p. 801-802.
5. Sönnichsen, C. and A.P. Alivisatos, Gold Nanorods as Novel Nonbleaching Plasmon-Based Orientation Sensors for Polarized Single-Particle Microscopy. Nanoletters, 2005. 5(2): p. 310-304.
6. Perez-Juste, J., et al., Gold nanorods: Synthesis, characterization and applications. Coordination Chemistry Reviews, 2005. 249: p. 1870-1901.
7. Templeton, A.C., W.P. Wuelfing, and R.W. Murray, Monolayer-Protected Cluster Molecules. Accounts of Chemical Research, 2000. 33(1): p. 27-36.
8. Pellegrino, T., et al., On the Development of Colloidal Nanoparticles towards Multifunctional Structures and their Possible Use for Biological Applications. Small, 2005. 1(1): p. 48-63.
9. Kanaras, A.G., et al., Thioalkylated tetraethylene glycol: a new ligand for water soluble monolayer protected gold clusters. Chem. Comm., 2002. 2002: p. 2294-2295.
10. Liz-Marzán, L.M., M. Giersig, and P. Mulvaney, Synthesis of Nanosized Gold-Silica Core-Shell Particles. Langmuir, 1996. 12(18): p. 4329-4335.
11. Zanchet, D., et al., Electrophoretic isolation of discrete Au nanocrystal/DNA conjugates. Nanoletters, 2001. 1(1): p. 32-35.
12. Levy, R., et al., A Generic Approach to Monofunctionalized Protein-Like Gold Nanoparticles Based on Immobilized Metal Ion Affinity Chromatography. chembiochem, 2006. 7(4): p. 592-594.
13. Hermanson, G.T., Bioconjugate Techniques. 1996, San Diego: Academic Press.
14. Sperling, R.A., et al., Electrophoretic separation of nanoparticles with a discrete number of functional groups. Advanced Functional Materials, 2006. 16(7): p. 943-948.
15. Demers, L.M., et al., A Fluorescence-Based Method for Determining the Surface Coverage and Hybridization Efficiency of Thiol-Capped Oligonucleotides Bound to Gold Thin Films and Nanoparticles. Analytical Chemistry, 2000. 72(22): p. 5535-5541.
16. Pellegrino, T., et al., Gelelectrophoresis of Gold-DNA nano-conjugates. Journal of Biomedicine and Biotechnology, 2008. in press.
17. Chithrani, B.D., A.A. Ghazan, and C.W. Chan, Determining the Size and the Shape dependence of gold nanoparticle uptake into mammalian cells. Nano Letters, 2006. 6(4): p. 662-668.
18. Patra, H.K., et al., Cell selective response to gold nanoparticles. Nanomedicine-Nanotechnology Biology And Medicine, 2007. 3(2): p. 111-119.

19. Albrecht, M.A., C.W. Evans, and C.L. Raston, Green chemistry and the health implications of nanoparticles. Green Chemistry, 2006. 8(5): p. 417-432.
20. Connor, E.E., et al., Gold nanoparticles are taken up by human cells but do not cause acute cytotoxicity. Small, 2005. 1(3): p. 325-327.
21. Kirchner, C., et al., Cytotoxicity of Colloidal CdSe and CdSe/ZnS Nanoparticles. Nanoletters, 2005. 5(2): p. 331-338.
22. Shukla, R., et al., Biocompatibility of Gold Nanoparticles and Their Endocytotic Fate Inside the Cellular Compartment: A Microscopic Overview. Langmuir, 2005. 21: p. 10644-10654.
23. Goodman, C.M., et al., Toxicity of Gold Nanoparticles Functionalized with Cationic and Anionic Side Chains. Bioconjugate Chemistry, 2004. 15(4): p. 897-900.
24. Pan, Y., et al., Size-dependent cytotoxicity of gold nanoparticles. Small, 2007. 3(11): p. 1941-1949.
25. Pernodet, N., et al., Adverse effects of citrate/gold nanoparticles on human dermal fibroblasts. Small, 2006. 2(6): p. 766-773.
26. Tsoli, M., et al., Cellular Uptake and Toxicity of Au_{55} Clusters. Small, 2005. 1(8-9): p. 841-844.
27. Schmid, G.? Acoounts on Chemical Research, 2008. same volume as this article.
28. Huang, X.H., et al., Gold nanoparticles: interesting optical properties and recent applications in cancer diagnostic and therapy. Nanomedicine, 2007. 2(5): p. 681-693.
29. Sonnichsen, C., et al., Plasmon resonances in large noble-metal clusters. New Journal Of Physics, 2002. 4.
30. Tkachenko, A.G., et al., Cellular Trajectories of Peptide-Modified Gold Particle Complexes: Comparison of Nuclear Localization Signals and Peptide Transduction Domains. Bioconjugate Chem., 2004. 15(3): p. 482-490.
31. Souza, G.R., et al., Networks of gold nanoparticles and bacteriophage as biological sensors and cell-targeting agents. Proceedings of the National Academy of Sciences, 2006. 103(5): p. 1215-1220.
32. Jin, R., et al., Photoinduced Conversion of Silver Nanospheres to Nanoprisms. Science, 2001. 294(30 November): p. 1901-1903.
33. Boyer, D., et al., Photothermal imaging of nanometer-sized metal particles among scatterers. Science, 2002. 297(5584): p. 1160-1163.
34. Berciaud, S., et al., Photothermal heterodyne imaging of individual nonfluorescent nanoclusters and nanocrystals. Physical Review Letters, 2004. 93(25).
35. Mallidi, S., et al., Molecular specific optoacoustic imaging with plasmonic nanoparticles. Optics Express, 2007. 15(11): p. 6583-6588.
36. Kim, K., et al., Photoacoustic imaging of early inflammatory response using gold nanorods. Applied Physics Letters, 2007. 90(22).
37. Wilcoxon, J.P., et al., Photoluminescence from nanosize gold clusters. The Journal of Chemical Physics, 1998. 108(21): p. 9137-9143.
38. Wang, G.L., et al., Near-IR luminescence of monolayer-protected metal clusters. Journal Of The American Chemical Society, 2005. 127(3): p. 812-813.
39. Roth, J., The silver anniversary of gold: 25 years of the colloidal gold marker system for immunocytochemistry and histochemistry. Histochemistry and Cell Biology, 1996. 106(1): p. 1-8.
40. Hainfeld, J.F., et al., Gold nanoparticles: a new X-ray contrast agent. British Journal Of Radiology, 2006. 79(939): p. 248-253.
41. Gosselin, R.E., THE UPTAKE OF RADIOCOLLOIDS BY MACROPHAGES IN VITRO - A KINETIC ANALYSIS WITH RADIOACTIVE COLLOIDAL GOLD. The Journal of General Physiology, 1956. 39(5): p. 625-649.

42. Faulk, W.P. and G.M. Taylor, An immunocolloid method for the electron microscope. Immunochemistry, 1971. 8(11): p. 1081.
43. Mey, J.D., et al., Visualization of Microtubules in Interphase and Mitotic Plant Cells of Haemanthus Endosperm with the Immuno-Gold Staining Method. Proceedings of the National Academy of Sciences, 1982. 79(6): p. 1898-1902.
44. Kusumi, A., et al., PARADIGM SHIFT OF THE PLASMA MEMBRANE CONCEPT FROM THE TWO-DIMENSIONAL CONTINUUM FLUID TO THE PARTITIONED FLUID: High-Speed Single-Molecule Tracking of Membrane Molecules. Annual Review of Biophysics and Biomolecular Structure, 2005. 34(1): p. 351-378.
45. Felsenfeld, D.P., D. Choquet, and M.P. Sheetz, Ligand binding regulates the directed movement of beta 1 integrins on fibroblasts. Nature, 1996. 383(6599): p. 438-440.
46. Cang, H., et al., Confocal three dimensional tracking of a single nanoparticle with concurrent spectroscopic readouts. Applied Physics Letters, 2006. 88(22).
47. Lasne, D., et al., Single nanoparticle photothermal tracking (SNaPT) of 5-nm gold beads in live cells. Biophysical Journal, 2006. 91(12): p. 4598-4604.
48. Cognet, L., et al., Single metallic nanoparticle imaging for protein detection in cells. PNAS, 2003. 100(20): p. 11350-11355.
49. Wang, Y.L., J.D. Silverman, and L.G. Cao, Single particle tracking of surface receptor movement during cell division. J. Cell Biol., 1994. 127(4): p. 963-971.
50. Dahan, M., et al., Diffusion Dynamics of Glycine Receptors Revealed by Single – Quantum Dot Tracking. Science, 2003. 302(17 October): p. 442-445.
51. Kim, D., et al., Antibiofouling polymer-coated gold nanoparticles as a contrast agent for in vivo x-ray computed tomography imaging. Journal Of The American Chemical Society, 2007. 129(24): p. 7661-7665.
52. Hainfeld, J.F., D.N. Slatkin, and H.M. Smilowitz, The use of gold nanoparticles to enhance radiotherapy in mice. Physics in Medicine and Biology, 2004(18): p. N309-N315.
53. Ballou, B., et al., Noninvasive Imaging of Quantum Dots in Mice. Bioconjugate Chemistry, 2004. 15(1): p. 79-86.
54. Kim, S., et al., Near-infrared fluorescent type II quantum dots for sentinel lymph node mapping. Nature Biotechnology, 2004. 22(1): p. 93-97.
55. Albrecht-Buehler, G., The Phagokinetic Tracks of 3T3 Cells. Cell, 1977. 11: p. 395-404.
56. Albrecht-Buehler, G., Phagokinetic Tracks of 3T3 Cells: Parallels between the Orientation of Track Segments and of Cellular Structures Which Contain Actin or Tubulin. Cell, 1977. 12: p. 333-339.
57. Albrecht-Buehler, G., The angular distribution of directional changes of guided 3T3 cells. Journal of Cell Biology, 1979. 80: p. 53-60.
58. Pellegrino, T., et al., Quantum dot-based cell motility assay. Differentiation, 2003. 71(9-10): p. 542-548.
59. Chen, D.-R., C.H. Wendt, and D.Y.H. Pui, A Novel Approach for Introducing Bio-Materials Into Cells. Journal of Nanoparticle Research, 2000. 2(2): p. 133-139.
60. Yang, N., et al., In vivo and in vitro Gene Transfer to Mammalian Somatic Cells by Particle Bombardment. Proceedings of the National Academy of Sciences, 1990. 87(24): p. 9568-9572.
61. Hilber, U.W., et al., Biolistic transformation of conidia of Botryotinia fuckeliana. Current Genetics, 1994. 25: p. 124-127.
62. Yepes, L.M., et al., Biolistic transformation of chrysanthemum with the nucleocapsid gene tomato spotted wilt virus. Plant Cell Reports, 1995. 14: p. 694-698.
63. Kuriyama, S., et al., Particle-mediated gene transfer into murine livers using a newly developed gene gun. Gene Therapy, 2000. 7(13): p. 1132-1136.

64. Wagner, E., D. Curiel, and M. Cotten, Delivery Of Drugs, Proteins And Genes Into Cells Using Transferrin As A Ligand For Receptor-Mediated Endocytosis. Advanced Drug Delivery Reviews, 1994. 14(1): p. 113-135.
65. Yang, P.-H., et al., Transferrin-Mediated Gold Nanoparticle Cellular Uptake. Bioconjugate Chemistry, 2005. 16(3): p. 494-496.
66. Dixit, V., et al., Synthesis and grafting of thioctic acid-PEG-folate conjugates onto Au nanoparticles for selective targeting of folate receptor-positive tumor cells. Bioconjugate Chemistry, 2006. 17(3): p. 603-609.
67. Jain, P.K., I.H. El-Sayed, and M.A. El-Sayed, Au nanoparticles target cancer. Nano Today, 2007. 2(1): p. 18-29.
68. Chithrani, B.D. and W.C.W. Chan, Elucidating the mechanism of cellular uptake and removal of protein-coated gold nanoparticles of different sizes and shapes. Nano Letters, 2007. 7(6): p. 1542-1550.
69. de_la_Fuente, J.M. and C.C. Berry, Tat peptide as an efficient molecule to translocate gold nanoparticles into the cell nucleus. Bioconjugate Chemistry, 2005. 16(5): p. 1176-1180.
70. Lewin, M., et al., Tat peptide-derivatized magnetic nanoparticles allow in vivo tracking and recovery of progenitor cells. Nature Biotechnolgy, 2000. 18(4): p. 410-414.
71. Koch, A.M., et al., Transport of surface-modified nanoparticles through cell monolayers. Chembiochem, 2005. 6(2): p. 337-345.
72. Murriel, C.L. and S.F. Dowdy, Influence of protein transduction domains on intracellular delivery of macromolecules. Expert Opin Drug Deliv, 2006. 3(6): p. 739-46.
73. Xu, Z.P., et al., Inorganic nanoparticles as carriers for efficient cellular delivery. Chemical Engineering Science, 2006. 61(3): p. 1027-1040.
74. Han, G., et al., Light-Regulated Release of DNA and Its Delivery to Nuclei by Means of Photolabile Gold Nanoparticles. Angewandte Chemie International Edition, 2006. 45(19): p. 3165-3169.
75. Salem, A.K., P.C. Searson, and K.W. Leong, Multifunctional nanorods for gene delivery. Nature Materials, 2003. 2: p. 668-671.
76. Sullivan, M.M.O., J.J. Green, and T.M. Przybycien, Development of a novel gene delivery scaffold utilizing colloidal gold-polyethylenimine conjugates for DNA condensation. Gene Therapy, 2003. 10(22): p. 1882-1890.
77. Rosi, N.L., et al., Oligonucleotide-modified gold nanoparticles for intracellular gene regulation. Science, 2006. 312(5776): p. 1027-1030.
78. Rojo, J., et al., Gold Glyconanoparticles as New Tools in Antiadhesive Therapy. ChemBioChem, 2004. 5: p. 291-297.
79. Sokolov, K., et al., Optical systems for in vivo molecular imaging of cancer. TECHNOLOGY IN CANCER REARCH AND TREATMENT, 2003. 2(6): p. 491-504.
80. Kumar, S., et al., Plasmonic nanosensors for imaging intracellular biomarkers in live cells. Nano Letters, 2007. 7(5): p. 1338-1343.
81. Govorov, A.O., et al., Gold nanoparticle ensembles as heaters and actuators: melting and collective plasmon resonances. Nanoscale Research Letters, 2006. 1(1): p. 84-90.
82. Pissuwan, D., S.M. Valenzuela, and M.B. Cortie, Therapeutic possibilities of plasmonically heated gold nanoparticles. Trends in Biotechnology, 2006. 24(2): p. 62-67.
83. Choi, M.R., et al., A cellular Trojan horse for delivery of therapeutic nanoparticles into tumors. Nano Letters, 2007. 7(12): p. 3759-3765.
84. Huff, T.B., et al., Hyperthermic effects of gold nanorods on tumor cells. Nanomedicine, 2007. 2(1): p. 125-132.

85. Huang, X.H., et al., Determination of the minimum temperature required for selective photothermal destruction of cancer cells with the use of immunotargeted gold nanoparticles. Photochemistry And Photobiology, 2006. 82(2): p. 412-417.
86. Lowery, A.R., et al., Immunonanoshells for targeted photothermal ablation of tumor cells. International Journal Of Nanomedicine, 2006. 1(2): p. 149-154.
87. Huang, X., et al., Plasmonic photothermal therapy (PPTT) using gold nanoparticles. Lasers in Medical Science, online first. in press(DOI:10.1007/s10103-007-0470-x).
88. Pankhurst, Q.A., et al., Applications of magnetic nanoparticles in biomedicine. J. Phys. D: Appl. Phys., 2003. 36: p. R167-R181.
89. Hiergeist, R., et al., Application of magnetite ferrofluids for hyperthermia. Journal of Magnetism and Magnetic Materials, 1999. 201: p. 420-422.
90. Hamad-Schifferli, K., et al., Remote electronic control of DNA hybridization through inductive coupling to an attached metal nanocrystal antenna. Nature, 2002. 415(10 January): p. 152-155.
91. Stehr, J., et al., Gold Nano-Stoves for Microsecond DNA Melting Analysis. Nanoletters, 2007. in press.
92. Kogan, M.J., et al., Nanoparticle-mediated local and remote manipulation of protein aggregation. Nano Letters, 2006. 6(1): p. 110-115.
93. Angelatos, A.S., B. Radt, and F. Caruso, Light-Responsive Polyelectrolyte/Gold Nanoparticle Microcapsules. J. Phys. Chem. B, 2005. 109: p. 3071-3076.
94. Skirtach, A.G., et al., The Role of Metal Nanoparticles in Remote Release of Encapsulated Materials. Nanoletters, 2005. 5(7): p. 1371-1377.
95. Skirtach, A.G., et al., Laser-Induced Release of Encapsulated Materials inside Living Cells. Angew. Chem. Int. Ed., 2006. 45: p. 4612-4617.
96. Pitsillides, C.M., et al., Selective Cell Targeting with Light-Absorbing Microparticles and Nanoparticles. Biophys. J., 2003. 84: p. 4023-32.
97. Klar, T.A., Biosensing with plasmonic nanoparticles, in Nanophotonics with Surface Plasmons, S. V.M. and K. S., Editors. 2007, Elsevier: The Netherlands. p. 219-270.
98. Raschke, G., et al., Biomolecular recognition based on single gold nanoparticle light scattering. Nano Letters, 2003. 3(7): p. 935-938.
99. Jain, P.K., S. Eustis, and M.A. El-Sayed, Plasmon coupling in nanorod assemblies: Optical absorption, discrete dipole approximation simulation, and exciton-coupling model. Journal Of Physical Chemistry B, 2006. 110(37): p. 18243-18253.
100. Mirkin, C.A., et al., A DNA-Based Method For Rationally Assembling Nanoparticles Into Macroscopic Materials. Nature, 1996. 382: p. 607-609.
101. Elghanian, R., et al., Selective Colorimetric Detection of Polynucleotides Based on the Distance-Dependent Optical Properties of Gold Nanoparticles. Science, 1997. 277(August 22): p. 1078-1081.
102. Moller, R. and W. Fritzsche, Metal nanoparticle-based detection for DNA analysis. Current Pharmaceutical Biotechnology, 2007. 8(5): p. 274-285.
103. Nam, J.M., S.I. Stoeva, and C.A. Mirkin, Bio-Bar-Code-Based DNA Detection with PCR-like Sensitivity. J. Am. Chem. Soc., 2004. 126(19): p. 5932-5933.
104. Liu, J. and Y. Lu, Colorimetric Cu2+ detection with a ligation DNAzyme and nanoparticles. Chemical Communications, 2007(46): p. 4872-4874.
105. Zhao, W., et al., DNA Aptamer Folding on Gold Nanoparticles: From Colloid Chemistry to Biosensors. J. Am. Chem. Soc., 2008. in press.
106. Wang, W., et al., Aptamer biosensor for protein detection using gold nanoparticles. Analytical Biochemistry, 2008. 373(2): p. 213.

107. Wang, Z., et al., Kinase-Catalyzed Modification of Gold Nanoparticles: A New Approach to Colorimetric Kinase Activity Screening. J. Am. Chem. Soc., 2006. 128(7): p. 2214-2215.
108. Sonnichsen, C., et al., A molecular ruler based on plasmon coupling of single gold and silver nanoparticles. Nature Biotechnology, 2005. 23(6): p. 741-745.
109. Lakowicz, J.R., Principles of Fluorescence Spectroscopy. Third Edition ed. 2006, New York: Springer. 954.
110. Dulkeith, E., et al., Fluorescence Quenching of Dye Molecules near Gold nanoparticles: radiative and Nonradiative Effects. Physical Review Letters, 2002. 89(20): p. 203002-1 - 202002-4.
111. Dulkeith, E., et al., Gold Nanoparticles Quench Fluorescence by Phase Induced Radiative Rate Suppression. Nanoletters, 2005. 5(4): p. 585-589.
112. Oh, E., et al., Inhibition Assay of Biomolecules based on Fluorescence Resonance Energy Transfer (FRET) between Quantum Dots and Gold Nanoparticles. JACS, 2005. 127: p. 3270-3271.
113. Dubertret, B., M. Calame, and A.J. Libchaber, Single-mismatch detection using gold-quenched fluorescent oligonucleotides. Nature Biotechnology, 2001. 19(4): p. 365-370.
114. Wang, Z., et al., Enzymatic DNA processing on gold nanoparticles. Journal of Materials Chemistry, 2004. 14: p. 578-580.
115. Ray, P., et al., Gold Nanoparticle Based FRET for DNA Detection. Plasmonics, 2007. 2(4): p. 173.
116. Lakowicz, J., Plasmonics in Biology and Plasmon-Controlled Fluorescence. Plasmonics, 2006. 1(1): p. 5.
117. Szymanski, H.A., Raman Spektroskopy. 1 ed. 1967, New York: Plenum Press. 255.
118. Fleischmann, M., P.J. Hendra, and A.J. McQuillan, Raman spectra of pyridine adsorbed at a silver electrode. Chemical Physics Letters, 1974. 26(2): p. 163.
119. Campion, A. and P. Kambhampati, Surface-enhanced Raman scattering. Chemical Society Reviews, 1998. 27(4): p. 241-250.
120. Kneipp, K., H. Kneipp, and J. Kneipp, Surface-Enhanced Raman Scattering in Local Optical Fields of Silver and Gold Nanoaggregates-From Single-Molecule Raman Spectroscopy to Ultrasensitive Probing in Live Cells. Acc. Chem. Res., 2006. 39(7): p. 443-450.
121. Emory, S.N.a.S.R., Probing Single Molecules and Single Nanoparticles by Surface-Enhanced Raman Scattering. Science, 1997. 275(February 21): p. 1102-1106.
122. Krug, J.T., et al., Efficient Raman Enhancement and Intermittent Light Emission Observed in Single Gold Nanocrystals. Journal of the American Chemical Society, 1999. 121(39): p. 9208-9214.
123. Cao, Y.C., R. Jin, and C.A. Mirkin, Nanoparticles with Raman Spectroscopic Fingerprints for DNA and RNA Detection. Science, 2002. 297(5586): p. 1536-1540.
124. Ni, J., et al., Immunoassay Readout Method Using Extrinsic Raman Labels Adsorbed on Immunogold Colloids. Anal. Chem., 1999. 71(21): p. 4903-4908.
125. Qian, X., et al., In vivo tumor targeting and spectroscopic detection with surface-enhanced Raman nanoparticle tags. Nat Biotech, 2008. 26(1): p. 83.
126. Kneipp, J., H. Kneipp, and K. Kneipp, Two-photon vibrational spectroscopy for biosciences based on surface-enhanced hyper-Raman scattering. Proceedings of the National Academy of Sciences, 2006. 103(46): p. 17149-17153.
127. Wang, Z., et al., Microarray-Based Detection of Protein Binding and Functionality by Gold Nanoparticle Probes. Anal. Chem., 2005. 77(17): p. 5770-5774.
128. Wang, Z., et al., The Peptide Route to Multifunctional Gold Nanoparticles. Bioconjugate Chemistry, 2005. 16(3): p. 497-500.

129. Newman, G.R. and B. Jasani, Silver development in microscopy and bioanalysis: past and present. The Journal of Pathology, 1998. 186(2): p. 119-125.
130. Blab, G.A., et al., Optical readout of gold nanoparticle-based DNA microarrays without silver enhancement. Biophysical Journal, 2006. 90(1): p. L13-L15.
131. Reichert, J., et al., Chip-Based Optical Detection of DNA Hybridization by Means of Nanobead Labeling. Anal. Chem., 2000. 72(24): p. 6025-6029.
132. Moeremans, M., et al., Sensitive visualization of antigen-antibody reactions in dot and blot immune overlay assays with immunogold and immunogold/silver staining. Journal of Immunological Methods, 1984. 74(2): p. 353.
133. Joseph, W., Nanoparticle-Based Electrochemical Bioassays of Proteins. Electroanalysis, 2007. 19(7-8): p. 769-776.
134. Castañeda, M.T. and S.A.A. Merkoçi, Electrochemical Sensing of DNA Using Gold Nanoparticles. Electroanalysis, 2007. 19(7-8): p. 743-753.
135. Willner, B., E. Katz, and I. Willner, Electrical contacting of redox proteins by nanotechnological means. Current Opinion In Biotechnology, 2006. 17(6): p. 589-596.
136. Xiao, Y., et al., "Plugging into Enzymes": Nanowiring of Redox Enzymes by a Gold Nanoparticle. Science, 2003. 299(5614): p. 1877-1881.
137. Xiao, Y., H.-X. Ju, and H.-Y. Chen, Hydrogen peroxide sensor based on horseradish peroxidase-labeled Au colloids immobilized on gold electrode surface by cysteamine monolayer. Analytica Chimica Acta, 1999. 391(1): p. 73.
138. Yu, A., et al., Nanostructured Electrochemical Sensor Based on Dense Gold Nanoparticle Films. Nano Lett., 2003. 3(9): p. 1203-1207.
139. Zhao, J., et al., Direct electron transfer at horseradish peroxidase--colloidal gold modified electrodes. Journal of Electroanalytical Chemistry, 1992. 327(1-2): p. 109.

Chloroform- and water-soluble sol-gel derived Eu+++/Y2O3 (red) and Tb+++/Y2O3 (green) nanophosphors: synthesis, characterization and surface modification (Submitted)

Ashutosh Pandey1*, M. K. Roy2, Anjana Pandey3, Marco Zanella4, Ralph A. Sperling4, W. J. Parak4, A. B. Samaddar1 and H. C. Verma2

1Department of Chemistry; MNNIT Allahabad, INDIA
2 Department of Physics; IIT Kanpur, INDIA
3Nanotechnology and Molecular Biology Laboratory, Center of Biotechnology, University of Allahabad, INDIA
4 Center for Nanoscience, Ludwig Maximilians Universität München, GERMANY and Fachbereich Physik, Philipps Universität Marburg, GERMANY
* Corresponding Author: apandey70@yahoo.com

Abstract:
Eu+++ and Tb+++ ions have been incorporated into nano-dimensional yttrium oxide host matrices in both 0.02:1.0 and 0.2:1.0 (dopant ion:host matrix) molar ratios via a sol-gel process using Y5O(OPri)13 as precursor (OPri = iso-propoxy). The as-synthesised white powders have been annealed at different temperatures ranging from 400 0C to 800 0C for 5 hours. Photoluminescence (PL) spectroscopy and X-ray diffraction (XRD) have been used as tools for documenting the characteristics of these powders. For Eu+++ doped powders a comparison of the Eu+++ 5D0 7F1 and 5D0 7F2 peak intensities in the emission spectra reveals that the dopant ions are occupying unsymmetrical sites in the host yttrium oxide in all the samples. For Tb+++ doped powders the characteristic terbium 5D3 7Fn and 5D 7Fn (n=2-6) transitions were visible only in the samples that had been annealed above 500 0C. All the samples for 0.2 M doped Eu+++ and Tb+++ were suspended in chloroform by fragmenting the powder with and without sonification under the presence of trioctylphosphine oxide (TOPO), or a mixture of oleic acid and dioctyl ether, to give clear colorless (for Eu+++) and light green translucent (for Tb+++) solutions of the dispersed particles which respectively give red and green luminescence upon UV excitation. In addition, suspension in water has been achieved by fragmenting the powder in the presence of dichloroacetic acid. TEM investigation of the soluble particles shows single dispersed particles along with some agglomerates. The changes in the luminescence due to fragmentation of the particle powder and due the influence of the surfactant of the suspended colloidal particles are discussed.

Chloroform- and water-soluble sol-gel derived Eu^{+++}/Y_2O_3 (red) and Tb^{+++}/Y_2O_3 (green) nanophosphors: synthesis, characterization and surface modification

Ashutosh Pandey[1*], M. K. Roy[2], Anjana Pandey[3], Marco Zanella[4], Ralph A. Sperling[4], W. J. Parak[4], A. B. Samaddar[1] and H. C. Verma[2]

[1]Department of Chemistry; MNNIT Allahabad, INDIA
[2] Department of Physics; IIT Kanpur, INDIA
[3]Nanotechnology and Molecular Biology Laboratory, Center of Biotechnology, University of Allahabad, INDIA
[4] Center for Nanoscience, Ludwig Maximilians Universität München, GERMANY and Fachbereich Physik, Philipps Universität Marburg, GERMANY
* Corresponding Author: apandey70@yahoo.com

Abstract:

Eu^{+++} and Tb^{+++} ions have been incorporated into nano-dimensional yttrium oxide host matrices in both 0.02:1.0 and 0.2:1.0 (dopant ion:host matrix) molar ratios via a sol-gel process using $Y_5O(OPr^i)_{13}$ as precursor (OPr^i = iso-propoxy). The as-synthesised white powders have been annealed at different temperatures ranging from 400 ^{0}C to 800 ^{0}C for 5 hours. Photoluminescence (PL) spectroscopy and X-ray diffraction (XRD) have been used as tools for documenting the characteristics of these powders. For Eu^{+++} doped powders a comparison of the Eu^{+++} $^5D_0 \rightarrow {}^7F_1$ and $^5D_0 \rightarrow {}^7F_2$ peak intensities in the emission spectra reveals that the dopant ions are occupying unsymmetrical sites in the host yttrium oxide in all the samples. For Tb^{+++} doped powders the characteristic terbium $^5D_3 \rightarrow {}^7F_n$ and $^5D \rightarrow {}^7F_n$ (n=2-6) transitions were visible only in the samples that had been annealed above 500 ^{0}C. All the samples for 0.2 M doped Eu^{+++} and Tb^{+++} were suspended in chloroform by fragmenting the powder with and without sonification under the presence of trioctylphosphine oxide (TOPO), or a mixture of oleic acid and dioctyl ether, to give clear colorless (for Eu^{+++}) and light green translucent (for Tb^{+++}) solutions of the dispersed particles which respectively give red and green luminescence upon UV excitation. In addition, suspension in water has been achieved by fragmenting the powder in the presence of dichloroacetic acid. TEM investigation of the soluble particles shows single dispersed particles along with some agglomerates. The changes in the luminescence due to fragmentation of the particle powder and due the influence of the surfactant of the suspended colloidal particles are discussed.

Keywords: Nanophosphors, luminescent solutions, colloidal nanoparticles, particle suspension, photoluminescence spectroscopy, sol-gel process

---

1. Introduction

Rare-earth ion doped nanocrystalline metal oxides are a class of luminescent materials (also called upconverting phosphors) which has been proved to be excellent for applications such as in FEDs (field emission displays) and sensors [1,2]. Under UV irradiation a variety of colors is available in these systems. For example, Eu^{+++} doped Y_2O_3 is a red phosphor while Tb^{+++} and Tm^{+++} incorporated in Y_2O_3 are green and blue phosphors, respectively [2]. The "caged atoms" in the host matrix retain their own atomic levels within the band gap of the host material. This combination of host and impurity energy levels leads to a large excitation cross-section resulting in high phosphorescence. It is anticipated that, due to their high quantum efficiency they might serve as improved luminescent markers [3] for bio-molecule detection in comparison to the reported non oxide semiconductor quantum dots [4,5]. This has been further substantiated by the fact that the LD_{50} values for rare earth oxides are about 1000mg/kg [6], while for example for selenium oxide (which is present even in many quantum dots that do not contain the far more toxic cadmium) it is only about 1mg/kg. Therefore, it is recommendable to explore the suitability of aforementioned nanophosphors for bioconjugation. However, one of the key issues for biological applications is that these probes have to be suspended in water while retaining their characteristic colors along with high stability. The group of Caruso has first suspended rare earth doped fluorescent lanthanum phosphate nanoparticles in water by surface modification with aminohexanoic acid [7] and subsequently the particles have successfully been conjugated with biological molecules. Recently, nonaggregated green emitting nanophosphors [8] of a size range of 50-200nm have been incorporated and imaged in the worm Caenorhabditis elegans and have further been examined by SEM. Several methods are known for the synthesis of these doped nanocrystallites [9-26], whereby among them the Sol-Gel process has especially attractive features. We have recently reported the synthesis and characterization of Eu^{+++}/Y_2O_3 nanophosphors by using the sol-gel method in which the dopant ion : host matrix ratio was kept as 0.001 : 1.0 [26]. Although the europium emission spectra is clearly visible at such a low concentration, the powders and their transparent suspensions (surfactant coated) in organic solvents showed very faint red luminescence when examined by naked eye under UV irradiation. Furthermore, in order to use these materials for any water-based application first the particle-powder would have to be dispersed into single hydrophilic colloidally stable particles. In sol-gel hydrolytic systems, the particles are characterized by hydroxylated surfaces that lead to strong interparticle interaction, and therefore a suitable stabilization is needed during the sol processing stage. Otherwise, very large and unstable particles would be readily formed. The situation becomes even more complex if a dopant ion like Eu^{+++} (for which the red phosphorescence gets significantly quenched by the -OH groups) [27] is required within the framework of sol-gel derived metal oxide nanoparticle powders, which also generally have water or alcohol molecules trapped inside. Therefore, these nanoparticle powders have to be annealed to high temperatures (i.e. up to 500 ^{0}C) to completely remove these volatile molecules [26]. However, high temperatures at the same time often lead to sintering, resulting in wide particle size distributions within the interconnected particle powder. Due to this it becomes rather difficult to prepare stable suspensions consisting of doped monodisperse particles and so

far we are aware of only few reports in this direction [7, 9, 28, 29]. Very recently also microwave assisted synthesis of doped nanocrystals has been reported [25].

The aim of this study was to generate and characterize stable suspensions for both red and green nanophosphors which should exhibit bright luminescence. In this connection, we hereby report the synthesis and spectral characterization of solid nanophosphors with dopant ion : Y_2O_3 molar ratios of 0.02 : 1 and 0.2 : 1, which exhibit bright red (Eu^{+++}) and green (Tb^{+++}) luminescence by visual examination in UV light. These powders were then suspended as well in organic solvents as in aqueous solution. For dispersion in organic solvents the powders were fragmented to nanoparticles under the presence of both, Trioctyl phosphine oxide (TOPO) and oleic acid / dioctyl ether, to give clear and stable suspensions in chloroform. These particle suspensions show the characteristic bright color (under UV irradiation) and emission spectra of the dopant ions. Transmission electron micrograph (TEM) studies show single particles along with agglomerates. In a further step these hydrophobically capped particles might be modified with an amphiphilic polymer in order to transfer them into aqueous solution [5]. In an alternative route the powders were also suspended in water by fragmenting them under the presence of dichloroacetic acid, whereby also their characteristic luminescence was retained.

2. Experimental details

2.1. General: Proton and ^{13}C NMR spectra were recorded with a GEOL –300 MHz spectrometer at B.H.U. Varanasi, India. X-ray diffraction pattern were recorded on a Seifert powder diffractometer using Cu-K_P X-rays. Photoluminescence (PL) spectra of the solid powders were recorded on an ocean optics system with range of 200nm to 1800nm by using an excitation wavelength of 440 nm. TEM images of nanostructures were taken on a transmission electron microscope (JEOL JEM-1011). The solution PL spectra were recorded on a Fuoromax-3 (JOBIN YVON HORIBA) spectrometer at the excitation wavelength 255nm. For performing sonication a BANDELIN sonicator (Sonorex Super RK 103H) was used. The solvents were dried and purified by standard procedures. Water was double distilled and deionized before being used.

2.2. Synthesis of $Y_5O(OPr^i)_{13}$ precursor: $Y_5O(OPr^i)_{13}$ was used as precursor in the sol-gel process for making the yttrium oxide particles. The manipulations pertaining to synthesis of $Y_5O(OPr^i)_{13}$ precursor were performed under dry argon atmosphere using Schlenck techniques as reported [26]. For this, yttrium chips (Aldrich) were refluxed with isopropanol in toluene in the presence of $Hg(OAc)_2$ catalyst (all Qualigens) to give a turbid solution which was filtered while hot. Upon cooling the hot solution the precursor was obtained in 73% yield. It was characterized by elemental analysis (Found (%) C 38.15, H 7.70: Calculated C 38.12, H 7.12) and NMR spectroscopy {^1H NMR in ppm, 1.29 (doublet), 4.30 (septet)} in dry $CDCl_3$ and was in accordance with reported values.

2.3. Synthesis of Eu^{+++} and Tb^{+++} doped Y_2O_3 powders: 8.0 g of $Y_5O(OPr^i)_{13}$ was dissolved in 30 ml toluene to give a clear solution which was kept in a bath at –70 ^0C. A mixture of 0.278 g $Eu(NO_3)_3 \cdot 5H_2O$ (for 0.02M doping), 0.582 g water and 30 ml.

isopropanol was added to it dropwise under stirring. For 0.2 M doping 2.78 g $Eu(NO_3)_3 \bullet 5H_2O$ was utilized. After the addition was complete the mixture was allowed to warm to room temperature resulting in a white gel. The gel was left for two days and then was dried in an oven at 100 ^{0}C to give a white powder. It was subjected to heat treatment and samples treated with 400 ^{0}C, 500 ^{0}C, 600 ^{0}C, 700 ^{0}C and 800 ^{0}C were made. Upon heating to different temperatures both (0.02M and 0.2M doped) of the europium doped materials did not show any discernable change in white color of the starting powder. A similar procedure was applied for Tb^{+++} doped powders for which 0.283 g of $Tb(NO_3)_3 \bullet 5H_2O$ was used for 0.02 M doping and 2.83 g for 0.2 M doping. In both cases the resulting gel was left for two days and was then warmed in an oven at 100 ^{0}C to give a white powder. 0.02 M Tb^{+++} doped Y_2O_3 powders also did not undergo any color change upon heat treatments in the range of 400 ^{0}C to 800 ^{0}C. In contrast to the 0.2 M Eu^{+++} doped the 0.2M Tb^{+++} doped Y_2O_3 powders exhibited different colors after annealing at different temperatures. The samples heated to 400 ^{0}C and 500 ^{0}C have dusky orange and gray sand colors while the powders heated to 600 ^{0}C, 700 ^{0}C and 800 ^{0}C exhibit light magenta ash appearance.

2.4. Dissolution of 0.2M Eu^{+++} / Tb^{+++} : 1M Y_2O_3 powders in chloroform or toluene under the presence of trioctylphosphine oxide (TOPO): The following general procedure was applied for preparing suspensions of all types of annealed powders. 100 mg of the particle powder were added to 5ml of chloroform in a vial and stirred for 30 minutes. To this suspension 1.0 g of TOPO (Sigma-Aldrich 98 %) was added and stirring was continued for two hours (stirring for higher duration led to no further changes). The so obtained suspension was centrifuged at 1500 rpm for 5 minutes and a white residue (64.5 mg) was set aside and the supernatant was collected in another vial. To purify the particles in this solution methanol was added until turbidity appeared and the mixture was centrifuged at 2000 rpm for 5 minutes. The particle-containing precipitate was collected and re- dissolved in chloroform (2ml) giving a clear solution, whereas the supernatant was discarded. The so obtained solution was centrifuged at 3000 rpm for 5 minutes to give a small amount of residue which was discarded and the supernatant solution was collected and used for further experiments (PL and TEM). Toluene may also be used in place of chloroform. However, in toluene the phosphorescence of the particles in UV light was more quenched than in chloroform.

2.5. Dissolution of 0.2M Eu^{+++} / Tb^{+++} : 1M Y_2O_3 powders in chloroform/toluene by oleic acid/dioctyl ether: The following general procedure was applied for preparing suspensions of all types of annealed powders. 100 mg of the powder was transferred in a three neck flask fitted with condenser and stirred in 5ml chloroform for 30 minutes. Then the chloroform was removed under low vacuum. 500 mg oleic acid and 3 ml dioctyl ether were injected separately under stirring and the mixture was heated to 200 ^{0}C for 2 hours while stirring, which resulted in a clear solution. The solution was cooled to 50 ^{0}C and 50 ml methanol was quickly added to give a turbid solution. This solution was centrifuged at 2000 rpm for 5 minutes and the supernatant was discarded. The particle containing precipitate was dissolved in 2 ml chloroform to give a clear solution. For removal of aggregated particles the solution was centrifuged at 3000 rpm for 5 minutes to give a very small residue at the bottom of the vial. The precipitate containing agglomerated was

discarded and the particle containing supernatant was used for all further experiments (PL and TEM).

2.6. Dissolution of 0.2M Eu^{+++} / Tb^{+++} : 1M Y_2O_3 powders in water by dichloroacetic acid: The following general procedure was applied for preparing suspensions of all types of annealed powders. 100 mg of the particle powder were added to 5ml of water in a vial and stirred for 30 minutes. To this suspension 200mg of dichlororoacetic acid (Sigma-Aldrich, 98 %) was added dropwise and within the next 20 minutes a turbid solution was obtained. This solution was centrifuged at 1500 rpm for 5 minutes and the residue with the undissolved particle powder was discarded. To the clear supernatant with suspended particles 60 ml isopropanol was added and the mixture was stirred for 30 minutes resulting in a turbid solution. The solution was centrifuged at 2000 rpm for 5 minutes and the supernatant was discarded. To the residue which contained the particles 5 ml water was added together with a drop of dichloroacetic acid to get a clear solution which was used for all further experiments (PL and TEM).

3. Results and Discussion

The sol-gel derived and 100 ^{0}C warmed europium and terbium doped (both in 0.02M and 0.2M concentrations) Y_2O_3 white powders were annealed to 400 ^{0}C, 500 ^{0}C, 600 ^{0}C, 700 ^{0}C and 800 ^{0}C for five hours to prepare in total twenty samples ((Eu / Tb) x (0.02M / 0.02M) x (400, 500, 600, 700, 800°C) = 2 x 2 x 5 = 20). All europium doped powders showed bright red and the terbium doped samples bright green luminescence under UV light excitation. We have very recently published the XRD patterns of 0.001M Eu^{+++} : 1M Y_2O_3 particle powders obtained via the sol-gel method which were heated in a range of 400 ^{0}C to 800 ^{0}C [26]. In the present work we found similar X-ray diffractograms for the powders that had been heat-treated in the range from 400^{0}C to 800 ^{0}C as well for europium as for terbium doping for both concentrations. The average sizes of the crystalline domains in the particle powder calculated from XRD with respect to the annealing temperature were 17 nm (400 ^{0}C), 24nm (500 ^{0}C), 42 nm (700 ^{0}C) and 45nm (800 ^{0}C).

The distribution of the Eu^{+++} ions within the host yttrium oxide matrix has been worked out by examination of the photoluminescence (PL) spectra, which are shown in Figure 1 for the 0.2M Eu^{+++} : 1M Y_2O_3 particle powders (for spectra of 0.02M Eu^{+++} : 1M Y_2O_3 powders see the Supporting Information). The most intense emission in the photoluminescence spectrum of Eu^{+++} is observed at about 580-595 nm ($^5D_0 \rightarrow {}^7F_1$), 610-625 nm ($^5D_0 \rightarrow {}^7F_2$), and 675-690 nm ($^5D_0 \rightarrow {}^7F_4$) [27]. In general the sharp emission lines point towards the occupation of europium ions in those crystallographic sites which are situated in the interior of the nanocrystal. It is well known that the intensity ratio of the $^5D_0 \rightarrow {}^7F_2$ and $^5D_0 \rightarrow {}^7F_1$ transitions is a good indicator of the symmetry of the environment around the rare earth ion. This feature is apparent (see the Supporting Information) in our 0.02M samples annealed at 400 ^{0}C and 500 ^{0}C, where the $^5D_0 \rightarrow {}^7F_2$ transitions are much more intense than the $^5D_0 \rightarrow {}^7F_1$ emissions. It is important to point out here that for 0.001M Eu^{+++} : 1MY_2O_3 powders annealed (up to 700 ^{0}C) under similar conditions the

$^5D_0 \rightarrow {}^7F_1$ transitions were found to be very intense and it was concluded that the dopant ions are occupying only the symmetrical sites in the interior of the particles [26]. However, in the data obtained in the present study we find that with higher concentrations the europium ions are more accommodated in unsymmetrical environments at the surface of the nanoparticles. This is not surprising because in particle powders with nanocrystalline domains it is highly probable that the atoms in the grain boundary region may get displaced from their lattice positions to new, non lattice equilibrium positions. The distribution of atoms in these non lattice positions may be fully disordered or have short range order. The PL spectrum of the 0.02M Eu^{+++} : 1M Y_2O_3 particle powder which has been heated to 400 ^{0}C shows a broad $^5D_0 \rightarrow {}^7F_2$ emission (612nm) with a shoulder centered at 625nm. The $^5D_0 \rightarrow {}^7F_4$ transition which is found around 697 nm is most intense in the spectrum of the powder heated to 600 ^{0}C, while it is completely absent in the 500 ^{0}C annealed sample (see Supporting Information).

The PL spectra of all the 0.2M Eu^{+++} : 1M Y_2O_3 (Figure 1a) particle powders prominently show the $^5D_0 \rightarrow {}^7F_2$ transition and are in many ways similar to spectra reported before [14,17,27], except for the absence of the peak at 697 nm corresponding to the $^5D_0 \rightarrow {}^7F_4$ emission. The $^5D_0 \rightarrow {}^7F_4$ emission seems to be weakly present in the spectrum of the 0.2M doped Eu^{+++} / 1M Y_2O_3 particle powder that had been heated to 400 ^{0}C. The PL spectrum of the 0.2M Eu^{+++} : 1M Y_2O_3 particle powder that had been heated to 800 ^{0}C turns out to be completely different to the corresponding spectra of the 0.001 M [26] and 0.02 M doped particle powders (see Supporting Information). It clearly shows the $^5D_0 \rightarrow {}^7F_2$ peak (Figure 1a) accompanied with a tiny $^5D_0 \rightarrow {}^7F_1$ transition indicating the presence of Eu^{+++} ions in unsymmetrical sites. Therefore, it seems that for fairly high (i.e. 0.2 M) doping concentration enough europium ions are still present in unsymmetrical environments and/or at the surface of the nanocrystalline domains, even at 800 ^{0}C, to show their characteristic spectrum.

A TEM image of untreated 0.2 M Eu^{+++} : 1M Y_2O_3 particle powder is shown in Figure 1a which exhibits tremendous agglomeration of the particles. Therefore in the next step the particle powders were fractionated with the aim to obtain colloidal particles suspended in solution. Since these oxide particle powders are in first place insoluble as well in organic solvents as in aqueous medium, dispersion had to be provided by an appropriated surfactant on the particle surface. For suspending the particle powders in organic solvents such as chloroform and toluene we tested several pathways which included heating and stirring the particle powder under the presence of oleic acid in dioctyl ether, and stirring the particle powder in chloroform or toluene under the presence of trioctyl phosphine (TOP), trioctyl phosphine oxide (TOPO), aminohexanoic acid, octylamine, or decylamine. We found that treatment of the particle powders with trioctyl phosphine oxide (TOPO) and oleic acid in dioctyl ether to give best suspension of the particles in toluene and chloroform. Dispersion in TOPO was found to be the most promising method as it could be performed at ambient temperature and did not require heating as was the case with oleic acid in dioctly ether. TOPO and oleic acid molecules presumably stick with their polar headgroups to the oxide particle surface so that their hydrophobic tails point towards the solvent and thus provide repulsion and thus colloidal stability of the particles in organic solvents. The TOPO coated particles were found to yield clear

suspensions in both chloroform and toluene. However, in toluene the red luminescence of the phosphors under UV irradiation was quenched significantly, whereas in chloroform very bright phosphorescence was observed. Therefore, all further spectroscopic analysis of hydrophobic particles was performed in chloroform.

Figure 1b shows the PL spectra of TOPO coated 0.2M Eu^{+++} : 1M Y_2O_3 particles (of particle powders that had been annealed to 400 ^{0}C - 800 ^{0}C) suspended in $CHCl_3$. For all suspensions, in the PL spectrum the intensity ratio of the $^5D_0 \rightarrow {}^7F_2$ and $^5D_0 \rightarrow {}^7F_1$ transitions clearly confirms the occupation of unsymmetrical sites by the dopant ions within the Y_2O_3 matrix as also seen in the corresponding solid particles powders (cfg. Figure 1a). This confirms that fragmentation of the solid particle powders to colloidal TOPO capped particles suspended in chloroform retains the basic photoluminescence properties of europium doped particles. However, unlike the spectra of the corresponding solid particle powder (Figure 1a) for the colloidal particles made out of the powder and that had been annealed at 400 ^{0}C the $^5D_0 \rightarrow {}^7F_4$ peak is absent in solution (Figure 1b).

A TEM image of TOPO coated 0.2 M Eu^{+++} : 1M Y_2O_3 particles made out of a particle powder that had been annealed to 400 ^{0}C is shown in Figure 1b. Although the particles are relatively well dispersed and have a fair size distribution, some aggregates can also be seen that comprise several small particles. The average diameter of the particles seen in the TEM is clearly bigger than the average diameter of 17nm obtained with XRD for the crystalline domains for the particle powder. This suggests that the fragmentation procedure of the particle powder to colloidal particles under the presence of TOPO is not sufficient to break up all agglomerates present in the particle powder to primary single particles. However, in comparison to the uncoated powders (Figure 1a) significant fragmentation has taken place. We also performed sonification of the particle powder in the TOPO / chloroform mixture during the fragmentation process to further reduce the average size of the particles. However, we were never able to completely remove the particle aggregates. TEM examination of TOPO coated particles suspended in chloroform that had been made out of particle powders annealed at 500 ^{0}C -800 ^{0}C also clearly revealed larger agglomerates together with separated single particles (see Supporting Information). Similar observations were also found with other surfactants in the present work. Although for all these particles sonification helped to reduce the size of the aggregates no discernable change in the solution PL spectra was observed for all the three surfactants.

We also employed oleic acid in presence of dioctyl ether to disperse suspend particles in chloroform. The PL spectra of these transparent suspensions are shown in Figure 1c, whereby the characteristic europium peaks similar to the ones shown in Figure 1b are visible. Furthermore, the TEM images of particles obtained from the particle powder which had been heated to 400 ^{0}C heated powders are similar to the ones obtained for TOPO coated particles. This indicates that both TOPO and oleic acid / dioctyl ether are working similarly in regard to the fragmentation capability whereby the TOPO coating has the advantage that it can be performend at ambient temperature.

Alternatively the surface of the nanophosphor particle powders was etched with dichloroacetic acid to suspend them in aqueous solution. This fragmentation was significantly faster than the one reported above in chloroform under the presence of TOPO or oleic acid / dioctyl ether. Although water is reported to significantly quench the europium emission [27] we found that the clear aqueous suspensions of the particles showed red phosphorescence under UV light excitation. The chloroacetic acids might act similar to aminohexanoic acid [7] where chlorine atoms with lone pair are directed towards the surface of the nanoparticles while the hydrophilic carboxylic groups are pointing outside. The PL spectra for aqueous suspensions of particles from powders which before had been annealed at 400^0C - 800^0C is shown in Figure 1d. Similar to the above discussion the characteristic peaks of Eu^{+++} are clearly visible. As can be seen from the corresponding TEM image in Figure 1d the fragmentation of the particle powders with di-chloroacetic acid results in many particle aggregates. Compared to suspension in chloroform (Figures 1b and 1c) particles suspended in water showed more and larger aggregates. This also can be seen in the scattering at low wavelengths for the PL spectra of the particle solutions (Figure 1d).

Doping of yttrium oxide with Tb^{+++} ions leads to green phosphors. Terbium related spectra are characterized by a series of $^5D_3 \rightarrow {}^7F_n$ transitions wherein for n = 0, 1, 2, 3, 4, 5, and 6 the corresponding peaks are observed at 486nm, 481nm, 470nm, 456nm, 436nm, 414nm and 381nm. Besides these, $^5D_4 \rightarrow {}^7F_5$ (~ 544 nm), $^5D_4 \rightarrow {}^7F_4$ (~ 585 nm), and $^5D_4 \rightarrow {}^7F_3$ (~ 620 nm) transitions are also characteristic of terbium ions. In general, the preparation conditions including the nature of the host metal oxide matrix, concentration of terbium ions, thermal synthesis conditions and the conditioning regime are factors that influence photoluminescence characteristics of Tb^{+++} incorporated Y_2O_3 phosphor [20,21,22]. Furthermore, distinct differences in the optical behavior of the bulk and nanoparticles for the same material have also been observed. For example, the excitation spectra of the nanophosphors were systematically found to be blue-shifted relative to bulk spectra [20]. Tb^{+++} transitions for a 0.02 M doping concentration within the Y_2O_3 matrix for particle powders heated at different temperatures ranging from 400 ^{0}C to 800 ^{0}C are given in the Supporting Information. Evidently, in all the samples the $^5D_3 \rightarrow {}^7F_n$ transitions with n = 2 to 6 overlap which results in a very broad spectrum in the corresponding region which indicates simultaneous emission from sites with different crystal field splitting [28]. However, the particle powders annealed at 700 ^{0}C, and 800 ^{0}C clearly show the $^5D_3 \rightarrow {}^7F_0$ (486nm), $^5D_3 \rightarrow {}^7F_1$ (481nm) and $^5D_4 \rightarrow {}^7F_6$ (490nm) peaks which are characteristic of doped terbium ions. In comparison, the spectra of 0.2 M Tb^{+++} : 1M Y_2O_3 powders (Figure 2a) are more intense but unlike for the 0.02M doped samples (700 ^{0}C, and 800 ^{0}C heated) the $^5D_3 \rightarrow {}^7F_{0,1}$ and $^5D_4 \rightarrow {}^7F_6$ transitions are merged to give a broad feature in the spectra.

As with the 0.2M Eu^{+++} : 1M Y_2O_3 red phosphors we also fragmented the 0.2M Tb^{+++} : 1M Y_2O_3 green phosphor particle powders, as due to sintering they are in highly agglomerated state (Figure 2b). Suspension in chloroform under the presence of TOPO yielded transparent light green solutions. Under UV excitation these solutions were found to give green luminescence. The PL spectra of the suspensions of TOPO coated green phosphors are shown in Figure 2b. Notably in all spectra a prominent peak is visible at around 348 nm which may be attributed to the $^5D_3 \rightarrow {}^7F_6$ transition. Generally for particle

powders in solid state this peak is found at 381nm [20], but it appears that in the presence of surfactant (in solution) it has shifted. However, the visibility of the $^5D_3 \rightarrow {}^7F_5$ (414 nm) and $^5D_3 \rightarrow {}^7F_4$ (436nm) transitions in 700 ^{0}C and 800 ^{0}C annealed samples confirms the presence of terbium ions in the host oxide matrix [20, 21]. The TEM image (Figure 2b) of a grid made by placing a drop of the particle suspension in chloroform (derive from the particle powder that had been heated to 400 ^{0}C) is almost similar to the corresponding europium doped sample (Figure 1b). The presence of a small fraction of aggregates further confirms the above discussed limitation of TOPO with regard to fragmentation capability in the given set of experimental conditions.

0.2M Tb^{+++} doped 1M Y_2O_3 particle powders were also fragmented in chloroform by coating with oleic acid/dioctyl ether. They were also found to be luminescent at UV light excitation. Their solution PL spectra are shown in Figure 2c. Evidently here also a peak is present around 348 nm, which as mentioned above, may be due to the $^5D_3 \rightarrow {}^7F_6$ transition. This is also accompanied with some other aforementioned transitions. TEM pictures (Figure 2c) of the corresponding particles coated with oleic acid/dioctyl ether were again found to be fairly similar to the corresponding red phosphors as shown in Figure 1c. Also for Tb^{+++} doping dispersed particles together with some aggregates were found to be present.

Finally, the PL spectra of aqueous suspensions of dichloroacetic acid capped 0.2M Tb^{+++} / 1M Y_2O_3 particles were recorded (Figure 2d). Each had a peak at 348 nm, which may be assigned to the $^5D_3 \rightarrow {}^7F_6$ transition, along with the other usual peaks as shown in Figures 2b and 2c. Similar to the corresponding red phosphors agglomeration of the particles can be seen in the scattering in the PL spectra. Furthermore, as the red phosphors, fragmentation in aqueous solution results in a higher number and also in bigger particle aggregates than fragmentation in chloroform, as is evident from the TEM images.

Therefore, in the present investigation we find that both, TOPO and oleic acid/di-octyl ether are capable of fragmenting and suspending the sol-gel derived and annealed doped yttrium oxide particles in organic solvents, whereas chloroacetic acids can suspend them in water yielding transparent suspensions that are stable for months at ambient temperature. In terms of the particle size distributions the performance of both TOPO and oleic acid/di-octyl ether is about similar. The advantage of using TOPO is that it does not require high temperature reaction conditions. In comparison, although di-chloroacetic acid could not provide single primary particles, it leads to well conserved PL characteristics of the dopant ions which are known to be quenched in the presence of hydroxyl groups.

4. Conclusions

The sol-gel process is an efficient way to dope rare earth ions into nano dimensional yttrium oxide. For Eu^{+++} doping with 0.02 M and 0.2 M doping concentration the europium ions are preferentially residing in unsymmetrical sites in the Y_2O_3 matrix for particle powders annealed in the range of 400 ^{0}C to 800 ^{0}C which are red phosphors. For

Tb^{+++} doping with 0.02 M and 0.2 M doping concentration the terbium ions are also incorporated into the Y_2O_3 matrix and the particle powders annealed in the range of 400 ^{0}C to 800 ^{0}C are green phosphors. The phosphor particle powders have been fragmented and suspended in chloroform by coating their surface with either TOPO or oleic acid/dioctyl ether. These colloidal suspensions retain the characteristic PL spectra of the particle powders and exhibit luminescence upon UV excitation. TEM pictures reveal the presence of dispersed particles along with particle aggregates. In presence of dichloroacetic acid the particle powders can also be suspended in water. Again, their PL properties are conserved, though water is known to significantly quench Eu^{+++} spectra. However, in contrast to colloidal particles suspended in chloroform the particles suspended in aqueous medium exhibit many aggregates.

Acknowledgements

Anjana Pandey, Ashutosh Pandey and Wolfgang J Parak are thankful to DST New Delhi and DAAD Germany for funding support. The German partner also acknowledges funding from the European Union (STREP SA-Nano) and the Deutsche Forschungsgemeinschaft (Emmy Noether grant).

References

[1] R. N. Bhargava, D. Gallagher and T. Walker, Doped nanocrystals of semiconductors - a new class of luminescent materials, J. Luminescence 60 (1994) 275-280.

[2] J Hao, S A Studenikin and M Cocivera, Blue, green and red cathodoluminescence of Y_2O_3 phosphor films prepared by spray pyrolysis, J. Luminescence 93 (2001) 313-319.

[3] M Darbandi, W Hoheisel and T Nann, Silica coated, water dispersible and photoluminescent Y (V,P)O4:Eu^{3+},Bi^{3+} nanophosphors, Nanotechnology 17 (2006) 4168-4173.

[4] W. J Parak., T. Pellegrino and C. Planck, Labelling of cells with quantum dots Nanotechnology, 16 (2005) R9-R25

[5] T. Pellegrino, L.Manna, S.Kudera, T. Liedl, D.Koktysh, A. L.Rogach., S.Keller, J Rädler., G. Natile and W. J. Parak., Hydrophobic nanocrystals coated with an amphiphilic polymer shell: A general Route to water soluble nanocrystals, Nanoletters 4 (2004) 703-707.

[6] R J Palmer, J L Butenhoff and J B Stevens, Cytotoxicity of the rare earth metals cerium, lanthanum, and neodymium in vitro: Comparisons with cadmium in a pulmonary macrophage primary culture system, Environ. Res. 43 (1987). 142-156.

[7] F Meiser, C Cortez and F Caruso, Biofunctionalization of Fluorescent Rare-Earth-Doped Lanthanum Phosphate Colloidal Nanoparticles, Angew. Chem. Int. Ed 43 (2004). 5954-5957.

[8] F L Shuang, R Riehn, W S Ryu, N Khanarian, C K Tung, D Tank, and R H Austin, In vivo and scanning electron microscopy imaging of upconverting nanophosphors in caenorhabditis elegans Nano letters 6 (2006) 169-174.

[9] Wet-Chemical Synthesis of Doped Colloidal Nanomaterials: Particles and Fibers of LaPO4:Eu, LaPO4:Ce, and LaPO4:Ce,Tb, H Meyssamy, R Riwotzki, A Kornowski, S Naused and M Haase, Adv. Mater 11(1999). 840-844.

[10] F Wang, F Xianping M Wang and Y Zhang, Multicolour PEI/NaGdF4:Ce3+,Ln3+ nanocrystals by single-wavelength excitation, Nanotechnology 17(5) (2006) 1527-1532.

[11] M Danek, K F Jensen, C B Murray and MG Bawendi, Synthesis of Luminescent Thin-Film CdSe/ZnSe Quantum Dot Composites Using CdSe Quantum Dots Passivated with an Overlayer of ZnSe, Chem Mater 8 (1996) 173-180.

[12] E T Goldbert, B Kulkarni, R N Bhargava, J Taylor and M Libera, Size dependent efficiency in Tb doped Y_2O_3 nanocrystalline phosphor, J. Luminisence 72-74 (1997), 190-192.

[13] B M Tissue, Synthesis and Luminescence of Lanthanide Ions in Nanoscale Insulating Hosts, Chem Mater10 (1998) 2837-2845.

[14] J A Nelson, E L Brant and M J Wagner, Nanocrystalline Y_2O_3:Eu Phosphors Prepared by Alkalide Reduction, Chem Mater15 (2003) 688-693.

[15] K Devlin, O Kelly, Z R Tang, C McDonagh and J F McGilp, A structural study of the sol-gel process by optical fluorescence and decay time spectroscopy J. Noncrystalline solids 135 (1991) 8-14.

[16] P K Sharma, MH Jilavi, R Nass and H Schmidt , Tailoring the particle size from μm→nm scale by using a surface modifier and their size effect on the fluorescence properties of europium doped yttria, J Lumin. 82 (1999).187-193.

[17] T Hirai, T Hirano and I Komasawa , Preparation of Y_2O_3 Eu^{3+} phosphor fine particles using an emulsion liquid membrane system , J. Mater. Chem .10 (2000) 2306-2310.

.[18]X Lingling, B Wei, Z Zhang, L Zhe, G Hong and Y Zhang, Synthesis and luminescence of europium doped yttria nanophosphors via a sucrose-templated combustion method, Nanotechnology 17 (2006) 4327-4331.

[19] O L Hersh and N Herbert, Concentration dependence curves of cathodoluminescence of Y_2O_2S:Tb Applied Physics Letters 28 (1976) 727-729.

[20] L G Jacobsohn, B L Bennett, R E Muenchausen, J F Smith, DW Cooke, Optical structural characterization of nanostructured Y_2O_3:Tb, Proceedings of SPIE on Nanophotonic Materials III, Edited by Gaburro, Zeno; Cabrini, Stefano, 6321 (2006) 63210-63213.

[21] N Hiromitsu and M Toshiyuki, Correlation between Y_2O_3 concentration and photoluminescence excitation spectra of Tb3+ impurity in Y_2O_3-stabilized ZrO2, Journal of Applied Physics 97 (2005) 023503-023506.

[22] J Weiyi, W Yanyun, F Fernandez, X Wang, S Huang and W M Yen, Photoluminescence of Ce^{3+},Tb^{3+}: Y_2O_3 nanoclusters embedded in SiO_2 sol-gel glasses, Materials Science and Engineering C 16 (1-2) (2001) 55-58.

[23] M A F Gonzalez, G Ledoux, S Roux, K Lebbou, P Perriat and O Tillement, Preparing nanometer scaled Tb-doped Y_2O_3 luminescent powders by the polyol method, Journal of Solid State Chemistry, 178(4) (2005) 989-997.

[24] L . Mursean, E J Popovici, A Hristea, E Indrea and M Vasilescu, Spectral investigation on terbium activated yttrium oxysulphide phorphors, SPIE ROMOPTO Seventh Conference on Optics, 775 (2003) 5581-5584.

[25] G. Buhler and C. Feldmann, Microwave-Assisted Synthesis of Luminescent $LaPO_4$:Ce,Tb Nanocrystals in Ionic Liquids, Angew. Chem. Int. Ed. 45 (2006) 4864 –4867

[26] A Pandey, A Pandey, M K Roy and H C Verma, Sol–gel synthesis and characterization of Eu^{+++}/Y_2O_3 nanophosphors by an alkoxide precursor, Mat. Chem. Phy 96 (2006). 466-470.

[27] F Paraspour, D F Kelley and R S Williams, Spectroscopy of Eu^{3+}-Doped PtS_2 Nanoclusters, J. Phys. Chem B 102 (1998) 7971-7977.

[28] K Kömpe, O Lehmann and M Haase, Spectroscopic Distinction of Surface and Volume Ions in Cerium(III)- and Terbium(III)-Containing Core and Core/Shell Nanoparticles, Chem Mater 18 (2006) 4442-4446.

[29] K Kömpe, H Borchert, J Storz, A Lobo, S Adams, T Möller and M Haase, Green-Emitting CePO4:Tb/LaPO4 Core-Shell Nanoparticles with 70 % Photoluminescence Quantum Yield Angew. Chem. Int. Ed. 42 (2003) 5513-5516.

Figures

Figure 1: a**)** Photoluminescence spectra of 0.2 M europium doped Y_2O_3 particle powders that had been annealed at temperatures ranging from 400 ^{0}C to 800^{0}C at 440 nm excitation wavelength and a corresponding TEM image of the particle powder (for the particles annealed at 400^{0}C). b) Photoluminescence spectra of solutions with TOPO coated colloidal 0.2M Eu^{+++} / Y_2O_3 nanoparticles in $CHCl_3$ at 250 nm excitation wavelength. Before transferring the particles from the powder to solution they had been annealed in the powder state at temperatures ranging from 400 ^{0}C to 800 ^{0}C. The TEM image corresponds to TOPO coated particles from the particle powder that had been annealed at 400^{0}C. c) Photoluminescence spectra of solutions with oleic acid/di-octyl ether coated colloidal 0.2M Eu^{+++} / Y_2O_3 nanoparticles in $CHCl_3$ at 250 nm excitation wavelength. Before transferring the particles from the powder to solution they had been annealed in the powder state at temperatures ranging from 400 ^{0}C to 800 ^{0}C. The TEM image corresponds to oleic acid/di-octyl ether coated particles from the particle powder that had been annealed at 400^{0}C. d) Photoluminescence spectra of solutions with di-chloro acetic acid coated colloidal 0.2M Eu^{+++} / Y_2O_3 nanoparticles in H_2O at 250 nm excitation wavelength. Before transferring the particles from the powder to solution they had been annealed in the powder state at temperatures ranging from 400 ^{0}C to 800 ^{0}C. The TEM image corresponds to di-chloro acetic acid coated particles from the particle powder that had been annealed at 400^{0}C.

Figure 2: a**)** Photoluminescence spectra of 0.2 M terium doped Y_2O_3 particle powders that had been annealed at temperatures ranging from 400 ^{0}C to 800^{0}C at 440 nm excitation wavelength and a corresponding TEM image of the particle powder (for the particles annealed at 400^{0}C). b) Photoluminescence spectra of solutions with TOPO coated colloidal 0.2M Tb^{+++} / Y_2O_3 nanoparticles in $CHCl_3$ at 250 nm excitation wavelength. Before transferring the particles from the powder to solution they had been annealed in the powder state at temperatures ranging from 400 ^{0}C to 800 ^{0}C. The TEM image corresponds to TOPO coated particles from the particle powder that had been annealed at 400^{0}C. c) Photoluminescence spectra of solutions with oleic acid/di-octyl ether coated colloidal 0.2M Tb^{+++} / Y_2O_3 nanoparticles in $CHCl_3$ at 250 nm excitation wavelength. Before transferring the particles from the powder to solution they had been annealed in the powder state at temperatures ranging from 400 ^{0}C to 800 ^{0}C. The TEM image corresponds to oleic acid/di-octyl ether coated particles from the particle powder that had been annealed at 400^{0}C. d) Photoluminescence spectra of solutions with di-chloro acetic acid coated colloidal 0.2M Tb^{+++} / Y_2O_3 nanoparticles in H_2O at 250 nm excitation wavelength. Before transferring the particles from the powder to solution they had been annealed in the powder state at temperatures ranging from 400 ^{0}C to 800 ^{0}C. The TEM image corresponds to di-chloro acetic acid coated particles from the particle powder that had been annealed at 400^{0}C.

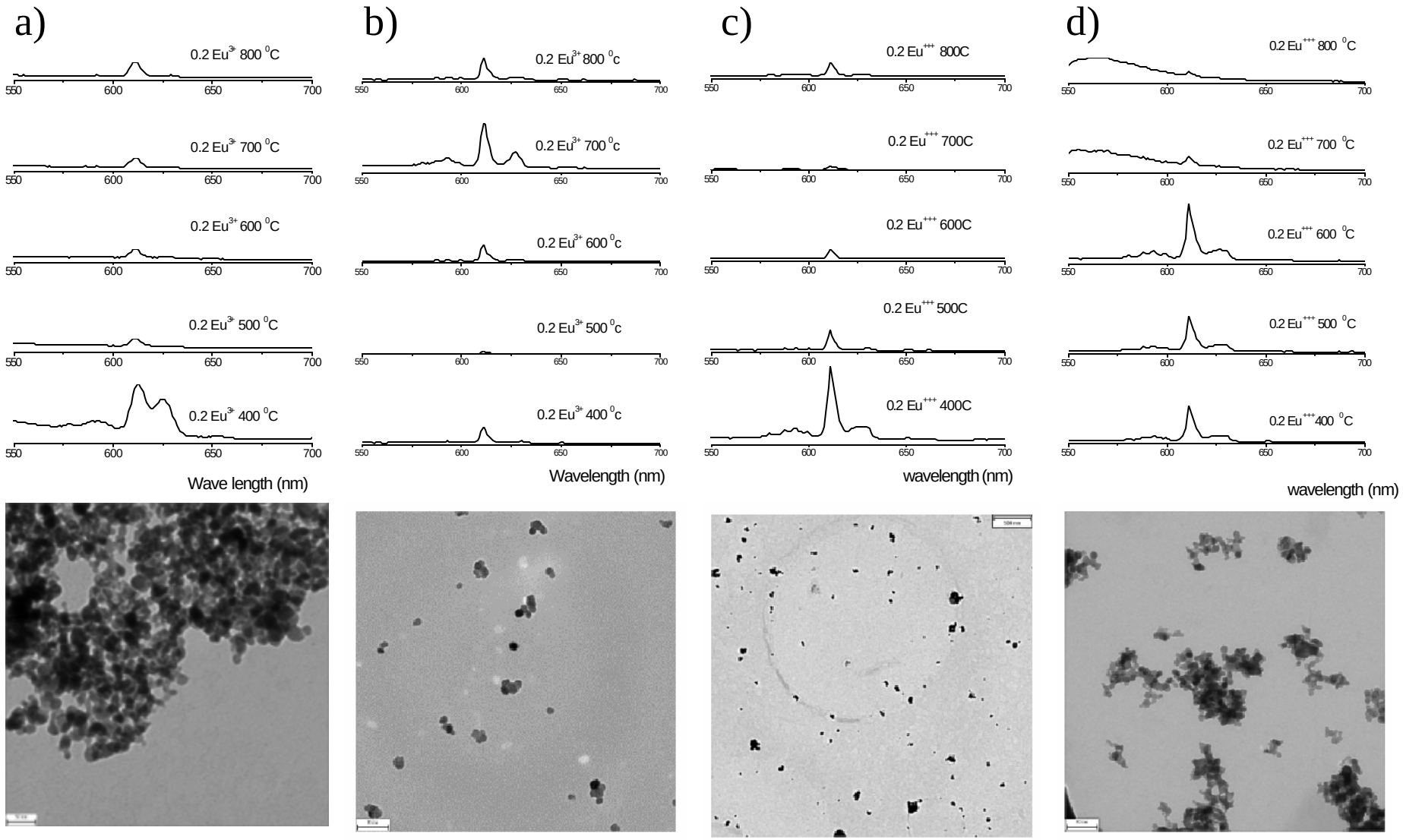
a)
b)
c)
d)
Counts
0.2 Eu3+ 800 0C
0.2 Eu3+ 700 0C
0.2 Eu3+ 600 0C
0.2 Eu3+ 500 0C
0.2 Eu3+ 400 0C
0.2 Eu3+ 800 0c
0.2 Eu3+ 700 0c
0.2 Eu3+ 600 0c
0.2 Eu3+ 500 0c
0.2 Eu3+ 400 0c
0.2 Eu+++ 800C
0.2 Eu+++ 700C
0.2 Eu+++ 600C
0.2 Eu+++ 500C
0.2 Eu+++ 400C
0.2 Eu+++ 800 0C
0.2 Eu+++ 700 0C
0.2 Eu+++ 600 0C
0.2 Eu+++ 500 0C
0.2 Eu+++400 0C
550
600
650
700
Wave length (nm)
Wavelength (nm)
wavelength (nm)
wavelength (nm)

Figure 1

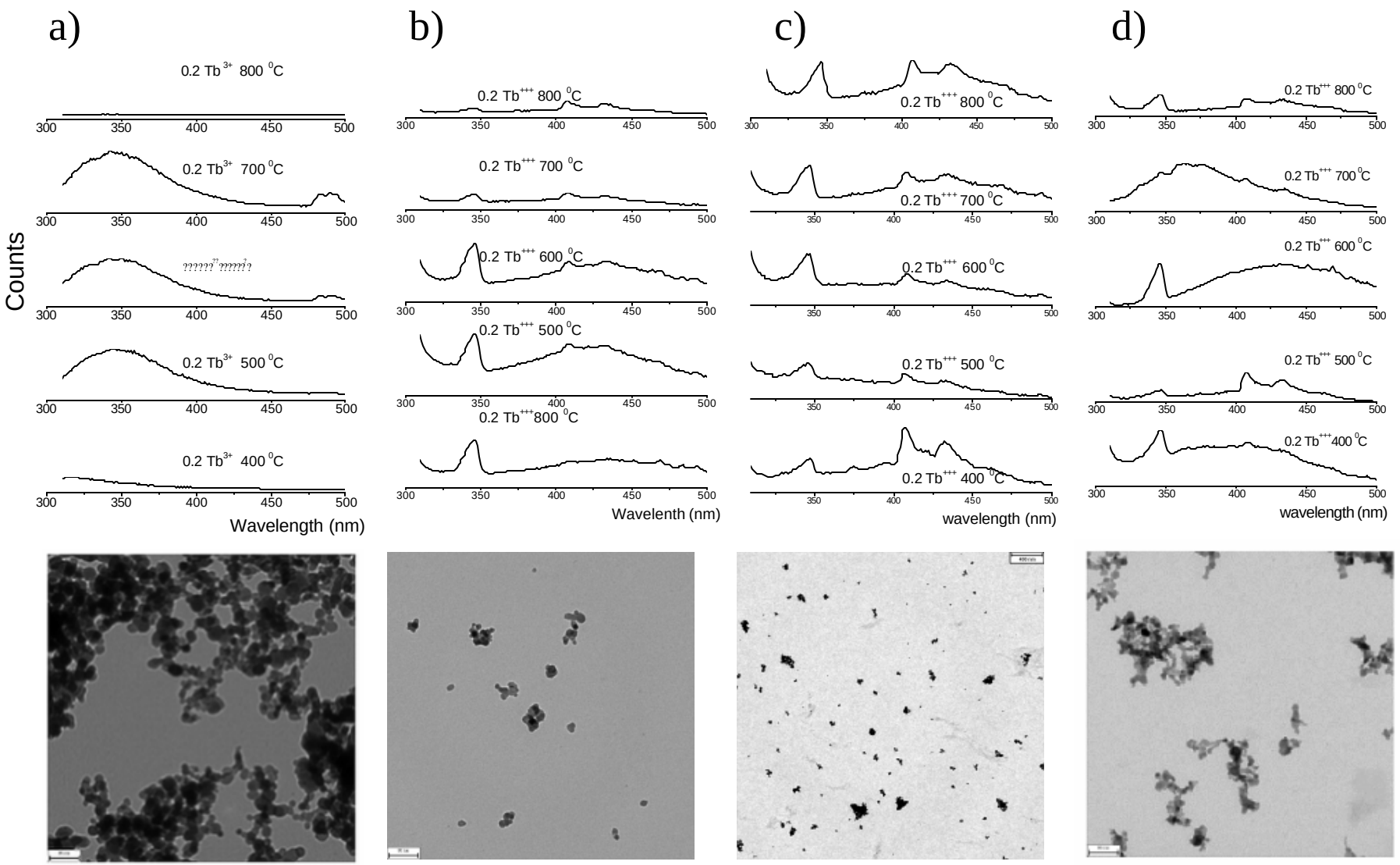
a)
b)
c)
d)
Counts
0.2 Tb 3+ 800 0C
0.2 Tb 3+ 700 0C
??????? ??????
0.2 Tb 3+ 500 0C
0.2 Tb 3+ 400 0C
Wavelength (nm)
0.2 Tb+++ 800 0C
0.2 Tb+++ 700 0C
0.2 Tb+++ 600 0C
0.2 Tb+++ 500 0C
0.2 Tb+++800 0C
Wavelenth (nm)
0.2 Tb+++ 800 0C
0.2 Tb+++ 700 0C
0.2 Tb+++ 600 0C
0.2 Tb+++ 500 0C
0.2 Tb+++ 400 0C
wavelength (nm)
0.2 Tb+++ 800 0C
0.2 Tb+++ 700 0C
0.2 Tb+++ 600 0C
0.2 Tb+++ 500 0C
0.2 Tb+++400 0C
wavelength (nm)

Figure 2

Chloroform- and water-soluble sol-gel derived Eu^{+++}/Y_2O_3 (red) and Tb^{+++}/Y_2O_3 (green) nanophosphors: synthesis, characterization and surface modification

Ashutosh Pandey[1*], M. K. Roy[2], Anjana Pandey[3], Marco Zanella[4], Ralph A. Sperling[4], W. J. Parak[4] , A. B. Samaddar[1] and H. C. Verma[2]

[1]Department of Chemistry; MNNIT Allahabad, INDIA
[2] Department of Physics; IIT Kanpur, INDIA
[3]Nanotechnology and Molecular Biology Laboratory, Center of Biotechnology, University of Allahabad, INDIA
[4] Center for Nanoscience, Ludwig Maximilians University of Munich, GERMANY and Fachbereich Physik, Phillips University Marburg, GERMANY
* Corresponding Author, e.mail: apandey70@yahoo.com

SUPPORTING INFORMATION

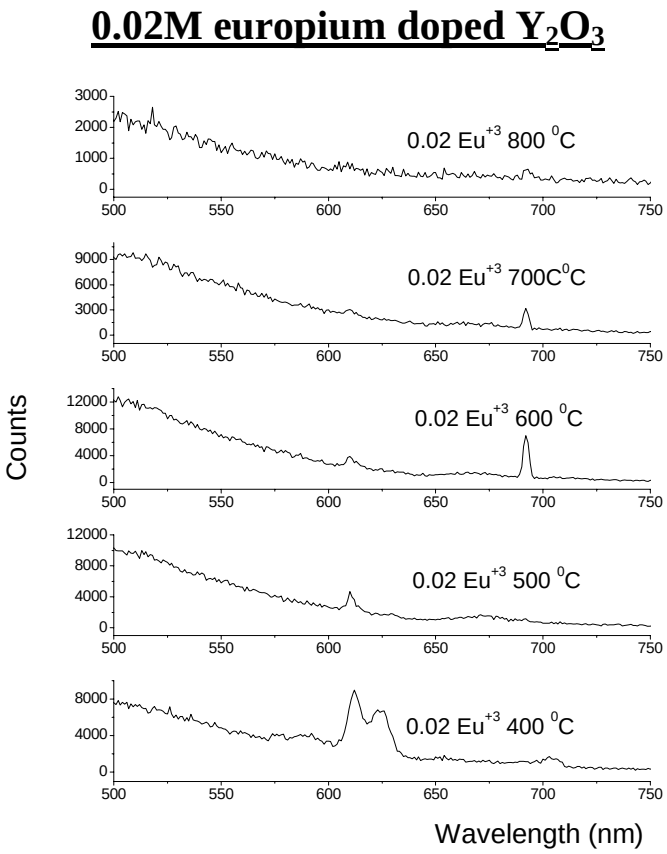

Figure 1: Photoluminescence spectra of 0.02M europium doped Y_2O_3 particle powders annealed from 400 ^{0}C to 800^{0}C at 440nm excitation.

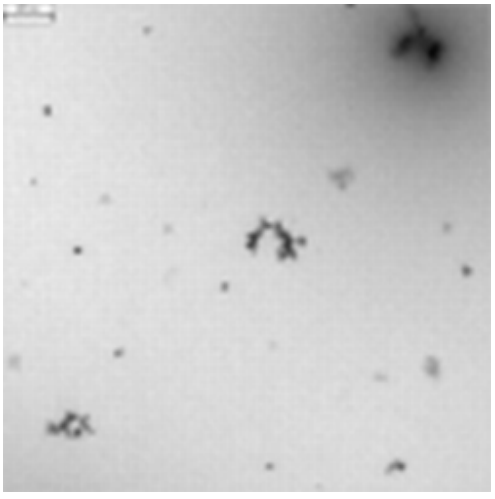

Figure 2: Transmission electron micrograph image of 0.2M Eu^{+++} doped Y_2O_3 particles annealed to 400 ^{0}C and sonicated before capping with TOPO. The scale bar corresponds to 480nm.

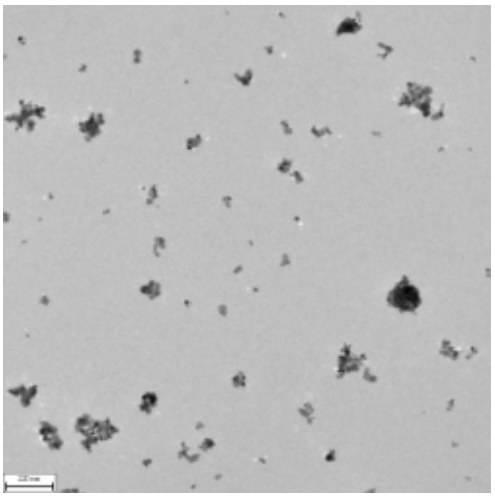

Figure 3: Transmission electron micrograph image of 0.2M Eu^{+++} dopedY_2O_3 particles annealed to 600 ^{0}C capped with TOPO. The scale bar corresponds to 220nm.

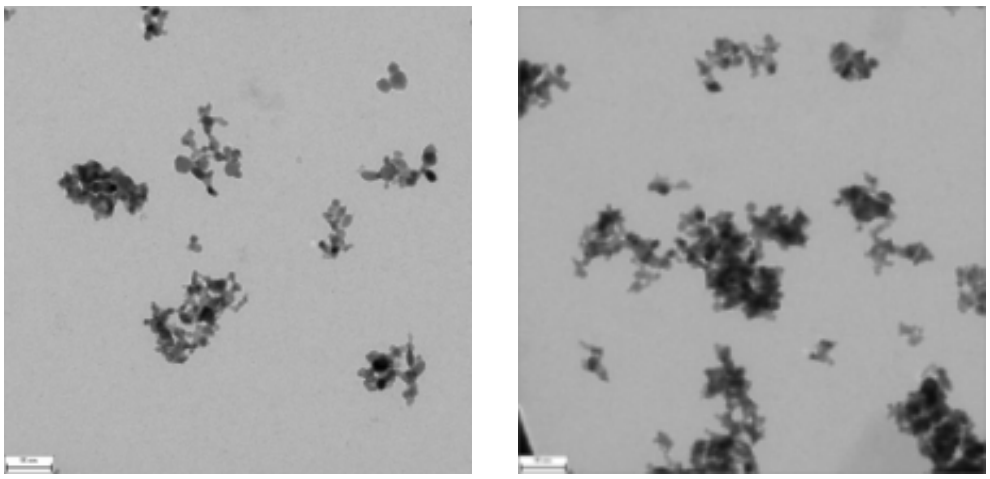

Figure 4: Transmission electron micrograph images of 0.2M Eu^{+++} doped Y_2O_3 particles annealed to 600 ^{0}C (on the left) and 800 ^{0}C (on the right) capped with DCA. The scale bars correspond to 90nm.

0.02M terbium doped Y_2O_3

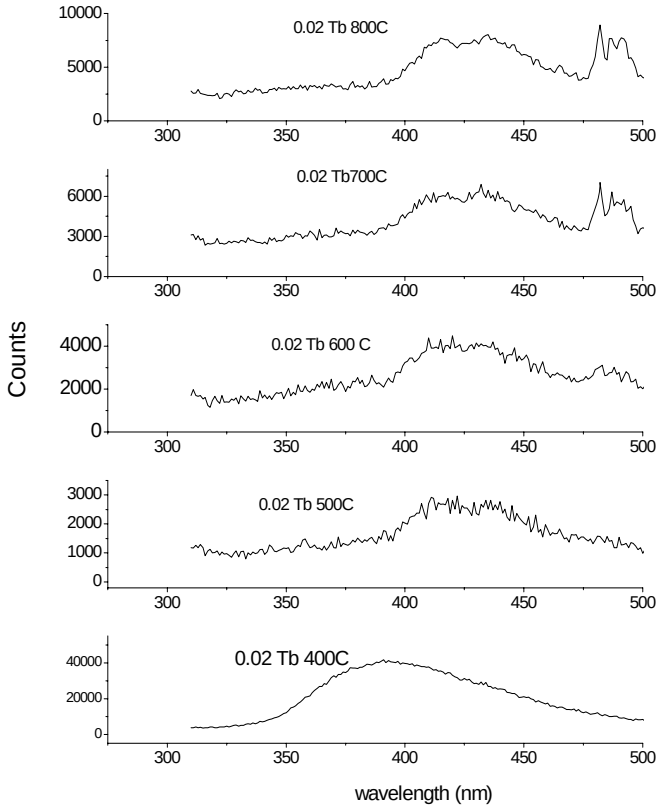

Figure 5: Photoluminescence spectra of 0.02M terbium doped Y_2O_3 particle powder annealed from 400 ^{0}C to 800^{0}C at 440nm excitation.

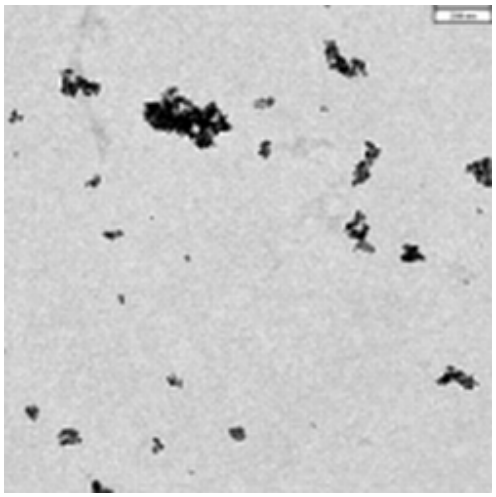

Figure 6: Transmission electron micrograph image of 0.2M Tb^{+++} doped Y_2O_3 particles annealed to 500 ^{0}C capped with oleic acid/di-octyl ether. The scale bar corresponds to 200nm.

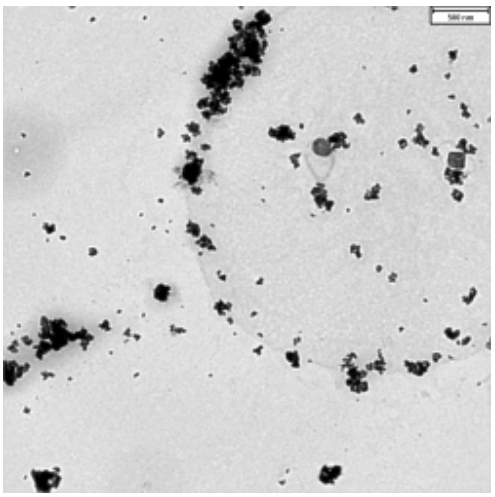

Figure 7: Transmission electron micrograph image of 0.2M Tb^{+++} dopedY_2O_3 particles annealed to 800 ^{0}C capped with oleic acid/di-octyl ether. The scale bar corresponds to 500nm.

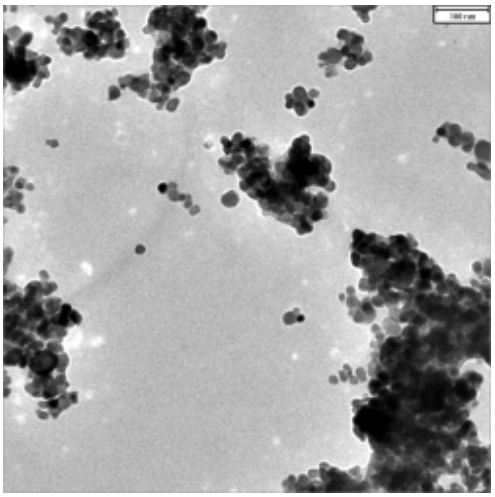

Figure 8: Transmission electron micrograph image of 0.2M Tb^{+++} dopedY_2O_3 particles annealed to 800 ^{0}C capped with DCA. The scale bar corresponds to 100nm.

Photoelectrochemical signal chain sensitive to superoxide radicals in solution

Ch. Stoll1, C. Gehring1#, M. Zanella2, W. J. Parak2, F. Lisdat*1

1 Biosystems Technology, Wildau University of Applied Sciences, 15745 Wildau, Germany,
2 Department of Physics, Philipps University Marburg, 35037 Marburg, Germany
*flisdat@igw.tfh-wildau.de, phone +49(0)3375508799, fax +49(0)3375508578
This article is dedicated to Claas Gehring who passed away during his engaged work on this project.

Abstract:
A photoelectrochemical signal chain sensitive to the presence of superoxide radicals was developed on the basis of CdSe/ZnS quantum dots which were immobilised on gold electrodes using a dithiol compound. The conditions of photo current generation under illumination have been characterized with respect to the dependence on the applied electrode potential, the wavelength of the light beam and the stability of the measurement.
Because of photoexcitation electron-hole pair generation is enforced enhancing the conductivity of the quantum dot layer. This was independently verified by impedance measurements.
In order to observe direct electron transfer with the redox protein cytochrome c different surface modifications of the quant um dots were investigated – mercaptopropionic acid, mercaptosuccinic acid and mercaptopyridine. Varying superoxide concentrations in solution can be detected by an enhanced conversion of superoxide-reduced cytochrome c and thus by an enhanced photo current at the quantum dot modified electrode. The electrode was found to be sensitive to higher nanomolar concentrations of the radical.

Photoelectrochemical signal chain sensitive to superoxide radicals in solution

Ch. Stoll[1], C. Gehring[1#], M. Zanella[2], W. J. Parak[2], F. Lisdat*[1]

[1] Biosystems Technology, Wildau University of Applied Sciences, 15745 Wildau, Germany,

[2] Department of Physics, Philipps University Marburg, 35037 Marburg, Germany

*flisdat@igw.tfh-wildau.de, phone +49(0)3375508799, fax +49(0)3375508578

This article is dedicated to Claas Gehring who passed away during his engaged work on this project.

Abstract

A photoelectrochemical signal chain sensitive to the presence of superoxide radicals was developed on the basis of CdSe/ZnS quantum dots which were immobilised on gold electrodes using a dithiol compound. The conditions of photo current generation under illumination have been characterized with respect to the dependence on the applied electrode potential, the wavelength of the light beam and the stability of the measurement. Because of photoexcitation electron-hole pair generation is enforced enhancing the conductivity of the quantum dot layer. This was independently verified by impedance measurements.

In order to observe direct electron transfer with the redox protein cytochrome c different surface modifications of the quantum dots were investigated – mercaptopropionic acid, mercaptosuccinic acid and mercaptopyridine. Varying superoxide concentrations in solution can be detected by an enhanced conversion of superoxide-reduced cytochrome c and thus by an enhanced photo current at the quantum dot modified electrode. The electrode was found to be sensitive to higher nanomolar concentrations of the radical.

Key words: nanoparticles, CdSe/ZnS, cytochrome c, superoxide, photoexcitation, gold electrode

1. Introduction

The incorporation of nanoparticles in analytical detection systems or sensors is an actual and intensively investigated area (Lin et al. 2007). Besides metal nanoparticles and carbon nanotubes, semiconductor nanoparticles - or quantum dots - have gained considerable interest. This is because of their unique photophysical properties such as size-controlled flourescence and stability against photobleaching. Particularly the first allows a highly parallel, multiplexed analysis. Binding molecules can be linked to this kind of label with the same coupling strategy since the different labels (nanoparticles) differ only in size but not in surface chemistry. The progress in chemical synthesis of these particles but also in surface modification strategies provides the basis for an increasing use of quantum dots also in bioanalysis (Mednitz et al. 2005, Alivisatos 2004, Chan et al. 2002). Thus, the particles have been applied in immunoassays (Goldman et al. 2004a,b, Hoshino et al. 2005) and the detection of nucleic acids (Gerion et al. 2003, Pathak et al. 2001, Xiao and Parker 2004, Kim et al. 2007). Another important fearture of quantum dots is going along with their electronic structure and consists in the generation of electron-hole pairs during photoexcitation. This provides the basis for the application of these nanoparticles on electrodes (Bakkers et al. 2000, Sharma et al. 2003). When sufficiently long-lived electron-hole pairs are generated this allows the ejection of conduction band electrons to the electrode or the injection of electrons from the electrode into the valence band of the particle. Thus, a photo current can be detected which is much enhanced when electron donors or acceptors are present in solution. The use of quantum dots on electrodes may thus lead to the development of light-switchable devices (such as the light-addressable potentiometric sensors LAPS: Parak et al. 1997), energy conversion systems (such as solar cells: Huynh et al. 2002) or sensors where the recognition event controls the photo current. Sensorial applications for the combination of quantum dots with DNA have been shown with several systems (Willner et al. 2001, Freeman et al. 2007). However, only few

examples are reported in the combination with proteins. In accordance with the concept of biosensors of the first generation (i.e. detection of a product of an enzymatic conversion) actylcholine esterase was coupled to the quantum dot surface which was immobilised on an electrode. The biocatalytic conversion of the substrate acetylthiocholine was detected by an electron exchange of the produced thiocholine with the illuminated quantum dots (Pardo-Yissar et al. 2003). Following the concept of biosensors of the 3rd generation (direct electrochemical communication of the redox protein with an electrode) proteins can also be coupled to the quantum dot in such a way that a direct electron exchange is feasible.

Surface modification is necessary here and has been shown first with mercaptopropionic acid on CdSe/ZnS QD and cytochrome c (Stoll et al. 2006). Oxidized cytochrome c can act as electron acceptor for the photoexcited quantum dots which are subsequently reduced by the electrode. Such a system can be further developed by combining cytochrome c with enzymes such as lactat dehydrogenase (Katz et al. 2006). This results in a signal chain starting from lactat in solution via the enzyme, cytochrome c and finally via the quantum dots towards the electrode. Here an anodic photo current was generated in the presence of lactat.

In this study we present results coupling quantum dots and cytochrome c to gold electrodes in order to construct a photoelectrochemical signal chain which is sensitive to superoxide radicals in solution. This is based on the use of cytochrome c as a recognition element in superoxide sensors (Cooper et al. 1992, Lisdat et al. 1999, Gobi and Mizutani 2000, Ge and Lisdat 2002). These electrodes also rely on direct electron transfer from cyt. c to a promoter-modified gold electrode and allow a concentration dependent radical analyis. The use of a quantum dot layer on the electrode provides a photo-switchable interlayer allowing the spatial read-out of a sensor surface. In this study the basic features of a signal chain from the short lived radical in solution via the protein and the quantum dot towards the electrode will be demonstrated.

2. Experimental

2.1. Materials

The CdSe/ ZnS nanoparticles were prepared according to a procedure described previously (Reiss et al 2002 , Dabbousi et al. 1997). The hard-core diameter of the inorganic CdSe/ZnS core/shell particles was ~5 nm with an absorbance peak at 527 nm. The concentration was determined by UV/VIS- spectroscopy (extinction coefficient 78000 $M^{-1}cm^{-1}$, Yu et al. 2003).

4-Dithiane and 1,4-benzene dithiol were purchased from Lancaster (Frankfurt/ Main, Germany). Mercaptopropionic and mercaptosuccinic acid, propane dithiol, hexane dithiol, cytochrome c (from horse heart), 4-mercaptopyridine, hypoxanthine and all buffer salts were from Sigma (Taufkirchen, Germany). Sodium dithionite (80%) and ethanol (99%) were obtained from Merck (Darmstadt, Germany). Xanthine oxidase *from cow milk* (XOD) was provided by Roche diagnostics. All aqueous solutions were prepared using 18MΩ ultra purified water (SG Wasseraufbereitung und Regenerierstation Ltd. Germany).

2.2. Electrode modification

The Au electrodes (from BASi, UK) were polished with Al_2O_3 powder of decreasing grain size (1µm, 0.05µm), voltammetrically cycled in 1M NaOH (-800mV to +200mV, scan rate 300 mV/s), rinsed with water, cycled in 0.5M H_2SO_4 (-250mV to +1.75V, scan rate 300 mV/s) and were again rinsed with ultra pure water.

Electrodes were coated with either dithiane or benzene dithiol. In the first case the cleaned electrodes were incubated in a saturated dithiane solution in ethanol at 65°C for 5 days with an intense ethanol rinsing afterwards. To immobilize the nanoparticles the dithiane modified electrodes were immersed into a 14µM particle suspension (CdSe/ZnS) in chloroform for 3 days at 50°C. In the second case, for the benzene dithiol modification the cleaned electrodes were incubated in a 10mM dithiol solution in chloroform for 40 hours at

room temperature. The dithiol modified electrodes were intensively rinsed with chloroform, immersed into the nanoparticle solution (14µM CdSe/ZnS) and incubated "upside down" for 2 days at room temperature.

In a final step the surface of the nanoparticles immobilized to the gold electrode was alternatively modified with mercaptopropionic acid, mercaptosuccinic acid, or mecaptopyridine. The modification of the nanoparticle surface fixed at the gold electrode with mercaptopropionic and mercaptosuccinic acid was done by incubation of the modified electrode in a 10% solution of the latter compounds in water for 3 days at 50°C. The modification with mercaptopyridine was achieved by incubation of the particle modified electrode in a 20mM aqueous solution of the compound for 30 hours at room temperature.

2.3. Cytochrome c reduction

A stock solution of 1-5mM oxidized cytochrome c was incubated with sodium dithionite for 5 minutes at room temperature (1g of the salt per mmol protein). The excess salt was removed using a NAP 25 column (Amersham Biociences). The concentration of reduced cytochrome c was determined by UV/ VIS spectroscopy evaluating the absorption at 550nm prior to use (van Gelder and Slater 1962). The solution was stored for a maximum of 24 hours at 4°C.

2.4. Electrode characterisation

All electrochemical measurements were performed in a home made cell using a 3-electrode arrangement. The nanoparticle modified electrode was the working electrode, the reference electrodes was an Ag/AgCl, 1M KCl electrode from Biometra (Germany) and a Pt wire served as counter electrode. The volume of the measuring cell was 1ml. Opposite to the working electrode a wave guide was fixed allowing the illumination of the full working electrode area from a defined distance of 1cm.

For the amperometric and voltammetric measurements an Autolab PGSTAT 12 (Methrom, Germany) with the GEPS 4.9 electrochemical data evaluation software was used. Impedimetric measurements were performed using a IM6e- potentiostat (Zahner-Elektrik, Germany). Here a 10mV ac perturbation voltage was used and the electrodes were characterized at open circuit potential in the frequency range: 50kHz – 50 mHz.

Within the transparent cell, the electrode surface was exposed to light for a period of 4-20s and the current response was recorded under the condition of a fixed dc potential. The light was emitted from a 150W Xe lamp purchased from L.O.T. ORIEL (Darmstadt, Germany) and the light pulses were generated by manually opening/ closing an aperture.

For wavelenght dependend measurements a monochromator, model 77250 (L.O.T., Germany) was coupled to the Xe lamp. The grating was 1200 l/mm and the entry slit was fully opened (3,2 mm). These settings cause a bandpass of +/- 10nm.

As supporting electrolyte 0,1M sodium phosphate buffer pH 7,4 was used. Hexacyanoferrate (II/III) was used in concentrations of 5mM each. The cytochrome c concentration was in the range of 1-12µM.

For the generation of superoxide radicals the xanthine oxidase catalysed conversion of hypoxanthine to uric acid was used. During this enzymatic conversion oxygen is reduced and thus hydrogen peroxide and superoxide are liberated simultaneously. The hypoxanthine concentration was 100µM and the xanthine oxidase (XOD) activity was varied from 9-100mU/ml in order to establish different steady-state superoxide concentrations in solution (Ge and Lisdat 2002).

3. Results and Discussion

In order to construct a signal chain for the detection of superoxide radicals which can be governed by illumination of the sensing electrode we first investigated the fixation of the CdSe/ZnS quantum dots on gold electrodes and their photoelectrochemical properties. In a

second step the electrochemical communication of the redox protein cytochrome c with the nanoparticle modified electrode was studied and finally the interaction with superoxide radicals in solution was characterized. In Scheme 1 the principle of the signal chain to be constructed is given. The system is based on the reduction of cytochrome c by the superoxide radical in solution. The reduced protein can be reoxidised by an electron transfer to the quantum dots provided they are photoexcited and a potential is applied sufficiently positive to allow an electron transfer from the particles to the electrode to occur. Thus, an enhanced photo oxidation current is generated when the radical is present in solution.

PLACE SCHEME 1 here

3.1. Quantum dots on gold

For the immobilisation of the nanoparticles on the gold surface dithiol compounds can be advantageously used. The thiol layer is not only important for the fixation but also for the blocking of the electrode surface for unwanted redox reactions of interfering substances in solution. In a previous study we could show that a dithiane layer is a feasable tool to achieve both goals (Stoll et al. 2006). However because of the rather time consuming and higher temperature demanding modification protocoll we replaced the compound by 1,4 benzene dithiol. Here a much faster modification can be obtained. The blocking properties of this thiol layer are comparable to layers of dithiane as can be seen from cyclic voltammetric measurements in ferri-/ferrocyanide solution (data not shown).

After the thiol modification the electrode was incubated within a solution of the nanoparticles and the particles were immobilized using the solution exposed free thiol groups by a ligand exchange process. The electrodes were tested for several characteristics. First the photo current generation was examined. Fig.1A shows an overlay of photo current measurements after the different modification steps of the electrode. It has to be noted that

in contrast to the dithian modification the benzene dithiol modified electrode already showed a small photo current of 1-1,5 nA at a potential of -0,2 V vs Ag/AgCl. However, after the fixation of the CdSe/ZnS quantum dots a much higher current was detected under illumination.

PLACE FIG 1 here

In order to verify that the photo current is related to the properties of the quantum dots the wavelength dependence of the current was examined. The results of these experiments are summarized in Fig. 2. The photo current of the particle modified electrode follows the absorption spectrum of CdSe/ZnS particles with a peak current between 520-540nm. The photo induced response for 1,4 benzedithiol, in contrast, gave much smaller values with an increase in the range 280- 310nm (data not shown). Thus, the latter effect was most likely due to the absorbtion of the aromatic ring structure while the photo current in the gold/dithiol/quantum dot- system showed a response clearly based on the specific wavelength absorbance and the resulting electron- hole pair generation inside the CdSe/ZnS particles.

PLACE FIG.2 here

The quantum dot modified electrode was further investigated with respect to the potential dependence of the photo current. Fig. 3 shows a linear sweep voltammogram with regularly applied short light pulses. As can be seen not only the magnitude of the photo current but also the direction is strongly influenced by the electrode potential. From this measurement the formal redox potential of the CdSe/ZnS nanoparticles can be estimated to be 103mV $\pm$ 10mV. For potentials more negative one can observe a reduction current, whereas at higher potentials particle oxidation is enforced (Kucur et al. 2003).

The particle decomposition in the absence of a redox partner in solution can also be seen from the peak shape of the photo current at higher potentials which is not stable but show an exponential decline during illumination. Particularly high oxidative potentials have a

high destructive impact on the quantum dots. Close to the formal potential the photo current was however rather constant during the duration of the light pulse (several seconds).

PLACE FIG. 3 here

For a further examination of this effect a set of repeated photo current measurements was performed. At applied potentials of +130mV and + 76mV the electrode was exposed to multiple light pulses (n= 35). The effect of repeated measurements on the magnitude of the photo current at the lower potential is negligible since the mean value of 6nA fluctuated during the whole experimental series with an average relative standard deviation of +/-5% but did not show a significant decrease related to the number of light pulses. However, at the higher potential, an initial drop of the photo current (~25%) was observed before a stable photo current could be detected at the electrode.

These experiments clearly show the importance of the electrode potential for the stability of the quantum dot modified electrode. However, at potentials close to the formal potential sufficient stability for repeated measurements can be provided.

The layer of quantum dots on the electrode surface should work as a switch allowing electron transfer from a redox component on the solution side (here cytochrome c) to the electrode under illumination and hindering this process in the absence of light. This means that the quantum dots should change their resistance in dependence of light exposure. Thus, the electrode was investigated by electrochemical impedance spectroscopy. The results are plotted as Nyquist diagram in Fig. 1B. The interfacial impedance can be simply described by a parallel circuit of the interfacial capacity and the charge transfer resistance. After modification of the gold surface with the thiol and the nanoparticles this interfacial impedance is rather high although the particle immobilisation is lowering the blocking properties of the thiol layer. However, during illumination the electrode impedance decreased drastically. This is mainly related to a diminished resistance i.e. an enhanced

charge transfer on the interface since the capacity was only slightly changed. The experiment thus illustrates clearly the basic idea of a photo-switchable layer on the electrode.

3.2. Quantum dot modified electrode and cytochrome c

As shown previously CdSe/ZnS- quantum dots are not only able to exchange electrons with the electrode or small redox mediators in solution but also with proteins (Stoll et al. 2006). This, however, requires a surface modification to create a chemical environment for a productive interaction of the nanoparticles with the biomolecule. For the detection of superoxide radicals cytochrome c is a suitable recognition element. To optimise the interaction of cyt.c with the surface fixed quantum dots 3 different modifications of the particles were investigated with respect to facilitate the protein electrode interaction, stability and ease of preparation. Thus quantum dot modified electrodes were incubated with short chain thiols such as mercaptopropionic acid, mercaptosuccinic acid or 4 mercaptopyridine.

These electrodes were investigated with respect to an electron transfer with oxidised cyt.c in solution. For all three particle modifications an increased photo current was observed when the redox protein was present in solution. This verifies that an electron transfer chain from the electrode via the particles towards cyt c can be established. However the concentration dependence of the photo current clearly shows the differences between the three modifiers. This is illustrated in Fig.4. The measurements were evaluated with respect to the concentration range where the photo current can follow the protein concentration in solution and the magnitude of the photo current. Mercaptosuccinic acid and mercaptopyridine gave the largest dynamic range from about 0,2 – 6µM, whereas mercaptopyridine modification results in the highest photo current. Additionally it was observed that the modification with mercaptosuccinic acid and mercaptopropionic acid

became instable after a set of measurements which resulted in a loss of cytochrome c interactivity (data not shown). Although the surface modification of mercaptopyridine was optimised using oxidised cyt. c the modification also works with reduced cyt.c resulting in a photo current which is concentration dependent in the same concentration range as shown for the oxidised protein (0,2-6µmolar). Since 4- mercaptopyridine enabled a stable electrochemical interaction of the electrode with both forms of cyt. c it was chosen as quantum dot modification for further experiments.

PLACE FIG. 4 here

3.3. Superoxide sensitive signal chain

The electrode system gold/benzenedithiol/quantum dots/mercaptopyridine was used together with cyt c to show that a photoelectrochemical signal chain sensitive for superoxide radicals can be established. The basic principle is given in Scheme 1. The formal redox potential of cytochrome c at modified electrodes is known to be around 0mV vs Ag/AgCl. Thus, with an applied potential of +130mV vs Ag/AgCl only reduced protein should be detectable (as enhanced photo oxidation current) and no photo current enhancement should be measured with oxidized cytochrome c. This was verified experimentally.

For the generation of superoxide radicals in solution the xanthine oxidase (XOD) catalysed conversion of hypoxanthine to uric acid was chosen. Thus, first the influence of the substrate and the enzyme alone on the photo current was studied. No photo current enhancement was found at the chosen potential of +130mV indicating that hypoxanthine and XOD can not directly exchange electrons with the quantum dot modified electrode.

When the generation of superoxide radicals was started in a solution of cyt.c and hypoxanthine by addition of XOD an enhanced photo current has been observed. This indicates that generated O_2^- radicals reduce the oxidized cytochrome in solution. Upon

illumination the cytochrome c was re-oxidized at the electrode which was visible by the increasing photo current. Since the photo current has been detected at several time intervals after start of the radical production, the process of cyt.c reduction by the radical can be followed. This is illustrated in Fig.5. From these measurements the rate of protein reduction can be calculated. This process should show a defined dependence on the radical concentration in solution. Different superoxide concentrations can be easily established by varying the XOD activity used for the radical generation. Superoxide radicals are not stable after formation, but dismutate in a concentration dependent manner to oxygen and hydrogen peroxide. In the counterbalance of generation and decomposition steady-state concentrations can be observed. It was previously shown that the steady-state radical concentration follows the square root of the XOD activity (McCord and Fridovich 1968, Ge and Lisdat 2002).

When the rate of photo current increase at the electrode after start of radical generation is plotted against the square root of the XOD activity used a linear dependence was obtained. This indicates that the system can follow the concentration dependent cytc reduction and thus the radical concentration. The behaviour was investigated with XOD activities from 4 mU/ml to 100mU/ml corresponding to superoxide concentrations from about 0,25 to 1,3µmol/l. The measurements demonstrate that the quantum dot modified electrode can linearly detect nanomolar superoxide concentrations.

PLACE FIG.5 here

4. Conclusions

Semiconductor nanoparticles of CdSe with a ZnS shell can be immobilised on gold electrodes with 1,4-dithiolbenzene and show a potential dependent photo current. When no electron acceptor or donor is in solution the photo current resulted in a partial decomposition of the particles. Stable photo current could be obtained near to the formal

potential of 100mV vs Ag/AgCl. The current under electrode illumination can be clearly attributed to the absorption properties of the nanoparticles although the dithiol layer shows a minor contribution. In order to establish communication with the redox protein cyt.c the surface of the particles was preferably modified with mercaptopyridine. This resulted in a photo current of the nanoparticle modified gold for oxidised and reduced cyt.c in concentrations of a few µmol/l. The generation of superoxide radicals in solution can be detected by following the cyt.c re-oxidation at the illuminated electrode. The photo current increase was found to correlate to the steady-state superoxide concentration in solution. Thus, the electrodes were found to be sensitive for nanomolar concentrations of this short-lived species.

Acknowledgements:

This was work was partially supported by the MWFK Brandenburg (HWP project 24#2597-04/339; 2004) and the Deutsche Forschungsgemeinschaft (project Li 706/2-1, PA 794/3-1). The authors also want to thank Daniel Schäfer for his help during the technical preparation of the manuscript.

Captions

Scheme 1 Schematic drawing of the photoelectrochemical signal sensitive for superoxide ions and based on quantum dots immobilized on gold electrodes. Superoxide can reduce cytochrome c which subsequently can tranfer electrons to the photo-excited quantum dots from which they can be further transfered to the polarised electrode. In the dark this signal chain is blocked.

Fig.1 A) Photo current measurement of a gold electrode (a), after 1,4-benzene dithiol modification (b), and after quantum dot (CdSe/ZnS) immobilisation (c). (V= -200 mV vs Ag/AgCl). B) Impedance spectra of the quantum dot modified gold electrode in 0,1M phosphate buffer pH 7,4 in the dark (points) and after illumination (squares).

Fig.2 Wave length dependence of the measured photo current at the quantum dot modified gold electrode (Au/benzenedithiol, CdSe/ZnS, V= -200mV vs AgAgCl, 5s light pulses). The inset shows the wavelength dependence of the absorption of a CdSe/ZnS solution (c= 5µM).

Fig.3 Linear sweep voltamogramm of the quantum dot modified gold electrode with light pulses applied every 20s (Au/benzenedithiol, CdSe/ZnS) in a phosphate buffer solution pH 7,4 (v= 1mV/s, duration of the light pulses 10s).

Fig.4 Comparison of the photo current measurement of the quantum dot modified gold electrode in dependence of the cytochrome c concentration (oxidized) in solution and the modification of CdSe/ZnS surface, a- mercaptopropionic acid, b- mercaptosuccinic acid, c- 1,4-mercaptopyridine (V= +76 mV vs Ag/AgCl, phosphate buffer pH 7,4)

Fig.5 A) Photo current measurement at the mercaptopyridine modified quantum dot – gold electrode (Au/benzenedithiol, CdSe/ZnS, 4-mercaptopyridine) in a phosphate buffer solution pH 7,4 containing 5µM cytochrome c after different time periods (a-0s, b-40s, c-205s, d-560s) after start of superoxide generation in solution by using 100 µM hypoxanthine and 20mU/ml XOD. B) Plot of the rate of photo current increase against the square root of XOD activity used for superoxide generation (the latter value is proportional to the steady-state superoxide concentration in solution).

293

References

Alivisatos, P., 2004, Nature Biotechnology 22, 47.

Bakkers, E.P.A.M., Roest, A.L., Marsman, A.W., Jenneskens, L.W., de Jong van Steensel, L.I., Kelly, J.J., Vanmaekelbergh, D., 2000, Journal of Physical Chemistry B 104, 7266-7272.

Baughman, R.H., Zakhidov, A.A., de Heer, W.A., 2002, Science 297 (5582), 787-792.

Chan, W.C.W., Maxwell, D.J., Gao, X., Bailey, R.E., Han, M., Nie, S., 2002, Current Opinion Biotechnology 13, 40.

Cooper, J.M., Greenough, K.R., McNeil, C.J., 1993, Journal of Electroanalytical Chemistry 347, 267-275.

Dabbousi, B.O., Rodriguez-Viejo, J., Mikulec, F.V., Heine, J.R., Mattoussi, H., Ober, R., Jensen, K.F., Bawendi, M.G., 1997, Journal of Physical Chemistry B 101 (46), 9463-9475.

Freeman, R., Gill, R., Beissenhirtz, M.K., Willner, I., 2007, Photochemical &. Photobiological Sciences 6, 416-422.

Fridovich, I., 1997, Journal of Biological Chemistry 272 (30), 18515-18517.

Ge, B., Lisdat, F., 2002, Analytica Chimica Acta. 454, 53-64.

Gerion, D., Chen, F., Kannan, B., Fu, A., Parak, W.J., Chen, D.J., Majumdar, A., Alivisatos, A.P., 2003, Analytical Chemistry 75, 4766.

Gill, R., Patolsky, F., Katz, E., Willner, I., 2005, Angewandte Chemie, Int. Ed. 44, 4554.

Gobi, K.V., Mizutani F., 2000, Journal of Electroanalytical Chemistry 484, 172-181.

Goldman, E.R., Balighian, E.D., Mattoussi, H., Kuno, M.K., Mauro, J.M., Tran, P.T., Anderson, G.P., 2002, Journal of the American Chemical Society 124, 6378-6382.

Goldman, E.R., Clapp, A.R., Anderson, G.P., Uyeda, H.T., Mauro, J.M., Medintz, I.L., Mattoussi, H., 2004, Analytical Chemistry 76, 684-88.

Hoshino, A., Fujioka, K., Manabe, N., Yamay, S., Goto, Y., Yasuhara, M., Yamamoto, K., 2005, Microbiology and Immunology 49(5) 461-470.

Huynh, W.U., Dittmer, J.J., Alivisatos, A.P., 2002, Science 295 (29), 2425-2427.

Katz, E., Zayats, M., Willner, I., Lisdat, F., 2006, Chemistry Communications 13, 1395-1397.

Kim, J.H., Chaudhary, S., Ozkan, M., 2007, Nanotechnology 18, 195105.

Kucur, E., Riegler, J., Urban, G.A., Nann, T., 2003, Journal of Chemical Physics 119 (4), 2333-2337.

Lin, C.-A.J., Liedl T., Sperling, R.A., Fernandez-Arguelles, M.T.,Costa-Fernandez, J.M. Pereiro, R., Sanz-Medel, A., Chang, W.H., Parak, W.J., 2007, J. Materials Chemistry. 17 (14), 1343-1346.

Lisdat, F., Ge, B., Ehrentreich-Förster, E., Scheller, F. W., 1999, Analytical Chemistry 71, 1359-1365.

McCord JM and Fridovich I, 1968, Journal of Biological Chemistry 243 5753.

Medintz, I.L., Uyeda, H.T., Goldmann, E.R., Mattoussi, H., 2005, Nature Materials 4, 435.

Meng, X., Wu, X., Wang, Z., Cao, X., Zhang, Z., 2001, Bioelectrochemistry 54 (2), 125-129.

Parak, W.J., Hofmann, U.G., Gaub, H.E., Owicki, J.C., 1997, Sensors and Actuators A 63, 47-57.

Pardo-Yissar, V., Katz, E., Wassermann, J., 2003, Journal of the American Chemical Society 125, 622-623.

Pathak, S., Choi, S.K., Arnheim, N., Thompson, M.E., 2001, Journal of the American Chemical Society 123, 4103-4104.

Reiss, P., Bleuse, Pron, A., 2002, Nanoletters 2 (7), 781-784.

Riklin, A., Katz, E., Willner, I., Stocker, A., Bückmann, A.F., 1995, NATURE. 376, 672-675.

Sharma, S.N., Pillai, Z.S., Kamat, P.V., 2003, Journal of Physical Chemistry B 107, 10088-10093.

Stoll, Ch., Kudera, S., Parak, W.J., Lisdat, F., 2006, SMALL. 2 (6), 741-743.

Van Gelder, B.F., and Slater, E.C. 1962, Biochimica Biophysica Acta, 58, 593-595.

Willner, I., Patolsky, F., Wassermann, J., 2001, Angewandte Chemie, Int. Ed. 40, 1861.

Xiao, Y., Barker, P.E., 2004, Nucleic Acids Research 32, e28.

Yu, W.W., Qu, L.H., Guo, W.Z., Peng, X.G., 2003, Chemistry of Materials 15 (14), 2854-2860.

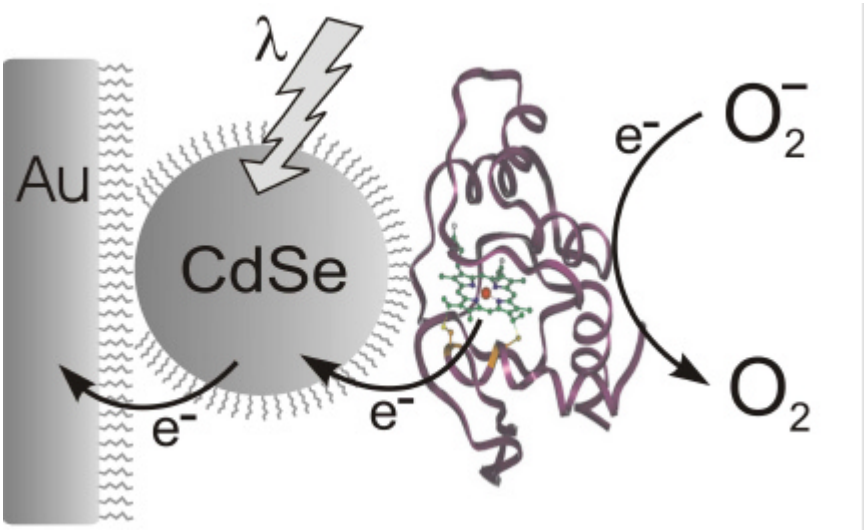

Scheme 1

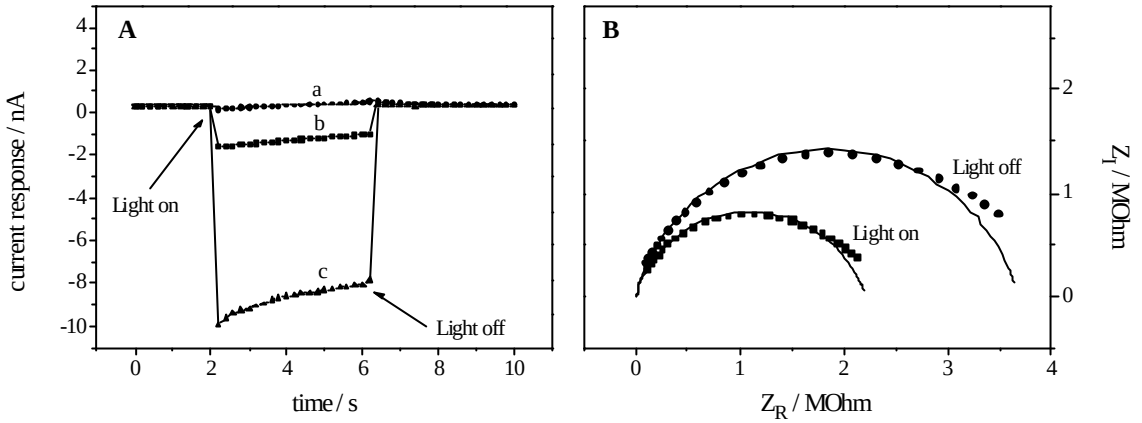
A
B
current response / nA
time / s
a
b
c
Light on
Light off
Light off
Light on
Z_I / MOhm
Z_R / MOhm

Fig.1

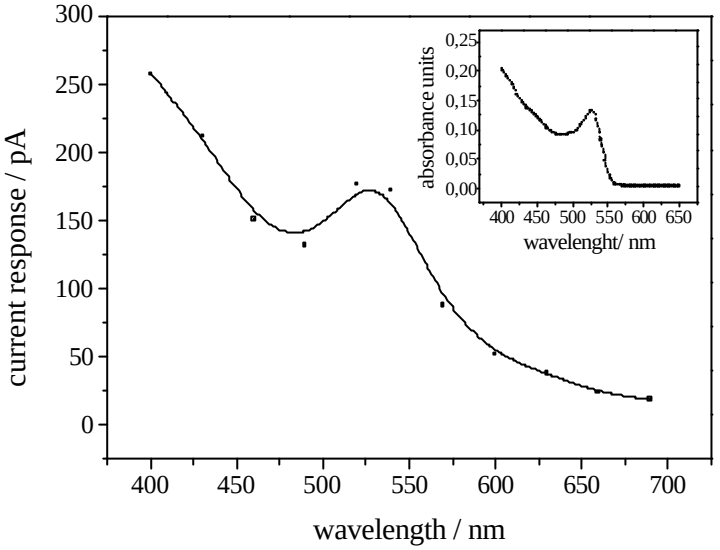
current response / pA
wavelength / nm
absorbance units
wavelenght/ nm

Fig.2

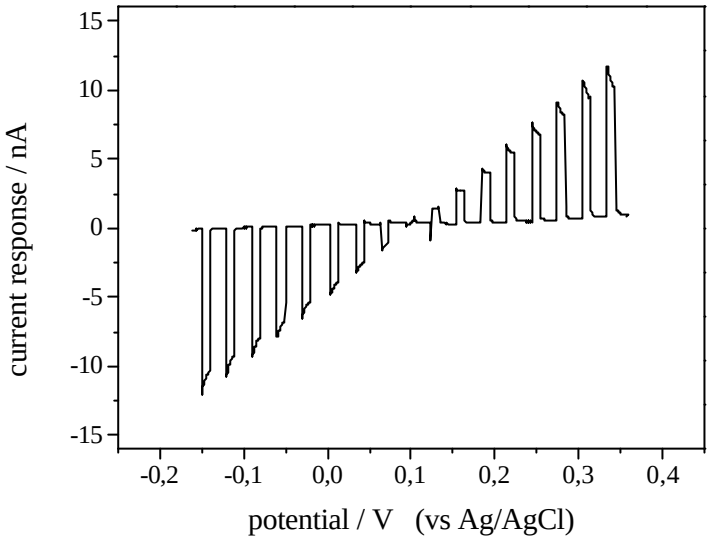
15
10
5
0
-5
-10
-15
current response / nA
-0,2
-0,1
0,0
0,1
0,2
0,3
0,4
potential / V (vs Ag/AgCl)

Fig.3

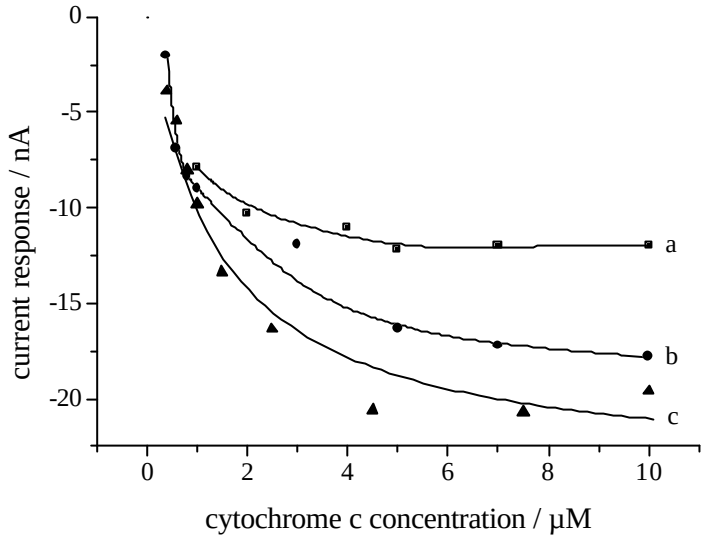
0
-5
-10
-15
-20
current response / nA
0
2
4
6
8
10
cytochrome c concentration / µM
a
b
c

Fig.4

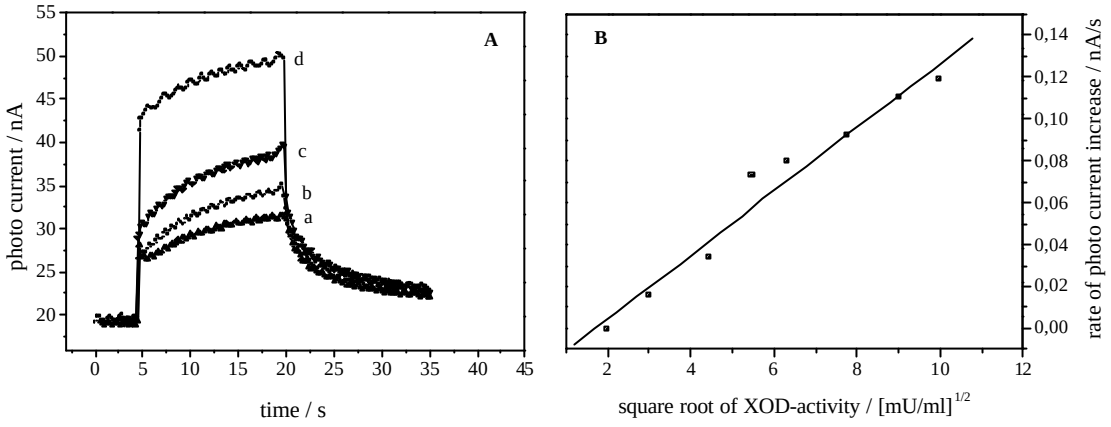
A
B
d
c
b
a
photo current / nA
time / s
rate of photo current increase / nA/s
square root of XOD-activity / [mU/ml] 1/2

Fig.5

VII. Acknowledgements.

I would like to express my gratitude to the following people:

Wolfgang Parak to have accepted the challenge to let me develop my own ideas.

Libero Manna for the incredible niceness, experience and for being the first person who introduced me to the fascinating world of nanocrystals research.

Stefan Kudera for all the things he taught me in the short time we worked together.

Dr. Andreas Schaper and Michael Hellwig for their courtesy and competence.

Maria Casula and Andrea Falqui for their niceness and for all the things I learnt from them.

Frau Thomas, Sabine Faust and all the people who had the patience to help me with the academic and non bureaucracy.

My students and colleagues Azhar Abbasi, Waqas Kalid and the last but not least Zhao Yue. Actually I had to kick their asses a little at the beginning of their training but after the “medicine” their performances improved considerably.

VIII.Academic Curriculum Vitae

Marco Zanella

Born Thiene (Italy), 05.02.1976

PhD in physics:

June 2007-May 2008: Senior PhD student in Prof. Dr. Wolfgang J. Parak group at Marburg Philipps University. Research interests: Synthesis and characterisation of colloidal nanocrystals, application of semiconductor nanoparticles for biosensing.

November 2004-May2007: PhD student in Dr. Wolfgang J. Parak group at LMU Muenchen. Research topic: Synthesis and characterisation of colloidal nanocrystals.

Degree in physics:

July 2004: I received the degree in Physics at Dipartimento di fisica Galileo Galilei, Università degli studi di Padova (Italy). Thesis title: Molecular Electronics at Nanoscale. The experimental part of this thesis was performed at the National Nanotecnology Laboratory (NNL) of Lecce (Italy).

High school diploma: At Technical Industrial Institute "G. Chilesotti", Thiene in 1995. Therefore I have theoretical and practical experience on digital and analogic electronics, telecommunications and noise in electronic devices.

Middle school diploma: At State Middle School "F. Bassani", Thiene. 1987-1989.

Elementary school: At Elementary school "Vianelle", Thiene 1981-1986.

Marburg, 25 April 2008